Integrated Analytical Systems
Series Editor: Radislav A. Potyrailo

Alexandre Dmitriev *Editor*

Nanoplasmonic Sensors

Springer

Integrated Analytical Systems

Series Editor:

Radislav A. Potyrailo

For further volumes:
http://www.springer.com/series/7427

Alexandre Dmitriev
Editor

Nanoplasmonic Sensors

Springer

Editor
Alexandre Dmitriev
Department of Applied Physics
Chalmers University of Technology
Göteborg, Sweden

ISBN 978-1-4614-3932-5 ISBN 978-1-4614-3933-2 (eBook)
DOI 10.1007/978-1-4614-3933-2
Springer New York Heidelberg Dordrecht London

Library of Congress Control Number: 2012942184

Printed on acid-free paper

Springer is part of Springer Science+Business Media (www.springer.com)

Preface

Plasmonics is the science of light-matter coupling through surface plasmon polaritons (SPPs) or surface plasmons. Simply put, surface plasmons are optically excited collective oscillations of the free electrons at a metal surface. Formally, SPPs are the quanta of charge density collective oscillations that are tightly confined at the interface of materials with negative and positive permittivities. However, surface plasmons can be comfortably described in the classical electrodynamics without evoking quantum mechanics. They represent actual mechanical oscillations (with very small displacements though) of the electron gas under the influence of the electromagnetic field of the incoming light.

Nanoplasmonics explores surface plasmon modes confined in the nanosized, i.e., subwavelength metal structures—localized surface plasmons (LSP). Although light interaction with nanoscopic matter has been observed for centuries, like stained glass goblets manufactured in the Roman Empire or spectacular windows in medieval churches, and was theoretically described already by Michael Faraday and Gustav Mie more than a century ago, only recently our ability to fabricate and control the matter at a nanoscale brought to life what is known as nanoplasmonics. Over the past decade nanoplasmonics has developed into a burgeoning field, where exciting opportunities are opening for the increasing number of application areas, including photonics, biomedical imaging and sensing, (photo)catalysis, and molecular spectroscopy to name a few.

The key features that enable such development are subwavelength confinement, large cross-section for scattering and absorption of light, and most important for sensing applications, strongly enhanced electromagnetic fields in the direct proximity of the nanostructures. Through such field enhancement nanoplasmonic resonances sensitively depend on the minute variations of the surrounding dielectric medium. This fact essentially forms the basis for nanoplasmonic sensing—a merely refractive index sensing, but with the powerful extension that the probed volumes are in the nanoscale. Small enough so a presence of even single biological or chemical molecular species becomes detectable in various nanoplasmonic sensing schemes.

With the present book we attempt to overview the current status of nanoplasmonic sensing, with the relevant highlights of the past decade of its extensive development and looking in the nearest future for this science and technology area. In Chap. 1 we start with the general principles of biosensors, outline surface plasmon resonance basics and applications such as in drug discovery, food industry, medical diagnostics, review the advantages of localized surface plasmon resonances (LSPR) from the basic physics of SPPs, and describe the principles of sensing with LSPR—"bulk" and "thin/molecular layer" approaches. This chapter further gives hints on the comparison of the propagating vs. localized plasmons for bulk refractive index (RI) and molecular sensing, substrate effects, and the importance of electromagnetic fields confinement. It ends with highlighting the single-molecule detection with LSPR. Chapter 2 focuses on the unique characteristics of LSPR: short EM fields decay for study of protein conformational changes and gas sensors in combination with metal-organic frameworks; going from single-nanoparticle sensing to wide-field single-nanoparticles imaging and spectroscopy; coupling LSPR with molecular identification through surface enhanced Raman scattering (SERS) and laser desorption ionization mass spectroscopy (LDI-MS). It gives the historical retrospect on the development of RI LSPR sensing, and gives the recipes for improving the limits of detection, for example, by using resonant molecules (chromophores) or utilizing plasmonic nanoparticles as labels. Chapter 3 presents nanoplasmonics combined with the studies of artificial cell membranes: the design nanoplasmonic biosensor for particular life science application. Further, here nanoplasmonic sensing is combined with quartz crystal microbalance with dissipation (QCM-D) mass and viscosity sensing technique. Chapter 4 brings nanoplasmonic sensors inside the living cells and helps to map with nanoplasmonic sensing time-resolved intracellular biochemical distribution. With specially designed plasmonic nanostructures it is possible to utilize the antenna effect for light and convert far-field radiation into local heat, earning intracellular nanoplasmonic gene switches through photothermal DNA dehybridization and gene silencing on-demand. Nanoplasmonics here defines the properties of intracellular plasmon resonant energy transfer (PRET) biosensors. Addition of magnetic layer to plasmonic nanostructures moves nanoplasmonic sensing towards externally controllable sensors. Nanoplasmonic molecular rulers—DNA-conjugated Au nanoparticles—are also outlined in this chapter. Chapter 5 focuses on the single plasmonic nanoparticle biosensing that dramatically reduces detection limits and in general allows miniaturizing of the sensor and the fluidic system. In Chapter 6 array-based nanoplasmonic sensors that move towards the point-of-care applications are featured. This includes multianalyte detection (multiplexing), handling of complex analyte media, and performing kinetic analysis of the complex fluids, addressing nonspecific binding to the sensor surface. Chapter 7 highlights optical tweezers in combination with SERS. This allows for manipulation of nanoplasmonic particles sensors, sensing in confined (intracellular) volumes, and addressing sensing interactions in colloidal systems. Nanoplasmonic

sensing for applications in nanomaterials science and catalysis is the emphasis of Chapter 8. It details the concepts of direct and indirect nanoplasmonic sensing and features nanoplasmonic sensors for optical gas detection. Direct sensing encompasses the sensing modality when nanoplasmonic particles act as sensors and the studied entities; it is used in studies of oxidation and corrosion, metal hydrides formation, liquid–solid phase transition, chemical surface reactions, and surface charge transfer. With indirect sensing plasmon nanoparticles function as sensors of processes on or in adjacent (nano)materials. It is used for gas sensing at metal oxide composite films, in heterogeneous catalysis (CO and H_2 oxidation on Pt), optical calorimetry, hydrogen storage, and polymer phase transitions. In Chapter 9 plasmonic crystals—arrays of nanoholes or nanoposts, fabricated via soft nanoimprint lithography—are highlighted. They are used for the prime RI sensing: for example, probing polyethylene glycol concentrations in thin films, mechanical deformation of hydrogels resulting from pH changes, and allowing 2D chemical imaging of protein thin films. Interestingly, such quasi 3D plasmonic crystals can be characterized by the concepts used for crystalline matter in solid state physics—for example, they feature the "plasmonic" Brillouin zone. Chapter 10 evaluates the general performance of nanoplasmonic sensors. It gives the definition of noise, stability, detection limit, dynamic range, sensitivity vs. resolution, diffusion vs. reversible binding of analytes, and figure-of-merit (FOM) of nanoplasmonic sensors. The chapter further discusses the importance of surface chemistry, probe affinity and density. Strategies are given for performance maximization. In Chapter 11 you will find the discussion of the spatial and spectral plasmonic modes engineering for biochemical sensors in relation to "top-down" nanoplasmonics. One the fine practical examples of such engineering are nanoplasmonic dimers, by the interparticle distance calibration adopted for the target analyte positioning. Result is the biosensing down to single-molecule detection limit. Chapter 12 comprehensively presents the integration of nanoplasmonic sensing elements with optical fiber technology, as the latter is very important transducer in analytical sciences to probe environments prohibitive for traditional spectroscopic probes. Such sensor scheme includes plasmonics inside or on the tip of the fibers for remote SPR and SERS measurements. The FOM—quotient between sensitivity and width of the resonance, a parameter that is equivalent both in wavelength and energy scales—is presented in Chapter 13. To maximize FOM it is shown on the example of gold nanoparticles that the existence of the optimized spectral region is needed, coinciding with the region where quotient of real to imaginary parts of the metal dielectric function reaches maximum. The importance of the supporting substrate and adhesion layer for the sensor is also discussed. Chapter 14 presents random evaporated gold island films—bottom-up nanoplasmonic sensors and transducers. It is in fact one of the earliest techniques for the preparation of LSPR systems and further use them for sensing. Details of the technique are given, the sensitivity of resulting transducer platform and biosensing case studies of immunoglobulin antibody–antigen recognition are outlined, with a

special focus on improving the stability of the sensing platform. Finally, Chapter 15 introduces the electrical detection of surface plasmons that is very relevant for the integrated biosensing. Evaluation of the sensitivity and FOM is given, and the metal-semiconductor-metal plasmons launch and detection are discussed in detail.

Göteborg, Sweden Alexandre Dmitriev

Contents

Chapter 1
An Introduction to Plasmonic Refractive Index Sensing

Mikael Svedendahl, Si Chen, and Mikael Käll

Abstract This chapter introduces the basics of plasmon-based refractometric sensing, its application in label-free biomolecular analysis, and discusses differences between propagating plasmons and localized plasmons in terms of refractive index sensitivity, sensing volume and measurement methodology. Based on some recent nanoplasmonic sensing studies, we discuss plasmon–substrate interactions and the possibility to perform long-range nanoplasmonic sensing. We also discuss an experimental comparison between particle-based and thin film plasmonic biosensing, and we describe a method to enhance the sensitivity of nanoplasmonic sensing towards the single molecule limit using enzymatic signal amplification.

Introduction

Since the introduction of surface plasmon resonance (SPR) refractive index sensing of gas and biomolecules based on thin metal films by Nylander et al. and Liedberg et al. [1, 2] almost three decades ago, the interest in plasmon-based sensing technology has increased tremendously. The technological advances in conventional SPR sensing have been remarkable and the commercialization of instruments has greatly expanded the user community. Conventional thin film SPR sensing is now a mature technology that inevitably will serve as a benchmark for novel nanoplasmonic sensor solutions. The progress in conventional surface plasmon biosensing has been accelerated by developments in several "enabling technologies," in particular development of effective surface chemistry and advanced liquid handling systems.

M. Svedendahl • S. Chen • M. Käll (✉)
Department of Applied Physics, Chalmers University of Technology, Göteborg 41296, Sweden
e-mail: mikael.kall@chalmers.se

A. Dmitriev (ed.), *Nanoplasmonic Sensors*, Integrated Analytical Systems,
DOI 10.1007/978-1-4614-3933-2_1,

Similarly, the present rapid development of refractive index sensing based on localized surface plasmon resonances (LSPRs) in metal nanostructures would not have been possible without enormous progress in nanofabrication technologies and computational electrodynamics.

There are three basic components of a plasmonic biosensor: the biorecognition layer, designed for specific binding of an analyte; the transducer, which converts the molecular interaction to a measurable physical property such as resonance angle or wavelength; and the auxiliary electronics, used to present and interpret the transducer signal. The biorecognition layer and the analytes could be antibodies, antigens, nucleic acids, lipid membranes, viruses, cells, enzymes, etc. [3] while the transducer could be a thin gold film on a prism or a layer of metal nanoparticles. In any case, the principle advantage of plasmonic sensing is that it is "label free," which means that no labeling of analyte molecules is needed. Techniques based on radioactivity and fluorescence require availability of specific molecular tags that can be difficult to obtain and that may affect analyte interactions. As a direct consequence of the "label free" transduction principle, plasmonic sensors enable real-time measurement of analyte binding to the sensor surface. The resulting kinetic data can, for example, be used to determine molecular affinity constants, interaction specificity, and reaction kinetics, thereby providing a clear advantage compared to endpoint measurement techniques, such as ELISA (enzyme-linked immunosorbent assay).

The conventional SPR sensor has had considerable impact on the life science research community, and it is now a widespread tool for studying the interactions of molecules with weights as low as 200 Da [4]. One of its main applications in the pharmaceutical industry is within the drug discovery process, where one wants to identify new drugs and/or new drug targets through molecular interaction studies. The disadvantage of SPR is that it has relatively low throughput, which makes it less suitable for primary drug screening. However, the throughputs are acceptable for secondary screening, in which a more focused search for leads is performed [5]. Importantly, the further downstream in drug discovery process one gets, the more important becomes the detailed information provided by SPR. A new trend in pharmaceutical research is to use molecular fragments for leads [6]. By screening functional groups instead of whole molecules, the library of possible interactions becomes considerably smaller. Unfortunately, the bindings of the fragments are also much weaker. SPR has the sensitivity to monitor the kinetics of weak bindings [7], which makes it a very interesting alternative to slow and costly traditional techniques [8]. In addition, several different strategies to increase the throughput for drug screening using conventional SPR-based sensors have been developed recently. This includes assay development that involves spotting thousands of molecular fragments on the sensor surface for subsequent protein interaction studies [9] and fully automated systems that is able to screen thousands of interactions in a few hours. It is thus likely that we have only seen the beginning of the use of SPR in pharmaceutical research, in particular when it comes to drug discovery applications.

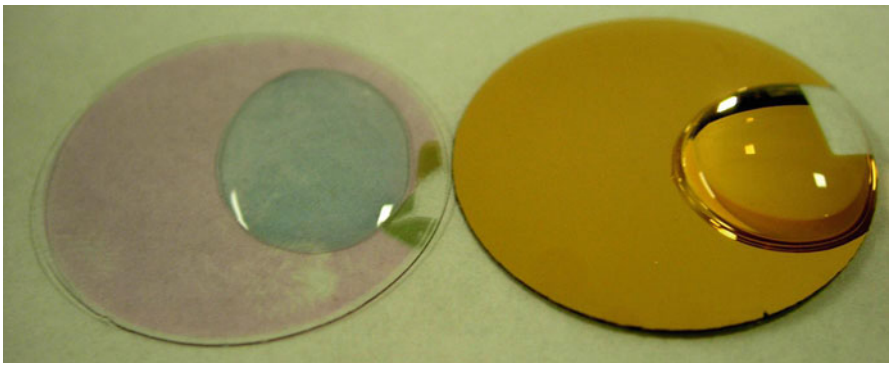

Fig. 1.1 Illustration of colorimetric refractive index sensing using LSPR. The photograph shows a gold nanodisk array (*left*) and a thin gold film (*right*) with water droplets on *top*. The localized surface plasmon resonance in the nanodisks is always excitable, which is why a clear plasmon shift/color change can be seen between the areas covered by air and water. The surface plasmons in the thin film, on the other hand, cannot be excited without additional optics and therefore no color change can be seen

Another important application area of SPR sensors is in the food industry, where analysis often focuses on hazardous contents, like pesticides, residuals from veterinary drugs, or bacterial toxins. SPR sensors has been used to analyze a variety of foods, including juice [10], milk [11], and meat [12], and excellent correlations have been found with conventional analysis methods, such as HPLC and ELISA [13]. The advantage here mainly lies in the simple sample preparation and in reduced reaction times, but it was also shown that SPR analysis can give up to ten times lower frequency of false positives compared to conventional immuno-assays [14].

SPR sensors also show important potential in the area of medical diagnostics, as demonstrated by detection of viruses in serum samples [15], of bacterial toxins in urine [16] and through therapeutic drug monitoring in saliva [17]. However, although SPR sensing clearly has the sensitivity and specificity required for many applications in clinical environments, the acceptance of the SPR technique has been rather low within the medical community. Possible reasons for this may include doubts regarding refractive index sensing as such, for example that the difficulty of discriminating between specific and nonspecific binding may result in false positives, and that traditional SPR sensors are perceived as costly and advanced diagnostic tools that require specially trained personnel. However, the latter problems might be countered by development of novel nanoplasmonic sensing structures.

Figure 1.1 illustrates one of the principal advantages of LSPR sensing compared to plasmon sensing based on thin metal films, that is the simplicity of plasmon excitation. A short-range ordered array of 50 nm tall and 80 nm wide gold nanodisks on glass is compared to a 50 nm gold film under ordinary white light illumination. The LSPR of the particles is such that the array looks reddish in air but the color changes to greenish in water due to the plasmon refractive index sensitivity. The gold film, in contrast, has a distinct “golden” color irrespective of dielectric

environment because the surface plasmons of the film are not excited unless special illumination conditions are fulfilled.

LSPRs were indirectly utilized for biosensing and immunoassays already in the 1980s and 1990s, for example in colorimetric assays based on the large optical cross sections of noble metal nanoparticles and in aggregation assays based on color change induced by clustering. However, it took until 1998 before the first experimental demonstration of label free refractometric LSPR sensing was reported: Engelbienne et al. showed that the color of colloidal gold nanoparticles in aqueous solution shifted upon molecular adsorption [18] and that the particles thus could be used for label free sensing in much the same way as propagating plasmons on thin metal films. An important consequence of the relaxed LSPR excitation requirements is that instruments can be made compact and even portable [19]. This also lowers the instrumental cost, thereby promoting applications in, e.g., food safety [20] and clinical diagnostics [21, 22]. Other factors that might favor LSPR sensors include the short field penetration depth, which makes the sensor less sensitive to refractive index changes in the solvent far from the metal surface, for example induced by temperature fluctuations [23]. LSPR also provides a versatile platform for a variety of novel sensing applications, such as monitoring catalytic reactions [24]. During the last decade, most LSPR refractive index sensing studies has focused on nanoparticles immobilized on a substrate [23, 25–29]. Surface bound nanoparticles enable more convenient liquid handling systems and much higher flexibility when optimizing both the individual nanoparticle LSPRs through the shape and size of the particles and the inter-nanoparticle coupling via the array parameters. Additionally, the sensing characteristics of particles on a substrate can be straightforwardly compared to the thin film plasmons introduced below.

Sensing Based on Propagating Plasmons

The reason for the relatively complicated excitation geometries required in traditional SPR sensors is that energy and momentum conservation both have to be fulfilled in the interaction between light and plasmons propagating along semi-infinite metal surfaces. Light directly incident from the ambient will not couple energy to the plasmon because the momentum, proportional to the wave number k, of the plasmon is considerably larger than the momentum of light in the ambient dielectric. A nanoparticle, on the other hand, has no translational symmetry, and the LSPR therefore has no well-defined k. This means that LSPR excitation in general only requires the right photon energy and polarization, but no particular magnitude or direction of the incident light momentum.

The relationship between the energy and the momenta of surface plasmons in thin films can be approximated by the dispersion relation for plasmons running along a boundary between two semi-infinite spaces, the metal and a dielectric

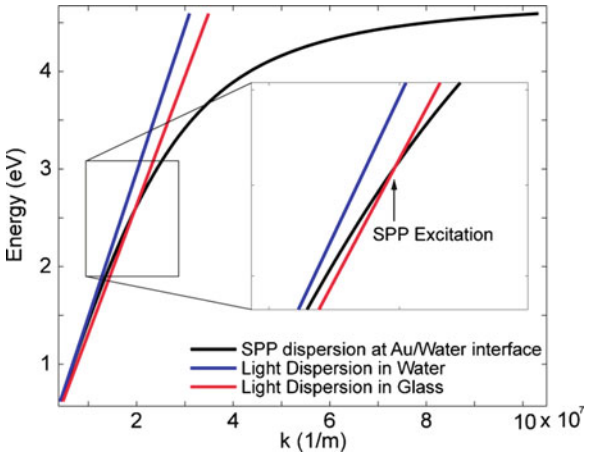

Fig. 1.2 Dispersion of surface plasmons and light. For any given energy, the surface plasmon at a gold–water interface possesses larger momentum than light in water ($n = 1.33$), but excitation is possible if one utilizes a glass ($n = 1.5$) prism in order to couple light to the plasmon. The figure illustrates this by visualizing that the light line in the water never crosses the plasmon dispersion line, while the light line in glass does

ambient. By applying the continuity condition of Maxwell's equations, one can then derive the dispersion relation for the surface plasmon according to:

$$k(\omega) = \frac{\omega}{c}\sqrt{\frac{\varepsilon_{\text{metal}}\varepsilon_{\text{d}}}{\varepsilon_{\text{metal}} + \varepsilon_{\text{d}}}} \tag{1.1}$$

Here ε_{d} is the frequency dependent and complex dielectric function of the metal, $\varepsilon_{\text{d}} = {n_{\text{d}}}^2$ is the dielectric constant of the ambient with refractive index n_{d}, and c is the speed of light in vacuum. By inserting an analytic function or tabulated values for the metal dielectric function one can calculate the dispersion relation $\omega(k)$. This is done in Fig. 1.2 for the case of surface plasmons propagating along a gold–water interface. The figure also shows the dispersion ("the light line") of light propagating parallel to the metal interface in water. Since the two curves never cross, it is impossible to convert photons propagating in water to surface plasmons and at the same time conserve both energy and momentum. However, if the photons instead propagate in glass, their momenta would increase in accordance with the refractive index and coupling to the plasmon would become possible. This is the idea behind the so-called Kretschmann configuration [30], in which a thin metal film is deposited on a glass prism and plasmons can be excited at the metal-ambient interface via illumination through the prism.

The most common method to measure plasmon excitation in a thin film is to study the reflected light in the Kretschmann geometry. A dip in the reflectance then indicates successful conversion of photons to plasmons [31]. This effect can be

simulated using Fresnel's equations for layered media, which gives the reflection coefficient from the prism/metal film/ambient system as:

$$R = |r_{\mathrm{pmd}}|^2 = \left|\frac{E_{\mathrm{r}}}{E_{\mathrm{inc.}}}\right|^2 = \left|\frac{r_{\mathrm{pm}} + r_{\mathrm{md}} e^{2ikt}}{1 + r_{\mathrm{pm}} r_{\mathrm{md}} e^{2ikt}}\right|^2 \tag{1.2}$$

Here r_{AB} is the Fresnel coefficient of reflection at the interface of medium A to B, with respective permittivity ε; p denotes the prism, m the metal film, and d the dielectric ambient, and t is the film thickness. From this equation it is clear that the minimum in reflectance also can be viewed as destructive interference between the light reflected from the prism/metal interface and light from the metal/ambient boundary. Optimum coupling is accomplished when the reflectance is as small as possible for a certain wavelength, which requires that the nominator in (1.2) is minimized. The depth of the reflectance minimum is therefore strongly related to the thickness of the film. Consequently, for given plasmon frequency and momentum, corresponding to a certain incident angle and wavelength, optimum coupling is achieved for a specific thickness of the metal film. For gold films on glass in water and plasmon excitation in the red, the optimum film thickness turns out to be around 50 nm.

Figure 1.3a–d illustrates the most common excitation and detection geometries of surface plamons in thin metal films. As discussed above, the most commonly used method of excitation is the Kretschmann configuration, shown in Fig. 1.3a, b [30]. Incident p-polarized light is coupled via a high refractive index prism to the metal film using an incidence angle above the critical angle. The propagation constant of the light at the prism/thin film interface is thus dependent on the incident angle, which, using (1.1), yields the following condition for SPP excitation:

$$k_{\mathrm{inc.}} = \frac{\omega}{c} n_{\mathrm{prism}} \sin\theta = \frac{\omega}{c}\sqrt{\frac{\varepsilon_{\mathrm{metal}}\varepsilon_{\mathrm{d}}}{\varepsilon_{\mathrm{metal}} + \varepsilon_{\mathrm{d}}}} = k_{\mathrm{SPP}} \tag{1.3}$$

In Fig. 1.3b, white light incident via a prism toward the thin metal film is used. The wavelength of the radiation that couples most effectively to the SPP will vary depending on the (fixed) incident angle and the refractive index of the ambient. This is analyzed by studying the decreased reflectivity spectroscopically. The reflectance spectrum shows a dip, with a minimum at the SPR wavelength, which can be used for tracking the refractive index changes of the ambient.

In Fig. 1.3a, the wavelength of the incident light is instead kept constant, while illumination now takes place from multiple incident angles. This yields a range of propagation constants, k, along the metal film. With the light focused on the film, the reflected light is diverging, and an intensity minimum is found at the angle where the energy and momentum coupling conditions are met simultaneously.

An often used alternative to prism coupling in the Kretchmann geometry is to use so-called grating coupling. The metal film is then deposited on a diffraction grating instead of at a flat surface. Because of the new periodicity introduced by the grating,

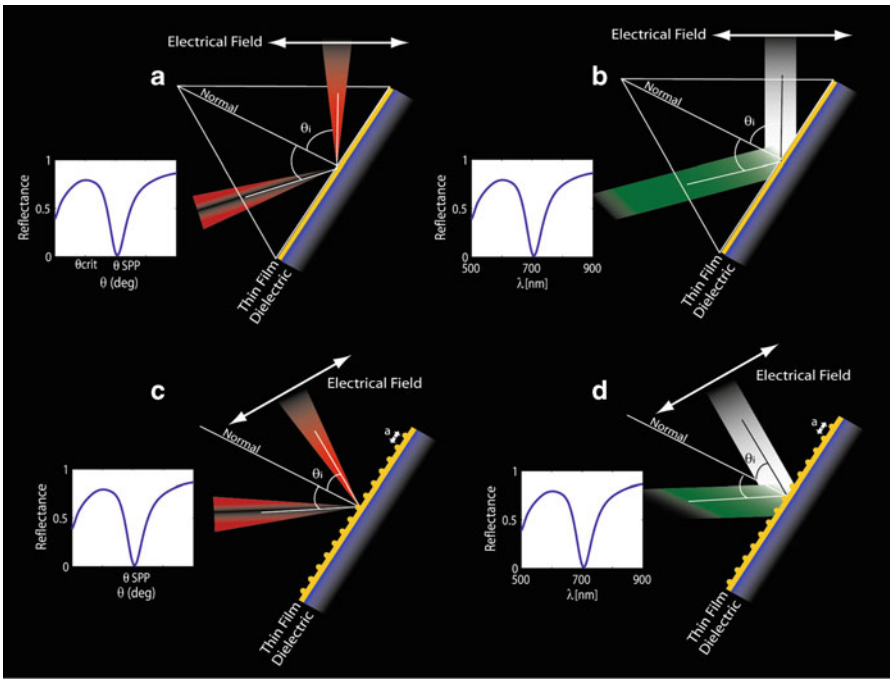

Fig. 1.3 Detection methods of surface plasmon resonances in thin films. (**a**, **b**) Illustrates angular and wavelength detection using Kretschmann geometry, respectively. (**c**, **d**) Are examples of grating coupling excitation of the SPP with angular and wavelength detection, respectively. θ_i denotes the light angle of incidence

the incident photons can gain or lose virtual momentum ("crystal momentum") in units governed by the grating constant a. This leads to the coupling condition:

$$k_{\text{diffracted}} = k_{\text{d}} + m\frac{2\pi}{a} = k_{\text{SPP}}, \quad (m = \pm 0, 1, 2, \ldots) \tag{1.4}$$

where $k_{\text{diffracted}}$ here denotes the propagation constant of the diffracted light in the ambient in the plane of the grating and m is the diffraction order. By adding the second term for the momentum, it is now possible to excite the plasmon from the ambient side. Grating coupling to the surface plasmon is illustrated in Fig. 1.3c, d. Both spectroscopic and angular detection methods can be used for probing refractive index changes [32–34], just as in the Kretschmann configuration above. Even though grating-based SPR sensors may show a smaller bulk refractive index sensitivity compared to the prism geometry, both exhibit similar detection limits [35]. Additionally, as the dip in grating coupled SPR can be designed to be sufficiently narrow, low cost light sources such as light emitting diodes (LEDs) may be used as light sources, thus making the grating coupled SPR a low cost alternative to conventional SPR prism sensors [34].

Naturally, monitoring the intensity at a fixed wavelength and incident angle is possible in both grating- and prism-based SPR sensors, although this implementation suffers from a smaller dynamic range as the intensity fluctuations only can be monitored within the width of the resonance. By exchanging the detector to a camera or a CCD detector, this detection method can be used for detection of multiple analytes simultaneously, using imaging SPR [36–38]. To overcome the low dynamic range, it is also possible to take images with varying incident angles or wavelength, creating a stack of images from which the resonance position can be determined [39, 40]. The latter methodology has some disadvantages though, as imaging from varying angles may create different image distortions. For a much more extensive treatment of thin film SPR sensing, the reader should consult the excellent recent book by Homola [41].

Localized Plasmons

To introduce refractometric sensing based on localized surface plasmons, it is convenient to start from the quasi-static polarizability of a spherical particle that is much smaller than the incident wavelength, the so-called Clausius–Mossotti polarizability:

$$\begin{aligned}\alpha &= 4\pi a^3 \frac{\varepsilon_{\text{metal}}(\omega) - \varepsilon_{\text{d}}}{\varepsilon_{\text{metal}}(\omega) + 2\varepsilon_{\text{d}}} \\ &= 4\pi a^3 \left[\frac{\omega_0^2}{\omega_0^2 - \omega^2 - i\omega\gamma} - \frac{\omega^2 + i\omega\gamma}{\omega_0^2 - \omega^2 - i\omega\gamma} \frac{1 - \varepsilon_{\text{d}}}{1 + 2\varepsilon_{\text{d}}} \right]\end{aligned} \tag{1.5}$$

Here, a is the radius of the sphere and the dielectric function of the metal has been approximated by the Drude model:

$$\varepsilon_{\text{Drude metal}}(\omega) = 1 - \frac{\omega_{\text{p}}^2}{\omega^2 + i\omega\gamma} \tag{1.6}$$

The resonance frequency is given by $\omega_0 = \omega_0/\sqrt{1 + 2\varepsilon_{\text{d}}}$, which clearly shows that the LSPR will redshift with increasing dielectric constant of the surrounding. By noting that resonance is achieved when the denominator in the polarizability function is minimized, i.e., when $\text{Re}[\varepsilon_{\text{metal}} + 2\varepsilon_{\text{d}}] = 0$, one can also illustrate the refractive index sensitivity as in Fig. 1.4. Since the dielectric function in the metal becomes more negative for longer wavelengths, the resonance condition will redshift as the dielectric constant in the medium increases.

By inserting the Drude dielectric function for $\varepsilon_{\text{metal}}$, thereby assuming a perfect free-electron metal, in the Clausius–Mossotti polarizability expression of (1.5), one finds that the dominant term describes a Lorentzian line shape. This means that the conduction electrons collectively respond as a damped harmonic oscillator.

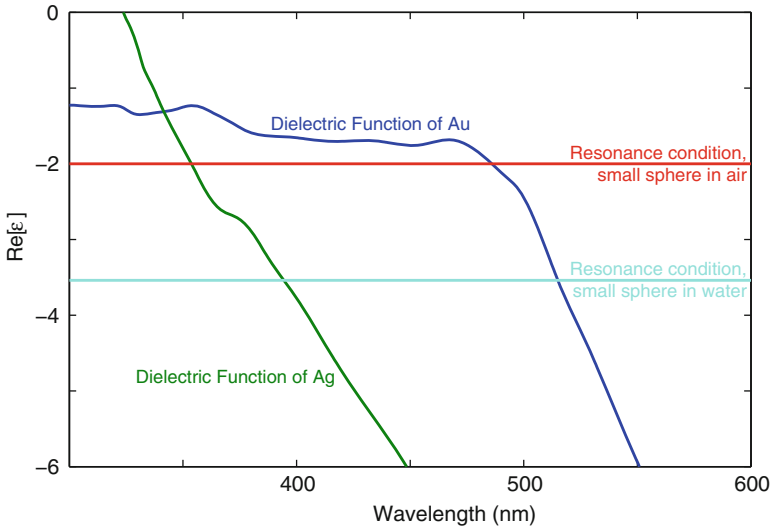

Fig. 1.4 The real dielectric functions of gold and silver. The *horizontal lines* show the resonance conditions for small spheres in air and water medium, see (1.5)

The resonating surface charges driven by the external field in turn produce an induced field inside and outside the particle that acts to restore charge neutrality. The corresponding restoring force will decrease, meaning that the resonance redshifts, if the field lines pass through a medium with a high dielectric constant. Plasmonic refractive index sensing is thus ultimately due to dielectric screening of surface charges and the sensitivity of the plasmon can be related to the ease with which the electrons are polarized and the strength of the restoring force, which is a function of the material but also of the geometrical shape of the particle. For example, the field lines associated with a plasmon oscillating along the long axis of an elongated particle will pass through a proportionally larger fraction of the surrounding medium and therefore be more sensitive to a refractive index change than a spherical particle plasmon. Similarly, a plasmon localized to a gap between two metal surfaces will be highly susceptible to dielectric screening inside the gap.

The discussion above focused on the *bulk* refractive index sensitivity. However, when one studies molecular adsorption at or very close to the surface of a nanostructure, the extension of the resonant field into the ambient naturally becomes of prime importance. Although a thin homogeneous layer with a certain refractive index can model a monolayer of molecules to some extent, individual molecules are described by their polarizability. A model that takes the polarizabilities of both the nanoparticle and the molecule(s) into account is therefore a more appropriate starting point for discussing nanoplasmonic biosensing. In the so-called coupled dipole approximation (CDA), one approximates the nanoparticle and the molecule as point dipoles that are coupled self-consistently through their induced fields. Solving the coupled dipole equations then yields new modified point dipole

polarizabilities with modified resonance conditions. In the case of one particle and a single molecule, we can write the two dipole moments as:

$$P_{\mathrm{NP}} = \alpha_{\mathrm{NP}}(E_0 - \mathrm{AP}_{\mathrm{molecule}}) \tag{1.7}$$

$$P_{\mathrm{molecule}} = \alpha_{\mathrm{molecule}}(E_0 - \mathrm{AP}_{\mathrm{NP}}) \tag{1.8}$$

where α_{NP} and $\alpha_{\mathrm{molecule}}$ are the respective polarizabilities of the two objects and E_0 is the incident field. The interaction between the individual dipoles is described using the matrix A, so that AP_{NP} corresponds to the field induced by the nanoparticle at the location of the molecule and vice versa for $AP_{molecule}$. We can describe the dipole polarizabilities as:

$$\alpha_{\mathrm{NP}} = 4\pi a_{\mathrm{NP}}^3 \frac{\omega_0^2}{\omega_0^2 - \omega^2 - i\omega\gamma} \tag{1.9}$$

$$\alpha_{\mathrm{molecule}} = 4\pi a_{\mathrm{molecule}}^3 \frac{n^2 - n_{\mathrm{d}}^2}{n^2 + 2n_{\mathrm{d}}^2} \tag{1.10}$$

where a_{NP} and a_{molecule} are the radii of the nanoparticle and the molecule, respectively, ω_0 is the resonance frequency of the nanoparticle, and γ is a damping factor. Further, n and n_{d} are the refractive indices of the small molecule and the surrounding medium respectively. Inserting P_{molecule} into the equation of P_{NP} and assuming $n > n_0$, we find a redshift of the particle resonance according to:

$$\tilde{\omega}_0^2 = \omega_0^2 \left(1 - \left(a_{\mathrm{molecule}}/a_{\mathrm{NP}}\right)^3 \frac{n^2 - n_{\mathrm{d}}^2}{n^2 + 2n_{\mathrm{d}}^2} \left(a_{\mathrm{NP}}^3 A\right)^2\right) \tag{1.11}$$

We see that the redshift is determined by three terms: the volume ratio between the molecule and the particle, which determines the "stiffness" of the particle resonance; a term describing the refractive index contrast between the molecule and the surrounding medium; and a coupling term that is directly related to the local intensity enhancement factor at the location of the molecule. The last term indicate that molecular adsorption will yield different shifts depending on the adsorption position with respect to the induced dipole moment of the nanoparticle and that local "hot spots" with high enhancement, for example sharp edges or crevices between particles, can be expected to yield large responses.

As mentioned above, the excitation conditions for LSPR sensing are much more relaxed than for sensing using propagating plasmons. Figure 1.5 illustrates the most common optical setups for micro- and macroscopic LSPR sensing. Dark field spectroscopy is a popular technique for measuring the response of single nanoparticles [42–45]. The excitation light is incident at high angles and the scattered light is collected using low numerical aperture optics that does not pick up the directly transmitted light. Using dark-field imaging it is also possible to study a large number of single particles simultaneously [43], thereby improving measurement statistics and potentially enabling multiplexed measurements of several analytes.

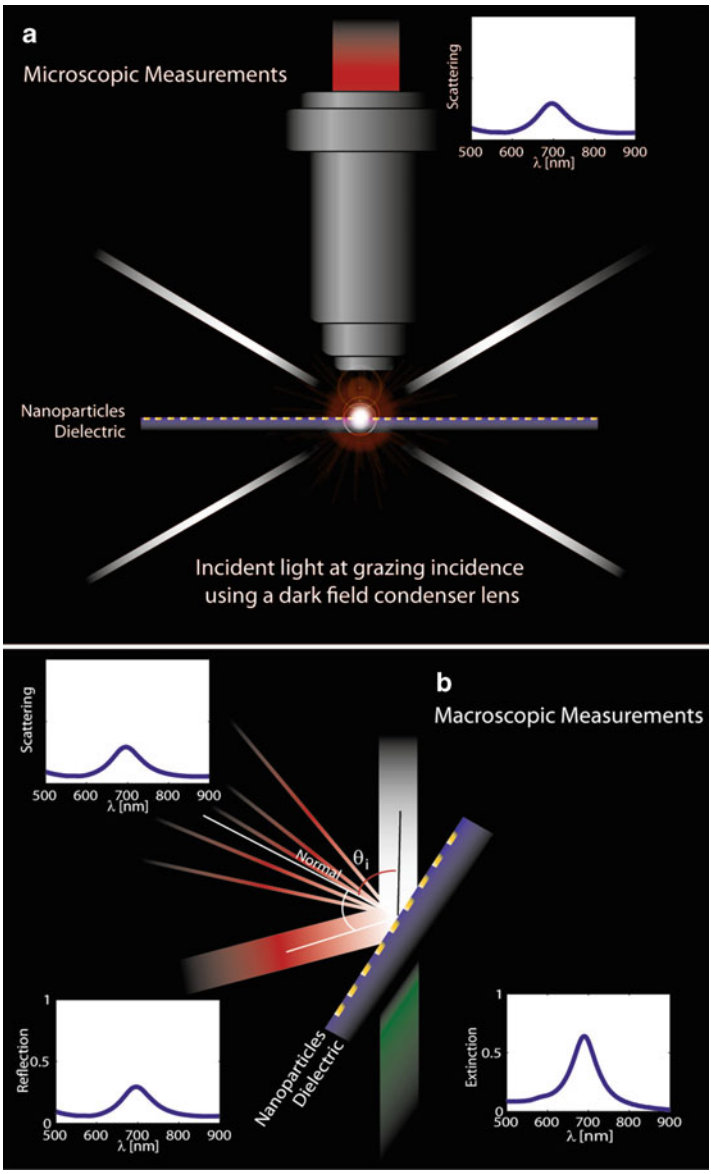

Fig. 1.5 Illustration of LSPR detection setups. (**a**) Dark field spectroscopy in an optical microscope. (**b**) Macroscopic measurements of a layer of supported nanoparticles using extinction, specular reflection and diffuse scattering

Although dark field measurements, or scattering measurements in general, are usually advantageous at low particle densities, the highest signal-to-noise ratios for dense samples have been obtained using extinction measurements, see Fig. 1.5b, which utilizes both absorption and scattering losses [21, 46, 47]. It can also be

advantageous to record specular reflection, since a dense layer of nanostructures behaves similar to a homogeneous "metamaterial" surface. In the case of a low interparticle coupling and low reflectance from the substrate supporting the particle layer, the specular reflectance spectrum will show characteristics similar to a single-particle scattering spectrum [23].

Propagating Versus Localized Plasmons: Bulk Refractive Index Sensitivity

Propagating plasmons in thin metal films and localized plasmons in nanoparticles clearly have the same physical origin and they are both sensitive to the surrounding refractive index. The obvious question is then if one is superior to the other. To address this question, Svedendahl et al. recently performed an experimental comparison between SPR sensing, based on a 50 nm gold film, and LSPR sensing based on a layer of gold nanodisks. Apart from the necessity of using prism coupling in the SPR measurement, the same optical excitation and detection schemes were used in the two measurements [23].

Keeping the initial resonance position of the LSPR and the SPR at around 700 nm, bulk refractive index sensitivity measurements showed the thin film plasmon to be much more sensitive, with a resonance shift of about 3,300 nm/RIU, while the LSPR only shifted 180 nm/RIU, as seen in Fig. 1.6. As suggested in ref. [48], a figure of merit for a plasmonic sensor can be defined as FoM $= (\partial\lambda_{\mathrm{res}}/\partial n)/\mathrm{FWHM}$, that is the ratio between the bulk sensitivity and the full width at half maximum (FWHM) of the resonance. The motivation behind this quality measure is simply that it is easier to detect a small shift using a sharp

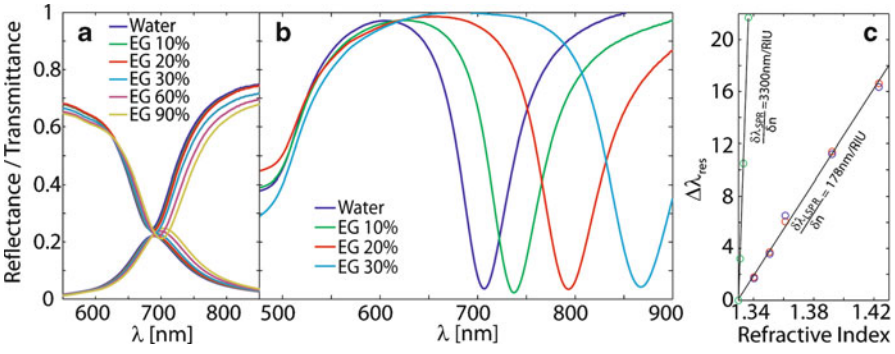

Fig. 1.6 Bulk refractive index sensing with localized and propagating plasmons. (**a**) Transmission and reflection spectra for Au nanodisks in contact with water/glycol mixtures of increasing refractive index *n*. (**b**) Corresponding data for propagating plasmons on a 50 nm thin gold film. (**c**) Resonance shift vs. bulk refractive index extracted from (**a**) and (**b**). Reprinted with permission from Svedendahl et al. [23]. Copyright 2009 American Chemical Society

resonance than using a broad one. In the present case, the SPP resonance turned out to be slightly sharper than the LSPR, resulting in an FoM above 50, of the order 25 times higher than for the nanodisk LSPR.

The differences in bulk sensing properties between SPR and LSPR sensors, illustrated in Fig. 1.6, can be understood from simplified theoretical models. Homola et al. showed that the SPR bulk sensitivity can be derived from the SPP dispersion relation given by (1.1) by differentiating k_{SPP} with respect to n [41]. Miller and Lazarides showed that the sensitivity of LSPR can be derived in a similar manner from the dipole polarizability of an ellipsoidal particle [49]. The resulting expressions are:

$$\frac{\partial \lambda_{res}^{SPR}}{\partial n} = -\frac{2\varepsilon^2}{n^3(\partial\varepsilon/\partial\lambda_{res})} \tag{1.12}$$

$$\frac{\partial \lambda_{res}^{LSPR}}{\partial n} = \frac{2\varepsilon}{n(\partial\varepsilon/\partial\lambda_{res})} \tag{1.13}$$

Equations (1.12) and (1.13) indicate that the bulk RI sensitivity of plasmons is mainly determined by the wavelength-dependent metal dielectric function and the refractive index of the surrounding. In particular, the bulk sensitivity expression for LSPR explains why nanostructures of different shapes but with the same composition and resonance wavelength exhibit very similar bulk RI sensitivities.

Returning to the FoM, it can be shown that the widths of the resonances can be written as [50]

$$\mathrm{FWHM}_{SPR} = \frac{4\varepsilon''}{|\partial\varepsilon'/\partial\lambda_{res}|} \tag{1.14}$$

$$\mathrm{FWHM}_{LSPR} = \frac{2\varepsilon''}{|\partial\varepsilon'/\partial\lambda_{res}|} \tag{1.15}$$

Combining (1.12)–(1.15) then yield the FoM for the two methodologies as

$$\mathrm{FoM}_{SPR} = \left|\frac{\varepsilon'}{2n^3\varepsilon''}\right| \tag{1.16}$$

$$\mathrm{FoM}_{LSPR} = \left|\frac{\varepsilon'}{n\varepsilon''}\right| \tag{1.17}$$

The theoretical FoM and bulk sensitivities discussed above are plotted in Fig. 1.7 using the experimentally dielectric data for gold [51]. Note that the analytical expression and the experimental results for the LSPR case do not fully agree. The

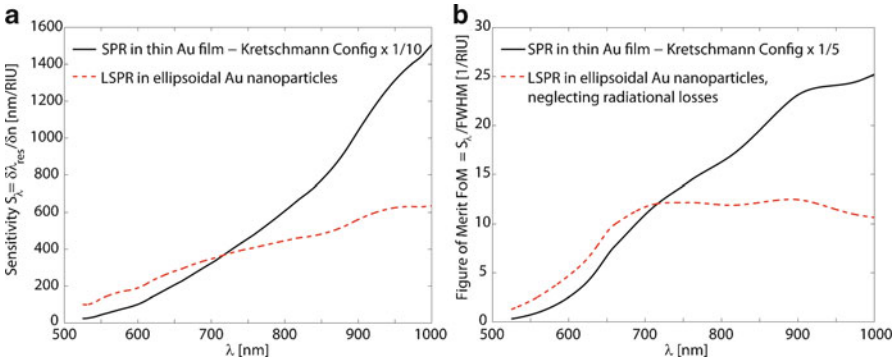

Fig. 1.7 Theoretical comparison of LSPR in Au ellipsoidal nanoparticles and thin film SPRs. Bulk refractive index sensitivity (**a**) and the figure of merit (**b**) of propagating SPR and Localized SPR in ellipsoidal particles in water ambient medium, using (1.12), (1.13) and (1.16), (1.17) with dielectric function of gold from [51]

discrepancy can be explained by two main factors. First, since the nanodisks are immobilized on a glass substrate, about half of the plasmon induced field to reside in the glass rather than in the ambient. This effectively decreases the sensitivity by ~50% compared to a particle in a homogeneous environment. Second, the FWHM derivation above is based on the assumption that there are no radiation losses and no inhomogeneous broadening, which together broadens the LSPR resonance considerably.

Substrate Effects

As mentioned above, supported nanostructures usually have a large fraction of their sensing volume blocked by the substrate. If the refractive index of the substrate is significantly higher than that of the sensing medium, one even expects that a dominant part of the plasmon field is pushed down into the substrate [52, 53]. This effect was investigated further by Brian et al. for the case of nanoholes in thin metal film [54]. This system constitutes an interesting combination of localized "hole plasmons" coupled through antisymmetric propagating plasmons [55]. The bulk sensitivity could be measured as a function of resonance position by altering the nanohole separation. The result was a higher sensitivity for longer resonance wavelengths, as expected from the data in Fig. 1.7. However, from the discussion above, one anticipates it is possible to additionally enhance the refractive index sensitivity by fabricating the nanohole arrays on low index substrates. To test this hypothesis, Brian et al. utilized SiO_2, Teflon, and TiO_2 substrates. The fabrication method used, colloidal lithography, results in nanoholes with a fixed diameter and a fixed average separation distance but short-range lateral order.

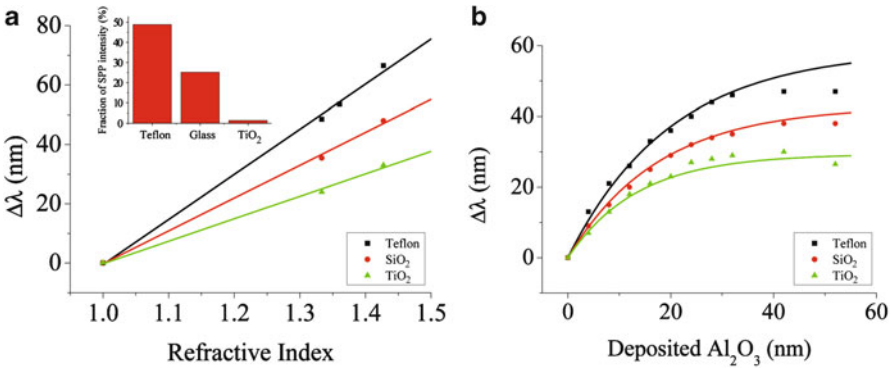

Fig. 1.8 The influence of nanoparticle substrates. (**a**) The plasmon resonance shift is higher for samples fabricated on low index substrates. (**b**) Resonance shift as a function of the thickness of a layer of Al_2O_3. Note the correlation between the plasmon induced field fraction in the ambient medium, calculated with the transfer matrix method [60] (*inset* in (**a**)), and the resonance shifts in (**a**) and (**b**). Adapted from Brian et al. [54]

A clear blue and redshift of the plasmon resonance was detected for the Teflon and TiO_2 substrates, respectively, compared to the more frequently used SiO_2 substrate. Given the previous finding that the bulk sensitivity should increase with resonance wavelength, this would imply a decrease of the Teflon sample sensitivity. However, as seen in Fig. 1.8, it was found that both the bulk refractive index sensitivity and the thin layer sensitivity increased substantially compared to the SiO_2 case. In fact, the effective improvement obtained using Teflon supported nanoholes compared to the SiO_2 and TiO_2 was as high as a factor of 1.6 and 3, respectively. The reason for this effect is thus that a low substrate index pushes the plasmon induced field into the sensing medium. This is illustrated by the calculation in the inset of Fig. 1.8, which indicates that the fraction of the plasmon field within the aqueous ($n = 1.33$) sensing region increases from ~5% to almost 50% when the substrate index decreases from $n = 2.4$ (TiO_2) to $n = 1.34$ (Teflon). See also ref [56–59] for related methods of increasing the plasmon sensitivity using optimized substrates.

Molecular Sensing: The Role of Field Confinement

Thus far we have only discussed the plasmon resonance condition in terms of the refractive index of the entire surrounding volume, but the dominant part of the plasmon induced field is evanescent and bound to the metal interface. Fortunately, this is precisely where the target molecules probed in biosensing experiments accumulate. To discuss the role of field confinement, it is useful to introduce an *effective refractive index* of the medium probed by the plasmon induced near-field. For propagating plasmons in thin films, the electric field decays exponentially from

the metal surface into the ambient media. An effective refractive index weighted by the field decay can then be defined as [61]:

$$n_{\text{effective}} = \frac{2}{L}\int_0^\infty n(z)E(z)^2 \mathrm{d}z = \frac{2}{L}\int_0^\infty n(z)e^{-2z/L}\mathrm{d}z \tag{1.18}$$

where L is the plasmon field decay length into the ambient medium and z is the distance from the metal surface. The decay length can be approximated as [62]:

$$L_{\text{SPR}} = \frac{\lambda}{2\pi}\sqrt{\frac{\varepsilon'_{\text{metal}} + n^2}{n^4}} \tag{1.19}$$

where $\varepsilon'_{\text{metal}}$ is the real part of the dielectric constant of the metal at the measurement wavelength λ. Typically, the decay length is of the order of 2–300 nm for gold films in the visible and near infra-red. Now assume that a layer of molecules with thickness d and refractive index n_1 is adsorbed on the substrate. This gives rise to a response of the sensor:

$$\Delta\lambda = \Delta n \frac{\partial\lambda_{\text{res}}}{\partial n}(1 - e^{-2d/L}) \tag{1.20}$$

where $\Delta\lambda$ is the wavelength shift, Δn is the refractive index change $n_{\text{eff}} - n_0$, with n_0 the index of the surrounding, and $\partial\lambda_{\text{res}}/\partial n$ is the bulk refractive index sensitivity of the sensor. Equation (1.20) can be used to convert from plasmon shift to refractive index change and from there to the amount of adsorbed molecules. This is typically done in terms of the adsorbed molecular mass per sensor area unit, Γ, which can be estimated from:

$$\Gamma_{\text{ads}} = \frac{\Delta n}{\partial n/\partial c} d \tag{1.21}$$

where $\mathrm{d}n/\mathrm{d}c$ is the molecule specific refractive index increment.

Even though the exponential decay model is excellent for thin film SPR measurements, it is not obvious that it can be used also for localized plasmons. Xu et al. theoretically studied the response of gold and silver spheres immobilized on glass substrates, thereby simulating experiments by Okamoto et al. [25] on supported colloidal particles covered with varying thicknesses of nanometric PMMA layers [63]. Using extended Mie theory for core-shell particles, and including the effects of the surrounding medium, particle–particle and particle–substrate interactions, the influence of the adsorption layers on the plasmon resonance position was investigated for different particle sizes, see Fig. 1.9b.

Both experiments and theory showed that the plasmon shifted faster with the coating thickness, d, for smaller particles, as shown in Fig. 1.9c, d. The results were interpreted in terms of a particle-dependent field decay and it was concluded that

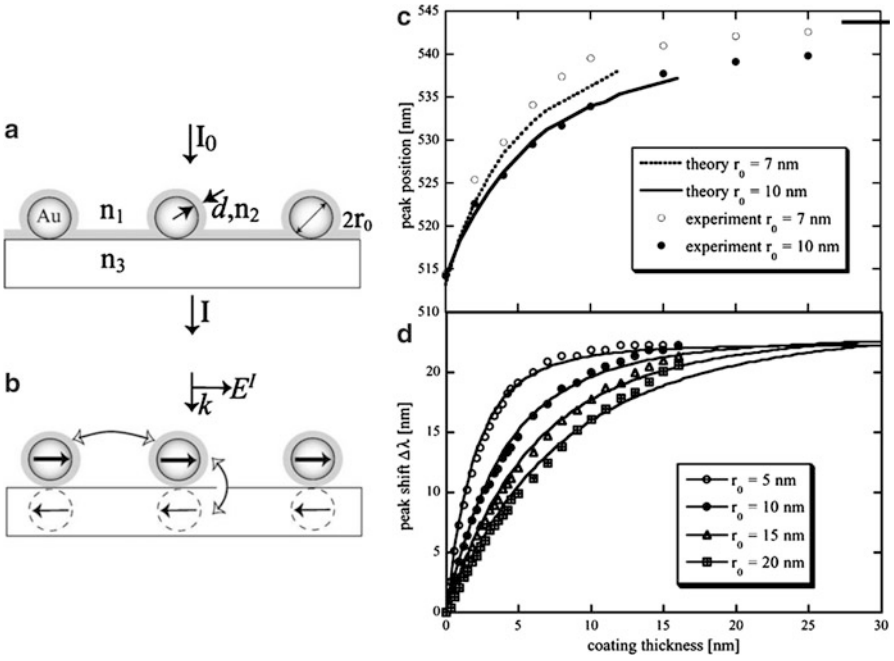

Fig. 1.9 Illustration of the sensing volume of supported gold colloids. (**a**) Schematic illustration of the experimental sensor configuration used by Okamoto et al [25]. (**b**) The core-shell Mie theory model used by Xu et al. to simulate this configuration [63]. Metal nanoparticles of radius r_0 are adsorbed on a substrate with refractive index n_3 in a medium with refractive index n_1. The model accounts for interparticle coupling effects within the dipole-approximation and image multipoles in the substrate. (**c**) Comparison between calculated and measured resonance wavelengths of 10 and 7 nm radius Au particles vs. the PMMA coating thickness d. The horizontal bar marks the resonance of a supported particle layer embedded in PMMA. (**d**) Calculated resonance shifts vs. d for various particle radii together with single-parameter fits. Adapted from Xu et al. [63], with permission from Elsevier

the plasmon induced field in the vicinity of the nanoparticle drops as $(r_0/r)^6$, where r_0 is the particle radius. This is the expected result for a dipolar plasmon resonance, which dominates the induced field for a sub-wavelength metal particle. Using the dipolar power-law decay, it is then straightforward to define an effective refractive index n_{eff} in the same manner as for the SPR case:

$$\begin{aligned} n_{\text{effective}} &= \frac{n_2 \int_{r_0}^{r_0+d} 4\pi r^2 (R_0/r)^6 \mathrm{d}r + n_1 \int_{r_0+d}^{\infty} 4\pi r^2 (R_0/r)^6 \mathrm{d}r}{\int_{r_0}^{\infty} 4\pi r^2 (R_0/r)^6 \mathrm{d}r} \\ &= n_2 - \frac{n_2 - n_1}{\left[1 + (d/R_0)\right]^3} \end{aligned} \tag{1.22}$$

Equation (1.22) does not show much resemblance with the thin film case, although the field falls off rapidly from the metal surface. Using the dielectric

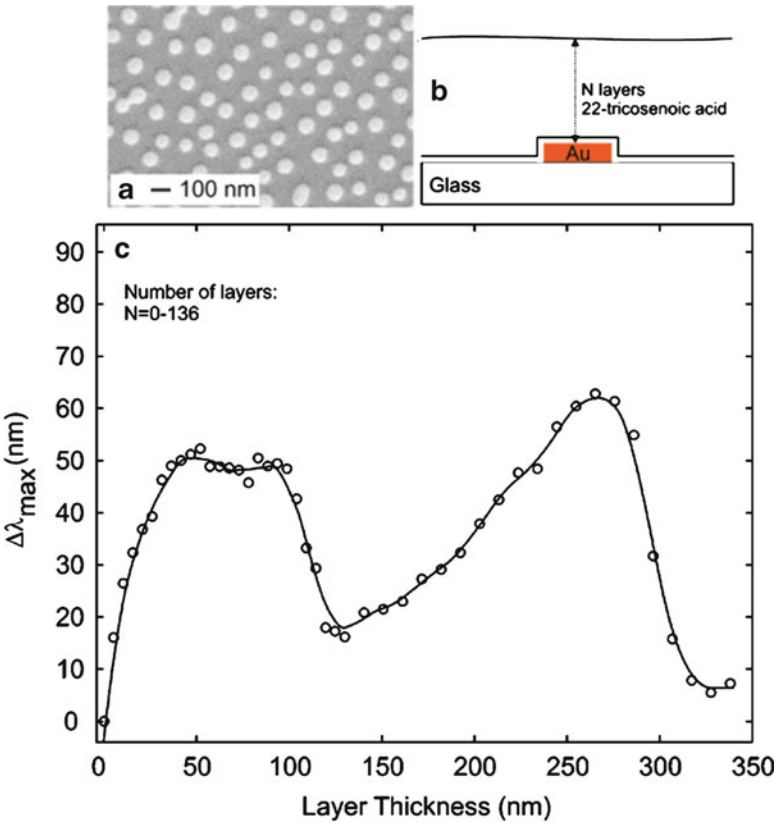

Fig. 1.10 Long-range LSPR sensing. (**a**) SEM image of 70 nm Au nanodisks on glass. (**b**) Schematics of the nanostructures coated with an LB film composed of *N* layers of 22-tricosenoic acid. (**c**) Plasmon resonance shift as a function of LB layer thickness, demonstrating high-slope/high-sensitivity regions at ~100 and ~300 nm from the particle surface. Adapted with permission from Rindzevicius et al. [64]. Copyright 2007 American Chemical Society

function of gold and the resonance condition of colloidal nanoparticles, $\varepsilon'_{\text{metal}} + 2n^2_{\text{effective}} = 0$, the plasmon wavelength shift can be written as $\Delta\lambda \approx (2/(\partial\varepsilon / \partial\lambda))[n_2^2[1-(1-n_1/n_2)/(1+d/r_0)^3]]^2$. This function was then used to obtain the curve fits shown in Fig. 1.9c, d.

The $(r_0/r)^6$ power law in Fig. 1.6, as well as the coupled dipole analysis discussed previously, demonstrates that the optical near-field intensity distribution is crucial for understanding LSPR sensing. However, nanostructures positioned in more complicated dielectric environments can exhibit much more complex sensing characteristics. This is illustrated by the study of Rindzevicius et al., who showed that long-range LSPR sensing is possible by utilizing interference and dipolar interactions [64]. The study focused on the layer refractive index sensitivity of nanodisk and nanohole gold structures covered by Langmuir–Blodgett (LB) films up to 350 nm in thickness, see Fig. 1.10a. In contrast to the colloid example above,

where ~75% of the saturated shift was expected for a layer thickness equal to the radius of the nanosphere, the LB system showed an oscillatory behavior as a function of layer thickness, see Fig. 1.10c for the case of 70 nm wide and 20 nm tall Au nanodisks. In particular, there were high-sensitivity regions as far away as 100 and 300 nm from the metal surface, which is far outside the expected near-field decay length. The results can be explained by taking into account that the particle dipole is driven not only by the incident field but also by the induced dipole field reflected back from the LB layer/ambient interface. The reflected field can add up in or out of phase with the incident field, depending on the distance between particle dipole and the substrate, and this results in oscillations of the resonance position with a period of about $\lambda_{LSPR}/2n$, where n denotes the refractive index of the LB film. This type of long-range LSPR sensing might be advantageous because the nanostructures are protected from the environment, for example from oxidation, and because the presence of only one type of surface open to the environment may facilitate chemical functionalization.

Propagating Versus Localized Plasmons: Biosensing

Thus far we have established that both the bulk sensitivity and the decay length are about one order of magnitude larger for thin film plasmons compared to localized plasmons. However, these two parameters need to be combined in order to effectively compare the two methodologies for biosensing purposes. Considering the vast differences in FoM seen in Fig. 1.7, one might anticipate that classical SPR is the better alternative for sensing in general. To test whether this is actually the case when it comes to biosensing, Svedendahl et al. studied biorecognition reactions between streptavidin (SA) and biotin using flat film and nanodisk plasmons [23]. Figure 1.11 shows the corresponding SPR and LSPR shifts vs. time during functionalization with biotinylated bovine serum albumin (bBSA), an intermediate step of BSA adsorption that passivate unfunctionalized areas, and the final introduction of SA. Although the LSPR measurements seem to give a smaller overall response, in particular during the functionalization step, the shifts induced by biorecognition, that is SA binding to bBSA, are surprisingly similar: 0.55 nm for SPR compared to 0.57 and 0.63 nm shifts for LSPR measured in extinction and reflection mode, respectively. These results demonstrate that the FoM is not the only factor determining plasmonic sensing capabilities. The decay length, which is at least one order of magnitude smaller for LSPR compared to SPR sensors [21, 65, 66], is just as important. Thus, in the case of molecular adsorption near the metal surface, the high confinement of the LSPR induced field compared to the SPR case leads to a much more efficient use of the bulk refractive index sensitivity, which is why the peak-shifts seen in Fig. 1.11 are so similar. One might also point out that the gold film used in the comparison had a more or less optimum thickness (50 nm) while both the bulk sensitivity, the FWHM and the field distribution of the LSPR,

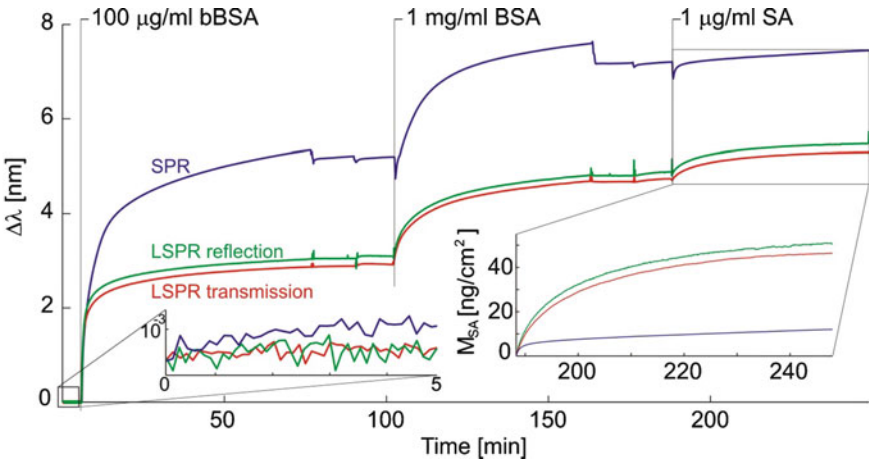

Fig. 1.11 Biosensing using localized and propagating plasmons. The temporal evolution of the resonance shifts for localized plasmons in Au nanodisks and propagating plasmons on a 50 nm planar gold film. The *vertical lines* specify the injection of different biomolecules into the sample chamber. The *insets* show the fluctuations of the resonance wavelength for blank samples (*left*) and the adsorbed mass after SA injection (*right*). Reprinted with permission from Svedendahl et al. [23]. Copyright 2009 American Chemical Society

probably could be improved quite substantially by fine-tuning the size, shape, and positioning of the nanoparticles [67–73].

One of the ultimate aims of biosensing research is to generate a label-free methodology that makes it possible to count single target molecules with high efficiency in complex media and at low concentrations. Although optical label-free methods, such as SPR and LSPR, are ideal for studying molecular interactions in real time, it is not obvious that the techniques have the specificity and sensitivity necessary to achieve "robust" single molecule (SM) detection. Plasmonic detection of single biomacromolecules based on structures with ultra-high field-enhancement has been reported using SERS [75] as well as LSPR sensing [45], but the question is whether detection using "hot spots" is robust enough to constitute an analytical alternative to methods based on target amplification, such as PCR, or signal amplification, such as ELISA [76]. As an alternative, Chen et al. recently presented an approach that combines enzymatic amplification with LSPR refractive index sensing using gold nanodisks, a structure that can be expected to exhibit rather uniform enhancement properties [74]. The aim of the study was to develop a simple colorimetric end-point assay with robust SM detection capabilities, thus trading kinetic resolution for sensitivity. The study was based on dark-field measurements using a variable band-pass liquid crystal tunable filter (LCTF) inserted into the illumination path of the optical microscope. Using stacks of images obtained at varying wavelengths, spectral information from up to a hundred individual nanodisks could be obtained in parallel. As illustrated in Fig. 1.12b, Chen studied the interaction between biotin and avidin conjugated to the enzyme horse radish

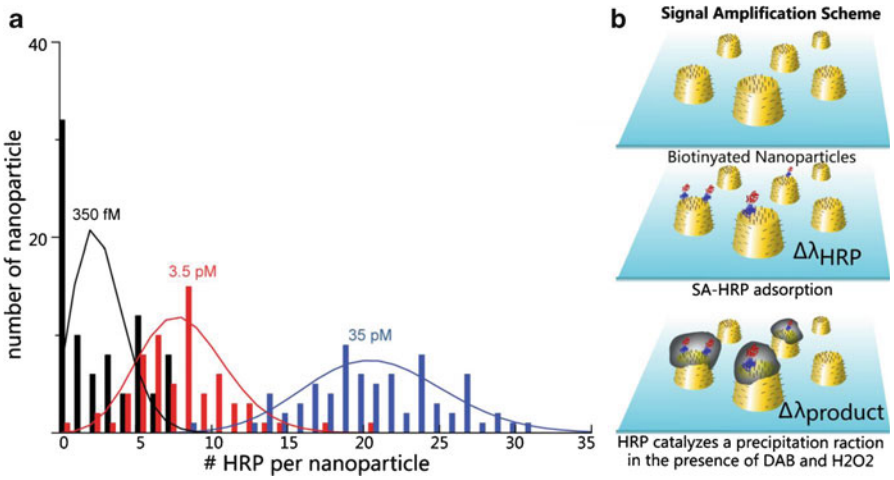

Fig. 1.12 Molecular detection using a combined LSPR-ELISA methodology. The enzyme horse radish peroxidase (HRP) conjugated to streptavidin binds to biotinylated gold nanodisks and catalyzes a local precipitation that amplify the optical mass sensed by the LSPR (**b**). By calibrating the response at low concentrations, it is possible to resolve LSPR shifts that correspond to a very low number of HRP (**a**). The spread in values are in excellent agreement with what can be expected for a Poisson distribution (*solid lines*) calculated from the average number of molecules per nanodisk. Adapted with permission from Chen et al. [74]. Copyright 2009 American Chemical Society

peroxidase (HRP), which catalyzes the polymerization of a precipitate in the final step of the assay. These precipitates have a large refractive index, thus enhancing the refractometric footprint of individual binding events by up to two orders-of-magnitude. When the peak-shifts measured for single particles were converted to number of molecules, as in Fig. 1.12a, the assay was found to have a sensitivity at or close to the SM limit, a conclusion supported by both the statistical signal distribution and computer simulations of the molecular diffusion and binding processes [74]. Although this study is only a model of a real sandwich assay, the method is likely transferrable to more complex sample solutions and may pave the way for highly sensitive diagnostic applications of nanoplasmonic sensing.

Summary and Outlook

This chapter has summarized some of the basic characteristics of SPR sensors. In particular, we compared sensors that utilize LSPRs in nanostructures with the much more mature and already commercialized technology based on propagating surface plasmons in thin films. It was shown that the bulk refractive index sensitivity and the so-called figure-of-merit of classical SPR sensors exceed the theoretical LSPR

limits and that the difference increases towards longer resonance wavelengths. The higher bulk sensitivity gives a clear advantage in, for example, gas detection but also makes an SPR sensor very sensitive to temperature fluctuations in the sensing medium. However, LSPR and SPR sensors have similar capabilities in detecting biorecognition reactions that occur close to the metal surface. The reason is that the decay length of the LSPR induced electromagnetic field is much better matched to the thickness of a biomolecular film, thus compensating for the higher SPR bulk sensitivity.

One of the main advantages of LSPR sensing is the simpler excitation requirement compared to SPR sensing. Because of the relaxed momentum conservation requirements, high-sensitivity LSPR data can be collected using miniature light sources and spectrometers applied in simple transmission or reflection measurements. This could be important for development of, for example, handheld sensors for use "in the field" or for point-of-care diagnostics. Nanofabricated samples are, on the other hand, more costly and complicated to produce, although this is likely to change with the growth of parallel nanofabrication methods such as nanoimprint lithography. Another potential drawback is that surface functionalization becomes more complicated because two surface types, i.e., metal and substrate, are exposed to the sensing medium in a typically LSPR sensor chip.

The discussion in this chapter has been based on the rather artificial division of plasmon resonances into "localized" and "propagating" modes. In reality, of course, real sensing structures have neither negligible nor infinite size and all plasmon resonances therefore exhibit some degree of localization and propagation. In fact, several recent research directions in plasmonics focus on metal systems of intermediate size, such as nanowires and groups of particles that are ordered on the micron length scale, where field retardation can be used to induce spectacular directionality effects [52, 53, 77] as well as line-sharpening due to Fano resonance [78]. Another prominent research direction concerns metamaterials, such as layers of strongly coupled plasmonic nanowires that exhibit collective guided modes with high refractive index sensitivity [79]. Moreover, the possibility to combine plasmonic sensing with other label-free or label-based measurement technologies has just begun to be explored. We have discussed one such example here, i.e., the combination with ELISA, while other published examples include hybrid LSPR- QCM (quartz crystal microbalance) [80, 81] and LSPR-WGM (whispering gallery mode) sensors [82–85]. Altogether, given the already successful SPR technology and the extremely rapid development of the plasmonic field, we can expect many more exciting discoveries and novel applications of plasmonic sensing.

References

1. Nylander C, Liedberg B, Lind T. Gas-detection by means of surface-plasmon resonance. Sens Actuators. 1982;3(1):79–88.
2. Liedberg B, Nylander C, Lundstrom I. Surface-plasmon resonance for gas-detection and biosensing. Sens Actuators. 1983;4(2):299–304.

3. Karlsson R. SPR for molecular interaction analysis: a review of emerging application areas. J Mol Recognit. 2004;17(3):151–61.
4. Campbell CT, Kim G. SPR microscopy and its applications to high-throughput analyses of biomolecular binding events and their kinetics. Biomaterials. 2007;28(15):2380–92.
5. Wassaf D, et al. High-throughput affinity ranking of antibodies using surface plasmon resonance microarrays. Anal Biochem. 2006;351(2):241–53.
6. Rees DC, et al. Fragment-based lead discovery. Nat Rev Drug Discov. 2004;3(8):660–72.
7. Mozsolits H, Thomas WG, Aguilar MI. Surface plasmon resonance spectroscopy in the study of membrane-mediated cell signalling. J Pept Sci. 2003;9(2):77–89.
8. Navratilova I, Hopkins AL. Fragment screening by surface plasmon resonance. ACS Med Chem Lett. 2010;1(1):44–8.
9. Neumann T, et al. SPR-based fragment screening: advantages and applications. Curr Top Med Chem. 2007;7(16):1630–42.
10. Taylor AD, et al. Quantitative and simultaneous detection of four foodborne bacterial pathogens with a multi-channel SPR sensor. Biosens Bioelectron. 2006;22(5):752–8.
11. Guidi A, et al. Comparison of a conventional immunoassay (ELISA) with a surface plasmon resonance-based biosensor for IGF-1 detection in cows' milk. Biosens Bioelectron. 2001;16 (9–12):971–7.
12. Wei D, et al. Development of a surface plasmon resonance biosensor for the identification of *Campylobacter jejuni*. J Microbiol Methods. 2007;69(1):78–85.
13. Ferguson JP, et al. Detection of streptomycin and dihydrostreptomycin residues in milk, honey and meat samples using an optical biosensor. Analyst. 2002;127(7):951–6.
14. Crooks SRH, et al. Immunobiosensor-an alternative to enzyme immunoassay screening for residues of two sulfonamides in pigs[dagger]. Analyst. 1998;123(12):2755–7.
15. Nilsson CE, et al. A novel assay for influenza virus quantification using surface plasmon resonance. Vaccine. 2010;28(3):759–66.
16. Naimushin AN, et al. Detection of *Staphylococcus aureus* enterotoxin B at femtomolar levels with a miniature integrated two-channel surface plasmon resonance (SPR) sensor. Biosens Bioelectron. 2002;17(6–7):573–84.
17. Fu E, et al. SPR imaging-based salivary diagnostics system for the detection of small molecule analytes. In: Malamud D, Niedbala RS, editors. Oral-based diagnostics. Blackwell; 2007. p. 335–44.
18. Englebienne P. Use of colloidal gold surface plasmon resonance peak shift to infer affinity constants from the interactions between protein antigens and antibodies specific for single or multiple epitopes. Analyst. 1998;123(7):1599–603.
19. Neuxil P, Reboud J. Palm-sized biodetection system based on localized surface plasmon resonance. Anal Chem. 2008;80(15):6100–3.
20. Hiep HM, et al. A localized surface plasmon resonance based immunosensor for the detection of casein in milk. Sci Technol Adv Mater. 2007;8(4):331–8.
21. Chen S, et al. Ultrahigh sensitivity made simple: nanoplasmonic label-free biosensing with an extremely low limit-of-detection for bacterial and cancer diagnostics. Nanotechnology. 2009;20(43):9.
22. Guo ZR, et al. Fabrication of anti-human cardiac troponin I immunogold nanorods for sensing acute myocardial damage. Nanoscale Res Lett. 2009;4(12):1428–33.
23. Svedendahl M, et al. Refractometric sensing using propagating versus localized surface plasmons: a direct comparison. Nano Lett. 2009;9(12):4428–33.
24. Larsson EM, et al. Nanoplasmonic probes of catalytic reactions. Science. 2009;326 (5956):1091–4.
25. Okamoto T, Yamaguchi I, Kobayashi T. Local plasmon sensor with gold colloid monolayers deposited upon glass substrates. Opt Lett. 2000;25(6):372–4.
26. Nath N, Chilkoti A. A colorimetric gold nanoparticle sensor to interrogate biomolecular interactions in real time on a surface. Anal Chem. 2002;74(3):504–9.
27. Malinsky MD, et al. Chain length dependence and sensing capabilities of the localized surface plasmon resonance of silver nanoparticles chemically modified with alkanethiol self-assembled monolayers. J Am Chem Soc. 2001;123(7):1471–82.

28. Himmelhaus M, Takei H. Cap-shaped gold nanoparticles for an optical biosensor. Sens Actuators B Chem. 2000;63(1–2):24–30.
29. Haes AJ, Van Duyne RP. A nanoscale optical blosensor: sensitivity and selectivity of an approach based on the localized surface plasmon resonance spectroscopy of triangular silver nanoparticles. J Am Chem Soc. 2002;124(35):10596–604.
30. Kretschm E, Raether H. Radiative decay of non radiative surface plasmons excited by light. Z Naturforsch A. 1968;A23(12):2135.
31. Novotny L, Hecht B. Principles of nano optics. Cambridge: Cambridge University Press; 2006.
32. Vukusic PS, Bryanbrown GP, Sambles JR. Surface-plasmon resonance on gratings as a novel means for gas sensing. Sens Actuators B Chem. 1992;8(2):155–60.
33. Cullen DC, Brown RGW, Lowe CR. Detection of immuno-complex formation via surface-plasmon resonance on gold-coated diffraction gratings. Biosensors. 1987;3(4):211–25.
34. Piliarik M, et al. Compact and low-cost biosensor based on novel approach to spectroscopy of surface plasmons. Biosens Bioelectron. 2009;24(12):3430–5.
35. Piliarik M, Homola J. Surface plasmon resonance (SPR) sensors: approaching their limits? Opt Express. 2009;17(19):16505–17.
36. Hickel W, Rothenhausler B, Knoll W. Surface plasmon microscopic characterization of external surfaces. J Appl Phys. 1989;66(10):4832–6.
37. Rothenhausler B, Knoll W. Surface–plasmon microscopy. Nature. 1988;332(6165):615–7.
38. Nelson BP, et al. Surface plasmon resonance imaging measurements of DNA and RNA hybridization adsorption onto DNA microarrays. Anal Chem. 2001;73(1):1–7.
39. Brockman JM, Nelson BP, Corn RM. Surface plasmon resonance imaging measurements of ultrathin organic films. Annu Rev Phys Chem. 2000;51:41–63.
40. Andersson O, et al. Gradient hydrogel matrix for microarray and biosensor applications: an imaging SPR study. Biomacromolecules. 2008;10(1):142–8.
41. Homola J. Surface plasmon resonance based sensors. In: Wolfbeis OS, editor. Springer series on chemical sensors and biosensors. Berlin: Springer; 2006.
42. Rindzevicius T, et al. Plasmonic sensing characteristics of single nanometric holes. Nano Lett. 2005;5(11):2335–9.
43. Bingham JM, et al. Localized surface plasmon resonance imaging: simultaneous single nanoparticle spectroscopy and diffusional dynamics. J Phys Chem C. 2009;113(39):16839–42.
44. Raschke G, et al. Biomolecular recognition based on single gold nanoparticle light scattering. Nano Lett. 2003;3(7):935–8.
45. Mayer KM, et al. A single molecule immunoassay by localized surface plasmon resonance. Nanotechnology. 2010;21(25):255503.
46. Dahlin AB, Tegenfeldt JO, Hook F. Improving the instrumental resolution of sensors based on localized surface plasmon resonance. Anal Chem. 2006;78(13):4416–23.
47. Dahlin AB, et al. High-resolution microspectroscopy of plasmonic nanostructures for miniaturized biosensing. Anal Chem. 2009;81(16):6572–80.
48. Sherry LJ, et al. Localized surface plasmon resonance spectroscopy of single silver triangular nanoprisms. Nano Lett. 2006;6(9):2060–5.
49. Miller MM, Lazarides AA. Sensitivity of metal nanoparticle surface plasmon resonance to the dielectric environment. J Phys Chem B. 2005;109(46):21556–65.
50. Kvasnicka P, Homola J. Optical sensors based on spectroscopy of localized surface plasmons on metallic nanoparticles: sensitivity considerations. Biointerphases. 2008;3(3):FD4–11.
51. Johnson PB, Christy RW. Optical-constants of noble-metals. Phys Rev B. 1972;6(12):4370–9.
52. Shegai T, et al. Angular distribution of surface-enhanced Raman scattering from individual Au nanoparticle aggregates. ACS Nano. 2011;5(3):2036–41.
53. Shegai T, et al. Unidirectional broadband light emission from supported plasmonic nanowires. Nano Lett. 2011;11(2):706–11.
54. Brian B, et al. Sensitivity enhancement of nanoplasmonic sensors in low refractive index substrates. Opt Express. 2009;17(3):2015–23.
55. Alaverdyan Y, et al. Optical antennas based on coupled nanoholes in thin metal films. Nat Phys. 2007;3(12):884–9.

56. Dmitriev A, et al. Enhanced nanoplasmonic optical sensors with reduced substrate effect. Nano Lett. 2008;8(11):3893–8.
57. Aouani H, et al. Crucial role of the adhesion layer on the plasmonic fluorescence enhancement. ACS Nano. 2009;3(7):2043–8.
58. Jiao XJ, et al. Localization of near-field resonances in bowtie antennae: influence of adhesion layers. Plasmonics. 2009;4(1):37–50.
59. Zhang SP, et al. Substrate-induced Fano resonances of a plasmonic: nanocube: a route to increased-sensitivity localized surface plasmon resonance sensors revealed. Nano Lett. 2011;11(4):1657–63.
60. Sepúlveda B, Lechuga LM, Armelles G. Magnetooptic effects in surface-plasmon-polaritons slab waveguides. J Lightwave Technol. 2006;24(2):945.
61. Jung LS, et al. Quantitative interpretation of the response of surface plasmon resonance sensors to adsorbed films. Langmuir. 1998;14(19):5636–48.
62. Raether H. Surface-plasmons on smooth and rough surfaces and on gratings Springer tracts in modern physics, Vol. 111. New York: Springer; 1988. p. 1–133.
63. Xu HX, Kall M. Modeling the optical response of nanoparticle-based surface plasmon resonance sensors. Sens Actuators B Chem. 2002;87(2):244–9.
64. Rindzevicius T, et al. Long-range refractive index sensing using plasmonic nanostructures. J Phys Chem C. 2007;111(32):11806–10.
65. Jain PK, Huang WY, El-Sayed MA. On the universal scaling behavior of the distance decay of plasmon coupling in metal nanoparticle pairs: a plasmon ruler equation. Nano Lett. 2007;7 (7):2080–8.
66. Murray WA, Auguie B, Barnes WL. Sensitivity of localized surface plasmon resonances to bulk and local changes in the optical environment. J Phys Chem C. 2009;113(13):5120–5.
67. Sonnichsen C, et al. Drastic reduction of plasmon damping in gold nanorods. Phys Rev Lett. 2002;88(7):077402.
68. Evlyukhin AB, et al. Detuned electrical dipoles for plasmonic sensing. Nano Lett. 2010;10 (11):4571–7.
69. Henzie J, Lee MH, Odom TW. Multiscale patterning of plasmonic metamaterials. Nat Nanotechnol. 2007;2(9):549–54.
70. Sonnefraud Y, et al. Experimental realization of subradiant, superradiant, and Fano resonances in ring/disk plasmonic nanocavities. ACS Nano. 2010;4(3):1664–70.
71. Hao F, et al. Symmetry breaking in plasmonic nanocavities: subradiant LSPR sensing and a tunable Fano resonance. Nano Lett. 2008;8(11):3983–8.
72. Hao F, et al. Tunability of subradiant dipolar and Fano-type plasmon resonances in metallic ring/disk cavities: implications for nanoscale optical sensing. ACS Nano. 2009;3(3):643–52.
73. Dondapati SK, et al. Label-free biosensing based on single gold nanostars as plasmonic transducers. ACS Nano. 2010;4(11):6318–22.
74. Chen S, et al. Plasmon-enhanced colorimetric ELISA with single molecule sensitivity. Nano Lett. 2011;11(4):1826–30.
75. Xu HX, et al. Spectroscopy of single hemoglobin molecules by surface enhanced Raman scattering. Phys Rev Lett. 1999;83(21):4357–60.
76. Rissin DM, et al. Single-molecule enzyme-linked immunosorbent assay detects serum proteins at subfemtomolar concentrations. Nat Biotechnol. 2010;28(6):595–9.
77. Curto AG, et al. Unidirectional emission of a quantum dot coupled to a nanoantenna. Science. 2010;329(5994):930–3.
78. Luk'yanchuk B, et al. The Fano resonance in plasmonic nanostructures and metamaterials. Nat Mater. 2010;9(9):707–15.
79. Kabashin AV, et al. Plasmonic nanorod metamaterials for biosensing. Nat Mater. 2009;8 (11):867–71.
80. Dahlin AB, et al. Synchronized quartz crystal microbalance and nanoplasmonic sensing of biomolecular recognition reactions. ACS Nano. 2008;2(10):2174–82.

81. Jonsson MP, Jonsson P, Hook F. Simultaneous nanoplasmonic and quartz crystal microbalance sensing: analysis of biomolecular conformational changes and quantification of the bound molecular mass. Anal Chem. 2008;80(21):7988–95.
82. Shopova SI, et al. Plasmonic enhancement of a whispering-gallery-mode biosensor for single nanoparticle detection. Appl Phys Lett. 2011;98(24):243104.
83. Vollmer F, Arnold S. Whispering-gallery-mode biosensing: label-free detection down to single molecules. Nat Methods. 2008;5(7):591–6.
84. Min BK, et al. High-Q surface-plasmon-polariton whispering-gallery microcavity. Nature. 2009;457(7228):455–8.
85. White IM, Gohring J, Fan XD. SERS-based detection in an optofluidic ring resonator platform. Opt Express. 2007;15(25):17433–42.

Part I
Biological and Chemical Sensing

Chapter 2
Exploring the Unique Characteristics of LSPR Biosensing

Julia M. Bingham*, W. Paige Hall*, and Richard P. Van Duyne

Abstract Plasmonic biosensors based on the localized surface plasmon resonance (LSPR) of metal nanoparticles have been developed using both nanoparticle arrays and single nanoparticles. We introduce LSPR biosensing by describing the initial experiments performed using both model systems and disease biomarkers. LSPR shift-enhancement methods, exploitation of the short electromagnetic field decay length, and single nanoparticle sensors are discussed as pathways to further exploit the strengths of LSPR biosensing. Coupling molecular identification to LSPR spectroscopy is a significant aspect of biosensing. Therefore, examples from surface-enhanced Raman spectroscopy and laser desorption ionization mass spectrometry are provided. This chapter highlights examples which emphasize the unique characteristics of LSPR biosensing.

Introduction

In 1998, the first use of localized surface plasmon resonance (LSPR) biosensing was reported by Englebienne [1]. At that time, the Van Duyne group had been utilizing the unique properties of LSPR for over 2 decades, but from within the framework of a different field: that of surface-enhanced Raman spectroscopy (SERS). Beginning with the successful observation and explanation of surface-enhanced Raman

*The authors Julia M. Bingham and W. Paige Hall contributed equally to this work.

J.M. Bingham
Department of Chemistry, Saint Xavier University, 3700 W 103rd Street, Chicago, IL 60655, USA
e-mail: bingham@sxu.edu

W.P. Hall • R.P. Van Duyne (✉)
Department of Chemistry, Northwestern University, 2145 Sheridan Road, Evanston, IL 60208, USA
e-mail: windsorhall2010@u.northwestern.edu; vanduyne@northwestern.edu

A. Dmitriev (ed.), *Nanoplasmonic Sensors*, Integrated Analytical Systems,
DOI 10.1007/978-1-4614-3933-2_2,

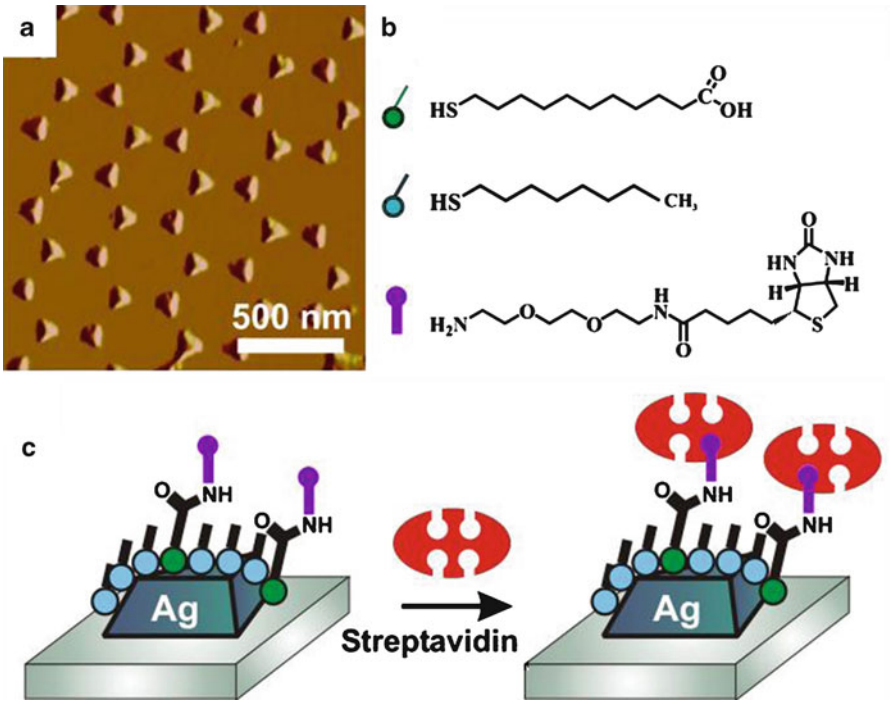

Fig. 2.1 Nanoparticle substrates for LSPR sensing. (**a**) AFM image of a Ag PPA. (**b**) SAM molecules used for biosensing: 11-MUA (*green*), octanethiol (*blue*) and amine-functionalized biotin (*purple*). (**c**) Streptavidin binding to biotinylated surface. Reprinted with permission from ref. [11]. Copyright 2002 American Chemical Society

scattering in 1977 by Van Duyne [2] and Creighton and colleagues [3], our group began fabricating roughened silver surfaces displaying LSPR properties for use in SERS. In 1993, we reported our first use of Ag film over nanosphere (AgFON) surfaces that had more well-defined surface roughness and periodicity [4]. These surfaces were made by depositing over one or more layers of nanoscale polystyrene spheres. Two years later, we began depositing silver films over monolayers of polystyrene spheres and removing the spheres from the substrate post metal deposition, creating arrays of silver nanoprisms on the substrate surface (Fig. 2.1a) [5]. These periodic particle arrays (PPAs) displayed the hallmarks of a plasmonic sensing material: selective wavelength absorption, as evidenced by a distinct maximum in the extinction band in the visible wavelength region, and enhanced electromagnetic fields at the particle surface, as evidenced by both theoretical calculations [6, 7] and experimental observations of enhanced Raman scattering of molecules at the particle surfaces [8].

While Englebienne had demonstrated a new application for plasmonic materials, he did not exploit the shift in extinction maximum for unaggregated colloids. The colorimetric properties of gold colloids were already well known, and had been used previously as a reporter for enzyme immunoassays [9] and DNA

hybridization [10]. Bioassays performed using solution-phase gold colloids were inherently limited, however, by the finite stability of the colloids themselves. For example, high ionic concentrations lead to colloid aggregation and precipitation, and the basic pH required for biomolecule-colloid attachment can denature proteins. Several research groups, including our own, had developed methods of fabricating surfaces coated with colloidal metal structures that could overcome the limitations of solution-phase colloids, but these were primarily used in SERS applications. In 1999, we began to tune the properties of our film-over-nanosphere (FON) and PPA substrates in order to optimize their optical properties, and we demonstrated the powerful refractive index sensitivity of these surfaces [11, 12]. Three years later, we applied these plasmonic surfaces to the detection of biotin-streptavidin interactions [11], in what was the first quantitative report of $\Delta\lambda_{max}$ for LSPR biosensing.

Because proteins have a relatively high refractive index (RI ~ 1.5), probing protein interactions was a natural choice for utilizing the refractive index sensitivity of nanoparticles. In addition, the short electromagnetic (EM) field decay length (l_d ~ 5–10 nm) of localized surface plasmons is on the same size scale as proteins, making biomolecules an ideal sensing target. In an early demonstration of LSPR biosensing using silver PPAs, Haes and Van Duyne demonstrated the quantitative detection of streptavidin-biotin interactions (Fig. 2.1c) [11]. The LSPR extinction maximum (λ_{max}) shifted to redder wavelengths upon streptavidin (SA) binding, with the magnitude of the shift increasing with SA concentration.

Plotting these shifts as a function of SA concentration and fitting to (2.1)

$$\frac{\Delta R}{\Delta R_{max}} = \frac{K_{a,surf}[SA]}{1 + K_{a,surf}[SA]} \tag{2.1}$$

revealed a binding constant, $K_{a,surf}$, of 10^{11} M^{-1} (Fig. 2.2), where ΔR is the measured response and ΔR_{max} is the maximum response possible. The maximum response, ΔR_{max}, was calculated from (2.2)

$$\Delta R = m(n_A - n_E)\left[1 - \exp\left(\frac{-2d}{l_d}\right)\right] \tag{2.2}$$

in which m is the refractive index sensitivity, n_A is the adsorbate refractive index, n_E is the external environment refractive index (N_2 in this experiment), d is the adsorbate layer thickness, and l_d is the decay length thickness. Not only does (2.2) determine the maximum response expected, but it also depicts which experimental factors affect the LSPR λ_{max} response: refractive index sensitivity of the nanoparticles, change in refractive index, decay length of the nanoparticles, and adsorbate thickness. Based on measurements of the standard deviation in λ_{max}, the smallest detectable wavelength shift for this system was 1.5 nm, providing a limit of detection of less than 1 pM. In subsequent work, Riboh et al. characterized biotin and anti-biotin interactions using the same silver nanoprism arrays [12]. This work revealed larger shifts for anti-biotin binding than for SA binding, a result that was expected based on the larger size of antibiotin (MW ~ 150 kDa) compared to SA (MW ~ 63 kDa). However, despite larger shifts in λ_{max}, the detection limit for

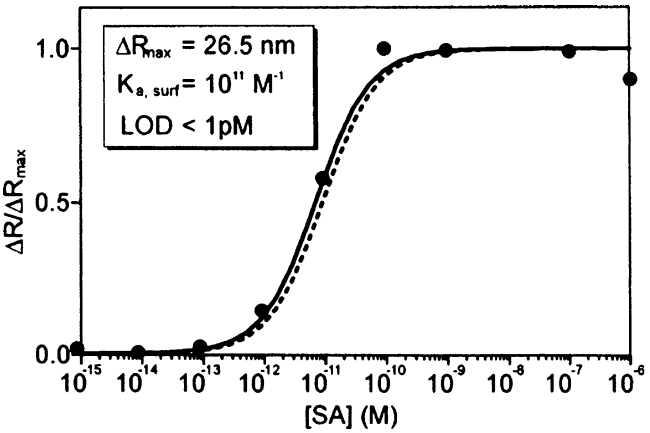

Fig. 2.2 Normalized LSPR shift, $\Delta R/\Delta R_{max}$, vs. [SA] response curve for the specific binding of SA to a biotinylated Ag nanobiosensor. The normalized experimental LSPR responses (*solid circles*) were calculated by subtracting $R_{layer\ 1}$ for the biotinylated Ag nanobiosensor from $R_{layer\ 2}$ after exposure to SA and dividing by ΔR_{max}. All extinction measurements were collected in a N_2 environment. Reprinted with permission from ref. [11]. Copyright 2002 American Chemical Society

this system was only ~1 nM due to the weaker binding affinity between biotin and anti-biotin ($K_a = 4.5 \times 10^7\ M^{-1}$).

Although biotin-streptavidin and biotin-anti-biotin interactions provide an ideal system for biosensor development due to their well-studied interactions and predictable binding affinities, these systems have limited utility in real-world sensing applications. In a compelling demonstration of the potential of LSPR sensors to be used as clinical diagnostic devices for disease detection, Haes et al. detected an oligomeric form of the Alzheimer's disease biomarker amyloid beta, known as amyloid-beta derived diffusible ligands (ADDLs) [13]. Using a sandwich assay format analogous to an enzyme-linked immunosorbent assay (ELISA), the binding of synthetic ADDLs to an antibody-functionalized silver nanoprism array was detected by redshifts in the nanoprism λ_{max}, the magnitude of which depended on ADDL concentration. The concentration of synthetic ADDLs exposed to the sensor was varied from 10^{-15} to 10^{-5} M in order to characterize the sensor response and determine affinity constants. Two affinity constants emerged with values on the order of 10^8 and $10^{12}\ M^{-1}$, with variations most likely due to size-dependent differences in epitope recognition. Finally, the LSPR sensor was used to detect ADDLs in clinical samples from both living and deceased patients. Although the total number of samples evaluated was too small to define sensor accuracy, a comparison between diseased samples and age matched controls revealed significant differences in sensor response. In an assay for the presence of ADDLs in cerebral spinal fluid (CSF), the Alzheimer's sample induced a total λ_{max} shift of 33.9 nm, compared to a shift of 7.2 nm for the aged-matched control. Although additional studies are needed to prove that the LSPR sensor can meet standards

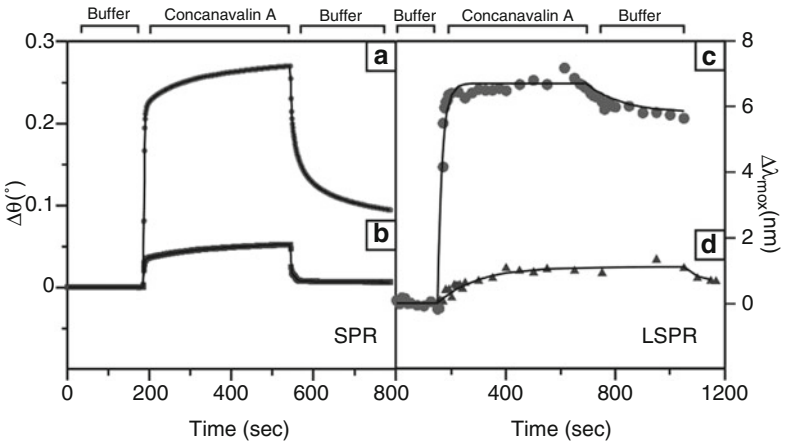

Fig. 2.3 Real-time response of sugar-functionalized sensor as 19 μM of Concanavalin A was injected in the cell following buffer injection. (**a**) Mannose-functionalized SPR sensor, (**b**) galactose-functionalized SPR sensor, (**c**) mannose-functionalized Ag nanosensor, and (**d**) galactose-functionalized Ag nanosensor. The points are the experimental data. The *solid line* for the SPR measurement is composed of straight line segments connecting the experimental data. The *solid line* in LSPR measurement is a first-order adsorption kinetics fit to the data and should only be interpreted as a guide to the eye. Reprinted with permission from ref. [14]. Copyright 2004 American Chemical Society

required for clinical detection of Alzheimer's disease, this study demonstrated the potential for LSPR assays to fill unmet needs in disease detection.

Finally, as the field of LSPR biosensing continues to grow, it is important to ask: what advantages do we gain by using nanoparticle-based sensors? As the predecessor to LSPR, surface plasmon resonance (SPR) sensors serve as a point of comparison. The introduction chapters of the book outlined the differences in these two sensing modalities, including the large differences in EM field decay length at the sensor surface. These differences in the EM field decay length between LSPR and SPR surfaces create an important advantage for LSPR sensing when detecting nanoscale analytes. As the name suggests, the LSPR response is dominated by events happening within a highly localized (~5–10 nm) region at the nanoparticle surface. Binding of nanoscale analytes, such as proteins, induces large shifts in the LSPR λ_{max}, while refractive index changes in the bulk media do not. Work by Yonzon et al. demonstrated the impact of these sensing volume differences in a study describing the binding of Concanavalin A to saccharide monolayers [14]. SPR and LSPR sensors functionalized with either mannose or galactose were exposed to micromolar concentrations of the lectin-binding protein Concanavalin A. During the dissociation phase, the SPR signal decreased by 60%, while the LSPR signal decreased by only 14% (Fig. 2.3). The larger signal decrease for the SPR sensor can be explained by the fact that a larger fraction of the SPR response arises from bulk media changes due to its relatively long EM field decay length. In fact, it was shown that by changing the aspect ratio of the silver

nanoprisms of the LSPR sensor, the EM field decay length can be tuned to allow more or less detection of bulk media changes [6, 15]. For applications in which the analyte is small (<10 nm) and binding occurs close to the substrate surface, LSPR provides improved sensitivity and spatial resolution compared to its SPR counterpart. That sensitivity, coupled with the vast variety of plasmonic nanostructures and surface chemistries available for use in LSPR sensing, make nanoparticles an ideal sensing substrate for a multitude of systems. The following sections of this chapter will outline how the unique properties of LSPR sensors can be exploited to achieve even greater sensitivity and used in conjunction with other analytical techniques to achieve molecular identification.

Improving the Limit of Detection of LSPR Sensors

Methods to Enhance the LSPR Shift

The introduction discussed the first experiments in LSPR biosensing that were based on the local refractive index change induced by biomolecules adsorbing close to the nanoparticle surface. The change in the local dielectric due to molecule adsorption was measured by a shift in the LSPR λ_{max}. An ideal biosensor is both specific and sensitive to the target analyte. While experiments continually aim to quantify and improve biosensor specificity, sensitivity is often inherent to the specific biosensor system. Therefore, new methods are examined to increase the biosensor sensitivity; that is, increase the λ_{max} shift from the same amount of analyte.

The LSPR λ_{max} shifts are dependent on the nanoparticle sensitivity and the size of the bound molecules. Nanoparticle sensitivity can be experimentally determined by systematically changing the refractive index environment—for example, by adding successive layers of a dielectric material or changing the ambient solvent—and plotting λ_{max} shifts as a function of a refractive index. A linear fit to the data will reveal the nanoparticle sensitivity factor, m, which is particular to nanoparticle composition, size, and morphology. The linear relationship is described in (2.3),

$$\Delta\lambda_{max} = m\Delta n \tag{2.3}$$

where n is the refractive index. In general, nanoparticles with a higher aspect ratio are more sensitive to the local dielectric environment [6, 15]. The shift is also roughly proportional to the adsorbate molecule mass [6, 7, 15]. As such, a protein is expected to produce a significantly larger LSPR λ_{max} shift than a small molecule. However, in the last several years, methods have been developed to detect unexpectedly large shifts from molecules binding to the metal nanoparticle [16–18]. These large shifts are the result of a chromophore coupling to the LSPR of a nanoparticle and have also been observed from small molecules binding to protein receptors on metal nanoparticles. A different way to enhance the λ_{max} shift is to use plasmonic labels such as gold nanoparticles [11]. This section discusses in detail the methods to increase the LSPR λ_{max} shift using both resonant molecules and plasmonic labels.

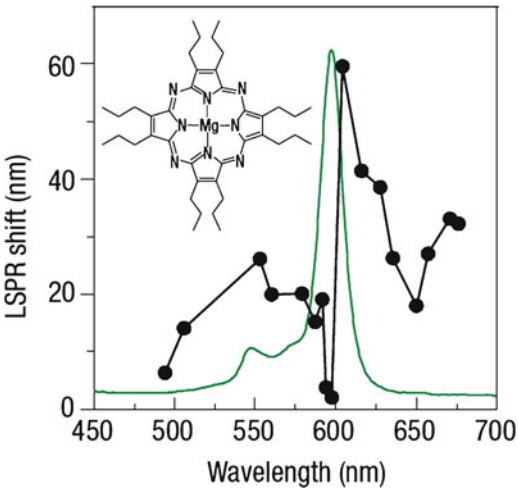

Fig. 2.4 LSPR shift induced by a monolayer of MgPz (*inset*) is depicted by the *black line* with *solid black circles*. The *green line* is the solution absorption spectrum of MgPz. Reprinted with permission from ref. [16]. Copyright 2006 American Chemical Society

Resonant Molecules

The interaction between the molecular resonance of a chromophore and the plasmon resonance of a nanoparticle was examined using several different chromophores [16]. A monolayer of non-resonant molecules would be expected to yield a shift consistent with (2.2). However, when a monolayer of chromophores resonant with the LSPR was probed, shifts were significantly larger or smaller than expected and were highly dependent on the overlap of the chromophore absorbance and plasmon resonance.

Work by Haes et al. examined the interaction between the molecular resonance of [2,3,7,8,12,13,17,18-octakis(propyl)porphyrazinato]magnesium (II) (MgPz), and the plasmon resonance of Ag nanoparticles [16]. As depicted in Fig. 2.4, the experiments demonstrated that the shift was highly dependent on the amount of overlap between the molecular absorbance of MgPz and the LSPR. In Fig. 2.4, the λ_{max} shift due to the MgPz monolayer was plotted as a function of initial LSPR λ_{max} with the molecular absorbance of MgPz overlaid. It was observed that when the absorbance maximum of MgPz directly overlapped with the LSPR λ_{max}, only a 2 nm redshift was observed. However, when the LSPR λ_{max} was slightly redder than the molecular absorbance peak, a large redshift of ~60 nm was observed. These resonant cases contrast drastically with the non-resonant conditions (where there is little overlap between the molecular chromophore resonance and Ag nanoparticle plasmon resonance), in which ~20 nm redshifts were observed. It was determined that the λ_{max} shift observed from a monolayer of MgPz tracked with the real component of the wavelength-dependent refractive index, which was extracted by the Kramers-Kronig transformation. (Note that the molecular absorbance spectrum is representative of the imaginary component of the refractive index.) The measured shift was largest when the real part of

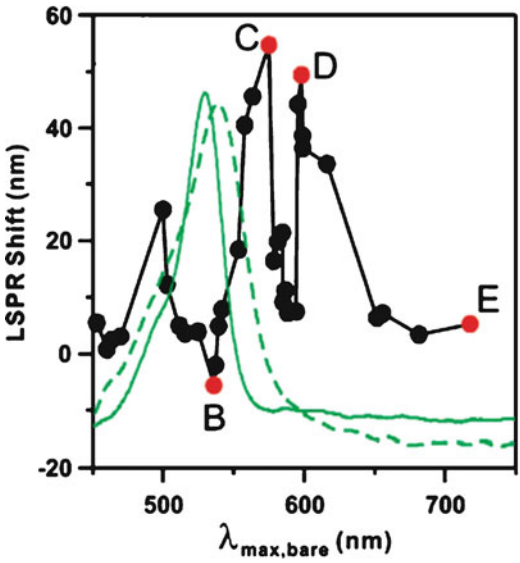

Fig. 2.5 The wavelength-dependent LSPR shift induced by a monolayer of R6G is depicted by the *black line* with *solid black circles*. The *solid green line* is the solution absorption spectrum of R6G in ethanol. *Green dashed line* is the absorption spectrum of R6G on a 200 nm Ag film. Reprinted with permission from ref. [18]. Copyright 2007 American Chemical Society

the wavelength-dependent refractive index of the dye was greatest. These experiments demonstrated the LSPR shift enhancement that is possible by using a molecule resonant with the LSPR, a significant result considering many biological targets containing chromophores.

To extend the chromophore-plasmon research to a dye used in many SERS experiments (especially single-molecule SERS), Zhao et al. used rhodamine 6G (R6G) to probe the chromophore-plasmon interaction in a similar fashion to the MgPz work [18]. The LSPR λ_{max} shift due to a monolayer of R6G was plotted as a function of initial LSPR λ_{max} along with the absorbance spectrum of R6G (Fig. 2.5). It is significant to note that three maxima were observed in the LSPR shift, whereas only two maxima are apparent in the R6G absorbance spectrum. Contrasting with results from the MgPz work, the LSPR shift from R6G did not track with only the real component of the dielectric (extracted by the Kramers-Kronig transformation). To probe the unique spectral features, the absorbance was measured using different R6G concentrations on a Ag surface and it was determined that three different forms of R6G were present: H-dimers, J-dimers, and monomers, each with slightly different absorbances. The three maxima of the LSPR λ_{max} shift in Fig. 2.5 were attributed to the three forms of R6G present on the Ag nanoparticle surface. Therefore, it was concluded that the LSPR λ_{max} shifts tracked with the dielectric constants (real and imaginary) of the three forms of dimers. These findings demonstrated that LSPR spectroscopy could provide information on electronic structural changes of adsorbates.

The work based on chromophores coupled to Ag nanoparticles motivated the study by Zhao et al. to examine the shift observed when the small molecule camphor (molecular weight = 152.25 g mol^{-1}) bound to the protein cytochrome

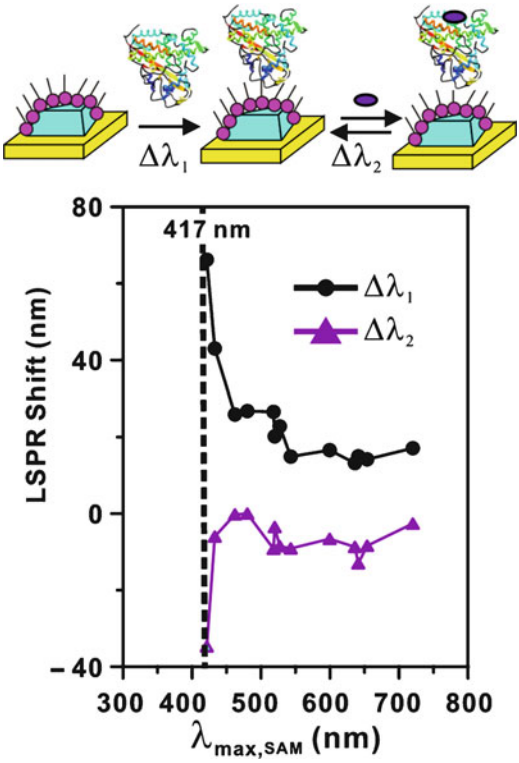

Fig. 2.6 Schematic representation of camphor binding to CYP101 on a Ag nanoparticle. Plots of the LSPR shift vs. $\lambda_{max,SAM}$ of CYP101 binding to the nanoparticle ($\Delta\lambda_1$) and camphor binding to CYP101 ($\Delta\lambda_2$). Reprinted with permission from ref. [17]. Copyright 2006 American Chemical Society

P450cam (CYP101) [17]. The absorption spectrum maximum of CYP101 changes from 417 to 391 nm upon camphor binding. The peak shift is due to camphor replacing the water coordinated to the Fe^{3+} of CYP101, causing the spin state of the heme iron to change from low to high spin [19–21].

To probe the effect of the molecular absorbance change of CYP101-Fe^{3+} on the LSPR of nanoparticles, CYP101-Fe^{3+} was covalently attached to a carboxylic acid-terminated SAM on the Ag nanoparticles via EDC coupling chemistry. Camphor was then added to the CYP101-functionalized nanoparticles. The LSPR λ_{max} shift was measured after CYP101 bound to the SAM-Ag nanoparticle surface ($\Delta\lambda_1$) and after camphor binding to the CYP101 on the Ag surface ($\Delta\lambda_2$). Shifts were measured relative to the initial λ_{max} of the SAM-functionalized Ag nanoparticles ($\lambda_{max,SAM}$) and the experiment was repeated for multiple Ag nanoparticle samples with varying LSPR λ_{max} to probe the interaction of overlapping molecular and plasmon resonances. The results, depicted in Fig. 2.6, demonstrated the shifts were highly dependent on the LSPR $\lambda_{max,SAM}$ relative to the molecular absorbance of CYP101. When the plasmon was slightly red-shifted from the CYP101 absorbance, a large shift of over 60 nm was observed due to CYP101 binding. As the LSPR λ_{max} moved farther from the CYP101 absorption, the red-shift ($\Delta\lambda_1$) decreased dramatically. When camphor bound to the CYP101, a blueshift was observed ($\Delta\lambda_2$).

When the LSPR $\lambda_{max,SAM}$ was close to the CYP101 absorbance, a large blueshift (nearly 40 nm) occurred. The $\Delta\lambda_2$ decreased as the plasmon resonance was tuned farther from the molecular absorbance; however, a blueshift was still observed.

If camphor did not affect the electronic state of CYP101, a small redshift would have been expected, given an increase in the local refractive index. However, the camphor altered the molecular absorbance of the CYP101 when it bound, specifically shifting the absorbance to bluer wavelengths and therefore blue-shifting the LSPR λ_{max} [17]. This report was significant, as a small molecule binding to a protein may not have been a large enough refractive index change to induce a visible LSPR shift.

Plasmonic Labels

While the λ_{max} shift enhancement due to resonant interactions between chromophoric molecules and nanoparticle plasmons is dramatic, this signal enhancement technique is limited to dyes and biomolecules with specific absorption properties. To observe the same type of signal enhancement from non-chromophoric molecules, it was necessary to develop an alternative technique. Inspired by previous work on SPR sensors [22–24], we decided to explore the properties of nanoparticle-labeled biomolecules. In 1993 Buckle et al. described the first reported use of gold nanoparticle-labeled proteins for SPR response enhancement [24]. Human serum albumin (HSA) proteins were electrostatically conjugated to gold colloids, and then exposed to an SPR surface functionalized with anti-HSA antibodies. The detection limit for this assay was improved 1,000-fold compared to the nanoparticle-free assay.

Due to the very short (5–10 nm) decay length of LSPR sensors, large sensitivity losses arise when detection platforms utilize longer surface ligands or molecules, such as in the sandwich-style ELISA, that place the detecting molecule far from the nanoparticle surface and outside the sensing volume. We therefore hypothesized that nanoparticle-labeled detection molecules could have a large impact on the LSPR sensor λ_{max} shift by increasing the analyte mass close to the nanoparticle surface. To test this hypothesis, we used the well-studied biotin/anti-biotin binding pair. Biotin was covalently immobilized on a Ag PPA surface, and subsequently exposed to anti-biotin that had been electrostatically conjugated to 20 nm Au colloids. As expected, the λ_{max} shift was enhanced, with the degree of enhancement varying with the concentration of anti-biotin-nanoparticle (AB-NP) conjugate (Fig. 2.7) [25]. The enhancement peaked near 400%, at a concentration close to the K_D of the biotin/anti-biotin interaction.

Based on previous theoretical [26–28] and experimental [26, 28–30] observations, we attributed the enhancement to two sources: (1) the larger refractive index of nanoparticle-labeled antibodies compared to un-labeled antibodies, and (2) plasmonic coupling between the Ag PPA and the Au colloid label. In contrast to a simple dielectric label (such as a glass bead), Au nanoparticle labels have the potential to induce much larger signal enhancements due to plasmonic coupling.

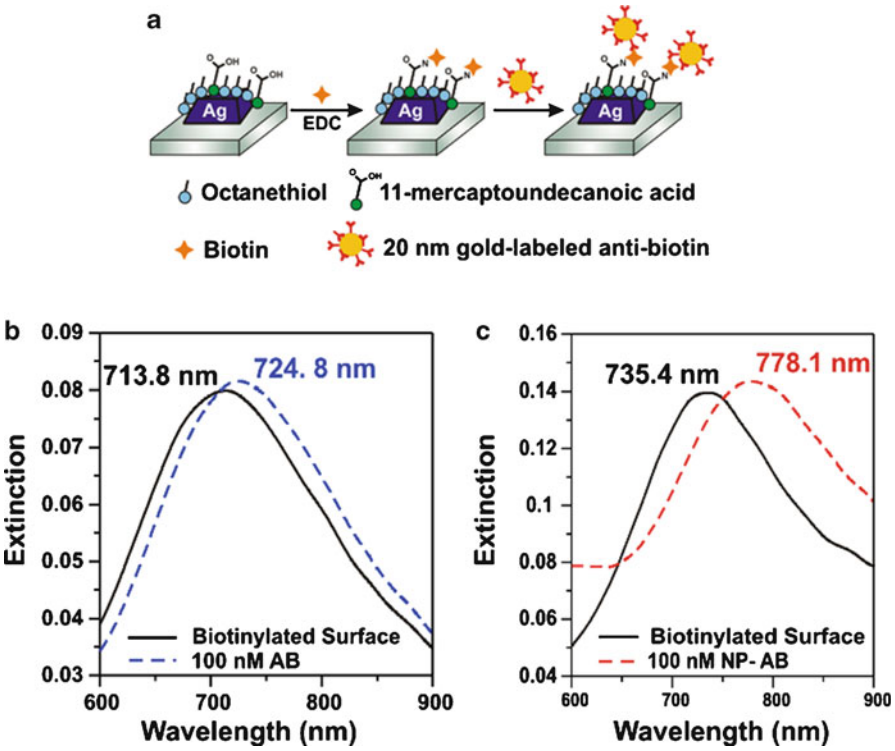

Fig. 2.7 Experiment schematic and LSPR spectra. (**a**) Biotin is covalently linked to the nanoparticle surface using EDC coupling agent, and anti-biotin labeled gold nanoparticles are subsequently exposed to the surface. LSPR spectra are collected before and after each step. (**b**) LSPR spectra before (*solid black*) and after (*dashed blue*) binding of native anti-biotin, showing a $\Delta\lambda_{max}$ of 11 nm. (**c**) LSPR spectra before (*solid black*) and after (*dashed red*) binding of anti-biotin labeled nanoparticles, showing a $\Delta\lambda_{max}$ of 42.7 nm. Adapted and reprinted with permission from ref. [25]. Copyright 2011 American Chemical Society

The existence of plasmonic coupling is evident in this study by the increase in full width half max (FWHM) of the LSPR sensor extinction peak that occurs upon AB-NP binding. The FWHM broadening is not observed for un-labeled anti-biotin. By optimizing both nanoparticle substrate and nanoparticle label in order to achieve the greatest plasmon overlap, we believe that even larger shift enhancements than what were reported in this study can be realized.

A fortuitous by-product of the antibody-nanoparticle conjugation was an increase not only in λ_{max} shift, but also in binding affinity between biotin and anti-biotin. This increase can be attributed to the antibody polyvalency gained upon nanoparticle conjugation. Based on surface area calculations, each gold colloid is functionalized with between 8 and 30 antibodies, depending on antibody orientation. This means that each binding event between the biotinylated surface and the gold colloids is likely mediated by more than one antibody. It is well known that

polyvalent antibodies bind to antigens with higher affinity compared to antibody monomers. Because biosensor sensitivity is inherently dependent on the strength of the binding interaction between surface and analyte, the improved affinity induced by nanoparticle-antibody conjugation offers an additional source of sensitivity for the plasmonic label-enhanced LSPR sensor.

Exploiting the Short EM Decay of LSPR

As mentioned briefly in the introduction, one of the chief advantages of LSPR sensors is the very short decay length of the EM field at the nanoparticle surface. This short decay length is an inherent property to LSPR, and arises due to the confined nature of the plasmons in a nanoscale material [31]. As a result of this short decay length, LSPR sensors are most sensitive to refractive index changes occurring within 5–10 nm of the nanoparticle surface [6, 7]. This highly localized sensitivity confers huge advantages when the analyte in question is on the nanoscale, or when refractive index changes occur very close to the nanoparticle surface. In this section we discuss the advantages of LSPR in detecting nanoscale materials utilizing protein conformational studies by Hall et al. as the prime example [32]. Additionally, the short EM field decay length of LSPR can even be advantageous for gaseous analytes incorporated into a partition layer.

Protein Conformational Changes

Biological and materials research often requires tools that can characterize dynamic changes in protein conformation and immobilized molecules. Techniques based on NMR [33], FRET [34], and X-ray scattering [35] are widely used. SPR sensors have been used to detect conformational changes in proteins, but due to the large sensing volume at the SPR surface, detection generally requires that the protein be immobilized in 3D dextran layers, where observed signals are convoluted by matrix effects [36]. LSPR sensors have been used to detect lipid membrane formation over a hole-array substrate [37] and solution-phase colloid aggregation induced by protein denaturation [38]. LSPR-based approaches are advantageous because, in addition to highly localized detection capabilities, they provide an intense signal that does not bleach and allow non-destructive measurements over long periods of time. Limits of detection of LSPR sensors have been reduced in recent years by the development of instrumentation capable of accurately measuring spectral shifts of only hundredths of nanometers [32, 39]. Chapter 11 of this book highlights some of the advances that have been made in LSPR instruments, advances that contributed to our ability to detect small wavelength shifts in response to conformational changes.

The intracellular calcium-binding protein calmodulin (CaM) was used to illustrate the sensitivity of LSPR sensors to surface-adsorbate conformation. Calmodulin

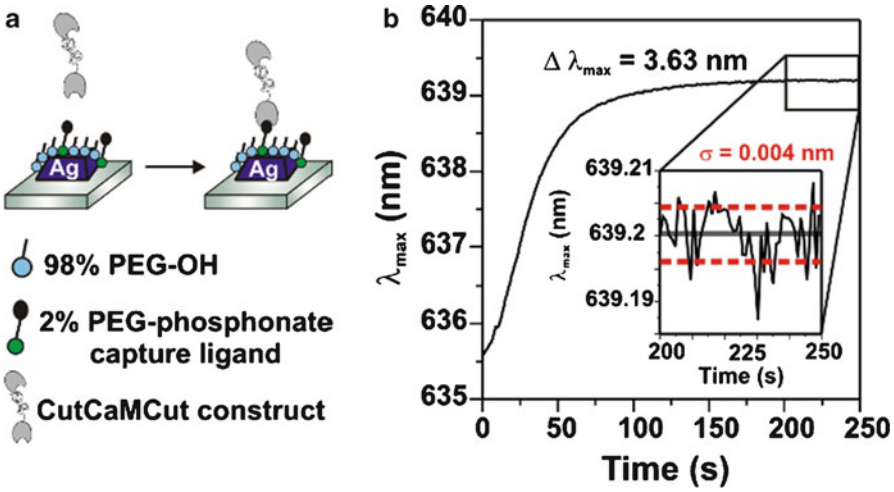

Fig. 2.8 (**a**) Schematic representation of the binding of the CutCaMCut fusion protein to a phosphonate functionalized Ag nanoparticle sensor; (**b**) plot of changes in λ_{max} in real-time as CutCaMCut binds to the sensor surface in solution. *Inset*: Closeup after the reaction is complete, showing a noise level of 4×10^{-3} nm averaged over 50 s. Reprinted with permission from ref. [32]. Copyright 2008 American Chemical Society

regulates cellular signaling pathways via calcium ion-dependent switching between open and closed conformational states. A recombinant cutinase-calmodulin-cutinase (CutCaMCut) construct was used to flexibly tether CaM to the surface [40] (Fig. 2.8a). Binding of CutCaMCut to the LSPR sensor was accompanied by a 3.6 nm redshift in the sensor λ_{max}, with a standard deviation in λ_{max} of only 4×10^{-3} nm (Fig. 2.8b). Thus, the signal:noise ratio for this immobilization was over 900.

Exposure of the CutCaMCut functionalized LSPR surface to 2 mM $CaCl_2$ resulted in a λ_{max} redshift of 2.2 nm. This redshift was reversed upon chelation of the calcium ions using 2 mM ethylene glycol tetraacetic acid (EGTA). The λ_{max} shifts induced by calcium binding and unbinding were reproducible over several cycles, with a standard deviation in $\Delta\lambda_{max}$ of 0.18 nm (Fig. 2.9b). To verify that the changes in λ_{max} were a result of protein conformation, two controls were performed using a sensor with no surface bound protein and a sensor functionalized with a non-calcium sensitive cutinase-cutinase (CutCut) construct. Both controls exhibited only small reversible $\Delta\lambda_{max}$ changes which were opposite in trend to what was observed in the presence of calmodulin, demonstrating that the conformational changes in calmodulin were the source of the observed spectral shifts.

Finally, the ability to monitor λ_{max} in real-time enabled the determination of opening and closing rates for the calmodulin conformational change (Fig. 2.9c). First-order exponential fits to the real-time λ_{max} shifts using (2.4),

$$\lambda_{max} = \lambda_{max(0)} + A\exp(-t/\tau) + Bt \tag{2.4}$$

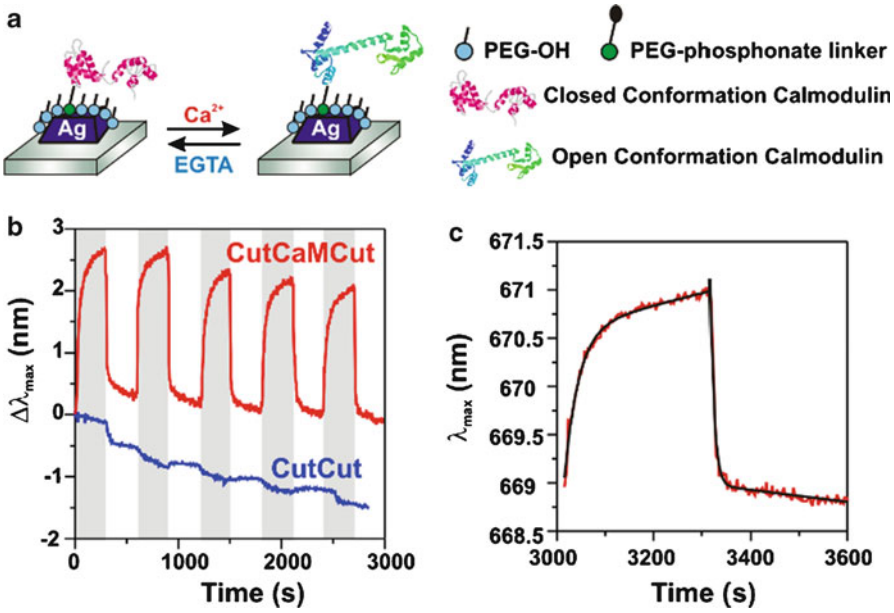

Fig. 2.9 (**a**) Schematic representation of the reversible conformational changes of CutCaMCut immobilized on the LSPR nanosensor. (**b**) Plot of changes in the extinction maximum (1 Hz collection) of the sensor as the buffer is cycled between 2 mM $CaCl_2$ and 2 mM EGTA, a calcium chelator. (**c**) Closeup of one $CaCl_2$/EGTA cycle, with an exponential fit of $\lambda_{max} = \lambda_{max(0)} + A \exp(-t/\tau) + Bt$ (*black*) to the experimental data (*red*), where $\tau_{(open)} = 30$ s, $\tau_{(close)} = 8$ s, and $|B| < 0.0013$ nm s^{-1}. Reprinted with permission from ref. [32]. Copyright 2008 American Chemical Society

where $\lambda_{max(0)}$ is the initial λ_{max} value, τ is the rate in seconds, and Bt is a correction factor for linear baseline drift, revealed an opening rate of 0.034 s^{-1} and a closing rate of ~0.127 s^{-1}. These rates are slower than reported rates in solution, which we attributed to steric interactions between proteins due to their immobilized density on the surface, as well as the added mass from the second cutinase moiety in the construct. Although we expect differences between solution measurements and measurements made on a surface, the demonstrated ability to measure rates of binding and conformational change is nonetheless significant because the rates of protein-mediated reactions play an integral role in regulating cellular pathways, and disruptions to these rates can lead to diseased states. Indeed, the surface measurements described in this study may offer a good model for observing the rates of proteins that are anchored in vivo, such as lipid membrane receptors and channels. In addition, the results from this study demonstrated a novel means to reversibly switch a plasmon signal using ionic concentration changes, and pave the way for more creative use of biomolecules in the development of small-molecule and ion sensors.

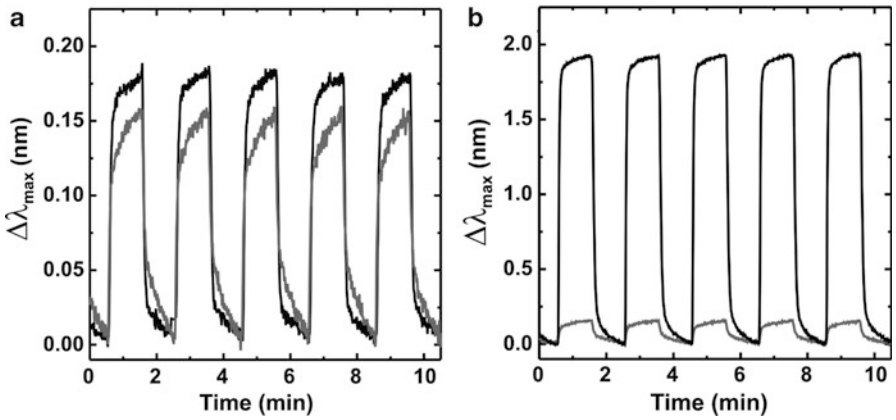

Fig. 2.10 (**a**) LSPR λ_{max} vs. time as the bulk environment switches on bare Ag nanoparticles between N_2 and CO_2 (*gray*) and N_2 and SF_6 (*black*) gas. (**b**) LSPR λ_{max} vs. time as the bulk environment switches between N_2 and CO_2 on bare Ag nanoparticles (*gray*) and MOF-coated Ag nanoparticles (*black*). Reprinted with permission from ref. [46]. Copyright 2010 American Chemical Society

Gas Sensing

Typical biomarker detection focuses on solution phase analytes; however, volatile biomarkers in the gaseous phase have been investigated for certain diseases, like lung cancer [41]. Therefore, it is significant to expand traditional solution phase detection schemes to gaseous media. Traditional SPR spectroscopy has been used for gas sensing due to the high sensitivity to bulk refractive index changes [42, 43]. Recent work in the Van Duyne lab has demonstrated that gas sensing is feasible using a high-resolution, low noise LSPR spectrometer. For example, N_2 and He have similar refractive indices, differing by only 2.62×10^{-4} refractive index units. However, it was demonstrated that even a small change in bulk refractive index was detectable using LSPR spectroscopy [44, 45]. More recently, Kreno et al. expanded LSPR gas sensing experiments to CO_2 and SF_6 gases [46]. Figure 2.10a depicts the λ_{max} as a function of time as the environment is switched between N_2 and CO_2 (gray) and N_2 and SF_6 (black). To increase the selectivity and sensitivity of the LSPR sensor, thin partition layers are required. The Ag nanoparticle substrate was functionalized with a metal-organic framework (MOF) such that select gaseous analytes of interest would be close to the nanoparticle surface, and therefore detected. Figure 2.10b compares the LSPR response of bare Ag nanoparticles (gray) to MOF-functionalized Ag nanoparticles (black) while switching between N_2 and CO_2. The MOF-functionalized nanoparticles demonstrated selectivity of CO_2 over SF_6 [46]. Since the EM field decay length of nanoparticles is only several nanometers, the environment beyond the partition layer is not detected. Therefore, the short EM field decay length utilized in LSPR spectroscopy is advantageous for gas sensing using a thin, selective partition layer, like a MOF.

Single-Nanoparticle Sensors: Toward the Ultimate Detection Limit

Measurements of single nanoparticles have several benefits to ensemble-averaged measurements. First, the single nanoparticles are readily implemented in multiplexed detection schemes since each unique nanoparticle possesses a distinguishable LSPR maximum. A second advantage is that the absolute detection limit (number of analyte molecules per nanoparticle) is significantly reduced. A third advantage of single-nanoparticle spectroscopy is the ability to measure the LSPR spectrum of individual particles with a high signal-to-noise ratio [47]. Additionally, single nanoparticles can be used for in vivo studies. These advantages provide motivation to examine the environmental dependence of single nanoparticle LSPR [47–49]. In this section, experiments utilizing resonant Rayleigh scattering spectroscopy to measure the LSPR λ_{max} of single Ag nanoparticles are described. The first part details the response of the λ_{max} of individual Ag nanoparticles to varying solvent environments, self-assembled monolayer formation, and protein adsorption [47, 49]. The second half describes a high-throughput wide-field single nanoparticle spectroscopy method. The wide-field method demonstrates the ability to not only measure ~10^2 single nanoparticles simultaneously, but also measure the single-particle trajectory and scattering spectra of moving single Ag nanoparticles [50].

Single Nanoparticle Sensing

McFarland and Van Duyne [47] and Raschke et al. [48]. independently reported the first sensing experiments with single nanoparticles. A dark-field scattering image of single Ag nanoparticles is depicted in Fig. 2.11a. McFarland and Van Duyne demonstrated sensitivity to SAM formation with multiple alkanethiols. Citrate-reduced Ag colloids were exposed to a hexadecanethiol (HDT) solution and a HDT monolayer formed on the Ag surface, displacing the citrate ions. These single-nanoparticle studies exhibited the adsorption of fewer than 60,000 HDT molecules on a single Ag nanoparticle resulting in a LSPR shift of 40.7 nm (Fig. 2.11b), thus demonstrating low zeptomole sensitivity [47].

The bulk refractive index sensitivity of individual citrate-reduced Ag colloids was measured by exposing the nanoparticles to various solvent environments and single nanoparticles with three different shapes were used to illustrate the effect of nanoparticle shape on refractive index sensitivity [47]. The nanoparticle shapes were inferred from TEM imaging [51], LSPR line shape, LSPR λ_{max}, and LSPR polarization dependence. Similar to the results from ensemble-averaged measurements, the LSPR λ_{max} shifted to longer wavelengths as the refractive index of the solvent was increased (Fig. 2.11c). The particle with the largest aspect ratio (a rod-shaped particle) exhibited the highest refractive index sensitivity (235 nm RIU^{-1}), consistent with predictions from Mie theory. The refractive index sensitivity decreased with decreasing particle aspect ratio and the spherical nanoparticle exhibited a refractive index sensitivity of 161 nm RIU^{-1} [47]. Additionally, the LSPR λ_{max} response was monitored in real-time as an octanethiol SAM

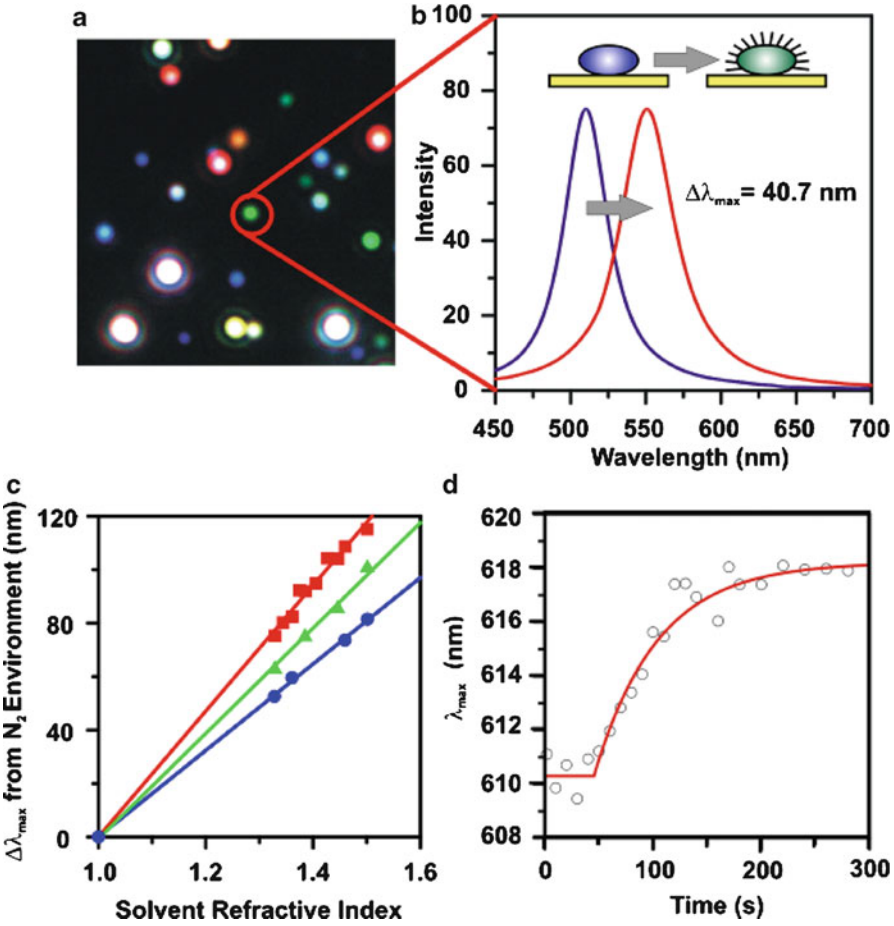

Fig. 2.11 (**a**) Dark-field scattering image of single Ag nanoparticles. (**b**) Single nanoparticle spectra of the selected Ag nanoparticle in (**a**) before and after a HDT monolayer. A shift of 40.7 nm was observed. (**c**) Refractive index sensitivity of three different nanoparticles: spherical particle (*filled circle*) 161 nm RIU^{-1}, triangular particle (*filled triangle*) 197 nm RIU^{-1}, rodlike particle (*filled square*) 235 nm RIU^{-1}. (**d**) Real-time LSPR response of a single Ag nanoparticle as a SAM of octanethiol forms on the nanoparticle. The line is a first order response profile with a rate constant of 0.0167 s^{-1}. Adapted and reprinted with permission from ref. [47]. Copyright 2003 American Chemical Society

formed on the nanoparticle surface (Fig. 2.11d). The response exhibits first-order kinetics with a rate constant of 0.0167 s^{-1}, demonstrating that single-nanoparticle sensing platforms provide the same advantageous real-time behavior as nanoparticle arrays and SPR sensors [47].

The feasibility of single Ag nanoparticles for biosensing was demonstrated using the streptavidin-biotin system. The single Ag nanoparticles were functionalized with a mixed monolayer with carboxyl terminal groups, and amine-functionalized biotin was covalently attached to the nanoparticle via amide bond formation.

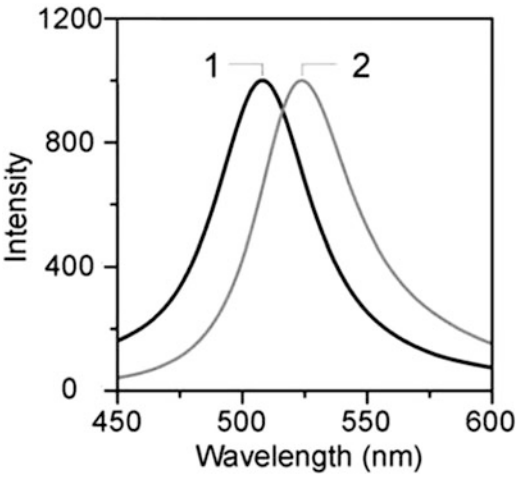

Fig. 2.12 Scattering spectrum of a biotinylated single Ag nanoparticle before (1) and after (2) exposure to 10 nM streptavidin. Reproduced with permission from ref. [49]

The biotinylated Ag nanoparticles were incubated in 10 nM streptavidin, rinsed, and dried in N_2. The λ_{max} of the nanoparticle shifted +12.7 nm as a result of the streptavidin binding to the biotinylated Ag surface (Fig. 2.12). This shift is approximated to result from less than 700 streptavidin molecules binding to the single Ag nanoparticle [49]. Similarly, Raschke et al. demonstrated the use of single biotinylated-Au nanoparticles to detect streptavidin binding [48].

Single-nanoparticle sensing has proven to be an effective method for detecting small amounts of molecules. However, it has been an under-exploited area of research because it is an extremely low-throughput method, as only one particle can be measured at a time. Additionally, it has been a challenge to measure the LSPR spectra of moving single nanoparticles. In the next part of this section, a high-throughput wide-field apparatus is described, in which moving particles can be measured and characterized.

Wide-Field Single Nanoparticle Imaging and Spectroscopy

Typical methods of measuring single nanoparticle LSPR spectra require the nanoparticle to be isolated in a narrow field of view determined by the slit width of the spectrometer [47, 52, 53]. This method is inefficient for collecting multiple single nanoparticle spectra and limits experiments to particles that are immobile. Spatial tracking of moving single particles has been of interest to the biological community due to the new information it provides on the organization of cell membranes, particle movement on cell surfaces, and the effects of the external cell environment [54–60]. Single particle tracking is used to determine the diffusion coefficients of individual particles, allowing for modes of motion inside cells to be characterized. The work reported here describes results obtained from a wide-field LSPR imaging apparatus which was used to simultaneously track and collect scattering spectra from hundreds of mobile nanoparticles.

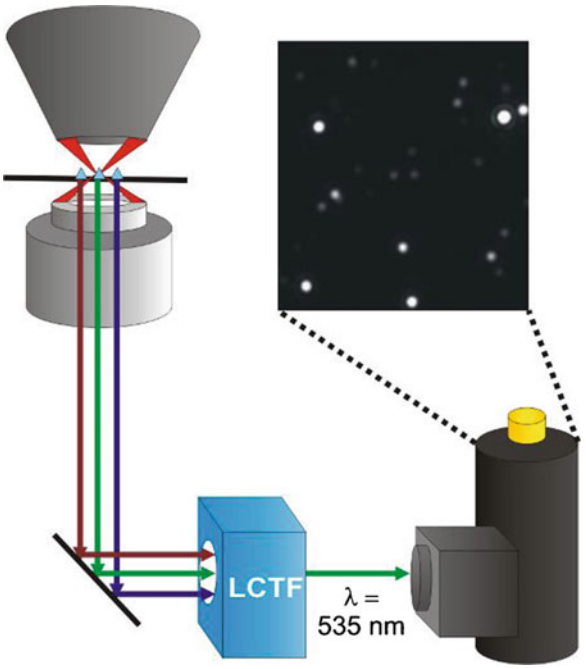

Fig. 2.13 Wide-field imaging apparatus. The scattered light from multiple nanoparticles is collected by the objective and sent through the LCTF, where only the specified wavelength of light is transmitted to the CCD (535 nm shown here) and is seen as an intensity image of the nanoparticles. Reprinted with permission from ref. [50]. Copyright 2009 American Chemical Society

The wide-field imaging method utilized dark-field microscopy and an LCTF to measure the resonant Rayleigh scattered light from multiple nanoparticles. The scattered light was sent through an LCTF, which has a continuously tunable transmission from 400 to 720 nm, to a CCD detector (Fig. 2.13). A wide-field intensity image was obtained from light scattered by multiple nanoparticles at each specified wavelength and the intensity of the scattering was integrated as a function of wavelength to construct single nanoparticle spectra. This wide-field method allowed for hundreds of single nanoparticle spectra to be measured simultaneously, providing a plasmon distribution of the specific nanoparticle sample [50].

Not only did each intensity frame have wavelength information, but it also had time information, since the LCTF was scanned with a specific time interval. This feature made it possible to measure moving particles. The location of each particle at a given time in the wide-field image was known, allowing diffusional dynamics of moving particles to be characterized (Fig. 2.14). Figure 2.14a, b display the LSPR scattering spectra and the single-particle trajectories, respectively, of three single Ag nanoparticles. The mean square displacement ($\langle r^2 \rangle$) was calculated from the nanoparticle trajectories and plotted as a function of time lag, t (Fig. 2.14c) demonstrating a linear relationship. For Brownian diffusion in two dimensions, the relationship between $\langle r^2 \rangle$ and t is expected to be linear with the slope equal to $4D$, where D is the diffusion coefficient. From the linear fit in Fig. 2.14c, particles 1, 2, and 3 were determined to have diffusion coefficients of 1.33×10^{-10} cm^2 s^{-1}, 8.75×10^{-11} cm^2 s^{-1}, and 5.73×10^{11} cm^2 s^{-1}, respectively. Using the Stokes-Einstein relationship, the nanoparticles were found to

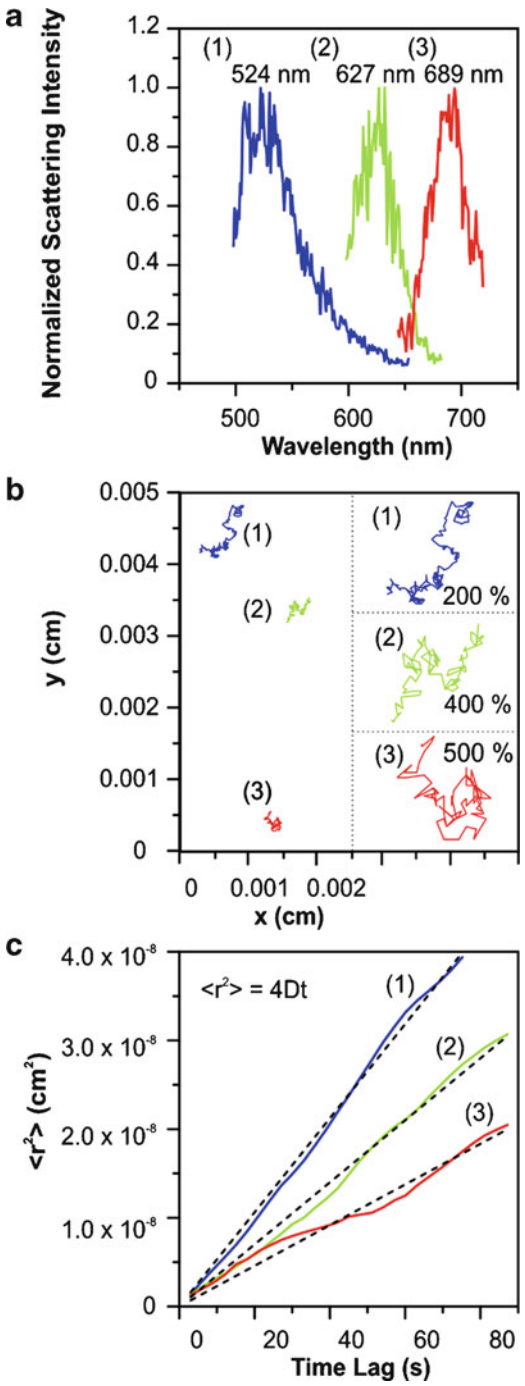

Fig. 2.14 Characterization of three single moving nanoparticles. (**a**) The normalized LSPR scattering spectra of particles 1, 2, and 3 with λ_{max} of 524, 627, and 689 nm, respectively. The scattering spectra were obtained while the particles were moving according to the trajectories in (**b**). (**b**) Two-dimensional trajectories of particles 1, 2, 3. The *insets* show a magnification of the trajectories at 200, 400, and 500% for particles 1, 2, and 3, respectively. (**c**) The mean square displacement, $\langle r^2 \rangle$, is plotted as a function of the time lag, t, for particles 1, 2, and 3 and fit with a linear regression. Adapted and reprinted with permission from ref. [50]. Copyright 2009 American Chemical Society

have sizes of 177 nm, 269 nm, and 410 nm for particles 1, 2, and 3, respectively. Using this method, the particle size was approximated within a factor of ~2–3 of the actual nanoparticle size of 80–100 nm [61].

Although the sizes of the Ag nanoprisms were larger than expected by a factor of ~2–4, this work demonstrated the first time both spectra and diffusion coefficients of single nanoparticles were correlated in real-time. Wide-field LSPR imaging and spectroscopy has proven to be an effective and efficient method for obtaining many single nanoparticle spectra for both stationary and moving particles. With high throughput methods and particle tracking capabilities, it is feasible that LSPR spectroscopy can reach the ultimate level of detection, single molecule.

Coupling Molecular Identification to LSPR Spectroscopy

LSPR spectroscopy is a sensitive method for measuring the local refractive index changes surrounding noble metal nanoparticles. The LSPR spectrum shifts when adsorbates bind close to the nanoparticle, allowing for the quantitative determination of adsorbate concentrations. LSPR spectroscopy methods obtain specificity from nanoparticle functionalization with molecular recognition elements like antibodies, SAMs, or other specific interactions. However, LSPR spectroscopy methods are not well-suited to identify unknown analytes. Therefore, the versatility of LSPR assays can be improved by coupling with molecular identification techniques such as SERS and laser desorption ionization mass spectrometry.

Surface-Enhanced Raman Spectroscopy

Light scattering by molecules can occur elastically (i.e., Rayleigh) or inelastically (i.e., Raman). Raman scattered photons are shifted in frequency from the incident photons by the energy difference necessary to excite a vibrational mode, a process known as normal Raman scattering (NRS). Raman scattering spectrum is unique to a molecule and can be viewed as a molecular "fingerprint." For example, the dye rhodamine 6G (R6G-d_0) and its isotopologue R6G-d_4 (which is identical to R6G-d_0 with the exception of four deuterium atoms in place of hydrogen atoms) have unique Raman spectra [62]. However, Raman scattering is a weak effect. When molecules are in proximity to a plasmonic nanoparticle, the enhanced local electromagnetic field increases the Raman scattering by a factor of 10^6–10^8, known as surface-enhanced Raman scattering [2, 8]. The field enhancement results from Raman excitation and emission coupling with the nanoparticle LSPR. The enhancement is greatest when the LSPR λ_{max} falls between the excitation wavelength and the wavelength of the scattered photon [8]. Therefore the complementary nature of LSPR and SERS makes them ideal techniques for biomolecular recognition and detection. SERS substrates can be fabricated with a

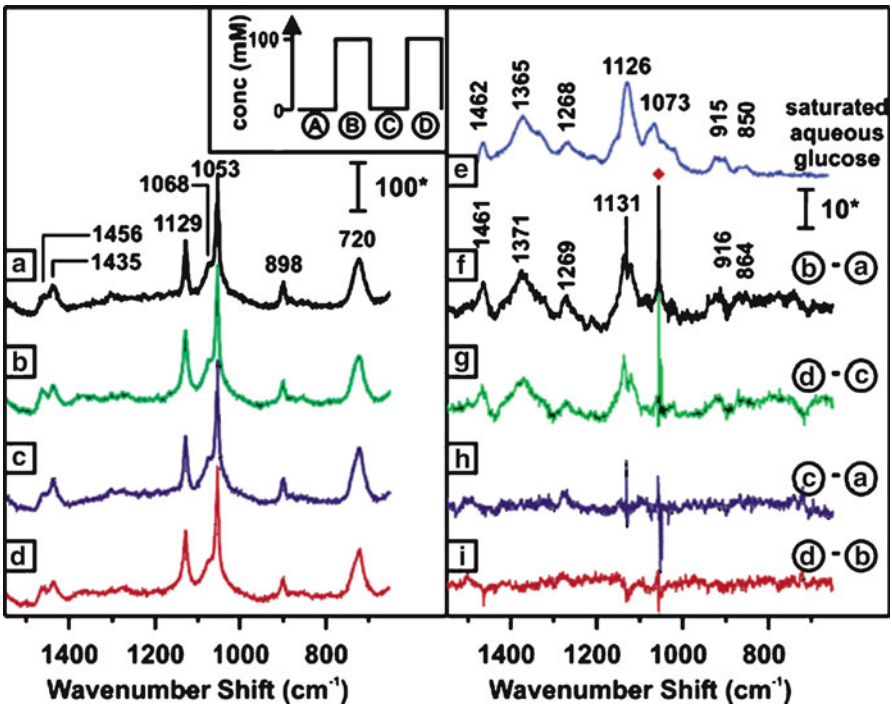

Fig. 2.15 Glucose pulsing sequence on the SAM-modified AgFON surface (*inset*). SER spectra of the sample cycled between 0 and 100 mM aqueous glucose solutions (**a**–**d**). Normal Raman spectrum of aqueous saturated glucose solution (**e**). Difference spectra showing partitioning/departitioning of glucose (**f**–**i**). An *asterisk* (*) denotes adu·mW^{-1} min^{-1}. Reproduced with permission from ref. [63]. Copyright 2005 American Chemical Society

specific LSPR so that the enhancement is maximized. This section discusses the detection of glucose and calcium dipicolinate (CaDPA) using SERS-based sensors.

A critical aspect in the management of diabetes is the quantitative, real-time detection of glucose. Lyandres and Shah et al. demonstrated the feasibility of a SERS-based glucose sensor using Ag FON substrates [63]. For the development of a SERS glucose sensor, a partition layer on the metal nanoparticle surface was necessary. The partition layer increased the affinity of glucose for the sensor surface, and allowed glucose to bind reversibly in order to accurately reflect fluctuations in glucose levels. The partition layer consisted of a mixed monolayer of decanethiol (DT) and mercaptohexanol (MH), which possessed both hydrophobic and hydrophilic properties making it well-suited for in vivo use [63]. The SERS glucose sensor provided stable glucose level measurements in bovine plasma over 10 days. To establish the reversibility of the sensor, the DT/MH AgFON was exposed to cycles of water and 100 mM glucose solutions. Difference spectra demonstrated partitioning and departitioning of glucose into and out of the DT/MH SAM (Fig. 2.15). Recently, the glucose SERS sensor was successfully transitioned

from in vitro models to in vivo testing in the Sprague–Dawley rat [64]. The in vivo studies were compared to a commercial glucose sensor (Ascensia ELITE) and both were successful in monitoring glucose concentration fluctuations with similar trends.

SERS-based sensors have also been used for biological warfare agent detection. In addition to being specific and sensitive, the SERS biowarfare agent sensor must exhibit a fast response time. Work by Zhang et al. demonstrated sensitive and rapid detection of CaDPA, a biomarker for anthrax, using a portable Raman spectrometer [65]. Extracted from *Bacillus subtilis* spores, (a harmless stimulant of *Bacillus anthracis*), the CaDPA was drop coated on bare AgFON surfaces, which were optimized for 750 nm laser excitation. The intensity of the characteristic 1,020 cm^{-1} CaDPA peak increased linearly with spore concentration initially, then saturated at higher concentrations. The LOD was determined to be 2,600 spores, which is below the anthrax infectious dose of 10^4 spores. When the AgFON substrates were functionalized with alumina, fabricated by atomic layer deposition (ALD), the LOD for the spores was improved to 1,400 spores [66]. Alumina has a strong affinity for carboxylate groups, making the alumina-AgFON an ideal candidate for *Bacillus* spore detection using CaDPA.

Laser Desorption Ionization Mass Spectrometry

Mass spectrometry (MS) is a highly utilized analytical technique that allows the identification of unknown analytes via their unique mass or mass fragmentation pattern [67]. Analysis first requires that the sample be ionized to create a mobile charged species, and the mass/charge ratio is subsequently measured by a detector. Variations in ionization techniques allow the analysis of a wide range of analytes, from gases to small molecules to proteins. Matrix-assisted laser desorption ionization time of flight (MALDI-TOF) MS is a technique that was developed to allow intact detection of very large molecules such as proteins. In this technique, the analyte is embedded in a small-molecule matrix and ionized using a laser source. The matrix absorbs at or near the incident laser wavelength, assisting in energy transfer to the analyte (desorption), as well as ionizing the analyte via proton transfer. MALDI-TOF MS functions for analytes over a mass range from 500 Da to upwards of 250,000 Da, and is widely used in the biological community to study protein composition [68]. As an analytical tool, it provides information that complements LSPR bioassays.

Anker et al. demonstrated the first combination of LSPR and MALDI-TOF MS (Fig. 2.16) [69]. LSPR bioassays and MALDI-TOF MS analysis were performed serially in order to first detect, and then identify ADDLs, a biomarker for Alzheimer's disease. It was shown that an anti-ADDL detection antibody could specifically detect ADDLs adsorbed to the LSPR sensor, and that subsequent MALDI-TOF MS could identify ADDLs by the characteristic mass peak at 4,516 Da. A matrix was spotted directly onto the LSPR sensor post-assay to

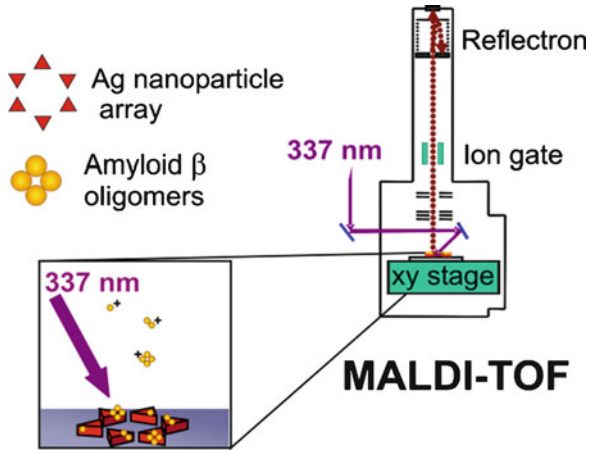

Fig. 2.16 Schematic of LSPR sensor made of an array of silver nanoparticles and the MALDI-TOF instrument used for MS analysis of the sensor surface. Reprinted with permission from ref. [69]. Copyright 2009 American Chemical Society

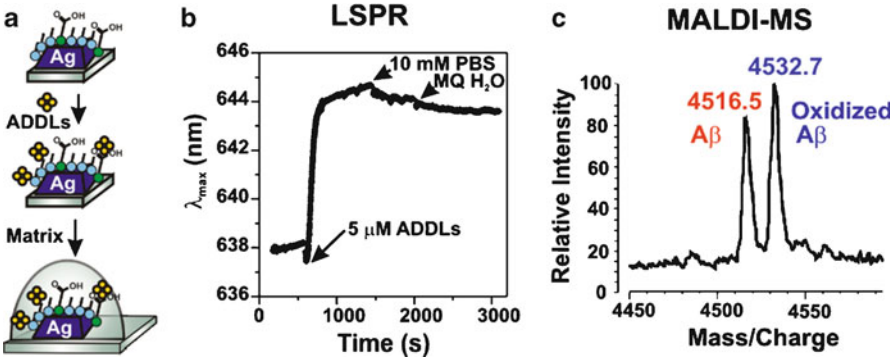

Fig. 2.17 (**a**) Experimental protocol. (**b**) Real-time detection of ADDLs binding to octanethiol/11-MUA functionalized nanoprisms. (**c**) MALDI mass spectrum of Aβ monomers bound to the nanoprisms, using a layer of sinapinic acid as the matrix. Reprinted with permission from ref. [69]. Copyright 2009 American Chemical Society

facilitate ionization, with no further sample preparation required (Fig. 2.17a). Real-time data collection during the LSPR assays (Fig. 2.17b) allowed for the determination of kinetic rates of binding interactions. In addition to demonstrating the ease and utility of combined LSPR-MS analysis, this study identified a modified form of the ADDLs monomer, with a mass peak shifted by 16 Da (Fig. 2.17c). It was proposed that this second mass peak resulted from a post-translational modification to the ADDLs protein, which may be correlated with ADDLs toxicity. Although this investigation reported the detection of purified, synthetic analytes,

applications to clinical diagnostics can be inferred. LSPR sensors can be patterned with arrays of antibodies to allow multiplexed detection and quantification of multiple biomarkers in a single sample. MS can subsequently verify the identity of the biomarkers immobilized on the antibody array, as well as identify structural modifications which may not be distinguishable in an immunoassay, but which are important indicators of disease progression. Thus, the combination of LSPR bioassays with mass spectrometry provides new information about biological systems that cannot easily be obtained using any other single technique.

Raman Tags

An additional way to couple LSPR spectroscopy with molecular information is to use SERS-nanotags. SERS-nanotags are typically composed of a plasmonic nanoparticle coated with a Raman-active molecule. Wustholz et al. characterized single SERS-nanotags by correlating the nanotag structure with both the LSPR spectrum and SER spectrum [70]. Raman tags have been used for in vivo tumor targeting and detection [71] as well as multiplexed imaging in living mice [72]. Additionally, SERS nanotags have been used for sensing applications in SERS immunoassays. The SERS immunoassays are based on the sandwich-type assay utilizing antibodies, with the SERS-nanotag attached to the detection antibody. Both the SER spectrum and the LSPR of the sample are measured and the SER spectrum intensity can be quantitatively correlated to the analyte concentration [73]. When used in a similar fashion to the Au plasmonic labels (AB-NPs) described in section "Plasmonic Labels," an enhanced LSPR shift will likely be observed, but an additional detection method will be available by examining the SER spectra of the nanotags. Ultimately, by coupling molecular identification methods with LSPR spectroscopy, more specific and sensitive biosensing platforms can be developed.

Future Directions

The field of nanotechnology has been rapidly expanding for over a decade, and devices that utilize the LSPR property of nanoparticles will continue to be the focus of numerous fields of research. As demand for these devices grows, it will become increasingly important to have a thorough understanding of structure–property relationships. Despite significant gains in the theoretical understanding of LSPR, we are far from having a comprehensive and predictive model for how structure affects LSPR properties. Mock et al. was among the first to report a systematic study of the effects of size and shape on the spectral features of single Ag nanoparticles by combining TEM imaging and optical spectroscopy [51]. Since then, research has continued to focus on understanding how nanoparticle features, such as tip sharpness, rounding, size, and anisotropy, give rise to specific spectral

features, like peak position, line shape, and line width [70, 74–76]. The ultimate goal of structural-spectral correlation experiments is to develop a structure-plasmonic function correlation in order to drive rational nanoparticle design. For example, in sensing and SERS applications, it is important to know what specific structure is the most sensitive to the external environment or has the most enhanced EM field. With the continuation of correlated structural-spectral studies, these questions can be answered.

In addition to rationally designed nanostructures, the successful commercialization of plasmonic sensors will require the development of scalable fabrication techniques and fast, user-friendly readout capabilities. Parallel fabrication strategies, such as Dip Nanolithography [77], wet chemical syntheses, photolithography, and templated syntheses [78] create highly reproducible nanoscale structures over large areas and should translate well to industrial settings. On the user end, utility will be improved by designing devices with a multiplexed array format, where readout is performed serially using an automated device, or in parallel via imaging technologies. As diagnostics, nanoparticles have been used as imaging contrast agents, force probes, colorimetric or electrochemical detectors, and optical signal-enhancing agents. On the therapeutics side, nanoparticles are utilized to enhance drug bioavailability, tag cancerous cells for subsequent therapy, or act as targeted drug delivery vectors [28, 79–82]. The development of techniques for nanoparticle tracking within cells has enabled researchers to gain insight into the dynamic behavior of cellular components [83]. Further advances in the field of nanotechnology will continue to impact the utility of plasmonic devices as medical diagnostic and therapeutic devices, and may one day enable us to address major challenges in medicine.

Acknowledgment This research was supported by the National Science Foundation (Grants EEC-0647560, CHE-0911145, and BES-0507036), the NSF MRSEC (DMR-0520513) at the Materials Research Center of Northwestern University, the AFOSR/DARPA Project BAA07-61 (FA9550-08-1-0221), the NIH (5R56DK078691-02), the NCI (1 U54 CA119341-01), and a Ryan Fellowship to W.P.H.

References

1. Englebienne P. Use of colloidal gold surface plasmon resonance peak shift to infer affinity constants from the interactions between protein antigens and antibodies specific for single or multiple epitopes. Analyst. 1998;123:1599–603.
2. Jeanmaire DL, Van Duyne RP. Surface Raman spectroelectrochemistry part I: heterocyclic, aromatic, and aliphatic amines adsorbed on the anodized silver electrode. J Electroanal Chem. 1977;84:1–20.
3. Albrecht MG, Creighton JA. Anomalously intense Raman spectra of pyridine at a silver electrode. J Am Chem Soc. 1977;99:5215–9.
4. Hulteen JC, Treichel DA, Van Duyne RP. Atomic force microscopy and surface-enhanced Raman spectroscopy. I. Ag island films and Ag film over polymer nanosphere surfaces supported on glass. J Chem Phys. 1993;99:2101–15.

5. Hulteen JC, Van Duyne RP. Nanosphere lithography: a materials general fabrication process for periodic particle array surfaces. J Vac Sci Technol A. 1995;13:1553–8.
6. Haes AJ, Zou S, Schatz GC, Van Duyne RP. A nanoscale optical biosensor: the long-range distance dependence of the localized surface plasmon resonance of noble metal nanoparticles. J Phys Chem B. 2004;108:109–16.
7. Haes AJ, Zou S, Schatz GC, Van Duyne RP. A nanoscale optical biosensor: short range distance dependence of the localized surface plasmon resonance of noble metal nanoparticles. J Phys Chem B. 2004;108:6961–8.
8. McFarland AD, Young MA, Dieringer JA, Van Duyne RP. Wavelength-scanned surface-enhanced Raman excitation spectroscopy. J Phys Chem B. 2005;109:11279–85.
9. Leuvering JH, Thal PJ, van der Waart M, Schuurs AH. Sol particle immunoassay (SPIA). J Immunoassay. 1980;1:77–91.
10. Elghanian R, Storhoff JJ, Mucic RC, Letsinger RL, Mirkin CA. Selective colorimetric detection of polynucleotides based on the distance-dependent optical properties of gold nanoparticles. Science. 1997;277:1078–81.
11. Haes AJ, Van Duyne RP. A nanoscale optical biosensor: sensitivity and selectivity of an approach based on the localized surface plasmon resonance spectroscopy of triangular silver nanoparticles. J Am Chem Soc. 2002;124:10596–604.
12. Riboh JC, Haes AJ, McFarland AD, Yonzon CR, Van Duyne RP. A nanoscale optical biosensor: real-time immunoassay in physiological buffer enabled by improved nanoparticle adhesion. J Phys Chem B. 2003;107:1772–80.
13. Haes AJ, Chang L, Klein WL, Van Duyne RP. Detection of a biomarker for Alzheimer's disease from synthetic and clinical samples using a nanoscale optical biosensor. J Am Chem Soc. 2005;127:2264–71.
14. Yonzon CR, Jeoung E, Zou S, Schatz GC, Mrksich M, Van Duyne RP. A comparative analysis of localized and propagating surface plasmon resonance sensors: the binding of concanavalin A to a monosaccharide functionalized self-assembled monolayer. J Am Chem Soc. 2004;126:12669–76.
15. Whitney AV, Elam JW, Zou S, Zinovev AV, Stair PC, Schatz GC, et al. Localized surface plasmon resonance nanosensor: a high-resolution distance-dependence study using atomic layer deposition. J Phys Chem B. 2005;109:20522–8.
16. Haes AJ, Zou S, Zhao J, Schatz GC, Van Duyne RP. Localized surface plasmon resonance spectroscopy near molecular resonances. J Am Chem Soc. 2006;128:10905–14.
17. Zhao J, Das A, Zhang XY, Schatz GC, Sligar SG, Van Duyne RP. Resonance surface plasmon spectroscopy: low molecular weight substrate binding to cytochrome P450. J Am Chem Soc. 2006;128:11004–5.
18. Zhao J, Jensen L, Sung J, Zou S, Schatz GC, Van Duyne RP. Interaction of plasmon and molecular resonances for rhodamine 6G adsorbed on silver nanoparticles. J Am Chem Soc. 2007;129:7647–56.
19. Lipscomb JD, Gunsalus IC. Structural aspects of the active site of cytochrome P-450cam. Drug Metab Dispos. 1973;1:1–5.
20. Schlichting I, Berendzen J, Chu K, Stock AM, Maves SA, Benson DE, et al. The catalytic pathway of cytochrome P450cam at atomic resolution. Science. 2000;287:1615–22.
21. Sligar SG. Coupling of spin, substrate, and redox equilibriums in cytochrome P450. Biochemistry. 1976;15:5399–406.
22. He L, Musick MD, Nicewarner SR, Salinas FG, Benkovic SJ, Natan MJ, et al. Colloidal Au-enhanced surface plasmon resonance for ultrasensitive detection of DNA hybridization. J Am Chem Soc. 2000;122:9071–7.
23. Lyon LA, Musick MD, Natan MJ. Colloidal Au-enhanced surface plasmon resonance immunosensing. Anal Chem. 1998;70:5177–83.
24. Buckle PE, Davies RJ, Kinning T, Yeung D, Edwards PR, Pollard-Knight D. The resonant mirror: a novel optical sensor for direct sensing of biomolecular interactions part II: applications. Biosens Bioelectron. 1993;8:355–63.

25. Hall WP, Ngatia SN, Van Duyne RP. LSPR biosensor signal enhancement using nanoparticle-antibody conjugates. J Phys Chem C. 2011;115:1410–4.
26. Gunnarsson L, Rindzevicius T, Prikulis J, Kasemo B, Kall M, Zou SL, et al. Confined plasmons in nanofabricated single silver particle pairs: experimental observations of strong interparticle interactions. J Phys Chem B. 2005;109:1079–87.
27. Su KH, Wei QH, Zhang X, Mock JJ, Smith DR, Schultz S. Interparticle coupling effects on plasmon resonances of nanogold particles. Nano Lett. 2003;3:1087–90.
28. Jain PK, Huang WY, El-Sayed MA. On the universal scaling behavior of the distance decay of plasmon coupling in metal nanoparticle pairs: a plasmon ruler equation. Nano Lett. 2007;7:2080–8.
29. Sonnichsen C, Reinhard BM, Liphardt J, Alivisatos AP. A molecular ruler based on plasmon coupling of single gold and silver nanoparticles. Nat Biotechnol. 2005;23:741–5.
30. Reinhard BM, Sheikholeslami S, Mastroianni A, Alivisatos AP, Liphardt J. Use of plasmon coupling to reveal the dynamics of DNA bending and cleavage by single EcoRV restriction enzymes. Proc Natl Acad Sci U S A. 2007;104:2667–72.
31. Schatz GC, Van Duyne Richard P. Electromagnetic mechanism of surface-enhance spectroscopy. In: Chalmers JM, Griffiths PR, editors. Handbook of vibrational spectroscopy. Chichester: Wiley; 2002.
32. Hall WP, Anker JN, Lin Y, Modica J, Mrksich M, Van Duyne RP. A calcium-modulated plasmonic switch. J Am Chem Soc. 2008;130:5836–7.
33. Ishima R, Torchia DA. Protein dynamics from NMR. Nat Struct Biol. 2000;7:740–3.
34. Heyduk T. Measuring protein conformational changes by FRET/LRET. Curr Opin Biotechnol. 2002;13:292–6.
35. Lipfert J, Doniach S. Small-angle X-ray scattering from RNA, proteins, and protein complexes. Ann Rev Biophys Biomol Struct. 2007;36:307–27.
36. Paynter S, Russell DA. Surface plasmon resonance measurement of pH-induced responses of immobilized biomolecules: conformational change or electrostatic interaction effects? Anal Biochem. 2002;309:85–95.
37. Jonsson MP, Joensson P, Dahlin AB, Hoeoek F. Supported lipid bilayer formation and lipid-membrane-mediated biorecognition reactions studied with a new nanoplasmonic sensor template. Nano Lett. 2007;7:3462–8.
38. Chah S, Hammond MR, Zare RN. Gold nanoparticles as a colorimetric sensor for protein conformational changes. Chem Biol. 2005;12:323–8.
39. Dahlin AB, Tegenfeldt JO, Hook F. Improving the instrumental resolution of sensors based on localized surface plasmon resonance. Anal Chem. 2006;78:4416–23.
40. Hodneland CD, Lee Y-S, Min D-H, Mrksich M. Selective immobilization of proteins to self-assembled monolayers presenting active site-directed capture ligands. Proc Natl Acad Sci U S A. 2002;99:5048–52.
41. Deng C, Zhang X, Li N. Investigation of volatile biomarkers in lung cancer blood using solid-phase microextraction and capillary gas chromatography-mass spectrometry. J Chromatogr B. 2004;808:269–77.
42. Nylander C, Liedberg B, Lind T. Gas detection by means of surface plasmon resonance. Sens Actuators. 1982;3:79–88.
43. Liedberg B, Nylander C, Lunström I. Surface plasmon resonance for gas detection and biosensing. Sens Actuators. 1983;4:299–304.
44. Bingham JM. PhD Dissertation, Fundamental and applied localized surface plasmon resonance spectroscopy studies from nanoparticle arrays to single nanoparticles. Northwestern University; 2010.
45. Bingham JM, Anker JN, Kreno LE, Van Duyne RP. Gas sensing with high-resolution localized surface plasmon resonance spectroscopy. J Am Chem Soc. 2010;132:17358–9.
46. Kreno LE, Hupp JT, Van Duyne RP. Metal–organic framework thin film for enhanced localized surface plasmon resonance gas sensing. Anal Chem. 2010;82:8042–6.
47. McFarland AD, Van Duyne RP. Single silver nanoparticles as real-time optical sensors with zeptomole sensitivity. Nano Lett. 2003;3:1057–62.

48. Raschke G, Kowarik S, Franzl T, Sonnichsen C, Klar TA, Feldmann J, et al. Biomolecular recognition based on single gold nanoparticle light scattering. Nano Lett. 2003;3:935–8.
49. Van Duyne RP, Haes AJ, McFarland AD. Nanoparticle optics: sensing with nanoparticle arrays and single nanoparticles. Proc SPIE Int Soc Opt Eng. 2003;5223:197–207.
50. Bingham JM, Willets KA, Shah NC, Andrews DQ, Van Duyne Richard P. Localized surface plasmon resonance imaging: simultaneous single nanoparticle spectroscopy and diffusional dynamics. J Phys Chem C. 2009;113:16839–42.
51. Mock JJ, Barbic M, Smith DR, Schultz DA, Schultz S. Shape effects in plasmon resonance of individual colloidal silver nanoparticles. J Chem Phys. 2002;116:6755–9.
52. Sherry LJ, Chang S-H, Schatz GC, Van Duyne RP, Wiley BJ, Xia Y. Localized surface plasmon resonance spectroscopy of single silver nanocubes. Nano Lett. 2005;5:2034–8.
53. Sherry LJ, Jin R, Mirkin CA, Schatz GC, Van Duyne RP. Localized surface plasmon resonance spectroscopy of single silver triangular nanoprisms. Nano Lett. 2006;6:2060–5.
54. Nallathamby PD, Lee KJ, Xu X-H. Design of stable and uniform single nanoparticle photonics for in vivo dynamics imaging of nanoenvironments of zebrafish embryonic fluids. ACS Nano. 2008;2:1371–80.
55. Qian H, Sheetz MP, Elson EL. Single particle tracking: analysis of diffusion and flow in two-dimensional systems. Biophys J. 1991;60:910–21.
56. Saxton MJ. Single-particle tracking: the distribution of diffusion coefficients. Biophys J. 1997;72:1744–53.
57. Saxton MJ, Jacobson K. Single-particle tracking: applications to membrane dynamics. Annu Rev Biophys Biomol Struct. 1997;26:373–99.
58. Suzuki KGN, Fujiwara TK, Sanematsu F, Iino R, Edidin M, Kusumi A. GPI-anchored receptor clusters transiently recruit Lyn and Galpha for temporary cluster immobilization and Lyn activation: single-molecule tracking study 1. J Cell Biol. 2007;177:717–30.
59. Vrljic M, Nishimura SY, Brasselet S, Moerner WE, McConnell HM. Translational diffusion of individual class II MHC membrane proteins in cells. Biophys J. 2002;83:2681–92.
60. Vrljic M, Nishimura SY, Moerner WE, McConnell HM. Cholesterol depletion suppresses the translational diffusion of class II major histocompatibility complex proteins in the plasma membrane. Biophys J. 2005;88:334–47.
61. Jin RC, Cao YW, Mirkin CA, Kelly KL, Schatz GC, Zheng JG. Photoinduced conversion of silver nanospheres to nanoprisms. Science. 2001;294:1901–3.
62. Dieringer JA, Lettan II RB, Scheidt KA, Van Duyne RP. A frequency domain existence proof of single-molecule surface-enhanced Raman spectroscopy. J Am Chem Soc. 2007;129:16249–56.
63. Lyandres O, Shah NC, Yonzon CR, Walsh Jr JT, Glucksberg MR, Van Duyne RP. Real-time glucose sensing by surface-enhanced Raman spectroscopy in bovine plasma facilitated by a mixed decanethiol/mercaptohexanol partition layer. Anal Chem. 2005;77:6134–9.
64. Lyandres O, Yuen JM, Shah NC, VanDuyne RP, Walsh Jr JT, Glucksberg MR. Progress toward an in vivo surface-enhanced Raman spectroscopy glucose sensor. Diabetes Technol Ther. 2008;10:257–65.
65. Zhang X, Young MA, Lyandres O, Van Duyne RP. Rapid detection of an anthrax biomarker by surface-enhanced Raman spectroscopy. J Am Chem Soc. 2005;127:4484–9.
66. Zhang X, Zhao J, Whitney AV, Elam JW, Van Duyne RP. Ultrastable substrates for surface-enhanced Raman spectroscopy: Al_2O_3 overlayers fabricated by atomic layer deposition yield improved anthrax biomarker detection. J Am Chem Soc. 2006;128:10304–9.
67. Burlingame AL, Boyd RK, Gaskell SJ. Mass spectrometry. Anal Chem. 1996;68:599R–651.
68. Aebersold R, Mann M. Mass spectrometry-based proteomics. Nature. 2003;422:198–207.
69. Anker JN, Hall WP, Lambert MP, Velasco PT, Mrksich M, Klein WL, et al. Detection and identification of bioanalytes with high-resolution LSPR spectroscopy and MALDI mass spectrometry. J Phys Chem C. 2009;113:5891–4.

70. Wustholz KL, Henry A-I, Bingham JM, Kleinman SL, Natan MJ, Freeman RG, et al. Exploring single-molecule SERS and single-nanoparticle plasmon microscopy. Proc SPIE Int Soc Opt Eng. 2009;7394.
71. Qian X, Peng X-H, Ansari DO, Yin-Goen Q, Chen GZ, Shin DM, et al. In vivo tumor targeting and spectroscopic detection with surface-enhanced Raman nanoparticle tags. Nat Biotechnol. 2008;26:83–90.
72. Zavaleta CL, Smith BR, Walton I, Doering W, Davis G, Shojaei B, et al. Multiplexed imaging of surface enhanced Raman scattering nanotags in living mice using noninvasive Raman spectroscopy. Proc Natl Acad Sci U S A. 2009;106:13511–6.
73. Porter MD, Lipert RJ, Siperko LM, Wang G, Narayanan R. SERS as a bioassay platform: fundamentals, design, and applications. Chem Soc Rev. 2008;37:1001–11.
74. McMahon JA, Wang YM, Sherry LJ, Van Duyne RP, Marks LD, Gray SK, et al. Correlating the structure, optical spectra, and electrodynamics of single silver nanocubes. J Phys Chem C. 2009;113:2731–5.
75. Munechika K, Smith JM, Chen Y, Ginger DS. Plasmon line widths of single silver nanoprisms as a function of particle size and plasmon peak position. J Phys Chem C. 2007;111:18906–11.
76. Stiles RL, Willets KA, Sherry LJ, Roden JM, Van Duyne RP. Investigating tip-nanoparticle interactions in spatially correlated total internal reflection plasmon spectroscopy and atomic force microscopy. J Phys Chem C. 2008;112:11696–701.
77. Piner RD, Zhu J, Xu F, Hong S, Mirkin CA. Dip Pen nanolithography. Science. 1999;283:661–3.
78. Gates BD, Xu Q, Stewart M, Ryan D, Willson CG, Whitesides GM. New approaches to nanofabrication: molding, printing, and other techniques. Chem Rev. 2005;105:1171–96.
79. Brigger I, Dubernet C, Couvreur P. Nanoparticles in cancer therapy and diagnosis. Adv Drug Deliv Rev. 2002;54:631–51.
80. Ferrari M. Cancer nanotechnology: opportunities and challenges. Nat Rev Cancer. 2005;5:161–71.
81. Nie S, Xing Y, Kim GJ, Simons JW. Nanotechnology applications in cancer. Annu Rev Biomed Eng. 2007;9:257–88.
82. Davis ME, Chen Z, Shin DM. Nanoparticle therapeutics: an emerging treatment modality for cancer. Nat Rev Drug Discov. 2008;7:771–82.
83. Cognet L, Berciaud S, Lasne D, Lounis B. Photothermal methods for single nonluminescent nano-objects. Anal Chem. 2008;80:2288–94.

Chapter 3
Nanoplasmonic Sensing Combined with Artificial Cell Membranes

Magnus P. Jonsson, Andreas B. Dahlin, and Fredrik Höök

Abstract This chapter is dedicated to nanoplasmonic sensing systems made compatible with studies of artificial cell membranes. After a short motivation to the opportunity of sensors designed for such studies to fill an existing technological gap, we introduce basic features of cell membranes and common mimics of the cell membrane that have been proven useful in various bioanalytical sensing applications.

With suitable examples from the literature, subsequent sections exemplify how nanoplasmonics can be used to study different reactions that are associated with cell membranes. In particular, focus is on unique possibilities provided by different types of nanoplasmonic structures. For example, while discrete nanoplasmonic particles can be used as mobile probes attached to cell membranes, conductive nanoplasmonic hole structures can be used for combined optical and electrical transduction. Examples on how the latter possibility has enabled cell membrane-related reactions to be investigated with nanoplasmonic sensing combined with quartz crystal microbalance with dissipation monitoring are presented. Another key aspect of nanoplasmonic structures is that the plasmonic field (and hence the refractive index sensitivity) is strongest at the sensor surface and decays rapidly away from the surface. We describe how this feature provides a means to monitor structural changes of molecules on the surface, such as the spontaneous rupture of lipid vesicles into a supported lipid bilayer on silicon oxide-coated nanoplasmonic holes.

M.P. Jonsson (✉)
Department of Bionanoscience, Kavli Institute of NanoScience, Delft University of Technology, Lorentzweg 1, 2628 CJ Delft, The Netherlands

Department of Applied Physics, Chalmers University of Technology, Göteborg 41296, Sweden
e-mail: magnus@mpjonsson.com

A.B. Dahlin • F. Höök (✉)
Department of Applied Physics, Chalmers University of Technology, Göteborg 41296, Sweden
e-mail: fredrik.hook@chalmers.se

A. Dmitriev (ed.), *Nanoplasmonic Sensors*, Integrated Analytical Systems,
DOI 10.1007/978-1-4614-3933-2_3,

Introduction

As discussed in this book, the concept of nanoplasmonics has shown great promise as a powerful tool for bioanalytical sensing applications. Optimization with respect to refractive index (RI) sensitivity and noise minimization is important and of general interest for most applications. Hence, significant efforts have been directed towards developing "the ultimate" nanoplasmonic sensor. In this context, bulk RI sensitivity in terms of resonance peak shift and the figure of merit (see Chap. 10 and 13) are two common parameters used to compare different nanoplasmonic sensors. However, when designing a nanoplasmonic sensor for a particular application, other properties of the structure are often as important. For example, the choice of surface materials may be essential to allow for material-specific surface modifications or for a specific biomolecular reaction to occur in a desired way. In other applications, the surface topography or the electrical properties of the sensor may be more important parameters. In this chapter, we discuss such issues with respect to the design of nanoplasmonic sensors made compatible with studies of artificial cell membranes and biomolecular recognition reactions controlled by cell membranes.

The Cell Membrane

The core structural element of the cell membrane, also called the plasma membrane, is a 5 nm thick lipid bilayer shell that surrounds the living cell. It is a vital part of life as it makes it possible to maintain (and protect) molecules and functioning organelles (which themselves are surrounded by lipid bilayer membranes) inside a confined compartment. The main constituents of the cell membrane are amphiphilic lipid molecules. While the hydrophilic head group of a lipid prefers to be exposed to water, its hydrophobic tail prefers not to be in contact with water. In an aqueous environment, the lipids therefore spontaneously self-assemble into a bilayer-like structure. The tails are shielded from the aqueous solutions by pointing towards each other and the polar head groups are facing the two liquid environments inside and outside of the cell, as depicted schematically in Fig. 3.1. The resulting lipid bilayer structure thus acts as a hydrophobic barrier. This barrier limits the membrane permeability with respect to large, charged, and polar molecules as well as atomic ions and thereby allows for molecular gradients that are essential for life to be maintained.

Still, the cell membrane can also enable selective transport of molecules in and out of the cell, and it is also responsible for signaling between cells, adhesion of cells to surfaces and to other cells, and more. These important properties are controlled by different kinds of proteins and protein complexes that are embedded inside the cell membrane (signaling receptors, ion channels, aquaporins, etc.) [1]. In fact, around 30% of the around 20,000–25,000 human genes [2] codes for

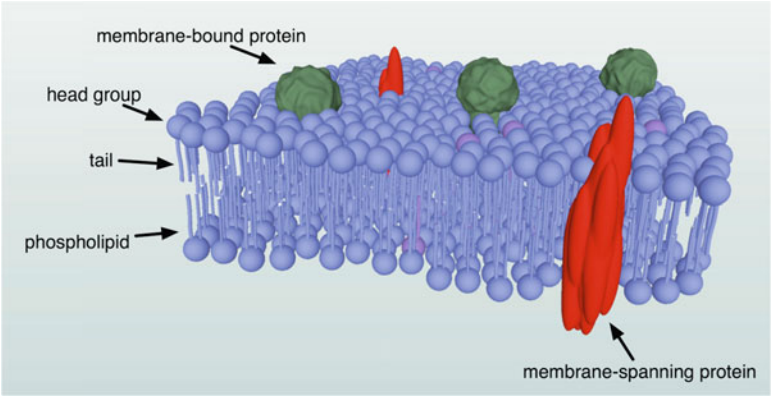

Fig. 3.1 A simplified schematic illustration of the cell membrane

proteins that are embedded in the cell membrane or in other ways associated with membrane-related processes [3].

It should also be pointed out that the complexity of the cell membrane is not restricted to its composition. The cell membrane is also constantly undergoing changes, both in shape and also by lateral movement of membrane components within the lipid bilayer. The lateral fluidity is important, as it makes the membrane self-healing, but also because it allows embedded proteins to form complexes and lipids to be able to organize into domains (often referred to as rafts) [4]. Such organized structures, in turn, play essential functional roles in for example membrane-fusion processes as well as in the pathogenesis of various diseases [4–7].

The important role of the cell membrane is manifested by the fact that more than half of the most common drugs are directed towards membrane-residing proteins [3]. However, despite their vital importance, the knowledge about the structure and function of membrane proteins is still very limited. This is, to a large extent, due to their low natural abundance and the difficulty to produce and purify them [8]. Furthermore, to preserve their function, membrane proteins should be maintained in a native-like environment, that is, in a lipid bilayer. Biosensors that are compatible with studies of lipid bilayer assemblies are therefore particularly appealing for functional investigations of membrane proteins, both from a fundamental perspective, but also with respect to the development of applications for medical diagnostics and drug development.

Supported Cell Membrane Mimics

In order to study processes associated with the cell membrane in a controllable way, it is valuable to use model membranes that are less complex than the native cell membrane. We will here focus on the two artificial membrane concepts that so

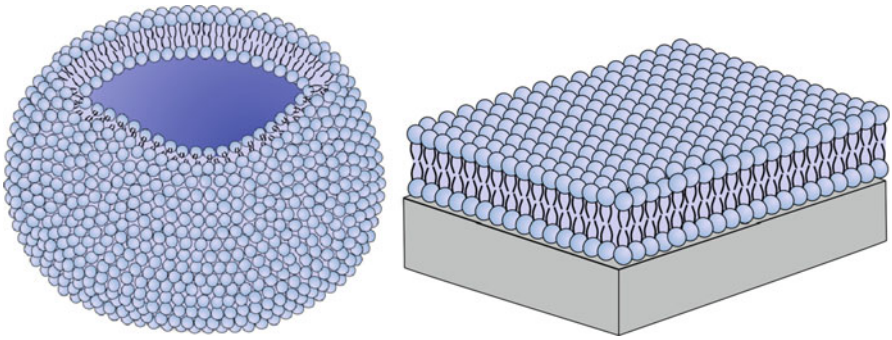

Fig. 3.2 Schematic illustrations of a lipid vesicle (*left*) and a SLB (*right*)

far have been most widely used in combination with surface-based sensors [3], including nanoplasmonic sensing. These are the lipid vesicle and the supported lipid bilayer (SLB).

Lipid Vesicles

One popular artificial cell-membrane mimic is the lipid vesicle, also known as liposome (see Fig. 3.2 left). It is spherical lipid bilayer shell that can be thought of as a small cell filled with aqueous solution. Depending on preparation method, lipid vesicles may have multiple shells (like an onion, multilamellar vesicles) or single shells (unilamellar vesicles). Unilamellar lipid vesicles, which we will focus on in this chapter, can be formed using different methods, such as tip sonication and extrusion [9–11]. In the extrusion method, which has been used in most of the examples presented below, an unordered lipid suspension is forced through a polymer membrane containing multiple nanopores. This results in lipid vesicles being formed in a process similar to that of blowing soap bubbles. The method enables the preparation of vesicles with different lipid compositions and with diameters ranging from tens to hundreds of nanometers [11].

The possibility to tether lipid vesicles to a surface [12] is highly valuable for bioanalytical sensing applications, because the transduction mechanisms of many sensors are based on biomolecule-induced optical, electrical, or mechanical changes at or close to the sensor surface. One popular means of attaching vesicles to a surface is to prepare the vesicles with a small fraction of biotin-modified lipids. These vesicles can then be bound to a surface modified with avidin (or streptavidin or NeutrAvidin) [13]. An increasingly popular approach is to use DNA as surface tethers. A lipid vesicle modified with single-stranded DNA can be site-selectively bound to a surface modified with complementary DNA strands [14, 15]. Because the hybridization process is highly specific, this strategy has the potential for multiplexed automatic sorting of vesicles, which may be of particular value for array-based membrane-proteomics [16]. DNA tethers can be attached to lipid

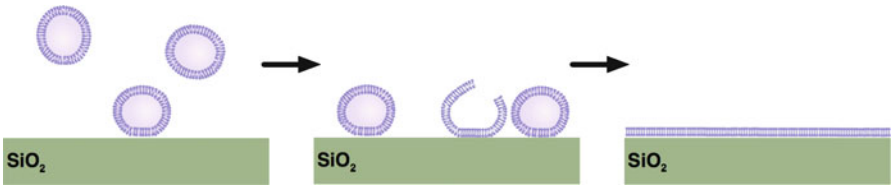

Fig. 3.3 Simplified schematic illustration of supported lipid bilayer formation from vesicles on SiO_2

vesicles by, for example, covalently attaching DNA to lipids modified with reactive head groups [17]. One can also use cholesterol-tagged DNA, which spontaneously incorporates into lipid bilayers [18, 19]. In this case, the hydrophobic cholesterol part self-incorporate into the hydrophobic part of the lipid bilayer, making the concept highly attractive in combination with, for example, lipid vesicles derived directly from native cell membranes [20].

The Supported Lipid Bilayer

An alternative to immobilized lipid vesicles is the concept of planar SLBs [21–23]. A SLB is a planar lipid bilayer that rests on a support, which may be part of a surface-based sensor system. Silica-based supports (i.e., glass) are most popular by far, mainly because of the simple SLB preparation procedure. On silica, mica and some metal oxides, such as titanium dioxide, SLBs can be formed spontaneously by adsorption and spontaneous rupture of lipid vesicles, without the need of prefunctionalization of the surface apart from normal cleaning procedures [24–26]. In contrast, under normal conditions, vesicles do not rupture on other materials, including the metals (e.g., gold and silver) that are typically used in nanoplasmonic biosensors. Instead, the vesicles adsorb and remain nonruptured on such surfaces. A simplified schematic illustration of the SLB formation process on silicon dioxide (SiO_2) is presented in Fig. 3.3.

Analogous to the lateral fluidity of a real cell membrane, the lipids in a SLB have a high lateral diffusivity, although somewhat reduced compared with that of lipid vesicles [27]. Note also that the lateral mobility of a lipid bilayer membrane is dependent on the temperature. Above a certain, lipid-specific, melting temperature, the membrane is in the *fluid phase* with a high lateral mobility. Below the melting temperature, the membrane is in a *gel phase* with a significantly reduced mobility. In one of the last examples in this chapter we describe how nanoplasmonics can be used to investigate the transition between these two phases [28].

Similarly to lipid vesicles, SLBs can be modified with different components, including membrane proteins [29]. Further, SLBs have been proven successful in studies of crystallization of water-soluble proteins [25, 30–33], multivalent interactions [34], and cell adhesion [21], to mention a few important examples.

By forming a SLB from vesicles that contain a small fraction of fluorescently labeled lipids (typically 0.1–1%), the final SLB also becomes fluorescent.

Except from traditional fluorescence-based imaging, this enables the characterization of the lateral mobility in the artificial cell membrane using, for example, fluorescence recovery after photobleaching (FRAP) [35, 36]. In FRAP, fluorescent molecules in a small region (typically around 10 μm in diameter) of the microscope's field of view are photobleached. For a fluid SLB that is considerably larger than the bleached region, nonbleached lipids will diffuse into the bleached area and the fluorescence will recover with time. In contrast, if the mobility is low, as for or a SLB in gel phase, or if the diffusion is limited to within regions smaller than the bleached area, as for a layer of vesicles, there is essentially no fluorescence recovery. This makes FRAP a powerful tool in the characterization of cell membrane mimics. Further, in the case of SLBs formed on nanostructures, the diffusion coefficient can be used to determine if a SLB follows the contour of the nanostructured surface or not [37, 38], which is of high relevance when SLBs are combined with nanoplasmonic sensors.

Other variants of supported cell membrane mimics include tethered and polymer-SLBs [39, 40]. For certain applications, these are promising alternatives to conventional SLBs, because they can be formed also on materials that do not promote spontaneous SLB formation from vesicles and also because they provide a liquid reservoir under the lipid bilayer. The latter property may be particularly beneficial when working with membrane-protruding proteins, such as ion channels. Another concept is that of free-hanging membranes [41] (SLBs that span apertures), which also provides space under the membrane and liquid reservoirs on both sides of the lipid bilayer.

Patterns of Cell Membrane Mimics

One of the attractive features of nanoplasmonic sensing is the possibility of miniaturization (down to sensing of single nanostructures) [42–46] and the potential for array based sensing [47]. In this respect, formation of SLB and vesicle patterns may be useful. In the case of vesicles, the DNA-controlled immobilization strategies discussed above are promising for multiplexed sorting of vesicles on the sensor surface [16]. DNA-controlled binding, combined with materials-specific surface modifications, can also be used to attach vesicles specifically to the most sensitive regions of a nanosensor [48]. This is particularly relevant with respect to nanoplasmonic sensors, which are known to provide sensitive fields that are highly localized to the nanostructure. It is in this context worth mentioning that such specific binding to high-sensitivity regions can be used to improve the performance of nanoplasmonic sensors [49].

Several techniques have been developed to create patterns or patches of SLBs. For example, barriers on a SiO_2 surface can be used to hinder lipids from diffusing between two adjacent fluid SLB patches [50]. As discussed in more detail below, this principle was utilized to form around 100 nm in diameter SLB patches in the bottom of nanoplasmonic holes [51]. Although to our knowledge not yet combined

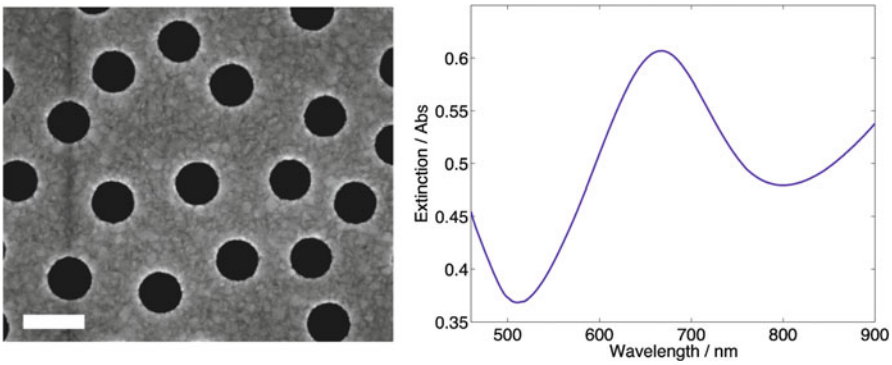

Fig. 3.4 (*Left*) Scanning electron microscopy image of a typical sample with short-range ordered nanoholes (diameter around 130 nm) in a 30 nm thick gold film supported on glass. The scale bar is 200 nm. (*Right*) Extinction spectrum of the sample shown in *left*. The left SEM image is adapted with permission from ref. [37] Copyright 2008 American Chemical Society

with nanoplasmonic sensing, microcontact printing with patterned stamps is another attractive approach to create SLB patches [52] and more serial techniques include dip-pen nanolithography [53], and nanoshaving [54]. SLBs have also been formed on nanostructured surfaces, both from a self-spreading technique [55], via the vesicle fusion principle [56] and most recently, by driving a preformed lipid bilayer [57] over a nanostructured surface using the hydrodynamic shear force generated by a liquid flow [38].

Introduction to Short-Range Ordered Nanoplasmonic Holes in Thin Metal Films

Many of the examples that are presented in this chapter are based on the optical properties of short-range ordered holes in a thin gold film. The short-range order refers to a nonperiodic arrangement of holes, but where there is a characteristic distance between neighboring holes [58] (see Fig. 3.4 left). Short-range ordered holes in thin gold films have similar sensing behavior to that of discrete plasmonic particles, such as gold nanodisks [59]. This includes a lower bulk refractive index sensitivity compared with that of conventional surface plasmon resonance (SPR) sensors based on both flat metal films as well as metal films with gratings or periodic arrays of holes in thicker metal films [60–62]. On the other hand, the average decay length of the plasmonic field associated with nanoholes in thin metal films [63] and plasmonic nanoparticles [64] is around one order of magnitude shorter (tens of nanometers) than that of conventional SPR sensors [61, 62] (typically hundreds of nanometers). From the perspective of measuring thin biomolecular films, these two properties compensate each other, leading to comparable sensing behavior for the two cases [65].

Nanoplasmonics and Artificial Cell Membranes

As explained above, lipid vesicles interact differently with different surfaces, where gold and silica-based materials may be the most well studied materials. Both of these materials are stable in typical buffer solutions. These materials are also possible to modify chemically (and specifically without cross-modification) in order to either promote or prevent binding of biomolecules [66]. Together with material-specific surface modifications, which enable either of the two materials to be selectively modified, this makes nanoplasmonic systems based on gold nanostructures on glass substrates ideally suited for biosensing applications in general. In particular, tuning the design of nanoplasmonic structures, including the chemical surface modifications, enables self-assembly of different artificial cell membrane mimics on such sensor surfaces.

Nanoplasmonic Structural Sensing: SLB Formation

To perform nanoplasmonic sensing of cell membrane mimics, it is desirable to be able to form SLBs on nanoplasmonic sensor surfaces. Because lipid vesicles rupture into SLBs on glass and silicon oxide, but not on gold, this is not straightforward, but may be achieved by coating the structure with a thin layer of silicon oxide (or another material that allows for SLB formation). This possibility was investigated by us using silicon oxide-coated short-range ordered nanoholes in a thin gold film (see Fig. 3.5) [37]. Using a small fraction of fluorescently labeled lipids in the vesicles, fluorescence-based microscopy investigations, including FRAP [36], were used to verify that macroscopic SLBs were formed on the substrate. The SLB was shown to be fluid with a high, long-range lateral mobility. From a reduction in diffusivity of around 20% compared with that of a SLB formed on flat silicon oxide, it was concluded that the SLB followed the contour of the substrate in a similar manner to that depicted in Fig. 3.5.

The SLB formation process was investigated in real-time by monitoring the temporal variation in the plasmon resonance, as shown in Fig. 3.6. The nanoplasmonic sensor structure was mounted in a flow cell that was filled with buffer.

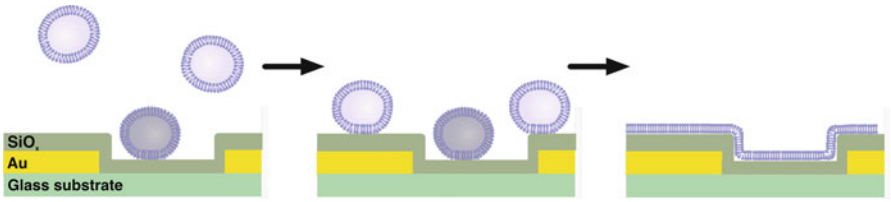

Fig. 3.5 Schematic illustration of SLB formation from vesicles on a silicon oxide-coated nanoplasmonic hole surface

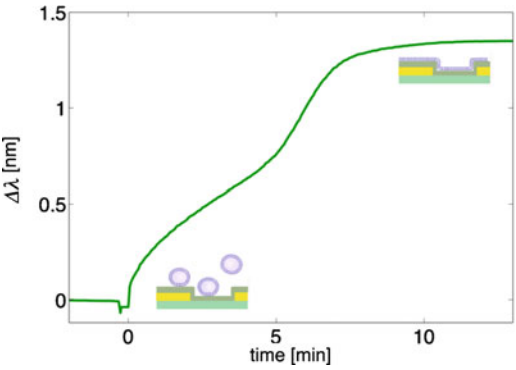

Fig. 3.6 Temporal variation in the plasmon resonance during SLB formation on silicon oxide-coated nanoplasmonic holes. The kink around 5 min is attributed to vesicle rupture. Modified with permission from ref. [63] Copyright 2008 American Chemical Society

Lipid vesicles were injected into the flow cell at 0 min and subsequent adsorption to the surface induced local changes in RI resulting in a corresponding increase in the plasmon resonance (plasmon resonance shift is denoted $\Delta\lambda$ in Fig. 3.6). At around 5 min, the sensor response accelerated before it finally saturated after around 10 min. The acceleration and corresponding kink in the response curve is attributed to the structural change during vesicle rupture.

The observed signature for bilayer formation can be understood based on the strong confinement of the plasmonic field to the sensor surface. A molecule with a refractive index (RI) different from that of the surrounding solution that enters the plasmonic field will induce a shift in the plasmon resonance (for example measured as a redshift of the wavelength at maximum extinction). This forms the base for using nanoplasmonics for RI-based sensing. However, the magnitude of the shift induced by the molecule is related to the square of the plasmonic field strength (that is, the field intensity), which is strongest at the surface of the nanoplasmonic structure and decays rapidly away from the surface [60, 67]. A molecule that binds directly on the surface will therefore induce a larger plasmonic shift than a molecule that binds (or in other ways becomes located) at a certain distance away from the surface (for example a tethered molecule). As a result, if a molecule that is placed at a distance from the surface moves closer to the surface, it would induce a redshift in the plasmon resonance wavelength. Hence, not only binding of molecules, but also the movement of molecules closer or further away from the surface can be monitored through shifts in the plasmon resonance. The acceleration of the response shown in Fig. 3.6 was therefore attributed to rupture of vesicles, resulting in a movement of the average lipid distribution closer to the surface and hence into a stronger plasmonic field [37].

The concept of using nanoplasmonics to probe biomolecular structural changes has also proven capable of resolving reversible conformational changes in proteins induced by changes in concentration of calcium (Ca^{2+}) [68]. Further, conformational or structural changes of biomolecules have been studied using so-called plasmon rulers [69]. In this method, plasmonic nanoparticles are attached to each end of the biomolecule of interest. The plasmon coupling between the two particles and hence their optical properties are highly sensitive to changes in the distance

between the particles. Because this distance will change upon a structural change in the molecule, this phenomenon can be used to study structural changes of, for example, DNA molecules [69].

Specific Protein Binding to SLBs on Nanoplasmonic Sensors

For many applications, not the least within medical diagnostics and drug development, it is essential to be able to investigate the interaction of molecules with membrane-embedded receptors. In fact, this was accomplished already in the first combination of nanoplasmonic RI sensing and artificial cell membranes using functionalized SLB patches in the bottom of nanoplasmonic holes [51].

There are mainly two criteria for the surface chemistry that are important in order to enable the investigation of specific binding reactions using surface-based sensors. First, it should be possible to modify the sensor surface with one of the two binding partners so that the interacting partner can bind specifically to the sensor. As discussed above, SLBs can be modified with a wide range of receptors and molecules, although it may for certain applications be beneficial to use other cell mimics, such as free-hanging membranes or lipid vesicles. Second, when subsequently adding the target molecule it is important that the sensor response corresponds only to specific interaction between the added target molecule and the immobilized receptor. It is therefore important to minimize unspecific adsorption of both the target as well as other biomolecules to the sensor surface, because such adsorption events will result in false positives. Fortunately, nonfunctionalized SLBs are known to provide surfaces with extremely low unspecific adsorption of biomolecules [70]. SLBs are therefore suitable to be used for studies of specific binding reactions to membrane receptors. Figure 3.7 shows an example where the protein NeutrAvidin binds specifically to biotin-modified lipids in a SLB formed on silicon oxide-coated nanoplasmonic holes. The first part in the curve shows the successful formation of a SLB from biotin-modified vesicles, manifested by the signature discussed above. After rinsing, NeutrAvidin was added to the flow cell (marked by the arrow) and the binding reaction could be investigated in real-time by monitoring the temporal variation in the plasmon resonance peak position.

Biomolecular interactions on surface-supported artificial cell membranes have been studied also with other types of nanoplasmonic sensors. This includes the use of nonperiodic nanoplasmonic holes without silicon oxide coating [51], periodic arrays of plasmonic holes [71] as well as nanoplasmonic systems that are based on discrete nanostructures, including both gold [46, 72] and silver nanostructures [73, 74]. For example, Baciu et al. recently formed lipid bilayers over surface supported gold nanorods and showed that protein–membrane interactions could be probed by monitoring the plasmonic resonance of single gold nanorods [46].

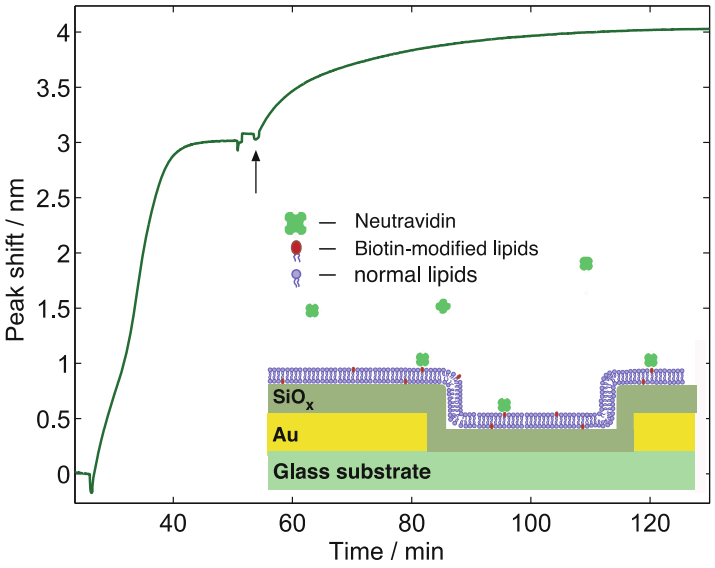

Fig. 3.7 Temporal variation in the plasmon resonance peak position of silicon oxide-coated plasmonic holes during SLB formation and subsequent binding of NeutrAvidin. The *arrow* marks the addition of the NeutrAvidin. The schematic *inset* illustrates the binding reaction

Estimation of the Decay Length of the Nanoplasmonic Field Using a SLB

A SLB forms a continuous and very homogeneous around 5 nm thick film on silicon oxide. Hence, the volume of the decaying evanescent field that is occupied by a SLB is relatively well defined, which makes the system suitable for estimates of the decay length of the nanoplasmonic field. This stems from the fact that the sensitivity to changes in bulk RI after SLB formation will be reduced compared with a bare substrate due to the volume occupied by the SLB.

The bulk RI sensitivity of a nanoplasmonic sensor is generally measured by probing the variation in the plasmon resonance during immersion in solutions of varying RI (e.g., different concentrations of glycerol). The slope of a linear fit to the peak shift ($\Delta\lambda$) vs. changes in the RI of the liquid environment represents the bulk RI sensitivity. The shift in the plasmon resonance induced by a bulk RI change is proportional to the field strength squared integrated over the whole volume that is probed. Assuming that the field decays exponentially from the surface with an average decay length, L, the peak shift induced by a bulk change on a bare sensor can then be written as [75]:

$$\Delta\lambda = \Delta n \cdot \frac{2S_{\text{bare}}}{L} \int_0^\infty \mathrm{e}^{-2z/L}\,\mathrm{d}z = \Delta n \cdot S_{\text{bare}} \tag{3.1}$$

where S_{bare} is the bulk sensitivity of the bare sensor and z is the distance from the sensor surface. Note that (3.1) is normalized with $2/L$ in order to directly obtain S_{bare} as the bulk sensitivity of the bare sensor.

The bulk sensitivity of a nanoplasmonic sensor is expected to decrease upon addition of an adsorbed film on the surface. The reason is that the adsorbed film will occupy a significant fraction of the sensitive volume of the sensor and thus exclude this volume from the bulk sensitivity measurement. Only the plasmonic field outside the adsorbed film ($z > t$) should now be considered, and the shift induced by a change in RI outside the adsorbed film is (corresponding to that in (3.1)):

$$\Delta\lambda = \Delta n \cdot \frac{2S_{\text{bare}}}{L} \int_t^\infty \mathrm{e}^{-2z/L}\,\mathrm{d}z = \Delta n \cdot S_{\text{bare}} \cdot \mathrm{e}^{-2t/L} = \Delta n \cdot S_{\text{film}} \tag{3.2}$$

where S_{film} is the measured bulk RI sensitivity after film adsorption. Interestingly, from the last equality in (3.2) it is clear that the thickness and the sensitivity measured before (S_{bare}) and after (S_{film}) film adsorption provides an estimate on the average field decay length according to:

$$L = \frac{2t}{\ln(S_{\text{bare}}/S_{\text{film}})} \tag{3.3}$$

With the adsorbed film being homogeneous, as in the case of a SLB, the average decay length can be directly obtained from (3.3) using measured values of S_{bare} and S_{film}.

Figure 3.8a shows the temporal variation in the peak position of a sample with silicon oxide-coated short-range ordered nanoholes during (i) bulk sensitivity measurement using increasing concentrations of glycerol, (ii) the formation of a SLB from lipid vesicles and (iii) a second bulk sensitivity measurement.[1] The slopes of the blue and red curves in Fig. 3.8b correspond to the bulk RI sensitivity measured before (S_{bare}) and after (S_{film}) bilayer formation. As expected, the sensitivity was lower after bilayer formation and with a SLB thickness of around 5 nm, as measured with a quartz crystal microbalance (QCM), this yielded an average field decay length of around 40 nm [63]. The corresponding decay length of the sensitivity was thus 20 nm, in agreement with both an independent study using the same combined setup [76] and with numerical simulations of similar nanoplasmonic holes [77].

[1] Note that although these three steps are sufficient for this analysis, the data also includes the adsorption of NeutrAvidin to the bilayer (a small fraction of biotinylated lipids were used as in the example above) and a third bulk sensitivity measurement. These steps are discussed in the next section.

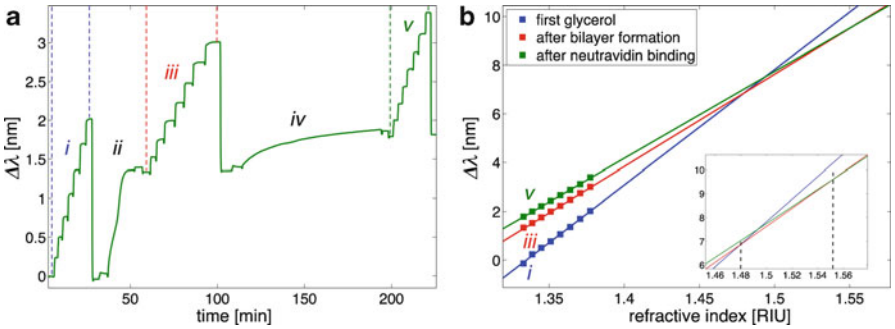

Fig. 3.8 (**a**) Temporal variations of the peak position during the following sequential steps: (i) bulk sensitivity measurement using increasing concentrations of glycerol, (ii) SLB formation from lipid vesicles, (iii) bulk sensitivity measurement, (iv) adsorption of NeutrAvidin to the functionalized bilayer, and (v) bulk sensitivity measurement. (**b**) The peak shift vs. the refractive index for the experimental values (*squares*) extracted from (**a**) for the glycerol cycle before (*blue*), after bilayer formation (*red*) and after adsorption of NeutrAvidin (*green*). The *full lines* are linear fits to the experimental data. The inset is a close up of the same graph and the *dashed lines* mark the intersections that represent the refractive index of the SLB and NeutrAvidin, respectively. Adapted with permission from ref. [63]. Copyright 2008 American Chemical Society

Estimation of the Refractive Index of SLBs and Adsorbed Molecules

In a similar manner, bulk sensitivity measurements before and after biomolecular binding can provide information on the (absolute) refractive index of the adsorbed molecules. Importantly, in this case the adsorbed biomolecular film does not need to be homogeneous. This concept was first used by Haes et al. to determine the absolute refractive index of hexadecanethiols adsorbed on silver nanoparticles [78]. The principle is exemplified here for both a SLB and for NeutrAvidin bound to the SLB using the same measurements as described in the previous section (Fig. 3.8). Bulk sensitivity measurements were performed before and after both the SLB formation and the NeutrAvidin binding reaction. The corresponding sensitivity curves are shown in Fig. 3.8b. Note that the curves are separated by the shifts induced by the SLB and the NeutrAvidin, respectively. Those shifts, in turn, are dependent on the difference in RI of the molecules and the RI of the surrounding medium. Hence, the separations of the curves in Fig. 3.8b were done at the RI of the surrounding buffer solution. This also means that the plasmon resonance shifts would have been smaller if the buffer would have had an RI closer to that of the molecules. In fact, there would be no shift at all if the buffer and the molecules would have had the same RI, simply because the binding reaction would in that case not induce a RI contrast within the probed volume. This means that the interceptions between the curves in Fig. 3.8b (the two interceptions that are marked with dashed lines in the inset) will correspond to the refractive indices of the SLB and the NeutrAvidin, respectively. In this particular example, this approach yields values of around 1.48 and 1.55 for the SLB and the protein, respectively [63], which are in excellent agreement with literature data.

Combined Nanoplasmonic and QCM-D Sensing of Artificial Cell Membranes

In this section we present how the conductive properties of nanoplasmonic hole sensors enables a direct combination with the quartz crystal microbalance with dissipation (QCM-D) monitoring technique. In particular, we describe how this setup provides two independent measures on structural changes, such as the one occurring during SLB formation.

The reader is advised to previously published reports for detailed presentations of the QCM-D technique [79]. In brief, the QCM-D technique is based on the mechanical oscillation of a piezoelectric quartz crystal, whose resonance frequency will decrease upon binding of a biomolecular film on the surface. Similarly to the nanoplasmonic sensing concept, the QCM-D method can thus be used for label-free investigation of biomolecular binding events in real-time, but instead of measuring changes in refractive index, it gives a measure on the change in the mass that couples to the mechanical oscillation of the crystal. Further, changes in the energy dissipation (the damping of the crystal, which is inversely proportional to the quality factor of the resonator) can be used to investigate changes in the viscoelastic properties of the adsorbed film.

The QCM crystal is typically driven electrically using one electrode on the sensing side that is immersed in liquid and one electrode on the backside of the crystal. Because a perforated nanoplasmonic hole film is electrically conductive, it can be used as the sensing electrode and thereby enable combined nanoplasmonic and QCM-D sensing [63, 76]. By making a small hole in the backside electrode, the nanoplasmonic response can be measured using conventional transmission spectroscopy as depicted schematically in Fig. 3.9.

The formation of a SLB from adsorption and rupture of lipid vesicles will be used to exemplify the combined setup. In 1998, the Kasemo group showed that both the frequency and the dissipation of the QCM-D setup provide clear signatures for the rupture of lipid vesicles into a planar SLB [80]. This feature was nicely reproduced also for the QCM-D signals in the combined setup (Fig. 3.10a), where the SLB was formed on a surface with silicon oxide coated nanoplasmonic holes. The origin of the peculiar QCM-D response relates to the fact that not only the mass of the lipid bilayer shells of adsorbed lipid vesicles contributes to the response, but also the liquid contained inside and between the vesicles. This results in a relatively large decrease in the frequency upon initial vesicle adsorption. However, when the vesicles rupture (at around 5–6 min in Fig. 3.10a), the hydrodynamically coupled liquid is decoupled and no longer sensed by the crystal. The rupture process therefore results in a decrease in the effective mass on the sensor and a corresponding increase in the frequency until saturation is reached at around −25 Hz (for a QCM with resonance close to 5 MHz normalized with the overtone number). The dissipation signal, in turn, reflects the viscoelastic properties of the system, yielding an increase in dissipation as the lipid vesicles adsorb on the surface. During rupture, an acoustically more rigid

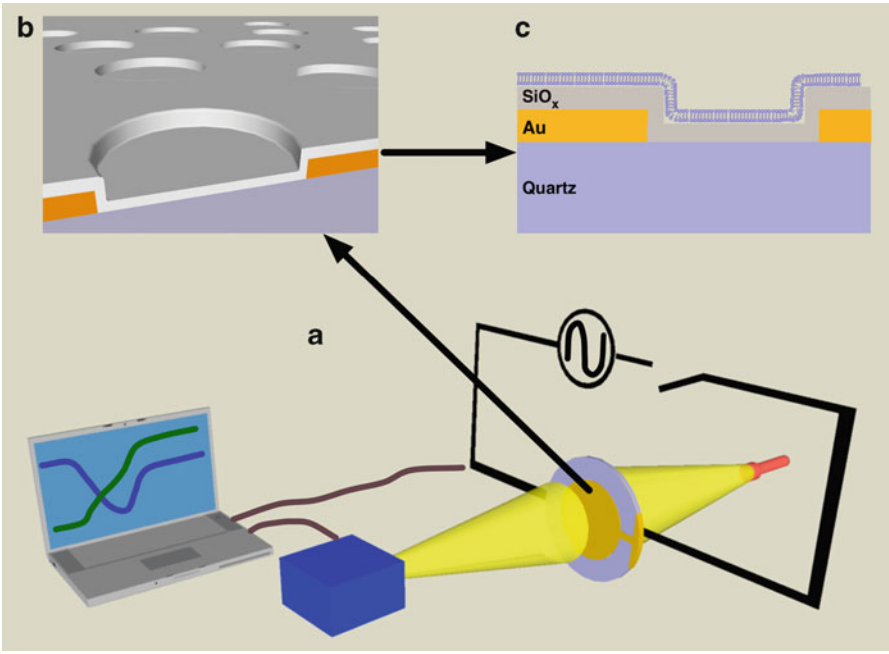

Fig. 3.9 Schematic illustration of the combined sensor principle for simultaneous nanoplasmonic and QCM-D measurements on the same surface of, for example, SLB formation. Adapted with permission from ref. [63]. Copyright 2008 American Chemical Society

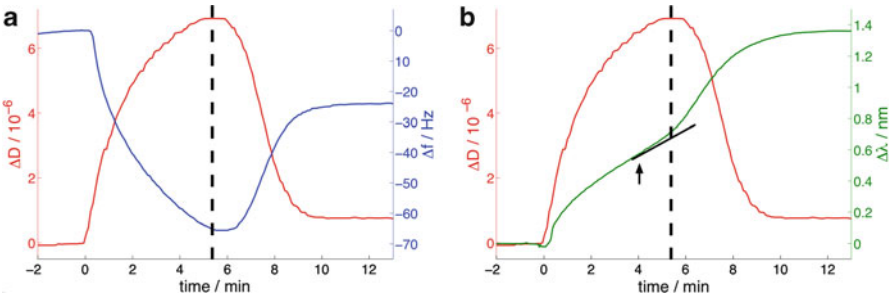

Fig. 3.10 (**a**) Temporal variation of the dissipation, ΔD (*red*) and the frequency, $\Delta f/3$, (*blue*) at the third overtone during SLB formation on the nanostructured surface. (**b**) Same as in (**a**), but instead showing the dissipation (*red*) and the LSPR peak shift, $\Delta\lambda$ (*green*). An initial (at around 0 min) drop in peak shift due to a wavelength dependence on the light scattering of vesicles has been removed. The *vertical dashed lines* in both (**a**) and (**b**) are there as visual aids and to demonstrate the temporal correlation between the turnover in the dissipation and the LSPR kink, respectively. The *short black line* and the *arrow* demonstrate the possibility to investigate the initiation of vesicle rupture from the kinky LSPR response. Adapted with permission from ref. [63]. Copyright 2008 American Chemical Society

layer is formed and the dissipation decreases to a relatively small value of around 5×10^{-7} for the final SLB.

In Fig. 3.10b, the change in dissipation of the QCM crystal is plotted together with the nanoplasmonic response, demonstrating a clear correlation in time between the two signatures for SLB formation. Note also that the nanoplasmonic response provides an estimate of the start of the vesicle rupture process, corresponding to the time at which the curve starts to deviate from the initial binding curve (marked with arrow).

The combined sensor setup contributes to improved quantification of the bound mass, in particular via the information about effective film thickness that can be obtained from the QCM-D response. It is also worth noting that the combination of two different sensor techniques, such as the one presented here, generally provide more information about a reaction then the two separate techniques do alone. In this particular case, it was possible to verify that the acceleration in the nanoplasmonic response actually reflects the structural transformation that occurs during vesicle rupture into a SLB. This added value stems mainly from the fact that the responses of different sensor methods originate from different physical processes. In this example, the nanoplasmonic response was due to local changes in refractive index, while the QCM-D response corresponds to the damping of the oscillating crystal. Recently, it was also shown that the QCM-D can be operated by using the liquid itself as an electrode, enabling QCM-D to be combined also with nonconductive nanoplasmonic sensor systems, such as an array of gold nanodisks on a blank crystal [72].

Positioning of SLBs and Lipid Vesicles in Nanoplasmonic Holes

We have so far discussed artificial membranes in combination with nanoplasmonic systems where the sensor surface consists of one material only. However, in many nanoplasmonic sensors there are two or more materials available for biomolecular interactions. Typically, one material provides the plasmonic properties (e.g., gold or silver) and the other material is the supporting substrate (e.g., glass or other dielectric materials). To function properly, such systems require material-specific surface modifications. First, this is a key aspect in order to avoid nonspecific adsorption and potential false signals, but it can also be used to control positioning of molecules. In the first report on nanoplasmonic sensing of artificial cell membranes this concept was utilized to form nanoscale SLBs in the bottom of short-range ordered holes (110 nm in diameter) in a thin gold film (20 nm) on a glass (quartz) substrate [51]. This structure was thus mainly composed of gold, except for the bottom of the holes, which were made of glass. The gold surface was made inert to vesicle adsorption by incubation of the substrate in a solution containing biotin-modified bovine serum albumin (biotin-BSA),which binds selectively to gold and not to the glass regions [14]. In this way, the glass in the bottom of the holes becomes the only region of the sensor that is available for vesicle binding, where formation of SLB patches was shown possible if calcium (Ca^{2+}) was added to the buffer.

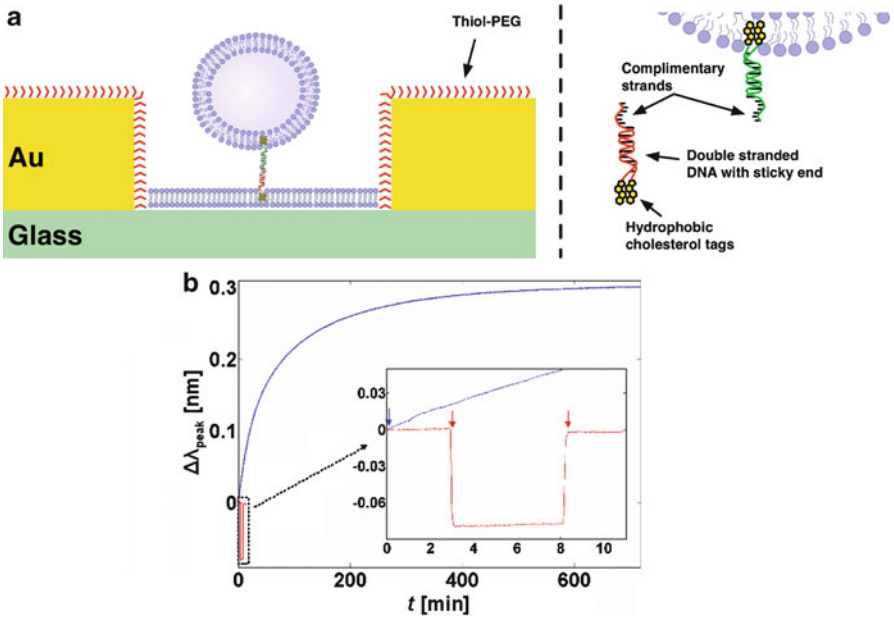

Fig. 3.11 (**a**) Schematic illustration of a vesicle tethered to a SLB in a nanoplasmonic hole using cholesterol anchored DNA. Not to scale. (**b**) Temporal variation in the plasmon resonance wavelength during addition of vesicles. The *blue curve* shows efficient binding (hybridization) and the *red curve* shows the response when noncomplementary DNA is used. (**b**) Is adapted from ref. [48]. Copyright Wiley-VCH Verlag GmbH & Co. KGaA, reproduced with permission

This concept has recently been extended to selective tethering of lipid vesicles to SLB-patches in the bottom of similar nanoplasmonic holes [48]. In this study, the gold surface was first made inert using thiol-modified poly(ethylene glycol) (thiol PEG, 3 kD average molecular weight). SLB patches could then be formed preferentially in the bottom of the holes in a way similar to that used in the previous example. Subsequently, cholesterol-modified DNA with a sticky end (a short single-stranded part) was added to the flow cell, leading to self-incorporation into the SLB patches. Lipid vesicles (around 100 nm in diameter) modified with DNA complementary to that of the DNA on the SLB patches were subsequently added (see Fig. 3.11). The vesicle binding reaction could be monitored optically through the temporal variation in the plasmon resonance (see Fig. 3.11b), yielding strong contrasts between unmodified and DNA-modified vesicles. Complementary fluorescence-based methods were used to verify that single vesicles were bound to single holes. We anticipate the positioning of lipid vesicles into the high plasmonic field strength in the void of the holes as an interesting system to probe both molecular binding to the lipid membrane as well changes in the refractive index inside the vesicles, in a way similar to the use of conventional SPR for this purpose [81].

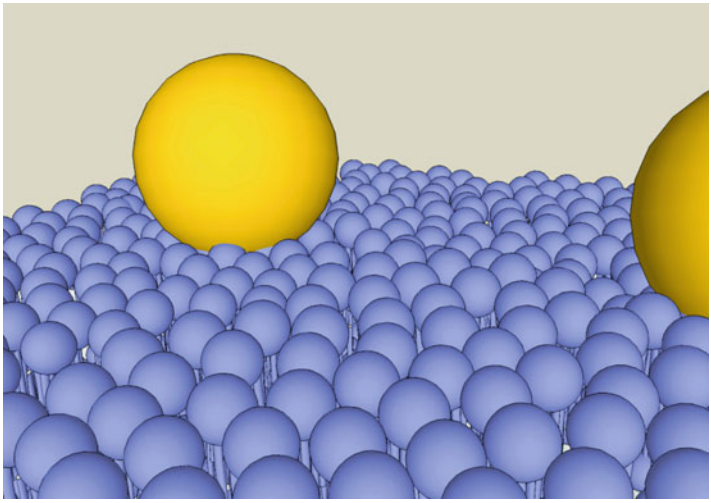

Fig. 3.12 Schematic illustration of mobile plasmonic nanoparticle probes attached to a lipid bilayer

Nanoplasmonic Particles for Imaging and Heating of Cell Membranes

With respect to the investigation of lipid bilayer membranes and associated reactions, discrete nanoplasmonic particles hold great promise, because they can be used as mobile optical probes in or on the cell membrane [82], as illustrated in Fig. 3.12.

The strong light scattering at the plasmon resonance wavelength makes it possible to image nanoplasmonic particles using, for example, confocal or dark field microscopy [83, 84]. Plasmonic particles can hence be used as labels or contrast agents for imaging in solution (as compared to surface-based nanoplasmonic systems) and even *in vivo*. For example, Xu et al. [85] used this concept to investigate the transport of silver nanoparticles through the outer and inner lipid membrane of living microbial cells. Because the particle plasmon resonance and corresponding color is dependent on the size of the particle, the particle size distribution accumulated in the cells could be measured and related to the membrane permeability and porosity at the nanometer scale.

Apart from transport through cell membranes, plasmonic particles can also be designed to bind to cell membranes. For example, Sokolov et al. functionalized gold particles with monoclonal antiepidermal growth factor receptor (anti-EGFR) antibodies [83]. The EGFR is a transmembrane glycoprotein that typically is over expressed in epithelial cancers (e.g., lung cancer). The functionalized particles could therefore be bound preferentially to cancer cells, which could thus be differentiated from healthy cells. Moreover, plasmonic particles do not only scatter light, but plasmonic excitations in general also have an absorbing component that

rapidly converts into heat [86]. This makes it possible not only to use plasmonic particles for imaging and diagnostics, but also for photothermal therapy by light-induced local heating and corresponding cell death [87].

With respect to nanoplasmonics combined with cell membranes, plasmonic heating can be used also for other purposes than therapy. Urban et al. recently used the concept to induce and investigate the transition between the gel phase (low lateral mobility) and the fluid phase (high lateral mobility) of a lipid bilayer [28]. Gold nanoparticles modified with cetyl trimethyl ammonium bromide (CTAB) were attached to the lipid membrane of a giant vesicle (tens of μm in diameter). The movements of single particles on the membrane were tracked in real-time using dark-field microscopy. At room temperature, the lipid bilayer was in the gel phase (membrane melting temperature = 41°C) and the particles attached to the membrane showed a low diffusivity. The membrane was then heated extremely locally by illuminating single gold nanoparticles with a laser. This resulted in a significant increase in the diffusivity of the same particle, illustrating that the transition from gel to fluid phase could be achieved locally and in a controlled manner with plasmonic heating.

For over 20 years, position-tracking of strongly scattering gold particles has served as a useful tool to reveal new insights about the cell membrane [82, 88]. Recently, this concept was extended to utilize also plasmon coupling between particles [89]. As mentioned above, the plasmon resonance wavelength of a particle pair is dependent on the separation between the particles [90]. Rong et al. [89] made use of this feature using nanoplasmonic particles attached to the surface of a cell. In contrast to tracking of single plasmonic particles, which can provide an excellent position determination [91], the coupling of particles could be used to determine also the distance between particles with subdiffraction limited resolution. This was successfully used to study the short-range interactions between gold nanoparticle-labeled integrin surface receptors in living cells [89].

Concluding Remarks and Outlook

The development of nanoscale sensors made compatible with cell-membrane mimics and studies of the various biological reactions that they control is very likely to contribute with important new fundamental insights. These sensor systems may also have a large impact on both medical diagnostics and drug development. The aim of this chapter is to provide an overview of how these visions so far have been approached using nanoplasmonic sensing. In particular, we have highlighted some of the unique possibilities with various nanoplasmonic systems, ranging from utilizing electrically conducting structures to discrete mobile particles in combination with cell-membrane mimics.

It is worth mentioning that the strong electromagnetic fields associated with plasmonic excitations in metal nanostructures can be beneficial in other contexts than those discussed herein. For example, the evanescent near-field inside a

nanohole in an aluminum film can be used to locally excite fluorescent molecules inside the holes. Edel et al. [92] used this concept to carry out fluorescence correlation spectroscopy to study the lateral diffusion of lipids in the membrane. Moreover, apart from tuning fluorescence emission with nanoplasmonics, the strong electromagnetic fields may also be used to enhance signals that are intrinsic to the biomolecules themselves. An interesting example that may be useful in combination with artificial cell membranes is surface-enhanced Raman spectroscopy (SERS) [67].

We also anticipate that several new applications will emerge in the near future. For example, an interesting extension of the nanoplasmonic holes formed in thin gold films on solid supports is nanoplasmonic pores that provide liquid access at both sides of the substrate [71, 93, 94]. These may become useful, for example, in combination with so-called pore-spanning lipid membranes [41], because molecular transport through such membranes could then be probed through changes in the plasmonic properties. This would, in turn, complement existing methods based on electrical readout [41] by making it feasible to study transport also of noncharged molecules. In fact, a similar concept was already proven successful using lipid vesicles and conventional SPR [81, 95]. In addition, electrical impedance spectroscopy (EIS) is well established for studies of the electrical properties of lipid membranes tethered on e.g., planar gold substrates [96]. Current work focused on the understanding of nanoplasmonics in combination with electrochemistry and EIS [97] may using, for example, conductive substrates similar to those used in combination with QCM-D measurements, open up entirely new avenues in this line of research.

By having provided a basic overview of the current knowledge on the interaction of lipid bilayers with materials of relevance for nanoplasmonic systems, we hope to have guided the readers to contribute to the further optimization of nanoplasmonic sensors systems designed for studies of cell membrane mimics.

References

1. Gouaux E, MacKinnon R. Principles of selective ion transport in channels and pumps. Science. 2005;310(5753):1461–5.
2. International Human Genome Sequencing Consortium. Finishing the euchromatic sequence of the human genome. Nature. 2004;431(7011):931–45.
3. Cooper MA. Advances in membrane receptor screening and analysis. J Mol Recognit. 2004;17(4):286–315.
4. Simons K, Ikonen E. Functional rafts in cell membranes. Nature. 1997;387(6633):569–72.
5. Campbell SM, Crowe SM, Mak J. Lipid rafts and HIV-1: from viral entry to assembly of progeny virions. J Clin Virol. 2001;22(3):217–27.
6. Fortin DL, et al. Lipid rafts mediate the synaptic localization of alpha-synuclein. J Neurosci. 2004;24(30):6715–23.
7. Salaun C, James DJ, Chamberlain LH. Lipid rafts and the regulation of exocytosis. Traffic. 2004;5(4):255–64.

8. Alves ID, Park CK, Hruby VJ. Plasmon resonance methods in GPCR signaling and other membrane events. Curr Protein Pept Sci. 2005;6(4):293–312.
9. Barenholz Y, et al. Simple method for preparation of homogeneous phospholipid vesicles. Biochemistry. 1977;16(12):2806–10.
10. Hope MJ, et al. Production of large unilamellar vesicles by a rapid extrusion procedure—characterization of size distribution, trapped volume and ability to maintain a membrane-potential. Biochim Biophys Acta. 1985;812(1):55–65.
11. Patty PJ, Frisken BJ. The pressure-dependence of the size of extruded vesicles. Biophys J. 2003;85(2):996–1004.
12. Christensen SM, Stamou D. Surface-based lipid vesicle reactor systems: fabrication and applications. Soft Matter. 2007;3(7):828–36.
13. Boukobza E, Sonnenfeld A, Haran G. Immobilization in surface-tethered lipid vesicles as a new tool for single biomolecule spectroscopy. J Phys Chem B. 2001;105(48):12165–70.
14. Svedhem S, et al. Patterns of DNA-labeled and scFv-antibody-carrying lipid vesicles directed by material-specific immobilization of DNA and supported lipid bilayer formation on an Au/SiO_2 template. Chembiochem. 2003;4(4):339–43.
15. Yoshina-Ishii C, Boxer SG. Spatially encoded and mobile arrays of tethered lipid vesicles. Biophys J. 2003;84(2):379A.
16. Städler B, et al. Creation of a functional heterogeneous vesicle array via DNA controlled surface sorting onto a spotted microarray. Biointerphases. 2006;1(4):142–5.
17. Yoshina-Ishii C, et al. General method for modification of liposomes for encoded assembly on supported bilayers. J Am Chem Soc. 2005;127(5):1356–7.
18. Pfeiffer I, Höök F. Bivalent cholesterol-based coupling of oligonucleotides to lipid membrane assemblies. J Am Chem Soc. 2004;126(33):10224–5.
19. Pfeiffer I, Höök F. Quantification of oligonucleotide modifications of small unilamellar lipid vesicles. Anal Chem. 2006;78(21):7493–8.
20. Bailey K, et al. G-protein coupled receptor array technologies: site directed immobilisation of liposomes containing the H1-histamine or M2-muscarinic receptors. Proteomics. 2009;9(8):2052–63.
21. Brian AA, McConnell HM. Allogeneic stimulation of cytotoxic T cells by supported planar membranes. Proc Natl Acad Sci U S A. 1984;81(19):6159–63.
22. Castellana ET, Cremer PS. Solid supported lipid bilayers: from biophysical studies to sensor design. Surf Sci Rep. 2006;61(10):429–44.
23. Richter RP, Berat R, Brisson AR. Formation of solid-supported lipid bilayers: an integrated view. Langmuir. 2006;22(8):3497–505.
24. McConnell HM, et al. Supported planar membranes in studies of cell-cell recognition in the immune-system. Biochim Biophys Acta. 1986;864(1):95–106.
25. Richter RP, et al. On the kinetics of adsorption and two-dimensional self-assembly of annexin A5 on supported lipid bilayers. Biophys J. 2005;89(5):3372–85.
26. Rossetti FF, et al. Interactions between titanium dioxide and phosphatidyl serine-containing liposomes: formation and patterning of supported phospholipid bilayers on the surface of a medically relevant material. Langmuir. 2005;21(14):6443–50.
27. Przybylo M, et al. Lipid diffusion in giant unilamellar vesicles is more than 2 times faster than in supported phospholipid bilayers under identical conditions. Langmuir. 2006;22(22):9096–9.
28. Urban AS, et al. Controlled nanometric phase transitions of phospholipid membranes by plasmonic heating of single gold nanoparticles. Nano Lett. 2009;9(8):2903–8.
29. Salafsky J, Groves JT, Boxer SG. Architecture and function of membrane proteins in planar supported bilayers: a study with photosynthetic reaction centers. Biochemistry. 1996;35(47):14773–81.
30. Horton MR, et al. Structure and dynamics of crystalline protein layers bound to supported lipid bilayers. Langmuir. 2007;23(11):6263–9.

31. Larsson C, Rodahl M, Höök F. Characterization of DNA immobilization and subsequent hybridization on a 2D arrangement of streptavidin on a biotin-modified lipid bilayer supported on SiO_2. Anal Chem. 2003;75(19):5080–7.
32. Reviakine I, et al. Two-dimensional crystallization of annexin A5 on phospholipid bilayers and monolayers: a solid-solid phase transition between crystal forms. Langmuir. 2001;17 (5):1680–6.
33. Reviakine I, Brisson A. Streptavidin 2D crystals on supported phospholipid bilayers: toward constructing anchored phospholipid bilayers. Langmuir. 2001;17(26):8293–9.
34. Shi J, et al. GM1 clustering inhibits cholera toxin binding in supported phospholipid membranes. J Am Chem Soc. 2007;129(18):5954–61.
35. Axelrod D, et al. Mobility measurement by analysis of fluorescence photobleaching recovery kinetics. Biophys J. 1976;16(9):1055–69.
36. Jönsson P, et al. A method improving the accuracy of fluorescence recovery after photobleaching analysis. Biophys J. 2008;95(11):5334–48.
37. Jonsson MP, et al. Supported lipid bilayer formation and lipid-membrane-mediated biorecognition reactions studied with a new nanoplasmonic sensor template. Nano Lett. 2007;7(11):3462–8.
38. Jönsson P, Jonsson MP, Höök F. Sealing of sub-micrometer wells by a shear-driven lipid bilayer. Nano Lett. 2010;10(5):1900–6.
39. Atanasov V, et al. A molecular toolkit for highly insulating tethered bilayer lipid membranes on various substrates. Bioconjug Chem. 2006;17(3):631–7.
40. Sackmann E, Tanaka M. Supported membranes on soft polymer cushions: fabrication, characterization and applications. Trends Biotechnol. 2000;18(2):58–64.
41. Römer W, Steinem C. Impedance analysis and single-channel recordings on nano-black lipid membranes based on porous alumina. Biophys J. 2004;86(2):955–65.
42. McFarland AD, Van Duyne RP. Single silver nanoparticles as real-time optical sensors with zeptomole sensitivity. Nano Lett. 2003;3(8):1057–62.
43. Mock JJ, et al. Shape effects in plasmon resonance of individual colloidal silver nanoparticles. J Chem Phys. 2002;116(15):6755–9.
44. Raschke G, et al. Biomolecular recognition based on single gold nanoparticle light scattering. Nano Lett. 2003;3(7):935–8.
45. Rindzevicius T, et al. Plasmonic sensing characteristics of single nanometric holes. Nano Lett. 2005;5(11):2335–9.
46. Baciu CL, et al. Protein-membrane interaction probed by single plasmonic nanoparticles. Nano Lett. 2008;8(6):1724–8.
47. Endo T, et al. Multiple label-free detection of antigen-antibody reaction using localized surface plasmon resonance-based core-shell structured nanoparticle layer nanochip. Anal Chem. 2006;78(18):6465–75.
48. Dahlin AB, Jonsson MP, Höök F. Specific self assembly of single lipid vesicles in nanoplasmonic apertures in gold. Adv Mater. 2008;20(8):1436–42.
49. Feuz L, et al. Improving the limit of detection of nanoscale sensors by directed binding to high-sensitivity areas. ACS Nano. 2010;4(4):2167–77.
50. Groves JT, Ulman N, Boxer SG. Micropatterning fluid lipid bilayers on solid supports. Science. 1997;275(5300):651–3.
51. Dahlin A, et al. Localized surface plasmon resonance sensing of lipid-membrane-mediated biorecognition events. J Am Chem Soc. 2005;127(14):5043–8.
52. Hovis JS, Boxer SG. Patterning and composition arrays of supported lipid bilayers by microcontact printing. Langmuir. 2001;17(11):3400–5.
53. Lenhert S, et al. Massively parallel dip-pen nanolithography of heterogeneous supported phospholipid multilayer patterns. Small. 2007;3(1):71–5.
54. Shi JJ, Chen JX, Cremer PS. Sub-100 nm patterning of supported bilayers by nanoshaving lithography. J Am Chem Soc. 2008;130(9):2718–9.

55. Furukawa K, et al. Supported lipid bilayer self-spreading on a nanostructured silicon surface. Langmuir. 2007;23(2):367–71.
56. Huang SCJ, et al. Formation, stability, and mobility of one-dimensional lipid bilayers on polysilicon nanowires. Nano Lett. 2007;7(11):3355–9.
57. Jonsson P, et al. Shear-driven motion of supported lipid bilayers in microfluidic channels. J Am Chem Soc. 2009;131(14):5294–7.
58. Hanarp P, et al. Control of nanoparticle film structure for colloidal lithography. Colloids Surf A. 2003;214(1–3):23–36.
59. Prikulis J, et al. Optical spectroscopy of nanometric holes in thin gold films. Nano Lett. 2004;4(6):1003–7.
60. Jonsson MP, et al. Nanoplasmonic biosensing with focus on short-range ordered nanoholes in thin metal films. Biointerphases. 2008;3(3):FD30–40.
61. Homola J, Yee SS, Gauglitz G. Surface plasmon resonance sensors: review. Sensors Actuators B. 1999;54(1–2):3–15.
62. Brolo AG, et al. Surface plasmon sensor based on the enhanced light transmission through arrays of nanoholes in gold films. Langmuir. 2004;20(12):4813–5.
63. Jonsson MP, Jönsson P, Höök F. Simultaneous nanoplasmonic and quartz crystal microbalance sensing: analysis of biomolecular conformational changes and quantification of the bound mass. Anal Chem. 2008;80(21):7988–95.
64. Haes AJ, et al. A nanoscale optical biosensor: the long range distance dependence of the localized surface plasmon resonance of noble metal nanoparticles. J Phys Chem B. 2004;108 (1):109–16.
65. Svedendahl M, et al. Refractometric sensing using propagating versus localized surface plasmons: a direct comparison. Nano Lett. 2009;9(12):4428–33.
66. Marie R, et al. Generic surface modification strategy for sensing applications based on Au/SiO_2 nanostructures. Biointerphases. 2007;2(1):49–55.
67. Willets KA, Van Duyne RP. Localized surface plasmon resonance spectroscopy and sensing. Annu Rev Phys Chem. 2007;58:267–97.
68. Hall WP, et al. A calcium-modulated plasmonic switch. J Am Chem Soc. 2008;130(18):5836–7.
69. Sönnichsen C, et al. A molecular ruler based on plasmon coupling of single gold and silver nanoparticles. Nat Biotechnol. 2005;23(6):741–5.
70. Glasmästar K, et al. Protein adsorption on supported phospholipid bilayers. J Colloid Interface Sci. 2002;246(1):40–7.
71. Lesuffleur A, et al. Plasmonic nanohole arrays for label-free kinetic biosensing in a lipid membrane environment. In: 31st annual international the conference of the IEEE EMBS. Minneapolis, Minnesota. September 2-6, 2009. p. 1481–4.
72. Larsson EM, et al. A combined nanoplasmonic and electrodeless quartz crystal microbalance setup. Rev Sci Instrum. 2009;80(12):125105.
73. Das A, et al. Screening of type I and II drug binding to human cytochrome P450-3A4 in nanodiscs by localized surface plasmon resonance spectroscopy. Anal Chem. 2009;81 (10):3754–9.
74. Galush WJ, et al. A nanocube plasmonic sensor for molecular binding on membrane surfaces. Nano Lett. 2009;9(5):2077–82.
75. Jung LS, et al. Quantitative interpretation of the response of surface plasmon resonance sensors to adsorbed films. Langmuir. 1998;14(19):5636–48.
76. Dahlin AB, et al. Synchronized quartz crystal microbalance and nanoplasmonic sensing of biomolecular recognition reactions. ACS Nano. 2008;2(10):2174–82.
77. Rindzevicius T, et al. Nanohole plasmons in optically thin gold films. J Phys Chem C. 2007;111(3):1207–12.
78. Haes AJ, et al. Nanoscale optical biosensor: short range distance dependence of the localized surface plasmon resonance of noble metal nanoparticles. J Phys Chem B. 2004;108 (22):6961–8.

79. Höök F, Kasemo B. The QCM technique for biomacromolecular recognition: technical and theoretical aspects. In: Wolfbeis OS, editor. The Springer series on chemical sensors and biosensors. Berlin: Springer; 2006.
80. Keller CA, Kasemo B. Surface specific kinetics of lipid vesicle adsorption measured with a quartz crystal microbalance. Biophys J. 1998;75(3):1397–402.
81. Brändén M, Dahlin S, Höök F. Label-free measurements of molecular transport across liposome membranes using evanescent-wave sensing. Chemphyschem. 2008;9(17):2480–5.
82. Sheetz MP, et al. Nanometer-level analysis demonstrates that lipid flow does not drive membrane glycoprotein movements. Nature. 1989;340(6231):284–8.
83. Sokolov K, et al. Real-time vital optical imaging of precancer using anti-epidermal growth factor receptor antibodies conjugated to gold nanoparticles. Cancer Res. 2003;63 (9):1999–2004.
84. El-Sayed IH, Huang X, El-Sayed MA. Surface plasmon resonance scattering and absorption of anti-EGFR antibody conjugated gold nanoparticles in cancer diagnostics: applications in oral cancer. Nano Lett. 2005;5(5):829–34.
85. Xu X-HN, et al. Real-time probing of membrane transport in living microbial cells using single nanoparticle optics and living cell imaging. Biochemistry. 2004;43(32):10400–13.
86. El-Sayed MA. Some interesting properties of metals confined in time and nanometer space of different shapes. Acc Chem Res. 2001;34(4):257–64.
87. Jain PK, et al. Review of some interesting surface plasmon resonance-enhanced properties of noble metal nanoparticles and their applications to biosystems. Plasmonics. 2007;2:107–18.
88. Suzuki KGN, et al. GPI-anchored receptor clusters transiently recruit Lyn and G alpha for temporary cluster immobilization and Lyn activation: single-molecule tracking study 1. J Cell Biol. 2007;177(4):717–30.
89. Rong G, et al. Resolving sub-diffraction limit encounters in nanoparticle tracking using live cell plasmon coupling microscopy. Nano Lett. 2008;8(10):3386–93.
90. Rechberger W, et al. Optical properties of two interacting gold nanoparticles. Opt Commun. 2003;220(1–3):137–41.
91. Nan XL, Sims PA, Xie XS. Organelle tracking in a living cell with microsecond time resolution and nanometer spatial precision. Chemphyschem. 2008;9(5):707–12.
92. Edel JB, et al. High spatial resolution observation of single-molecule dynamics in living cell membranes. Biophys J. 2005;88(6):L43–5.
93. Jonsson MP, et al. Locally functionalized short-range ordered nanoplasmonic pores for bioanalytical sensing. Anal Chem. 2010;82(5):2087–94.
94. Eftekhari F, et al. Nanoholes as nanochannels: flow-through plasmonic sensing. Anal Chem. 2009;81(11):4308–11.
95. Brändén M, et al. Refractive-index based screening of membrane-protein mediated transfer across biological membranes. Biophys J. 2010;99:1–10.
96. Knoll W, et al. Solid supported lipid membranes: new concepts for the biomimetic functionalization of solid surfaces. Biointerphases. 2008;3(2):FA125–35.
97. Sannomiya T, et al. Electrochemistry on a localized surface plasmon resonance sensor. Langmuir. 2009;26(10):7619–26.

Chapter 4
Dual Functions of Nanoplasmonic Optical Antennas: Nanoplasmonic Gene Switches and Biosensors

Somin Eunice Lee, Younggeun Park, Taewook Kang, and Luke P. Lee

Abstract Within a living cell, the intracellular distribution is spatially nonuniform and dynamically changing over time in response to environmental cues. By focusing on electromagnetic fields down to dimensions smaller than the diffraction limit, nanoplasmonic optical antennas, functioning as nanoplasmonic gene switches, enable on- demand and spatially precise regulation of genetic activity to give rise to location-specific function. In addition to on-demand gene regulation, nanoplasmonic optical antennas also function as *label-free* biosensors that significantly enhance spectral information for plasmon resonance energy transfer, surface-enhanced Raman spectroscopy, and nanoplasmonic molecular rulers. "Spectral snapshots" (i.e., spectroscopic imaging) of the dynamically changing intracellular biochemical distribution can be obtained over time.

S.E. Lee • L.P. Lee (✉)
Department of Bioengineering, University of California-Berkeley, UCSF/UCB Joint Graduate Group in Bioengineering, Berkeley Sensor & Actuator Center, 408C Stanley Hall, Berkeley, CA 94720-1762, USA
e-mail: lplee@berkeley.edu

Y. Park
Department of Bioengineering, University of California-Berkeley, UCSF/UCB Joint Graduate Group in Bioengineering, Berkeley Sensor & Actuator Center, 408C Stanley Hall, Berkeley, CA 94720-1762, USA

Department of Chemical and Biomolecular Engineering, Sogang University, Seoul, South Korea

T. Kang
Department of Chemical and Biomolecular Engineering, Sogang University, Seoul, South Korea

A. Dmitriev (ed.), *Nanoplasmonic Sensors*, Integrated Analytical Systems,
DOI 10.1007/978-1-4614-3933-2_4,

Introduction

A living cell dynamically responds to its perpetually changing environment, such that signaling proteins, transcription factors, and enzymes are constantly synthesized, transported from one organelle to another, and finally shuttled to their appropriate locations to give rise to cell function. The intracellular distribution of these molecular complexes is spatially nonuniform and dynamically changing over time in response to environmental cues [1]. Quantitative knowledge of the intracellular biochemical distribution is critical for understanding intracellular organization and function in developmental processes, growth, differentiation, apoptosis, and disease.

Intracellular manipulation in conjunction with real-time imaging can provide unparalleled insight into the dynamic biochemical distribution as a result of local environmental changes. Recent advancements in nanotechnology and nanoplasmonics now enable sub-nanometer and nanometer tools to directly interface with intracellular processes. By focusing on electromagnetic fields down to dimensions smaller than the diffraction limit, nanoplasmonic optical antennas—functioning as nanoplasmonic gene switches—enable spatially precise regulation of genetic activity to give rise to location-specific function. Nanoplasmonic optical antennas—functioning as biosensors—also focus electromagnetic fields to significantly enhance spectral information for plasmon resonance energy transfer (PRET) [2–4], surface-enhanced Raman spectroscopy (SERS) [5–13], and nanoplasmonic molecular rulers [14]. In this way, quantitative "spectral snapshots" (i.e., spectroscopic imaging) of the intracellular biochemical distribution can be obtained over time as function of changes in the local environment.

In this chapter, the dual functions of nanoplasmonic optical antennas as nanoplasmonic gene switches and biosensors are reviewed (Fig. 4.1). Because of their extraordinarily large surface-to-volume ratio, nanoplasmonic optical antennas are ideal carriers of cargo, such as DNA/RNA oligonucleotides. In the presence of light that is matched to their plasmon resonance wavelength, nanoplasmonic optical antennas behave as nanoplasmonic gene switches by photothermally releasing their DNA/RNA cargo, activating DNA/RNA functionality, and regulating intracellular genes on-demand. Nanoplasmonic optical antennas also serve as label-free biosensors to acquire enhanced spectral information. PRET biosensors [2–4] are described, where energy transfer results in biochemical-specific spectral information by matching the plasmon resonance spectrum of the biosensors to the absorption spectrum of the molecules-of-interest. SERS biosensors are also reviewed, where biochemical-specific spectral information is enhanced in proximity of the biosensor's surface. Nanoplasmonic molecular rulers for label-free measurement of DNA length and real-time kinetic studies of nuclease activity are also reviewed. Equipped with new dual-functional nanoplasmonic optical antennas to directly manipulate and image the intracellular environment, quantitative approaches

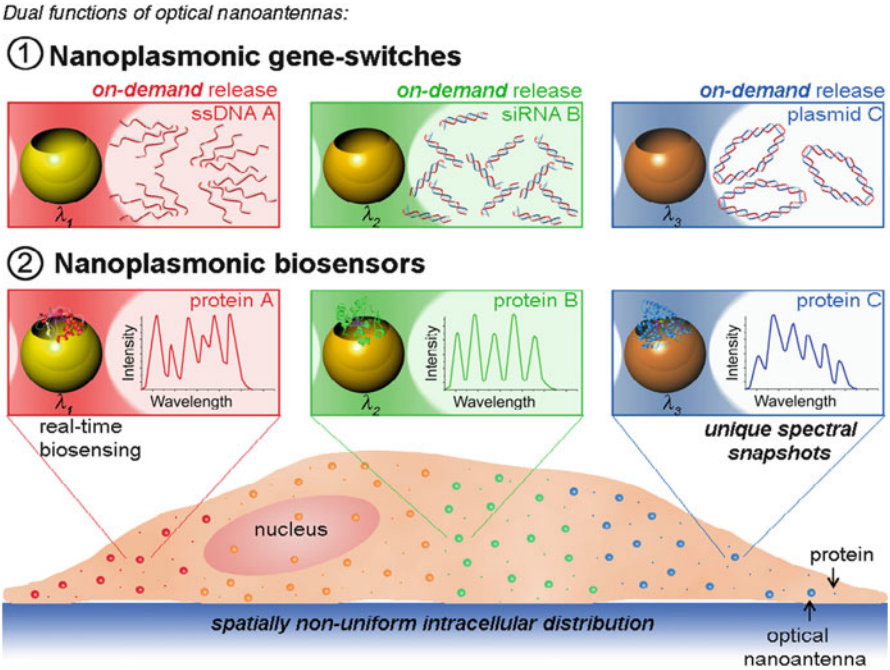

Fig. 4.1 Concept of optical nanoantennas for nanoplasmonic gene regulation and nanoplasmonic biosensing. The intracellular distribution is spatially nonuniform and dynamically changing over time in response to environmental cues. By focusing electromagnetic fields down to dimensions smaller than the diffraction limit, light-absorbing optical nanoantennas—functioning as nanoplasmonic gene switches—enable spatiotemporally precise regulation of genes. Light-scattering optical nanoantennas—functioning as nanoplasmonic biosensors—enhance spectral information for plasmon resonance energy transfer (PRET) and surface-enhanced Raman spectroscopy (SERS). "Spectral snapshots" of the dynamically changing intracellular biochemical distribution can be obtained over time using multiple optical nanoantennas with distinct plasmon resonance wavelengths matched to incident light wavelengths λ_1, λ_2, and λ_3. Reprinted with permission from Lee et al Current opinion in biotechnology, vol 21, pp 489–497, Copyright 2010 Elsevier

should capture dynamic "spectral snapshots" of the intracellular biochemical distribution of living systems that were otherwise previously impossible to detect using conventional methods.

Dual Functions of Nanoplasmonic Optical Antennas

Dual-functional nanoplasmonic optical antennas are powerful biological tools for on-demand gene regulation and label-free biosensing. A nanoplasmonic optical antenna receives, focuses, and transmits incoming optical and near-infrared (NIR) electromagnetic radiation as an analogous, classical antenna receives, focuses, and

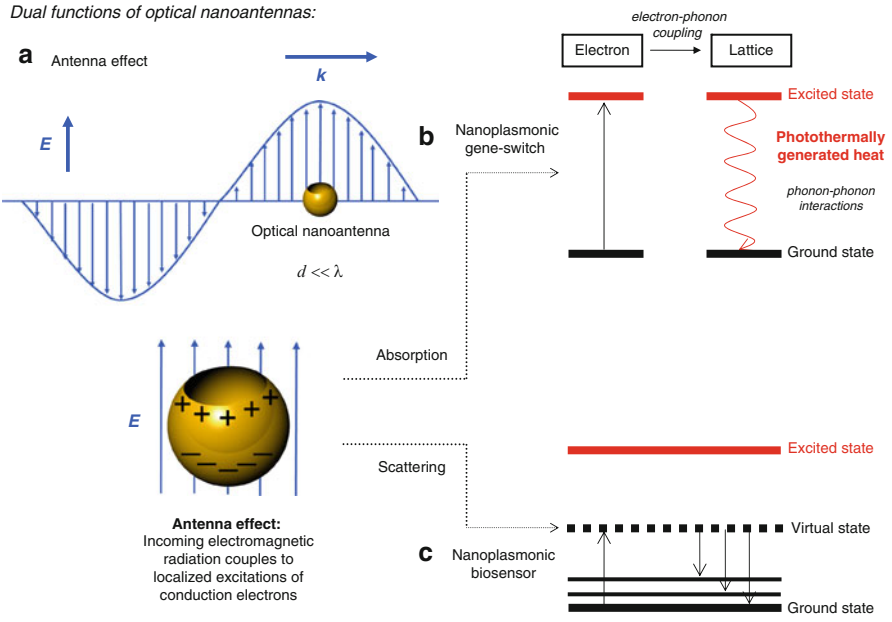

Fig. 4.2 Design and mechanism of the dual functions of optical nanoantennas. (**a**) When the diameter d of an optical nanoantenna is much smaller than the wavelength λ of incoming electromagnetic radiation: an optical nanoantenna focuses incoming electromagnetic radiation down to dimensions smaller than the diffraction limit, otherwise known as the antenna effect, by coupling the incoming electromagnetic radiation to the localized excitation of conduction electrons at the conductor-dielectric interface of the optical nanoantenna. **(b)** Nanoplasmonic gene-switches are geometrically designed such that their absorption cross-sections dominate over their scattering cross-sections. Therefore, when the incoming electromagnetic radiation is coupled to the localized excitation of conduction electrons at the conductor-dielectric interface of the nanoplasmonic gene-switch, these conduction electrons are excited from the ground (unexcited) state. Energy is then transferred from the excited conduction electrons to the lattice through electron–phonon collisions. As the system relaxes back to the ground state, the absorbed energy is finally dissipated as heat through phonon-phonon interactions. **(c)** Nanoplasmonic biosensors are designed such that their scattering cross-sections dominate over their absorption cross-sections in order to substantially enhance scattering spectra of biomolecules in proximity of the biosensors. Therefore, when the incoming electromagnetic radiation is coupled to the localized excitation of conduction electrons at the conductor-dielectric interface of the biosensor, a momentary transition from the ground state to a virtual state occurs. Transitions are related to the biochemical composition. Enhanced Raman scattering, utilized in SERS, results when the transition is immediately to a vibrational level of the ground state. Enhanced Rayleigh scattering, utilized in PRET, results when the transition is immediately back to the ground state

transmits radio-frequency electromagnetic radiation. A nanoplasmonic optical antenna focuses incoming electromagnetic radiation down to dimensions smaller than the diffraction limit, otherwise known as the antenna effect, by coupling the incoming electromagnetic radiation to the localized excitation of conduction electrons at the conductor-dielectric interface of the nanoplasmonic optical antenna (Fig. 4.2a). This antenna effect is prominent when the incoming electromagnetic

radiation is matched to the plasmon resonance of the nanoplasmonic optical antenna, and as a result, the conduction electrons at the conductor-dielectric interface of the nanoplasmonic optical antenna collectively oscillate in phase on resonance.

Nanoplasmonic optical antennas, functioning as nanoplasmonic gene switches, utilize the antenna effect to convert absorbed light energy into surface-localized heat, otherwise known as photothermal conversion [15–17]. Nanoplasmonic gene switches are geometrically designed such that their absorption cross-sections dominate over their scattering cross-sections for efficient photothermal conversion. Therefore, when the incoming electromagnetic radiation is coupled to the localized excitations of conduction electrons at the conductor-dielectric interface of the nanoplasmonic gene switch, these conduction electrons are excited from the ground (unexcited) state (Fig. 4.2b). Treating the electrons and the lattice as two coupled systems [17], energy is then transferred from the excited conduction electrons to the lattice through electron–phonon collisions. As the system relaxes back to the ground state, the absorbed energy is finally dissipated as heat through phonon–phonon interactions. This photothermally generated heat transfer from the surface of nanoplasmonic gene switches' to the surrounding cellular environment is highly localized, decaying exponentially within a few nanometers [15, 18, 19] and therefore is thought to have minimal adverse effects on cells. Additionally, the plasmon resonance of the nanoplasmonic gene switches is also tuned to the near-infrared (NIR) during fabrication, since tissues and cells are essentially transparent in the NIR wavelength regime [20]. Nanoplasmonic gene switches utilize photothermally generated heat to liberate surface-bound cargo, such as single-stranded DNA, small interfering RNA (siRNA), or plasmid DNA, in a highly localized manner (Fig. 4.3a).

Nanoplasmonic optical antennas, functioning as label-free biosensors, also utilize the antenna effect. To increase biosensor sensitivity, the geometry and structure of biosensors are specifically designed to substantially enhance the antenna effect by utilizing (1) the plasmon coupling between closely positioned geometrical features of the biosensor and (2) the lightning rod effect [21] at sharp geometrical features of the biosensor. Biosensors are designed such that their scattering cross-sections dominate over their absorption cross-sections in order to substantially enhance scattering spectra of molecular complexes in proximity of the biosensors. Therefore, when the incoming electromagnetic radiation is coupled to the localized excitations of conduction electrons at the conductor-dielectric interface of the biosensor, intense scattered radiation is generated. Molecules in proximity undergo a momentary transition from the ground state to a virtual state occurs (Fig. 4.2c). Transitions are related to the biochemical composition. Enhanced Raman scattering, utilized in SERS, results when the transition is immediately to a vibrational level of the ground state. Enhanced Rayleigh scattering, utilized in PRET, results when the transition is immediately back to the ground state. In this way, biosensors enable a highly sensitive and label-free spectral readout of the biochemical composition in the local environment.

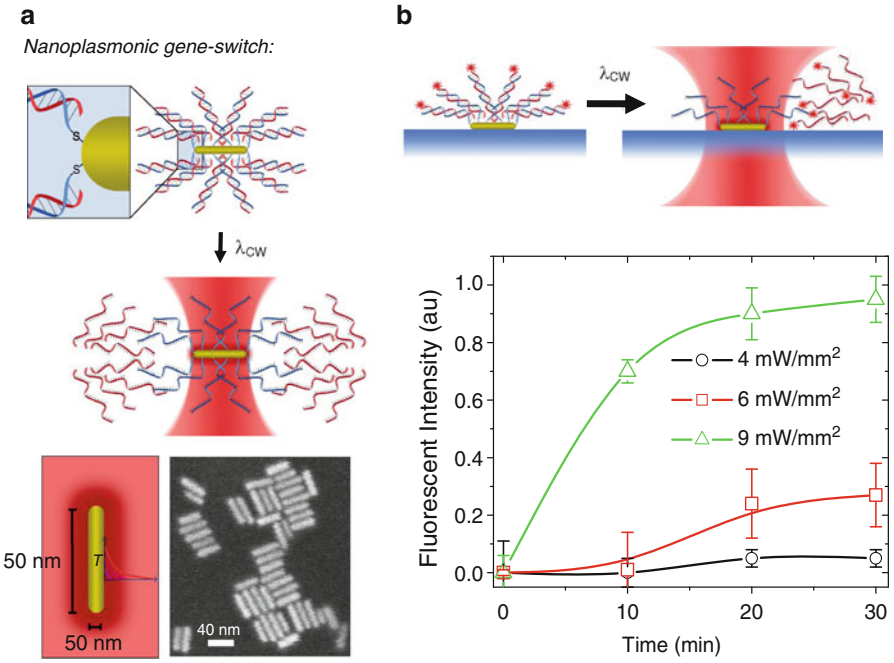

Fig. 4.3 Nanoplasmonic gene-switch. (**a**) Duplexes of thiol-modified sense and antisense DNA are covalently bound to the gold rod-shaped nanoplasmonic gene-switch. In the presence of continuous-wave illumination, the antisense DNA strands photothermally dehybridize while the thiol-modified sense strands remain attached to the gene-switch. The photothermally generated heat transfer from the surface of the gene-switch to the surrounding cellular environment is highly localized, decaying exponentially within a few nanometers. Scanning electron microscopy image of gold rod-shaped nanoplasmonic gene-switches. (**b**) Fluorescently-labeled antisense DNA are hybridized to thiolated complementary sense DNA and bound to the gene-switch's surface through gold-thiol covalent bonds. Gene-switches conjugated with sense-antisense DNA are immobilized onto a glass substrate. Photothermal dehybridization is monitored by observing the fluorescence intensity in an area away from the gene-switches. Initially, the fluorescence intensity in the background is zero. Immobilized gene-switches are then illuminated with light at varying power densities. The resulting dehybridization of fluorescently-labeled antisense DNA is observed by visualizing an increase in the background fluorescence intensity over time. Reprinted with permission from [18], Copyright 2009 American Chemical Society

Intracellular Nanoplasmonic Gene Switches

Nanoplasmonic gene switches enable on-demand and spatially precise intracellular regulation of genetic activity. Using remote-controlled NIR light as a trigger to release free oligonucleotides and "activate" their functionality, endogenous intracellular genes can be silenced on-demand. In addition to the inhibitory effects, exogenous foreign genes can also be introduced and expressed on-demand.

Because of their extraordinarily large surface-to-volume ratio, nanoplasmonic gene switches—in this case rod-shaped nanoplasmonic optical antennas—are ideal

carriers of oligonucleotides, such as short single-stranded DNA, siRNA, and plasmid DNA (Fig. 4.1). For example, short single-stranded DNA, otherwise known as antisense DNA, are hybridized to thiolated complementary sense DNA and bound to the switch's surface through the gold-thiol covalent bond [18] (Fig. 4.3a). While attached to the switches, oligonucleotides are rendered inactive due to steric hindrances between the tightly-packed DNA. In the presence of continuous-wave incident light that is matched to their plasmon resonance wavelength, antisense DNA is photothermally dehybridized from its carrier to freely interact with the local environment. To demonstrate controlled photothermal dehybridization, fluorescently labeled antisense DNA are hybridized to thiolated complementary sense DNA and bound to the switch's surface through the gold-thiol covalent bond (Fig. 4.3b). Switches conjugated with double-stranded DNA are immobilized onto a glass substrate. Photothermal dehybridization is monitored by observing the fluorescent intensity in an area away from the switches. Initially, the fluorescent intensity in the background is zero. Immobilized switches are then illuminated with light at varying power densities. The resulting dehybridization of fluorescently-labeled antisense DNA is observed by visualizing an increase in the background fluorescent intensity over time. Antisense DNA has also been photothermally dehybridized from other antenna structures, such as gold nanoshells [22] and gold nanoprisms [23]. Release of circular plasmid DNA [24, 25], linearized plasmid DNA [26], siRNA [27], and directly conjugated single-stranded DNA [28] has also been demonstrated by photothermally melting the carrier. This strategy of photothermal dehybridization offers several notable advantages. Firstly, no chemical modifications are made to the antisense DNA strand itself since a thiolated complementary strand is used to directly conjugate to the switch's surface. Because chemical modifications can interfere with nucleic acid functionality and gene silencing efficacy, unmodified antisense DNA is highly desirable. Secondly, gold-thiol covalent bonds are stable after illumination, such that the switch's surface remains covered with the thiolated complementary sense strands. With respect to cytotoxicity, this surface coating of complementary strands after illumination is critical. While the gold core is widely accepted as being biocompatible, bare nanoparticles have been shown to interact with proteins and induce misfolding at physiological conditions [29]. Maintaining surface coverage with complementary strands after illumination also prevents reattachment of antisense DNA strands back onto the switch since rehybridization events are thermodynamically unfavorable due to steric hindrances and electrostatic repulsive forces at the switch's surface [30]. Finally, the structural integrity of the switches is uncompromised after illumination. Maintaining structure after illumination allows unique nano-scale optical properties to be retained, thereby enabling the same incident light wavelength to be used. Repetitive or finely-graded release of cargo is conceivable for future applications requiring precise temporal patterns of cargo release. Maintaining structure after illumination is also crucial for in vivo applications, where the size, geometry, coating material, and core material of nanoparticles are precisely designed and carefully characterized for proper biodistribution [31].

Using nanoplasmonic gene switches, endogenous intracellular genes are silenced on-demand. As illustrated in Fig. 4.4a, the duplex of thiol-modified sense and unmodified antisense DNA is covalently bound to nanoplasmonic gene switches and internalized in BT-474 cells. In the presence of continuous-wave illumination, antisense DNA strands dehybridize and release into the cytosol, while the thiol-modified sense strands remain attached to the switches. The unbound antisense DNA then binds to a portion of the mature mRNA corresponding to ERBB2. Once the mRNA/antisense DNA heteroduplex is formed, it is recognized and degraded by RNase H enzymes in the cytosol, thereby silencing ERBB2. As seen in Fig. 4.4b, on-demand silencing of ERBB2 expression is qualitatively demonstrated using immunofluorescence imaging and quantitatively shown using flow cytometry [18]. Since RNase H is ubiquitously present in both the cytosol and the nucleus [32, 33], an alternative model [32] suggests that unbound antisense DNA transports to the nucleus. In the nucleus, the antisense DNA binds to the premature mRNA. Once this heteroduplex is formed, it is recognized and degraded by RNase H enzymes in the nucleus. Intracellular genes can also be nanoplasmonically silenced using siRNA [27]. In addition to the inhibitory effects of interfering oligonucleotides, exogenous foreign genes can also be nanoplasmonically expressed on-demand [26]. In this way, nanoplasmonic gene switches can enable spatially precise regulation of intracellular activity to give rise to location-specific function.

Intracellular PRET Biosensors

In addition to on-demand gene regulation, nanoplasmonic optical antennas can also serve as label-free biosensors to significantly enhance spectral information for PRET. Plasmon resonance energy can be transferred from nanoplasmonic optical antennas to molecules in proximity. When the plasmon resonance spectrum of an antenna is intentionally matched to the absorption spectrum of the molecules, energy transfer by PRET [2–4] results in wavelength-specific quenching in the Rayleigh scattering spectrum (Fig. 4.5a). For instance, when the plasmon resonance energy of the biosensors is transferred to adsorbed cytochrome *c*, wavelength-specific quenching is observed in the Rayleigh scattering spectrum of the biosensor [2, 4]. The quenching positions exactly correspond to the absorbance peaks of cytochrome *c*. PRET efficiency is dependent on the extent of the spectral overlap, as shown in Fig. 4.5b with biosensors of different plasmon resonances. Therefore, the greater the spectral overlap, the higher the PRET efficiency and plasmon quenching intensity.

Real-time production of cytochrome *c* in living cells can be dynamically imaged using PRET spectroscopy [4]. It is well known that cytochrome *c* is released from the mitochondria to the cytoplasm in response to pro-apoptotic stimuli, such as ethanol, due to increased permeability of the outer membrane of the mitochondria [34]. Therefore, when carboxylic acid-terminated biosensors are internalized into HepG2 cells and cells are then exposed to ethanol, the production of intracellular

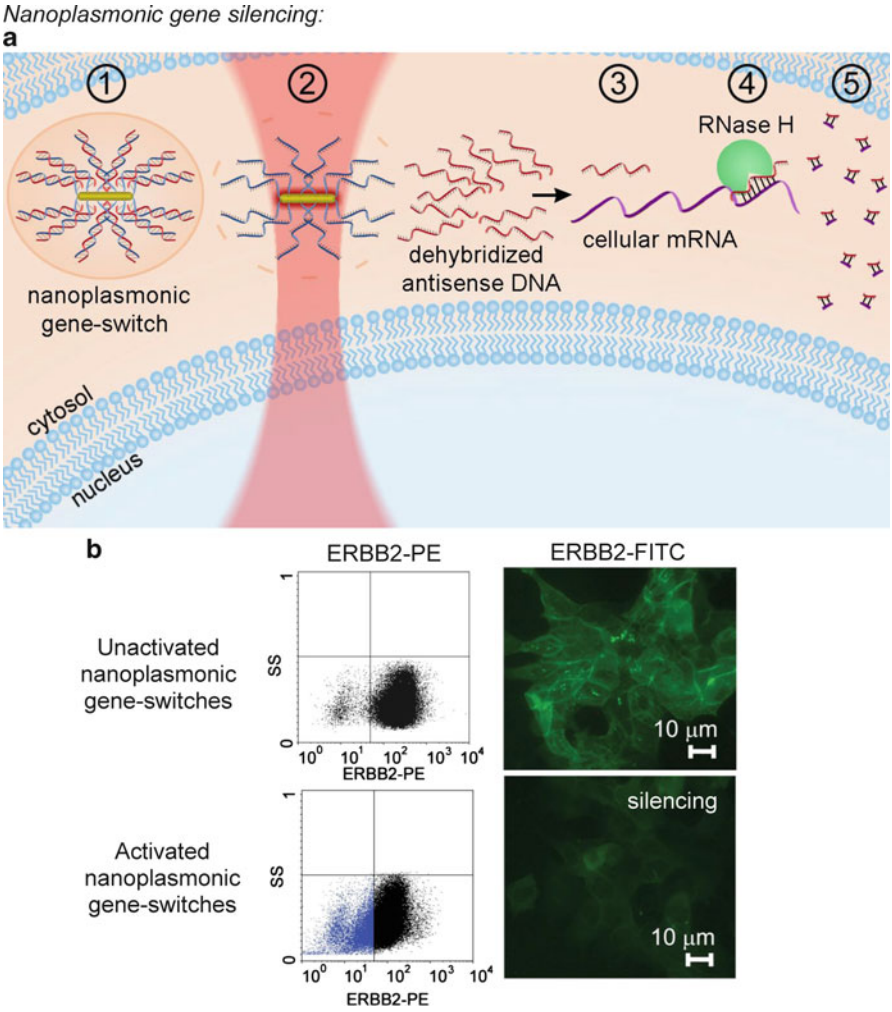

Fig. 4.4 Nanoplasmonic gene silencing. (**a**) Concept of nanoplasmonic gene silencing of human epidermal growth factor 2 (HER2/neu, also known as ERBB2) in human BT-474 breast carcinoma cells. In step 1, duplexes of thiol-modified sense and unmodified antisense DNA are covalently bound to gene-switches and internalized in BT-474 cells. In step 2, in the presence of continuous-wave illumination, antisense DNA strands dehybridize and release into the cytosol, while the thiol-modified sense strands remain attached to the gene-switches. In step 3, the unbound antisense DNA then binds to a portion of the mature mRNA corresponding to the ERBB2 gene. In step 4, once the mRNA/antisense DNA heteroduplex is formed, it is recognized by RNase H enzymes. In step 5 RNase H enzymes degrade the heteroduplex, thereby silencing the ERBB2 gene. (**b**) Flow cytometric data and immunofluorescent images showing nanoplasmonic gene silencing of ERBB2 using activated nanoplasmonic gene-switches in BT-474 cells. Flow cytometric data and immunofluorescent images of the control showing no silencing using unactivated nanoplasmonic gene-switches. Part (**a**) reprinted with permission from Lee et al Current opinion in chemical biology, vol 14, pp 623–633, Copyright 2010 Elsevier. Part (**b**) reprinted with permission from [18], Copyright 2009 American Chemical Society

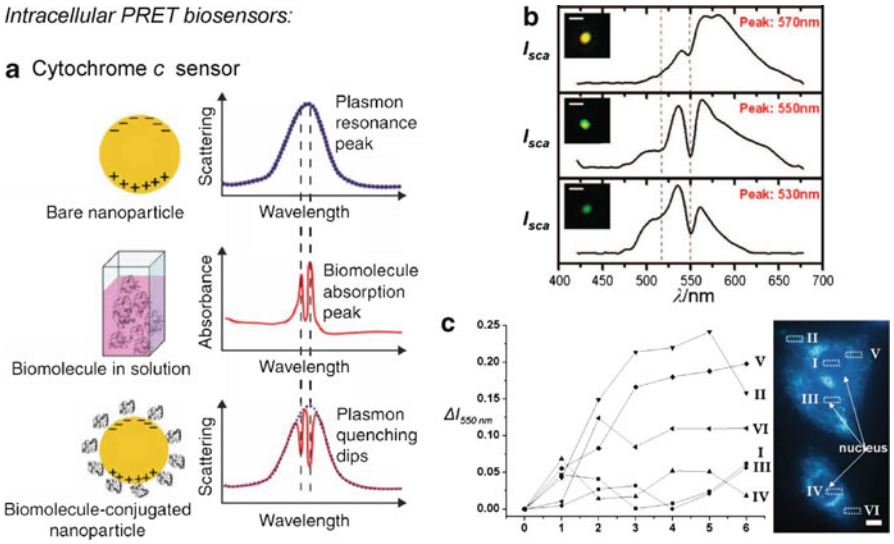

Fig. 4.5 Intracellular biosensor for PRET imaging of cytochrome *c*. (**a**) Typical Rayleigh scattering spectrum of bare gold nanoparticles. Typical absorption spectra of biomolecules in bulk solution. When the plasmon resonance spectrum of the biosensors is intentionally matched to the absorption spectrum of these biomolecules, plasmon resonance energy transfer (PRET) results in wavelength-specific quenching in the Rayleigh scattering spectra of the biosensors that is specific to the biomolecules. (**b**) Representative Rayleigh scattering spectra and corresponding colors. PRET efficiency depends on the extent of spectral overlap between the plasmon resonance spectrum of the biosensor and the absorption spectrum of cytochrome *c*. The greater the spectral overlap, the higher the PRET efficiency and plasmon quenching intensity. (**c**) Dynamic imaging of intracellular cytochrome *c* using PRET. Intracellular cytochrome *c* production is induced using 100 mM ethanol. Representative dark-field image of human HepG2 liver hepatocellular carcinoma cells with internalized biosensors. Part (**a**) reprinted with permission from [2], Copyright 2007 Nature Publishing Group. Part (**b**, **c**) reprinted with permission from [4], Copyright 2009 American Chemical Society

cytochrome *c* results in distinguishable wavelength-specific quenching in the scattering spectra over time. In Fig. 4.5c, the positions I, III, and IV correspond to the nucleus, whereas the positions II, V, and VI correspond to the cytoplasm. Dynamic quenching as a function of time is shown at different positions. Before exposure to ethanol, no quenching was observed at these intracellular positions. On the other hand, after exposure to ethanol, significant quenching at 550 nm occurred. The observed quenching at 550 nm in the scattering spectra is attributed to the release of cytochrome *c* from mitochondria to cytoplasm induced by ethanol.

In addition to cytochrome *c* sensing, highly sensitive and selective metal ion sensing is also enabled by PRET spectroscopy. When the transition metal ion (blue) binds with the matching ligand (red), *d* orbitals are split, generating a new absorption band of the metal-ligand complex in the visible range [3] (Fig. 4.6a). Due to this new absorption band, Rayleigh scattering energy from the biosensor can be transferred to the metal-ligand complex. There is no spectral overlap between

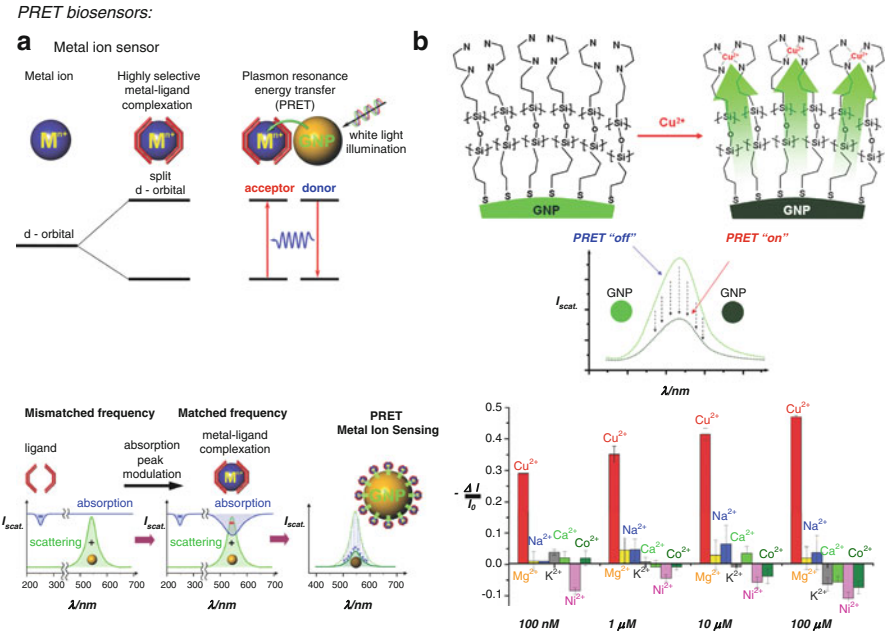

Fig. 4.6 Biosensor for PRET imaging of metal ions. (**a**) When the transition metal ion (*blue*) binds with the matching ligand (*red*), *d* orbitals are split, generating a new absorption band of the metal-ligand complex in the visible range. Due to this new absorption band, Rayleigh scattering energy from the biosensor can be transferred to the metal-ligand complex. There is no spectral overlap between ligands and the biosensor in the absence of the metal ion. When the electronic absorption frequency of the metal-ligand complex matches with the Rayleigh scattering frequency, the selective energy transfer is induced by this spectral overlap and distinguishable resonant quenching in the resonant Rayleigh scattering spectrum is observed. (**b**) Concept of PRET sensing of Cu^{2+} between a single nanoparticle and the conjugated resonant complexes $[Cu(TMSen)_2]^{2+}$ and resulting Rayleigh scattering profile. Biosensor response is compared for biologically relevant metal ions (Cu^{2+}, K^+, Ca^{2+}, Mg^{2+}, and Na^+) and transition metal ions (Co^{2+} and Ni^{2+}). With the exception of Cu^{2+}, no energy transfer or color change is observed in the presence of other metal ions. Reprinted with permission from [3], Copyright 2009 Nature Publishing Group

ligands and the biosensor in the absence of the metal ion. When the electronic absorption frequency of the metal-ligand complex matches with the Rayleigh scattering frequency, the selective energy transfer is induced by this spectral overlap and distinguishable resonant quenching in the resonant Rayleigh scattering spectrum is observed [3] (Fig. 4.6a). PRET biosensors enable high spatial resolution due to the small nanometer-scale size of the biosensor, as well as highly sensitive biosensing that is up to 100–1,000 times higher sensitivity compared to conventional organic reporter-based methods.

High selectivity of metal ions by PRET can be achieved by the selective formation of metal ion complexes and selective resonant quenching of the biosensor by the conjugated complexes. Here, this biosensor is composed of a gold

nanoparticle, which allows for the surface-binding of an ethylenediamine moiety for selective recognition of aqueous Cu^{2+}. Using this biosensor, PRET sensing of Cu^{2+} is visualized in the Rayleigh scattering profile [3] in Fig. 4.6b. To demonstrate the highly selectivity for Cu^{2+} by this PRET biosensor, its response to other biologically relevant metal ions (Cu^{2+}, K^{+}, Ca^{2+}, Mg^{2+}, and Na^{+}) and other transition metal ions (Co^{2+} and Ni^{2+}) are compared in Fig. 4.6b. With the exception of Cu^{2+}, no energy transfer or color change is observed when using other metal ions in the presence of the PRET biosensor. This remarkable selectivity is attributed to two key features of this detection system: exclusive complex formation with only the target metal ion and energy transfer only in the case of a frequency-matching condition between the biosensor and the metal–ligand complex. This approach can easily be extended to detect other metal ions and various molecules by either substituting another resonant metal-ligand pair or by modulating the biosensor's plasmon resonance positions. This highly resolved sensing ability can be also used for mapping location-specific metal ions concentrations in living systems.

Interestingly, PRET sensing of cytochrome *c* and metal ion Cu^{2+} result in distinctly different effects evident in the Raleigh scattering spectrum. Depending on the spectral bandwidth of the molecule's absorption spectrum, an amplitude decrease or wavelength-specific spectral quenching is observed in the Raleigh scattering spectrum of the biosensor. In the case of cytochrome *c*, its absorption spectrum consists of the spectrally narrow bandwidths. Therefore, PRET biosensing of cytochrome *c* results in wavelength-specific spectral quenching in the Raleigh scattering spectrum, where the quenching positions exactly correspond to the absorbance peaks of cytochrome *c* at 525 nm (FWHM ~ 20 nm) and 550 nm (FWHM ~ 12 nm). In contrast, the exclusive complex formation with the target metal ion Cu^{2+} results in an absorption spectrum with a spectrally wide bandwidth. As a result, PRET biosensing of metal ion Cu^{2+} results in an amplitude decrease in the Raleigh scattering spectrum. More experimental and theoretical approaches are needed to address the effects of the extinction coefficient strength, plasmon dependence, surface coverage, and distance dependence on energy transfer by PRET.

SERS Biosensors

For biological and biomedical applications, the ideal biologically functional nanoplasmonic optical antenna must exhibit non-toxicity, plasmon resonance in the NIR regime, high local field enhancement, and mobility under physiological conditions. Therefore, the material, size, and structure of the nanoplasmonic optical antenna are designed to simultaneously achieve the aforementioned features. Gold is selected since it is widely accepted as a biocompatible material. The nano-scale size and dimensions of the nanoplasmonic optical antenna are selected to achieve plasmon resonance tunability in the NIR regime between 700 and 1,300 nm, where tissues and cells are essentially transparent [20]. Finally, a nanocrescent structure is

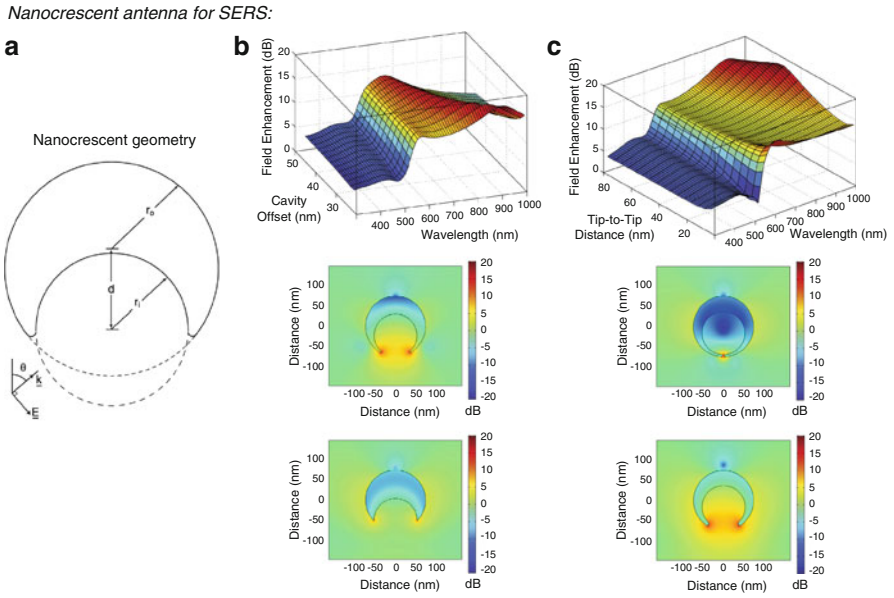

Fig. 4.7 Nanocrescent antenna for SERS. (**a**) Diagram of the nanocrescent illustrating key geometric parameters: outer radius r_o; an inner radius r_i; the center-to-center distance between the circles (cavity offset) d; and the filet radius of the sharp tips s. (**b**) Maximum local field enhancement as a function of cavity offset d and incident free-space wavelength λ_0. Field distribution for $d = 21$ nm, $\lambda_0 = 785$ nm. Field distribution for $d = 46$ nm, $\lambda_0 = 785$ nm ($r_o = 70$ nm, $r_i = 50$ nm, $s = 1$ nm, $\theta = 0\,^\circ$). (**c**) Maximum local field enhancement as a function of tip-to-tip distance and incident free-space wavelength λ_0. Field distribution for $t = 5$ nm, $\lambda_0 = 1{,}000$ nm and (**c**) field distribution for $t = 70$ nm, $\lambda_0 = 1{,}000$ nm ($r_o = 70$ nm, $r_i = 50$ nm, $d = 15$ nm, $\theta = 0\,^\circ$). Reprinted with permission from [37], Copyright 2008 IOP Science

specifically designed to substantially enhance the antenna effect by utilizing the plasmon coupling between closely-spaced crescent tips and the lightning rod effect [21] at the sharp geometrical features of the nanocrescent.

A systematic numerical analysis is used to optimize the geometry of the nanocrescent to show high local field enhancement and plasmon resonance tunability in the NIR regime. A finite element model is used to solve the time-harmonic Maxwell equations over the domain-of-interest, which reduces to the Helmholtz equation [35]. The domain consists of the 2D nanocrescent in free space (vacuum) with a transverse magnetic (TM) plane wave incident at an angle θ measured from the vertical axis. The permeability of gold is assumed to be $\mu_r = 1$ and the complex permittivity ε is assumed to be a function of wavelength [36]. The geometry of the nanocrescent is defined by four parameters: an outer radius r_o; an inner radius r_i; the center-to-center distance between the circles (cavity offset) d; and the filet radius of the sharp tips s (Fig. 4.7a).

Significant plasmon band tuning can be seen by varying the overall nanocrescent size or by varying the cavity offset d, keeping the other parameters constant [37]. As shown in Fig. 4.7b, by decreasing d, the plasmon resonance peak can be brought well into the NIR regime. Varying d affects the tip-to-tip distance of the nanocrescent, and as d is reduced, dipole-like coupling increases between the tips. High local field enhancement can be achieved by varying the tip-to-tip distance t. As shown in Fig. 4.7c, as t becomes less than 10 nm, strong coupling occurs between the tips and high local field enhancement occurs, concentrated in a small region near the tips. Therefore, by varying the nanocrescent geometry, the plasmon resonance peak can be tuned to the NIR and the local field enhancement can be increased significantly, with maximum enhancement of the electric field amplitude of approximately 100 for realistic geometries.

Having optimized geometrical features by numerical analysis, biologically functional gold nanocrescent antennas are batch-fabricated for use as SERS biosensors (Fig. 4.8a). Firstly, a monolayer of sacrificial spherical polystyrene nanospheres is cast onto a photoresist-coated glass substrate (Fig. 4.8b). Secondly, a thin gold layer is coated onto the surface of the polystyrene nanospheres using electron beam evaporation. During this deposition, the sample is rotated at an angle with respect to the gold target. The plasmon resonance and enhancement factor can be tuned during fabrication by selecting the size of the sacrificial polystyrene nanospheres, varying the thickness of the thin gold layer, and varying the deposition angle. The gold-coated polystyrene nanospheres are then lifted off from the glass substrate. Finally, the sacrificial polystyrene is dissolved. The resulting gold nanocrescent antennas exhibit plasmon resonance in the NIR regime. High local field enhancement is achieved due to the lightning rod effect at the sub-10 nm sharp edges and plasmon coupling between the closely-spaced crescent tips.

To characterize biosensor functionality, different concentrations of Rhodamine 6G (R6G) are adsorbed onto the surface of antennas, since the biochemical composition and the Raman scattering spectra of R6G are well known. A NIR laser source, matched to the plasmon resonance of the antenna, is used to induce the antenna effect. SERS spectra are then collected from a single gold nanocrescent antenna. Nanocrescent antennas significantly enhance the Raman scattering of R6G [9]. As seen in Fig. 4.8c, vibrational peaks (e.g., 615 cm^{-1}), corresponding to the aromatic ring bending and stretching of R6G, are significantly enhanced, with an estimated Raman enhancement factor of larger than 10 [10], by using a nanocrescent antenna as a biosensor.

When nanoplasmonic optical antennas are internalized in living cells for use as intracellular biosensors, their intracellular position and orientation are random. However, the specific intracellular position of a nanoplasmonic optical antenna is critical for biosensing since the intracellular biochemical distribution is spatially nonuniform. Additionally, the orientation of asymmetrical antennas with respect to the incoming electromagnetic radiation is also crucial for enabling large local field enhancement and therefore high biosensor sensitivity. As shown in Fig. 4.9a, the maximum local field enhancement occurs when the propagation direction of the incoming electromagnetic radiation is parallel to the symmetry line of the

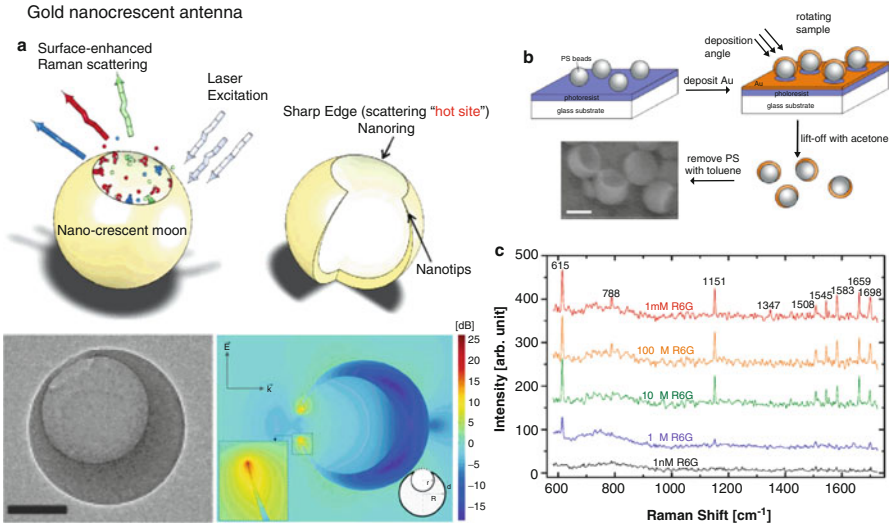

Fig. 4.8 Gold nanocrescent antenna functioning as biosensor for SERS. (**a**) Concept of gold nanocrescent antenna functioning as a biosensor for SERS. The gold surface can be functionalized with target ligands to recognize specific biomolecules. High local field enhancement is achieved due to the lightning rod effect at the sub-10 nm sharp edges and plasmon coupling between the closely-spaced crescent tips. Nanocrescent antenna enhances the Raman scattering intensity of biomolecules in proximity of the antenna. Transmission electron microscope images of gold nanocrescent antenna. The scale bar is 100 nm. Local electric field amplitude distribution of a nanocrescent antenna at its 785 nm scattering peak wavelength. The geometry of the nanocrescent is shown in the inset schematics where r is the inner radius, R is the outer radius, and d is the center-center distance as shown as two partially overlapping circles. For this nanocrescent antenna, $r = 150$ nm, $R = 200$ nm, $d = 51$ nm. The shown field amplitude is normalized with respect to the incident field amplitude. The direction of light incidence is from left to right. (**b**) Batch fabrication of gold nanocrescent antennas. Firstly, a monolayer of sacrificial spherical polystyrene nanospheres is cast onto a photoresist-coated glass substrate. Secondly, a thin gold layer is coated onto the surface of the polystyrene nanospheres using electron beam evaporation. During this deposition, the sample is rotated at an angle with respect to the gold target. The gold-coated polystyrene nanospheres are then lifted off from the glass substrate. Finally, the sacrificial polystyrene is dissolved. Scanning electron microscopy image of resulting gold nanocrescent antennas. The scale bar is 200 nm. (**c**) SERS spectra of different concentrations of Rhodamine 6G (R6G) adsorbed on a single gold nanocrescent antenna. Reprinted with permission from [9], Copyright 2005 American Chemical Society

nanocrescent structure. To enable external control of position and orientation by an external magnetic field, magnetic nanocrescent antennas have been designed and fabricated (Fig. 4.9a, b). Magnetic nanocrescent antennas consist of multi-layers of gold, silver, iron, and gold (Au/Ag/Fe/Au). The fabrication of magnetic nanocrescent antennas is similar to the fabrication of gold nanocrescent antennas, except that thin layers of Au, Ag, Fe, and Au are sequentially deposited onto the surface of polystyrene nanospheres using electron beam evaporation. Similar to gold nanocrescent antennas, magnetic antennas also exhibit plasmon

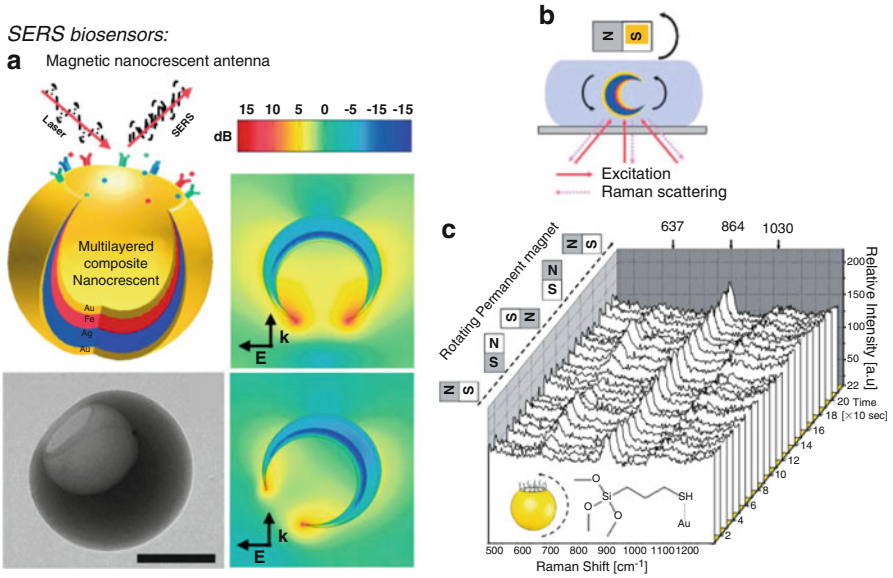

Fig. 4.9 Magnetic nanocrescent antenna functioning as biosensor for SERS. (**a**) Concept of magnetic nanocrescent antenna functioning as a biosensor for SERS. A magnetic nanocrescent antenna consists of multilayers of gold, silver, iron, and gold. The gold surface can be functionalized with target ligands to recognize specific biomolecules. High local field enhancement is achieved due to the lightning rod effect at the sub-10 nm sharp edges and plasmon coupling between the closely-spaced crescent tips. Nanocrescent antenna enhances the Raman scattering intensity of biomolecules in proximity of the nanoantenna. Transmission electron microscope images of gold nanocrescent antenna. The scale bar is 100 nm. Simulated local electric-field-amplitude enhancement in dB by a single magnetic nanocrescent oriented 0 ° and 45 ° with respect to the 785 nm light incident direction. (**b**) Concept of externally controllable biosensor using an external magnetic field. (**c**) MPTMS is covalently bound to the surface of magnetic nanocrescent antennas. A NIR laser source, matched to the plasmon resonance wavelength of the biosensor, is used to induce the antenna effect. An external magnet is continuously rotated 20 ° to systematically control the position and orientation of this magnetic biosensor. SERS spectra are then collected from single particles at different positions and orientations. Reprinted with permission from [8], Copyright 2005 John Wiley and Sons

resonance in the NIR regime. Large local field enhancement is also achieved due to the lightning rod effect at the sub-10 nm sharp edges and plasmon coupling between the closely-spaced crescent tips.

To demonstrate the magnetic nanocrescent antenna as an externally controllable and highly sensitive biosensor, 3-mercaptopropyltrimethoxysilane (MPTMS) is covalently bound to the surface of magnetic nanocrescent antennas. A NIR laser source, matched to the plasmon resonance of the biosensor, is used to induce the antenna effect. An external magnet is continuously rotated 20 ° to systematically control the position and orientation of this magnetic biosensor. SERS spectra are then collected from single particles at different positions and orientations. As seen in Fig. 4.9c, the vibrational peak at 637 cm^{-1}, corresponding to MPTMS, is significantly enhanced by the biosensor when its structural symmetry line is parallel

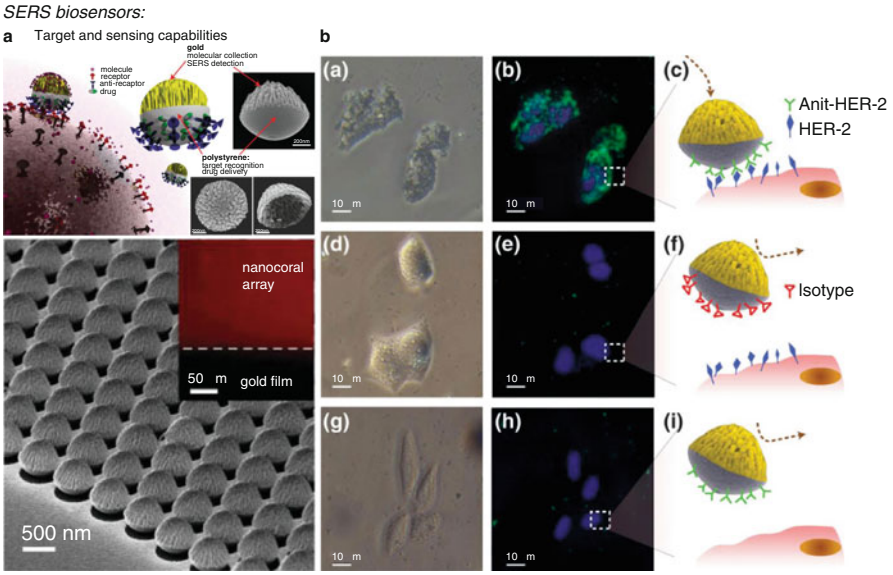

Fig. 4.10 Biosensor for SERS with target and sensing capabilities. (**a**) Concept of nanocoral biosensor for target and sensing. Insets show scanning electron microscopy images of fabricated nanocoral biosensors; the polystyrene (PS) template has been etched in the bottom right inset. (**b**) Targeting capabilities of nanocoral biosensors. (*a*) bright-field, (*b*) fluorescent, and (*c*) schematic images of 300-nm nanocoral biosensors attached to human BT-474 breast carcinoma cell surfaces with HER-2/anti-HER-2 binding; fluorescent PS nanospheres are used as the nanocoral template; (*d*) bright-field, (*e*) fluorescent, and (*f*) schematic images for a control experiment where PS is functionalized with isotype antibodies and very few nanocoral biosensors bind to the cells; (*g*) bright-field, (*h*) fluorescent, and (*i*) schematic images for a control experiment for human HeLa cervical carcinoma cells with PS functionalized with anti HER-2 and very few nanocoral biosensors bind to the cells. Reprinted with permission from [38], Copyright 2010 John Wiley and Sons

with the propagation direction of the incoming NIR electromagnetic radiation [8]. These externally controllable and highly sensitive biosensors will be useful for obtaining location-specific biochemical information in living systems.

Biosensors can also be chemically functionalized to target specific cellular entities for location-specific biochemical information. Achieving both targeting and sensing via SERS by a single nanoplasmonic optical antenna is challenging because targeting ligands attached on the surface will inevitably impede SERS measurement of the molecules-of-interest. Therefore, a portion of the antenna surface must be kept ligand-free to prevent blockage of the SERS sensing surface and interference of mixed signals, while the other portion of the antenna surface is conjugated with targeting ligands. Therefore, a new type of nanoplasmonic optical antenna, called a nanocoral [38], is designed which combines cellular-specific targeting with biochemical sensing, yet decouples the two functional modes (Fig. 4.10a). Analogous to natural sea corals that use roughened surfaces to maximize surface area for efficient capture of light and food particles, nanocoral antennas utilize a highly roughened surface at the

nanoscale, on one hemisphere, to increase analyte adsorption capacity and create a high density of SERS hotspots for large local field enhancement. The other polystyrene hemisphere of the nanocoral is then selectively functionalized with antibodies to target the receptors of specific cells (Fig. 4.10b). This functionalization leaves the roughened gold region of the nanocoral specifically for SERS measurements. Therefore, the targeting and sensing mechanisms are decoupled and can be separately engineered for a particular experiment.

Nanoplasmonic Molecular Rulers

Biosensors functioning as nanoplasmonic molecular rulers enable label-free measurement of DNA length, real-time kinetic studies of nuclease activity, and real-time detection of specific binding activities between proteins and DNA. Nanoplasmonic molecular rulers are ideal for long-term kinetic studies because they do not suffer from photobleaching or blinking. Nanoplasmonic molecular rulers utilize double-stranded DNA as an enzymatic substrate and calibration standard. In Fig. 4.11a, the double-stranded DNA is designed to contain cleavage sites for endonucleases *HindIII*, *XhoI*, *SalI,* and *KpnI*, centered at nucleotide positions 12, 24, 36, and 48, respectively. This double-stranded DNA is then tethered onto the biosensors, in this case gold nanoparticles. Scattering images and spectra of individual biosensors are acquired using a dark-field microscope, a true-color imaging charge-coupled device (CCD) camera, and a spectrometer. Figure 4.11b shows typical scattering spectra and plasmon resonance wavelengths for biosensors conjugated with double-stranded DNA after cleavage reactions with *HindIII*, *XhoI*, *SalI,* and *KpnI* [14]. After 1 h of cleaving, the plasmon resonance wavelength blueshifts approximately 67, 62, 45, 28, 10, and 0 nm, respectively. An average wavelength shift of approximately 1.24 nm is observed per DNA base pair. The change in plasmon resonance wavelength corresponds to a change in the dielectric layer around the biosensor when bound DNA is digested. Therefore, a plasmon resonance shift is related to the length of the DNA which can be measured with sub-nanometer axial resolution.

Using this nanoplasmonic molecular ruler, nuclease enzymatic kinetics can be studied in real-time. For example, the exonuclease enzyme, *Bal31*, is known to degrade both 3′ and 5′ termini of double-stranded DNA. When *Bal31* is in the presence of biosensors conjugated with DNA, *Bal31* degrades double-stranded DNA from the untethered end (Fig. 4.11c). After introduction of *Bal31*, the plasmon resonance wavelength of the biosensor conjugated with DNA blueshifts approximately 52 nm in 20 min (Fig. 4.11d). By taking advantage of the high quantum efficiency of Rayleigh scattering in comparison to fluorescence or Raman scattering, the time resolution of this nanoplasmonic molecular ruler can be as high as one spectrum per second. Therefore, kinetic reactions can be measured on the timescale of seconds. The ability to resolve a single nanoparticle without the need for radioactive or fluorescent labeling also makes it possible for eventual integration with microfluidic devices [13, 39, 40] for high-throughput screening.

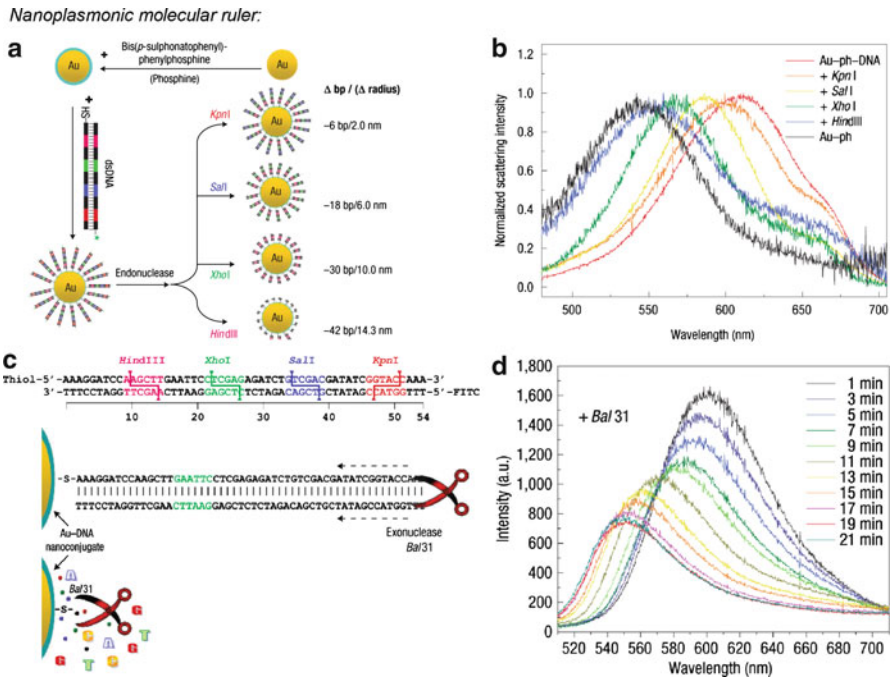

Fig. 4.11 Nanoplasmonic molecular ruler. (**a**) Design of the nanoplasmonic molecular ruler. The double-stranded DNA contains endonuclease incision sites positioned at 12, 24, 36 and 48 bp from the tethered end of the gold nanoparticles. The fluorescent labeling with fluorescein isothiocyanate (FITC) is only for further confirmation of the nuclease reactions, and is not necessary for plasmon resonance measurements. The 20-nm gold nanoparticle modified with a phosphine surfactant monolayer is enclosed by a layer of synthesized 54-bp double-stranded DNA. A thiol group and the fluorophore (as indicated by a *green star*) are present at each end of the dsDNA, respectively. Through the thiol–Au chemistry, the double-stranded DNA is tethered onto the gold nanoparticles. (**b**) Typical scattering spectra of gold nanoparticles functionalized with double-stranded DNA after cleavage reactions with four endonuclease enzymes, *HindIII*, *XhoI*, *SalI,* and *KpnI*. (**c**) Concept of real-time sensing of nuclease enzymatic kinetics. *Bal31* degrades both 3′ and 5′ termini of double-stranded DNA. When *Bal31* is in the presence of biosensors conjugated with DNA, *Bal31* degrades double-stranded DNA from the untethered end. (**d**) After introduction of *Bal31*, the plasmon resonance wavelength blueshifts approximately 52 nm in 20 min. Reprinted with permission from [14], Copyright 2006 Nature Publishing Group

Conclusions

In conclusion, the dual functions of nanoplasmonic optical antennas as nanoplasmonic gene switches and biosensors have been reviewed. Functioning as nanoplasmonic gene switches, nanoplasmonic optical antennas enable on-demand and spatially precise intracellular regulation of genetic activity. Functioning as label-free biosensors, nanoplasmonic optical antennas enable PRET-based and SERS-based biosensing for spectroscopic imaging in living cells as well as in vitro molecular

detection. Nanoplasmonic molecular rulers for label-free measurement of DNA length and real-time kinetic studies of nuclease activity have also been reviewed. Equipped with new dual-functional nanoplasmonic optical antennas to directly manipulate and image the intracellular environment, quantitative approaches should capture dynamic "spectral snapshots" of the intracellular biochemical distribution of living systems that were otherwise previously impossible to detect using conventional methods.

Acknowledgements The authors thank all current and previous BioPOETS for their invaluable scientific contribution to projects discussed in this book chapter. The authors acknowledge the National Institutes of Health (NIH) Nanomedicine Development Center for the Optical Control of Biological Function (PN2 EY018241) for financial support. The authors acknowledge the Siebel Foundation for graduate support S.E. Lee (Siebel Scholarship, Class of 2010). The authors acknowledge the Center for Nanostructured Materials and Technology (CNMT) of the Korea government for support of Y. Park.

References

1. Alberts B, Johnson A, Lewis J, Raff M, Roberts K, Walters P. Molecular biology of the cell. 4th ed. New York: Garland Science; 2002.
2. Liu GL, Long Y, Choi Y, Kang T, Lee LP. Quantized plasmon quenching dips nanospectroscopy via plasmon resonance energy transfer. Nat Methods. 2007;4:1015–7.
3. Choi Y, Park Y, Kang T, Lee LP. Selective and sensitive detection of metal ions by plasmon resonance energy transfer-based nanospectroscopy. Nat Nanotechnol. 2009;4:742–6.
4. Choi Y, Kang T, Lee LP. Plasmon resonance energy transfer (PRET)-based molecular imaging of cytochrome c in living cells. Nano Lett. 2009;9:85–90.
5. Nikoobakht B, Wang J, El-Sayed MA. Surface-enhanced Raman scattering of molecules adsorbed on gold nanorods: off-surface plasmon resonance condition. Chem Phys Lett. 2002;366:17–23.
6. Nie S, Emory SR. Probing single molecules and single nanoparticles by surface-enhanced Raman scattering. Science. 1997;275:1102–6.
7. Willets KA, Van Duyne RP. Localized surface plasmon resonance spectroscopy and sensing. Annu Rev Phys Chem. 2007;58:267–97.
8. Liu GL, Lu Y, Kim J, Doll JC, Lee LP. Magnetic nanocrescents as controllable surface-enhanced Raman scattering nanoprobes for biomolecular imaging. Adv Mater. 2005;17:2683–8.
9. Lu Y, Liu GL, Kim J, Mejia YX, Lee LP. Nanophotonic crescent moon structures with sharp edge for ultrasensitive biomolecular detection by local electromagnetic field enhancement effect. Nano Lett. 2005;5:119–24.
10. Kniepp K, Kniepp H, Itzkan I, Dasari RR, Feld MS. Ultrasensitive chemical analysis by Raman spectroscopy. Chem Rev. 1999;99:2957–75.
11. Jackson JB, Halas NJ. Surface-enhanced raman scattering on tunable plasmonic nanoparticle substrates. Proc Natl Acad Sci U S A. 2004;101:17930–5.
12. Cho H, Lee B, Liu GL, Agarwal A, Lee LP. Label-free and highly sensitive biomolecular detection using SERS and electrokinetic preconcentration. Lab Chip. 2009;9:3360–3.
13. Choi D, Kang T, Cho H, Choi Y, Lee LP. Additional amplifications of SERS via an optofluidic CD-based platform. Lab Chip. 2009;9:239–43.
14. Liu GL, Yin Y, Kunchakarra S, Mukherjee B, Gerion D, Jett SD, et al. A nanoplasmonic molecular ruler for measuring nuclease activity and DNA fingerprinting. Nat Nanotechnol. 2006;1:47–52.

15. Cortie M, Xu X, Chowdhury H, Zareie H, Smith G. Plasmonic heating of gold nanoparticles and its exploitation. Proc SPIE. 2005;5649:565–73.
16. Khlebtsov B, Zharov V, Melnikov A, Tuchin V, Khlebtsov N. Optical amplification of photothermal therapy with gold nanoparticles and nanoclusters. Nanotechnology. 2006;17:5167–79.
17. Link S, El-Sayed M. Shape and size dependence of radiative, non-radiative and photothermal properties of gold nanocrystals. Int Rev Phys Chem. 2000;19:409–53.
18. Lee SE, Liu GL, Kim F, Lee LP. Remote optical switch for localized and selective control of gene interference. Nano Lett. 2009;9:562–70.
19. Skirtach AG, Dejugnat C, Braun D, Susha AS, Rogach AL, Parak WJ, et al. The role of metal nanoparticles in remote release of encapsulated materials. Nano Lett. 2005;5:1371–7.
20. Svoboda K. Biological applications of optical forces. Annu Rev Biophys Biomol Struct. 1994;23:247–85.
21. Gersten J. Electromagnetic theory of enhanced Raman scattering by molecules adsorbed on rough surfaces. J Chem Phys. 1980;73:3023–37.
22. Barhoumi A, Huschka R, Bardhana R, Knight MW, Halas NJ. Light-induced release of DNA from plasmon-resonant nanoparticles: towards light-controlled gene therapy. Chem Phys Lett. 2009;482:171–9.
23. Jones MR, Millstone JE, Giljohann DA, Seferos DS, Young KL, Mirkin CA. Plasmonically controlled nucleic acid dehybridization with gold nanoprisms. Chemphyschem. 2009;10:1461–5.
24. Horiguchi Y, Niidome T, Yamada S, Nakashima N, Niidome Y. Expression of plasmid DNA released from DNA conjugates of gold nanorods. Chem Lett. 2007;36:952–3.
25. Takahashi H, Niidome Y, Yamada S. Controlled release of plasmid DNA from gold nanorods induced by pulsed near-infrared light. Chem Commun. 2005;2247–49 http://pubs.rsc.org/en/Content/ArticleLanding/2005/CC/b500337g.
26. Chen C, Lin Y, Wang C, Tzeng H, Wu C, Chen Y, et al. DNA-gold nanorod conjugates for remote control of localized gene expression by near infrared irradiation. J Am Chem Soc. 2006;128:3709–15.
27. Braun GB, Pallaoro A, Wu G, Missirlis D, Zasadzinski JA, Tirrell M, et al. Laser-activated gene silencing via gold nanoshell-siRNA conjugates. ACS Nano. 2009;3:2007–15.
28. Wijaya A, Schaffer SB, Pallares IG, Hamad-Schifferli K. Selective release of multiple DNA oligonucleotides from gold nanorods. ACS Nano. 2009;3:80–6.
29. Zhang D, Neumann O, Wang H, Yuwono VM, Barhoumi A, Perham M, et al. Gold nanoparticles can induce the formation of protein-based aggregates at physiological pH. Nano Lett. 2009;9:666–71.
30. Demers LM, Mirkin CA, Mucic RC, Reynolds RA, Letsinger RL, Elghanian R, et al. A fluorescence-based method for determining the surface coverage and hybridization efficiency of thiol-capped oligonucleotides bound to gold thin films and nanoparticles. Anal Chem. 2000;72:5535–41.
31. Brayner R. The toxicology impact of nanoparticles. Nanotoday. 2008;3:48–55.
32. Dean NM, Bennett CF. Antisense oligonucleotide-based therapeutics for cancer. Oncogene. 2003;22:9087–96.
33. Marcusson EG, Bhat B, Manoharan M, Bennett CF, Dean NM. Phosphorothioate oligodeoxyribonucleotides dissociate from cationic lipids before entering the nucleus. Nucleic Acids Res. 1998;26:2016–23.
34. Nakayama N, Eichhorst ST, Müller M, Krammer PH. Ethanol-induced apoptosis in hepatoma cells proceeds via intracellular Ca2+ elevation, activation of TLCK-sensitive proteases, and cytochrome c release. Exp Cell Res. 2001;269:202–13.
35. Jackson JD. Classical electrodynamics. 3rd ed. New York: Wiley; 1999.
36. Etchegoin PG, Le Ru EC, Meyer M. An analytic model for the optical properties of gold. J Chem Phys. 2006;125:164705.

37. Ross B, Lee LP. Plasmon tuning and local field enhancement maximization of the nanocrescent. Nanotechnology. 2008;19:275201.
38. Wu L, Ross BM, Hong S, Lee LP. Bioinspired nanocorals with decoupled cellular targeting and sensing functionality. Small. 2010;6:503–7.
39. Liu GL, Kim J, Lu Y, Lee LP. Optofluidic control via photothermal nanoparticles. Nat Mater. 2006;5:27–32.
40. Liu GL, Doll JC, Lee LP. Nanowell surface enhanced Raman scattering arrays fabricated by soft-lithography for label-free biomolecular detections in integrated microfluidics. Appl Phys Lett. 2005;87:074101.

Chapter 5
Individual Plasmonic Nanostructures as Label Free Biosensors

Greg Nusz and Ashutosh Chilkoti

Abstract This chapter reviews our work and that of other groups in the use of *individual* plasmonic nanostructures that are presented by a substrate for the label-free detection of biomolecular binding events. This class of single particle nanosensors is based on the local surface plasmon resonance (LSPR) behavior of noble metal nanostructures that enables optical transduction of binding events at their surface into an optical signal [1–5]. The LSPR peak location and intensity are sensitive to the local refractive index surrounding the nanoparticle, which is altered by the binding of biomolecular targets to receptor-functionalized nanostructures, and forms the basis of their utility as label-free biosensors [6].

We have previously shown that this transduction modality allows label-free, optical biomolecular detection in a chip-based format [7, 8]; this ensemble approach has also been validated by other groups [9–14]. Most work on LSPR biosensors has been based on interrogation of an *ensemble* of nanoparticles. In an effort to push this technology to its limits, we and others have explored *single* plasmonic nanostructures as transducers of biomolecular binding events, with the ultimate goal of single molecule detection of proteins (and other biomolecules) from complex mixtures. These developments are reviewed in this chapter.

There are two primary motivations that direct work into the exploration of label-free sensors based on individual nanoparticles. First, the miniaturization of the

G. Nusz
Department of Chemistry, University of Colorado, Denver, CO 80201, USA

Department of Biomedical Engineering, Duke University, Durham, NC 27708-0281, USA

A. Chilkoti (✉)
Department of Biomedical Engineering, Duke University, Durham, NC 27708-0281, USA

Center for Biologically Inspired Materials and Materials Systems, Duke University, Durham, NC 27708-0281, USA
e-mail: chilkoti@duke.edu

A. Dmitriev (ed.), *Nanoplasmonic Sensors*, Integrated Analytical Systems,
DOI 10.1007/978-1-4614-3933-2_5,

entire transduction system down to the nanometer scale offers many distinct advantages regarding sensor manufacture and performance. Second, by analyzing individual nanostructures—the quantum unit by which all plasmonic detection systems are built—a greater understanding of these systems can be achieved allowing for optimization and rational design of any system utilizing plasmonic nanostructures. This chapter is hence divided into two primary sections. The first describes the motivation and practical application of biosensing with individual nanostructures. The second illustrates an example of nanostructure optimization and discusses its impact on overall sensor performance as well as its implications toward the development of future generations of sensors.

Single-Nanoparticle Biosensing

The power of a nanoparticle-based sensor comes from its size. A single plasmonic nanoparticle has characteristic dimensions in the 10–100 nm size range. Thus, by miniaturizing a detection system down to a single nanoparticle, the entire sensing platform is in the same size regime as the target analyte molecules. This offers advantages to minimizing detection limits at least in terms of the minimum number of molecules that can be detected and opens the door for label-free detection of individual molecular binding events. It should be noted that the ability to detect single molecules will not, per se, provide a gain in sensitivity as defined by the lowest concentration of the analyte that can be detected, primarily because of mass transport limitations [15–17]. Rather, miniaturizing the sensor to a single nanoparticle is of interest because it is a useful test of the limits of this technology for biosensing and also because it provides a potentially useful biophysical tool for the interrogation of single binding events that is complementary to other transduction modalities under development for single molecule, stochastic sensing [18–21].

Additionally, with concomitant miniaturization of the fluid handling system, sample volumes can be greatly reduced, which is likely to be important in the design of clinical diagnostics where analysis is constrained by the available sample volume (e.g., in neonatal diagnosis and archival samples), or by the high cost of reagents. The miniaturization of a biosensor down to the nanoscale also allows for measurements to be made in regions not accessible by macroscopic sensors, such as within live cells [22]. As single nanostructure detection systems advance, the realization of optical, label-free single molecule is becoming a reality [23, 24]. Such detectors offer the chance to study molecular interactions in a real-time, stochastic manner, enabling further exploration into the fundamental nature of these reactions. Single nanoparticle interrogation also offers a method to bypass LSPR peak broadening present in ensemble studies introduced by the heterogeneous size and shape distribution of nanoparticle. By interrogating single nanoparticles, individual resonance peaks are analyzed independently, each with a much narrower line-width than the ensemble average, thereby increasing the ability to discern peak shifts and thus increase the overall measurement accuracy [25].

Just as many of the advantages of single nanostructure detection methods are derived from their scale, so are many of their disadvantages. Signals generated by individual nanoparticles are obviously quite small, so specialized equipment is typically necessary to detect these signals. As a result, single nanostructure detection systems are typically more expensive and complex than those needed for ensemble measurements, which can be performed by a conventional visible spectrophotometer. Additionally, the smaller absolute signal that emanates from a single nanoparticle also results in low a signal-to-noise ratio (SNR) limiting the reliability of measuring small spectral resonance shifts. These smaller signals also typically require a longer acquisition time, which increases the SNR of each measurement but also reduces the temporal frequency at which measurements can be made, thereby limiting the time-resolution of dynamic measurements. Despite these disadvantages, the LOD for detection of proteins by single nanostructures are competitive with both conventional planar SPR and ensemble LSPR techniques, with protein detection limits in the 0.02–2 ng/mL range [9, 26–30].

Even though individual plasmonic nanostructures exhibit very large extinction cross sections relative to their physical size, detecting optical signals from individual structures presents some challenges. The most common means of detection relies on the scattering component of the plasmon resonance. Light scattered by individual nanostructures can be easily separated from the overwhelming illumination light by using darkfield microscopy, a technique commonly used to visualize light scattered by individual nanostructures. Under darkfield illumination, the incident light is directed such that it will illuminate the sample area, but will not be collected by the imaging objective. The only light that reaches the collecting optics is that which has been scattered by objects within the sample. There are several experimental configurations that produce darkfield illumination. The first is referred to as reflection mode, and it is achieved by introducing the incident light at a shallow angle to the sample surface [31–33]. This configuration is illustrated in Fig. 5.1a. Because of the shallow angle, the reflected beam is not collected by the imaging objective, so only light scattered by the sample surface is collected. While relatively simple to assemble, reflection mode darkfield is restricted to samples that have no reflective surfaces above the scatterers because this reflected light may be collected by the objective. However, reflection mode darkfield modes have the advantage of being able to image samples on opaque substrates. For example, this technique has been used to collect micrographs of scattered light of gold nanospheres on a gold surface [34]. A second darkfield configuration is the well-studied Kretschmann configuration, which is commonly used for conventional planar SPR studies. Also known as total internal reflection, in the Kretschmann configuration light is incident at a shallow angle through an index-matched prism on the back side of the sample [35]. Because of the lower refractive index of the medium above the substrate, the incident beam totally internally reflects providing the dark background necessary to achieve darkfield illumination. The evanescent field created at the point of total internal reflection excites nanostructures on the substrate, causing them to scatter light, which is collected by the microscope objective as shown in Fig. 5.1b. It is important to note that the function of the prism in this configuration is simply to provide a relatively high refractive index

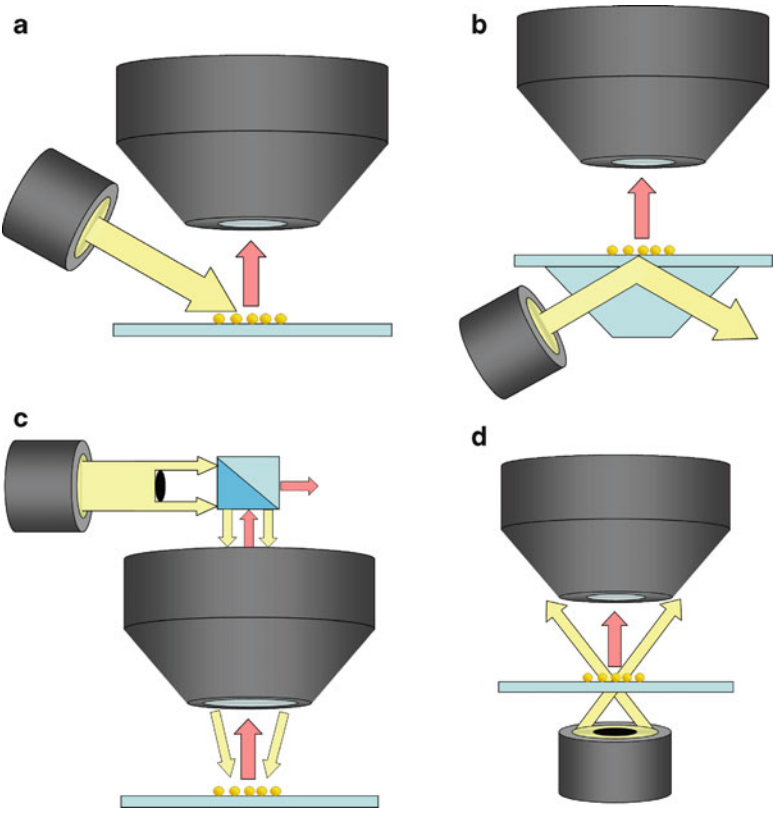

Fig. 5.1 Schematics of darkfield illumination techniques. Incident light and scattered light are depicted by *yellow* and *red arrows* respectively. (**a**) Reflected darkfield (**b**) total internal reflection (Kretschmann) configuration, (**c**) epiillumination darkfield (**d**) transmission darkfield

medium to facilitate total internal reflection of the incident beam and is not required to modify the momentum of the incident light to allow coupling into the nanoparticle electron resonance as in the case of conventional planar surface plasmon resonance. A third experimental means of achieving darkfield illumination is referred to as epiillumination, which involves using the imaging objective for both illumination of the sample as well as collecting scattered light. As shown in Fig. 5.1c, this is accomplished by using a beam-splitter to separate incident light from light reflected by the sample. This light is then further separated by a field stop to isolate light scattered from the sample surface from reflected illumination light [36]. This approach is particularly useful for imaging structures under a confined environment that does not allow simple optical access to the sample surface such as in a fluid cell, or an incubator for the imaging of live cells [37]. The fourth approach to achieve darkfield illumination is by the use of commercially available darkfield condensers that focus collimated illumination light at an angle steeper than can be collected by the objective. Figure 5.1d shows an illustration describing transmission

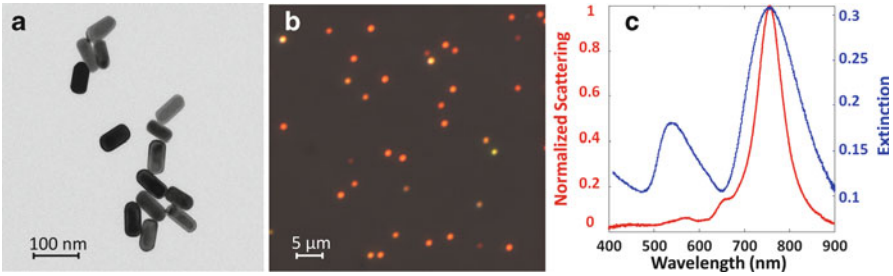

Fig. 5.2 (**a**) TEM micrograph of gold nanorods. (**b**) Darkfield micrograph of gold nanorods. (**c**) Extinction spectrum of an ensemble of gold nanorods (*blue*) and of a single gold nanorod (*red*). Figure reprinted with the permission of the American Chemical Society [42]

darkfield illumination. This technique has been used by many groups [23, 25, 38–43], to collect scattering spectra of individual nanostructures.

Because of their subwavelength dimensions, plasmonic nanostructures are imaged as diffraction-limited spots in darkfield microscopy, and exhibit the familiar and well-characterized Airy pattern. Thus, the resulting optical micrographs of plasmonic nanostructures under darkfield illumination are bright spots corresponding to light scattered by individual nanoparticles against a dark background. Although the nanostructure size is far below the typical resolution limits of optical microscopy, plasmon resonant nanostructures are visible in darkfield optical microscopy (under far field conditions) because they exhibit very large scattering cross sections. A scattering cross section represents a hypothetical disk around a nanoparticle such that all light incident upon that area is scattered. For example, a 30 nm diameter gold nanosphere has a scattering cross section of 90 nm^2 at resonance whereas a polystyrene bead with 30 nm diameter has a scattering cross section of approximately 0.1 nm^2 at visible wavelengths [44]. The large scattering cross section of plasmonic nanostructures hence allows the collection of high signal-to-noise images of individual nanoparticles with darkfield microscopy. In fact, individual nanoparticles scatter enough light that they can be easily visualized by eye through a darkfield microscope. As an illustrative example, chemically synthesized gold nanorods characterized by transmission electron micrograph (Fig. 5.2a) could be easily visualized individually by darkfield microscopy of gold nanorods that were sparsely immobilized on glass; these images were collected with an integration time of 200 ms with a typical RGB (red-blue-green) CCD showing the ease with which they can be optically imaged (Fig. 5.2b). These images have spectroscopic content as well; the red trace in Fig. 5.2c shows a typical scattering spectrum of a single nanorod that is obtained by darkfield illumination using a slit-imaging spectrometer [42]. This spectrum of an isolated gold nanorod by darkfield imaging spectroscopy with an acquisition time of 10 s has a high SNR of 80 and a low FWHM of ~60 nm. This is in contrast to the blue trace that shows an extinction spectrum of an ensemble of the same nanorods measured with a conventional spectrophotometer (Cary 300-Bio). This ensemble measurement interrogates a macroscopic area of several square millimeters, which includes on the order of

10^9 nanorods. The ensemble spectrum exhibits heterogeneous broadening compared to the single Lorentzian peak observed for each resonance of a single nanoparticle. This broadening is simply due to the fact that even the most careful chemical synthesis will yield nanoparticles with a distribution of size and shapes, and as the LSPR behavior of a nanoparticle is strongly dependent upon these structural parameters, this structural inhomogeneity leads to a broadening of the ensemble LSPR peaks. Additionally, the location and amplitude of smaller scattering peaks corresponding to plasmonic resonances other than the longitudinal resonance of the nanorod are observed for the isolated nanorod. The location and magnitude of these minor peaks has been shown to be highly dependent on nanorod end cap geometry and thus tends to vary widely between chemically synthesized nanorods [45].

The LSPR properties of metal nanostructures are derived from their surface conduction electrons. The electric field from incident light provides an oscillating driving force that pushes the conduction electrons away from the metal lattice core. A restoring force is then provided by the coulomb attraction between the displaced electrons and the positively charged metal lattice. When driven at resonance, the oscillating electrons behave as a single dipole, emitting photons as it oscillates. Thus, individual nanoparticles behave as elastic light scatterers, preferentially scattering light, which couples resonantly with the oscillating electrons. Any change in the system that alters the resonant energy of the plasmon will therefore change the scattering properties of the nanoparticle. In particular, nanoparticle composition, geometry, proximity to other conductors, chemical bonds to lattice atoms, and the local refractive index (RI) are all parameters that have been shown to alter the LSPR spectrum of plasmonic nanoparticles.

The RI sensitivity of plasmon resonant nanostructures is particularly useful for label-free, optical detection of biomolecular binding. Changing the dielectric properties of the medium surrounding the nanostructure alters the energy associated with the electric field oscillation. As most biological materials are nonabsorbing and nonmagnetic, a change in dielectric can be directly translated to a change in RI. Generally this effect is observed as a red shift in the LSPR peak of a nanostructure upon an increase in the local RI. This effect can be exploited for biosensing by functionalizing the nanoparticle surface with a specific "receptor," and observing the LSPR change as the local RI increases upon binding of a target analyte [46]. Ensemble measurements of receptor-analyte binding were first demonstrated using gold nanospheres in suspension to determine the affinity of protein–ligand interactions [6]. This approach was then extended by our group to gold spheres immobilized on a surface in a chip-based format allowing for easier nanoparticle functionalization [8, 47]. Since then, several groups have reported the measurement of biomolecular interactions by observing ensemble LSPR shifts of particles immobilized to a surface using gold rods [12], silver triangular prisms [9], silicon–gold core–shell nanoparticles [48] and other nanoparticles [15]. Biomolecular detection limits in the subnanomolar range have been reported for ensemble-based LSPR sensors with a dynamic range of four to five orders of magnitude of analyte concentration [12, 49].

Using darkfield illumination techniques, these LSPR sensors can be miniaturized down to the single nanostructure level. The specific recognition of streptavidin by

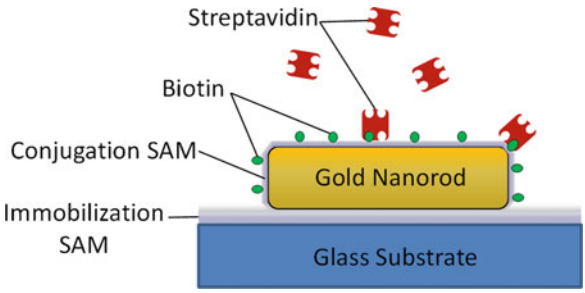

Fig. 5.3 Cartoon depicting a label-free biodetection system based on the plasmonic resonance shifts of individual gold nanorods

individual, biotin-conjugated gold nanorods is discussed below as an example. For this example, gold nanorods were selected as plasmonic transducers of biomolecular binding events for two reasons: first, gold was selected over silver, even though silver nanoparticles exhibit a higher bulk refractive index sensitivity than gold particles of the same shape and size [50], because the greater reactivity of silver as compared to gold makes it less suitable for use in biologically relevant media. Second, nanorods were chosen over many other possible shapes because gold nanorods can be conveniently synthesized to desired geometries by appropriately tuning chemical synthesis methods [51]. Because the primary LSPR sensing metrics—the refractive index sensitivity and electric field enhancement—are dictated by the particle geometry, the ability to tune the plasmon behavior by control of two orthogonal variables—the size and aspect ratio of gold nanorods—provides a degree of synthetic control over plasmonic properties that are enormously useful in optimizing a LSPR sensor for a specific receptor–analyte pair of interest.

Figure 5.3 shows a cartoon illustrating the basic assembly and operation of a gold nanorod biosensor. First, a glass substrate is treated with a self-assembled monolayer (SAM) of a silane to enable chemisorption of chemically synthesized nanoparticles to the surface. In order to do so, the silane SAM typically presents a thiol or amine group to which the gold rods bind by chemisorption. After the nanorods are immobilized, a second thiol-terminated SAM is formed around the nanorod that is a mixed monolayer of two molecules: one that is amine-terminated to which biotin receptor molecules are conjugated, and the other is terminated with an oligo(ethylene glycol) group which serves to both space the biotin molecules and also to prevent nonspecific adsorption to the nanorod surface. Detection occurs when streptavidin molecules bind to the biotin conjugated to the nanorod surface as shown in Fig. 5.3. The increase in the local RI caused by the binding of streptavidin molecules to the biotin presented by the nanorods induces an shift in the plasmon resonance of the nanorod.

This resonance shift can be quantified by observing the LSPR peak wavelength shift of a single diffraction-limited spot. Figure 5.4a–d show typical LSPR spectra, collected using a slit-imaging spectrometer [42], of streptavidin binding to an individual biotin-functionalized gold nanorod utilized by the scheme illustrated in Fig. 5.3. In Fig. 5.4a, b, the blue trace is the LSPR spectrum of a single nanorod that has been immobilized on a glass substrate and treated with a silane SAM.

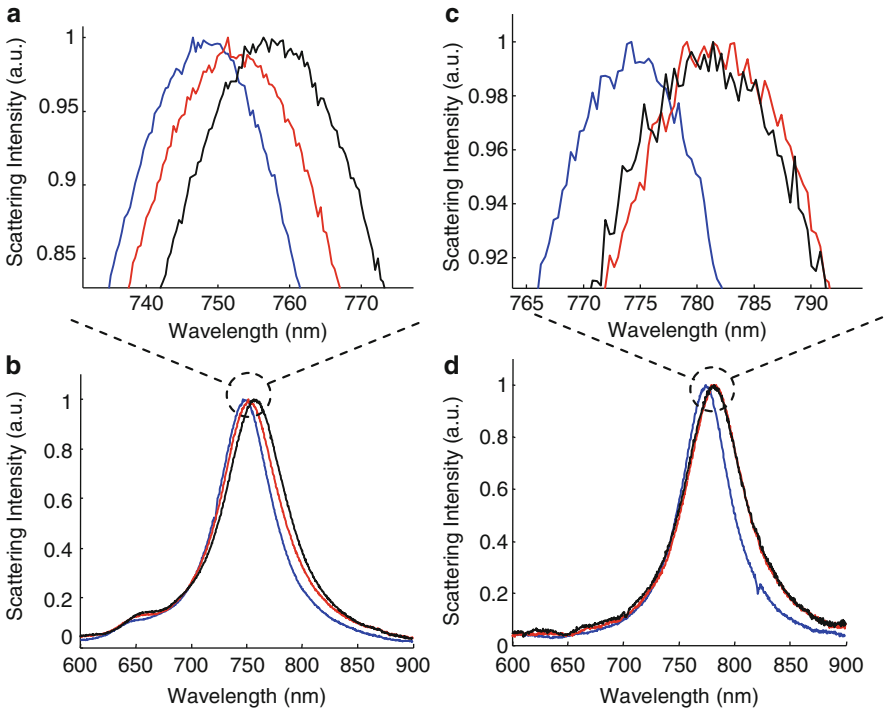

Fig. 5.4 (**a**, **b**) Scattering spectra of a bare single gold nanorod after sequential incubation of the conjugation SAM (*blue*), biotin (*red*), and 130 nM streptavidin (*black*). (**c**, **d**) Scattering spectra of a single gold nanorod after sequential incubation of the conjugation SAM (*blue*), biotin (*red*), and 1 μM streptavidin presaturated with free biotin (*black*). Figure reprinted with the permission of the American Chemical Society [42]

The red trace is the LSPR spectrum of the same particle after conjugation of biotin molecules. A 5 nm LSPR shift is observed upon attachment of biotin, which resulted from the increase in local RI from conjugation of the biotin to the nanorod. The black trace is the LSPR spectrum of the same gold nanorod after reaching saturation in a solution of 130 nM streptavidin. The resulting 5.2 nm shift indicated that streptavidin binding occurred on the surface of the biotinylated nanorod. Figure 5.4c, d show the results of a control experiment after incubation of biotin-functionalized nanorods in a 1 μM solution of streptavidin that had been previously saturated with free biotin. The characteristic 5 nm LSPR shift resulting from the biotin coupling was observed, consistent with the previous experiment, which indicated that biotin was successfully conjugated to the gold nanorods. However, there was no further shift in the LSPR peak upon incubation with the biotin-saturated streptavidin, which clearly demonstrated that the saturation of biotin-binding sites on the streptavidin prevents binding of streptavidin to the biotin-functionalized nanoparticle surface. These results also suggest that the mixed SAM on the nanorod surface successfully prevented nonspecific adsorption of streptavidin because the

streptavidin molecules did not nonspecifically adsorb to the nanorods when their biotin-binding sites were blocked. Together, these results strongly suggest that the measured LSPR shifts observed for streptavidin binding to the biotin-functionalized nanorods are caused by molecular recognition of biotin by streptavidin.

At the time of writing this chapter, the authors were aware of only four other studies that have explored specific biomolecular interactions at the single nanoparticle level, in addition to those described above utilizing gold nanorods [23, 42]. The first example of biodetection with individual nanoparticles was demonstrated by Raschke et al. who used spherical gold nanoparticles functionalized with biotin to detect streptavidin binding, albeit at the much higher detection level of 50 μg/mL level in 2004 [38]. The following year, Rindzevicius et al. reported the detection of 1 mg/mL neutravidin to biotin-BSA using single plasmonic nanoholes in a gold film as a plasmonic transducer [52]. This was followed in 2008 by our report of the detection of streptavidin to biotin-functionalized gold nanorods at a much lower detection limit of 50 ng/mL, as described above [42]. Also in 2008, Baciu et al. reported the detection of streptavidin at 1 μg/mL on single gold nanorods that have been activated by depositing a biotin-containing lipid bilayer over the entire sensor surface [53]. This was followed by a report in March 2009 of the detection of avidin with a detection limit of 1.3 μg/mL was reported using gold spheres decorated with an oligonucleotide aptamer [54].

Nanostructure Optimization

It is important to note that all of the single nanoparticle biodetection studies described above are essentially proof-of-concept experiments. In order to exploit the full potential of these miniaturized biosensors, these systems need to be optimized. Ideally, the nanoparticle transducer itself would be optimized for a specific analyte, as would the optical detection system. Single nanostructure systems offer the most direct route towards optimization because the effects of design perturbations on system performance can be directly observed. The resulting optimized system components, for example an ideal nanostructure geometry, can then be used as a building block with which to construct the next generation of LSPR-based biosensors.

As an example illustrating how such optimizations can be performed and also to describe the potential benefits of such optimization, we return again to the example of gold nanorods. Motivated by the goal of rationally designing LSPR sensors, we integrated recent progress in understanding the structural details of metal nanoparticles that control their plasmonic behavior with various measurement system parameters into a quantitative model. The resulting analytical model quantifies the LSPR shift of a gold nanorod caused by the local refractive index increase from the presence of analyte molecules as a function of system design parameters.

The utility of this model is twofold. First, it provides an analytical model that allows a priori design of a LSPR sensor with figures-of-merit such as the molecular detection limit (MDL) and dynamic range (DR) that can be analytically calculated completely as a function of sensor components for a given receptor–analyte pair. Because the model calculates LSPR shifts for individual bound binding events, the MDL is defined as the smallest number of bound molecules that are measurable by the system, and the dynamic range is the maximum number of molecules that can be detected by a single nanostructure. We define the MDL in term of minimum number of particles detected per nanoparticle so that the focus of model is the interaction of the bound analyte with the plasmonic nanoparticles and the LSPR signal that is generated, and not the mass transport kinetics of the sensor system. Therefore, the optimal nanoparticle can be determined for a proposed analyte strictly by using the model to predict which geometry will offer the lowest MDL. To illustrate its experimental utility, the model was used to identify the optimal gold nanorod geometry (length and width) that was predicted by the model to yield the lowest MDL for the detection of streptavidin by a biotin-functionalized gold nanorod LSPR sensor. This model is useful because it allows the contribution of different system parameters to overall sensitivity to be individually parsed. Thus, the effects of potential system enhancements can be approximated, thereby providing a framework to guide the design of future detection systems. With the ultimate goal of label-free, single molecule detection by LSPR sensors, we conclude with a discussion of optimization of the system within realistic physical and current technological constraints that might allow the fabrication of an LSPR detection system that is capable of detecting the binding of individual analyte molecules.

The goal of the analytical model was to provide an estimate of the MDL and dynamic range of a LSPR sensor for a specific analyte–receptor pair based on the geometric dimensions of the gold nanorod used. To do so, an equation was developed that calculates these two figures-of-merit as a function of nanorod length and diameter, as well as the RI and volume occupied by the analyte. A cartoon illustrating the geometry of the model is shown in Fig. 5.5.

To formulate an analytically simple relationship between these variable, several approximations and assumptions were made. First, it was assumed that the nanorods are cylindrical in shape with a length (l) and diameter (d). It is noted that the assumption that the nanorods are perfect cylinders is an approximation because transmission electron micrographs of chemically synthesized nanorods indicate that the nanorods are only approximately cylindrical, as they have "end-caps" with visible curvature on their ends as seen in Fig. 5.2a. This approximation will introduce some error, as it has been shown that end-cap geometry has an impact on the optical scattering spectra of nanorods [45, 55].

The basis of the model is the assumption that the LSPR peak shift, $\Delta\lambda_{\mathrm{LSPR}}$, is directly proportional to the change in local refractive index. While this relationship is theoretically not perfectly linear, over the relatively small range of refractive indices considered a linear approximation is appropriate—indeed, the refractive index sensitivity of plasmonic structures reported in the literature are calculated as the linear proportionality constant of this relationship. This is extended to describe discrete, local increases in RI caused by bound analytes by

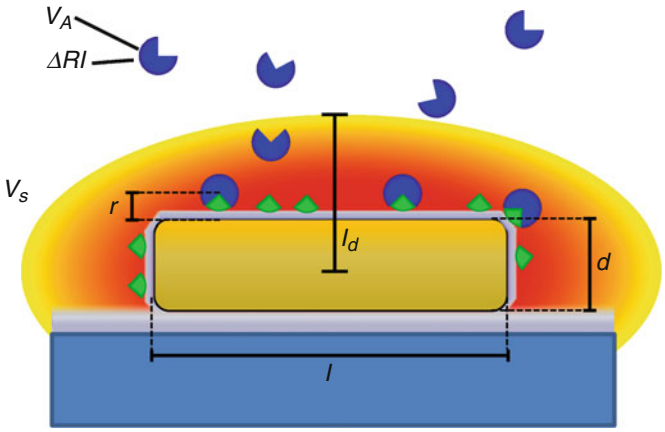

Fig. 5.5 Schematic illustrating the geometry of the nanorod detection model. Variables shown are the analyte volume V_A, the refractive index increment of the analyte ΔRI, the nanorod sensing volume V_S, the decay length of the sensitivity l_d, the binding distance r, the nanorod length l and nanorod diameter d

assuming that the $\Delta\lambda_{LSPR}$ induced by a single bound analyte is proportional to the total LSPR shift that is expected if the entire surrounding medium increased to the RI of the analyte. The proportionality constant is the fraction that the analyte volume occupies of the total sensing volume of the nanorod. For example, if analytes occupy 50% of the total nanorod sensing volume, then the resulting $\Delta\lambda_{LSPR}$ would be half of that if the entire sensing volume were filled. These assumptions yield the following relationship

$$\Delta\lambda_{LSPR} = \frac{S_0}{V_S}\Delta RI \cdot N \cdot V_A \tag{5.1}$$

where $\Delta\lambda_{LSPR}$ is the induced LSPR shift, S_0 is the bulk RI sensitivity of the nanorod, ΔRI is the difference between the RI of the analyte and the surrounding medium, N is the number of analyte molecules bound, and V_A is the volume of a single analyte molecule. In order to determine the MDL of the system, we replace $\Delta\lambda_{LSPR}$ in (5.1) with U, the measurement uncertainty of the optical system in detecting wavelength shifts—that is, the smallest wavelength shift that can be reliably measured by the detection system. By this substitution, the right hand side of (5.1) becomes an expression of the bound optical mass that would induce the minimum detectable LSPR wavelength shift. In this case, solving for N yields an expression for L_M, the MDL of the system in terms of the minimum detectable number of bound biomolecules.

$$L_M(l,d) = N = \frac{V_S}{V_A} \cdot \frac{U}{S_0 \cdot \Delta RI} \tag{5.2}$$

where L_M is a function of the length l and diameter d of the nanorod.

This equation, however, assumes that the RI sensitivity of the nanoparticle is uniform in space, with a distinct cutoff at a fixed distance. This is an oversimplification as the spatial extent of the sensitivity is correlated with the plasmonic electric field enhancement [56], which has a more complex spatial distribution. It has been shown that LSPR shifts induced by local RI have a strong distance-dependence as a result of the exponential decrease in electric field enhancement further from the nanoparticle surface [57]. Specifically, it has been shown that the LSPR associated electric field is enhanced near the ends of nanorods [58, 59]. These observations indicate that the location at which a target analyte binds to the nanorod (i.e., along the sides or at the ends) will affect the magnitude of the induced LSPR shift. The detector-analyte system described in this chapter provides reasonable certainty in estimating the average binding distance r, which is determined by the length of the receptor conjugated to the nanorod (biotin in the experimental case tested herein) and its binding site. Hence, we model sensitivity as being a function solely of the distance r from the surface of the nanorod $S(r)$. The effect of this assumption is that the model effectively outputs the LSPR response of the *average* bound analyte at a fixed distance r from the surface of the nanorod. This is a simplification of the physical phenomenon because of the known complexity of the electric field enhancement distribution. Nevertheless, this model is the closest representation to the actual detection experiments because the actual binding locations cannot be controlled, nor can the fraction of analytes that bind along the nanorod ends vs. sides be accurately estimated. In such a case, it has been shown that an exponential decay model can be reliably extended to describe LSPR response of individual nanoparticles despite exhibiting a high degree of electric field localization [49, 57]. Thus, the model is formulated assuming that the spatial distribution of the sensitivity is an exponentially decaying function as a function of the binding distance, r. This exponential decay is described by a characteristic decay length l_d that relates the rate of sensitivity decay with increasing distance and is a function of the nanorod length and diameter. Incorporating these considerations into (5.2) yields the following expression:

$$L_M(l,d) = \frac{V_S}{V_A \cdot \Delta RI} \cdot \frac{U}{\exp\left(\frac{-2r}{l_d}\right) \cdot (3S_0)} \tag{5.3}$$

where the 2 in the exponential is a result of the fact that RI sensitivity scales with the square of the electric field intensity and the 3 in the denominator is a normalization factor so that the volume integral of the sensitivity is equal to the bulk RI sensitivity, S_0 [23]. Since S_0 can be determined analytically from nanorod dimensions [60, 61], now every variable on the right hand side of the expression is either characteristic of the detection system (U, V_A and ΔRI) or a function of nanorod length and diameter. Figure 5.6 shows the theoretical MDL for streptavidin binding to biotin decorated gold nanorods as predicted by (5.3) for single nanorods of arbitrary dimensions when measured in the microspectroscopy system we used,

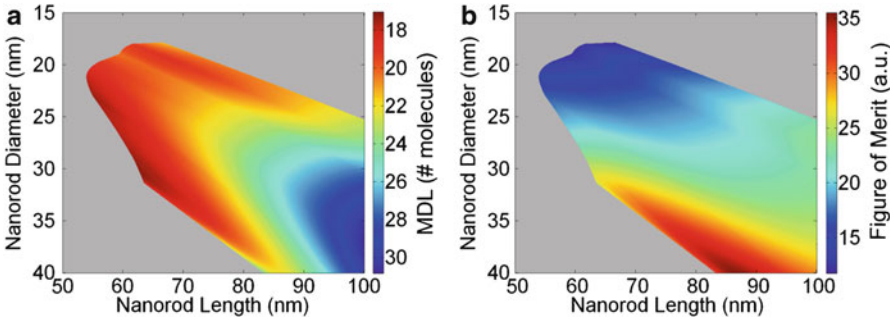

Fig. 5.6 (**a**) Calculated molecular limits of detection for gold nanorods of arbitrary dimension based on (5.3). (**b**) Composite figure-of-merit (FOM) for nanorods of arbitrary dimensions. The composite FOM is calculated as the maximum number of bound molecules divided by the minimum number of detectable molecules. The surrounding gray regions in both are indicative of nanorod geometries that were not considered in this model because they either had resonances outside the visible spectrum or had scattering cross-sections that are insufficient to collect spectra with SNR greater than 30. Figure reprinted with the permission of the American Chemical Society [23]

which has been determined to have a U of 0.3 nm. The simulation was restricted to nanoparticles that have LSPR peak wavelengths in the range 300–900 nm because that is the range observable in the microspectroscopy system. We also applied a minimum SNR threshold of 30 to exclude particles with small scattering cross sections that cannot produce enough scattered light to be visualized in the darkfield microscopy setup with a SNR above 30. The streptavidin molecules are assumed to have a volume [62] of 114 nm^3 and a RI of 1.57 [56]. Figure 5.6 shows that nanorods with a length between 55 and 65 nm in length and between 25 and 33 nm in diameter offer the lowest MDL of ~18 streptavidin molecules. It is important to note that the nanorod MDL predicted by (5.3) are a monotonic function of several detection system and analyte parameters. Although the absolute value of the MDL will vary across detection systems and receptor–analyte pairs, the relative performance of a nanorod with a specified geometry will not vary, so that once the optimal rod geometry has been identified for a target analyte, it will always offer the lowest MDL across detection systems and different receptor-ligand configurations.

In addition to the absolute MDL, the dynamic range (DR) is an important quantitative figure-of-merit (FOM) of a biomolecular sensor. Within the context of this model, the DR is defined as the theoretical maximum number of analyte molecules that are detectable by a single nanorod. This definition was chosen because it is consistent with the model output, which is quantified as the number of bound molecules. The DR was determined by calculating the total surface area available for binding, and dividing it by the footprint of a bound analyte molecule. This value was then scaled by a factor of 0.9, which assumes a hexagonal packing density of hard spheres, which would yield the highest possible coverage that could be achieved in practice.

By this definition, a larger nanorod will obviously exhibit a higher DR because of its larger surface area. However, larger nanorods also tend to have higher MDLs

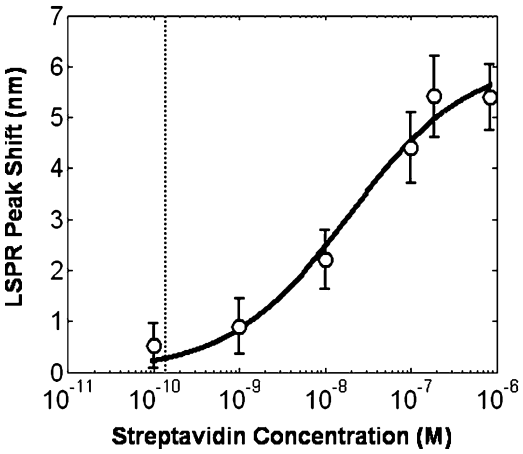

Fig. 5.7 LSPR peak shift of individual, biotin-activated gold nanorods vs. concentration of streptavidin. *Open circles* are the mean LSPR shift of 15 nanorods per measurement at each concentration and the error bars indicate 95% confidence interval. The *solid line* is a sigmoidal fit to the data. The *dotted line* indicates the detection limit as defined by LSPR peak shift measurement uncertainty. This occurs at a concentration of 160 pM (8 ng/mL). Figure reprinted with the permission of the American Chemical Society [23]

because of the increased sensing volume. To balance these considerations, we calculate a composite FOM for nanorods that includes both the DR and MDL of these nanorod plasmonic sensors operating in the single nanorod mode. The composite FOM is calculated simply as the ratio of the DR vs. its MDL. Figure 5.6b shows the composite FOM for nanorods of arbitrary dimensions, and shows that rods with a length of 85 nm and diameter 40 nm offer the highest composite FOM with the potential to bind ~35 times as many molecules as are required to generate its lowest detectable signal. Although nanorods of those dimensions may exhibit a MDL of ~22, their higher dynamic range indicates they may be more useful as a streptavidin sensor over a wider range of analyte concentrations.

To experimentally test the results provided by the model, gold nanorods were synthesized with dimensions that were as close to the geometry predicted by (5.3), and visually represented in Fig. 5.6a as having the lowest streptavidin MDL. These nanorods were shown by TEM to have a length of 63.3 $\pm$ 8.2 nm and a diameter of 24.9 $\pm$ 4.9 nm ($N = 319$). Equation (5.3) calculates that these rods have a mean MDL of 20 molecules and a composite FOM of 22. To experimentally test the predictions of the model, streptavidin binding experiments were performed with these nanorods after biotin functionalization.

A dose–response curve for streptavidin–biotin binding was determined by incubating identical samples of biotin-functionalized gold nanorods that were chemisorbed on glass slides in streptavidin solutions that spanned a range of protein concentration. Sensor fabrication of all samples and streptavidin incubation were performed identically as described previously in this chapter. Figure 5.7 shows the steady-state LSPR shift of single nanorods as a function of streptavidin

concentration. A sigmoidal fit was applied to these data, and the concentration at which the fit crosses the LSPR peak measurement uncertainty of 0.3 nm was defined as the experimental minimum detection limit [25]. The optimized nanorod sensor has a minimum streptavidin detection limit of 160 pM (8 ng/mL) which is an improvement by a factor of 6 over the best previously reported gold nanorod sensor operating in single nanorod mode [42].

As a further check of the relevance of the MDLs predicted by our model, we observe that the mean LSPR shift at saturation is 4.4 nm (Fig. 5.7). Using (5.3), we calculate that this shift arises from the binding of approximately 280 streptavidin molecules to the nanorod surface. For the nanorods used in these experiments, approximately 8,000 nm^2 of biotin-activated surface is available for the binding of streptavidin molecules. Each streptavidin molecule is a tetramer of four identical biotin binding subunits, and the entire tetramer is roughly ellipsoidal with axes 5.4 × 5.8 × 4.8 nm [63, 64]. Thus, the footprint that a streptavidin molecule would occupy on the binding surface is approximately 25 nm^2. In this orientation, a maximum of only 320 molecules would be expected to fit on the nanorod surface. Approximating the streptavidin molecules as hard spheres, the model of random sequential adsorption [65] predicts a packing ratio of 0.54 which would translate to only 170 bound molecules. Whereas the highly ordered method of hexagonal packing predicts a packing ratio 0.9, allowing for up to 290 streptavidin molecules. Therefore, the 280 molecules bound at saturation as determined by (5.3) is reasonable and suggests a more ordered arrangement of bound streptavidin molecules.

Prospects for Sensor Improvement

The described analytical model can also be used to systematically explore the parameters in (5.3) within physically realistic limits to determine which parameters can be modified in order to develop a LSPR sensor with a single molecule MDL.

The product $V_A \cdot \Delta RI$ is a parameter of the analyte and of the surrounding medium. For proteins with a RI commonly near 1.57, detection in water (RI = 1.33) yields a typical ΔRI of 0.24. By drying the samples and taking measurements in air (RI = 1.00) ΔRI can be increased to 0.57. Thus, a factor of 2.4 improvement in MDL is possible through this method. We note that this approach would preclude real-time detection, and require further processing steps of the sample, which detracts from the strength of label-free detection. However, this drying methodology has been successfully utilized by Van Duyne and coworkers [9].

The total sensing volume V_S of the nanoparticle is determined by the nanoparticle shape and decay length l_d. Smaller V_S and l_d are indicative of nanostructures with small, intense electric field enhancements. In general, the sensing volume will vary proportionally with the cube of the decay length simply because it is a three dimensional volume subtended by the decay length. In the case of rods, smaller rods have shorter decay lengths. So ideally, one would want to use the smallest nanorods

possible. However, smaller rods also exhibit smaller scattering cross-sections C_{SCA}, which means they scatter less light under darkfield illumination. For rods in particular, C_{SCA} varies approximately as the square of the rod length and proportionately to rod diameter [60]. So if the length and diameter of a nanorod were both reduced by a factor of 2, C_{SCA} would be reduced by about a factor of 8. On the other hand, to maintain an adequate SNR of the collected spectra, the intensity of the illumination source must be increased. An upper limit to this intensity exists because at some point the nanorods will melt due to photothermal effects [66, 67]. The use of a broadband illumination source, such as a supercontinuum fiber laser, would allow the complete scattering spectrum to be collected and would provide a light output that is 6–10-fold more intense than the tungsten filament used in the experimental setup used here. Hence, (5.3) predicts that a physically realistic increase in illumination intensity by a factor of 10 could enable the visualization of smaller nanorods, effectively reducing the size of the rod by about 1.5, thereby reducing the sensing volume and decay length, which would ultimately reduce the MDL by a factor of 7.

The decay length of the electric field enhancement l_d is determined by the geometry of the nanoparticles. Equation (5.3) assumes a uniform decay length for nanorods. The actual electric field enhancement has a more complicated geometry and in particular has been shown to exhibit larger enhancements near the ends of the rod [59, 68–70]. Thus, analyte molecules that bind near the end of the nanorod will cause a greater LSPR shift than those binding on the lateral portion. For this reason, (5.3) is applicable to a MDL that stems from the LSPR response of individual biomolecules that are spatially averaged around the nanorod surface. It is reasonable to make this approximation for the experiments described here, because the streptavidin molecules are adsorbed a fixed distance r from the nanorod surface, but no further spatial localization is possible. However, if analyte binding can be limited to only within these regions, it is reasonable to assume a concurrent sensitivity increase can be realized due to the reduction of sensing volume. A recent paper offers describes selective functionalization of nanoparticle vertices by a thiol-replacement strategy that reportedly provides a route to site-specific functionalization of nanorods with initial reports citing a reduction in concentration detection limits by a factor of 500 [71]. As a rough estimate as applied to the MDL model, we assume molecular binding can be restricted to only the end-caps of the nanorod while maintaining the same net LSPR shift upon saturation. This results in the reduction of the available binding area, and thus number of molecules bound at saturation by a factor of 4. Further, if we restrict binding to only the end-cap edges, this factor is increased to 9.

The binding distance r is the physical distance that the analyte binds from the surface of the nanoparticle. It is determined by the length of the receptor which is approximated to be 2.4 nm for the experiments presented herein. EDC-NHS coupling is used to conjugate amine-terminated biotin to the carboxyl-terminated monolayer applied to the gold surface. We employ this binding moiety because it offers easy translation to other amine-terminated receptors, such as antibodies or aptamers [12]. It would be possible to employ a smaller receptor that would cause

the target analyte to bind closer to the surface of the nanoparticle where the field enhancement, and thus RI sensitivity, is greater. For example, using thiol-terminated biotin has been successfully employed as a receptor for streptavidin detection with single nanoparticles [72]. This would reduce r by as much as a factor of 2, which in return would reduce the overall MDL by a factor of $\exp(l_d^{-1})$. For the case of nanorods with a decay length l_d that is generally on the order of 10–20 nm, this results in a factor of 1.1 improvement (i.e., 10% decrease in MDL). In most practical situations, however, the size of the receptor–analyte pair is likely to be significantly larger than the model biotin–streptavidin pair used here (e.g., antibody-protein), so that some of the gains realized from the optimization of the parameters discussed here are likely to be offset by the size of the receptor–analyte pair. Nevertheless, these results suggest that minimizing the size of the receptor while retaining high binding affinity and specificity for its analyte is an important factor in extracting the minimum MDL of which LSPR sensors are capable. In this regard, the use of smaller receptors such as aptamers [73, 74] or smaller, engineered antibody fragments such as single chain antibodies are preferable to intact antibodies, which to date are the most commonly used class of receptors in biosensors [4, 75–77].

The bulk RI sensitivity of a nanostructure S_0 is dependent on its size, shape and material composition. However, Miller and Lazarides have observed that S_0 is correlated with the LSPR peak wavelength, regardless of nanoparticle shape [61, 78]. Thus, for a nanostructure of known material composition, its bulk RI sensitivity can be predicted simply by characterizing its LSPR peak. Because longer wavelength resonances exhibit higher bulk RI sensitivities, the highest sensitivities will be from particles with LSPR peaks in the red end of the spectrum. Assuming the detection is to remain in the visible light spectrum, LSPR peaks at wavelengths up to 800 nm could be measured. Thus, bulk RI sensitivities as high as 600 nm/RIU could be expected. This is more than a twofold improvement over the 260 nm/RIU sensitivity of nanorods used in this study. However it is worth noting that for the case of nanorods, longer resonances correspond to larger rods with larger sensing volumes and longer decay lengths. Equation (5.3) was used to balance the contributions for these effects to optimize sensor performance using the nanorod geometry. Thus, for this factor of 2 increase to be realistic, an alternative nanoparticle geometry would be sought that could indeed have a resonance far into the red without such large geometries. Additional sensitivity could be achieved by structuring the sensor to operate in near-IR wavelengths where the bulk RI sensitivities are higher, although the optics and instrumentation could be potentially more challenging. Also, silver nanoparticles exhibit sensitivities typically 1.5-fold higher than gold particles at similar resonant wavelengths. However, as mentioned above the high reactivity of silver makes it less suitable as a sensor for use in biologically relevant media.

The peak measurement uncertainty U represents the most direct way at improving sensor detection limits. Obviously, the smaller the wavelength shifts that can be reliably detected, the greater the accuracy and lower the overall MDL will be. For the system used in these experiments U was found to be 0.3 nm. However, an in-depth

Table 5.1 Theoretical improvement factors that can reduce the molecular detection limit of a label-free, single particle LSPR sensor based on the modulation of parameters from (5.3)

Technique summary	Variable from (5.3) involved	Potential enhancement factor
Drying	ΔRI	2.4
Brighter illumination source	C_{SCA}, V_S and l_d	7
Shorter binding moiety	r	1.1
LSPR peaks in IR	S_0	2
Silver nanoparticles	S_0	1.5
High spectral resolution detection system	U	15
Isolation to rod edges	V_S	9
	Total	~7,200

analysis of the contributing factors to U found that a large portion of the uncertainty is the result of physical system stability [25]. In particular, it was found that stability in microscope focus and sample stage drift account for the largest contributions in uncertainty. It is proposed that by using active feedback hardware to control microscope focus and XY-sample location, U can theoretically be reduced to the order of 0.02 nm resulting in a 15-fold decrease in MDL [25].

These possible enhancement factors are displayed in Table 5.1. From here it is seen that the estimated possible enhancement factors could potentially provide an 7,200-fold improvement over the 18 molecule detection limit described herein. Thus, it is shown that the ultimate limit of label-free detection of single molecule binding events is theoretically possible within the framework of (5.3).

We have presented a simple mathematical model that analytically relates physical detection parameters of a single nanoparticle LSPR sensor to the minimum number of detectable analyte molecules. The utility of this model is twofold. It can be used to select the optimum nanoparticle geometry for a desired detection system completely analytically, forgoing otherwise necessary comprehensive, experimental characterization. The minimum number of detectable molecules can be estimated as well as the number of molecules detected at saturation which provides insight into the dynamic range of the system. Equation (5.3) was used to predict the optimal nanorod geometry to for the detection of streptavidin molecules. A factor of 6 reduction in the minimum detectable concentration was established over previous work using a nonoptimized nanorod detection system. The second application of the model is that a framework is provided through which the effects of potential system improvements can be assessed. Analysis of the theoretical limits of the dependent variables of (5.3) indicates that a 7,200-fold reduction of the MDL for the detection system described herein is possible. Clearly, not all of these potential avenues for MDL reduction can be realized concurrently. However, because our current MDL is 18 streptavidin molecules, we propose it is theoretically possible to design a system capable of detecting single molecule binding events by careful optimization of system parameters, as described herein.

In conclusion, we have reviewed developments in the field of LSPR biosensors that use isolated plasmonic nanostructures on a surface. Our results and those of

other groups show that miniaturization of LSPR sensors down to a single nanostructure is possible, with metrics that approach those of ensemble LSPR sensors that interrogate a large field of view of plasmonic nanostructures. Although the FOM of individual nanostructure based LSPR sensors are no better than ensemble LSPR sensors, they offer the intriguing possibility of detecting individual binding events in real time. Our results show that this goal is tantalizingly within reach, and we present a roadmap of improvements that may allow us to optimize current LSPR sensors to reach this exciting goal.

References

1. Yguerabide J, Yguerabide EE. Light-scattering submicroscopic particles as highly fluorescent analogs and their use as tracer labels in clinical and biological applications—II. Experimental characterization. Anal Biochem. 1998;262:157–76.
2. Alivisatos P. The use of nanocrystals in biological detection. Nat Biotechnol. 2004;22:47–52.
3. Penn SG, He L, Natan MJ. Nanoparticles for bioanalysis. Curr Opin Chem Biol. 2003;7:609–15.
4. Iqbal SS, Mayo MW, Bruno JG, Bronk BV, Batt CA, Chambers JP. A review of molecular recognition technologies for detection of biological threat agents. Biosens Bioelectron. 2000;15:549–78.
5. Storhoff JJ, Elghanian R, Mucic RC, Mirkin CA, Letsinger RL. One-pot colorimetric differentiation of polynucleotides with single base imperfections using gold nanoparticle probes. J Am Chem Soc. 1998;120:1959–64.
6. Englebienne P. Use of colloidal gold surface plasmon resonance peak shift to infer affinity constants from the interactions between protein antigens and antibodies specific for single or multiple epitopes. Analyst. 1998;123:1599–603.
7. Nath N, Chilkoti A. Label free colorimetric biosensing using nanoparticles. J Fluoresc. 2004;14:377–89.
8. Nath N, Chilkoti A. A colorimetric gold nanoparticle sensor to interrogate biomolecular interactions in real time on a surface. Anal Chem. 2002;74:504–9.
9. Haes AJ, Stuart DA, Nie SM, Van Duyne RP. Using solution-phase nanoparticles, surface-confined nanoparticle arrays and single nanoparticles as biological sensing platforms. J Fluoresc. 2004;14:355–67.
10. Frederix F, Friedt JM, Choi KH, Laureyn W, Campitelli A, Mondelaers D, et al. Biosensing based on light absorption of nanoscaled gold and silver particles. Anal Chem. 2003;75:6894–900.
11. Dahlin A, Zach M, Rindzevicius T, Kall M, Sutherland DS, Hook F. Localized surface plasmon resonance sensing of lipid-membrane-mediated biorecognition events. J Am Chem Soc. 2005;127:5043–8.
12. Marinakos SM, Chen S, Chilkoti A. Plasmonic detection of a model analyte in serum by a gold nanorod sensor. Anal Chem. 2007;79:5278–83.
13. Fujiwara K, Watarai H, Itoh H, Nakahama E, Ogawa N. Measurement of antibody binding to protein immobilized on gold nanoparticles by localized surface plasmon spectroscopy. Anal Bioanal Chem. 2006;386:639–44.
14. Chen C-D, Cheng S-F, Chau L-K, Wang CRC. Sensing capability of the localized surface plasmon resonance of gold nanorods. Biosens Bioelectron. 2007;22:926–32.
15. Gervais T, Jensen KF. Mass transport and surface reactions in microfluidic systems. Chem Eng Sci. 2006;61:1102–21.

16. Dejardin P, Vasina EN. An accurate simplified data treatment for the initial adsorption kinetics in conditions of laminar convection in a slit: application to protein adsorption. Colloids Surf B Biointerfaces. 2004;33:121–7.
17. Nair PR, Alam MA. Performance limits of nanobiosensors. Appl Phys Lett. 2006;88:233120.
18. Cui Y, Wei QQ, Park HK, Lieber CM. Nanowire nanosensors for highly sensitive and selective detection of biological and chemical species. Science. 2001;293:1289–92.
19. Gu LQ, Braha O, Conlan S, Cheley S, Bayley H. Stochastic sensing of organic analytes by a pore-forming protein containing a molecular adapter. Nature. 1999;398:686–90.
20. Besteman K, Lee JO, Wiertz FGM, Heering HA, Dekker C. Enzyme-coated carbon nanotubes as single-molecule biosensors. Nano Lett. 2003;3:727–30.
21. Bayley H, Martin CR. Resistive-pulse sensing—from microbes to molecules. Chem Rev. 2000;100:2575–94.
22. Wax A, Sokolov K. Molecular imaging and darkfield microspectroscopy of live cells using gold plasmonic nanoparticles. Laser Photon Rev. 2009;3:146–58.
23. Nusz GJ, Curry AC, Marinakos SM, Wax A, Chilkoti A. Rational selection of gold nanorod geometry for label-free plasmonic biosensors. ACS Nano. 2009;3(4):795–806.
24. Armani AM, Kulkarni RP, Fraser SE, Flagan RC, Vahala KJ. Label-free, single-molecule detection with optical microcavities. Science. 2007;317:783–7.
25. Curry A, Nusz G, Chilkoti A, Wax A. Analysis of total uncertainty in spectral peak measurements for plasmonic nanoparticle-based biosensors. Appl Opt. 2007;46:1931–9.
26. Gillis EH, Gosling JP, Sreenan JM, Kane M. Development and validation of a biosensor-based immunoassay for progesterone in bovine milk. J Immunol Methods. 2002;267:131–8.
27. Rosi NL, Mirkin CA. Nanostructures in biodiagnostics. Chem Rev. 2005;105:1547–62.
28. Mitchell JS, Wu YQ, Cook CJ, Main L. Sensitivity enhancement of surface plasmon resonance biosensing of small molecules. Anal Biochem. 2005;343:125–35.
29. Neely A, Perry C, Varisli B, Singh AK, Arbneshi T, Senapati D, et al. Ultrasensitive and highly selective detection of Alzheimer's disease biomarker using two-photon rayleigh scattering properties of gold nanoparticle. ACS Nano. 2009;3:2834–40.
30. Kreuzer MP, Quidant R, Salvador JP, Marco MP, Badenes G. Colloidal-based localized surface plasmon resonance (LSPR) biosensor for the quantitative determination of stanozolol. Anal Bioanal Chem. 2008;391:1813–20.
31. Mock JJ, Barbic M, Smith DR, Schultz DA, Schultz S. Shape effects in plasmon resonance of individual colloidal silver nanoparticles. J Chem Phys. 2002;116(15):6755–9.
32. Mock JJ, Smith DR, Schultz S. Local refractive index dependence of plasmon resonance spectra from individual nanoparticles. Nano Lett. 2003;3:485–91.
33. Schultz DA, Mock JJ, Schultz S, Smith DR. Single-target molecule detection with nonbleaching multicolor optical immunolabels. Proc Natl Acad Sci U S A. 2000;97:996–1001.
34. Mock JJ, Hill RT, Degiron A, Zauscher S, Chilkoti A, Smith DR. Distance-dependent plasmon resonant coupling between a gold nanoparticle and gold film. Nano Lett. 2008;8(8):2245–52.
35. Sonnichsen C, Geier S, Hecker NE, von Plessen G, Feldmann J, Ditlbacher H, et al. Spectroscopy of single metallic nanoparticles using total internal reflection microscopy. Appl Phys Lett. 2000;77:2949–51.
36. Curry A, Hwang WL, Wax A. Epi-illumination through the microscope objective applied to darkfield imaging and microspectroscopy of nanoparticle interaction with cells in culture. Opt Express. 2006;14:6535–42.
37. Curry AC, Crow M, Wax A. Molecular imaging of epidermal growth factor receptor in live cells with refractive index sensitivity using dark-field microspectroscopy and immunotargeted nanoparticles. J Biomed Opt. 2008;13(1):014022.
38. Raschke G, Kowarik S, Franzl T, Sonnichsen C, Klar TA, Feldmann J, et al. Biomolecular recognition based on single gold nanoparticle light scattering. Nano Lett. 2003;3:935–8.
39. Liu GL, Doll JC, Lee LP. High-speed multispectral imaging of nanoplasmonic array. Opt Express. 2005;13:8520–5.

40. Rodriguez-Fernandez J, Novo C, Myroshnychenko V, Funston AM, Sanchez-Iglesias A, Pastoriza-Santos I, et al. Spectroscopy, imaging, and modeling of individual gold decahedra. J Phys Chem C. 2009;113:18623–31.
41. McFarland AD, Van Duyne RP. Single silver nanoparticles as real-time optical sensors with zeptomole sensitivity. Nano Lett. 2003;3:1057–62.
42. Nusz GJ, Marinakos SM, Curry AC, Dahlin A, Höök F, Wax A, et al. Label-free plasmonic detection of biomolecular binding by a single gold nanorod. Anal Chem. 2008;80:984–9.
43. Curry A, Nusz G, Chilkoti A, Wax A. Substrate effect on refractive index dependence of plasmon resonance for individual silver nanoparticles observed using darkfield micro-spectroscopy. Opt Express. 2005;13:2668–77.
44. Yguerabide J, Yguerabide EE. Light-scattering submicroscopic particles as highly fluorescent analogs and their use as tracer labels in clinical and biological applications—I. Theory. Anal Biochem. 1998;262:137–56.
45. Prescott SW, Mulvaney P. Gold nanorod extinction spectra. J Appl Phys. 2006;99:123504.
46. Kreibig U, Gartz M, Hilger A. Mie resonances: sensors for physical and chemical cluster interface properties. Ber Bunsen Gesellsch Phys Chem Chem Phys. 1997;101:1593–604.
47. Nath N, Chilkoti A. Label-free biosensing by surface plasmon resonance of nanoparticles on glass: optimization of nanoparticle size. Anal Chem. 2004;76:5370–8.
48. Raschke G, Brogl S, Susha AS, Rogach AL, Klar TA, Feldmann J, et al. Gold nanoshells improve single nanoparticle molecular sensors. Nano Lett. 2004;4:1853–7.
49. Haes AJ, Van Duyne RP. A nanoscale optical biosensor: sensitivity and selectivity of an approach based on the localized surface plasmon resonance spectroscopy of triangular silver nanoparticles. J Am Chem Soc. 2002;124:10596–604.
50. Chumanov G, Sokolov K, Gregory BW, Cotton TM. Colloidal metal films as a substrate for surface-enhanced spectroscopy. J Phys Chem. 1995;99:9466–71.
51. Nikoobakht B, El-Sayed MA. Preparation and growth mechanism of gold nanorods (NRs) using seed-mediated growth method. Chem Mater. 2003;15:1957–62.
52. Rindzevicius T, Alaverdyan Y, Dahlin A, Hook F, Sutherland DS, Kall M. Plasmonic sensing characteristics of single nanometric holes. Nano Lett. 2005;5:2335–9.
53. Baciu CL, Becker J, Janshoff A, Sonnichsen C. Protein-membrane interaction probed by single plasmonic nanoparticles. Nano Lett. 2008;8:1724–8.
54. Hernandez FJ, Dondapati SK, Ozalp VC, Pinto A, O'Sullivan CK, Klar TA, et al. Label free optical sensor for avidin based on single gold nanoparticles functionalized with aptamers. J Biophotonics. 2009;2:227–31.
55. Xu XD, Cortie MB. Shape change and color gamut in gold nanorods, dumbbells, and dog bones. Adv Funct Mater. 2006;16:2170–6.
56. Jung LS, Campbell CT, Chinowsky TM, Mar MN, Yee SS. Quantitative interpretation of the response of surface plasmon resonance sensors to adsorbed films. Langmuir. 1998;14:5636–48.
57. Haes AJ, Van Duyne RP, Zou SL, Schatz GC. Nanoscale optical biosensor: short range distance dependence of the localized surface plasmon resonance of noble metal nanoparticles. J Phys Chem B. 2004;108:6961–8.
58. Hao E, Schatz GC. Electromagnetic fields around silver nanoparticles and dimers. J Chem Phys. 2004;120:357–66.
59. Imura K, Okamoto H, Nagahra T. Plasmon mode imaging of single gold nanorods. J Am Chem Soc. 2004;126:12730–1.
60. Kuwata H, Tamaru H, Esumi K, Miyano K. Resonant light scattering from metal nanoparticles: practical analysis beyond Rayleigh approximation. Appl Phys Lett. 2003;83:4625–7.
61. Miller MM, Lazarides AA. Sensitivity of metal nanoparticle plasmon resonance band position to the dielectric environment as observed in scattering. J Opt A Pure Appl Opt. 2006;8: S239–49.

62. Neish CS, Martin IL, Henderson RM, Edwardson JM. Direct visualization of ligand-protein interactions using atomic force microscopy. Br J Pharmacol. 2002;135:1943–50.
63. Weber PC, Ohlendorf DH, Wendoloski JJ, Salemme FR. Structural origins of high-affinity biotin binding to streptavidin. Science. 1989;243:85–8.
64. Hendrickson WA, Pahler A, Smith JL, Satow Y, Merritt EA, Phizackerley RP. Crystal-structure of core streptavidin determined from multiwavelength anomalous diffraction of synchrotron radiation. Proc Natl Acad Sci U S A. 1989;86:2190–4.
65. Hinrichsen EL, Feder J, Jossang T. Geometry of random sequential adsorption. J Stat Phys. 1986;44:793–827.
66. Link S, El-Sayed MA. Spectroscopic determination of the melting energy of a gold nanorod. J Chem Phys. 2001;114:2362–8.
67. Chang SS, Shih CW, Chen CD, Lai WC, Wang CRC. The shape transition of gold nanorods. Langmuir. 1999;15:701–9.
68. Muskens OL, Bachelier G, Del Fatti N, Vallee F, Brioude A, Jiang XC, et al. Quantitative absorption spectroscopy of a single gold nanorod. J Phys Chem C. 2008;112:8917–21.
69. Link S, El-Sayed MA. Spectral properties and relaxation dynamics of surface plasmon electronic oscillations in gold and silver nanodots and nanorods. J Phys Chem B. 1999;103:8410–26.
70. Link S, Mohamed MB, El-Sayed MA. Simulation of the optical absorption spectra of gold nanorods as a function of their aspect ratio and the effect of the medium dielectric constant. J Phys Chem B. 1999;103:3073–7.
71. Beeram SR, Zamborini FP. Selective attachment of antibodies to the edges of gold nanostructures for enhanced localized surface plasmon resonance biosensing. J Am Chem Soc. 2009;131:11689.
72. Dahlin AB, Tegenfeldt JO, Hook F. Improving the instrumental resolution of sensors based on localized surface plasmon resonance. Anal Chem. 2006;78:4416–23.
73. Kim DK, Kerman K, Hiep HM, Saito M, Yamamura S, Takamura Y, et al. Label-free optical detection of aptamer-protein interactions using gold-capped. Anal Biochem. 2008;379:1–7.
74. Frank Jeyson H, Srujan Kumar D, Ozalp VC, Alessandro P, Ciara KOS, Thomas AK, et al. Label free optical sensor for Avidin based on single gold nanoparticles functionalized with aptamers. J Biophotonics. 2009;2:227–31.
75. Stewart ME, Anderton CR, Thompson LB, Maria J, Gray SK, Rogers JA, et al. Nanostructured plasmonic sensors. Chem Rev. 2008;108:494–521.
76. Qavi AJ, Washburn AL, Byeon JY, Bailey RC. Label-free technologies for quantitative multiparameter biological analysis. Anal Bioanal Chem. 2009;394:121–35.
77. Hoa XD, Kirk AG, Tabrizian M. Towards integrated and sensitive surface plasmon resonance biosensors: a review of recent progress. Biosens Bioelectron. 2007;23:151–60.
78. Miller MM, Lazarides AA. Sensitivity of metal nanoparticle surface plasmon resonance to the dielectric environment. J Phys Chem B. 2005;109:21556–65.

Chapter 6
Plasmon Biophotonic Arrays for Multi-analyte Biosensing in Complex Media

Andrew M. Shaw, Rouslan V. Olkhov, Artem Jerdev, and William L. Barnes

Abstract The design of plasmon-based sensors for analysis of complex media such as serum is sensitive to the effects of non-specific binding. A simple analysis is presented to provide insight into the orders of magnitude involved in the kinetics of the problem and how label-free Immuno-kinetic assays may compensate for these effects. We then consider some specific challenges including sensitivity and non-specific binding discussed in terms of the kinetic and thermodynamic parameters of the protein–protein interactions which define the extent of fouling of the target sensor surface. Nanoparticle plasmon arrays have some fundamental advantages in multi-analyte sensing in complex media such as blood and the advantages of multiple measurements are considered in the context of a global mechanistic, kinetic analysis to profile the complex medium composition.

Overview

Many differential diagnoses are made on the basis of a single biomarker in the blood, for example prostate specific antigen and prostate cancer [1], however not all diseases may be diagnosed in this way and measurement of the relative and absolute concentrations of a number of markers may prove to be a more reliable diagnosis [2]. Most biomarker analyses are performed in the clinical chemistry laboratory on large ELISA assay instruments which require significant sample preparation. The alternative is a point-of-care multi-analyte sensing platform which will take diagnosis out of the laboratory and into the doctor's surgery and has the potential to revolutionise health care [3]. A necessary pre-requisite is the discovery of the

A.M. Shaw (✉) • R.V. Olkhov
School of Biosciences, University of Exeter, Exeter, EX4 4QD, UK

A. Jerdev • W.L. Barnes
School of Physics, University of Exeter, Stocker Road, Exeter, EX4 4QL, UK
e-mail: W.L.Barnes@exeter.ac.uk

A. Dmitriev (ed.), *Nanoplasmonic Sensors*, Integrated Analytical Systems,
DOI 10.1007/978-1-4614-3933-2_6,

diagnostic patterns, the choice of biomarkers and an array-based platform that requires little or no sample preparation. Many different approaches to biomarker discovery [4] and biomarker patterns have been investigated, notably mass spectroscopy [5, 6] where patterns in large collections of molecules, perhaps even the entire metabolome, have been investigated although there are some doubts about the validity of this approach [6]. Once biomarkers have been discovered these are transferred onto presumptive tests on fluorescence-based array platforms [7, 8]. However, development of a point-of-care device remains elusive owing to problems associated with the need for sample preparation to eliminate the effects of the large blood proteome on the assays.

Here we address some of the challenges for point-of-care devices for multi-analyte differential diagnosis, notably for label-free surface plasmon resonance (SPR) based platforms where minimal sample preparation and user skill is required [9]. If a diagnostic is to proceed to clinical application there are many tests that need to be performed to optimise the design of the assay, ensuring reproducibility, sensitivity, accuracy and specificity. Once the assay has been optimised, confidence in the diagnostic must be achieved via a clinical trial before regulatory approval can be sought. In what follows, we assess the factors involved in the assay design on label-free plasmon platforms in complex fluids, specifically blood. Here, the major challenge is maintaining the assay sensitivity, specificity and accuracy against the significant problem of non-specific binding of blood proteins such as human serum albumin (HSA) which are in significant and varying concentration from patient to patient.

The use of SPRs for biosensing has an extensive history over several decades [10] and will not be reviewed here. The principal advantage of SPR is that it offers a label-free approach removing the need to tag target analytes thereby significantly reducing the overhead time required for sample preparation. Biospecificity is achieved by binding a highly specific capture molecule, typically an antibody, to the gold plasmon surface. The specificity of the biosensor then depends on the immunological specificity of the target analyte binding to the antibody against a background of non-specific binding [11]. The sensitivity and accuracy of the assay depend on the measurement of the protein mass change at the plasmon surface. The plasmon mode that was originally developed for biosensing applications was the propagating surface plasmon resonance (PSPR) [11–13]. It involves a surface plasmon mode that is bound to a metal surface in much the same way that light is guided by an optical fibre. Importantly, the surface plasmon mode is sensitive to the optical environment near the metal surface—the optical field associated with the plasmon mode decays exponentially with distance from the metal surface, with a typical decay length of ~200 nm [14]. The metal of choice in SPR biosensing is gold since it provides a combination of good surface plasmon properties with suitable surface chemistry. More recently sensors based on the localised particle SPRs associated with metallic nanostructures have been developed as biosensors [12, 15]. Whilst the raw sensitivity of these sensors is less than that of those based on PSPR, the shorter field decay length, ~20 nm [16], is advantageous—it reduces sensitivity to changes in the bulk: assays based on PSPR and localised surface plasmon resonance (LSPR) thus have a comparable performance [17–19].

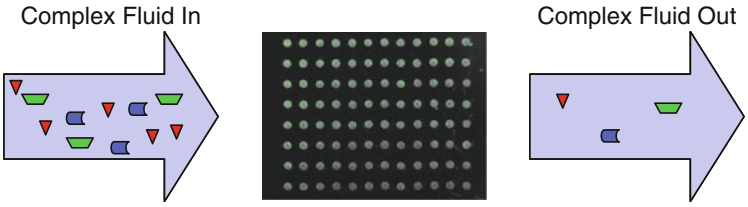

Fig. 6.1 Biophotonic array functionalised for different target molecules with control spots

The general approach of array-based plasmon sensors [15, 20] for the analysis of multi-analytes in complex solutions in shown schematically in Fig. 6.1. For PSPR a planar gold film is functionalized by printing localised assays of the capture antibodies (ligands) with ligand-free gold surfaces between the arrays. The typical array spot pitch is 100–300 μm and is significantly greater than the plasmon decay length of ca. 200–300 nm into the medium above the surface and typically 60 μm propagation length along the surface. Thus crosstalk between functionalised spots is avoided and individual array spot areas can be interrogated independently and simultaneously with 2D camera sensor. In the case of the LSPR-based sensor, a glass substrate is coated with a number of spots that are made up of a large number of gold nanoparticles. Each of these spots is then functionalized by having ligands, e.g. antibodies, printed on top of the nanoparticles. The crosstalk between spots with different functionality is even less of a concern in this case because the plasmon field penetration depth is in the order of the particle radius, 20–50 nm. Sensing is accomplished by monitoring the reflection (PSPR) or extinction (or scattering) (LSPR) of light by the spots. The light scattered by the nanoparticles is collected in real time by a video camera from each of the array spots. As the fluid to be analysed is introduced both specific and non-specific binding occurs to the assay spots, and the scattered light optical signal intensity changes directly in proportion to the mass arriving within the plasmon field at the surface of the particle. This binding changes the effective refractive index of the medium in the surface plasmon field, i.e. close to the metal surface. A simple kinetic model, detailed below, shows that the time-dependent signal should change in an exponential way with the exponent being a product of the concentration of the analyte and the binding rate constant of the analyte–ligand interaction. The kinetic response may be calibrated against known concentrations so that the measured rate is proportional to the concentration of the analyte: an immuno-kinetic assay. As we discuss below, this simple kinetic picture is a crude approximation but allows the proof-of-principle to be demonstrated. By monitoring a number of differently functionalized spots the concentration of several different analytes can be monitored at once.

For single-analyte sensing the preferred instrumental configuration is a dual-channel SPR platform. Here, two flow channels are placed close to one another (separated by a few mm) on a continuous gold surface with one channel acting as a control for temperature and non-specific binding of an analyte. The dual-channel configuration is well established in the field with Biacore arguably the leading

commercial platform capable of detecting protein concentrations in ng mL^{-1} or pM. For the ultimate in sensitivity, differential SPR (dSPR) [21] and interferometric techniques [22] are best, perhaps two orders of magnitude more sensitive, but are not yet developed in array-format. Array-format biosensing using plasmonics has been explored by several groups [23, 24], and some are clearly making good progress [25]. In the next section we look at some of the issues that need to be addressed if the full potential is to be realised.

The Challenges of Biosensing Using Plasmonics

Refractive Index Sensitivity

The principle of SPR detection of biologically relevant molecules in aqueous solutions relies on the adsorption of analyte molecules to the sensor surface which forms part of the sensing volume of the plasmon field. For simplicity, proteins are assumed to have similar refractive indices as determined by methods comparing the change in the plasmon signal with alternative measures of absolute surface protein concentration such as radio-labelled proteins [26] or quartz crystal balance measurements [27, 28]. Measurement of the refractive index of proteins in layers on surfaces by complementary techniques [29] allow estimates in the range 1.33156–1.38483 [29] and up to 1.5 but only for a limited number of proteins. The independent techniques allow a dn/dc measurement (change in refractive index with change in surface concentration) to be made, $dn/dc = 0.182$ g^{-1} cm^3 [29]: SPR techniques are essentially mass sensors. In an angle-resolved measurement that uses the standard format of propagating surface plasmons on a planar metal surface, the smallest angular shift that can be detected is typically $10^{-4\circ}$. Using data from Biacore (BIAUser training presentation) this corresponds to a change of 10^{-6} refractive index units (10^{-6} refractive index units $\equiv 1$ RU), which in turn corresponds to 1 fg mm^{-2} of protein. Given these operational parameters, is this sensitivity appropriate for single biomarker sensing and what are the challenges in the extension to multi-analyte biosensing?

The dominant challenge to the integrity of the biomarker assay in a point-of-care device is the composition of the complex fluid (that is whole blood or serum) in which there are a large number of different proteins which provide a background against which the biomarker or panel of biomarkers should be detected [30]. The blood serum contains 60–80 g L^{-1} of various protein, the most abundant component, the protein serum albumin, is present at 35–55 g L^{-1} concentrations, followed by the immunoglobulin protein family at 10–35 g L^{-1}. The concentrations of the other proteins are orders of magnitude smaller, with the rest of the classic plasma proteins being about 10^3–10^6 less abundant than albumin, and known tissue leakage proteins (e.g. thyroglobulin ~ 10 ng mL^{-1}) and interleukins spanning the next six smaller orders of magnitude [30]. With the exception of a test for albumin,

these concentrations present major challenges for multi-analyte SPR sensing: we have to detect small amounts of the molecules of choice against a large background, a general and well-known problem of non-specific binding [26, 31–35].

To gain further insight into the kinetic analysis in complex fluids, it is useful to make some simple numerical estimates of mass-limited kinetics and concentration limited kinetics. For the purposes of illustration let us calculate how many molecules need to be detected if we are to be able to sense the presence of a typical complement protein in blood serum. We need to know: (1) the number density of surface sites to which analyte molecules may bind, (2) the number of analyte molecules in a given volume which can react with the surface in a given time and (3) the reaction rate. By way of example, let us take the following parameters as indicative, they come from the much-studied BSA—antibody to bovine serum albumin (aBSA) interaction and are:

- Time window, Δt: 1 s
- Reaction rate constant, k_a: 10^5 M^{-1} s^{-1}
- Analyte diff. coefficient, D: 6×10^{-11} m^2 s^{-1} (typical for albumin in water [36])
- Analyte surface coverage: 0 (maximal adsorption rate, no dissociation)
- Analyte concentration, $[A]$: 10 nM [30]
- Noise floor: ~2 RU (Biacore)

How many binding sites are there on the sensor surface? If we assume the separation between binding molecules is of order 10 nm then there will be 10^4 sites per μm^2. How reasonable is this estimate? A monolayer of IgG produces a response of ~2,000 RU (equivalent to 2×10^{-3} RIU), which corresponds to a protein mass load of ~2 ng mm^{-2}, when converted to number of molecules per μm^2, this yields:

$$\text{molecules per } \mu m^2 = \frac{\text{mass per } \mu m^2 \times N_a}{\text{molar mass}} = \frac{2 \times 10^9 \text{ g} \times 10^{-6} \times 6.022 \times 10^{23} \text{ M}^{-1}}{150,000 \text{ g M}^{-1}}$$
$$\approx 8 \times 10^3$$

i.e. ~10^4, the same as the number of sites estimated above from the size of the molecules.

Given the SPR sensitivity mentioned above, 1 fg mm^{-2}, the surface number density of binding sites we have just calculated, ~10^4 per μm^2, looks to be more than adequate, it corresponds to a protein mass load of ~2 ng mm^{-2}—if analyte molecules were to bind to all of these sites the resulting signal would be 10^3 above the noise floor. However, to estimate the mass of material that will actually bind to the surface, and thus gain an idea of how sensitive our detectors really need to be, we must go little further with the analysis. We need: (1) to examine how many analyte molecules will diffuse so as to interact with these binding sites (in the time interval) and (2) to determine how many molecules will bind to the surface in that time. Let us look at these in turn.

1. In 1 s, an albumin molecule can diffuse $\sqrt{2Dt} = \sqrt{2 \times 6 \times 10^{-11}\ \mathrm{m^2\ s^{-1}} \times 1\ \mathrm{s}}$ $\approx 11\ \mu\mathrm{m}$. As a result, the potential number of molecules that can collide with each $\mu\mathrm{m}^2$ of sensor surface is $\frac{10 \times 10^{-9}\ \mathrm{mol} \times N_\mathrm{a}}{10^{-3}\ \mathrm{m^3}} (1 \times 1 \times 11\ \ \mu\mathrm{m}^3) \approx 70$, i.e. many fewer than the 10^4 sites available.
2. The reaction rate or change in surface coverage, $\Delta\theta$, that takes place during the 1 s time interval is given by:

$$\begin{aligned}\Delta\theta &= \theta_{t=1\ \mathrm{s}} - \theta_{t=0} = (1 - \exp(-k_\mathrm{a}[A]t)) \\ &= 1 - \exp(-10^5\ \mathrm{M^{-1}\ s^{-1}} \times 10\ \mathrm{nM} \times 1\ \mathrm{s}) \approx 0.001\end{aligned}$$

   where θ_0 is the initial coverage and θ_t the coverage at the end then of the time period. From these estimates, less than 0.1% of the surface may react with the analyte in 1 s. (Note that this means that about 10% of the protein in the interaction volume above the surface is depleted in the 1 s of interaction time.)

Thus, the number of analyte molecules that we might expect to bind to the surface is $\leq$10 with a total mass load of ~1 pg mm^{-2}, well within the sensitivity range of standard SPR techniques. These benchmark calculations indicate that it would be possible to measure many of the molecules of interest in the blood proteome in a reasonable timescale of approximately 30 min. These measurements are not sensitivity limited.

The analysis above is extremely simplified with many assumptions made, we have ignored: dissociation, problems with unknown reaction rate constants, inhomogeneities in the flow of the solution and in surface chemistry; we have also assumed that the instrument response is reaction rather than mass-transport (diffusion) limited. The calculations also completely ignore the non-specific binding question. If the integrity and specificity of the biosensor are to be preserved then the sensitivity to protein load alone on the surface is insufficient to characterise the sensor performance as a biosensor [37]. In what follows, we look at the problem of non-specific binding in more detail and show that it is indeed a key limiting factor that must be overcome if an array-format multi-analyte platform is to be successfully developed.

Non-specific Binding: Finding the Needle in the Haystack

The SPR sensor is sensitive to any molecule retained near the surface which contributes to a change in the refractive index in the sensing, the technique does not discriminate between specific binding of the target molecules and non-specific binding of the other biomaterials that may be present in any given sample. The specificity of the sensor is instead determined by the functionalisation of the surface with biomolecular ligands which selectively bind the target analytes to the surface.

For the case of protein binding, the ligand choices include DNA/RNA/peptide aptamers [4, 38], affibodies [39] and antibodies, with the latter the most popular.

There are two broad categories of non-specific binding that need to be considered: (1) non-specific binding of the target molecules to regions of the sensor surface by means other than the desired ligand; and (2) binding of any non-target analyte components to the surface—an unwanted background. For a simple single-analyte solution this problem is easily addressed through a dual-channel measurement, as discussed in section "Binding of Target Molecules to the Sensor Surface by Means Other Than the Desired Ligand". The second non-specific binding problem is of more importance to multi-analyte sensing in complex fluids and involves the capture by ligand molecules of non-target molecules from the fluid. This problem is discussed in more detail in section "Multi-analyte Photonic Array Biosensing in Complex Media".

Binding of Target Molecules to the Sensor Surface by Means Other Than the Desired Ligand

Fitting of kinetic process parameters to data from multiple surface reactions has been tried by many groups to capture complex mechanisms of binding at the surface [31]. The global approach adopted by many is to write down the differential equation set for the chosen mechanism and solve the equations numerically, fitting the rate constants as parameters to the model directly. These models have been tried with pre-binding complexes for antibody–antigen interactions [31, 40] and including the effects of non-specific binding [35]. Myszka warns however [31] that a series of experiments with different concentrations is insufficient to produce an accurate description of the mechanism. One effect at the surface has been characterised accurately under ideal conditions and that is the Vroman effect [41, 42] where heavier proteins displace lighter proteins from the surface.

The multi-analyte sensor platform has potential to control for the presence of the competing background reactions by monitoring simultaneously the effects of the competing surface reactions on individual control spots within the array. The objective would be to measure the rates of the competing reactions on different control spots, fitting the data from assay spots and control spots simultaneously so as to produce a model with better defined parameters and therefore provide some insight into the binding processes at the surface. Here we present an analysis that can be extended to the presence of simultaneous assays. Some preliminary data looking at the measurement of total refractive index of some model sera are discussed and the potential for the design of the correct control spots is considered.

The simplest model that allows us to simulate the kinetic response of a sensor that includes the effect of this kind of non-specific binding is comprised of two types of surface region either on the same surface or on different surfaces such as on control spots, Fig. 6.2. An area L of surface is assumed to be covered with active

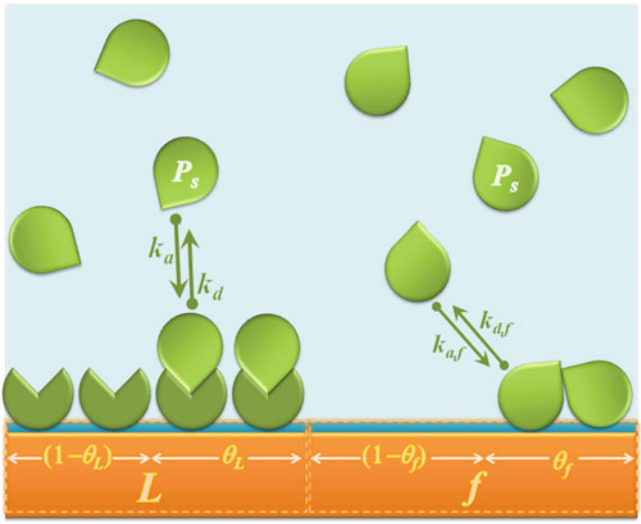

Fig. 6.2 Schematic for the interaction of target molecules (P_s) with the sensor surface. The *left-hand side* shows an area L of the surface that has been functionalised. A fraction of these ligand molecules are available for binding, $(1 - \theta_L)$ and the occupied fraction, θ_L. The *right-hand side* shows an area f that is un-functionalised: of this area a fraction θ_f is covered with analyte molecules

ligand molecules, an area f is assumed to be free of such active binding sites. The fraction of these surface areas to which analyte molecules are bound are θ_L and θ_f respectively. If we denote the fraction of the available surface covered with active binding sites as γ, where $\gamma = L/(L+f)$, than the fraction of the total surface, θ, to which any analyte molecules are bound can be written as

$$\theta = \gamma\theta_L + (1-\gamma)\theta_f. \tag{6.1}$$

The simplest one-to-one model describing the interaction of target analyte molecules with a ligand-functionalised surface requires the following parameters: the rate of association of the target molecules with surface binding sites and the rate of dissociation of thus formed complexes, as well as the rates of association and dissociation reactions for all other molecules present in analyte with the surface sites: the cross reactions. We can write the rate of change of these fractional surface occupations as follows:

$$\begin{aligned}\text{rate of change} = {} & \text{rate of association} - \text{rate of dissociation} \\ & + \text{rate of association of cross-reactants} \\ & - \text{rate of dissociation of cross-reactants.}\end{aligned}$$

In what follows these cross-reactants will be given the subscript i, whilst the specific target will be given the subscript s. More specifically, for the area of surface

coated with ligands, L, for the target analyte we can write the rate of change of the fractional occupation of available binding sites as,

$$\frac{\mathrm{d}\theta_{\mathrm{L}}}{\mathrm{d}t} = k_{\mathrm{a}}[P_{\mathrm{s}}](1-\theta_{\mathrm{L}}) - k_{\mathrm{d}}\theta_{\mathrm{L,s}} + \sum_{i,i\neq s} k_{\mathrm{a,L},i}[P_i](1-\theta_{\mathrm{L}}) - \sum_{i,i\neq s} k_{\mathrm{d,L},i}\theta_{\mathrm{L},i}, \tag{6.2}$$

where the first two terms are the specific binding association and dissociation of the target species for its ligand and the last two terms are the non-specific binding for all other proteins, P_i, to the specific sensor surface. For other parts of the same sensor surface that are non-functionalised, the same association and dissociation can occur for all proteins both the specific binding protein, P_{s} and the non-specific proteins, P_i,

$$\frac{\mathrm{d}\theta_{\mathrm{f}}}{\mathrm{d}t} = k_{\mathrm{a,f}}[P_{\mathrm{s}}](1-\theta_{\mathrm{f}}) - k_{\mathrm{d,f}}\theta_{\mathrm{f,s}} + \sum_{i,i\neq s} k_{\mathrm{a,f},i}[P_i](1-\theta_{\mathrm{f}}) - \sum_{i,i\neq s} k_{\mathrm{d,f},i}\theta_{\mathrm{f},i}. \tag{6.3}$$

In (6.2) and (6.3) $[P_i]$ is the concentration of the ith component (molecular species) in the fluid and $[P_{\mathrm{s}}]$ is the concentration of the target analyte, k_{a} and k_{d} are analyte-surface association and dissociation rate constants.

In the simplest case the analyte sample contains only target molecules, which may either specifically bind to respective surface ligands or non-specifically interact with the rest of the surface. These processes are represented in Fig. 6.2.

The commonest method used to find the concentration of the target analyte is based on using a dual-channel approach, a test channel and a reference channel. The single reference channel on a conventional instrument is subtracted from the test channel that is functionalised with the specific ligand. The reference channel is used in an attempt to compensate for all non-specific binding processes—processes which are assumed to contribute equally to the test channel and reference channel. For the single component experiment with the target protein in a buffer solution, $[P_i] = 0$, (6.1), (6.2) and (6.3) are combined to give:

$$\begin{aligned}
\text{test channel: } \frac{\mathrm{d}\theta}{\mathrm{d}t} &= \gamma\frac{\mathrm{d}\theta_{\mathrm{L}}}{\mathrm{d}t} + (1-\gamma)\frac{\mathrm{d}\theta_{\mathrm{f}}}{\mathrm{d}t} \\
&= \gamma k_{\mathrm{a}}[P_{\mathrm{s}}](1-\theta_{\mathrm{L}}) + (1-\gamma)k_{\mathrm{a,f}}[P_{\mathrm{s}}](1-\theta_{\mathrm{f}}) \\
&\quad -(1-\gamma)k_{\mathrm{d,f}}\theta_{\mathrm{f,s}} - \gamma k_{\mathrm{d,L}}\theta_{\mathrm{L,s}} \\
\text{reference: } \frac{\mathrm{d}\theta_{\mathrm{f}}}{\mathrm{d}t} &= k_{\mathrm{a,f}}[P_{\mathrm{s}}](1-\theta_{\mathrm{f}}) - k_{\mathrm{d,f}}\theta_{\mathrm{f,s}} \\
{}^{\gamma}\Delta\text{channel} = \text{test } - (1-\gamma)\text{reference: } \frac{1}{\gamma}\frac{\mathrm{d}\theta_{\mathrm{L}}}{\mathrm{d}t} &= k_{\mathrm{a}}[P_{\mathrm{s}}](1-\theta_{\mathrm{L}}) - k_{\mathrm{d,L}}\theta_{\mathrm{L,s}}
\end{aligned} \tag{6.4}$$

Measuring the γ-corrected difference response (${}^{\gamma}\Delta$ channel) allows corrections for temperature drift on the surface, assuming the reference surface is close to the test channel, and importantly allows k_{a} and k_{d} to be determined, provided γ is known.

Looking at the terms in the simple difference signal, test-reference, enables the effect of γ to be quantified which from (6.4) gives:

$$\Delta\text{channel} = \text{test-ref}:$$
$$\frac{1}{\gamma}\frac{d\theta_L}{dt} = k_a[P_s](1-\theta_L) - k_{d,L}\theta_{L,s} - k_{a,f}[P_s](1-\theta_f) + k_{d,f}\theta_{f,s}. \quad (6.5)$$

A simulated response based on (6.5) is shown in Fig. 6.3. Simulations were performed with γ taking the values 0.1, 0.5 and 0.9. For the purposes of modelling exercise the dissociation rate is assumed negligible, $k_d = 0$, and the association rate constant for specific binding to the L is set at 10^5 M^{-1} s^{-1} and for the non-specific binding of the target ligand to the un-functionalised surface is set at 5×10^3 M^{-1} s^{-1}: 20-fold less. For each of the three surface coverages the data from the test channel, reference channel and difference are simulated. The association rate constants, k_{obs}, determined by exponential fitting to the data from the test channel and the (test-reference) difference are compared with the true k_a. Note that k_{obs} derived from the difference channel is intrinsically an approximation since the data is the sum of two exponential processes whilst the fit is to a single exponential. In this particular model this leads to an overestimation of k_{obs} because an apparent coverage maximum decays faster than an initial reaction rate declines.

For low-surface ligand coverage the association to the bare surface is considerable with the k_{obs} for the test channel under estimating k_a, $k_{obs} = 0.62k_a$, but for the difference channel, $k_{obs} = 1.087k_a$, i.e. there is a small over-estimate. Similarly for the 0.5 coverage in the test channel $k_{obs} = 0.93k_a$ and in the difference channel $k_{obs} = 1.087k_a$, whilst for 90% ligand coverage, $k_{obs} = 0.99k_a$ and $k_{obs} = 1.087k_a$. Despite the range of values of γ, the difference channel allows for a constant 9% error in the over-estimate of k_a: on one hand the absolute error grows with increased γ owing to larger differences in ligand-free surface areas in test and reference channels but on the other hand the absolute specific response is also proportional to γ. Careful sensor surface design involving blocking steps to fill the gaps and controlling the hydrophobic/hydrophilic properties of the underlying surface means that only molecules binding to the ligands contribute to the mass change, the measured kinetics may then be used to produce accurate estimates of k_a and k_d which are close to those measured in solution and are reproducible to within 15% internationally [43]. There are other reasons for preferring to make γ smaller, notably reduced ligand crowding on the surface; these requirements have been discussed elsewhere [43, 44].

Multi-analyte Photonic Array Biosensing in Complex Media

The discussion of sensor response to single proteins using a two-channel platform represents the majority of current usage of SPR platforms commercially, there are a few exceptions, such as the 400-spot *Flexchip* platform from Biacore. Plasmonic

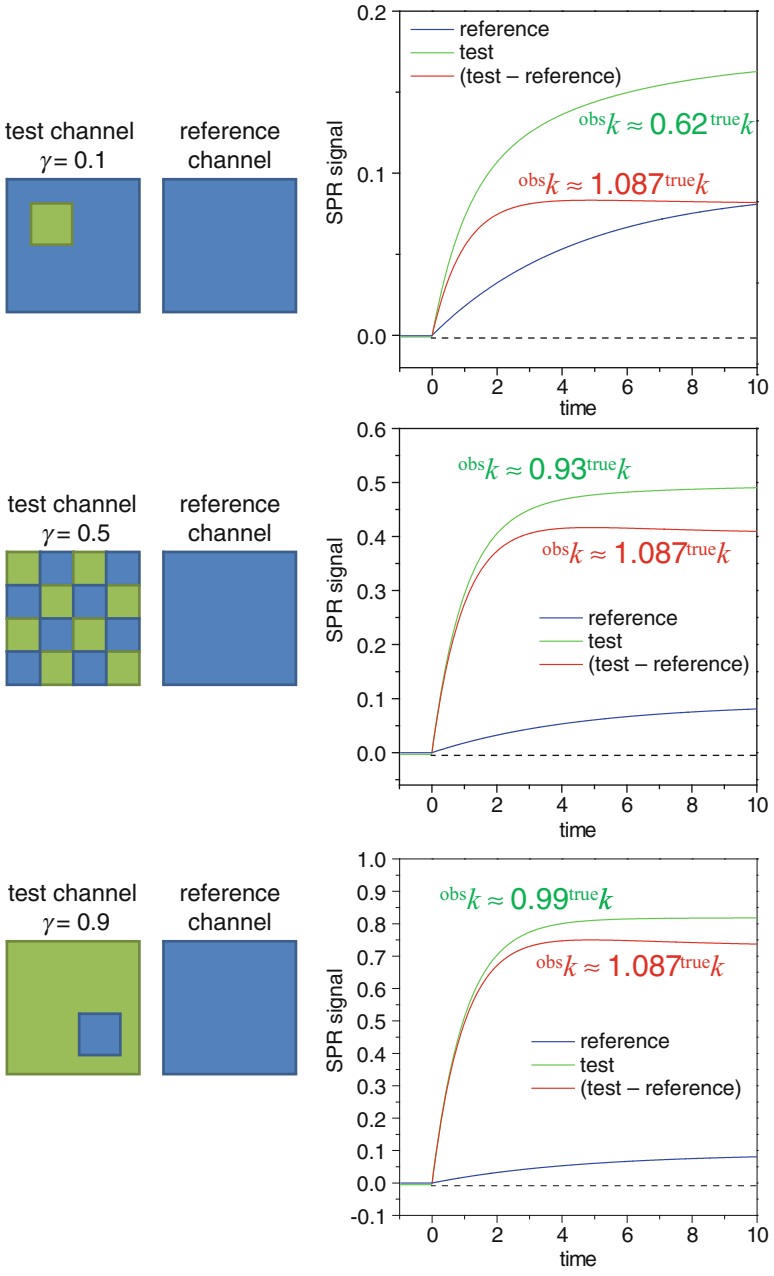

Fig. 6.3 Simulation of the response of the test channel (*green*), the reference channel (*blue*) and the difference (test-reference) (*red*) to exposure to a single-analyte solution

array imaging with nanoparticle-based arrays containing 96 spots has been performed using an array reader platform based on nanoparticles [15, 45, 46] which has the potential to measure many analytes simultaneously in complex media where a large number of control spots may be used to understand the effects of non-specific binding. The challenge is to design a series of control spots that let the non-specific effects to be considered quantitatively, thereby allowing the concentration of the target protein to be considered.

The detection of more than one protein against a background of a number of proteins landing on the sensor surface requires the discussion presented above to be extended to include the different mass contributions to the change in the refractive index, non-specific binding onto the sensor surface competing with the target binding and then a new series of surface displacement reactions which allow non-specific proteins to be displaced from the sensor surface. The mass correction needs to be introduced to convert the surface coverage of different mass proteins to the refractive index response of the sensor through the equation:

$$\frac{\mathrm{d}R}{\mathrm{d}t} = \frac{\mathrm{d}R}{\mathrm{d}\theta_{\mathrm{S}}}\frac{\mathrm{d}\theta_{\mathrm{S}}}{\mathrm{d}t} + \frac{\mathrm{d}R}{\mathrm{d}\theta_{\mathrm{NS}}}\frac{\mathrm{d}\theta_{\mathrm{NS}}}{\mathrm{d}t}, \tag{6.6}$$

where $\mathrm{d}R/\mathrm{d}\theta_{\mathrm{S}}$ is the specific protein mass and surface coverage dependent variation of the refractive index, and $\mathrm{d}R/\mathrm{d}\theta_{\mathrm{NS}}$ is the same for the non-specific proteins. Whilst these do not have to be absolute conversion factors, they must be scaled for the relative masses of the proteins. Hence in a two-protein system m_1 and m_2 the relative response is scaled in the ratio m_1/m_2.

Loosely Bound Surface Competition Reactions: Blood Serum Contamination

The interaction between proteins in complex fluids may not follow the simple loosely bound processes described above, more complex mechanisms may be present at the sensor surface. Adsorption of proteins onto hydrophobic surface sites may lead to conformational changes compromising their tertiary structure and lead to partial denaturing, which ultimately results in irreversibly bound proteins thereby changing the rate constants for the interactions. The surface denaturation is often combated by reducing the ligand concentration and increasing the amount of blocking protein on the surface in the same way as the minimisation of non-specific binding [31]. Molecules loosely bound to the surface may be exchanged with other molecules from the medium. Consequently, the simplified adsorption–desorption model presented above may be extended to include the exchange and displacement reactions shown schematically in Fig. 6.4.

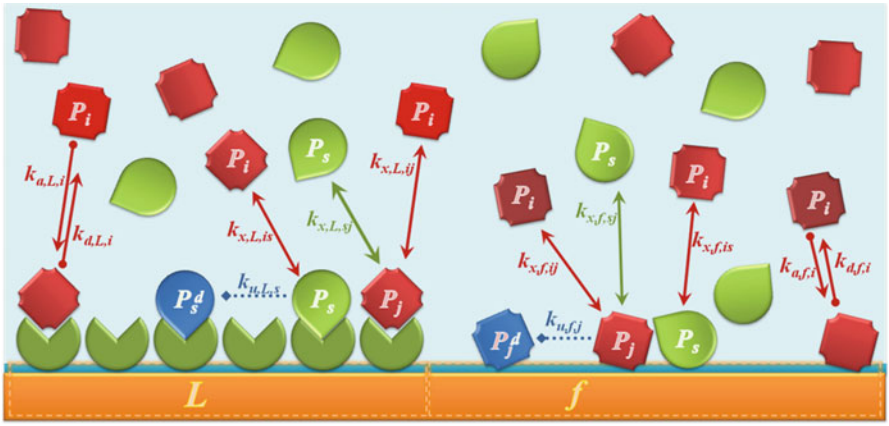

Fig. 6.4 Additional exchange and re-arrangement reactions when binding of non-target molecules is possible

The extended reaction model can be represented mechanistically as:

$$
\begin{aligned}
&(1)\ \text{adsorption: } P_i + S_{\mathrm{L/f}} \underset{k_{d,L/f,i}}{\overset{k_{a,L/f,i}}{\rightleftarrows}} P_i \cdot S_{\mathrm{L/f}} \\
&(2)\ \text{exchange: } P_i + P_j \cdot S_{\mathrm{L/f}} \underset{k_{x,L/f,ji}}{\overset{k_{x,L/f,ij}}{\rightleftarrows}} P_j + P_i \cdot S_{\mathrm{L/f}} \\
&(3)\ \text{rearrangement: } P_i \cdot S \xrightarrow{k_{u,i}} P_i^{\mathrm{d}} \cdot S
\end{aligned}
\tag{6.7}
$$

where in reaction 2 one adsorbed species, P_i , are exchanged with other species, P_j, from the bulk. A particular case of this reaction when low-mass adsorbed species are exchanged with higher-mass species from analyte corresponds to the Vroman effect [41]. Reaction 3 leads to deformed or (partly) denatured protein molecules permanently occupying the surface site. The exchange and re-arrangement rates are k_{x} and k_{u} respectively. An instance of the latter process is often induced on purpose before the sensor is used in a practical experiment and is known as a "blocking step": the sensor surface is exposed to a solution of non-target proteins (BSA and milk proteins are popular choices), which irreversibly interact with particularly active surface sites, thus blocking those sites from binding with other biomolecules. The following discussion is based on the assumption that non-specific binding significantly contributes to the observed SPR signal.

The association rate of any particular biomolecule with the sensor surface is proportional to the product of the corresponding rate constant and the concentration of the biomolecule in question, therefore, even if the non-specific association rate constants are smaller than the specific rate constants, the signal due to non-specific binding can outweigh the desired signal simply because of the higher concentration of the non-specific content of the sample. Consider the following reaction scheme and simulation values, Fig. 6.5.

Fig. 6.5 Reaction scheme and simulation values for high serum concentrations

$$[P_S]_0 = 10^{-8}\,M$$
$$[P_{\Sigma i}]_0 = 10^{-4}\,M$$
$$P_S + S \rightarrow P_S \bullet S \quad k_{a,P_S} = 10^5\,M^{-1}s^{-1}$$
$$P_S \bullet S \rightarrow P_S + S \quad k_{d,P_S} = 10^{-4}\,s^{-1}$$
$$P_{\Sigma i} + S \rightarrow P_{\Sigma i} \bullet S \quad k_{a,P_{\Sigma i}} = 10^2\,M^{-1}s^{-1}$$
$$P_{\Sigma i} \bullet S \rightarrow P_{\Sigma i} + S \quad k_{d,P_{\Sigma i}} = 10^{-2}\,s^{-1}$$
$$P_S + P_{\Sigma i} \bullet S \rightarrow P_{\Sigma i} + P_S \bullet S \quad k_{x,P_S,P_{\Sigma i}} = 2\times10^4\,M^{-1}s^{-1}$$

The first and second reactions are the association of the target protein to the surface with a rate constant consistent with a specific reaction giving a $K_D = 10^{-9}$ M corresponding to an interaction Gibbs free energy of -51.3 kJ mol^{-1}, which may be compared with the biotin-streptavidin $K_D = 10^{-13}$ M or -74.2 kJ mol^{-1}. The third and fourth reactions correspond to a non-specific interaction with $K_D = 10^{-4}$ M corresponding to a Gibbs free energy of -1.7 kJ mol^{-1}. Thermal energy (RT) at 298 K is -2.5 kJ mol^{-1} which suggests the non-specific complex will be unstable in the thermal bath and therefore can readily dissociate to free up the binding site. The final reaction is the displacement of the non-specific proteins from the target ligand which is set close to the association rate constant for the specific reaction implying the non-specific complex is easily broken.

The non-specific protein content of human serum albumin, HSA, in whole blood is in a concentration some 200 times the target protein; therefore the initial surface coverage is dominated by the rapid arrival of non-specific HSA protein covering the surface. However, the serum albumin layer is easily replaced with each thermal collision and the specific binding increases steadily with time, Fig. 6.6. The resulting test, reference and their difference channel responses are shown in Fig. 6.7. The reference channel shows a large initial change in refractive index associated with the arrival of the high concentration of non-specific proteins such as serum proteins with a similar rise in the test channel. The difference channel effectively removes the large step change allowing the recovery of a rate constant from the near-exponential trace with $k^{obs} = 0.7 \times k_a$ for the specific binding.

The effect of a loosely bound non-specific protein binding or fouling the sensor surface has been recently studied for the assay of the aBSA in model serum solutions containing varying concentrations of HSA from pure buffer to physiological concentrations of 450 μM [34]. The aBSA is detected absorbing specifically to BSA bound to the sensor surface with HSA acting as the interfering molecule. Large HSA concentrations interfere with aBSA binding to the surface as a decrease in k^{obs} of a factor of 3 is observed from the difference plots (Fig. 6.8).

There are two advantages associated with the multi-analyte array platform based on the nanoparticle plasmonics; (1) a number of control spots can be position around the array to control for the presence of a large concentration of the HSA; and (2) the particle plasmon field is sensitive only to the region immediately

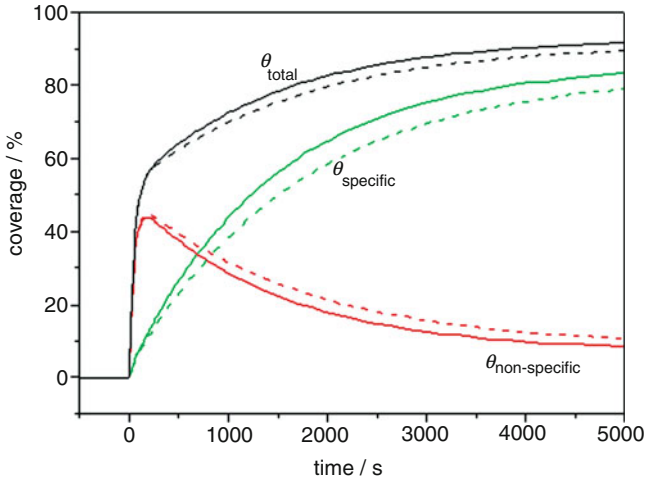

Fig. 6.6 Variation of surface coverage for the specific and non-specific interactions: *solid* and *dashed lines* represent simulations with and without surface exchange reactions, k_x, respectively, Fig. 6.5

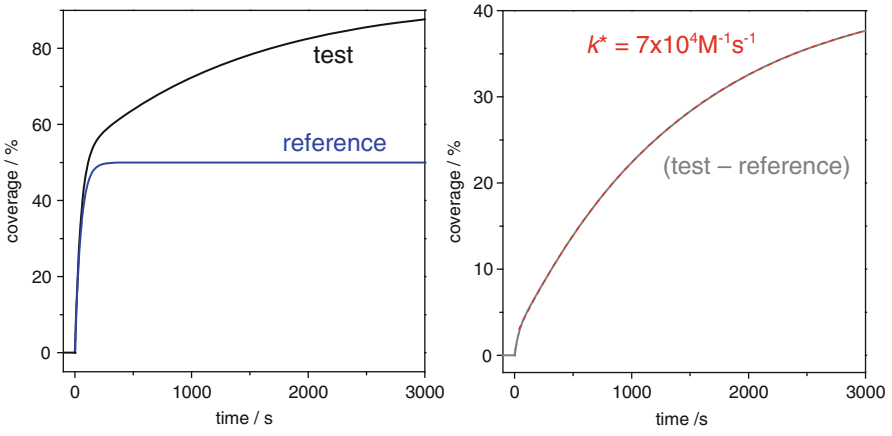

Fig. 6.7 Test and reference channel response (*left*) and the their difference (*right*) with the $k^{obs} = 7 \times 10^4\ M^{-1}\ s^{-1}$ compared with the simulation k_a value of $10^5\ M^{-1}\ s^{-1}$

above the particle, typically 20 nm. Both were exploited in the correction of the immuno-kinetic assay for aBSA in these experiments. A simple empirical correction was possible by measuring the bulk refractive index change on a control spot that showed little or no non-specific binding and which was constructed using a

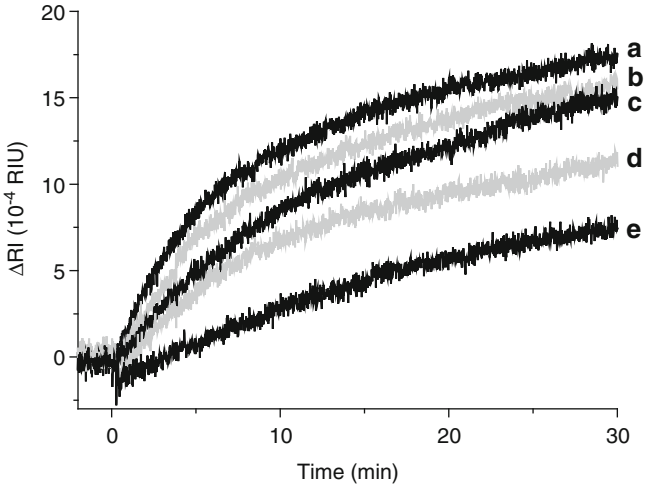

Fig. 6.8 aBSA-BSA assay with varying concentrations of HSA: (a) 0 μM; (b) 100 μM; (c) 200 μM; (d) 300 μM; (e) 450 μM (reproduced from ref. [34] with permission)

multi-layer fibrinogen-coated control spot. Printing a large concentration of fibrinogen into the control spot partially fills the plasmon field so that small changes in refractive index associated with non-specific binding are not observed making it an ideal control spot. The change in bulk refractive index is a measure of the total protein concentration in the serum sample which is therefore related directly to the rate of non-specific binding. Correlating the fast bulk index change observed in the reference channel with the rate of slower non-specific binding in the same reference channel provides an empirical correction which can be used to balance the effect of non-specific binding in test channels for all HSA concentrations producing a linear correlation between the assay parameters and the concentration of aBSA—a calibration curve, Fig. 6.9.

Surface Displacement Reactions

In the process of reaching equilibrium some reversibly bound molecules at the surface can change their place with other molecules from the solution, and a particular case of the substitution of lower-mass non-specifically adsorbed molecules with higher-mass components is the Vroman effect [41]. This is an energy competitive process which will be favoured by heavier masses.

Equations (6.2) and (6.3) can be modified to include the reactions indicated in (6.7) and shown in Fig. 6.4. The surface coverages can be expressed as sums of

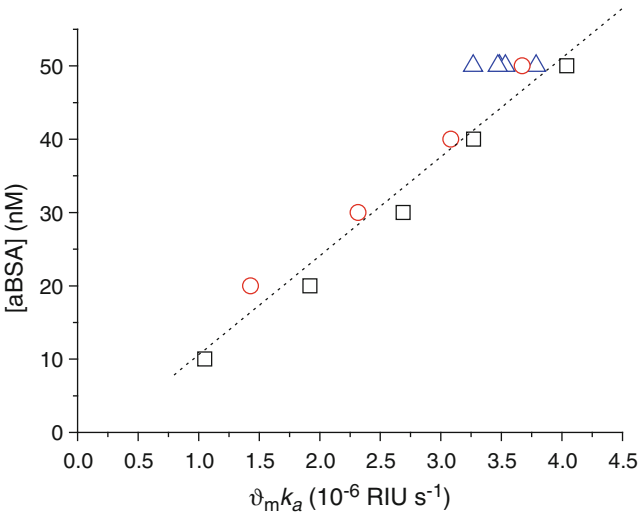

Fig. 6.9 Empirical correction of the immuno-kinetic assay for the variation of bulk [HSA], symbols denote several different experimental series. $\vartheta_m k_a$ parameter is equivalent to the initial rate of aBSA-BSA association reaction (reproduced with permission from ref. [34])

$\theta_{L/f,i}$—fractions of the surface covered with a particular analyte molecule P_i, where labels L/f refer, as before, to ligand-functionalised or ligand-free surface binding sites:

$$\frac{d\theta_{L/f}}{dt} = \sum_i \frac{d\theta_{L/f,i}}{dt} \tag{6.8}$$

and where

$$\begin{aligned}\frac{d\theta_{L/f,i}}{dt} &= k_{a,L/f,i}[P_i](1-\theta_{L/f}) - k_{d,L/f,i}\theta_{L/f,i} - k_{u,L/f,i}\theta_{L/f,i} \\ &+ \sum_{j,j\neq i} k_{x,L/f,ij}[P_i]\theta_{L/f,j} - \sum_{j,j\neq i} k_{x,L/f,ji}[P_j]\theta_{L/f,i}.\end{aligned} \tag{6.9}$$

The last two terms in (6.9) formally cancel each other when the summation over i is done so as to express $\theta_{L/f}$, but the SPR signal depends not only on the surface coverage, but also on the nature of the molecules covering the surface, notably their mass, therefore the individual θ_i needs to be used to discuss specific binding or the Vroman effect. Finally, the effect of the mass in the plasmon field also needs to be corrected.

The simplest model for the Vroman effect can be illustrated with the following assumptions:

- There are no specific binding sites on the surface for a given set of analytes
- The blocking step has been performed to minimise re-arrangement reactions, i.e. $k_u \approx 0$

Fig. 6.10 Reaction scheme and simulation values for the Vroman effect

$$[P_1]_0 = 10^{-4}\,M$$
$$[P_2]_0 = 10^{-6}\,M$$
$$P_1 + S \rightarrow P_1 \bullet S \quad k_{a,P_1} = 10^2\,M^{-1}s^{-1}$$
$$P_1 \bullet S \rightarrow P_1 + S \quad k_{d,P_1} = 10^{-2}\,s^{-1}$$
$$P_2 + S \rightarrow P_2 \bullet S \quad k_{a,P_2} = 5\times 10^2\,M^{-1}s^{-1}$$
$$P_2 \bullet S \rightarrow P_2 + S \quad k_{d,P_2} = 2\times 10^{-3}\,s^{-1}$$
$$P_2 + P_1 \bullet S \rightarrow P_1 + P_2 \bullet S \quad k_{x,2,1} = 10^2\,M^{-1}s^{-1}$$

– The non-specific affinity of analyte molecule P_i to the surface depends on the contact area, and therefore size/mass of P_i : $k_{\mathrm{x},ij} = k_{\mathrm{x}} f(P_i, P_j)$ and $K_{\mathrm{a},i} = K_{\mathrm{a}} f(P_i)$, such as $k_{\mathrm{x},ij} > k_{\mathrm{x},ji}$ and $K_{\mathrm{a},i} > K_{\mathrm{a},j}$ if mass of $P_i >$ mass of P_j

which, for two-component analyte, reduce (6.9) to:

$$\frac{\mathrm{d}\theta_1}{\mathrm{d}t} = k_{\mathrm{a},1}[P_1](1-\theta_1-\theta_2) - k_{\mathrm{d},1}\theta_1 + k_{\mathrm{x},1,2}[P_1]\theta_2 - k_{\mathrm{x},2,1}[P_2]\theta_1, \tag{6.10}$$

$$\frac{\mathrm{d}\theta_2}{\mathrm{d}t} = k_{\mathrm{a},2}[P_2](1-\theta_1-\theta_2) - k_{\mathrm{d},2}\theta_2 + k_{\mathrm{x},2,1}[P_2]\theta_1 - k_{\mathrm{x},1,2}[P_1]\theta_2. \tag{6.11}$$

This two-component mechanism can be simulated for the reaction scheme with sensible values of the kinetic rate constants presented in Fig. 6.10.

Here the first and second equations show a near-thermal binding energy for the association of protein P_1 with the surface -1.7 kJ mol^{-1}, P_2 has a stronger association of -30 kJ mol^{-1} about half the strength of an antibody–antigen interaction and a displacement reaction with P_2 changing places with P_1 with a rate constant of 10^2 M^{-1} s^{-1}. The channel responses have been simulated and are shown in Fig. 6.11.

Since the formal description of the Vroman effect and competition of specific vs. non-specific adsorption is the same, compare Figs. 6.5 and 6.10, the competitive binding for the limited number of specific ligand-functionalised surface sites can also be described using a similar approach:

– There are specific binding sites on the surface
– The blocking step has been performed to minimise re-arrangement reactions, $k_{\mathrm{u}} \approx 0$
– The affinity of analyte P_i to the surface largely defined by specific interaction when $i = s$: such as $K_{\mathrm{a,s}} \gg K_{\mathrm{a},i\neq s}$ and $k_{\mathrm{x,s},i} \gg k_{\mathrm{x},i\neq s,\mathrm{s}}$

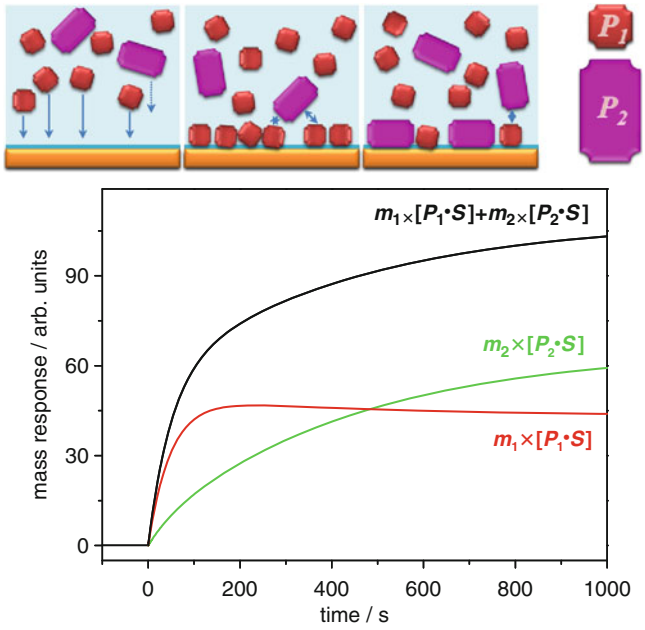

Fig. 6.11 The analyte contains two proteins of masses $m_2 = 5$ mL, k_a and k_d are taken to be proportional to the masses and the concentrations of the two proteins are $[P_1] = 100[P_2]$ (roughly corresponding to albumin and fibrinogen content of a serum sample). *Black trace* is the sensor response which is a sum of the *green trace*, heavy protein binding and *red trace*, light protein binding

again, (6.9) reduces to:

$$\frac{\mathrm{d}\theta_{\mathrm{L,s}}}{\mathrm{d}t} = k_{\mathrm{a,L,s}}[P_{\mathrm{s}}](1 - \theta_{\mathrm{L,s}} - \theta_{\mathrm{L,n}}) - k_{\mathrm{d,L,s}}\theta_{\mathrm{L,s}} + \sum_{i \neq s} k_{\mathrm{x,L,si}}[P_{\mathrm{s}}]\theta_{\mathrm{L},i}, \tag{6.12}$$

$$\begin{aligned}\frac{\mathrm{d}\theta_{\mathrm{L,n}}}{\mathrm{d}t} &= \sum_{i \neq s} \frac{\mathrm{d}\theta_{\mathrm{L},i}}{\mathrm{d}t} \\ &= \sum_{i \neq s} k_{\mathrm{a,L},i}[P_i](1 - \theta_{\mathrm{L,s}} - \theta_{\mathrm{L,n}}) - \sum_{i \neq s} k_{\mathrm{d,L},i}\theta_{\mathrm{L},i} - \sum_{i \neq s} k_{x,\mathrm{L,si}}[P_{\mathrm{s}}]\theta_{\mathrm{L},i}.\end{aligned} \tag{6.13}$$

Extracting the specific part of the signal by reference subtraction can be done only with respect to the surface which is free of specific ligand. This implies that (1) the reference is *always* subject to the variation of affinities of analyte components to the ligands used, and (2) the reference should ideally be functionalized with a ligand similar in properties to the ligand in the specific channel, but lacking the specific activity towards the target molecules. If such a reference can be created than, for this channel featuring ligand L',

$$\frac{\mathrm{d}\theta_{\mathrm{L}',n}}{\mathrm{d}t} = \sum_i \frac{\mathrm{d}\theta_{\mathrm{L}',i}}{\mathrm{d}t} = \sum_i k_{\mathrm{a,L}',i}[P_i](1-\theta_{\mathrm{L}',n}) - \sum_i k_{\mathrm{d,L}',i}\theta_{\mathrm{L}',i}. \tag{6.14}$$

If the degree of ligand functionalisation is γ, and $k_{\mathrm{L}} \approx k_{\mathrm{L}'}$, whilst $\theta_{\mathrm{L,s}}$ is small, then reference subtraction gives,

$$\begin{aligned}
&\text{test channel: } \frac{\mathrm{d}\theta}{\mathrm{d}t} = \gamma\left(\frac{\mathrm{d}\theta_{\mathrm{L,s}}}{\mathrm{d}t} + \frac{\mathrm{d}\theta_{\mathrm{L,n}}}{\mathrm{d}t}\right) + (1-\gamma)\frac{\mathrm{d}\theta_{\mathrm{f}}}{\mathrm{d}t} \\
&\text{reference: } \frac{\mathrm{d}\theta}{\mathrm{d}t} = \gamma\left(\frac{\mathrm{d}\theta_{\mathrm{L}',n}}{\mathrm{d}t}\right) + (1-\gamma)\frac{\mathrm{d}\theta_{\mathrm{f}}}{\mathrm{d}t} \\
&\Delta\text{channel} = \text{ test - reference : } \frac{\mathrm{d}\theta_{\mathrm{L}}}{\mathrm{d}t} = \gamma\left(\frac{\mathrm{d}\theta_{\mathrm{L,s}}}{\mathrm{d}t} + \frac{\mathrm{d}\theta_{\mathrm{L,n}}}{\mathrm{d}t} - \frac{\mathrm{d}\theta_{\mathrm{L}',n}}{\mathrm{d}t}\right) \\
&\approx \gamma\left[k_{\mathrm{a,L,s}}[P_{\mathrm{s}}](1-\theta_{\mathrm{L,s}}-\theta_{\mathrm{L,n}}) - k_{\mathrm{d,L,s}}\theta_{\mathrm{L,s}} + \sum_{i\neq s} k_{\mathrm{x,L,si}}[P_{\mathrm{s}}]\theta_{\mathrm{L},i}\right]_{\theta_{\mathrm{s}}} \\
&\quad - \gamma\left[k_{\mathrm{a,L}',\mathrm{s}}[P_{\mathrm{s}}](1-\theta_{\mathrm{L}',\mathrm{s}}-\theta_{\mathrm{L}',\mathrm{n}}) - k_{\mathrm{d,L}',\mathrm{s}}\theta_{\mathrm{L}',\mathrm{s}} + \sum_{i\neq s} k_{\mathrm{x,L,si}}[P_{\mathrm{s}}]\theta_{\mathrm{L},i}\right]_{\theta_{\mathrm{n}}}
\end{aligned} \tag{6.15}$$

Taking into account the fact that the SPR signal is proportional to the molecular mass of the adsorbed species, m:

$$\begin{aligned}
&\text{SPR responce: } \frac{\mathrm{d}\vartheta}{\mathrm{d}t} = m\frac{\mathrm{d}\theta}{\mathrm{d}t} \\
&\Delta\text{SPR channel} \approx \gamma\begin{pmatrix} m_{\mathrm{s}}(k_{\mathrm{a,L,s}} - k_{\mathrm{a,L}',\mathrm{s}})[P_{\mathrm{s}}](1-\theta_{\mathrm{L,s}}-\theta_{\mathrm{L,n}}) \\ - m_{\mathrm{s}}(k_{\mathrm{d,L,s}}\theta_{\mathrm{L,s}} - k_{\mathrm{d,L}',\mathrm{s}}\theta_{\mathrm{L}',\mathrm{s}}) + [P_{\mathrm{s}}]\sum_{i\neq s} k_{\mathrm{x,L,si}}(m_{\mathrm{s}}\theta_{\mathrm{L},i} - m_i\theta_{\mathrm{L},i}) \end{pmatrix}
\end{aligned} \tag{6.16}$$

and that the specific ligand L possesses a much higher affinity towards P_{s} than ligand L':

$$\begin{aligned}
&k_{\mathrm{a,L}',\mathrm{s}} \ll k_{\mathrm{a,L,s}} \quad \text{and} \quad \theta_{\mathrm{L}',\mathrm{s}} \ll \theta_{\mathrm{L,s}} \quad \text{therefore} \\
&\Delta\text{SPR channel} \approx \gamma\begin{pmatrix} m_{\mathrm{s}}k_{\mathrm{a,L,s}}[P_{\mathrm{s}}](1-\theta_{\mathrm{L,s}}-\theta_{\mathrm{L,n}}) - m_{\mathrm{s}}k_{\mathrm{d,L,s}}\theta_{\mathrm{L,s}} \\ + [P_{\mathrm{s}}]\sum_{i\neq s} k_{\mathrm{x,L,si}}\theta_{\mathrm{L},i}(m_{\mathrm{s}} - m_i) \end{pmatrix}.
\end{aligned} \tag{6.17}$$

The strength of the measured SPR signal benefits from the larger γ, this is different from the case of the single-analyte system since in complex media the specific analyte is generally a minor component and non-specific binding is mainly due to adsorption of other, non-target but more abundant biomolecules present in the sample.

A qualitative inspection of (6.17) shows that after initial fast loading of the surface with non-specific components of the complex sample, which may be corrected for by suitable referencing, the specific binding is described with the same k_a and k_d as was the case for the single-analyte system (section "Binding of Target Molecules to the Sensor Surface by Means Other Than the Desired Ligand"), with the important difference that the fraction of the free surface sites is diminished due to the non-specific load and therefore the observed transient response will be both slower and smaller in amplitude (section "Loosely Bound Surface Competition Reactions: Blood Serum Contamination", Fig. 6.7). Additionally, if exchange reactions are viable, their contribution can be both positive and negative depending on the mass difference of the participating biomolecules. The effect on the response curves, Fig. 6.6, is the same as was illustrated for the Vroman effect in Fig. 6.11.

Array-Based Plasmonic Sensor Advantages

The analysis of target analytes in complex media needs to be performed against the background of contaminating proteins that may be present in the medium and which induce an array of exchange and displacement reactions at the sensor surface. If the label-free immuno-kinetic assay is to be successful, sufficient simultaneous measurements must be performed to characterise the complex medium from which the concentration of the target species can be extracted with confidence to give a clinically useful sensitivity and accuracy. The interaction of proteins binding to the surface covers a Gibbs free energy spectrum from -2.5 kJ mol^{-1}, thermal energy, and -75 kJ mol^{-1} for a strongly bound interaction such as biotin-streptavidin. The energy scale is the same as that controlling all protein–protein interactions in biological systems. The energy scale is defined by the ratio of the dissociation rate constants to the association rate constants leading to protein interactions that quickly foul the sensor surface but leave rapidly at the thermal exchange rate, and proteins that foul surface and remain associated such as the HSA in the model sera experiments. Ascending the scale, specific binding at 50 kJ mol^{-1} such as for antibodies have favourable association and dissociation rate constants and remain attached at the surface. The interaction energy therefore confers a kinetic discrimination between target and background interactions.

Kinetic discrimination is regulated by the association and dissociation rates that control the level of disruption to the biosensing event with loosely bound molecules leaving rapidly no matter how large the rate of association from the large concentration. However, only knowledge of the K_D, (k_d/k_a), for all of the analyte components will identify the sources of significant interference, for example as discussed earlier in section "Loosely Bound Surface Competition Reactions: Blood Serum Contamination", near physiological amount of HSA has demonstrated threefold degradation effect on derived association rate constants for aBSA–BSA interaction.

The design of control spots on the arrays will need to ensure a number of spots with different protein–protein interaction energies from which the effect of multiple contaminants may be determined. The simplest control is a simple measurement of the bulk refractive index, as has been demonstrated, but this may be extended to look at non-specific binding explicitly. Antibodies and antigens not present in the medium may provide an assessment of the affect of non-specific binding to the antibody detection ligand. Hence a series of simultaneous measurements targeted from an array of control spots will provide multiple assessments of the composition, thereby allowing a global simulation model to be performed. The simultaneous measurements may allow details of the surface mechanisms to be extracted either directly or empirically to produce an accurate and sensitive determination of an analyte from solution.

Conclusions

We have looked at some of the challenges and fundamental limits to the measurement of analytes in complex media using a label-free detection platform based on the optical properties of surface plasmons. Both types of SPR sensors, propagating-SPR (PSPR) and localised-SPR (LSPR), act as mass sensors which are specific to target analytes only when functionalised with a biospecific molecule such as an antibody. However, such interactions are in general not infinitely specific so that the kinetic response is always the convolution of a number of competing reactions at the sensor surface. The nanoparticles used in the LSPR approach however are uniquely sensitive to the assay region within ~20 nm of the particle surface—a clear advantage over the PSPR that employs a continuous gold surface (~200 nm). The generic problem of non-specific binding, equally important in both PSPR and LSPR experimental techniques, particularly when complex biological samples are tested, has been characterised by the ratio of the dissociation and association rate constants, K_D, which defines the spectrum of non-specific interactions. Loosely bound proteins foul the surface but are quickly removed whereas more strongly bound proteins will permanently foul the sensor surface. Multiple analyte measurements however may allow the effect of complex media components to be assessed globally so as to allow the concentration of a given target analyte to be determined accurately. The use of such controls is essential if a particle plasmon platform is to be useful at the point-of-care where natural variations in the blood composition will cause variations in the accuracy of the assays. The challenges for plasmonic arrays in biosensing are:

- Well-designed target assays, preferentially with high affinity ligands.
- Well-designed control spots to profile complex media to preserve the immunokinetic assay.
- Sensitive and accurate determination of target analytes at clinically relevant concentrations.

Successfully addressing these challenges in the context of targeting well chosen clinical applications may provide a route to application of these technologies.

Acknowledgements The work was supported by the RCUK, Basic Technology Grant, EP/C52389X/1 and the Royal Society.

References

1. Zlotta AR, Djavan B, Marberger M, Schulman CC. Prostate specific antigen density of the transition zone: a new effective parameter for prostate cancer prediction. J Urol. 1997;157:1315–21.
2. Frank R, Hargreaves R. Clinical biomarkers in drug discovery and development. Nat Rev Drug Discov. 2003;2:566–80.
3. Giljohann DA, Mirkin CA. Drivers of biodiagnostic development. Nature. 2009;462:461–4.
4. Li Y, Lee HJ, Corn RM. Detection of protein biomarkers using RNA aptamer microarrays and enzymatically amplified surface plasmon resonance imaging. Anal Chem. 2007;79:1082–8.
5. Seibert V, Ebert MPA, Buschmann T. Advances in clinical cancer proteomics: SELDI-ToF-mass spectrometry and biomarker discovery. Brief Funct Genomic Proteomic. 2005;4:16–26.
6. Koomen JM, Li D, Xiao L-C, Liu TC, Coombes KR, Abbruzzese J, et al. Direct tandem mass spectrometry reveals limitations in protein profiling experiments for plasma biomarker discovery. J Proteome Res. 2005;4:972–81.
7. Yu X, Schneiderhan-Marra N, Joos TO. Protein microarrays for personalized medicine. Clin Chem. 2010;56:376–87.
8. Lee HJ, Wark AW, Corn RM. Microarray methods for protein biomarker detection. Analyst. 2008;133:975–83.
9. Anker JN, Hall WP, Lyandres O, Shah NC, Zhao J, Van Duyne RP. Biosensing with plasmonic nanosensors. Nat Mater. 2008;7:442–53.
10. Homola J. Surface plasmon resonance sensors for detection of chemical and biological species. Chem Rev. 2008;108:462–93.
11. Liedberg B, Nylander C, Lundstrom I. Surface plasmon resonance for gas detection and biosensing. Sens Actuators. 1983;4:299–304.
12. Yonzon CR, Jeoung E, Zou S, Schatz GC, Mrksich M, VanDuyne RP. A comparative analysis of localized and propagating surface plasmon resonance sensors: the binding of concanavalin A to a monosaccharide functionalized self-assembled monolayer. J Am Chem Soc. 2004;126:12669–76.
13. Zhao J, Zhang X, Yonzon CR, Haes AJ, Van Duyne RP. Localized surface plasmon resonance biosensors. Nanomedicine. 2006;1:219–28.
14. Barnes WL. Surface plasmon–polariton length scales: a route to sub-wavelength optics. J Opt A Pure Appl Opt. 2006;8:S87–93.
15. Olkhov RV, Shaw AM. Label-free antibody-antigen binding detection by optical sensor array based on surface-synthesized gold nanoparticles. Biosens Bioelectron. 2008;23:1298–302.
16. Murray AW, Suckling JR, Barnes WL. Overlayers on silver nanotriangles: field confinement and spectral position of localized surface plasmon resonances. Nano Lett. 2006;6:1772–7.
17. Haes AJ, Van Duyne RP. A unified view of propagating and localized surface plasmon resonance biosensors. Anal Bioanal Chem. 2004;379:920–30.
18. Svedendahl M, Chen S, Dmitriev A, Käll M. Refractometric sensing using propagating versus localized surface plasmons: a direct comparison. Nano Lett. 2009;9:4428–33.
19. Jensen TR, Duval ML, Kelly KL, Lazarides AA, Schatz GC, Van Duyne RP. Nanosphere lithography: effect of the external dielectric medium on the surface plasmon resonance spectrum of a periodic array of silver nanoparticles. J Phys Chem B. 1999;103:9846–53.

20. Homola J, Vaisocherová H, Dostálek J, Piliarik M. Multi-analyte surface plasmon resonance biosensing. Methods. 2005;37:26–36.
21. Hooper IR, Sambles JR, Pitter MC, Somekh MG. Phase sensitive array detection with polarisation modulated differential sensing. Sens Actuators B Chem. 2006;119:651–5.
22. Nikitin PI, Grigorenko AN, Beloglazov AA, Valeiko MV, Savchuk AI, Savchuk OA, et al. Surface plasmon resonance interferometry for micro-array biosensing. Sens Actuators A Phys. 2000;85:189–93.
23. Scarano S, Mascini M, Turner APF, Minunni M. Surface plasmon resonance imaging for affinity-based biosensors. Biosens Bioelectron. 2010;25:957–66.
24. Beusink JB, Lokate AMC, Besselink GAJ, Pruijn GJM, Schasfoort RBM. Angle-scanning SPR imaging for detection of biomolecular interactions on microarrays. Biosens Bioelectron. 2008;23:839–44.
25. Lausted C, Hu ZY, Hood L. Quantitative serum proteomics from surface plasmon resonance imaging. Mol Cell Proteomics. 2008;7:2464–74.
26. Edwards PR, Gill A, Pollardknight DV, Hoare M, Buckle PE, Lowe PA, et al. Kinetics of protein-protein interactions at the surface of an optical biosensor. Anal Biochem. 1995;231:210–7.
27. Su X, Wu Y-J, Knoll W. Comparison of surface plasmon resonance spectroscopy and quartz crystal microbalance techniques for studying DNA assembly and hybridization. Biosens Bioelectron. 2005;21:719–26.
28. Rickert J, Brecht A, Göpel W. Quartz crystal microbalances for quantitative biosensing and characterizing protein multilayers. Biosens Bioelectron. 1997;12:567–75.
29. Vörös J. The density and refractive index of adsorbing protein layers. Biophys J. 2004;87:553–61.
30. Anderson NL, Anderson NG. The human plasma proteome—history, character, and diagnostic prospects. Mol Cell Proteomics. 2002;1:845–67.
31. Myszka DG. Kinetic analysis of macromolecular interactions using surface plasmon resonance biosensors. Curr Opin Biotechnol. 1997;8:50–7.
32. Masson J-F, Battaglia T, Cramer J, Beaudoin S, Sierks M, Booksh K. Reduction of nonspecific protein binding on surface plasmon resonance biosensors. Anal Bioanal Chem. 2006;386:1951–9.
33. Brink G, Sigl H, Sackmann E. Near-infrared surface plasmon resonance in silicon-based sensor: new opportunities in sensitive detection of biomolecules from aqueous solutions by applying microstep for discriminating specific and non-specific binding. Sens Actuators B Chem. 1995;25:756–61.
34. van Vuuren BJ, Read T, Olkhov RV, Shaw AM. Human serum albumin interference on plasmon-based immuno-kinetic assay for antibody screening in model blood sera. Anal Biochem. 2010;405:114–20.
35. Sadana A, Chen Z. Influence of non-specific binding on antigen-antibody binding kinetics for biosensor applications. Biosens Bioelectron. 1996;11:17–33.
36. Atkins P, de Paula J. Physical chemistry for the life sciences. Oxford: Oxford University Press; 2005.
37. Matveeva EG, Gryczynski Z, Malicka J, Lukomska J, Makowiec S, Berndt KW, et al. Directional surface plasmon-coupled emission: application for an immunoassay in whole blood. Anal Biochem. 2005;344:161–7.
38. Garcia BH, Goodman RM. Use of surface plasmon resonance imaging to study viral RNA: protein interactions. J Virol Methods. 2008;147:18–25.
39. Wikman M, Steffen A-C, Gunneriusson E, Tolmachev V, Adams GP, Carlsson J, et al. Selection and characterization of HER2/neu-binding affibody ligands. Protein Eng Des Sel. 2004;17:455–62.
40. Karlsson R, Fält A. Experimental design for kinetic analysis of protein-protein interactions with surface plasmon resonance biosensors. J Immunol Methods. 1997;200:121–33.

41. Slack Steven M, Horbett Thomas A. The Vroman effect, proteins at interfaces II. Washington, DC: American Chemical Society; 1995. p. 112–28.
42. Choi S, Yang Y, Chae J. Surface plasmon resonance protein sensor using Vroman effect. Biosens Bioelectron. 2008;24:893–9.
43. Rich RL, Papalia GA, Flynn PJ, Furneisen J, Quinn J, Klein JS, et al. A global benchmark study using affinity-based biosensors. Anal Biochem. 2009;386:194–216.
44. Svitel J, Balbo A, Mariuzza RA, Gonzales NR, Schuck P. Combined affinity and rate constant distributions of ligand populations from experimental surface binding kinetics and equilibria. Biophys J. 2003;84:4062–77.
45. Olkhov RV, Fowke JD, Shaw AM. Whole serum BSA antibody screening using a label-free biophotonic nanoparticle array. Anal Biochem. 2009;385:234–41.
46. Olkhov RV, Shaw AM. Quantitative label-free screening for antibodies using scattering biophotonic microarray imaging. Anal Biochem. 2010;396:30–5.

Chapter 7
Laser Manipulation of Plasmonic Nanoparticles for SERS and Sensing

Lianming Tong and Mikael Käll

Abstract Optical tweezers have found widespread use in studies of biological macromolecules and in manipulation of microscopic objects, including biological cells and a variety of dielectric particles. But rapid progress over the last decade has demonstrated that optical tweezers also can be used as a powerful method for manipulation and control of plasmonic metal nanostructures. Here, we review our recent results in this area with a focus on the interaction between nanoparticles confined in an optical trap and applications in surface-enhanced Raman scattering spectroscopy.

Introduction

Optical tweezers are well established as a method for trapping and manipulation of dielectric objects on the micron scale [1–4]. However, since the pioneering work of Svoboda and Block [5], increasing attention has been devoted to laser trapping of metal nanoparticles. Noble metal nanoparticles are of course of particular interest because of their unique optical response in the visible to near-infrared wavelength range originating from the localized surface plasmon resonance (LSPR) phenomenon [5–7]. In the field of plasmonic sensing, optical tweezing has shown promising potential in the context of surface-enhanced spectroscopy based molecular detection [8–11]. A particularly important aspect of this application concerns near-field optical forces, which to a large extent determines the interaction between metal nanoparticles in an optical trap [12–14]. Near-field optical forces can, for example, lead to dimerization of metal nanoparticles and a concomitant large increase in the SERS efficiency [8]. However, the combination of optical manipulation

L. Tong • M. Käll (✉)
Department of Applied Physics, Chalmers University of Technology,
Göteborg 41296, Sweden
e-mail: mikael.kall@chalmers.se

A. Dmitriev (ed.), *Nanoplasmonic Sensors*, Integrated Analytical Systems,
DOI 10.1007/978-1-4614-3933-2_7,

and plasmonics offer many more avenues for novel sensing methodologies. One promising research direction, explored by several groups, focuses on the possibility of using surface supported plasmonic nanostructures to generate optical near-field distributions that can localize dielectric or metal objects with high spatial precision through nano-optical gradient forces [12, 15–17]. Other possibilities arise from the fact that plasmonic nanostructures in solution can be aligned and even rotated using polarization dependent optical forces [18–22] and from the observation that optical tweezers offer an opportunity for "sensing" the interaction potentials between individual colloidal metal nanoparticles in solution [22]. This chapter summarizes our recent research in the field of optical trapping and manipulation of metal nanoparticles for SERS and sensing [6, 8–10, 12, 14, 19, 22].

Experimental Considerations

All experiments discussed here utilize a so-called laser tweezers, that is a single laser beam with a Gaussian intensity profile that is focused to a diffraction limited spot by a high numerical aperture (NA) microscope objective [23]. It is important that the beam is expanded to cover the full back-aperture of the objective, implying that the full NA is utilized, since the peripheral rays of the beam contribute most to the optical gradient force.

Optical trapping of single metal nanoparticles has been demonstrated in both two and three dimensions using focused NIR beams [5–7]. However, due to their reflecting properties and small size, trapping of nanoscale metal structures is in general much more experimentally demanding than trapping of large dielectric objects. The most critical aspect typically concerns the balance between the gradient force and the radiation pressure in the direction along the optical axis [9]. In most of the experiments discussed here, we have circumvented this problem by blocking movement in this direction using a cover glass, i.e., we trap in two dimensions only. This approach has the added advantage that it makes it much simpler to combine laser tweezing with dark-field (DF) spectroscopy, which is the most convenient method for probing the plasmonic properties of isolated metal nanostructures.

A typical setup based on an inverted microscope is schemed in Fig. 7.1. The polarization status of the trapping laser can be tuned using retardation plates before it reaches the objective. Polarizers are also often used to select certain polarization component of the white light for bright- or dark-field illumination. The elastic/inelastic scattering from the particles or molecules is recorded by cameras for optical imaging and directed to spectrometers through free-space or fiber-coupling for spectral characterization.

The laser used for the optical tweezers can also conveniently be used to excite Raman scattering. However, many Raman studies require resonant excitation using visible or even ultraviolet wavelengths, while optical tweezing is best performed using near-infrared light to minimize laser induced heating of the aqueous medium or the sample itself. Two lasers can then be used, one for Raman excitation and one

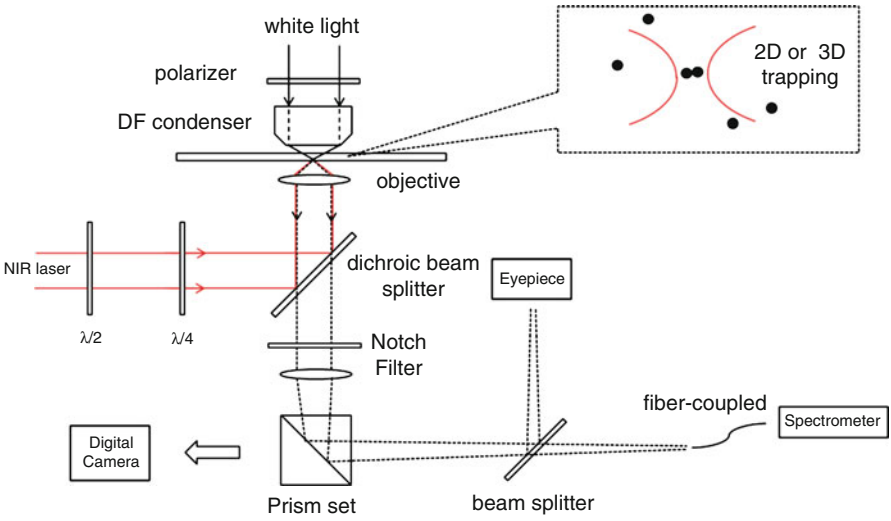

Fig. 7.1 Scheme of a typical experimental setup built around an inverted microscope. The NIR laser is reflected to the objective by a short pass dichroic beam splitter. A notch filter is used to remove the reflected laser light before the scattered white light reaches the detectors. Retarder plates can be used to control the polarization properties of the laser beam

for optical trapping, which means that the setup has to be equipped with suitable filters or dichroic mirrors in order to separate the tweezers and Raman light paths. Some experiments may even require the use of two separate microscope objectives facing each other, one for Raman microscopy and one for laser tweezing [24]. In any case, it is important to remember that a working Raman tweezers based on separate laser beams requires perfect overlap between the respective laser foci, which for widely separate excitation and tweezing wavelengths can be complicated due to, for example, chromatic aberrations.

Results and Discussion

Optical Characterization of Optically Trapped Nanoparticles

Figure 7.2 shows an example of how optical tweezers can be used to characterize individual nanoparticles in solution, in this case a silver colloid synthesized according to the Lee and Meisel protocol [6]. The ensemble extinction spectrum is strongly inhomogeneously broadened and DF and SEM images of surface-immobilized particles reveal a large heterogeneity in terms of color, size, and shape. Using a setup similar to the one shown in Fig. 7.1, individual diffusing particles could easily be trapped in 2D using a focused 830 nm laser beam.

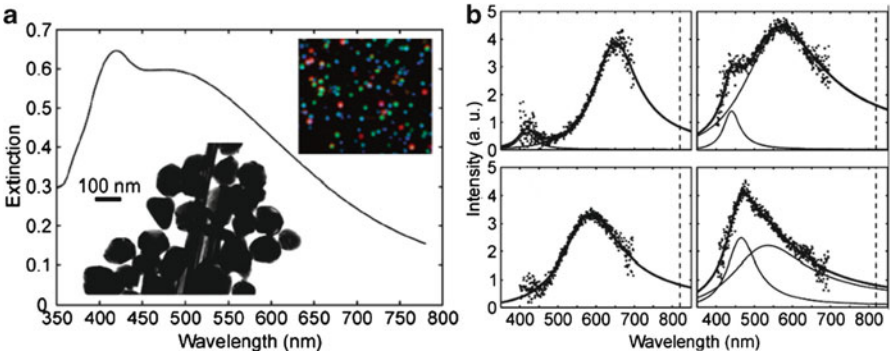

Fig. 7.2 (**a**) Extinction spectrum of a heterogeneous silver colloid solution with DF and SEM images shown as *insets*. (**b**) DF elastic scattering spectra of single trapped particles with corresponding Lorentzian fits (*solid curves*). The *dashed lines* indicate the wavelength of the trapping laser (830 nm)

We used an oil immersion objective with NA tuned to 0.7 to allow for dark-field measurements of elastic scattering spectra of single particles. Examples of such spectra shown in Fig. 7.2b exhibit widely varying LSPR characteristics, as anticipated from the color picture in the inset of Fig. 7.2a.

Alignment and Rotation of Optically Trapped Nanoparticles

The behavior of a metal nanostructure in an optical trap depends on its plasmonic properties, as determined by the particle size, shape, composition and environment, and the wavelength and polarization of the trapping laser [25–28]. A particularly important aspect of this dependence concerns the orientation of the nanostructure within the trap. An elongated metal nanoparticle, such as a nanorod, exhibits different polarizabilities along the long and short axes due to the different spatial confinements of the plasmon oscillations. In a NIR optical trap, gold and silver nanorods tend to self-align with their long axes parallel to the laser polarization to minimize the potential energy, which can be approximated as $U = -\langle P \cdot E \rangle = -1/2 \sum \mathrm{Re}\{\alpha_{ii}\} E_i^2,\ i = x, y, z$, where P is the induced dipole moment, E is the incident electric field and α_{ii} is the polarizability, respectively. If the polarization of the trapping laser is rotated by an angle of β with respect to the long axis of the rod, a torque is induced according to $\tau = |\langle P \cdot E \rangle| = -1/4(\alpha_{\parallel} - \alpha_{\perp}) \sin 2\beta \cdot E^2$ [29], where $\alpha_{\parallel}$ and $\alpha_{\perp}$ are the polarizability components parallel and perpendicular to the long axis of the nanorod, respectively. This torque drives the nanorod to realign parallel to the laser polarization, or to rotate if the linear polarization is rotated [19].

A nanoparticle dimer behaves similar to a nanorod in the sense that the polarizability is higher and the LSPR redshifted for polarization along the "long axis," i.e., along the dimer axis, than in the two perpendicular directions. Figure 7.3 shows DF

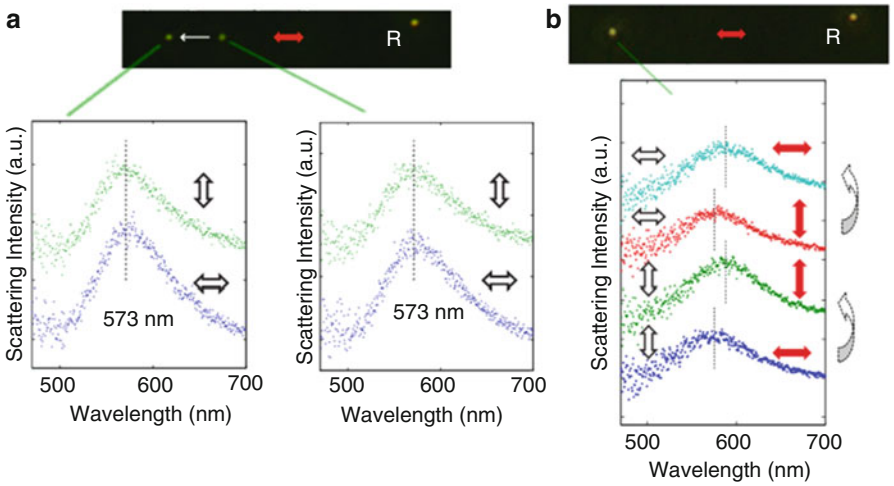

Fig. 7.3 Alignment and rotation of a dimer of gold nanoparticles (GNPs). *Red* and *white arrows* represent the laser polarization and white-light polarization, respectively. (**a**) DF scattering images and spectra of two individual GNPs. The left particle is fixed on the glass slide and the right one is trapped by the NIR beam. The particle marked as "*R*" is used as reference. (**b**) A dimer is created by moving the trapped particle close to the fixed one. The DF spectra show the alignment and rotation of the dimer

scattering images and spectra of two single spherical gold nanoparticles (GNPs) before (Fig. 7.3a) and after (Fig. 7.3b) they are dimerized in an optical trap. As seen in Fig. 7.3a, the isolated GNPs show identical LSPR peaks (~573 nm) at the two perpendicular polarization directions because of their spherical symmetry. However, after dimerization, the particles exhibit a clear polarization anisotropy. In the perpendicular polarization configuration (curve 2 and 4 from the top), for which the white light used for DF spectroscopy is polarized perpendicular to the trapping laser, the dimer shows a peak at ~575 nm, which is very close to the single particle LSPR position. However, the LSPR redshifts to ~588 nm in the parallel configuration (curve 1 and 3). This spectral shift arises due to near-field coupling, or hybridization, between the single particle LSPR's and can only be understood if one assumes that the particles dimerize in the trap and then align parallel to the laser polarization. The figure also illustrates rotation of dimers, as can be seen by comparing curve 1 and 2 (or curve 3 and 4) in Fig. 7.3b, for which the white-light polarization is fixed but the laser polarization is rotated by 90°.

It is worth noting that by continuously rotating the polarization of the trapping laser, elongated nanostructues and particle dimers will rotate in the optical trap [19]. Due to the viscous drag force of the surrounding medium, the long axis of the nanostructure will lag behind the laser polarization. The phase delay can be expected to depend on the surface structure of the trapped object, the viscosity of the medium around it, and the strength of the optical torque, which in turn will depend on the optical properties of the nanostructure. Furthermore, Ag nanowires can be made to

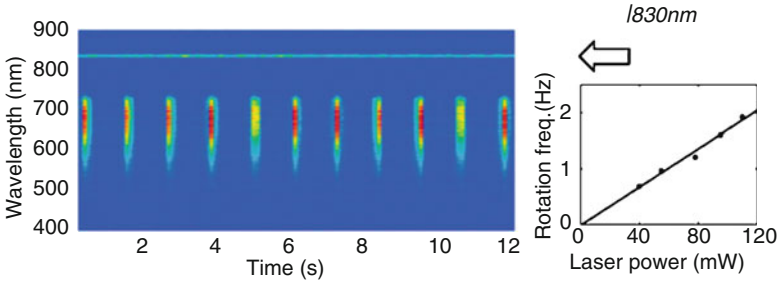

Fig. 7.4 Dark-field scattering from a trapped Ag nanowire rotated by a circularly polarized NIR laser beam. The rotation frequency in this example is ~1 Hz with 60 mW laser power. The power dependence of the rotation frequency is also shown. The wire passes through the measurement spot once per full turn

spin spontaneously if trapped by a circularly polarized laser beam. This effect is due to direct transfer of angular moment from the incident photons absorbed by the trapped nanowire. The rotation frequency is thus expected to be proportional to the laser power, which is indeed the case, see Fig. 7.4 for an example. The direction of rotation can be easily changed by changing the chirality of the circular polarization. Overall, the rotation dynamics of trapped plasmonic nanostructures could potentially be explored for the development of novel sensing modalities, such as nano-viscometers for measurements inside cells or other highly confined volumes.

Interaction Between Two Metal Nanoparticles in an Optical Trap

When two metal nanoparticles are in close vicinity of each other, as in an optical trap due to laser tweezing, their induced electromagnetic fields overlap and hybridize. This leads to drastic spectral changes, strong optical interparticle forces, and field-enhancement effects that can lead to extremely large optical gradient forces [12–14, 30]. As an example of the latter, Fig. 7.5 shows the estimated optical potentials, obtained from Mie theory, acting on a Rhodamine 6G molecule located near silver nanoparticle aggregates [12]. The spatial variation of the optical potential U is shown in units of k_BT ($T = 300$ K) around a three-sphere system ($R = 25$ nm) in water in Fig. 7.5a. The surface-to-surface separation is 1 nm and the aggregate is excited at a collective surface plasmon resonance (760 nm) polarized parallel to the trimer axis. Figure 7.5b shows the wavelength dependence of the optical potential in the gaps of the trimer and a similar dimer. At resonance and for an incident intensity of 10 mW/μm^2, the potential reaches a depth of ~6 k_BT for the trimer and ~4 k_BT for the dimer, which would lead to instantaneous trapping of a R6G molecule that passes through the trapping volume. Firm experimental evidence for optical trapping of molecules in plasmonic "hot spots" is, to the best of our knowledge, still lacking, but several recent works have demonstrated trapping of larger objects, including

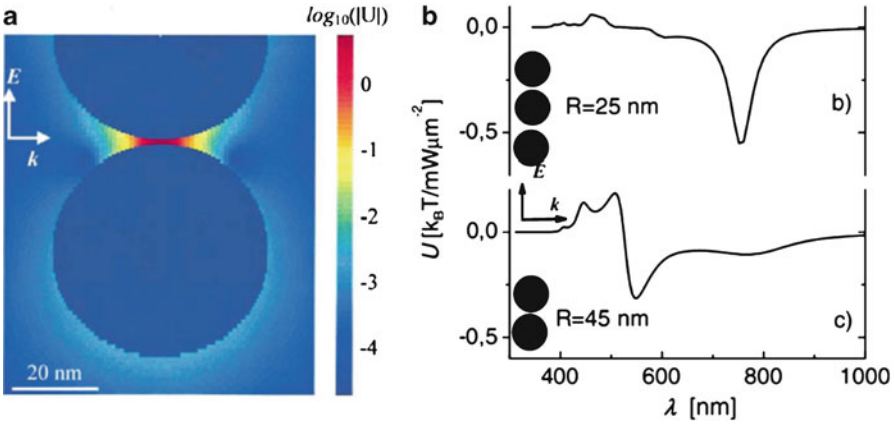

Fig. 7.5 (**a**) Spatial optical potential distribution around the lower half of a linear trimer of silver nanoparticles with 25 nm radius and 1 nm gap distance in water excited at the collective LSPR (760 nm) for a power density of 10 mW/μm^2. (**b**) Incident wavelength dependence of the optical potential at the gaps of a trimer and dimer with incident electric field parallel to the symmetry axes

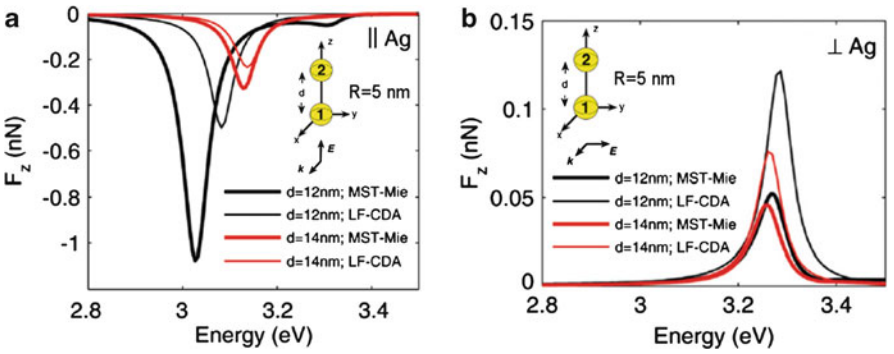

Fig. 7.6 Spectra of the optical force between two identical silver spheres with radii $R = 5$ nm and center-to-center distances $d = 12$ nm (*black curves*) and 14 nm (*red curves*) for an intensity of the incident field of 1 W/μm^2 at parallel (**a**) and perpendicular (**b**) polarization configurations, respectively. The forces are calculated using two different methods: an "exact" calculation based on the Maxwell's stress tensor formalism combined with Mie theory (MST-Mie) and an approximate method based on the Lorentz force and the coupled dipole approximation (LF-CDA)

biological cells, to surface supported nanostructures [15–17]. Another effect of the "plasmonic force" is the spontaneous dimerization and aggregation of nanoparticles in an optical trap. Figure 7.6 shows the calculated optical forces between two silver nanoparticles with radii 5 nm as a function of incident photon energy for the parallel (Fig. 7.6a, attractive force) and perpendicular (Fig. 7.6b, repulsive force) polarization configurations, respectively [14]. The incident power density is 1 W/μm^2. The figures also show simulations based on different calculation methods. Note in particular that the dipole simulations (Lorentz Force Coupled Dipole

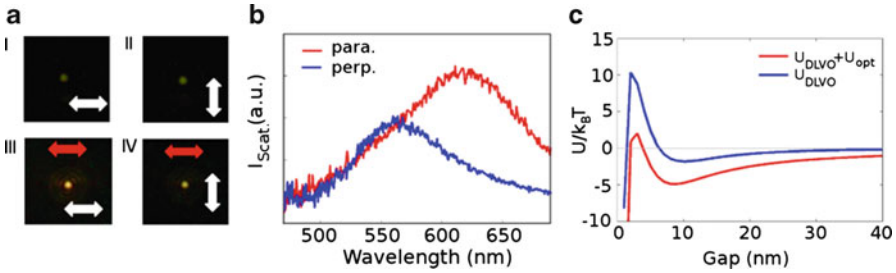

Fig. 7.7 (**a**) DF images of two single GNPs of diameter 80 nm before and after dimerization for white-light polarization (*white arrows*) parallel and perpendicular to the trapping laser polarization (*red arrows*), respectively. (**b**) Corresponding DF scattering spectra. (**c**) Total potentials of the dimer in a colloid with and without optical potential. The NaCl concentration in the colloid solution was 20 mM

Approximation, LF-CDA) underestimate the attractive force for the parallel polarization case and overestimate the repulsive force for the perpendicular configuration due to neglect of multipole couplings, while the Maxwell's Stress Tensor and Mie theory (MST-Mie) calculations are more accurate by including a large number of multipoles ($l_{max} = 13$ in this case). In any case, it is clear that the attractive force is of the order of nano Newton and ~10 times stronger than the repulsive force for small particle separations. These results thus indicate that the attractive optical force dominates strongly and lead to spontaneous dimerization even if there is a small component of the polarization perpendicular to the dimer axis, for example due to rotational Brownian motion.

Studying Colloid Interactions in an Optical Trap

Understanding colloidal stability is hugely important for many novel applications in nanoscience [31–33]. Colloidal particles are typically negatively charged due to the adsorption of ions, thus producing an electrostatic repulsion at close separation [34]. This screened Coulomb interaction depends on the number of surface charges and can be adjusted by changing the ionic strength of the solution. But there is also an attractive force, the van der Waals interaction, which is determined by the material specific Hamaker constant and the size of the particles. The Coulomb repulsion and the van der Waals attraction are combined in the well-known Derjaguin–Landau–Verwey–Overbeek (DLVO) theory of colloidal stability [34, 35]. The behavior of two particles in an optical trap thus depends on the combined effect of the DLVO interaction, the overall optical trapping potential, the aforementioned interparticle optical potentials, and the temperature dependent Brownian motion of the particles.

Figure 7.7a, b illustrates the dimerization of 80 nm diameter GNPs in a NIR (830 nm) optical trap using DF scattering images and spectra, respectively [22]. Compared to the example in Fig. 7.2, the hybridization induced redshift is much

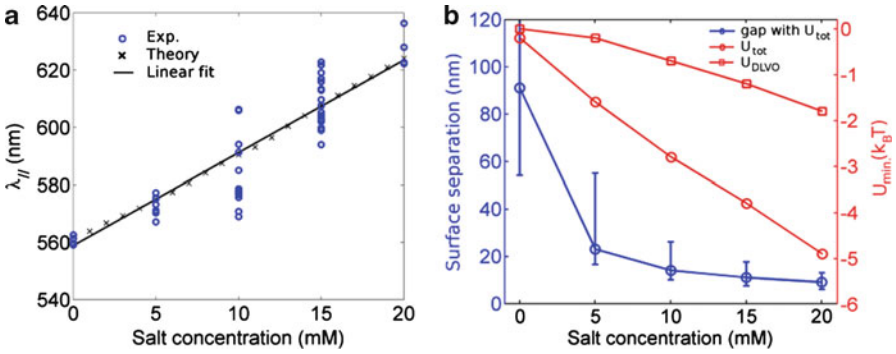

Fig. 7.8 (**a**) Experimental and simulated peak positions $\lambda_{\|}$ as a function of salt concentration. The *solid line* is a linear fit to the simulated results (*black crosses*). (**b**) Simulated surface separations (*blue*) and depth of $U_{\min}$ (*red*) at different salt concentrations. The error bars in the *blue curve* represent the separation ranges corresponding to a variation of 1 k_BT centered at $U_{\min}$ in the potential well. The theoretical simulations were based on a surface potential $\varphi_d = -53$ mV, approximated with the measured zeta-potential of the colloid stock solution, a Hamaker constant $A = 10^{-19}$ J based on AFM and chemical force microscopy studies [37, 38], a Debye screening length approximated as $\kappa \approx 0.3/[\text{NaCl}]$, $T = 300$ K and an effective laser intensity $I \approx 2.2$ mW/μm^2 [22]

more significant (~50 nm) due to a smaller surface separation caused by weaker electrostatic repulsion induced by adding salt (NaCl). Note that the data demonstrate that the dimer aligns parallel to the laser polarization. Figure 7.7c shows the calculated potential curves of the dimer with (red curve) and without (blue curve) the optical potential added, respectively. The dominant features are a deep primary minimum at near-zero separation and a potential barrier that prevents spontaneous permanent aggregation. There is also a shallow secondary minimum at ~15 nm separation in the absence of an optical potential. For some colloids and ionic strengths, this secondary minimum may result in spontaneous aggregation or flocculation [36], but here the depth is ~1 k_BT and not enough to induce stable dimerization in the presence of thermal Brownian motion. Consequently, the DLVO potential curve indicates that such a colloid should be stable against aggregation up to a salt concentration of at least 20 mM. However, as illustrated by the red curve in Fig. 7.7c, the secondary minimum deepens dramatically if the laser induced attractive optical potential is added. For a laser power of only 2 mW/μm^2 at $\lambda = 830$ nm, a potential well depth of ~5 k_BT at ~9 nm separation was obtained. This leads to stable dimerization and explains the significant redshift and strong plasmon hybridization seen in Fig. 7.7b.

Adding salt to a colloid solution leads to an increased screening of the surface charges through an accumulation of counter ions on the particle surfaces and within their immediate surroundings, the so-called electrical double layer [34]. Consequently, the electrostatic repulsion decreases for increasing salt concentration and the position of the secondary potential minimum seen in Fig. 7.7c should move towards smaller surface separations. This would in turn result in an increased spectral redshift. As shown in Fig. 7.8a, this is indeed the case: the experimental peak

positions (circles) of the longitudinal plasmon mode of a number of individual GNP dimers rapidly moves to the red for increasing NaCl concentrations. The perpendicular plasmon resonance, on the other hand, remains at the single particle resonance position (not shown).

As discussed above, the total interparticle potential affecting a trapped pair of particles can be approximated as $U_{\text{tot}} = U_c + U_{vdW} + U_{\text{opt}}$, where the first two terms constitute the DLVO potential and the third is the optical potential. The potentials yield a normalized probability distribution $(d) \propto \mathrm{e}^{-U_{\text{tot}}(d)/k_{\text{B}}T}$, describing the time-averaged probability of encountering a certain separation distance at temperature T. The corresponding dimer spectrum is then obtained as $S = \sum P(d)S(d)$, where $S(d)$ is the scattering spectrum for a specific separation computed from Mie theory and the sum runs over a reasonable range of separations. In this way, the theoretical peak positions can be obtained at different salt concentrations, as shown by the crosses in Fig. 7.8a. An approximately linear redshift in $\lambda_{\|}$ vs. [NaCl] is obtained in excellent agreement with the experimental results. The minimum expected separation between the two particles, as well as the depth of the secondary potential minimum, is also shown in Fig. 7.8b.

It is important to point out the considerable variation in redshift between different particle pairs measured under identical external conditions. The variation is considerably larger than the variance in λ_0 or $\lambda_{\perp}$ and indicates that the particle interaction is affected by slight differences in shape and surface properties of the individual GNPs. For example, if one translates the $\lambda_{\|}$ variation for [NaCl] = 15 mM to surface potential, one obtains values between −47 and −65 mV. This indicates that the methodology described provides a valuable tool for characterizing nanoparticle heterogeneities that are not accessible through ensemble-averaged measurements.

Optically Trapped Nanoparticle Dimers for SERS

The interparticle forces between trapped metal nanoparticles discussed above result in aggregation and create SERS "hotspots," i.e., particle junctions with strongly enhanced local fields. The dimerization of two isolated silver nanoparticles has been shown to produce high enough field enhancement for efficient SERS detection [9]. An example is shown in Fig. 7.9. In these experiments, a NIR laser (λ = 830 nm) was used for trapping while a separate laser beam (λ = 514.5 nm) was used for Raman excitation. Thiophenol (TP) molecules were chemically bound to the surface of the silver nanoparticles (radius 20 nm) as Raman probes. As shown in Fig. 7.9, a single silver nanoparticle immobilized on a glass slide or trapped by the focused NIR laser can be identified through dark-field imaging as a bluish spot, but no SERS intensity is detected (top and middle panels of Fig. 7.9a). However, a significant SERS signal appears when two single particles are paired up into a dimer (bottom panel of Fig. 7.9a). Figure 7.9b shows the calculated optical potential experienced by a diffusing silver nanoparticle in a Gaussian laser focus that overlaps with an immobilized single silver particle, thus simulating the experiment. It is clear that the mobile particle experience a deep potential minimum

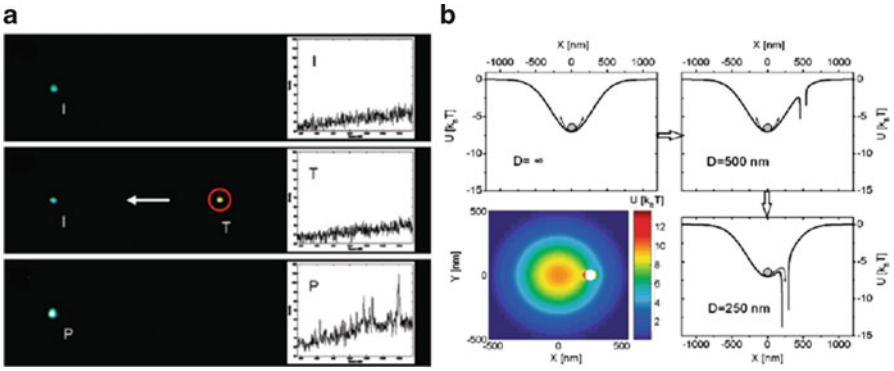

Fig. 7.9 (**a**) DF images and corresponding SERS spectra before and after dimerization of two silver nanoparticles ($R = 20$ nm). (**b**) Simulated optical potential under 830 nm laser irradiation experienced by a trapped silver nanoparticle with different separations to an immobilized one

when it approaches the immobilized particle, thus enabling spontaneous optical dimerization and the formation of an associated SERS "hotspots." It is likely that dimerization in the actual experiment is facilitated by the chemisorbed thiolphenol molecules, which can be expected to decrease the electrostatic repulsion between the particles even in the absence additional salt. As will be shown below, a higher SERS signal is generally observed for larger particle aggregates. The work by Tanaka et al. [39] is interesting in this respect. They showed that multiple silver nanoparticles simultaneously trapped by a NIR laser beam also tend to align parallel to the linear polarization and exhibit a pronounced SERS signal at a very low concentration (10^{-14} M) of the probe molecule pseudoisocyanine (PIC).

SERS Optical Tweezers Integrated with Microfluidics

The potential of optical tweezers for SERS sensing is further expanded by integration with microfluidics [10]. Using a microfluidic circuit, two separate input flows containing the metal colloid and the analyte solution, respectively, can be injected and allowed to mix in a common flow pipe before entering the microfluidic channel. The metal nanoparticles, pre-incubated with the molecules to be detected, can then be optically trapped and aggregated in the flow channel, resulting in an intense SERS signals. Figure 7.10a shows DF images of a growing aggregate created by NIR optical tweezing inside a microfluidic channel. The corresponding increase in SERS spectral intensity for two different probe molecules, thiophenol (TP) and 2-naphthalenethiol (2-NT) excited at 514 nm, are shown in Fig. 7.10b. Furthermore, the analyte flow through the microfluidic channel is easily interchangeable, enabling consecutive detection of a series of species. For example, alternate SERS spectra of TP and 2-NT can be obtained from the optically aggregated Ag nanoparticles in the microfluidic channel if the two solutions are injected to one of the input channels sequentially [10].

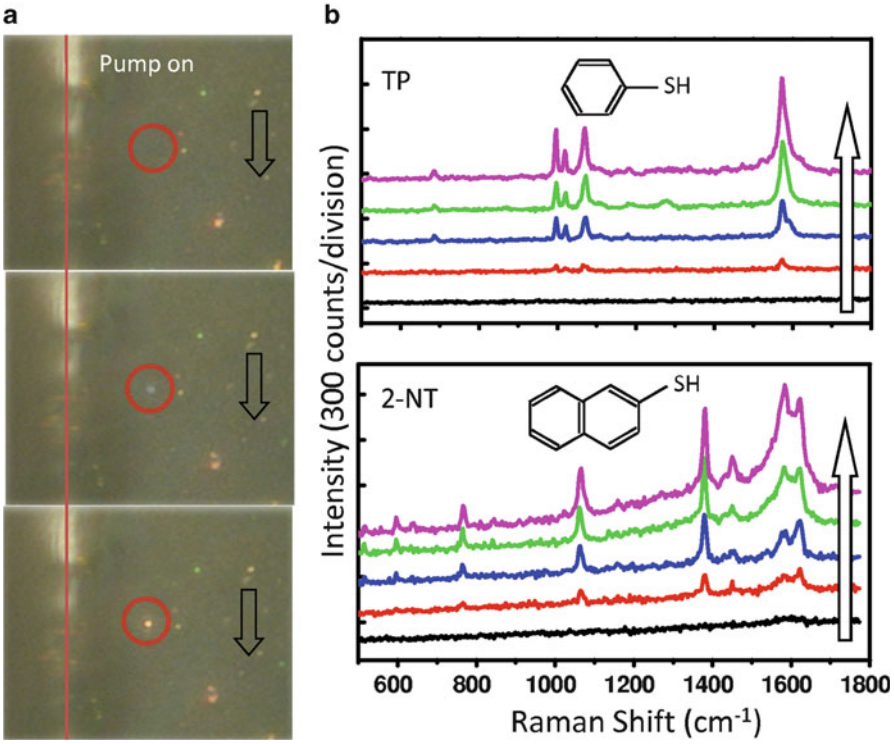

Fig. 7.10 (**a**) DF scattering images of silver nanoparticles trapped in a microfluidic channel. The trapping wavelength was 830 nm. (**b**) Corresponding SERS spectra from the optically induced aggregates. A separate laser line at 514.5 nm was used to excite the Raman probes

In an alternative approach, illustrated in Fig. 7.11, we used a Y-shaped microfluidic channel to mix the metal colloid and the analyte solution just before the laser tweezing site. A SERS signal could then be detected at the liquid interface where nanoparticles and analyte molecules mix, but the signal was weak. The principal difference compared to the previous scheme is that the colloid and analyte streams have much less time to mix. Incubation is further reduced through the laminar flow within the measurement channel, which only allows mixing through diffusion. However, SERS spectra are clearly observed from the optically aggregated nanoparticles at the interface between the two streams.

Summary and Outlook

We have reviewed our recent studies of optical manipulation of plasmonic nanostructures and discussed possible applications in SERS and sensing. Important results include the observation that GNP dimers align parallel to the laser

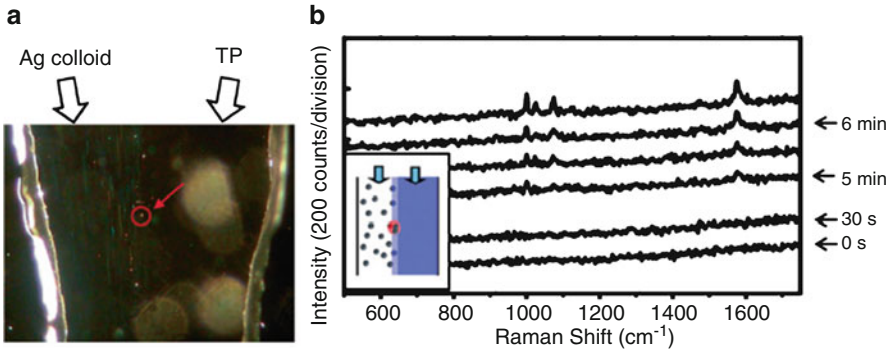

Fig. 7.11 (**a**) DF image of two laminar flows, Ag colloid and analyte solution, respectively, in a Y-shaped microfluidic channel. (**b**) Temporal SERS spectra from optically aggregated Ag nanoparticles at the interface highlighted by the *circle* and *arrow* in (**a**)

polarization, that nanowires can be rotated using circular polarized light, that the interaction between trapped particles can be understood from considering optical interparticle forces combined with DLVO theory, and that optical aggregation can be used for generating SERS from individual dimers as well as in microfluidic channels. But there are of course many more openings for innovative research and applications at the interface between laser tweezing and plasmonic nanostructures. For example, from theoretical simulations we expect that a variation of the trapping laser wavelength in relation to the plasmon spectrum should have profound impact on the gradient force as well as on optical interparticle interactions, but there are hardly any experimental studies that address such issues. Similarly, there is plenty of room for novel studies of nano-optical rotation phenomena and the influence of particle size, shape, chirality, and spectral properties. Rotating plasmonic nanostructures could potentially be used as effective "handles" for torsion experiments on biological macromolecules or for "nano-viscosity" measurements. From the SERS sensing perspective, extension to 3D trapping, perhaps using dielectric beads as carrier for metal nanoparticles [40, 41] or using non-Gausssian beam profiles that minimize radiation pressure, would facilitate Raman analysis in highly confined volumes, perhaps even inside biological cells.

References

1. Friese MEJ, Nieminen TA, Heckenberg NR, Rubinsztein-Dunlop H. Optical alignment and spinning of laser-trapped microscopic particles. Nature. 1998;394:348–50.
2. Nishimura Y, Misumi O, Matsunaga S, Higashiyama T, Yokota A, Kuroiwa T. The active digestion of uniparental chloroplast DNA in a single zygote of Chlamydomonas reinhardtii is revealed by using the optical tweezer. Proc Natl Acad Sci U S A. 1999;96:12577–82.
3. Grover SC, Skirtach AG, Gauthier RC, Grover CP. Automated single-cell sorting system based on optical trapping. J Biomed Opt. 2001;6:14–22.

4. Bonin KD, Kourmanov B, Walker TG. Light torque nanocontrol, nanomotors and nanorockers. Opt Express. 2002;10:984–9.
5. Svoboda K, Block SM. Optical trapping of metallic Rayleigh particles. Opt Lett. 1994;19:930–2.
6. Prikulis J, Svedberg F, Käll M, Enger J, Ramser K, Goksor M, Hanstorp D. Optical spectroscopy of single trapped metal nanoparticles in solution. Nano Lett. 2004;4:115–8.
7. Hansen PM, Bhatia VK, Harrit N, Oddershede L. Expanding the optical trapping range of gold nanoparticles. Nano Lett. 2005;5:1937–42.
8. Svedberg F, Li ZP, Xu HX, Käll M. Creating hot nanoparticle pairs for surface-enhanced Raman spectroscopy through optical manipulation. Nano Lett. 2006;6:2639–41.
9. Svedberg F, Käll M. On the importance of optical forces in surface-enhanced Raman scattering (SERS). Faraday Discuss. 2006;132:35–44.
10. Tong LM, Righini M, Gonzalez MU, Quidant R, Käll M. Optical aggregation of metal nanoparticles in a microfluidic channel for surface-enhanced Raman scattering analysis. Lab Chip. 2009;9:193–5.
11. Rao S, Raj S, Balint S, Fons CB, Campoy S, Llagostera M, Petrov D. Single DNA molecule detection in an optical trap using surface-enhanced Raman scattering. Appl Phys Lett. 2010;96:213701.
12. Xu HX, Käll M. Surface-plasmon-enhanced optical forces in silver nanoaggregates. Phys Rev Lett. 2002;89:246802.
13. Li ZP, Käll M, Xu H. Optical forces on interacting plasmonic nanoparticles in a focused Gaussian beam. Phys Rev B Condens Matter Mater Phys. 2008;77:085412.
14. Miljkovic VD, Pakizeh T, Sepulveda B, Johansson P, Käll M. Optical forces in plasmonic nanoparticle dimers. J Phys Chem C. 2010;114:7472–9.
15. Righini M, Zelenina AS, Girard C, Quidant R. Parallel and selective trapping in a patterned plasmonic landscape. Nat Phys. 2007;3:477–80.
16. Grigorenko AN, Roberts NW, Dickinson MR, Zhang Y. Nanometric optical tweezers based on nanostructured substrates. Nat Photonics. 2008;2:365–70.
17. Zhang WH, Huang LN, Santschi C, Martin OJF. Trapping and sensing 10 nm metal nanoparticles using plasmonic dipole antennas. Nano Lett. 2010;10:1006–11.
18. Pelton M, Liu MZ, Kim HY, Smith G, Guyot-Sionnest P, Scherer NE. Optical trapping and alignment of single gold nanorods by using plasmon resonances. Opt Lett. 2006;31:2075–7.
19. Tong LM, Miljkovic VD, Käll M. Alignment, rotation, and spinning of single plasmonic nanoparticles and nanowires using polarization dependent optical forces. Nano Lett. 2010;10:268–73.
20. Selhuber-Unkel C, Zins I, Schubert O, Sonnichsen C, Oddershede LB. Quantitative optical trapping of single gold nanorods. Nano Lett. 2008;8:2998–3003.
21. Liu M, Zentgraf T, Liu YM, Bartal G, Zhang X. Light-driven nanoscale plasmonic motors. Nat Nanotechnol. 2010;5:570–3.
22. Tong L, Miljkovic VD, Johansson P, Käll M. Plasmon hybridization reveals the interaction between individual colloidal gold nanoparticles confined in an optical potential well. Nano Lett. 2011;11:4505–8.
23. Ashkin A. Acceleration and trapping of particles by radiation pressure. Phys Rev Lett. 1970;24:156–9.
24. Ramser K, Enger J, Goksör M, Hanstorp D, Logg K, Käll M. A microfluidic system enabling Raman measurements of the oxygenation cycle in single optically trapped red blood cells. Lab Chip. 2004;5:431–6.
25. Jain PK, Lee KS, El-Sayed IH, El-Sayed MA. Calculated absorption and scattering properties of gold nanoparticles of different size, shape, and composition: applications in biological imaging and biomedicine. J Phys Chem B. 2006;110:7238–48.
26. Kelly KL, Coronado E, Zhao LL, Schatz GC. The optical properties of metal nanoparticles: the influence of size, shape, and dielectric environment. J Phys Chem B. 2003;107:668–77.

27. Mock JJ, Barbic M, Smith DR, Schultz DA, Schultz S. Shape effects in plasmon resonance of individual colloidal silver nanoparticles. J Chem Phys. 2002;116:6755–9.
28. Gunnarsson L, Rindzevicius T, Prikulis J, Kasemo B, Käll M, Zou SL, Schatz GC. Confined plasmons in nanofabricated single silver particle pairs: experimental observations of strong interparticle interactions. J Phys Chem B. 2005;109:1079–87.
29. Shelton WA, Bonin KD, Walker TG. Nonlinear motion of optically torqued nanorods. Phys Rev E Stat Nonlin Soft Matter Phys. 2005;71:036204.
30. Hallock AJ, Redmond PL, Brus LE. Optical forces between metallic particles. Proc Natl Acad Sci U S A. 2005;102:1280–4.
31. Tang ZY, Kotov NA, Giersig M. Spontaneous organization of single CdTe nanoparticles into luminescent nanowires. Science. 2002;297:237–40.
32. Yethiraj A, van Blaaderen A. A colloidal model system with an interaction tunable from hard sphere to soft and dipolar. Nature. 2003;421:513–7.
33. Bigioni TP, Lin XM, Nguyen TT, Corwin EI, Witten TA, Jaeger HM. Kinetically driven self assembly of highly ordered nanoparticle monolayers. Nat Mater. 2006;5:265–70.
34. Shaw DJ. Introduction to colloid and surface chemistry. 4th ed. Oxford: Butterworth-Heinemann; 2000.
35. Israelachvili JN. Intermolecular and surface forces. 2nd ed. San Diego: Academic; 1992.
36. Hahn MW, Abadzic D, O'Melia CR. Aquasols: on the role of secondary minima. Environ Sci Technol. 2004;38:5915–24.
37. Kane V, Mulvaney P. Double-layer interactions between self-assembled monolayers of omega-mercaptoundecanoic acid on gold surfaces. Langmuir. 1998;14:3303–11.
38. Ashby PD, Chen LW, Lieber CM. Probing intermolecular forces and potentials with magnetic feedback chemical force microscopy. J Am Chem Soc. 2000;122:9467–72.
39. Tanaka Y, Yoshikawa H, Itoh T, Ishikawa M. Surface enhanced Raman scattering from pseudoisocyanine on Ag nanoaggregates produced by optical trapping with a linearly polarized laser beam. J Phys Chem C. 2009;113:11856–60.
40. Jordan P, Cooper J, McNay G, Docherty FT, Graham D, Smith WE, Sinclair G, Padgett MJ. Surface-enhanced resonance Raman scattering in optical tweezers using co-axial second harmonic generation. Opt Express. 2005;13:4148–53.
41. Balint S, Kreuzer MP, Rao S, Badenes G, Miskovsky P, Petrov D. Simple route for preparing optically trappable probes for surface-enhanced Raman scattering. J Phys Chem C. 2009;113:17724–9.

Chapter 8
Nanoplasmonic Sensing for Nanomaterials Science, Catalysis, and Optical Gas Detection

Christoph Langhammer, Elin M. Larsson, Bengt Kasemo, and Igor Zoric

Abstract In this chapter *direct* and *indirect* nanoplasmonic sensing approaches for applications in nanomaterials science and catalysis, as well as for gas sensing are discussed. It is illustrated how the typical features of nanoplasmonic sensors, e.g., high local and absolute sensitivity, high temporal resolution, remote readout, simple experimental arrangement, and generic robustness, together with a wide range of possible application conditions make the latter a potentially very powerful experimental tool to study processes on the surface and in the bulk of nanosized systems. The possibility to locally measure temperature at the nanoscale with nanoplasmonic optical calorimetry will also be discussed. Furthermore, numerous examples of nanoplasmonic sensors for gas-sensing applications will be reviewed and the role and potential of novel plasmonic metals will be addressed.

Introduction

Nanoparticles and thin films (nanosized systems) are essential ingredients in many established or envisioned technological applications including sensors [1], heterogeneous catalysts [2], photovoltaics [3, 4], electronic and photonic devices [5], batteries [6, 7], hydrogen storage systems [8], drug delivery systems [9], and reinforced composite materials. In many of these applications the nanosized systems are in contact with gaseous or liquid environments and desired (e.g., in catalysis) or undesired (e.g., corrosion) interactions between gas or liquid molecules and the nanosized system may occur. Such interactions include oxide formation, corrosion, etching, surface functionalization, hydrogen embrittlement, and fouling.

C. Langhammer (✉) • E.M. Larsson • B. Kasemo • I. Zoric
Department of Applied Physics, Division for Chemical Physics, Chalmers University of Technology, Göteborg 412 96, Sweden
e-mail: clangham@chalmers.se

A. Dmitriev (ed.), *Nanoplasmonic Sensors*, Integrated Analytical Systems,
DOI 10.1007/978-1-4614-3933-2_8,

In heterogeneous catalysis nanosized systems catalyze surface reactions. In other situations a change of temperature or pressure may induce phase transitions like melting/freezing, magnetic/nonmagnetic, or metallic/insulating. Often the details of such transitions depend on the precise nanoscale dimension of the studied system and may influence the functionality.

In this context, for research applications, it is of particular importance to develop experimental tools for fast, sensitive, and reliable measurements of processes on/in nanosized systems under realistic, close-to-application, conditions. The latter often means working at high temperatures, at ambient or higher pressure (maybe even in liquid), and in harsh and corrosive environments. An experimental method intended to study such systems and processes should thus ideally be able to cover a wide range of pressures (from UHV to atmospheric pressure and above) and gas compositions in the gaseous environment and even be able to operate in a liquid. Furthermore, one would like to be able to study diverse nanosystems ranging from metals, semiconductors, and insulators to polymers and soft matter, and if possible with high temporal resolution to be able to scrutinize fast kinetic processes. A further desire is the ability to perform measurements on relatively small amounts of material, because samples may be scarce or expensive. Furthermore, sometimes measurements are preferably done on a single nanoparticle to avoid ensemble-averaging related effects.

Standard experimental techniques (like X-ray diffraction XRD, X-ray photoelectron spectroscopy XPS, Fourier transform infrared spectroscopy FTIR, scanning electron microscopy SEM, transmission electron microscopy TEM, scanning-tunneling microscopy STM, atomic force microscopy AFM, etc.), which can be used to characterize nanoparticles and processes on their surfaces or in their bulk, usually either require relatively large amounts of sample material and/or can only be used under idealized conditions (UHV, limited temperature range, etc.) and have poor temporal resolution. The first limitation often makes it necessary to work with powders, which are characterized by broad particle size distributions, complicating systematic studies of the role of nanoparticle size, shape, and chemical composition at the nanoscale on desired properties of the nanomaterials.

Typically, the size range of nanosized systems of interest stretches from 1 nm to ca. 500 nm. At the lower end of this size range, i.e., 1–10 nm, the nanosized systems typically have, for example, different electronic and crystal structure than larger particles and show novel thermodynamic, reactivity, and kinetic properties upon interaction with other materials and molecules. The limited number of atoms is one reason for these differences together with the large surface/bulk atom ratio, which makes surface related effects (gradients in electronic density, quantization of electronic states, novel local environment for surface atoms, etc.) important.

Nanosized systems in the size range 10–500 nm typically exhibit quite similar electronic and atomic structure, as well as thermodynamic and kinetic features as the corresponding bulk materials. Nevertheless, there are still some significant quantitative differences regarding e.g., exposed crystal facets, annealing behavior, defects like grain boundaries and dislocations, short diffusion path length, mechanical strength, and optical excitations.

In this chapter we describe how novel *direct* and *indirect* approaches based on nanoplasmonic sensing can be used to tackle the above-mentioned challenges. We will illustrate how the typical features of nanoplasmonic sensors, e.g., high local and absolute sensitivity and high temporal resolution, together with a wide range of possible application conditions (due to the method's remote sensing nature) make nanoplasmonic sensing a potentially unique and powerful experimental tool to study processes on and in nanosized systems of interest in nanomaterials science and catalysis. The possibility to locally measure temperature at the nanoscale in a nanoplasmonic optical calorimetry approach will also be discussed. Furthermore, we will indicate on numerous examples the potential of these approaches for novel types of optical nanoplasmonic sensors for mainly gas-sensing applications. The role and potential of novel plasmonic metals will also be addressed.

Novel Nanoplasmonic Metals

During the past decade's rapid development of nanoplasmonics the focus was almost entirely on Au and Ag as nanoplasmonic metals. The latter was due to the special dielectric (electronic) properties of Au and Ag in the vis-NIR spectral range, in particular low intrinsic losses in the visible, due to a lack of interband excitations at energies below the interband threshold at 2.3 or 3.9 eV for Au and Ag, respectively.

However, surface plasmons and localized surface plasmons, in principle, exist in any metal. Shifting the focus from the "classic" plasmonic metals, Au and Ag, to other metals, which have not yet received much attention as nanoplasmonic materials, leads to interesting novel opportunities. For example, one can combine the intrinsic material properties of the chosen plasmonic material with the possibility to explore these LSP excitations as transducers in novel nanoplasmonic sensing schemes. Of particular interest are applications as sensors to study processes on the surface and/or in the bulk of the plasmonically active nanoparticles themselves. Such processes are of high relevance and interest for (nano)materials science and may include, as will be shown below, chemical (e.g., catalytic) reactions, hydrogen absorption, oxide formation, liquid–solid phase transitions, etc. A brief discussion of the main features of plasmonic excitations in novel materials as well as a short literature review are therefore appropriate before discussing their application as nanoplasmonic sensors.

Figure 8.1 shows extinction spectra of random arrays of nanodisks of similar size, fabricated by Hole-mask Colloidal Lithography [10], for eight different metals. Clearly, despite the significantly different bulk dielectric properties of these metals, the confinement to nanodisk geometry with similar diameters and heights gives rise to well-defined LSPRs in the visible with similar spectral peak positions for all materials. We also observe spectral line-widths and optical cross-sections, which are strongly dependent on relevant, material specific damping processes.

A number of recent studies discuss plasmonic excitations in "novel" metals in more detail, e.g., Pt and Pd [11–14], Cu [15–17], Al [18–20], Sn [21] or several of the metals [22].

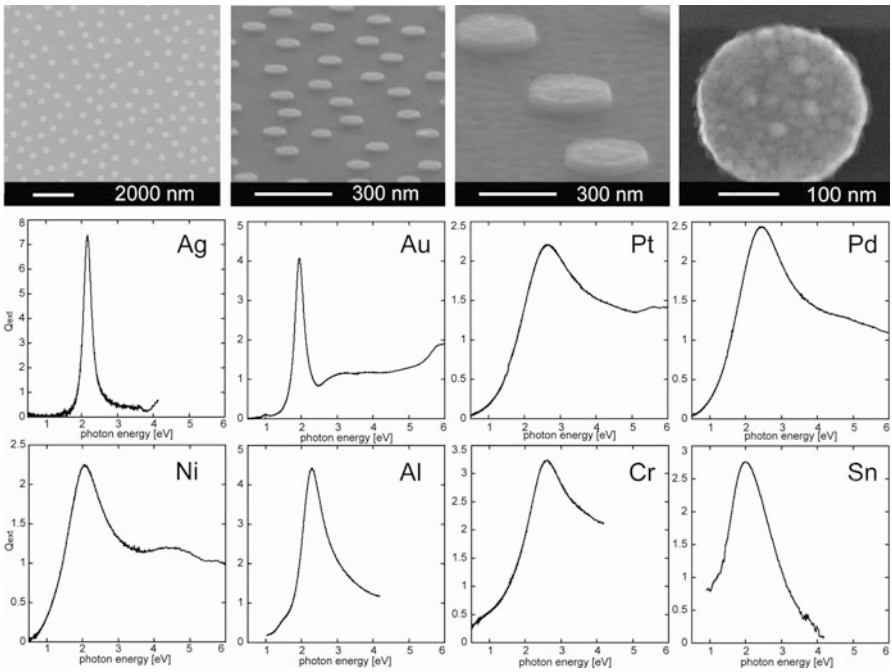

Fig. 8.1 Illustration of tunable LSPR in numerous metal nanodisks fabricated by the Hole-mask Colloidal Lithography method. The *top row* comprises different scanning electron microscopy (SEM) images of Pd nanodisks with a diameter $D = 300$ nm and height $h = 20$ nm. The *middle row* shows extinction spectra of Ag, Au, Pt, and Pd nanodisks with $D = 110$ nm and $h = 20$ nm [12]. The *bottom row* contains extinction spectra of Ni ($D = 110$ nm and $h = 20$ nm), Al ($D = 110$ nm and $h = 20$ nm) [18], and Cr ($D = 136$ nm, $h = 20$ nm), as well as Sn ($D = 107 \pm 10$ nm, $h = 52 \pm 6$ nm) nanodisks covered with 20 nm SiO_2 [21]

In the following section we will discuss the use of plasmonic excitations in various metals as local probes for real-time studies of processes in the bulk and on the surface of metallic nanoparticles. In these experiments the nanoparticles simultaneously constitute the sensor and the studied nano-entity. We therefore classify these types of experiments as "direct nanoplasmonic sensing."

Direct Nanoplasmonic Sensing: Plasmonic Nanoparticles as Coeval Sensors and Studied Nano-Entities

Metallic nanosized systems in the 10–100(s) nm size ranges are, as summarized in the introduction, finding more and more applications in functional systems and devices. Employing nanofabricated 2-D structures as model systems to study properties, fundamental mechanisms, and functionality of nanosized systems is a

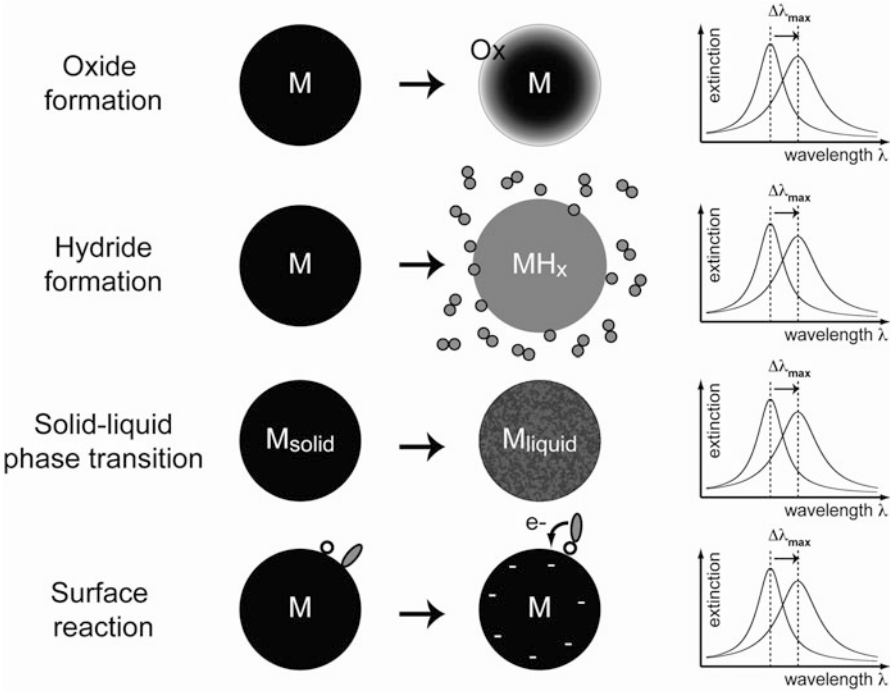

Fig. 8.2 Schematic depiction of processes on/in metallic nanoparticles that can be studied by direct nanoplasmonic sensing following the spectral response of the LSPR: (1) surface and bulk oxidation, (2) metal hydride formation, (3) solid–liquid phase transitions, (4) surface reactions inducing e.g., charge transfer from a reacting molecule to a metallic/plasmonic particle

very efficient approach to scrutinize the otherwise very complex processes. Using, for this purpose, the intrinsic LSPR in metallic functional nanostructures as a sensor, following the direct nanoplasmonic sensing scheme, is a very efficient way to study relevant interactions and processes in situ and in real time. In this way the role of particle size, geometry, microstructure, etc. can be scrutinized. If nanofabrication or size-selective synthesis approaches are used to prepare the samples, excellent control over the nano-dimensional parameters can be guaranteed. Furthermore, direct nanoplasmonic sensing can be carried out under a wide range of experimental conditions (UHV-high pressure, low-high temperature, etc.) owing to the remote detection principle.

During such experiments structural and/or electronic changes induced in/on the metallic nanoparticles by the studied process, are detected by real-time recording of (changes in) the LSPR response, e.g., spectral peak shifts. Schematic depictions of nanoscale processes that can be studied in this way are summarized in Fig. 8.2 and a literature overview is presented in the following subchapters.

Oxidation and Corrosion

Corrosion, in the most common use of this expression, refers to (electrochemical) oxidation of metals with an oxidizing agent such as oxygen or water, often with various co-factors that speed up the corrosion, e.g. sulfur or halogens. Typically, in a corrosion process, oxide(s), hydroxides and/or salt(s) of the corroding metal are formed. The corrosion process can take place very locally and form pits or cracks (pitting corrosion) or it can be spread more or less homogeneously over a surface, corroding the latter uniformly. For example, most metals, when exposed to clean, dry air, form a native protective oxide layer spontaneously, which, at low temperatures, passivates the surface against further oxidation/corrosion. For some systems like the alkali metals, the oxidation reaction can be quite violent while for other systems like Al, despite the very high enthalpy of formation of the oxide ($\Delta H(Al_2O_3) = -1675.7$ kJ mol), the oxidation under ambient conditions is a diffusion controlled process and practically terminates at room temperature with a protective oxide of a few nm thickness.

Corrosion has become a significant reliability concern and has received considerable attention in microelectronic devices, driven by ever-increasing demands for improved performance, reliability, miniaturization, and low-cost. Common problems encountered with integrated circuits and supporting microelectronic devices include galvanic corrosion causing increased contact resistance and/or electrical short circuits. Owing to the miniaturization of such components down to and below the micrometer regime, their dimensions approach or overlap already with the typical size range of plasmonically active nanostructures. Therefore, LSP excitations in metallic nanostructures can be used as very sensitive in-situ probes to study and scrutinize oxidation and corrosion processes at the nanoscale. Furthermore, applications as sensors to continuously monitor corrosion damage and/or to test corrosion inhibitors in, e.g., microelectronic devices can be envisioned.

Van Duyne and coworkers reported in 2007 how the presence of an oxide layer influences the LSPR in Cu nanotriangles fabricated with nanosphere lithography [16]. This is a very illustrative example of the idea presented above, because Cu is used in electronics applications and in miniaturized nanodevices, due to its high electrical conductivity. Cu is, however, also prone to surface oxidation (Cu_2O and CuO) upon exposure to ambient atmosphere at room temperature.

In their work, Van Duyne et al. studied the optical properties of 2-D arrays of Cu nanoparticles by implementing a simple oxide removal procedure using glacial acetic acid and relying on UV–vis extinction spectroscopy and electrodynamics calculations using the discrete dipole approximation (DDA) method. They demonstrated that removal of the copper oxide from the nanotriangle surface yields a dramatic difference in the observed LSPR (Fig. 8.3a) response.

An AFM investigation carried out by the authors indicated that the amount of copper oxides present on the surface of the Cu nanoparticles after 3–8 min exposure to ambient laboratory conditions at room temperature is most likely very thin

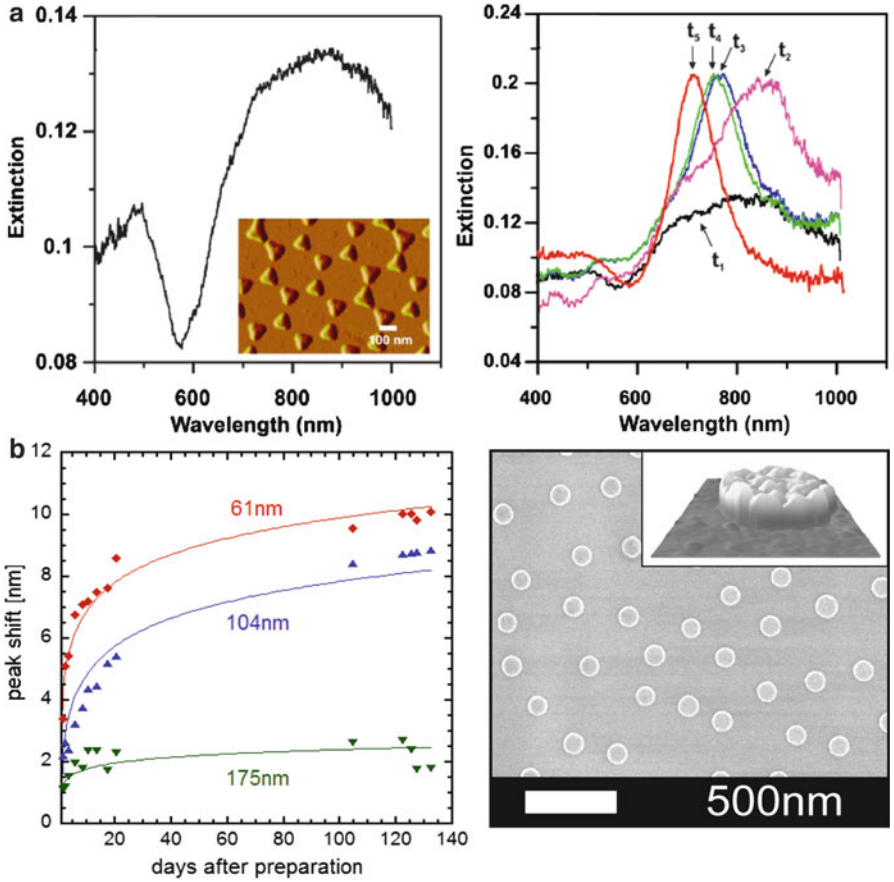

Fig. 8.3 (**a**) Extinction spectra of Cu nanotriangle arrays. *Left*: Extinction spectrum of an oxidized sample (*inset*: AFM image of the sample). *Right*: Real-time extinction spectra tracking the change in the LSPR during oxide removal with glacial acetic acid, where $t_1 = 0$ s (*black*), $t_2 = 2$ s (*light purple*), $t_3 = 10$ s (*blue*), $t_4 = 20$ s (*green*, $\lambda_{max} = 760$ nm) in acetic acid, and $t_5 =$ final (*red*, $\lambda_{max} = 710$ nm) in a N_2 environment. Adapted with permission from ref. [16]. Copyright 2007 American Chemical Society. (**b**) *Left*: Spectral peak shifts of the LSPR in Al nanodisks with different diameters and constant height ($h = 20$ nm) upon oxidation in air. *Right*: SEM micrograph and AFM image (*inset*) of a typical Al nanodisk sample. Adapted with permission from ref. [18]. Copyright 2008 American Chemical Society

(less than 1 nm). This illustrates quite impressively the sensitivity of the LSPR to the presence of a thin surface oxide since peak shifts of the order of 50 nm were observed upon removal of the oxide (Fig. 8.3a).

Another example, where LSPR was used as an in situ probe to study metal oxidation at the nanoscale, was performed in our laboratory by Langhammer et al. with Al nanodisks as the model system [18] (Fig. 8.3b). The presence and growth of an oxide layer was monitored by relying on two different inherent properties of LSPR: (1) the high LSPR sensitivity to refractive index changes

(caused by the growing oxide), and (2) the high sensitivity to size and shape changes of the particles (shrinking metallic core upon oxidation, possible surface roughening, etc.). The sum of these two contributions lies behind the total detected LSPR signal. The relative strengths of these two contributions are discussed in detail in the article by using electrostatic spheroid model calculations.

The obtained insight in the LSPR-based oxide sensing mechanism was then applied to study the native oxide formation on Al nanodisks under ambient conditions. In the study, the LSPR response of Al nanodisks with constant height and different diameters (61, 104 and 175 nm) was measured as a function of time after fabrication (Fig. 8.3b). The LSPR spectrally redshifted with time, with the largest shifts observed for the smallest nanodisks. Direct logarithmic kinetics, as expected for oxidation in humid air and in agreement with classic Cabrera–Mott theory of metal oxidation, were found.

Metal Hydride Formation

The solubility of hydrogen in metals has been and is to this day of great concern in the construction industry. The embrittlement of a metal or alloy by atomic hydrogen is caused by ingression of hydrogen into a component. This process can seriously reduce the ductility and load-bearing capacity, cause cracking and catastrophic brittle failures at stresses below the yield stress. An example of hydrogen embrittlement is the cracking of welds, hardened steels or high-strength aluminum alloys. A particular problem with hydrogen embrittlement is the difficulty of its (early stage) detection.

Another area where hydrogen in metals is explored extensively is for hydrogen storage, where metal hydrides have since long been proposed as an alternative reversible storage system for hydrogen, circumventing safety concerns related to storage of gas phase hydrogen in high pressure tanks [8]. Metal-hydrogen systems typically are characterized by a combination of the existence of an initial range of hydrogen solubility at very low concentrations (percentage range or less), which can be regarded as a solid solution of hydrogen atoms in the metal lattice (α-phase), followed by the formation of a crystallographically distinct new hydride (β-phase) at higher hydrogen contents. Hence, hydride formation in metals in general represents one of the best examples of first-order phase transitions in solids.

In this context, nanostructured hydride materials and nanoparticles have been proposed as a solution for faster response hydrogen storage systems. Nanosized storage entities offer short diffusion lengths and may differ from bulk materials both in their thermodynamic and kinetic properties [23]. Favorable thermodynamics and/or kinetics are often obtained by nanosizing and often in combination with alloying and addition of catalyst materials. Therefore, understanding the physical principles behind the influence of nanosizing on hydrogen storage performance is a key issue for developing efficient and competitive hydrogen

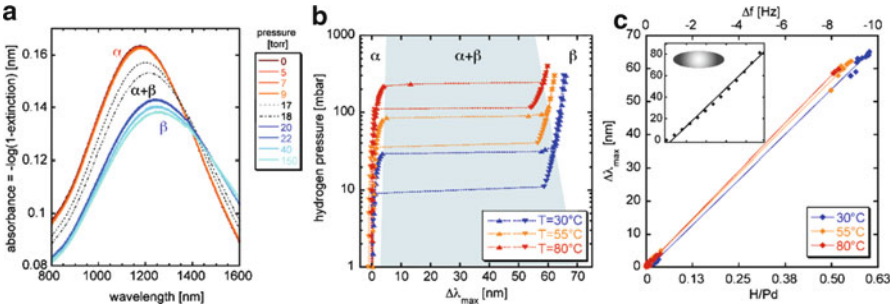

Fig. 8.4 (**a**) Series of measured extinction spectra for an array of Pd nanodisks ($D = 300$ nm, $h = 20$ nm) for increasing hydrogen pressure. A significant peak redshift ($\Delta\lambda_{max}$) and peak broadening as well as a decrease of the total cross section upon hydrogen uptake are observed. Adapted with permission from Ref. [24]. Copyright 2007 American Chemical Society. (**b**) p-$\Delta\lambda_{max}$ hydrogen sorption and desorption isotherms measured by LSPR for Pd nanodisks ($D = 290$ nm, $h = 60$ nm) at three different temperatures. (**c**) Linear scaling of $\Delta\lambda_{max}$ (LSPR) with the hydrogen concentration (QCM) in the nanodisks. The inset shows the scaling of $\Delta\lambda_{max}$ with hydrogen concentration calculated with electrostatic spheroid theory, confirming to a good first approximation the experimentally found linear dependence. Reproduced with permission from [26]. Copyright Wiley-VCH Verlag GmbH & Co

storage devices. For applications, nanosizing is achieved by ball-milling of precursor materials, yielding powders consisting of particles in the 10 nm to few 100 nm size range.

The direct nanoplasmonic sensing approach to study hydrogen sorption and desorption was first introduced by Langhammer et al. for a nanofabricated Pd nanodisk model system [24]. The essence of the study was to monitor the spectral LSPR response during hydrogen sorption and desorption as a function of hydrogen pressure. The observed changes in the plasmonic response of Pd nanodisks were then interpreted as a direct consequence of hydrogen-induced changes in the dielectric properties of the absorbing metal (metal hydrides can be metallic, as in the Pd-H system or insulators as in, e.g., the Mg-H system [25]) and of volume expansion of the nanodisks.

This first study was then followed by a more detailed quantitative work on Pd nanodisks and Pd nanorings by the same authors [26] including a "calibration" of the optical response to hydrogen concentration in the nanoparticles by using quartz crystal microbalance (QCM) measurements.

The typical optical response during hydrogen sorption measurements, i.e., a spectral peak shift and an increase of the line-width, are shown in Fig. 8.4a [24] with corresponding "optical isotherms" in Fig. 8.4b [26]. The latter were obtained by systematically reading out the plasmonic response for increasing/decreasing hydrogen pressure. They reflect very nicely the typical phase behavior of hydrogen-metal systems: (1) at low concentrations (small $\Delta\lambda_{max}$) the formation of an interstitial dilute solid solution (α-phase, of the order 1 % hydrogen) and (2),

at higher pressure and increasing hydrogen concentration, the formation of the hydride (β-phase), containing hydrogen atoms sitting in an ordered lattice in significant amounts [27] (host-material to H-atom-ratio is of order one). The calibration measurements with QCM demonstrated a linear scaling of the LSPR spectral peak shift with hydrogen concentration (Fig. 8.4c) [26]. This, at first, quite surprising result (in view of the fact that the found linear dependence stretches over a region of solid solution into a two-phase coexistence region with a first-order phase transition), was shown by the authors to be understandable in a straightforward way by theoretical calculations based on electrostatic spheroid theory and ab-initio electronic structure calculations for PdH_x [26]. Furthermore, quantitative analysis of the LSPR-based optical isotherms indicated that the enthalpies and entropies for α- and β-phase formation in these relatively large nanostructures are very much bulk like but that internal nanostructure (e.g., grain size as in the example of Pd nanorings [26]) significantly alters the general appearance of the isotherms and storage capacity.

Liquid–Solid Phase Transition

The melting and solidification of metals has been of great technological importance since ancient times. The LSPR of metallic nanoparticles was employed for the first time by Yeshchenko et al. [28] to study the size-dependent melting of spherical copper nanoparticles embedded in a silica matrix. Monitoring the temperature dependence of the spectral line-width of the LSP excitation in the Cu nanoparticles, two distinct melting regimes were observed. For particles smaller than 20 nm, the absorption spectrum changed monotonically with the temperature, which suggested a gradual solid–liquid phase transition of the nanoparticles or the existence of superheated solid. In contrast, for nanoparticles larger than 20 nm, a jump-like increase of the spectral line-width and a non-monotonic shift of spectral peak position with increasing temperature were observed below the bulk melting point, indicating a first-order melting phase transition similar to bulk copper.

A second study by Yeshchenko et al. [29] addressed the size dependent melting of Ag nanoparticles embedded in a silica matrix and a third study by the same authors [30] also addressed the liquid–solid transition in 5 nm spherical gold nanoparticles embedded in a polymer polytetrafluoroethylene matrix. In both works, the LSPR energy and line-width were used as readout parameters to monitor the melting.

Schwind et al. [21] studied the solid–liquid phase transition in Sn nanoparticles nanofabricated on a substrate by Hole-mask Colloidal Lithography (Fig. 8.5a) and encapsulated by a thin sputtered SiO_2 overlayer. The measurements were performed under controlled conditions in UHV and with high temporal resolution. They used the intrinsic LSPR of Sn nanoparticles (average diameter 107 and

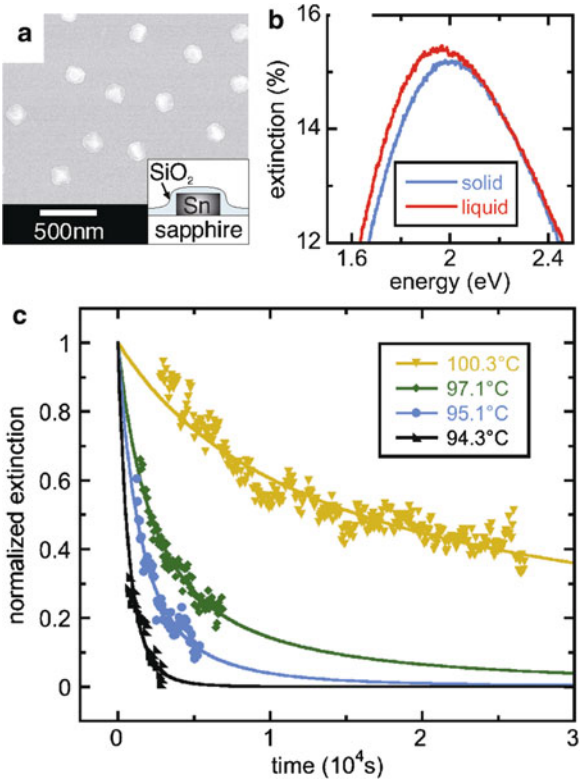

Fig. 8.5 (**a**) SEM picture of the Sn nanoparticles in the frozen state showing the sample after several heating and cooling cycles. The *inset* comprises a schematic drawing of the sample structure. (**b**) LSPR of solid (*blue*) and liquid (*red*) Sn nanoparticles at 27 and 247°C, respectively. (**c**) Sn nanoparticle freezing kinetics at four different temperatures. Adapted with permission from ref. [21]. Copyright 2010 American Chemical Society

52 nm height) (Fig. 8.5b) to study their kinetics of melting and freezing for increasing and decreasing temperature, respectively. During the temperature ramps, the kinetics was found to exhibit distinct hysteresis. Melting occurred near the bulk melting point while crystallization took place at much lower temperatures (ca. 130 K undercooling). The authors also investigated, for the first time, the crystallization kinetics at different fixed temperatures (Fig. 8.5c) in the hysteresis region. Furthermore, they successfully correlated their findings quantitatively with a theoretical model assuming the nucleation to occur on the edges of the nanoparticles and employing the classical nucleation theory with the corresponding modifications.

Chemical Surface Reactions on and Charge Transfer to Plasmonic Nanoparticles

Metal nanoparticles play a key role as catalytically active entities in many chemical processes and reactions. Exhaust emission-cleaning catalysis in vehicles is one of the most prominent examples. Typically catalysts consist of (often noble metal) nanoparticles in the few to few 10 nm size range. Plasmonic excitations in such particles potentially constitute sensitive probes for changes induced by chemical reactions on the particle surface. For direct nanoplasmonic sensing of such processes for most metals one is, however, limited to particle sizes above 30–40 nm for spectroscopic reasons, i.e., due to deep-UV LSPR excitations and strong damping and absorption (too small scattering cross section for e.g., dark-field scattering spectroscopy) in smaller systems.

A first example of a direct sensing application of a catalytic reaction was presented by Ung et al. [31] and relied on plasmonically active Ag nanoparticles. When the latter catalyzed a redox reaction they acquired a charge during the reaction via electron transfer to/from the nanoparticles, inducing changes in the plasmon resonance band. Using as an example the oxidation reaction of BH_4^- in the liquid phase, Ung et al. showed that the electron injection into Ag nanoparticles, catalyzing the reaction, could be monitored using time resolved UV-visible spectroscopy. Figure 8.6 shows the evolution of the absorption spectra of PAA stabilized silver nanoparticles upon the addition of 0.55 M $NaBH_4$.

When adding the $NaBH_4$ solution, the plasmon resonance was first seen to rapidly decrease in intensity (Fig. 8.6, upper panel, 0.5 min). This effect decreased with time and was likely due to the adsorption of borohydrate ions on the surface, with no immediate charge transfer. Subsequently, the plasmon resonance was observed to blueshift, the band to sharpen, and its intensity to increase (Fig. 8.6, upper panel), which was ascribed to the following charging process: $BH_4^- + Ag_n + 3H_2O \rightarrow BO_3^{3-} + Ag_n^{8-} + 10H^+$. Following the blueshift, the reverse process was observed, i.e., a redshift, band broadening and a decrease of maximum intensity (Fig. 8.6, lower panel). The latter observation was ascribed to a discharging process. Charging was observed to occur until the maximum charge density on the particle surface was achieved, and then the charge remained constant until the borohydride concentration was insufficient to maintain the electron density on the particles. Spontaneous "oxidation" of the surface was then observed, probably via reduction of water or other moieties resulting from borohydride oxidation. Mulvaney et al. made similar observations when studying the same redox reaction on gold nanorods in 2006 [32].

In 2008 Novo et al. [33] showed that dark field spectroscopy could be used to monitor the rate of the Au catalyzed oxidation of ascorbic acid on a single Au decahedral nanoparticle (tens of nm size). The authors determined the reaction rate by detecting, via the plasmon resonance position, the transferred electrons stored in a single catalyst particle and by quantifying the concentration in real time. Their results were the first direct measurements of the rates of redox catalysis on single

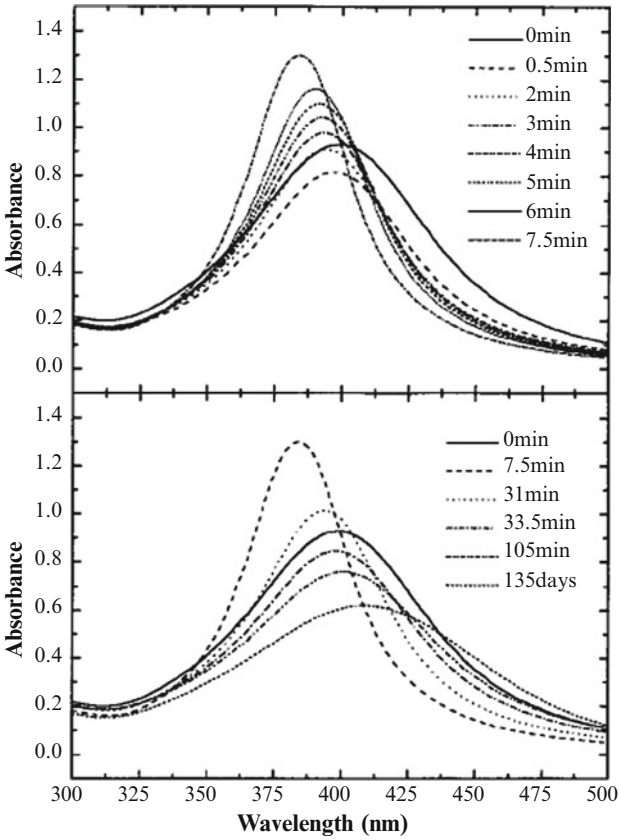

Fig. 8.6 Time evolution of the absorption spectra of the PAA stabilized silver nanoparticles upon the addition of 0.55 M $NaBH_4$. The upper graph shows the charging period and the lower graph shows the discharging period. Adapted with permission from ref. [31]. Copyright 1999 American Chemical Society

nanocrystals. Figure 8.7a shows the scattering spectra for a single gold nanocrystal as a function of the reaction time. In Fig. 8.7b the data has been analyzed to show the evolution of the peak position in time. Similarly to the experiments above, the plasmon absorption band was first observed to blueshift during more than 3 min as the electrons were injected. Subsequently, there was a plateau region where the gold particles had the highest electron density built up during the cycle. Following the plateau, the spectra redshifted back to the initial position reflecting the discharge of the excess electrons from the particle through the reduction of oxygen to water once the ascorbic acid had been oxidized. The study by Novo et al. provides a highly interesting route to determine the role of redox catalyst structure, etc. on the reaction rate.

This work was in 2009 followed by another study by Novo et al. [34] where they demonstrated a method for modulating the optical properties of single gold nanorods using electrochemical charge injection. Calculations included in this work indicated that surface plasmon spectroscopy may provide a potential route to the optical detection of single electrons.

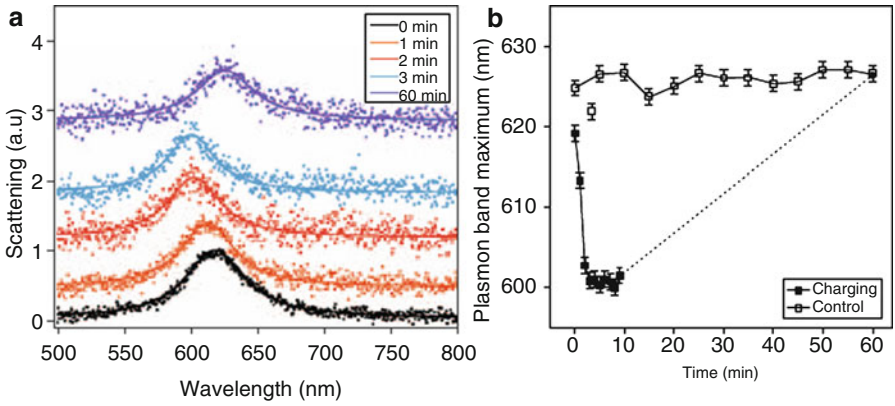

Fig. 8.7 (**a**) Gold-catalyzed oxidation of ascorbic acid. Scattering spectra of a single Au decahedron at 1, 2, 3 and 60 min after addition of ascorbic acid. (**b**) Spectral shift as a function of time for the catalytic reaction in (**a**) and for a control experiment. Reprinted by permission from Macmillan Publishers Ltd: Nature Nanotechnology ref. [33] copyright 2008

Summary: Direct Nanoplasmonic Sensing

The LSPR in nanoparticles and structures consisting of "classic" Ag and Au but also numerous "non-classic" metals like Al, Sn, and Pd have been presented as very powerful optical probes to study physical and chemical processes in and on the surface of nanosized (few 10 nm to few 100 nm) metallic systems. The presented sensing employed the direct nanoplasmonic sensing scheme, where the studied nanoparticles are sensor and studied nano-entity at the same time.

We note that this approach is generic and easily can be applied to study thermodynamics and kinetics of other bulk or surface modifications on metallic nanoparticles. The latter may include corrosion, surface functionalization, etching, etc., of nanoparticles since all these processes have in common that some molecules (via dissociation on the surface) or atoms in a nanoparticle's environment can reversibly (or irreversibly) enter the bulk of the nanoparticles and/or interact directly with their surfaces. For proper combinations of material, (gas- or fluid-phase) molecules and temperature, such processes could happen for, e.g., hydrocarbons, ammonia, oxygen, nitric oxides, etc. Technologically important situations where this might play a role are in nanoelectronic components (oxidation, corrosion), heterogeneous catalysis, hydrogen embrittlement of nanostructured materials, and nanoparticle based sensors.

The direct nanoplasmonic sensing approach has, however, one important limitation. It is not applicable to nanoparticles smaller than 10–20 nm for two main reasons: (1) Typically, for numerous non-classic nanoplasmonic metals, the LSPR energy is shifted into the UV spectral range [12, 18], which complicates the optical spectroscopy. (2) For metals with relatively strong interband damping channels, like e.g., Au,

Ag, Pt, and Pd, the optical cross-section of small nanoparticles is very low and the LSPR peaks are typically very broad, which decreases the signal to noise ratio and gives rise to low figures of merit of the sensor. Furthermore, the LSPR decay is predominantly absorptive, which makes e.g., dark-field scattering spectroscopy on single particles very difficult.

A possible solution to circumvent this problem efficiently will be discussed in section "Indirect Nanoplasmonic Sensing." Furthermore, other strategies employing LSPR to study processes in (nano) materials *adjacent to* the plasmonic (Au) nanoparticles e.g., for gas-sensing applications are discussed in the following section.

Plasmonic Nanoparticles as Sensors to Study Processes on/in Adjacent (Nano-) Materials

In this chapter nanoplasmonic sensing, in which the studied process occurs, upon interaction with the environment, in/on a material or nanosized system adjacent or in close vicinity to a plasmonically active sensing nano-entity, is described. Three different types of arrangements are principally possible, as schematically depicted in Fig. 8.8:

1. A thin layer of a nanomaterial or nanoparticles, which undergoes a bulk or surface chemical and/or structural change upon interaction with the environment, is in direct contact with a plasmonically active sensor nanoparticle. A typical change occurring in the layer may be a volume variation of the latter or a change of its refractive index after interaction with a reactant. Moreover it may also be e.g., a temperature-induced phase transition. The consequent changes of the effective refractive index in the particle nano-environment will induce a spectral shift of the sensor nanoparticle LSPR (Fig. 8.8a).
2. Changes occur on/within nanoparticles or a thin film separated from the plasmonically active sensing particles by an inert or chemically "active" dielectric spacer layer but still located within the enhanced near-field region (Fig. 8.8b). As for (1) changes of the effective refractive index in the particle nano-environment will induce a spectral shift of the sensor nanoparticle LSPR. Furthermore also e.g., charge transfer processes from/to the sensor nanoparticles and dielectric changes in the spacer layer induced by e.g., a chemical reaction may give rise to measurable peak shifts and thus be the sensing mechanism in certain applications. This sensing approach was first demonstrated in our laboratory by Larsson et al. [35] for catalysis and by Langhammer et al. [36] for hydrogen storage applications and is called *Indirect Nanoplasmonic Sensing* (INPS).
3. The plasmonic sensing nanoparticles are dispersed into a medium, which undergoes a change upon interaction with a surrounding medium or a temperature variation (Fig. 8.8c). The detected change can either be a change in the dielectric properties of the medium or a reaction occurring at the interface between the sensing particle and the supporting medium (giving rise to e.g., charge transfer or dielectric changes) upon exposure to the reactants.

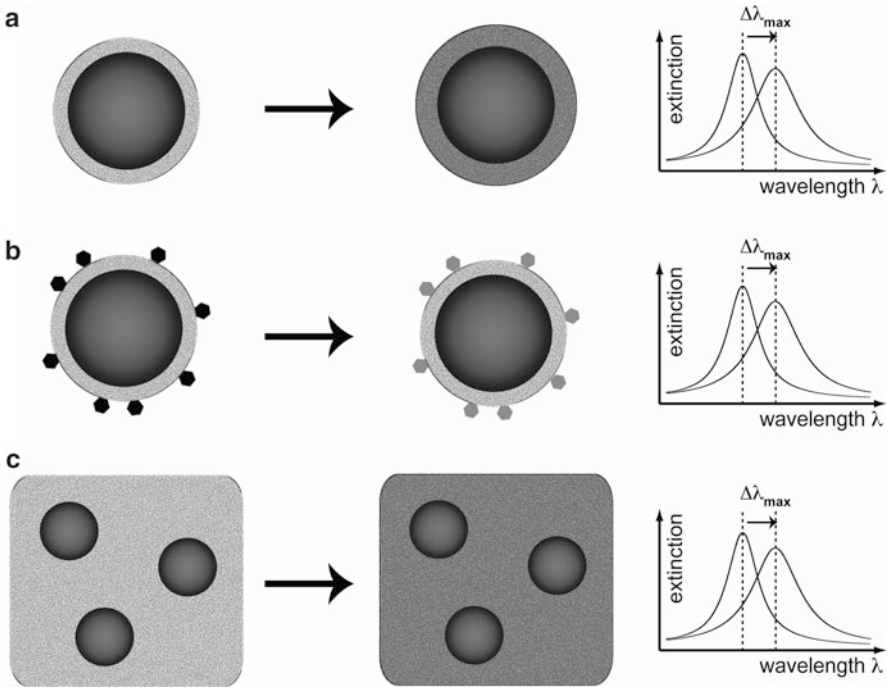

Fig. 8.8 Different types of arrangements to study changes on/in nanomaterials adjacent to plasmonic sensing nanoparticles. (**a**) A thin layer of a nanomaterial, in/on which a chemical and/or structural change takes place upon interaction with the environment, is in direct contact with a plasmonically active sensor nanoparticle. (**b**) Changes occur on/within nanoparticles or a thin film separated from the plasmonically active sensing particles by an inert or chemically active dielectric spacer layer. (**c**) The plasmonic sensing nanoparticles are dispersed into a medium, which undergoes a change upon interaction with a surrounding medium or a temperature variation

Nanoplasmonic Gas Sensing: Metal Oxide Composite Films

Optical sensors have several advantages over conventional charge transport-based gas sensors such as higher resistivity to electromagnetic noise, operability in fiber optic networks, and the potential of multi-gas detection using differences in the intensity, wavelength, phase, and polarization of the output light signals. Materials whose optical absorption properties change reversibly upon the interaction with gases are suitable for optical chemical sensors. In 1990 Haruta and coworkers investigated the gas-sensing performance of Au composite films of transition metal oxides [37]. By then it had already been shown that the catalytic activities of base metal oxides at low temperatures are enhanced by the presence of Au nanoparticles [38]. Haruta and coworkers first demonstrated enhanced gas-sensing performance for NiO films [37, 39, 40], but later found enhancement effects (compared to the metal oxide films without Au nanoparticles) for other composite

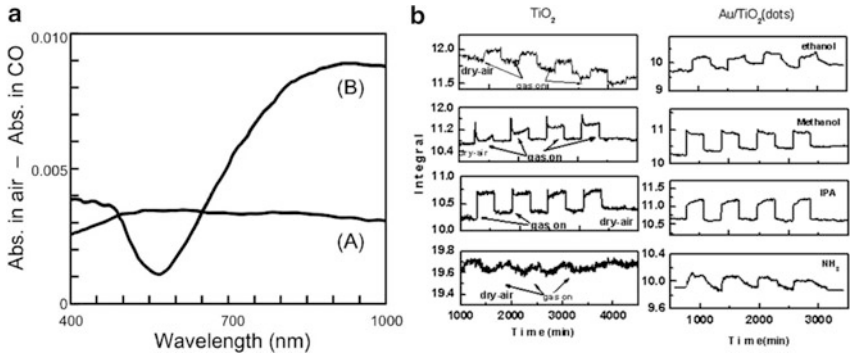

Fig. 8.9 (**a**) Difference spectra of the NiO films without (A) and with (B) Au nanoparticles in the presence and in the absence of 1 vol.% CO in air. Reprinted from ref. [37], copyright 1993, with permission from Elsevier. (**b**) Optical absorption curves for the TiO_2 films and the TiO_2 films with Au dots measured in the presence of dry air and spaced out repeatedly with different analytes: vapors of methanol (6,000 ppm), ethanol (6,000 ppm), isopropanol (IPA, 600 ppm), and NH_3 (50 ppm). The curves represent the change of the integrated intensity (*I*) under the absorption curve in the range of 300–600 nm. Reprinted from ref. [46], copyright 2008, with permission from Elsevier

systems as well, including CuO [41], WO [42], and Co_3O_4 [43]. The difference in absorbance when NiO (A) and NiO/Au (B) composite films were exposed to air and CO is shown in Fig. 8.9a [37]. As can be seen in the figure the absorbance change was greatly enhanced by depositing gold on the NiO film, except for in the wavelength region corresponding to the plasmon absorption of the colloidal Au, where a decrease was observed.

In 2009, Buso et al. used gold nanoparticle monolayers deposited using a fast chemisorption protocol for producing Au–NiO multilayer films which showed a reversible optical absorbance change when exposed to CO (100–10,000 ppm) at 300°C [44].

Haruta and coworkers attributed the improvements of metal oxide gas sensors that they obtained when adding colloidal Au to two different effects [45]: (1) An enhanced catalytic activity of the composite material compared to the pure transition metal oxide film. In this case the gas sensitive optical absorption change comes solely from the oxide film. (2) The dielectric constant of the transition metal oxide film changes during interaction with the gas causing a change in the plasmon absorption of the Au particles. They found that these two types of effects sometimes, but not always, occur at the same time. Ando et al. [45] for example, showed that the plasmon absorption in Au/CuO composite films was reversibly changed by CO and to a much smaller extent by H_2, providing a means for separating the signals from CO and H_2.

The pioneering work by Haruta et al. was in 2008 followed up in a study by Manera et al. [46] who performed optical gas-sensing measurements by SPR and LSPR on TiO_2/Au composite films, deposited by a sol–gel technique, when

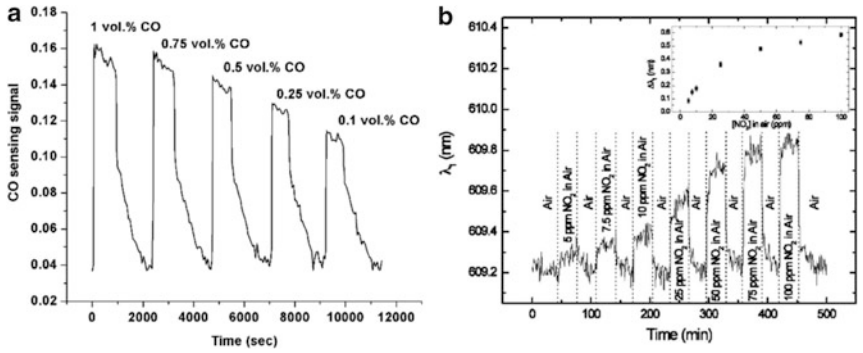

Fig. 8.10 (**a**) Sensing signal (i.e., distance between the two peaks in the CO-Air difference spectrum) response curve of the Au-YSZ nanocomposite film upon exposure to 1, 0.75, 0.5, 0.25, and 0.1 vol.% CO in air at 500°C. Adapted with permission from ref. [47]. Copyright 2006 American Chemical Society. (**b**) The plasmon peak position of the Au-YSZ film at 500°C under exposure to varying amounts of NO_2 in air. The inset displays the calibration curve obtained for exposure to NO_2 concentrations from 5 to 100 ppm in air. Adapted with permission from ref. [49]. Copyright 2008 American Chemical Society

interacting with alcohol vapors. A similar increase in the optical absorption in the spectral range 300–600 nm was observed upon exposure to all types of alcohols. The responses were larger than those recorded for TiO_2 thin films without Au particles. Figure 8.9b shows the optical responses when exposing TiO_2 and TiO_2/Au films to vapors of methanol, ethanol, isopropanol (IPA), and NH_3. The shown signal is the integrated intensity under the absorption curve in the range 300–600 nm. The SPR measurements suggested that the observed LSPR shifts were due to changes in the real part of the matrix refractive index or thickness due to the diffusion and adsorption of the analyte molecules.

Charge Transfer to Plasmonic Particles due to Chemical Reactions

Plasmon shifts induced by electron transfer can also be used for gas-sensing application as shown by Carpenter and coworkers who used nanocomposite materials consisting of Au nanoparticles in an yttrium stabilized zirconia (YSZ) matrix for CO [47], H_2 [48], and NO_2 [49] detection. Figure 8.10a shows the sensing signal (distance between the two peaks in the CO-Air difference spectrum) response when exposing the structure to CO concentrations ranging from 0.1 to 1 vol.% in air at 500°C. A linear dependence of the sensing signal with CO concentration was found. This behavior was not observed upon exposure to CO in an N_2 carrier gas, indicating an oxygen-dependent reaction mechanism. Additionally, no measurable signal was observed below temperatures of approximately 400°C. The latter two observations coupled with the oxygen ion formation and

conduction properties of the YSZ matrix are indicative of charge-transfer reactions occurring at the three-phase boundary region between oxygen, Au and YSZ, which results in a net charge transfer into the Au. In the presence of oxygen, electrons are removed from the Au nanoparticles during the dissociative adsorption and ionization of the oxygen species. A positively charged metal center is thus formed in the immediate vicinity of the nanoparticle-matrix interface. When the YSZ-Au nanocomposite is exposed to CO, ionized oxygen species are consumed by the CO oxidation reaction and electrons are transferred back to the Au nanoparticles [47].

To further demonstrate the gas-sensing capabilities of these Au-YSZ nanocomposite films, Rogers et al. [48] performed a detailed O_2/H_2 titration study. They found that the degree of charge transfer to Au was dictated by the equilibrium ratio ${pH_2}^{1/4}/{pO_2}^{1/8}$, contributing to oxygen ion diffusion into and out of the YSZ matrix. Similarly, they found that the Au-YSZ composite is sensitive to changes in the NO_2 concentration dictated by the ratio ${pO_2}^{-1/8}{pNO_2}^{-1/4}$ [49]. Figure 8.10b shows the plasmon peak position as a function of time upon the exposure of the Au-YSZ nanocomposite film to 5–100 ppm NO_2 in air. The detection limit is estimated to be 5 ppm NO_2.

Indirect Nanoplasmonic Sensing

Indirect Nanoplasmonic Sensing (INPS) is a technique that was developed by the authors to study nanoparticles and structures in the sub-10 nm size range as well as thin films. The "indirect" nature of the approach makes it possible to study systems (in contrast to direct nanoplasmonic sensing described above) that do not themselves support a plasmon resonance. The latter is either because they are nonmetallic or because they have very small optical cross-sections and plasmon energies in the UV spectral range, due to their small size, which complicates optical spectroscopy. Since the INPS platform is surface based, structural analysis of the studied sample nanomaterials by e.g., microscopic techniques (SEM, TEM, AFM) is straightforward and experiments with geometrically and chemically well-defined nanomaterials as well as on single particles are possible. Furthermore, the provided possibility of the method to with very high sensitivity *and* temporal resolution operate under realistic (for applications) pressure and temperature conditions with small sample amounts is very important. In this way the INPS method can overcome numerous shortcomings of other techniques, which often are related to pressure restrictions, large required sample material amounts, low sensitivity, non-isothermicity, and low temporal resolution.

The INPS platform consists of plasmonically active nanoparticles (typically Au) that are physically separated from the nanosized system to be studied by a thin dielectric spacer/substrate layer as schematically depicted in Fig. 8.11. The sensing elements or sensor (nano)particles, (i.e., the gold nanodisks in the presented

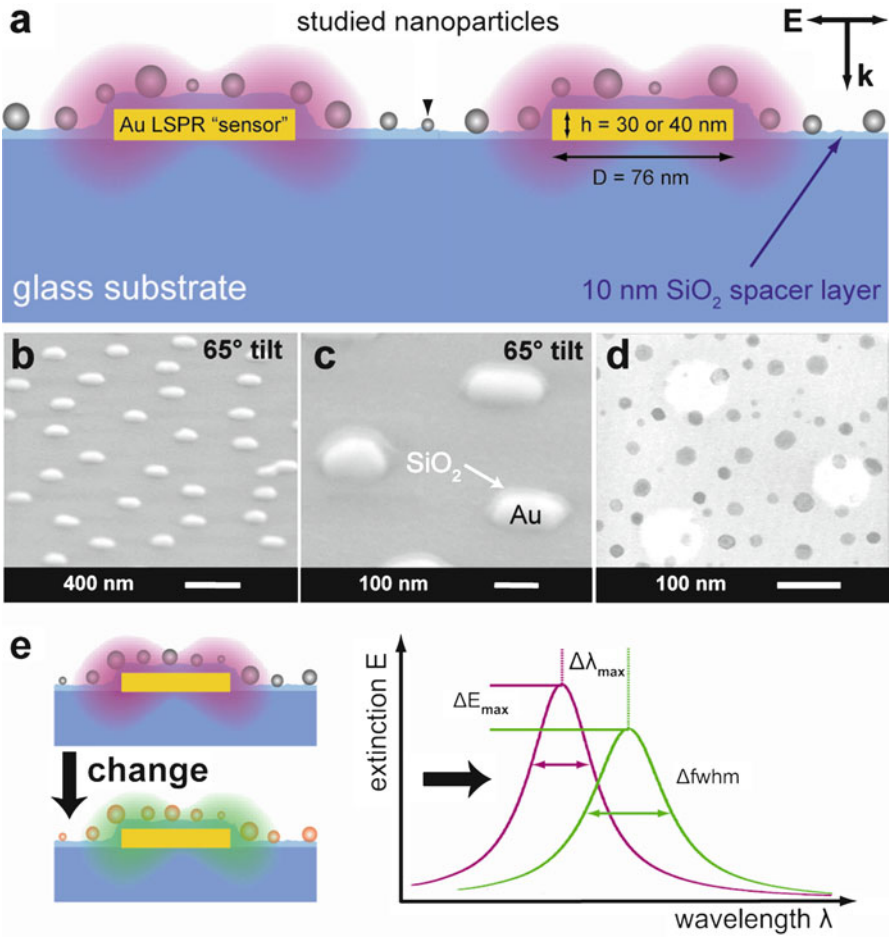

Fig. 8.11 (**a**) Schematic depiction the INPS platform. (**b**, **c**) SEM images of INPS chips decorated with Au nanodisks and 10 nm SiO_2 spacer layer. (**d**) Superimposed SEM (Au nanodisk sensors $\langle D \rangle = 76$ nm) and TEM (Pd nanoparticles $\langle D \rangle = 18.6$ nm) images with identical scales illustrating the typical number of nanoparticles in the sensing volume of an individual Au sensor when studying clusters as in several of the examples below. (**e**) Schematic illustration of the INPS detection and readout principle. Adapted with permission from ref. [51]

examples below), are thereby embedded in the sensor surface and not physically interacting with the studied nanomaterial, which is deposited onto the dielectric spacer (hence the name *indirect* sensing). The dipole field from the LSPR penetrates though the spacer layer and has considerable strength also on and in the proximity of its surface (Fig. 8.11) and can in this way e.g., sense dielectric changes there. Other possible sensing mechanisms are either related to the detection of dielectric changes within the spacer layer and/or charge transfer from/to the Au sensor particles induced by the studied process. Furthermore, as shown below,

INPS can be used to measure local temperature at the nanoscale by relying on an "optical nano-calorimetry" sensing principle, using the intrinsic temperature sensitivity of LSPR [50].

The presence of the dielectric spacer layer drastically widens the range of applicability of nanoplasmonic sensing in the following ways: (1) The spacer can have a purely protective function and prevents alloy formation or reactions between the sensor and the studied nanomaterials. (2) It makes measurements in harsh/abrasive environments and at high temperatures possible by e.g., retaining the shape of the sensor nanoparticles. (3) It provides a tailored surface chemistry for different applications since it basically can be chosen freely. (4) In the role of a substrate material it can either be chosen to be inert or to actively participate in the studied process and in this way, for example, increase the number of sensing mechanisms that can be exploited.

In the following, a number of application examples of INPS are presented. The INPS sensor chips in all these examples were very similar and consisted of nanofabricated amorphous 2-D arrangements of plasmonically active Au nanodisks deposited by Hole-mask Colloidal Lithography [10] onto a glass substrate, covered with a thin dielectric spacer layer, typically SiO_2.

Heterogeneous Catalysis

Heterogeneous catalysis is of vast economic and societal importance for the energy, chemical industry, and environmental sectors with the (probably) most well-known example being the catalytic converter for cars. During a catalytic reaction the reactants are converted to desired product on the surface of the catalyst (a material in the solid phase). For many applications the catalyst is composed of catalytically active nanoparticles (1–10 nm), which are dispersed on a porous, high surface area support material.

In 2009 Larsson et al. used INPS to study reactant surface coverage changes during heterogeneous catalytic reactions [35] on nanocatalysts under realistic application conditions. In particular it was shown that it is possible to monitor changes in the surface coverage of reactant molecules on a Pt nanocatalyst with a sensitivity of <0.1 monolayers of oxygen. As demonstrators the oxidation reaction of CO and H_2 and INPS chips decorated with Au nanodisks with a diameter of 76 nm, a height of 20 nm, and covered with a 10 nm SiO_2 spacer layer were used.

Figure 8.12a shows the result for a CO oxidation experiment, which was performed by step-wise varying the relative CO concentration, $\alpha^{CO} = [CO]/([CO] + [O_2])$, from carbon monoxide rich to oxygen rich and back again, while continuously recording $\Delta\lambda_{max}$ by measuring optical transmission through a quartz tube reactor with an INPS sensor chip placed inside. The sample temperature was measured with a thermocouple in contact with the sample/chip surface. The total reactant ($CO + O_2$) concentration was kept constant at atmospheric pressure. The most important result is the discontinuous step up (down) in $\Delta\lambda_{max}$ at a critical reactant mixture of $\alpha_{cr}^{CO} = 0.07$ (blue curves,

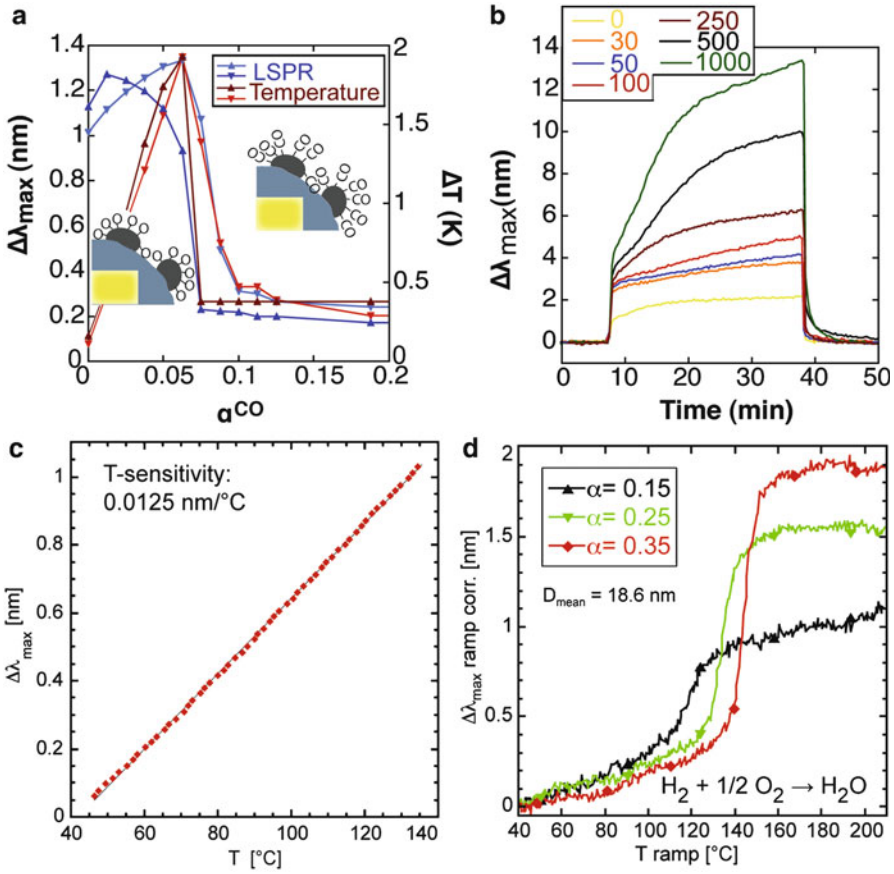

Fig. 8.12 (**a**) LSPR shift (*blue*) and temperature change (*red*) during sweeps of the relative CO concentration (α^{CO}) in Ar carrier gas at 506 K. The total reactant concentration (CO + O_2) was 8 %. The schematic depictions to the left and right of the step in $\Delta\lambda_{max}$ illustrate the change in surface coverage upon passing the kinetic phase transition. (**b**) NO_x storage and release (as N_2) from BaO. The curves show LSPR peak shifts during 30 min NO_2 storage for seven different concentrations (the numbers given in the figure are in ppm), in a constant oxygen background, and subsequent release by exposure to 2 % H_2. Adapted with permission from ref. [35]. (**c**) Optical nanocalorimetry: Depiction of the linear T-dependence of the LSPR of a INPS chip, yielding a temperature sensitivity of $\Delta\lambda_{max} = 0.0125$ nm/°C. (**d**) Catalytic light-off traces obtained for the hydrogen oxidation on Pd with $\langle D \rangle = 18.6$ nm for $\alpha = 0.15, 0.25, 0.35$ ($\alpha = [H_2]/([H_2] + [O_2])$ in Ar carrier gas at 4 % total reactant concentration. The displayed $\Delta\lambda_{max}$ values correspond to LSPR peak shifts induced by local heating of the Au sensor nanodisks by the exothermic reaction ($\Delta H = 250$ kJ/mol). Adapted with permission from ref. [51]. Copyright 2010 American Chemical Society

Fig. 8.12a). This is the kinetic phase transition in the CO + O_2 reaction from an oxygen to a CO covered Pt nanocatalyst surface. This transition occurred, where the overall reaction had a rate maximum, as reflected very clearly in the peak in temperature (exothermic reaction).

In the same work by Larsson et al., INPS was also used to monitor nitric oxide (NO_x) storage in and release from BaO. For the NO_x sensing, the spacer layer consisted of 30 nm evaporated BaO and the Au nanodisks had a diameter of 105 nm with a height of 30 nm. Pt clusters of ca. 2 nm size were used as catalyst and deposited onto the BaO spacer layer.

The latter is a practically important reaction in automotive emission cleaning for diesel and so-called "lean burn" engines, i.e., engines operated at oxygen excess, where the conventional 3-way catalyst cannot reduce NO_x efficiently. This has led to development of so-called NO_x storage/reduction catalysts, where NO_x is temporarily (~1min) accumulated (often as $Ba(NO_3)_2$) in the catalyst, while the engine operates at O_2 excess and then the stored NO_x is reduced to N_2 by switching the air/fuel mixture to excess fuel, hydrocarbons (or H_2) for a few seconds. Larsson et al. showed that the NO_x storage in and release from BaO could be easily monitored using INPS. A concentration and storage time dependent response of the plasmon peak position was obtained (Fig. 8.12b, 0–1,000 ppm NO_2), indicating (at least) 2 ppm sensitivity.

Optical Calorimetry

Calorimetry is a widely used technique for investigating the thermodynamic and kinetic aspects of catalytic reactions. Also other processes like phase transitions or chemical reactions in the solid state are often studied by approaches like differential scanning calorimetry (DSC). The principle behind calorimetry in general is that by measuring the energy dissipation from an exothermic process one obtains a direct measure for, e.g., the conversion efficiency of a catalyst or the latent heat of a phase transition.

The LSPR is sensitive to temperature [50] and INPS can, therefore, be used to measure nanoscale local temperature changes in optical calorimetry-type measurements, as first demonstrated by Langhammer et al. in 2010 [51]. INPS chips decorated with Au nanodisks with a diameter of 76 nm, a height of 20 nm, and covered with a 10 nm SiO_2 spacer layer were used.

Figure 8.12c depicts the spectra peak shift, $\Delta\lambda_{max}$, vs. T characteristics of the INPS chip, indicating linear T-dependence and a temperature sensitivity of $\Delta\lambda_{max} = 0.0125$ nm/°C for this particular sensing structure used here.

Figure 8.12d shows so-called catalytic light-off traces (external heating-rate 4°C/min) obtained by Langhammer et al. [51] for Pd nanocatalysts with average diameter 18.6 nm for three different relative H_2 and O_2 concentrations ($\alpha = [H_2]/([H_2] + [O_2])$) in Ar carrier gas. To obtain this graph the $\Delta\lambda_{max}$-values were corrected for the peak shift induced by *external* heating of the reactor chamber. Therefore, the plotted peak shifts are those induced by *local* heating of the Au sensor nanodisks caused by the dissipated heat from the exothermic $H_2 + \frac{1}{2} O_2 \rightarrow H_2O$ reaction ($\Delta H = 250$ kJ/mol) on the Pd catalyst particles. The general form of the curves is a first slow rise of temperature (i.e., of the reaction rate), until a fast rise begins

(transition from kinetic limitation to mass transport limitation) and then a flattening, when the reaction reaches the mass transport limited regime, and therefore becomes rather insensitive to further temperature rise.

Hydrogen Storage

Langhammer et al. successfully used INPS to study size-effects in hydride formation and decomposition thermodynamics [51, 52] and kinetics [36, 51] of small Pd nanoparticles ($D < 8$ nm). INPS chips decorated with Au nanodisks with a diameter of 76 nm, a height of 20 nm, and covered with a 10 nm SiO_2 spacer layer, onto which the studied Pd clusters were deposited, were used. The actual "sensing" in these experiments was achieved through the coupling of the plasmonic near-field of the Au nanodisks to the changing dielectric properties of Pd nanoparticles as they absorbed or released hydrogen and the hydride phase was formed (for details see [51]).

In their first INPS hydrogen storage study Langhammer et al. [36] investigated the size dependence of the hydriding and dehydriding kinetics in Pd nanoparticles at room temperature. The kinetics exhibited very strong size dependence and a large difference in the time scales for hydriding (Fig. 8.13b) and dehydriding, related to different rate limiting steps for the two situations. The (exothermic) hydriding of a nanoparticle is limited by diffusion of hydrogen atoms from the surface layer to the metallic core via the hydride shell formed in this process since the hydride formation itself results from attractive hydrogen–hydrogen interactions. In the dehydriding case, the effect of surface tension was demonstrated in the article to be especially important to understand how the time scale of the kinetics depends on nanoparticle size.

In a second INPS study Langhammer et al. [52] have measured hydrogen absorption/desorption isotherms in Pd nanoparticles with an average diameter from 1.8 to 8 nm at 30°C. The isotherms were found to be fully reversible at relatively low and high hydrogen pressures. At intermediate pressures, however, hysteresis related to the hydride formation and decomposition was observed, as expected. In their study they found, that this hysteresis shrinks with decreasing particle size and becomes negligible for particles smaller than 2.5 nm (Fig. 8.13c). The observation was explained in terms of a diminishing contribution of lattice strain to the free energy of hydride formation for decreasing particle size.

A "calibration" of the INPS platform for hydrogen storage measurements, i.e., a determination of the scaling of the plasmonic response of the INPS sensor with the absolute hydrogen concentration in the studied Pd nanoparticles, was carried out using complementary QCM measurements by Langhammer et al. in a third study [51]. For this purpose Pd nanoparticles were prepared on a 10 MHz SC-cut quartz crystal resonator and the measured frequency shift was converted to hydrogen concentration. A linear scaling of the INPS sensor LSPR signal with the hydrogen concentration in the Pd nanoparticles was found.

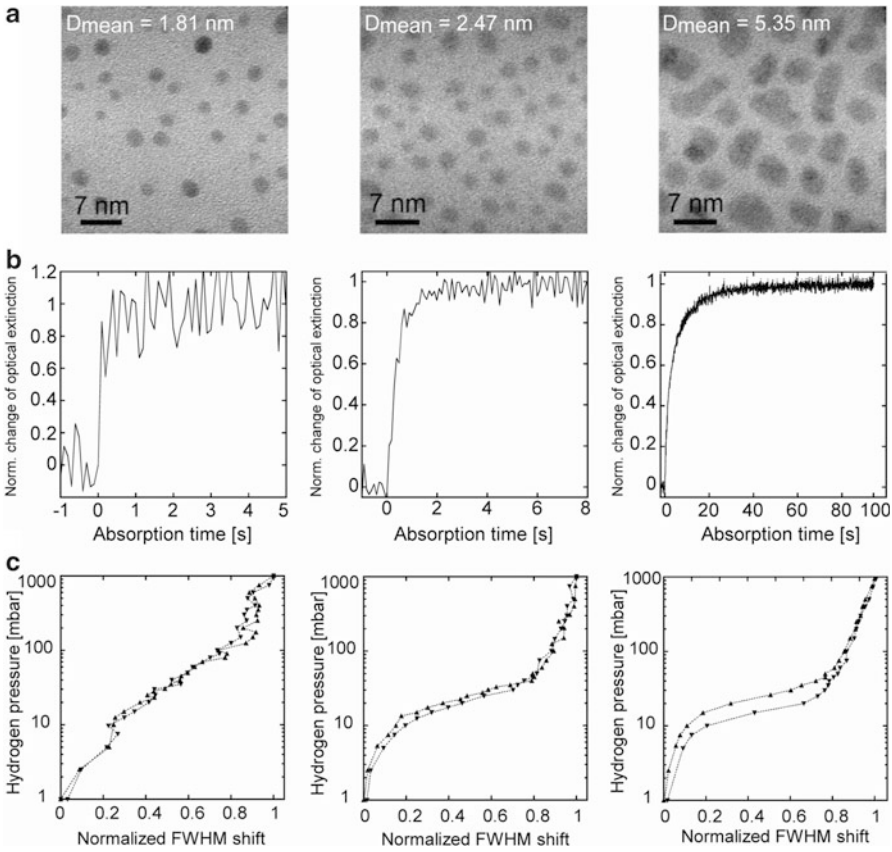

Fig. 8.13 (**a**) TEM images of the Pd nanoparticles studied with INPS. (**b**) Experimental hydriding kinetics for three different Pd nanoparticle diameters. The change of the optical extinction is normalized in such a way that "1" corresponds to 100 % conversion of Pd nanoparticles to the hydride phase. (**c**) Hydrogen absorption/desorption isotherms at 30°C for three different Pd nanoparticle sizes. The normalized FWHM shift is proportional to hydrogen concentration in the Pd particles. (**a**, **b**) Adapted with permission from ref. [36], copyright 2010 American Physical Society. (**c**) Adapted from ref. [52], copyright 2010, with permission from Elsevier

Polymer Phase Transitions

As yet another application example of INPS, Langhammer et al. [51] have studied phase transitions in polymers; in particular, the size-/thickness dependence of the glass transition temperature (T_g) in polystyrene (PS) nanoparticles and thin films of atactic poly(methyl methacrylate) (PMMA). This example illustrates the applicability of INPS to study confined *nonmetallic* systems and thin films. INPS chips decorated with Au nanodisks with a diameter of 76 nm, a height of 20 nm, and covered with a 10 nm SiO_2 spacer layer were used.

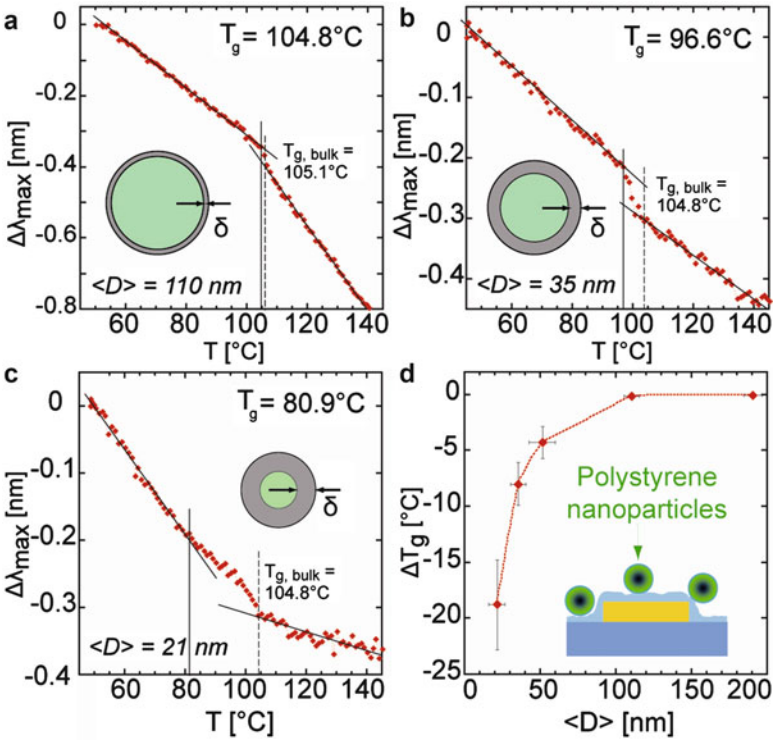

Fig. 8.14 (**a**) LSPR response of an INPS chip decorated with PS nanoparticles upon heating after subtracting the temperature response of the Au sensor. The change in slope of the LSPR response is attributed to the glass transition of the polymer. An upper and lower transition temperature can be defined. $T_{g,\ bulk}$ is attributed to the glass transition in the bulk of the nanosphere and T_g to the transition in a thin surface layer with higher molecular mobility and thickness δ. (**b**) Glass transition trace for $\langle D \rangle = 35$ nm. (**c**) Same as in (**a**, **b**) but for $\langle D \rangle = 21$ nm. (**d**) A plot of the transition temperature T_g vs. average particle diameter. The error bars on the *y*-axis represent three identical individual measurements. Adapted with permission from ref. [51]. Copyright 2010 American Chemical Society

The glass transition in polymers is related to significant slowing of the motion of polymer chain segments when cooled below a critical and material-specific temperature, the glass transition temperature T_g. In nanosystems T_g is known to become size/thickness dependent due to the existence of a near surface layer (few nanometers thick), where polymer segments have a different mobility (compared to the bulk) due to different steric constraints. For decreasing film thickness/particle size this surface/interface contribution becomes larger and the average dynamics becomes faster or slower (depending on the nature of the interface). This typically results in a decrease (or increase) of T_g and general broadening of the glass transition region.

Figure 8.14 shows T_g measurements, using INPS, on PS nanoparticles with average diameters ranging from 21 to 190 nm. The $\Delta\lambda_{max}$-values in the figure have been

corrected for the peak shift caused by external heating. Langhammer et al. defined T_g as the temperature at which $\Delta\lambda_{max}$ started deviating from a linear fit to the $\Delta\lambda_{max}$ vs. T curve (indicated by the black solid line) and found a very pronounced particle size dependence of T_g for $D < 100$ nm. The INPS measurements also showed the expected broadening of the glass transition T-range (indicated by the dashed vertical lines) for decreasing particle size.

Conclusions

Nanoplasmonic sensing, both direct and indirect approaches, is an excellent characterization tool for nanomaterials science, catalysis, and optical nano-calorimetry. Furthermore, LSPRs are very effective transducers for optical gas-sensing applications with great potential for miniaturization. Particular advantages for both types of applications, characterization tool and sensor, are the combination of broad applicability (real time in situ measurements on metallic and nonmetallic (nano)materials, nanoparticles and thin films), the quality of the obtainable information, the high absolute sensitivity and time resolution, as well as the general robustness. Furthermore, with appropriate design of the sensors and owing to the remote nature of the optical readout applications in harsh environments and at high temperatures are feasible. Thanks to the fact that the sensor platforms for research applications can be made surface based (as e.g., the INPS approach), combinatory studies with advanced electron microscopy (SEM, TEM) or other (surface-) spectroscopies are also possible (e.g., Fourier transformed infrared or Raman spectroscopy). Such combinatory approaches together with appropriate choice of active materials on the nanoplasmonic sensor may also facilitate multiplexing in the future, by e.g., using different areas on a single sample, optimized to detect different changes (e.g., temperature) or reactions/interactions of interest. Nanoplasmonic sensing is ideal for multiplexing approaches due to the very small "spot-size" (<10 μm) required for each measurement area.

References

1. Anker JN, et al. Biosensing with plasmonic nanosensors. Nat Mater. 2008;7:442–53.
2. Li Y, Somorjai GA. Nanoscale advances in catalysis and energy applications. Nano Lett. 2010;10(7):2289–95.
3. Atwater HA, Polman A. Plasmonics for improved photovoltaic devices. Nat Mater. 2010;9:205–13.
4. Zhu J, Cui Y. Photovoltaics: more solar cells for less. Nat Mater. 2010;9:183–4.
5. Maier SA, et al. Local detection of electromagnetic energy transport below the diffraction limit in metal nanoparticle plasmon waveguides. Nat Mater. 2003;2:229–32.
6. Arico AS, Bruce P, Scrosati B, Tarascon J-M, van Schalkwijk W. Nanostructured materials for advanced energy conversion and storage devices. Nat Mater. 2005;4:366–77.

7. Guo Y-G, Hu J-S, Wan L-J. Nanostructured materials for electrochemical energy conversion and storage devices. Adv Mater. 2008;20:2878–87.
8. Schlapbach L, Zuttel A. Hydrogen-storage materials for mobile applications. Nature. 2001;414:353–8.
9. Koo OM, Rubinstein I, Onyuksel H. Role of nanotechnology in targeted drug delivery and imaging: a concise review. Nanomedicine. 2005;1:193–212.
10. Fredriksson H, et al. Hole-mask colloidal lithography. Adv Mater. 2007;19:4297–302.
11. Langhammer C, Yuan Z, Zoric I, Kasemo B. Plasmonic properties of supported Pt and Pd nanostructures. Nano Lett. 2006;6:833–8.
12. Langhammer C, Kasemo B, Zoric I. Absorption and scattering of light by Pt, Pd, Ag, and Au nanodisks: absolute cross sections and branching ratios. J Chem Phys. 2007;26(19):194702.
13. Pakizeh T, Langhammer C, Zoric I, Apell P, Kall M. Intrinsic fano interference of localized plasmons in Pd nanoparticles. Nano Lett. 2009;9:882–6.
14. Bigall NC, et al. Monodisperse platinum nanospheres with adjustable diameters from 10 to 100 nm: Synthesis and distinct optical properties. Nano Lett. 2008;8:4588–92.
15. Wang H, Tam F, Grady NK, Halas NJ. Cu nanoshells: effects of interband transitions on the nanoparticle plasmon resonance. J Phys Chem B. 2005;109:18218–22.
16. Chan GH, Zhao J, Hicks EM, Schatz GC, Van Duyne RP. Plasmonic properties of copper nanoparticles fabricated by nanosphere lithography. Nano Lett. 2007;7:1947–52.
17. Duan JL, et al. Surface plasmon resonances of Cu nanowire arrays. J Phys Chem C. 2009;113:13583–7.
18. Langhammer C, Schwind M, Kasemo B, Zoric I. Localized surface plasmon resonances in aluminum nanodisks. Nano Lett. 2008;8:1461–71.
19. Chan GH, Zhao J, Schatz GC, Van Duyne RP. Localized surface plasmon resonance spectroscopy of triangular aluminum nanoparticles. J Phys Chem C. 2008;112:13958–63.
20. Ekinci Y, Solak HH, Löffler JF. Plasmon resonances of aluminum nanoparticles and nanorods. J Appl Phys. 2008;104:083107.
21. Schwind M, Zhdanov VP, Zoric I, Kasemo B. LSPR study of the kinetics of the liquid-solid phase transition in Sn nanoparticles. Nano Lett. 2010;10:931–6.
22. Gao HW, Henzie J, Lee MH, Odom TW. Screening plasmonic materials using pyramidal gratings. Proc Natl Acad Sci U S A. 2008;105:20146–51.
23. Berube V, Radtke G, Dresselhaus M, Chen G. Size effects on the hydrogen storage properties of nanostructured metal hydrides: A review. Int J Energ Res. 2007;31:637–63.
24. Langhammer C, Zoric I, Kasemo B, Clemens BM. Hydrogen storage in Pd nanodisks characterized with a novel nanoplasmonic sensing scheme. Nano Lett. 2007;7:3122–7.
25. Isidorsson J, Giebels I, Arwin H, Griessen R. Optical properties of MgH2 measured in situ by ellipsometry and spectrophotometry. Phys Rev B. 2003;68:115112.
26. Zoric I, Larsson EM, Kasemo B, Langhammer C. Localized surface plasmons shed light on nanoscale metal hydrides. Adv Mater. 2010;22(41):4628–33.
27. Fukai Y. The Metal-Hydrogen System. Berlin: Springer; 1993.
28. Yeshchenko OA, Dmitruk IM, Alexeenko AA, Dmytruk AM. Size-dependent melting of spherical copper nanoparticles embedded in a silica matrix. Phys Rev B. 2007;75:085434.
29. Yeshchenko OA, et al. Surface plasmon as a probe for melting of silver nanoparticles. Nanotechnology. 2009;21(4):045203.
30. Yeshchenko OA, et al. Influence of interparticle interaction on melting of gold nanoparticles in Au/polytetrafluoroethylene nanocomposites. J Appl Phys. 2009;105:094326.
31. Ung T, Liz-Marzan LM, Mulvaney P. Redox catalysis using Ag@SiO2 colloids. J Phys Chem B. 1999;103:6770–3.
32. Mulvaney P, Pérez-Juste J, Giersig M, Liz-Marzán L, Pecharromán C. Drastic surface plasmon mode shifts in gold nanorods due to electron charging. Plasmonics. 2006;1:61–6.
33. Novo C, Funston AM, Mulvaney P. Direct observation of chemical reactions on single gold nanocrystals using surface plasmon spectroscopy. Nat Nanotechnol. 2008;3:598–602.

34. Novo C, Funston AM, Gooding AK, Mulvaney P. Electrochemical charging of single gold nanorods. J Am Chem Soc. 2009;131:14664–6.
35. Larsson EM, Langhammer C, Zoric I, Kasemo B. Nanoplasmonic probes of catalytic reactions. Science. 2009;326:1091–4.
36. Langhammer C, Zhdanov VP, Zoric I, Kasemo B. Size-dependent kinetics of hydriding and dehydriding of Pd nanoparticles. Phys Rev Lett. 2010;104:135502.
37. Kobayashi T, Ando M, Haruta M. Enhancing effect of gold deposition in the optical detection of reducing gases in air by metal oxide thin films. Sensor Actuat B. 1993;13–14:545–6.
38. Haruta M, Yamada N, Kobayashi T, Iijima S. Gold catalysts prepared by coprecipitiation for low-temperature oxidation of hydrogen and carbon monoxide. J Catal. 1989;115:301–9.
39. Ando M, Kobayashi T, Haruta M. Enhancement in the optical CO sensitivity of NiO film by the deposition of ultrafine gold particles. J Chem Soc Farad T. 1994;90:1011–3.
40. Ando M, Zehetner J, Kobayashi T, Haruta M. Large optical CO sensitivity of NO2-pretreated Au-NiO composite films. Sensor Actuat B. 1996;35–36:513–6.
41. Ando M, Kobayashi T, Haruta M. Optical CO detection by use of CuO/Au composite film. Sensor Actuat B. 1995;24–25:851–3.
42. Ando M, Chabicovsky R, Haruta M. Optical hydrogen sensitivity of nobel metal—tungsten oxide composite films prepared by sputter deposition. Sensor Actuat B. 2001;76:13–7.
43. Ando M, Kobayashi T, Haruta M. Optical recognition of CO and H2 by use of a gas-sensitive Au-Co3O4 composite film. J Mater Chem. 1997;7:1779–83.
44. Buso D, et al. Self-assembled gold nanoparticle monolayers in sol-gel matrices: synthesis and gas sensing applications. J Mater Chem. 2009;19:2051–7.
45. Ando M, Kobayashi T, Iijima S, Haruta M. Optical CO sensitivity of Au-CuO composite film by use of the plasmon absorption change. Sensor Actuat B. 2003;96:589–95.
46. Manera MG, et al. Optical gas sensing of TiO2 and TiO2/Au nanocomposite thin films. Sensor Actuat B: Chem. 2008;132:107–15.
47. Sirinakis G, Siddique R, Manning I, Rogers PH, Carpenter MA. Development and characterization of Au-YSZ surface plasmon resonance based sensing materials: High temperature detection of CO. J Phys Chem B. 2006;110:13508–11.
48. Rogers PH, Sirinakis G, Carpenter MA. Direct observations of electrochemical reactions within Au-YSZ thin films via absorption shifts in the an nanoparticle surface plasmon resonance. J Phys Chem C. 2008;112:6749–57.
49. Rogers PH, Sirinakis G, Carpenter MA. Plasmonic-based detection of NO2 in a harsh environment. J Phys Chem C. 2008;112:8784–90.
50. Liu M, Pelton M, Guyot-Sionnest P. Reduced damping of surface plasmons at low temperatures. Phys Rev B. 2009;79:035418.
51. Langhammer C, Larsson EM, Kasemo B, Zoric I. Indirect nanoplasmonic sensing: ultrasensitive experimental platform for nanomaterials science and optical nano-calorimetry. Nano Lett. 2010;10(9):3529–38.
52. Langhammer C, Zhdanov VP, Zoric I, Kasemo B. Size-dependent hysteresis in the formation and decomposition of hydride in metal nanoparticles. Chem Phys Lett. 2010;488:62–6.

Chapter 9
Functional Nanoimprinted Plasmonic Crystals for Chemical Sensing and Imaging

An-Phong Le, Stephen K. Gray, Ralph G. Nuzzo, and John A. Rogers

Abstract We describe here nanoimprinted plasmonic crystals composed of highly uniform subwavelength metal nanohole and nanopost arrays and their application in surface-enhanced sensing and imaging. Soft nanoimprint lithography is a versatile, cost-effective method to precisely replicate these structures with well-characterized optical properties. These plasmonic crystals support multiple surface plasmon modes controlled by the design rules of the nanostructures, allowing us to optimize the devices for operation in a particular wavelength range. We have demonstrated the ability to spectroscopically measure bulk refractive index changes and mechanical deformation of hydrogels resulting from pH changes, thin film imaging with sensitivities down to submonolayer levels using a common optical microscope, and Raman signal enhancement using a single common device framework. These plasmonic crystals have the potential to overcome many of the technological limitations that have limited the widespread application and integration of surface-enhanced analytical techniques.

A.-P. Le
Department of Chemistry, University of Illinois at Urbana-Champaign, Urbana, IL 61801, USA

S.K. Gray
Center for Nanoscale Materials, Argonne National Laboratory, Argonne, IL 60439, USA

R.G. Nuzzo • J.A. Rogers (✉)
Department of Chemistry, University of Illinois at Urbana-Champaign, Urbana, IL 61801, USA

Department of Materials Science and Engineering, University of Illinois at Urbana-Champaign, Urbana, IL 61801, USA
e-mail: jrogers@ad.uiuc.edu

A. Dmitriev (ed.), *Nanoplasmonic Sensors*, Integrated Analytical Systems,
DOI 10.1007/978-1-4614-3933-2_9,

Introduction to Surface Plasmon Resonance and Plasmonic Nanostructure Fabrication

Surface plasmons are resonant oscillations of conduction electrons at the metal-dielectric interface excited by the coupling of incoming electromagnetic radiation to the metal surface which gives rise to an evanescent electric field that extends from the metal surface a few hundreds of nanometers into the surrounding medium [1–4]. Even small changes in the dielectric material's refractive index can generate large changes in the resonance conditions of these surface plasmons. This combination of refractive index sensitivity and a small sensing volume has attracted great interest in the application of surface plasmon resonance (SPR) for label-free chemical sensing applications [5, 6]. Indeed, SPR sensors are commonly used to quantitatively detect both chemical and biological analytes in their native state, side-stepping potential concerns related to the inclusion of fluorescent or radioactive labels.

Traditional SPR sensors use flat metal films (typically gold) to generate surface plasmon polaritons which can propagate tens to hundreds of microns along the metal-dielectric interface [7–9]. Light is coupled into the metal film at an angle using a prism in the Kretschmann configuration, exciting a single SPR in the metal film [10–12]. This resonance is identified by a minimum in the spectrum of light reflected from the metal film, and changes in the refractive index of the local environment result in changes in the position and magnitude of this reflectance minimum. Although the resulting data are relatively easy to interpret, the physical equipment can be cumbersome and difficult to integrate with other systems for low-cost or high-throughput detection schemes [13].

Metal grating-based and metal nanoparticle-based systems can give rise to localized surface plasmon resonances (LSPRs) in which the surface plasmon is confined within or around the nanostructure [4, 14–17]. (Metal gratings can take the form of one-dimensional or two-dimensional arrays and can generate both SPP and LSPR modes in the metal film [14, 18].) In contrast to propagating surface plasmon polaritons, these LSPRs can be used to make measurements of the local refractive index with higher spatial resolution. These nanostructured metals can efficiently couple light into surface plasmons with simpler optics, making them more amenable for lower cost devices. The electric field intensity of LSPRs can be higher than that of SPPs, attracting interest in using these substrates for other surface-enhanced spectroscopy techniques such as surface-enhanced Raman scattering (SERS) and surface-enhanced fluorescence [19–29]. Raman signal enhancements upwards of 10^{10} for a single molecule have been reported, providing chemically specific information without the need for additional labels with great sensitivity [20, 30–35].

The widespread application of surface-enhanced spectroscopies, in general, has been limited by the poor reproducibility of the substrates that give rise to the surface enhancement itself [20]. Production techniques for these substrates would ideally generate highly uniform structures over large areas at low cost. Photolithography

and thin film processing techniques can be used to fabricate large areas of high-quality nanostructures but at relatively high cost. Electron beam lithography and focused ion beam lithography are capable of creating a diverse array of nanostructures including holes[36, 37], grooves[38], slits[39], and nanoparticles [40, 41] with high reproducibility and fine control over structures' dimensions, but they are not easily scaled to large areas or high production rates.

Recent reports describe the use of soft interference lithography to create plasmonic nanostructures over large areas [42–45]. An elastomeric stamp is cast from a lithographically defined master and is used as a phase mask for phase-shifting photolithography. Subsequent metal deposition and etching steps can create both nanoparticles and free-standing nanostructured metal films with centimeter-scale areas. However, these substrates come at the expense of higher cost and processing complexity.

The use of close-packed nanospheres as a deposition template allows the formation of continuously structured metal-film-over-nanosphere structures which have generated very high SERS enhancement factors [46–48]. The close-packed nanosphere layer can also be used as a deposition mask to selectively allow metal nanoparticles to be deposited onto a substrate with high size and spatial control. These nanosphere lithography techniques can generate defect-free nanostructures over areas of 10–100 μm^2 [49]. The use of larger colloidal spheres adsorbed onto a surface has been used to generate different structures including rings and crescents, but these nanostructures are generally more randomly distributed [50–52].

Soft nanoimprint lithography addresses the need for a relatively low-cost fabrication technique that can generate high-quality, high-resolution, uniform nanostructures over large areas [4, 53–55]. Relatively simple changes in the fabrication process of these nanoimprinted plasmonic crystals can greatly shift the spectral sensitivity of the devices which can be harnessed for SPR spectroscopy and imaging. These plasmonic crystals can quantitatively detect binding events at even submonolayer levels, comparable to the sensitivity of more conventional SPR devices [4]. Their applications extend from bulk refractive index sensing via SPR spectroscopy to thin film imaging using SPR and SERS with micrometer-scale lateral resolution over square millimeter areas [4, 24, 56–59]. The fabrication and demonstrated applications of these nanoimprinted plasmonic crystals are herein discussed.

Soft Nanoimprint Lithography for the Facile Production of Plasmonic Crystals

A generalized summary of nanoimprint lithography for the production of plasmonic crystals is depicted in Fig. 9.1 [4, 24, 54, 56, 57]. A master consisting of a square array of holes is created in a photoresist (PR) layer on silicon from which an elastomeric stamp is cast. To replicate the nanohole array, a composite poly

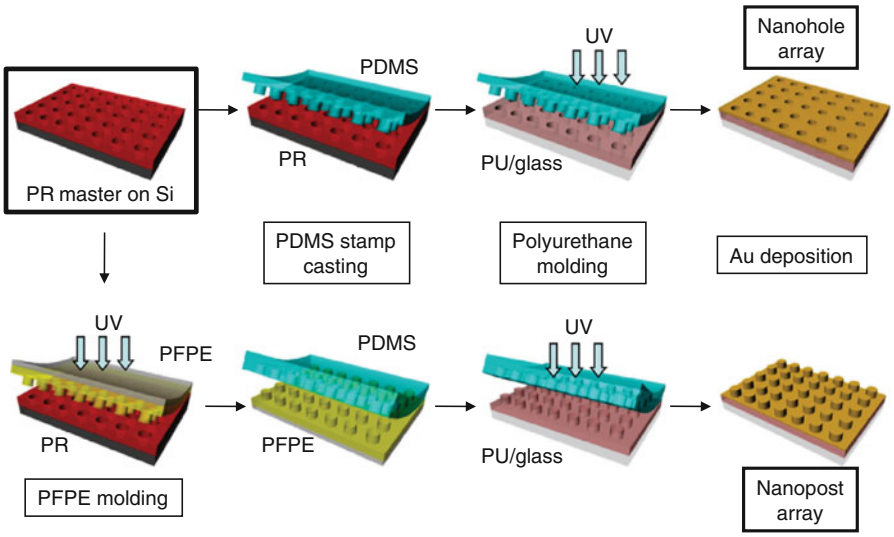

Fig. 9.1 Generalized procedure for nanoimprint lithography fabrication of nanohole (*top*) and nanopost (*bottom*) plasmonic crystals. A photolithographically defined layer of photoresist on silicon is used as a master. To create a nanohole array stamp, a polydimethylsiloxane (PDMS) stamp is cast directly from the master. A nanopost array stamp is fabricated by first casting and curing an acryloxy perfluoropolyether (PFPE) intermediate under ultraviolet (UV) light. This PFPE intermediate is then used to cast a PDMS stamp. The stamp is then used to mold a layer of photocurable polyurethane on a glass slide. Removal of the stamp leaves a nanohole or nanopost array which is then metalized to complete the plasmonic crystal. Reprinted and adapted with permission from [57]; copyright 2009 IOP Publishing Ltd

(dimethylsiloxane) (PDMS) stamp is cast [60–63], resulting in a stamp with the inverse of the original hole structure. To create a nanopost array from the nanohole master, an intermediate casting step is used where an acryloxy perfluoropolyether (a-PFPE) stamp is cast from the lithographically defined master. The a-PFPE layer is backed by a poly(ethylene terephthalate) film for mechanical support and is then used to cast a PDMS stamp which has the same nanohole structure as the photoresist master [57, 64]. The stamp material is not limited to PDMS—as evidenced in the production of the nanopost array stamp, other materials with low surface energy and good chemical compatibility can be used [64–67].

The PDMS stamp is then pressed into a layer of photocurable polyurethane cast onto a glass slide and exposed to ultraviolet light to generate either a nanohole or nanopost array, depending on the particular stamp used. This technique is not limited to polyurethanes—other molding materials are possible (such as an epoxy-type SU-8 photoresist precursor) [24, 57, 64]. After curing, the nanoimprinted array is metalized (typically with gold) to complete the plasmonic crystal. Although the original photoresist master is initially produced via a photolithography process, the expense of initial fabrication is mitigated by the PDMS stamp production itself. Several PDMS stamps can be cast from the same photoresist master, and each PDMS stamp can then be reused to produce many replicas.

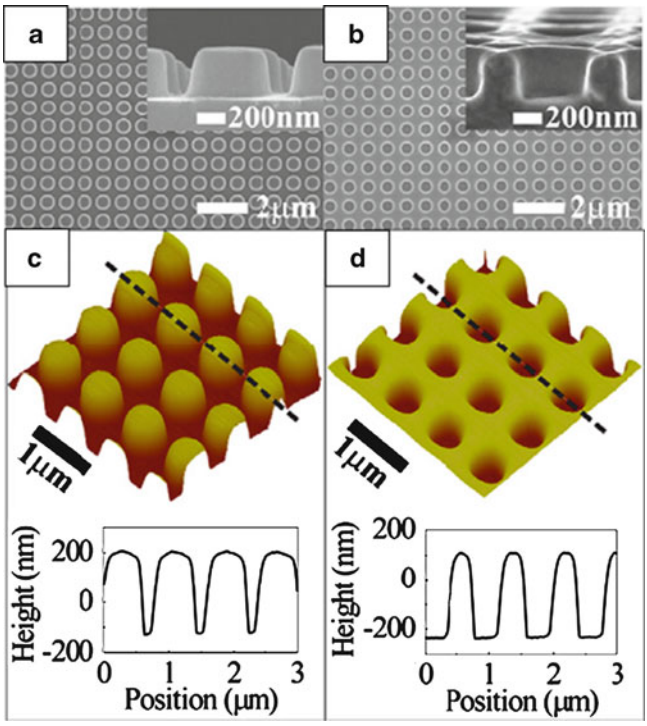

Fig. 9.2 (**a**, **b**) SEM images of nanopost (**a**) and nanohole (**b**) plasmonic crystals with cross-section *insets*. (**c**, **d**) AFM mappings of nanopost (**c**) and nanohole (**d**) plasmonic crystals with height profile *line cuts*. Reprinted and adapted with permission from [57]; copyright 2009 IOP Publishing Ltd

Figure 9.2a, b shows scanning electron microscope (SEM) images and cross-section insets for the nanopost and nanohole arrays, respectively, and Fig. 9.2c, d shows atomic force microscope (AFM) maps and line cuts for the same nanopost and nanohole arrays, respectively [57]. Both the SEM and AFM images show that the nanoimprinted features are precisely replicated across lengths of tens of microns with high spatial uniformity. Figure 9.3a shows an optical image of a nanohole plasmonic crystal with 16 arrays (4 mm on a side) varying in periodicity from 0.5 μm (hole diameter = 0.24 μm) to 1.74 μm (hole diameter = 1.06 μm). Diffraction of light from the grating arrays gives rise to the different colorations, and the uniform color across each array shows that the nanostructure pattern is in fact highly uniform across the entire millimeter-scale area. Spectroscopic measurements confirm this uniformity [68]. Figure 9.3b shows transmission spectra collected at five different areas within a single nanohole array, and the nearly identical spectra demonstrate the high nanostructure fidelity across the entire plasmonic crystal. Figure 9.3c shows transmission spectra for four different plasmonic crystal samples and shows that the optical properties remain consistent between samples.

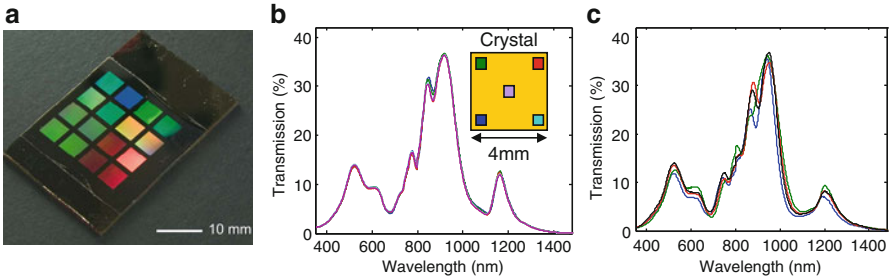

Fig. 9.3 (**a**) Optical image of a completed quasi 3D nanohole plasmonic crystal. Reprinted with permission from [24]; copyright 2009 American Institute of Physics. (**b**) Transmission spectra overlay for four different full 3D nanohole plasmonic crystals illustrating similar optical responses between samples. (**c**) Transmission spectra overlay for five points within the same full 3D nanohole plasmonic crystal illustrating highly reproducible optical response within a single sample over large areas. (**b**, **c**) Were collected on a plasmonic crystal with a periodicity of 748 nm, a hole diameter of 456 nm, and a relief depth of 350 nm. (**b**, **c**) Reprinted with permission from [68]; copyright 2010 Wiley-VCH Verlag GmbH & Co

Although the feature sizes replicated in these plasmonic crystals are relatively large, the ultimate resolution of soft nanoimprint lithography can be much smaller with the proper choice of stamp and molding materials. An a-PFPE stamp cast from a master consisting of single-walled carbon nanotubes on a silicon substrate successfully replicated those features in a layer of photocurable polyurethane with lateral resolutions approaching ~1 nm [61, 64]. Moreover, the fabrication steps required to achieve this resolution were not markedly different from the procedure described above, demonstrating that soft nanoimprint lithography is indeed capable of high resolution feature replication over large areas.

The design rules for these plasmonic crystals include not only the geometry (post or well) and nanostructure dimensions (diameter, depth or height, and spacing between the holes or posts) but also the thickness and distribution of the gold layer that supports the surface plasmons. Electron beam evaporation of gold onto the plasmonic crystal results in a directional coating of gold on the top surface of the plasmonic crystal as well as the formation of gold disks at the bottom of the nanowells [4]. The gold distribution in these devices is discontinuous (although small grains of gold may appear on the sidewalls of the nanoholes) and have been termed a "quasi 3D" plasmonic crystal. Figure 9.4a shows a SEM image of a quasi-3D nanohole plasmonic crystal, and the inset image shows a lack of metal on the nanohole sidewall. In contrast, sputtering of gold onto the plasmonic crystal results in a continuous, conformal coating of gold along the top, bottom, and sidewall surfaces which are referred to as "full 3D" plasmonic crystals [56, 58]. Figure 9.4b shows a SEM image of one of these structures along with a cross-section inset showing the continuous gold layer on all of the nanohole surfaces. The distribution of gold in these plasmonic crystals exerts great influence over their optical properties and sensitivities for sensing applications.

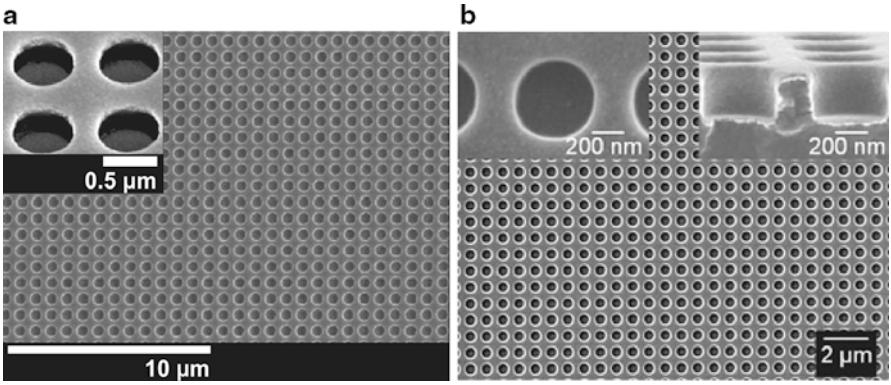

Fig. 9.4 (**a**) SEM image of a quasi 3D nanohole array with angled SEM image (*inset*) showing no gold on nanohole sidewalls. Reprinted and adapted with permission from [4]; copyright 2006 *National Academy of Sciences U S A*. (**b**) SEM image of full 3D nanohole array with magnified view of a single nanohole (*left inset*) and cross-section SEM image (*right inset*) showing continuous metal layer on top and bottom surfaces and on sidewalls of nanohole. Reprinted with permission from [56]; copyright 2008 Wiley-VCH Verlag GmbH & Co

Bulk Refractive Index Sensing Using Quasi 3D and Full 3D Plasmonic Crystals

The SPR modes supported by these nanoimprinted plasmonic crystals exhibit great sensitivity to changes in the local refractive index and have been applied as refractive index sensors. The plasmonic crystals are mounted in a flow cell through which aqueous solutions of poly(ethylene glycol) (PEG) of varying concentration and refractive index are introduced [4, 56, 57]. The flow cell itself is mounted in a spectrophotometer, allowing the time-resolved measurement of transmission through the plasmonic crystal.

Figure 9.5a shows a map of the change in transmission as a function of wavelength and time as aqueous solutions of PEG with different refractive indices are flowed past a quasi 3D plasmonic crystal [4]. The reference condition in these experiments was the initial transmission when water is flowed past the plasmonic crystal. Figure 9.5b shows a simplified version of the data presented in Fig. 9.5a where the time-resolved transmission change is plotted for four individual wavelengths. The data clearly show a change in transmission when the refractive index of the solution is changed as well as a return to the initial transmission when the aqueous PEG solution is replaced with water.

SPR refractive index measurements often report the change in wavelength or intensity for a single SPR supported by the plasmonic device. However, the data in Fig. 9.5a, b clearly show wavelengths where the transmission increases (1,033 and 1,187 nm), while other wavelengths show decreases (1,071 and 1,126 nm). Furthermore, Fig. 9.5a reveals transmission changes that vary across different

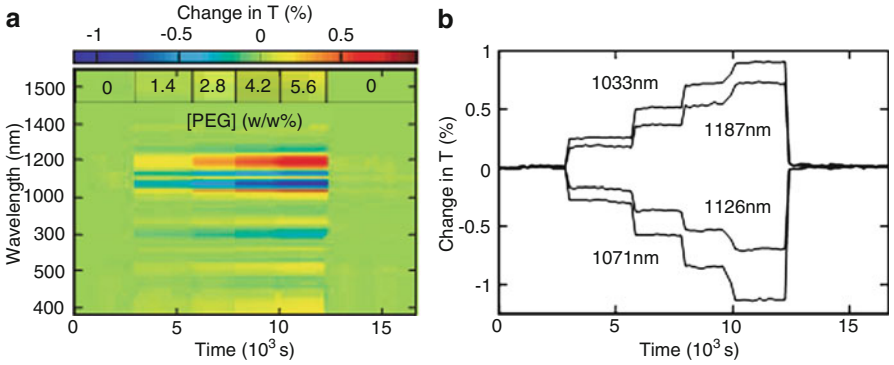

Fig. 9.5 (**a**) Time-resolved transmission difference map for a quasi 3D nanohole plasmonic crystal corresponding to serial injections of aqueous poly(ethylene glycol) (PEG) (*overlaid*). (**b**) Time-resolved transmission differences for serial injections of aqueous PEG at four selected wavelengths. Reprinted with permission from [4]; copyright 2006 *National Academy of Sciences U S A*

wavelengths. We have developed a multispectral analysis to account for these changes in transmission over all wavelengths. The absolute value of the change in transmission relative to the reference transmission at time $t = 0$ is calculated at each wavelength. These absolute changes are then integrated across the entire wavelength range to determine an integrated response. The integrated response is then plotted against the change in refractive index, and the slope of the regression line is used as the figure of merit for this multispectral analysis. A larger figure of merit corresponds to a larger change in the integrated response for a given refractive index change, akin to the peak wavelength shift or reflectance change reported in conventional single resonance SPR measurements [7].

Figure 9.6a, b shows transmission difference maps for a quasi 3D plasmonic crystal and a full 3D plasmonic crystal, respectively [4, 56, 68]. The quasi 3D difference map shows the grates changes at near-infrared wavelengths, while the full 3D difference map shows larger transmission changes throughout the measured spectrum. This is borne out in the integrated response and figure of merit calculations shown in Fig. 9.6c, d for the quasi 3D and full 3D cases, respectively. The integrated responses of the full 3D plasmonic crystal are approximately twice as large as those of the quasi 3D plasmonic crystal with a figure of merit also approximately twice as large. Furthermore, the sensitivity of the full 3D plasmonic crystal is more than three times greater than that of the quasi 3D system when the analysis is restricted to wavelengths between 350 and 1,000 nm (as shown in red in Fig. 9.6c, d).

We have conducted bulk refractive index sensitivity measurements using the nanopost arrays in a similar manner [57]. Gold was sputtered onto both the nanopost and nanowell, yielding continuous conformal metal films on the relief structures. In calculating the integrated responses for the nanopost and the full 3D

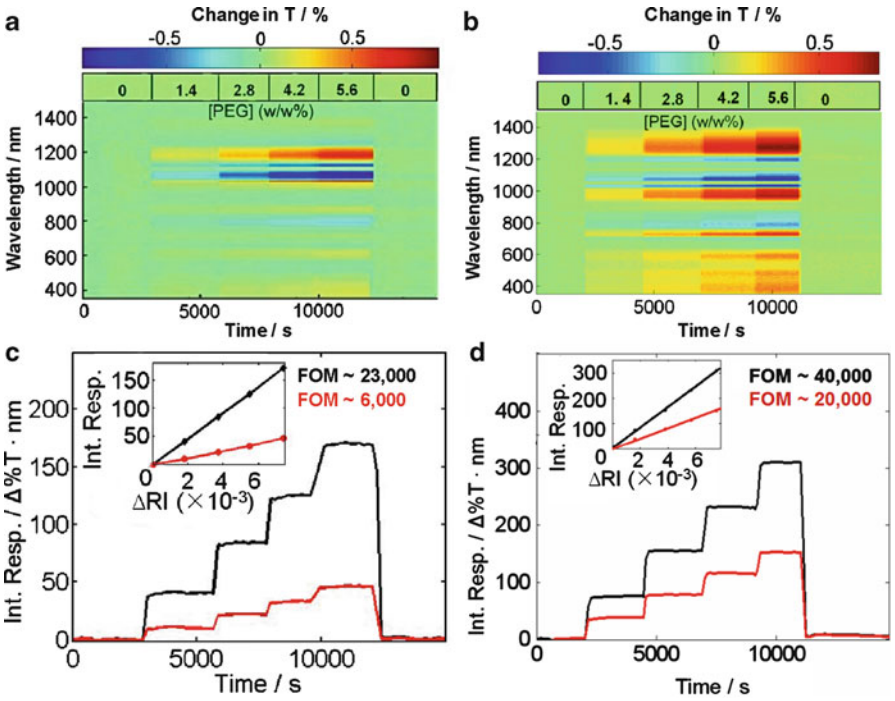

Fig. 9.6 (**a**, **b**) Transmission difference maps for bulk refractive index sensitivity of quasi 3D nanohole (**a**) and full 3D nanohole (**b**) plasmonic crystals. (**c**, **d**) Integrated response calculations and figure of merit calculations (*insets*) for bulk refractive index sensitivity of quasi 3D (**c**) and full 3D (**d**) nanohole plasmonic crystals. *Black curves* in (**c**, **d**) correspond to integration from 355 to 1,500 nm. *Red curves* in (**c**, **d**) correspond to integration from 355 to 1,000 nm. Reprinted with permission from [68]; Copyright 2010 Wiley-VCH Verlag GmbH & Co

nanohole arrays in this experiment, an additional step was introduced to normalize the absolute transmission change at each wavelength to the initial transmission at time $t = 0$. This change has the effect of giving greater weight to changes where the initial transmission is smaller. Figure 9.7 presents these normalized transmission differences for a nanopost (Fig. 9.7a, c) and a full 3D nanohole (Fig. 9.7b, d) array. The nanopost array exhibited ~70% greater sensitivity to bulk refractive index changes than the nanowell array, with much of the increase in sensitivity coming at wavelengths between 700 and 800 nm.

The linear change in integrated response to refractive index change of these plasmonic crystals is advantageous for their use in quantitative sensing and imaging. Each structure demonstrated sensitivity at different wavelengths spanning the visible and near-infrared wavelengths. Furthermore, the signal-to-noise ratio of the integrated response is greater than that associated with examinations of single wavelengths, improving the precision of these plasmonic crystals compared to other SPR-based measurements [4, 56].

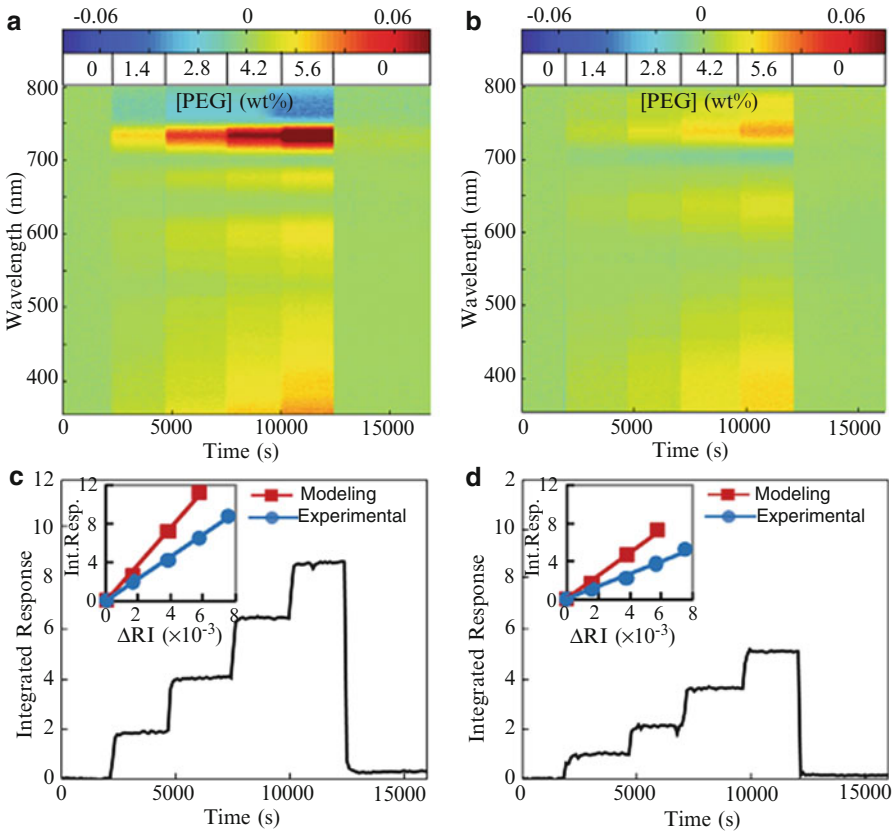

Fig. 9.7 (**a**, **b**) Normalized transmission difference maps for bulk refractive index sensitivity of nanopost (**a**) and full 3D nanohole (**b**) plasmonic crystals. (**c**, **d**) Integrated response calculations and figure of merit calculations (*insets*) for bulk refractive index sensitivity of nanopost (**c**) and full 3D nanohole (**d**) plasmonic crystals. *Insets* of (**c**, **d**) show experimentally determined integrated responses in blue in comparison with computationally predicted integrated responses in red. Reprinted with permission from [57]; Copyright 2009 IOP Publishing Ltd

Theoretical Modeling of Plasmonic Crystal Resonances

The design rules of these nanoimprinted nanohole and nanopost plasmonic crystals undoubtedly control not only the overall sensitivity of the devices but the spectral regions in which that sensitivity is greatest. Thus, a rational approach to altering those design rules must include the ability to understand and to model the underlying physics present. The plasmonic Brillouin zone (PBZ) of a quasi 3D nanohole array has been mapped using angle-dependent transmission measurements [54]. Additionally, the highly uniform nanostructures make these plasmonic crystals amenable to computational modeling using the finite-difference time-domain method [4, 56–58, 69].

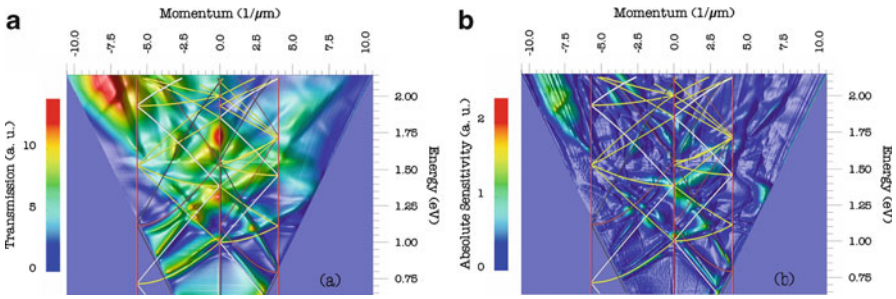

Fig. 9.8 (**a**) Plasmonic Brillouin zone map of a quasi 3D plasmonic crystal with overlaid surface plasmon polariton dispersion curves. (**b**) Absolute sensitivity map of quasi 3D plasmonic crystal after formation of a 1-hexadecanethiol self-assembled monolayer with overlaid surface plasmon polariton dispersion curves. Reprinted with permission from [54]; Copyright 2005 Optical Society of America

Plasmonic Brillouin Zone Mapping

Surface plasmon polaritons can be considered as propagating oscillations of the conduction electrons at the metal-dielectric interface. Because these oscillations travel across the periodic nanohole or nanopost arrays in these plasmonic crystals, a PBZ should exist that fully characterizes their behavior across the entire surface. Zero-order transmission data were collected for a quasi 3D nanohole plasmonic crystal as it was rotated around two axes, and the appropriate mathematical transformations result in the PBZ map presented in Fig. 9.8a [14, 54, 70, 71]. The flat blue regions in the lower corners of Fig. 9.8a correspond to angles that were not accessible in this experimental setup.

To provide insight into the PBZ, lines have been overlaid on the diagram using the surface plasmon polaritons dispersion relation for a flat metal-dielectric interface:

$$k_{\mathrm{SPP}} = \frac{\omega}{c}\sqrt{\frac{\varepsilon_{\mathrm{d}} \cdot \varepsilon_{\mathrm{m}}}{\varepsilon_{\mathrm{d}} + \varepsilon_{\mathrm{m}}}},$$

where k_{SPP} and ω are the respective momentum and frequency of the surface plasmon polaritons, c is the speed of light, and ε_{d} and ε_{m} are the respective dielectric constants of the dielectric and metal. The plotted SPP dispersion curves overlay well with some ridges of higher transmission in the PBZ map, although other areas of increased transmission are not fully described by this simpler model.

Following the initial PBZ mapping of the quasi 3D nanohole array, a self-assembled monolayer (SAM) of 1-hexadecanethiol was formed on the gold surface and similar angle-dependent transmission measurements were carried out. Figure 9.8b shows an absolute sensitivity map for the quasi 3D nanohole array obtained by taking the absolute value of the difference in the PBZ before and after formation of the SAM. Interestingly, regions of higher sensitivity in the map lie

close to areas where several SPP dispersion curves intersect, suggesting that the coupling of SPP modes may be responsible for the increased sensitivity. Although these simple SPP dispersion relations explain some of the behavior observed in the PBZ, other regions of higher sensitivity are found away from the plotted dispersion curves. Additional work is needed to fully characterize the PBZ of both the quasi 3D and full 3D nanohole arrays and the nanopost arrays.

Finite-Difference Time-Domain Computational Modeling and Optimization of Plasmonic Crystals

Although a more thorough understanding of the underlying physics of these devices is of interest, there is also a need to predict the optical properties of devices with arbitrary design rules without the expense of physical fabrication. While the PBZ maps clearly show the presence of propagating SPP modes, other plasmonic features are also supported by these plasmonic crystals. The periodic grating structure generates counterpropagating SPPs, giving rise to Bloch wave SPPs [72]. Additionally, the grating structure itself creates Wood anomalies, although these are diffractive phenomena rather than plasmonic ones [4, 15, 72]. The individual nanoholes and nanoposts can also support localized SPRs [19, 73, 74]. In lieu of a comprehensive physical modeling accounting for the presence and interaction between these features, we have extensively modeled these structures computationally using an implementation of the finite-difference time-domain method [72, 75].

A unit cell containing a single nanostructure (hole or post) with the appropriate dimensions and metal distribution is considered with appropriate boundary conditions to model an infinite square planar array. The unit cell itself is subdivided into a number of grid points with an arbitrary spacing in the x, y, and z dimensions. (A smaller grid spacing results in a more accurate description of the optical properties of the device, but comes at a large computational cost.) The interaction between the nanostructure and the electric and magnetic fields of propagating light is evaluated according to Maxwell's equations at each point in the unit cell for a predetermined length of time (on the order of 100 fs), and quantities such as the zero-order transmission of light are derived from these results.

Figure 9.9 shows a comparison between experimental transmission spectra and those calculated from the FDTD modeling for the nanopost (Fig. 9.9a) and full 3D nanohole (Fig. 9.9b) systems in air, and the correspondence between the experimental and modeled spectra is quite good for both systems [57]. Discrepancies may arise from a combination of effects, such as a physical geometry that differs slightly from that modeled, an incomplete approximation of the wavelength-dependent refractive indices of the metal and dielectrics, and nanoscale defects or variations in the actual metal layer thicknesses. Figure 9.10a shows a comparison between the experimental and modeled transmission spectra for a quasi 3D nanohole array [4].

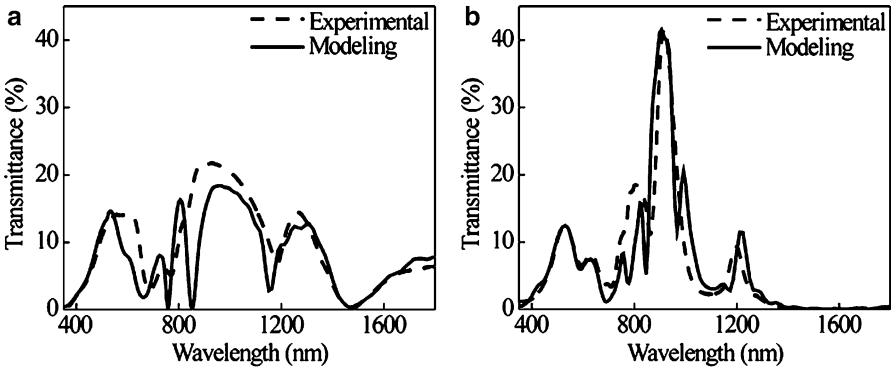

Fig. 9.9 Comparison of experimental transmission spectra with those calculated using the finite-difference time-domain method for nanopost (**a**) and full 3D nanohole (**b**) plasmonic crystals. Reprinted with permission from [57]; Copyright 2009 IOP Publishing Ltd

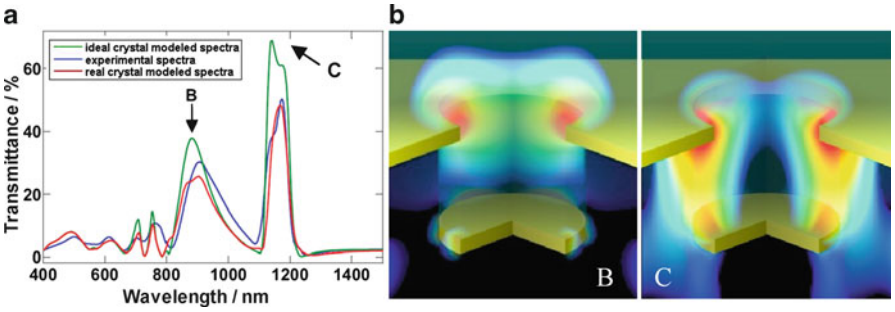

Fig. 9.10 (**a**) Experimental (*blue*) and computationally modeled (*red* and *green*) transmission spectra for a quasi 3D nanohole plasmonic crystal. The *green curve* represents an idealized gold distribution, and the *red curve* represents a more realistic gold distribution in which small nanograins of gold are included near the edge of the bottom gold disc. (**b**) Calculated electric field distributions for the spectral features marked "B" and "C" in (**a**). Reprinted with permission from [4]; Copyright 2006 *National Academy of Sciences U S A*

Although the ideal crystal-modeled spectrum correlates fairly well with the experimental transmission spectrum, the idealized crystal model does not include small gold grains (~20–30 nm in size) along the edge of the gold disc at the bottom of the nanohole which were experimentally observed. Inclusion of these features in the modeled structure gives the "real crystal" modeled spectrum and further improves the fit to the experimental data. Indeed, the optical properties of these nanoimprinted plasmonic crystals are well characterized by the FDTD method.

FDTD calculations of these structures can also reveal the electric fields associated with the active plasmonic resonances in these devices. Figure 9.10b shows the electric field distributions associated with the features marked "B" and "C" in the transmission spectra shown in Fig. 9.10a for a quasi 3D nanohole array [4]. The feature marked "B" shows a LSPR mode that is tightly confined

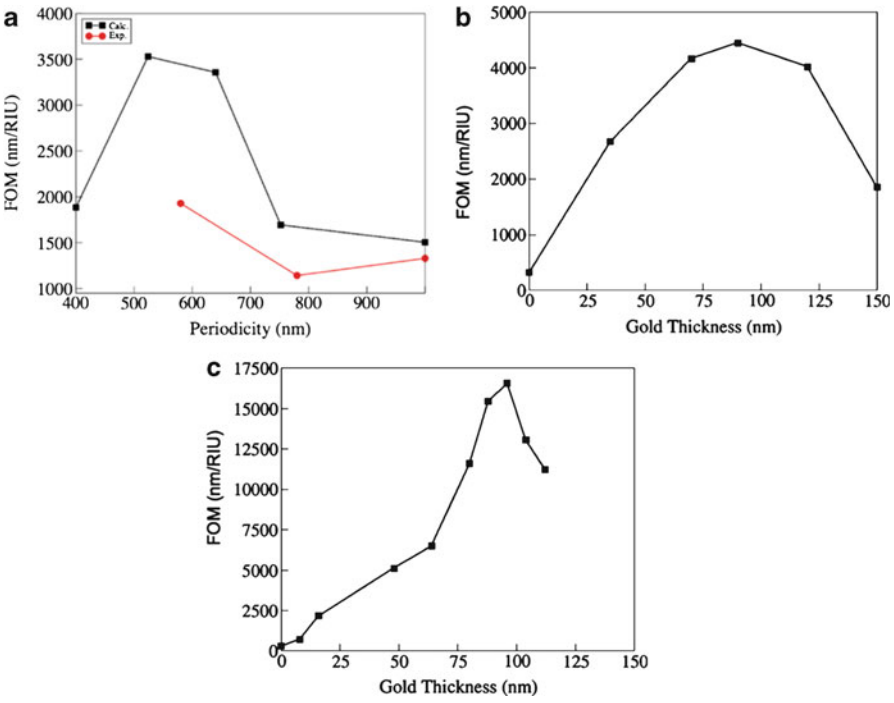

Fig. 9.11 Computationally modeled figures of merit for optimization of selected full 3D nanohole design parameters: (**a**) Periodicity of nanohole array variation (with hole diameter fixed as 60 % of the periodicity) (**b**, **c**) Gold thickness variation assuming a uniform thickness on the top, bottom, and sidewalls of the nanohole for (**b**) a structure with a 752 nm periodicity, 456 nm hole diameter, and 500 nm relief depth and (**c**) a structure with a 524 nm periodicity, 320 nm hole diameter, and 400 nm relief depth. Reprinted with permission from [69]; Copyright 2009 American Chemical Society

around the top rim of the nanohole. The feature marked "C" corresponds to overlapping Bloch wave SPP and Wood anomaly excitation at the interface between the gold film and the molded polymer that shows strong coupling between the gold disc at the bottom of the hole and the upper rim. The intensities and locations of these electric fields are of significant importance in applications such as SERS [24], and the ability to computationally model those fields makes possible the rational design and optimization of these nanostructures.

Further FDTD calculations were performed to optimize the figure of merit of full 3D nanohole plasmonic crystals for bulk refractive index sensing between 400 and 1,000 nm [69]. The parameters tuned were the relief depth, periodicity, and diameter of the nanoholes as well as the metal thicknesses on the top surface, on the sidewalls, and on the bottom surface of the nanohole. By simulating the transmission spectra for a series of bulk refractive indices, integrated responses and figures of merit can be computed and compared. Figure 9.11a shows the results of varying the periodicity of the nanohole array (nanohole diameter scaled as 60% of the

periodicity) with a constant relief depth of 350 nm and constant gold thicknesses. The calculations clearly show a peak in the sensitivity of this configuration for a periodicity of 524 nm (and hole diameter of ~314 nm). Although not all of the periodicity and hole diameter combinations were experimentally available, experimental results do support the trend revealed by the FDTD calculations.

Figure 9.11b, c shows similar optimization calculations in which the gold thickness (assumed to be uniform on the tops, bottoms, and sidewalls of the nanohole arrays) was varied for two different sets of relief depths, hole diameters, and periodicities. Although the figure of merit peaks at approximately the same gold thickness (~96 nm) in both systems, the behavior of the figure of merit is markedly different. Further experimental work is needed to verify these trends as well as to explore other nanostructure architectures, but these results serve to emphasize the intricate interdependencies between the design rule parameters. Additionally, while the sensitivity optimized here (over wavelengths between 400 and 1,000 nm) may not be appropriate for all possible uses, similar calculations can be carried out to optimize the performance of these devices as dictated by the application.

One-Dimensional Sensing Applications of Nanoimprinted Plasmonic Crystals

Despite the high sensitivity of these plasmonic crystals to bulk refractive index changes at visible and near-infrared wavelengths, their application in thin film sensing may be more analytically relevant. The evanescent nature of the electric field associated with SPRs affords these devices high sensitivity to refractive index changes at distances on the order of hundreds of nanometers from the metal-dielectric interface. The small sampling volume probed by these plasmonic crystals makes them inherently sensitive to thin film changes, and they have been used to measure the dynamic adsorption of biomolecules on the plasmonic crystal surface [4, 58]. Additionally, by coupling the plasmonic crystal with a pH-sensitive hydrogel, these plasmonic crystals can optically measure chemomechanical forces [76].

Antibody Assays Using Plasmonic Crystals

Antibody/antigen assays have been performed using full 3D nanohole plasmonic crystals with excellent quantitative results [58]. Antigoat IgG was immobilized on the plasmonic crystal surface and exposed to solutions of goat IgG of varying concentrations through a flow cell. The transmission changes (and thus the change in the integrated response) were measured as a function of the goat IgG

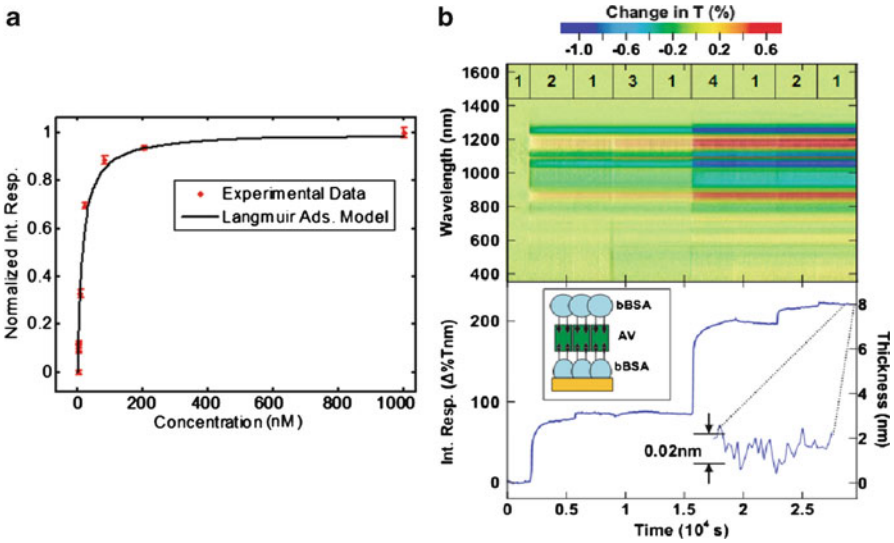

Fig. 9.12 (**a**) Quantitative goat IgG/antigoat IgG assay performed on full 3D plasmonic crystal with nonlinear data fit to Langmuir isotherm. Reprinted with permission from [58]; Copyright 2009 American Chemical Society. (**b**) Spectral difference map (*top*) and integrated response (*bottom*) for biotin-avidin assay performed on quasi 3D plasmonic crystal with representative schematic inset. Overlaid numbers on spectral difference map correspond to injection sequence of PBS (1), bBSA (2), BSA (3), and avidin (4). Integrated response inset illustrates noise-limited sensitivity corresponding to a layer thickness of 0.02 nm. Reprinted with permission from [4]; Copyright 2006 *National Academy of Science U S A*

concentration in the surrounding medium corresponding to surface coverage of goat IgG on the plasmonic crystal. The data presented in Fig. 9.12a show a change in the normalized integrated response that is well described by a Langmuir adsorption model. Fitting the data to a Langmuir isotherm results in an estimate of the surface-confined affinity constant of approximately 7×10^7 M^{-1}, consistent with previously reported results for other IgG/anti-IgG systems.

Figure 9.12b shows the results of a biotin-avidin sandwich assay carried out using a quasi 3D nanohole plasmonic crystal [4]. A biotinylated bovine serum albumin (bBSA) monolayer was nonspecifically adsorbed onto the plasmonic crystal using a flow cell, leading to the first plateau in the integrated response seen in Fig. 9.12b. Subsequent introduction of both phosphate buffered saline (PBS) and unmodified bovine serum albumin (BSA) resulted in no significant change in the integrated response, confirming that no additional material had adsorbed onto the plasmonic crystal surface. Injection of avidin led to a further increase in the integrated response as expected from the binding of an additional layer of material on the plasmonic crystal surface. Injection of a second bBSA layer did not generate as large a change in the integrated response as the first, although this is consistent with other experimental observations of layer-dependent mass coverage in similar assays [77, 78].

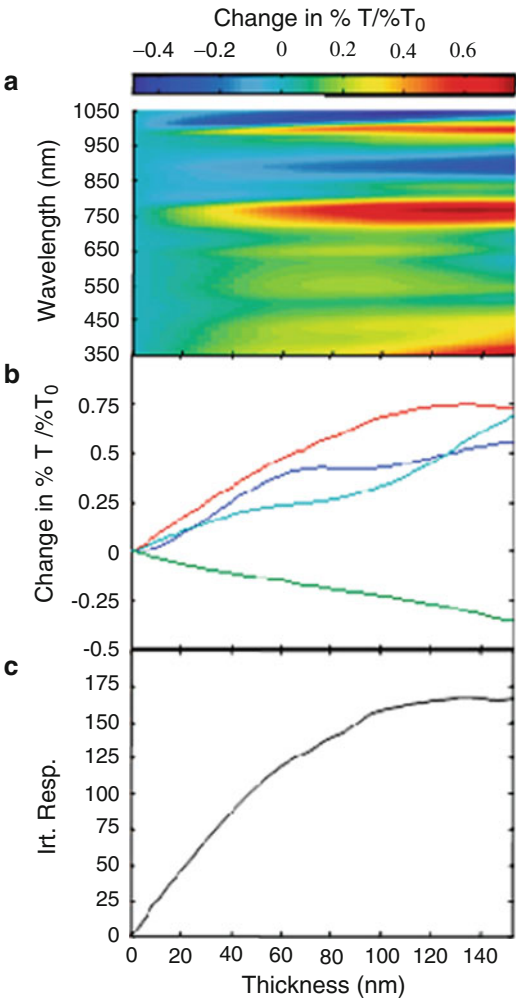

Fig. 9.13 (**a**) Normalized spectral difference map, (**b**) normalized transmission difference at 357 nm (*cyan*), 769 nm (*red*), 894 (*green*) and 996 nm (*blue*), and (**c**) integrated response as a function of polyelectrolyte layer thickness on a full 3D plasmonic crystal. Reprinted with permission from [58]; Copyright 2009 American Chemical Society

Thickness Measurements of Polyelectrolyte Thin Film Assemblies

Although the diminishing change in integrated response demonstrated in the biotin-avidin assay agrees with previous reports in the literature, it presents an opportunity to further investigate the impacts of the exponential decay of the electric field from the plasmonic crystal surface. Polyelectrolyte thin films were deposited on the surface of a full 3D nanohole plasmonic crystal via layer-by-layer assembly, and the change in transmission of the assembly in water was investigated as a function of the layer thickness [58]. Figure 9.13a presents a normalized transmission change map (normalized to the initial transmission when no polyelectrolyte layer was present) over wavelengths between 350 and 1,050 nm, and Fig. 9.13b presents the normalized transmission change for four selected wavelengths. The multiple SPP and

LSPR modes supported by these plasmonic crystals give rise to complex interactions between them and the surrounding environment, and this can be seen by the nonlinear behavior in the single wavelength transmission changes.

Integrated responses were calculated from the transmission data as a function of polyelectrolyte layer thickness and are presented in the Fig. 9.13c. The integrated response clearly increases with the polyelectrolyte layer thickness. However, the integrated response does not increase linearly ad infinitum and appears to saturate at polyelectrolyte thicknesses greater than ~95 nm, representing an upper film thickness limit to the use of the integrated response as an analytical measure for this particular plasmonic crystal. Single wavelength responses do continue to change at larger layer thicknesses and can be used for measurements past this limit. Despite this, the integrated response still responds linearly for layer thicknesses up to ~70 nm, and the continued use of the integrated response of these plasmonic crystals as an analytical metric still bears merit since the film thicknesses involved in most bioassays lie within this linear response regime.

Optical Measurement of pH Change Through Chemomechanical Forces

These nanoimprinted plasmonic crystals have demonstrated great sensitivity to changes in the bulk refractive index as well as to thin film changes at the plasmonic crystal surface. However, their utility is ultimately limited by the refractive index contrast present in the application. While numerous methods exist to measure pH colorimetrically and electrochemically, direct measurement of pH using only the refractive index contrast is extremely difficult. The refractive index change between buffered solutions of pH = 1.44 and 7.86 is extremely small, less than 1×10^{-4} refractive index units [76]. By instead modifying the plasmonic crystal with a hydroxyethyl methacrylate hydrogel sensitized to pH by a small amount of cross-linked acrylic acid, a change in the pH of the bulk environment results in changes in the protonation state of the acrylic acid, generating electrostatic interactions that swell or collapse the hydrogel. This pH change in the bulk results in a mechanical change in the hydrogel at the plasmonic crystal surface.

The data presented in Fig. 9.14 show the optical response of the hydrogel-modified plasmonic crystal with changes in pH. The spectral difference map presented in Fig. 9.14a clearly shows a change in transmission as the system is cycled between pH = 7.86 and pH = 1.44. Additionally, the changes are clearly reversible with the transmission returning to its original state, even after several cycles of pH change. The relative integrated response changes are presented in Fig. 9.14b for three different sets of pH changes—7.86–1.44 (blue), 6.42–5.13 (red), and 5.76–5.66 (black). Larger pH changes show correspondingly larger changes in the relative integrated response as a result of a greater change in hydrogel osmotic pressure and swelling. Impressively, even a change of only 0.10 pH units is clearly distinguishable as seen in the magnified inset.

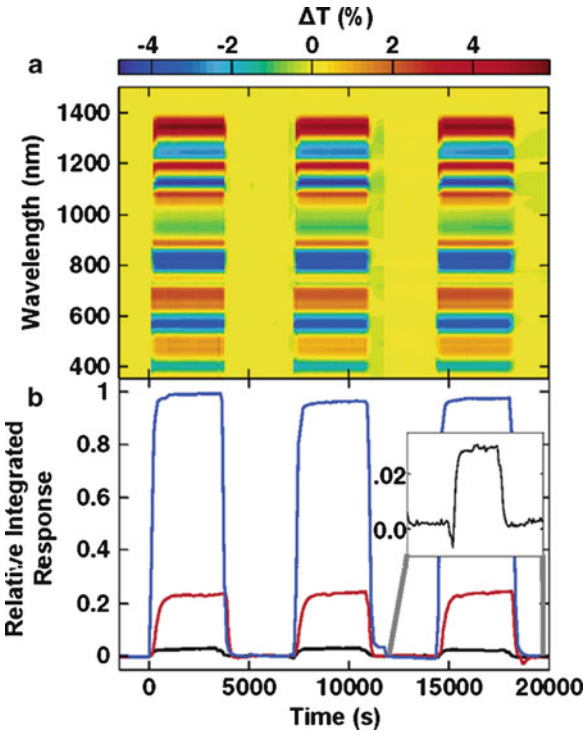

Fig. 9.14 (**a**) Transmission difference map for hydrogel-modified quasi 3D nanohole plasmonic crystal cycled from pH 7.86 to 1.44. (**b**) Relative integrated response for hydrogel-modified plasmonic crystal for pH changes of 7.86–1.44 (*blue*), 6.42–5.13 (*red*), and 5.76–5.66 (*black*). *Inset* shows a magnified view of the *black curve*. Reprinted with permission from [76]; Copyright 2007 American Chemical Society

Interestingly, the hydrogel layer is thicker than the distance penetrated by the evanescent electric field of the plasmonic crystal [4]. Because of the hydrogel thickness and the extremely small refractive index differences in the solutions used, the changes in optical response must have been the result of the change in hydrogel volume and the associated mechanical forces exerted electrostatically by the acrylic acid moieties in their different protonation states. By transducing chemical changes in the environment to mechanical forces at the plasmonic crystal surface, introduction of an appropriate sensing element in the hydrogel network can enable the direct measurement of analytes where the inherent refractive index contrast would otherwise be too small to measure.

Two-Dimensional Chemical Imaging Applications of Plasmonic Crystals

Besides their demonstrated utility in spectroscopic sensing, nanoimprinted plasmonic crystals offer great potential for applications in chemical imaging. The highly uniform patterning over millimeter-scale areas offers a large sensing area, and their demonstrated performance and sensitivity permit fully quantitative

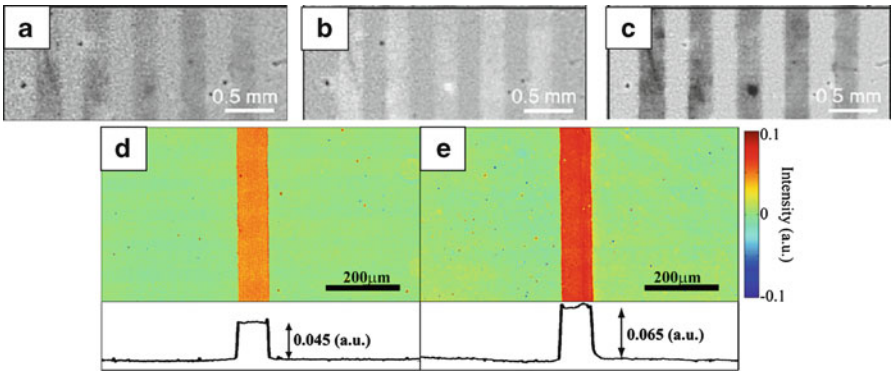

Fig. 9.15 (**a–c**) Background corrected spatial imaging of nonspecifically adsorbed fibrinogen lines on quasi 3D nanohole plasmonic crystals illuminated by (**a**) white light, (**b**) monochromatic 1,090 nm, (**c**) monochromatic 1,200 nm. (**a–c**) Reprinted and adapted with permission from [59]; Copyright 2007 American Institute of Physics. (**d**, **e**) Transmitted light image of fibrinogen nonspecifically adsorbed onto nanopost (**d**) and full 3D nanohole (**e**) plasmonic crystals with curves corresponding to the measured light intensity contrast determined from the images. Reprinted with permission from [57]; Copyright 2009 IOP Publishing Ltd

imaging. We have demonstrated the utility of these plasmonic crystals for high performance imaging at both near-infrared and visible wavelengths with exceptional sensitivity for surface-bound species [4, 56–58].

Protein Thin Film Imaging

Thin film imaging experiments complementary to the spectroscopic measurements previously described were performed using all of the nanoimprinted structure geometries previously described (quasi 3D and full 3D nanoholes, nanopost). The structures' complementary wavelength characteristics allow for their use in the near-infrared and the visible spectrum to image protein thin films. In these examples, fibrinogen was nonspecifically adsorbed onto the plasmonic crystal surface through a microfluidic channel to generate line patterns [57, 59]. Figure 9.15a presents the near-infrared transmission imaging of a single sample of nonspecifically adsorbed fibrinogen thin films onto the surface of a quasi 3D nanohole plasmonic crystal under white light illumination [59]. Even under white light, these 8 nm thick protein films are readily distinguished from the surrounding areas.

Spectrally resolved imaging of the fibrinogen layers demonstrates the previously observed response of the underlying SPRs to refractive index changes at the metal-dielectric interface. Spectroscopic bulk refractive index measurements in Fig. 9.5b revealed wavelength where the transmission increased with a change in refractive index, while the opposite behavior was observed at other wavelengths. This contrast

inversion is plainly evident in the single wavelength imaging presented in Fig. 9.15b (1,090 nm) and c (1,200 nm). Because the protein lines in Fig. 9.15a appear darker than the surrounding areas, the overall change in transmission across the entire wavelength range captured must be lower where the protein is adsorbed on the plasmonic crystal. However, the wavelengths at which the transmission actually increases when the protein is adsorbed will effectively reduce the observed image contrast under white light illumination, and spectrally resolved imaging that accounts for this factor can be exploited to increase the contrast. Despite this caveat, the high performance and sensitivity of the quasi 3D nanohole geometry in the near infrared allows for larger-area imaging of thin films at near-infrared wavelengths.

Fibrinogen layers were also imaged on full 3D nanohole and nanopost plasmonic crystals, and the imaging performance is compared between the nanopost crystal (Fig. 9.15d) and a full 3D nanohole crystal (Fig. 9.15e) [57]. Although the nanopost plasmonic crystal showed greater bulk refractive index sensitivity, the opposite appears to be true in this thin film imaging experiment—the nanohole plasmonic crystal shows a larger difference in image intensity between the fibrinogen line and the surrounding area. An important distinction to be made is that the bulk refractive index measurements were made in water, while the thin film images were captured in air. The complexity of the SPR behavior in different environments results in this seemingly paradoxical behavior is in fact confirmed by FDTD simulations of both systems under both conditions. The complexity of the SPR behavior in different environments results in performances of the different nanostructures (nanopost, quasi 3D nanohole, full 3D nanohole) that are, in practice, complementary to each other—the optimal device architecture is ultimately application-specific.

Molecular Rulers and Film Thickness Calibration of Plasmonic Crystals

The analytical power of these nanoimprinted plasmonic crystals has been demonstrated in molecular ruler imaging experiments carried out on full 3D nanohole arrays [58]. Thin films of proteins of known thickness were microfluidically deposited to establish a calibration between the observed imaging response and surface coverage. Figure 9.16a shows an optical image of three proteins adsorbed onto the plasmonic crystal (from left to right: fibrinogen, γ-globulins, and myoglobin), while Fig. 9.16b gives an average thickness profile. Once again, the protein lines are clearly visible because of the refractive index contrast with the protein-free regions, and estimates of the protein film thicknesses based on a calibration using a self-assembled monolayer were in good agreement with ellipsometric thickness measurements [79]. These visible spectrum measurements were made using white light illumination and a common silicon-based charge-coupled device (CCD) camera mated to a common optical microscope, demonstrating the practical sensitivity of the full 3D nanohole plasmonic crystal at visible wavelengths.

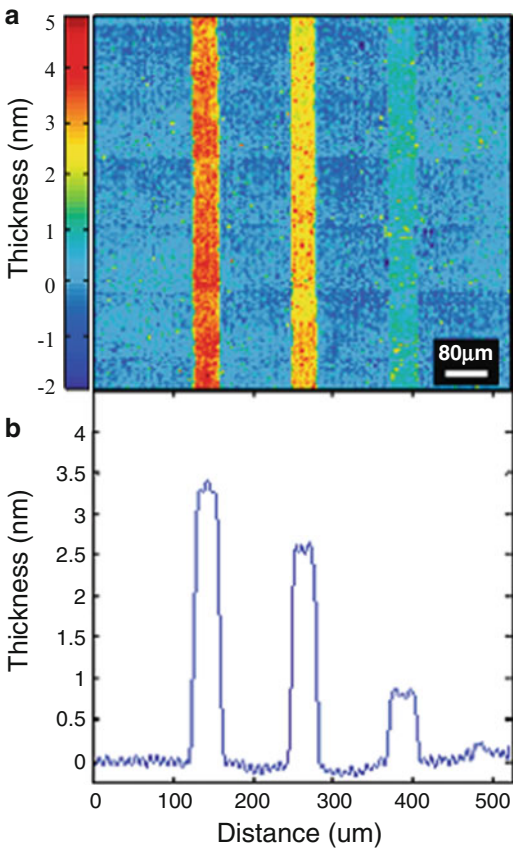

Fig. 9.16 (**a**) Quantitative transmission spatial imaging of (*left*), γ-globulins (*center*), and myoglobin (*right*) nonspecifically adsorbed on full 3D nanohole plasmonic crystal with corresponding layer thickness (**b**) Average height profile for image presented in (**a**). Reprinted and adapted with permission from [58]; Copyright 2009 American Chemical Society

The analytical sensitivity of the full 3D nanohole plasmonic crystals is demonstrated in Fig. 9.17. A self-assembled monolayer of 1-octadecanethiol (ODT) was patterned on the metal surface, and a visible light image of the pattern is shown in Fig. 9.17a [56]. The rest of the surface was backfilled with a layer of 1-hexadecanethiol (HDT), and the resulting image is shown in Fig. 9.17b. Although the ODT pattern is somewhat degraded as a result of infilling of HDT into defect areas in the ODT monolayer as well as dynamic exchange between the ODT on the surface and HDT in solution, the ODT pattern is still readily visible. Compared to the initial contrast between the ODT monolayer and the surroundings, the addition of HDT reduces the contrast to ~10% of its original value. This corresponds strikingly well with the ~11% difference in chain length between 1-octadecanethiol and 1-hexadecanethiol. Indeed, the use of these full 3D plasmonic crystals enables visible light imaging of high sensitivity (down to a difference of two methylene groups) using an inexpensive substrate and common laboratory equipment (optical microscope and CCD camera).

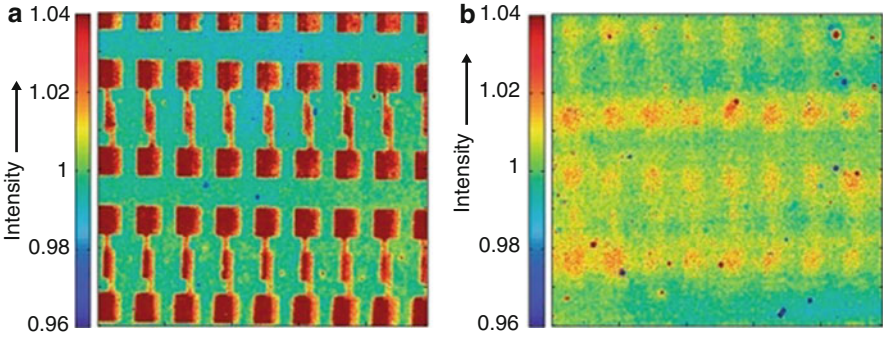

Fig. 9.17 Optical transmission images of a 1-octadecanethiol self-assembled monolayer patterned on a full 3D nanohole plasmonic crystal before (**a**) and after (**b**) backfilling with 1-hexadecanethiol for 5 min. Box ends of octadecanethiol pattern approximately 50 μm wide. Reprinted with permission from [56]; Copyright 2008 Wiley-VCH Verlag GmbH & Co

Surface-Enhanced Raman Scattering on Nanoimprinted Plasmonic Crystals

The underlying physics and evanescent electric fields associated with these nanostructured plasmonic crystals are responsible for their utility as SPR sensors, but these same phenomena are responsible, in large part, for SERS [19–24]. Despite the rich vibrational data obtained using Raman-related techniques, the lack of reproducible SERS substrates with large signal enhancements has significantly hampered the widespread adoption of SERS as an analytical tool [48]. To this end, soft nanoimprint lithography allows us to replicate nanostructures over large areas with high fidelity which we have shown to generate uniform SERS enhancements across the entire plasmonic crystal surface [24].

Benzenethiol (BT) was chosen as the SERS reporter molecule in these experiments, and a BT monolayer was formed on the surface of a quasi 3D nanohole plasmonic crystal [24]. The Raman spectra shown in Fig. 9.18a are in good agreement with previous reports from the literature [80], and subsequent analysis focused on the peak at ~1,073 cm^{-1}. The overlaid spectra in Fig. 9.18a show the spectra collected for nanohole arrays with three different sets of hole diameters and periodicities and show a dependence of the SERS signal enhancement on the design rules of the substrate, a reasonable expectation considering the dependence of the individual plasmonic modes on the device geometry. Analytical SERS enhancement factors from 10^4 to 10^5 were obtained on these substrates without further optimization, on par with other SERS substrates fabricated using serial processing procedures.

The Raman signal enhancement observed in these devices is attributed to a LSPR that establishes the enhanced electric field from which the SERS enhancement is derived. A maximum enhancement is expected when the spectral position of this LSPR is halfway between the laser excitation wavelength (785 nm in this work) and the wavelength of the Raman scattered photon (857 nm in this work,

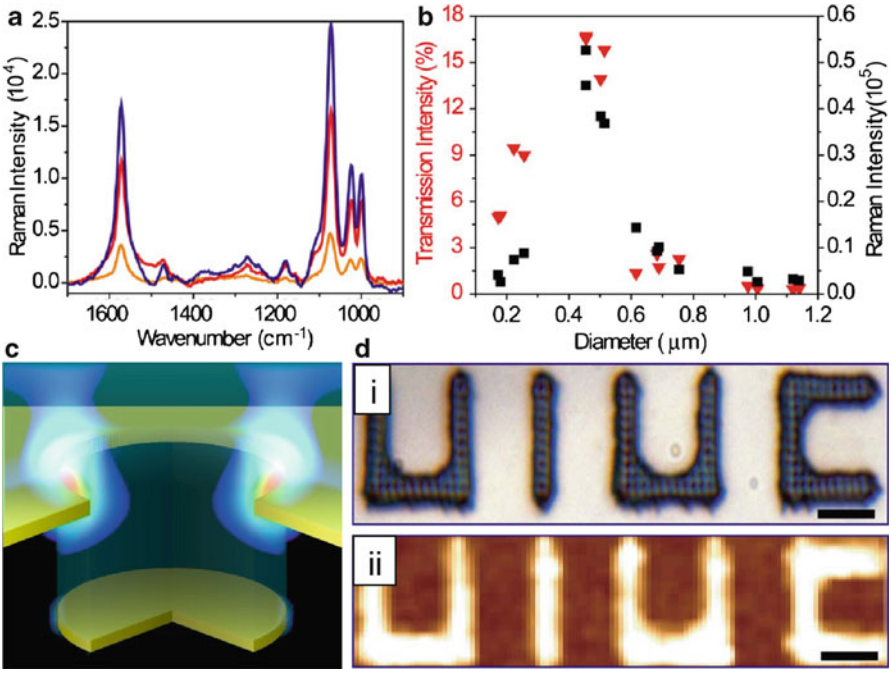

Fig. 9.18 (**a**) Raman spectra of benzenethiol monolayer on three quasi 3D nanohole plasmonic crystal with varying periodicity and hole diameter. (**b**) Comparison of transmission intensity at 826 nm and intensity of Raman feature at 1,087 cm^{-1} as a function of nanohole diameter (and periodicity). (**c**) Electric field plot of transmission spectral feature at 826 nm computed using FDTD modeling. (**d**) Optical image (*i*) of nanohole array embossed in photodefined SU-8 and SERS image (*ii*) of benzenethiol adsorbed onto the structure in (*i*). Scale bars are 5 μm. Figures reprinted with permission from [24]; Copyright 2009 American Institute of Physics

corresponding to a Raman shift of 1,073 cm^{-1}) [81], corresponding to a LSPR wavelength of 826 nm in this work. In fact, the transmission intensity at 826 nm for the 16 different nanohole arrays (of varying hole diameter and periodicity) is strongly correlated to the corresponding Raman signal intensity as shown in Fig. 9.18b.

Considering the LSPR wavelength as a design criterion leads to two conclusions: First, no single design rule can generate equivalent enhancements at all Raman shifts. Instead, an optimal design rule depends on both the excitation wavelength and the Raman shift desired. This could be exploited to preferentially enhance certain Raman bands over others, possibly reducing the complexity of the Raman data when multiple Raman-active analytes are present. Second, the strong correlation between the Raman intensity and the transmission intensity offers a ready metric for computational optimization of the Raman enhancement. Multiple design rules and nanostructure geometries can be investigated in silico to maximize transmission at the LSPR wavelength to optimize the Raman enhancement without the expense associated with physical fabrication of the nanostructures themselves. Figure 9.18c shows that the electric field from the LSPR in this experiment is localized at the upper rim of the nanohole. Knowledge of the electric field

distribution offers the potential for further device optimization by designing modifications that may trap analytes of interest at locations where the electric field is strongest, further enhancing the analytical sensitivity.

The large area, highly uniform nanostructures produced by the nanoimprinting process makes these substrates attractive for use in SERS imaging. The top image in Fig. 9.18d shows a plasmonic crystal that was molded in previously photodefined SU8, resulting in a structure in which the nanohole array is only embossed in the areas making up the letters "UIUC." Benzenethiol was adsorbed across the entire surface, but the Raman map (for the signal at 1,073 cm^{-1}) shown in the bottom panel of Fig. 9.18d shows that a Raman signal is only observed at areas where the nanohole array is present. Furthermore, the Raman intensity is uniform across the entire nanostructured surface. The inexpensive fabrication and uniform performance of these nanoimprinted plasmonic crystals make them promising substrates for further application in SERS sensing and imaging.

Future Prospects

Plasmonic crystals fabricated by soft nanoimprint lithography offer several advantages for use in chemical sensing and imaging applications: They are inexpensively fabricated while retaining high fidelity over large areas, making larger-area imaging and multiplexing possible. They offer high sensitivity when used in SPR sensing and imaging using common laboratory equipment without the need for chemical labels. The SPRs generated by these structures enable several analytical techniques, including SERS and surface-enhanced fluorescence, opening the possibility of using a single device for multimodal sensing. The ability to computationally model and predict the optical properties of these plasmonic crystals enables the rational design and optimization of nanostructures for specific applications.

Although we have demonstrated numerous capabilities of these nanostructured plasmonic crystals, other applications certainly remain. Miniaturization of the plasmonic crystal and integration into microfluidic lab-on-a-chip systems can enable portable, high performance sensing of chemical and biological analytes. Real time imaging of biochemical systems using both SERS and SPR is possible using these devices, and our preliminary data suggest that the dynamics of living cells and their responses to external stimuli on the plasmonic crystal surface can be monitored. Indeed, these nanoimprinted plasmonic crystals offer a versatile platform for a new generation of biological and chemical sensors with applications in analytical chemistry, biochemistry, and cell biology.

Acknowledgments We acknowledge the support of the U. S. Department of Energy, Materials Science Division under award number DE-FG02-07ER46471, through the Frederick Seitz Materials Research Laboratory at the University of Illinois, including the Center for Microanalysis of Materials. The work at Argonne National Laboratory was supported by the U. S. Department of Energy, Office of Science, Office of Basic Energy Sciences, under contract number DE-AC02-06CH11357.

References

1. Knoll W. Interfaces and thin films as seen by bound electromagnetic waves. Annu Rev Phys Chem. 1998;49:569–638.
2. Ozbay E. Plasmonics: merging photonics and electronics at nanoscale dimensions. Science. 2006;311:189–93.
3. Raether H. Surface plasmons on smooth and rough surfaces and on gratings. Berlin: Springer; 1988.
4. Stewart ME, Mack NH, Malyarchuk V, Soares JANT, Lee T-W, Gray SK, Nuzzo RG, Rogers JA. Quantitative multispectral biosensing and 1d imaging using quasi-3d plasmonic crystals. Proc Natl Acad Sci USA. 2006;103:17143–8.
5. Zhao J, Zhang X, Yonzon CR, Haes AJ, Van Duyne RP. Localized surface plasmon resonance biosensors. Nanomedicine. 2006;1:219–28.
6. Chau L-K, Lin Y-F, Cheng S-F, Lin T-J. Fiber-optic chemical and biochemical probes based on localized surface plasmon resonance. Sens Actuators B. 2006;113:100–5.
7. Homola J. Surface plasmon resonance sensors for detection of chemical and biological species. Chem Rev. 2008;108:462–93.
8. Nelson BP, Frutos AG, Brockman JM, Corn RM. Near-infrared surface plasmon resonance measurements of ultrathin films. 1. Angle shift and spr imaging experiments. Anal Chem. 1999;71:3928–34.
9. Wark AW, Lee HJ, Corn RM. Long-range surface plasmon resonance imaging for bioaffinity sensors. Anal Chem. 2005;77:3904–7.
10. Kretschmann E, Raether H. Radiative decay of nonradiative surface plasmons excited by light. Z Naturforsch A. 1968;23:2135.
11. Otto A. Exitation of nonradiative surface plasma waves in silver by the method of frustrated total reflection. Z Phys. 1968;216:398–410.
12. Homola J. Present and future of surface plasmon resonance biosensors. Anal Bioanal Chem. 2003;377:528–39.
13. Nath N, Chilkoti A. A colorimetric gold nanoparticle sensor to interrogate biomolecular interactions in real time on a surface. Anal Chem. 2002;74:504–9.
14. Barnes WL, Murray WA, Dintinger J, Devaux E, Ebbesen TW. Surface plasmon polaritons and their role in the enhanced transmission of light through periodic arrays of subwavelength holes in a metal film. Phys Rev Lett. 2004;92:107401.
15. Ebbesen TW, Lezec HJ, Ghaemi HF, Thio T, Wolff PA. Extraordinary optical transmission through sub-wavelength hole arrays. Nature. 1998;391:667–9.
16. Sherry LJ, Chang S-H, Schatz GC, Van Duyne RP, Wiley BJ, Younan X. Localized surface plasmon resonance spectroscopy of single silver nanocubes. Nano Lett. 2005;5:2034–8.
17. Yonzon CR, Jeoung E, Zou S, Schatz GC, Mrksich M, Van Duyne RP. A comparative analysis of localized and propagating surface plasmon resonance sensors: The binding of concanavalin a to a monosaccharide functionalized self-assembled monolayer. J Am Chem Soc. 2004;126:12669–76.
18. Barnes WL, Dereux A, Ebbesen TW. Surface plasmon subwavelength optics. Nature. 2003;424:824.
19. Stewart ME, Anderton CR, Thompson LB, Maria J, Gray SK, Rogers JA, Nuzzo RG. Nanostructured plasmonic sensors. Chem Rev. 2008;108:494–521.
20. Camden JP, Dieringer J, Zhao J, Van Duyne RP. Controlled plasmonic nanostructures for surface-enhanced spectroscopy and sensing. Acc Chem Res. 2008;41:1653–61.
21. Gordon R, Sinton D, Kavanagh KL, Brolo AG. A new generation of sensors based on extraordinary optical transmission. Acc Chem Res. 2008;41:1049–57.
22. Stuart DA, Haes AJ, Yonzon CR, Hicks EM, Van Duyne RP. Biological applications of localized surface plasmonic phenomena. IEE Proc Nanobiotechnol. 2005;152:13–32.
23. Willets KA, Duyne RPV. Localized surface plasmon resonance spectroscopy and sensing. Annu Rev Phys Chem. 2007;58:267–97.

24. Baca AJ, Truong TT, Cambrea LR, Montgomery JM, Gray SK, Abdula D, Banks TR, Yao J, Nuzzo RG, Rogers JA. Molded plasmonic crystals for detecting and spatially imaging surface bound species by surface-enhanced Raman scattering. Appl Phys Lett. 2009;94:243109.
25. Liebermann T, Knoll W. Surface-plasmon field-enhanced fluorescence spectroscopy. Colloid Surf A. 2000;171:115–30.
26. Liebermann T, Knoll W, Sluka P, Herrmann R. Complement hybridization from solution to surface-attached probe-oligonucleotides observed by surface-plasmon-field-enhanced fluorescence spectroscopy. Colloid Surf A. 2000;169:337–50.
27. Ekgasit S, Stengel G, Knoll W. Concentration of dye-labeled nucleotides incorporated into DNA determined by surface plasmon resonance-surface plasmon fluorescence spectroscopy. Anal Chem. 2004;76:4747–55.
28. Yu F, Persson B, Lofas S, Knoll W. Attomolar sensitivity in bioassays based on surface plasmon fluorescence spectroscopy. J Am Chem Soc. 2004;126:8902–3.
29. Feller BE, Kellis JT, Cascao-Pereira LG, Knoll W, Robertson CR, Frank CW. Fluorescence quantification for surface plasmon excitation. Langmuir. 2008;24:12303–11.
30. Johansson P, Xu H, Käll M. Surface-enhanced Raman scattering and fluorescence near metal nanoparticles. Phys Rev B. 2005;72:035427.
31. Kneipp K, Wang Y, Kneipp H, Perelman LT, Itzkan I, Dasari RR, Feld MS. Single molecule detection using surface-enhanced Raman scattering (SERS). Phys Rev Lett. 1997;78:1667.
32. Michaels AM, Jiang J, Brus L. Ag nanocrystal junctions as the site for surface-enhanced Raman scattering of single rhodamine 6g molecules. J Phys Chem B. 2000;104:11965–71.
33. Nie S, Emory SR. Probing single molecules and single nanoparticles by surface-enhanced Raman scattering. Science. 1997;275:1102–6.
34. Xu H, Bjerneld EJ, Käll M, Börjesson L. Spectroscopy of single hemoglobin molecules by surface enhanced Raman scattering. Phys Rev Lett. 1999;83:4357.
35. Xu HX, Aizpurua J, Kall M, Apell P. Electromagnetic contributions to single-molecule sensitivity in surface-enhanced Raman scattering. Phys Rev E. 2000;62:4318.
36. Dintinger J, Klein S, Ebbesen TW. Molecule-surface plasmon interactions in hole arrays: enhanced absorption, refractive index changes, and all-optical switching. Adv Mater. 2006;18:1267–70.
37. Przybilla F, Genet C, Ebbesen TW. Enhanced transmission through penrose subwavelength hole arrays. Appl Phys Lett. 2006;89:121115.
38. Bozhevolnyi SI, Volkov VS, Devaux E, Laluet J-Y, Ebbesen TW. Channel plasmon subwavelength waveguide components including interferometers and ring resonators. Nature. 2006;440:508–11.
39. Chang C-K, Lin D-Z, Yeh C-S, Lee C-K, Chang Y-C, Lin M-W, Yeh J-T, Liu J-M. Experimental analysis of surface plasmon behavior in metallic circular slits. Appl Phys Lett. 2007;90:061113.
40. Grand J, Adam P-M, Grimault A-S, Vial A, de la Chapelle ML, Bijeon J-L, Kostcheev S, Royer P. Optical extinction spectroscopy of oblate, prolate and ellipsoid shaped gold nanoparticles: experiments and theory. Plasmonics. 2006;1:135–40.
41. Rechberger W, Hohenau A, Leitner A, Krenn JR, Lamprecht B, Aussenegg FR. Optical properties of two interacting gold nanoparticles. Opt Commun. 2003;220:137–41.
42. Henzie J, Lee MH, Odom TW. Multiscale patterning of plasmonic metamaterials. Nat Nanotechnol. 2007;2:549–54.
43. Kwak E-S, Henzie J, Chang S-H, Gray SK, Schatz GC, Odom TW. Surface plasmon standing waves in large-area subwavelength hole arrays. Nano Lett. 2005;5:1963–7.
44. Henzie J, Lee J, Lee MH, Hasan W, Odom TW. Nanofabrication of plasmonic structures. Annu Rev Phys Chem. 2009;60:147–65.
45. Gao H, McMahon JM, Lee MH, Henzie J, Gray SK, Schatz GC, Odom TW. Rayleigh anomaly-surface plasmon polariton resonances in palladium and gold subwavelength hole arrays. Opt Express. 2009;17:2334–40.

46. Zhang X, Yonzon C, Duyne RPV. Nanosphere lithography fabricated plasmonic materials and their applications. J Mater Res. 2006;21:1083–92.
47. Zhang X, Whitney AV, Zhao J, Hicks EM, Van Duyne RP. Advances in contemporary nanosphere lithographic techniques. J Nanosci Nanotechnol. 2006;6:1920–34.
48. Stiles PL, Dieringer JA, Shah NC, Van Duyne RP. Surface-enhanced Raman spectroscopy. Annu Rev Anal Chem. 2008;1:601–26.
49. Haynes CL, Van Duyne RP. Nanosphere lithography: a versatile nanofabrication tool for studies of size-dependent nanoparticle optics. J Phys Chem B. 2001;105:5599–611.
50. Yang S-M, Jang SG, Choi D-G, Kim S, Yu HK. Nanomachining by colloidal lithography. Small. 2006;2:458–75.
51. Prikulis J, Hanarp P, Olofsson L, Sutherland D, Kaell M. Optical spectroscopy of nanometric holes in thin gold films. Nano Lett. 2004;4:1003–7.
52. Bukasov R, Shumaker-Parry JS. Highly tunable infrared extinction properties of gold nanocrescents. Nano Lett. 2007;7:1113–8.
53. Stewart ME, Motala MJ, Yao J, Thompson LB, Nuzzo RG. Unconventional methods for forming nanopatterns. Proc Inst Mech Eng Part N J Nanoeng Nanosyst. 2007;220:81–138.
54. Malyarchuk V, Hua F, Mack NH, Velasquez VT, White JO, Nuzzo RG, Rogers JA. High performance plasmonic crystal sensor formed by soft nanoimprint lithography. Opt Express. 2005;13:5669–75.
55. Truskett VN, Watts MPC. Trends in imprint lithography for biological applications. Trends Biotechnol. 2006;24:312–7.
56. Yao J, Stewart ME, Maria J, Lee T-W, Gray SK, Rogers JA, Nuzzo RG. Seeing molecules by eye: surface plasmon resonance imaging at visible wavelengths with high spatial resolution and submonolayer sensitivity. Angew Chem Int Ed. 2008;47:5013–7.
57. Truong TT, Maria J, Yao J, Stewart ME, Lee T-W, Gray SK, Nuzzo RG, Rogers JA. Nanopost plasmonic crystals. Nanotechnology. 2009;20:434011.
58. Stewart ME, Yao J, Maria J, Gray SK, Rogers JA, Nuzzo RG. Multispectral thin film biosensing and quantitative imaging using 3D plasmonic crystals. Anal Chem. 2009;81:5980–9.
59. Malyarchuk V, Stewart ME, Nuzzo RG, Rogers JA. Spatially resolved biosensing with a molded plasmonic crystal. Appl Phys Lett. 2007;90:203113.
60. Delamarche E, Schmid H, Michel B, Biebuyck H. Stability of molded polydimethylsiloxane microstructures. Adv Mater. 1997;9:741–6.
61. Hua F, Sun Y, Gaur A, Meitl MA, Bilhaut L, Rotkina L, Wang J, Geil P, Shim M, Rogers JA. Polymer imprint lithography with molecular-scale resolution. Nano Lett. 2004;4:2467–71.
62. Odom TW, Love JC, Wolfe DB, Paul KE, Whitesides GM. Improved pattern transfer in soft lithography using composite stamps. Langmuir. 2002;18:5314–20.
63. Schmid H, Michel B. Siloxane polymers for high-resolution, high-accuracy soft lithography. Macromolecules. 2000;33:3042–9.
64. Truong TT, Lin R, Jeon S, Lee HH, Maria J, Gaur A, Hua F, Meinel I, Rogers JA. Soft lithography using acryloxy perfluoropolyether composite stamps. Langmuir. 2007;23:2898–905.
65. Rolland JP, Hagberg EC, Denison GM, Cater KR, DeSimone JM. High-resolution soft lithography: enabling materials for nanotechnologies. Angew Chem Int Ed. 2004;43:5796–9.
66. Rothrock GD, Maynor B, Rolland JP, DeSimone JM. High-performance imprint lithography and novel metrology methods using multifunctional perfluoropolyethers. Proc SPIE. 2006;6152:61523F.
67. Rolland JP, Van Dam RM, Schorzman DA, Quake SR, DeSimone JM. Solvent-resistant photocurable “liquid teflon” for microfluidic device fabrication. J Am Chem Soc. 2004;126:2322–3.
68. Yao J, Le A-P, Gray SK, Moore JS, Rogers JA, Nuzzo RG. Functional nanostructured plasmonic materials. Adv Mater. 2010;22:1102–10.

69. Maria J, Truong TT, Yao J, Lee T-W, Nuzzo RG, Leyffer S, Gray SK, Rogers JA. Optimization of 3D plasmonic crystal structures for refractive index sensing. J Phys Chem C. 2009;113:10493–9.
70. Hohng SC, Yoon YC, Kim DS, Malyarchuk V, Muller R, Lienau C, Park JW, Yoo KH, Kim J, Ryu HY, Park QH. Light emission from the shadows: surface plasmon nano-optics at near and far fields. Appl Phys Lett. 2002;81:3239–41.
71. Chaemi HF, Thio T, Grupp DE, Ebbesen TW, Lezec HJ. Surface plasmons enhance optical transmission through subwavelength holes. Phys Rev B. 1998;58:6779–82.
72. Chang S-H, Gray SK, Schatz GC. Surface plasmon generation and light transmission by isolated nanoholes and arrays of nanoholes in thin metal films. Opt Express. 2005;13:3150–65.
73. Dahlin A, Zach M, Rindzevicius T, Kall M, Sutherland DS, Hook F. Localized surface plasmon resonance sensing of lipid-membrane-mediated biorecognition events. J Am Chem Soc. 2005;127:5043–8.
74. Hutter E, Fendler JH. Exploitation of localized surface plasmon resonance. Adv Mater. 2004;16:1685–706.
75. Taflove A, Hagness SC. Computational electrodynamics: the finite-difference time-domain. Boston: Artech House; 2005.
76. Mack NH, Wackerly JW, Malyarchuk V, Rogers JA, Moore JS, Nuzzo RG. Optical transduction of chemical forces. Nano Lett. 2007;7:733–7.
77. Lin L, Harris JW, Thompson GR, Brody JP. Surface plasmon resonance-based sensors to identify cis-regulatory elements. Anal Chem. 2004;76:6555–9.
78. Huang TT, Sturgis J, Gomez R, Geng T, Bashir R, Bhunia AK, Robinson JP, Ladisch MR. Composite surface for blocking bacterial adsorption on protein biochips. Biotechnol Bioeng. 2003;81:618–24.
79. Mack NH, Dong R, Nuzzo RG. Quantitative imaging of protein adsorption on patterned organic thin-film arrays using secondary electron emission. J Am Chem Soc. 2006;128:7871–81.
80. Brolo AG, Arctander E, Gordon R, Leathem B, Kavanagh KL. Nanohole-enhanced Raman scattering. Nano Lett. 2004;4:2015–8.
81. Haynes CL, Van Duyne RP. Plasmon-sampled surface-enhanced Raman excitation spectroscopy. J Phys Chem B. 2003;107:7426–33.

Part II
Techniques for Nanoplasmonic Sensing

Chapter 10
Performance of Nanoplasmonic Biosensors

Andreas B. Dahlin and Magnus P. Jonsson

Abstract This chapter aims to give an overview of how to optimize the performance of nanoplasmonic sensors. Specific biosensing challenges beyond the capability of current nanoplasmonic sensors will be discussed. Various methods to improve sensor performance will then be introduced, including solving issues related to surface chemistry. We distinguish the concept of signal enhancement, which is related to the choice of nanostructure and surface functionalization, from the concept of noise minimization, which is related to the spectroscopy techniques employed. The concepts of bulk sensitivity, figure of merit, nanostructure performance, and their relation to detection limit are discussed in detail.

The most important points addressed are:

- The challenges which require the development of nanoplasmonic sensors with better performance are diverse in nature. Different improvements will solve different problems.
- More effort needs to be put into improving surface functionalization for specific binding, especially if nanoplasmonic sensors are to be useful in medical diagnostics.
- The sensing performance of a plasmonic nanostructure is best defined in terms of relative intensity changes (e.g., extinction in absorbance units) per refractive index change, because this is what is measured by optical spectroscopy. The signals upon local changes in refractive index also depend on the extension of the plasmonic field.
- In most sensing situations, except single nanoparticle/hole analysis or imaging applications, extinction spectroscopy in transmission mode will outperform scattering spectroscopy under dark-field illumination.

A.B. Dahlin (✉)
Division of Bionanophotonics, Department of Applied Physics,
Chalmers University of Technology, Gothenburg, Sweden
e-mail: adahlin@chalmers.se

M.P. Jonsson
Division of Biological Physics, Department of Applied Physics,
Chalmers University of Technology, Gothenburg, Sweden

A. Dmitriev (ed.), *Nanoplasmonic Sensors*, Integrated Analytical Systems,
DOI 10.1007/978-1-4614-3933-2_10,

Sensor Terminology

Throughout this chapter, we will address several topics related to sensor performance. For one thing, we will consider the types of challenges the research field faces and how they differ from each other (section "Important Characteristic Challenges"). Surface functionalization strategies are then discussed (section "Surface Functionalization"), including the challenge of generating inert surfaces in order to suppress unspecific binding. We then continue with a detailed discussion on how to compare the sensing performance of various nanostructures (section "Sensitivity Maximization"), with particular focus on which parameter that best describes performance. Finally, we will describe various spectroscopy methods (section "Noise Minimization") and discuss which method is best to employ in a given situation. We will in this first section start with an introduction that goes through some of the basic terminology within sensor science.

For sensors designed for quantitative analysis, the *sensitivity* is usually defined as the slope of the curve acquired from a calibration experiment (IUPAC definition). A calibration is performed by recording the sensor response for different known values of whatever environmental variable (EV) the sensor is designed to measure (Fig. 10.1a). For instance, if the sensor is a thermometer, the EV can be controlled by an environment with known temperature and the response could be the height of a liquid mercury pillar. For refractometric nanoplasmonic sensors, the calibration experiment is instead related to how spectral changes depend on the refractive index around metallic nanostructures. As will be discussed below, one can define the sensor response in different ways, especially in real-time measurements. The sensitivity is usually determined from the calibration data by fitting a linear function. However, the calibration curve does not necessarily have to be linear, i.e., the sensitivity may vary with the value of the EV (Fig. 10.1a).

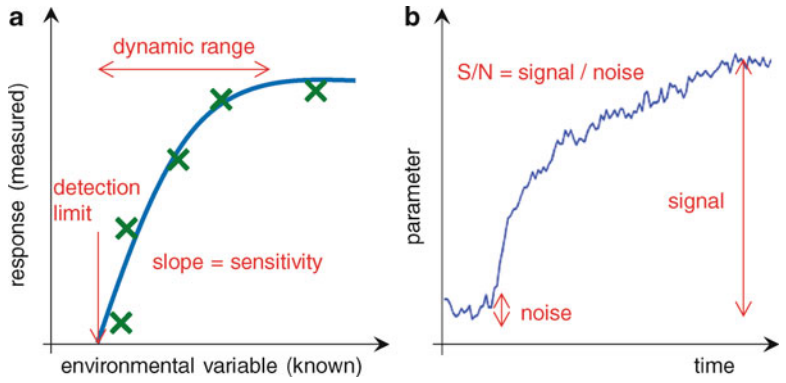

Fig. 10.1 Important terms in sensor science. In (**a**) is shown a calibration experiment, where the response is measured for different values of the environmental variable. In (**b**) is shown a typical sensing experiment using surface-based detection, where the change of a physical parameter is monitored

All systems exhibit *noise*, i.e., random fluctuations in the output. Noise is usually referred to as fluctuations on the short time scale (seconds), while *stability* refers to changes or drifts over longer time periods (hours). For a sensor that monitors a parameter in real-time, such as most nanoplasmonic systems, we here define the *signal* as the endpoint change in the monitored parameter (Fig. 10.1b). Finally, we define the signal to noise (S/N) simply as the ratio of these two quantities. At some value of the EV, the system will not generate a response high enough to be clearly distinguished from the noise level. This value of the EV, i.e., the lowest which can be detected, represents the detection limit of the system. Naturally, the detection limit is one of the most important parameter when evaluating sensor performance, although it does not always provide all the necessary information to give a complete picture.

Another important parameter of a sensor is its *dynamic range*, which is defined as the range of EV values which gives rise to different responses in the system. The lower end of the dynamic range is the detection limit, while the upper range may be infinite in theory. However, the system usually becomes saturated at some point depending on the physical transducer principle. On a surface, there is always a maximum coverage at which further binding is not possible. For instance, if one high (100 μM) and one extremely high (1 mM) concentration of target protein are added to a nanoplasmonic sensor, the corresponding (end point) signals can be indistinguishable. In this situation, binding kinetics can be monitored to reveal differences in concentration, given that the temporal resolution is sufficient. The dynamic range can be critical for applications where the quantitative result of the sensor really is what matters, such as the detection of biomarkers in blood. Many biomarkers, such as prostate-specific antigen (PSA), are always present, but at changed concentration in diseased patients [1].

It should be noted that although the definition of sensitivity as explained above represents the most common meaning of the word within quantitative and analytical sensor science, other interpretations do occur. For instance, for nonquantitative tests (output yes or no), sensitivity is normally defined as one minus the probability of a false negative result (The "sensitivity" of an ELISA test for HIV is >99%). In electronics, sensitivity is sometimes instead referred to as "responsivity," while sensitivity instead represents detection limit (the sensitivity of a microphone can be a critical sound volume required to activate it). For the purpose of this chapter, it should be noted that sensitivity and detection limit, as defined here, are different concepts that should not be mixed up. For nanoplasmonic sensors, sensitivity is related to the sensing capability of the nanostructure, while detection limit also depends on the instrumentation used for spectroscopy.

What physical parameters should represent response and EV (as well as noise and detection limit, respectively) in nanoplasmonic biosensors? There is no obvious answer to this question. Most of the experimental papers presented in the literature on nanoplasmonic sensing report sensitivity values of resonance peak wavelength (λ_{peak}) shift per refractive index (RI) unit change in the liquid environment. This value is indeed an important parameter, but it does not, as detailed below, provide the full picture of the performance of a nanoplasmonic sensor. Also, far more information is needed to determine the signal from actual biomolecular binding reactions compared to bulk RI changes, such as knowing the effective RI change caused by biomolecules [2, 3].

In terms of detection limit, the literature on nanoplasmonic sensing has so far focused mainly on defining detection limits in number of molecules inducing the smallest detectable signal. It can be argued that number of molecules is not the most relevant parameter, due to several reasons. For one thing, even if only 100 molecules bound to a single nanoplasmonic particle are causing the observed signal, the actual sample solution in such experiments always contains many orders of magnitude more molecules. Also, in many biomedical sensing applications the number of target molecules available is practically infinite, but detection is nevertheless challenging. As will be discussed below, it is in most situations the lowest detectable *surface coverage* that counts.

Important Characteristic Challenges

It is obvious from the literature on nanoplasmonic sensors that they are adequate for detecting typical protein targets (10–100 kD) when they are present at reasonably high concentrations in the sample solution, typically >1 nM [4]. When measuring in real-time, the noise level in these data is adequate for determining rate constants, although finding an accurate model describing the binding rate can be very challenging. This is mainly because the rate of binding often depends on both reaction kinetics and mass transport simultaneously. Concerning molecular binding to surfaces, there are two simple equations which need to be kept in mind. First, the Ilkovic equation for the case of *diffusion limited* binding under stagnant conditions gives the surface coverage Γ as [5]:

$$\Gamma(t) = 2c_0\sqrt{\frac{Dt}{\pi}} \tag{10.1}$$

Here c_0 is the concentration of molecules in the liquid bulk and D is their diffusion constant. Note that the unit used to define c_0 (mass or moles over volume) gives the unit for Γ. The surface is assumed to be infinitely large, just like the liquid bulk it is in contact with Equation (10.1) describes a surface that never saturates but keeps "devouring" molecules. Naturally, this is only valid as long as the surface coverage of molecules remains reasonably low and the model can therefore only describe the very initial part of an adsorption process *before* equilibrium is reached [5]. It should also be noted that the rate of binding will be higher than that described by (10.1) when there is a continuous flow of liquid next to the surface, which reduces the depletion zone. However, the effect of flow on binding rate is not always high [6, 7]. Also, higher flow means that more sample volume is consumed.

The other characteristic equation is the Langmuir isotherm describing *reversible* binding. When equilibrium is reached, the surface coverage Γ_{eq} is [5]:

$$\frac{\Gamma_{eq}}{\Gamma_{max}} = \frac{c_0}{c_0 + K_D} \tag{10.2}$$

Here Γ_{max} is the maximum possible surface coverage and K_D is the *dissociation constant* of the interaction. K_D is equal to the ratio of the rate constants for dissociation and binding $(K_D = k_{off}/k_{on})$. Therefore, only knowing K_D does not provide absolute values of k_{on} and k_{off} which are needed to know, e.g., the lifetime of the interaction. This illustrates one major advantage of being able to monitor binding and unbinding in real-time.

In reality, neither (10.1) nor (10.2) can describe a binding process precisely since the binding rate is determined by combined effects of mass transport, reversibility, and reaction kinetics. Still, the expressions are useful due to their simplicity and ability to illustrate important points. Mass transport limitation is generally promoted by systems that have high k_{on} and low D, but most importantly it is the current state of the surface Γ_{eq}/Γ_{max} that determines if (10.1) holds true. In theory, all systems reach equilibrium (10.2) eventually.

We will now look at some characteristic situations where the detection limit of current nanoplasmonic sensors is not sufficient. The importance in terms of biological or biomedical applications is described for each case. Possible future improvements of nanoplasmonic sensors in order to overcome these challenges will then be discussed. The characteristic challenges are illustrated in Fig. 10.2. At the end of this section, Table 10.1 summarizes the situations described.

Note that these are *characteristic* problems and that in reality one might face a biosensing challenge which is a combination of several of these situations. For instance, the analyte might be present at low concentration in a sample (Fig. 10.2c) which also has a small volume (Fig. 10.2b). As another example, we might want to have single molecule resolution (Fig. 10.2a) for a target molecule of low molecular weight (Fig. 10.2d). Such situations will create even higher demands on sensor performance. However, many situations can be described by only a single of these four different points and the summary in Table 10.1 can act as a guideline for which aspects of a sensor design are most important.

Single Molecule Resolution (Fig. 10.2a)

Single molecule resolution is achieved when a single molecular binding event gives rise to a signal which is significantly higher than the noise. In other words, S/N should be higher than the number of molecules causing the total signal. It is important to note that the possibility to observe single molecule-binding statistics does not necessarily make a sensor more suitable for biomedical applications. In brief, even if molecules that do bind are counted, it does not mean that *all* molecules in the sample will be counted. Single molecule resolution is also unnecessary for proper determination of binding rate constants, in which case it is actually better with ensemble measurements to achieve a higher statistical selection. However, observing single-binding events may provide additional information about the molecular interaction compared to ensemble measurements. For instance, if a pair of molecules can interact in different ways, single molecule resolution

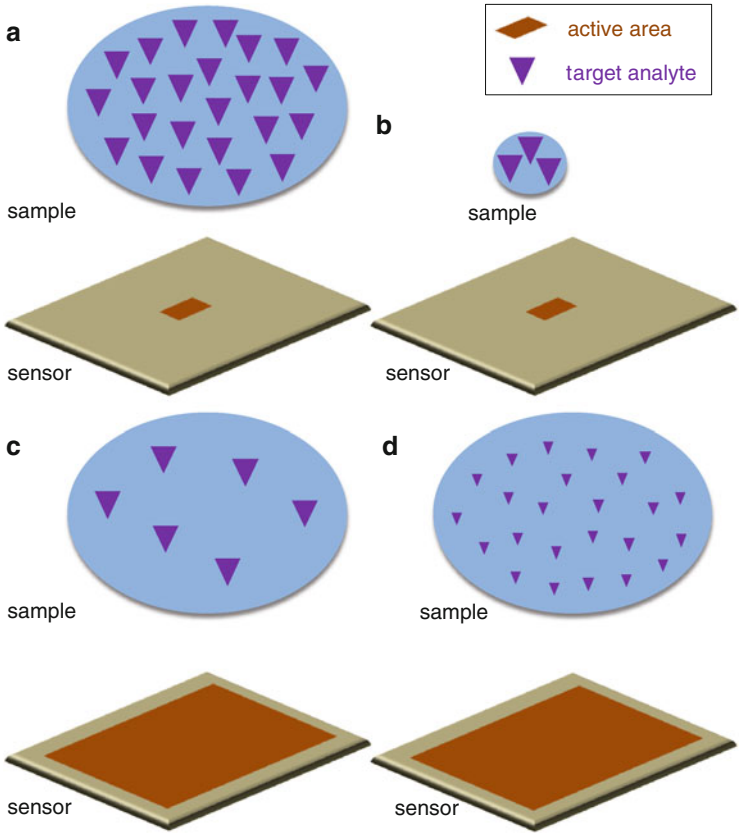

Fig. 10.2 Characteristic sensing challenges. The challenge of single molecule resolution is illustrated in (**a**), the problem of handling small sample volumes is shown in (**b**), a sample with low analyte concentration is shown in (**c**) and (**d**) illustrates the challenge of low molecular weight analytes

might be a way to discover such features. This type of information is harder to acquire in the case of ensemble measurements. On the other hand, in nanoplasmonic detection systems there is an additional complication from the fact that the signal from a molecule will depend on where in the nanostructure environment that molecule is located [2, 8].

For any surface-based biosensor, miniaturization is essential for resolving single-binding events. This is because the number of molecules captured on the surface will be proportional to the active area A, while S/N does not increase with A in this manner, but more slowly. For surface-based detection in general, increasing A means that more statistical data is included in the analysis and noise levels tend to, at best, follow a square root dependence on the amount of data generated. Thus, one tends to get closer to achieving a signal per molecule higher than the noise level

Table 10.1 A summary of the four characteristic sensing challenges, each of which represents a situation where the performance of current nanoplasmonic sensors usually is not sufficient

Challenge	Single molecule resolution	Detecting few molecules	Low analyte concentration	Low molecular weight analyte
Sample: volume available	Practically infinite, but detecting one binding event is still challenging	Typically small	Practically infinite, but detection is still challenging	Large, but detection is still challenging
Sample: concentration of analyte	High, but detecting one binding event is still challenging	Can be high if the sample volume is small	(Low)	High, but detection is still challenging
Sample: molecular weight of analyte	High, but detecting one single binding event is still challenging	High, but detection is still challenging	High, but detection is still challenging	(Low)
Sensor surface: number of molecules bound	Not relevant for this challenge	Low since typically only a few molecules are captured by the sensor	Absolute number of molecules can be quite high if the sensor is large	High, but detection is still challenging
Sensor surface: surface mass coverage generated	Not relevant for this challenging	Low since few molecules are captured by the sensor	will be low due to the equilibrium condition	Will be low due to the low molecular weight
Sensor surface: need of miniaturization	Very important for success	Very important for success	Meaningless when specifically addressing this challenge	Meaningless when specifically addressing this challenge
Notes on the molecular interaction	Detection will be easier if the lifetime of the interaction is longer	Detection is challenging for irreversible binding and even more difficult for reversible binding	Binding is usually reversible, detection normally feasible for an irreversible interaction	Detection is challenging even for irreversible binding, high receptor density desirable

The left column shows different factors describing the analyte, the sample, and the interaction with the sensor. Each other column represents one of the challenges. Note that although there are several real life examples for each challenge, one might also face a situation where more than one of the challenges need to be met. This table represents a summary of the section on characteristic challenges and details are given in the main text

for miniaturized systems [9–11]. Typically, for a miniaturized nanoplasmonic sensor, the amount of light collected by the detector will increase linearly with A and the noise will scale with the square root of this intensity (see below).

So far, most nanoplasmonic sensors that clearly aim for single molecule resolution are based on scattering spectroscopy of single nanoparticles under dark-field illumination [9, 11–14]. However, a microspectroscopy approach based on transmission mode is clearly competitive, because the noise level is much lower when measuring on a small ensemble of nanoparticles compared to a single particle [10]. Reported detection limits in terms of number of molecules giving rise to the minimum observable signal are slightly below 100 for typical proteins and theoretical estimates of the detection limit in an optimized system are on the order of tens of molecules [9]. An important challenge to be overcome is the additional noise due to mechanical instability associated with spectroscopy of few or single nanoparticles [9, 10]. The Vörös group actually reported single-binding events using such a system, although not yet in a label-free manner [15].

Another important feature to consider when aiming for single molecule resolution is the noise (and stability) of the system in relation to the rate of binding. For resolving a single molecule, it is only the noise between subsequent acquisitions which is important because binding events are virtually instantaneous [10]. However, the rate at which molecules arrive at (or are released from) the sensor area matters since it determines how many averaging operations can be performed without the risk of "smearing out" a binding event in the data of binding kinetics. In a hypothetical perfectly stable system, single molecule resolution can almost always be achieved if the target molecule concentration is low enough. In this case, the noise can always be reduced by averaging to the level corresponding to the signal of a binding event and it is just a matter of not having binding events occurring too often.

Detection of Few Molecules (Fig. 10.2b)

Single molecule resolution should not be confused with "single molecule detection," i.e., to detect the presence of a single target molecule in a sample. This represents the worst case of the more general challenge of detecting "few" molecules and it is a greater challenge than obtaining single molecule resolution since one also faces the problem of directing the few target molecules to the sensor elements. Other than this the same principles, e.g., miniaturization, apply as in the case of aiming for single molecule resolution. This situation typically occurs when the total sample volume is so low that few molecules are expected to be present in total. In this case, challenges associated with handling of small sample volumes have to be considered. Clever fluidics is essential also when few molecules are present in a larger volume (e.g., the same sample being diluted), because it becomes even more challenging to direct the few molecules to the sensor elements.

It is evident that detection of few molecules cannot be realized without effectively passivating all other surfaces in the system except the active sensing area. Also, the active spot must clearly be very small. For instance, if the sample is 1 μL, it is difficult to spread this volume on a 1 cm^2 sensor. Thus, surface functionalization becomes a great challenge, because only the very small sensor spot should be activated, while all other surfaces must be inert. For example, a single nanoparticle, if possible to probe with sufficient S/N, containing specific antibodies could be placed on an inert background and its spectrum recorded, but there must not be any other such nanoparticles present since they might then capture the targets instead.

It should be noted that even if the analyte would bind irreversibly to the sensor, the problem of directing the targets to the sensor remains. The challenge is basically a matter of efficient liquid handling ("getting the molecules there") and efficient microfluidics technology is a prerequisite for possible future applications. As explained by several numerical and analytical models (more sophisticated than (10.1)), the mass transport limits imposed by diffusion need to be overcome in order for detection to be sufficiently fast for practical sensor use [6, 7, 16]. Also, as long as the binding does not reach saturation or equilibrium, the molecules that do arrive at the surface should preferably bind at the most sensitive regions of the sensor [4].

Situations where the total sample volume is limited often occur in biology and medicine when the analyte is present in tissue or bodily fluids which cannot be extracted in large quantities. A characteristic example is single cell analysis, in which case the total sample volume obviously is extremely small [17]. Another typical example is the situation when a larger sample volume is processed in some way for purification (or perhaps for increasing the analyte concentration). Increasing the analyte concentration by reducing the sample volume may be helpful (see below), but it also introduces the problems related to handling small sample volumes.

Significant research efforts in the field of nanoplasmonic sensing have been focused on achieving single molecule resolution, while much less effort has been put into the requirements for detection from samples with low volume. In other words, the miniaturization issue has been addressed to a higher extent than the challenge of handling small liquid volumes. In future work, the challenge of efficient liquid handling must also be considered, since it is a key component for incorporation of sensors in practically applicable lab-on-a-chip devices. An efficient way to improve the mass transport rate to the sensor area is to utilize plasmonic nanopores with a liquid flow through the surface [18–20]. This type of setup, in combination with inert microfluidic channels above and below the pores, may substantially improve liquid handling and capture efficiency.

Low Analyte Concentration (Fig. 10.2c)

Another principle challenge is associated with low analyte concentration in a sample, which may have an essentially infinite volume. In this case the eventual surface coverage of targets on the active sensing area will normally be low due to the *reversibility* of most biomolecular interactions, even when equilibrium is reached (10.2). This situation thus differs from the other challenges discussed above, as illustrated in Fig. 10.2. For the case of low analyte concentration, we assume that the amount of sample solution available is practically unlimited. This is normally the case in sensing applications such as food product analysis and environmental monitoring, but is sometimes also true for biomedical sensing (see below). Therefore we may have plenty of molecules, but if the concentration is low, it will still be a major challenge to detect them, primarily because the interaction is usually reversible.

It is usually not a challenge to detect low concentrations when the analyte binding is irreversible and follows mass transport kinetics (such as (10.2)) as long as an infinite sample volume is available. This is because the rate of binding can be enhanced by flowing sample solution over the sensor [6, 7]. Although introducing flow cannot strongly improve the mass transport to miniaturized sensors with good capture efficiency (~1 μm) [6], high mass flux enhancements can be achieved for larger sensors (~1 mm) [7]. Since there is no need for sensor miniaturization when addressing this challenge (a relatively large analyte in an infinite sample volume), detection should thus normally be feasible for the case of irreversible binding under flow. Naturally, if the analyte concentration is extremely low, some of the challenge might still remain. This depends on the efficiency of the fluidic system introduced to the surface-based sensor. A high flow rate should preferably be used together with a narrow fluid channel above the (large) sensor, so that diffusion to the surface is fast [7].

There are examples of biomolecular interactions that are essentially irreversible, such as the common biotin–avidin interaction (K_D on the order of 10^{-15} M) [21]. In fact, this appears to be the most common model interaction chosen by us and others when evaluating the performance of a nanoplasmonic sensor, as evident when browsing through the literature. Although it is desirable to have such a standard interaction for comparison, the choice of avidin binding to biotin does not represent a typical situation in biomolecular interaction analysis. Because it is irreversible, it does not provide a way to illustrate the effect of reversible binding, which is more or less a standard feature among biomolecular interactions where proteins are involved [22]. One exception from the general rule of reversible binding is detection of DNA. Single-strand hybridization can be practically irreversible for longer strands (depending on temperature and salinity). However, it is often of greater interest to focus nanoplasmonic applications on biomolecular interactions related to proteins, simply because DNA sensing arrays are already developed and the technology behind them is working well [23].

A typical example of an application illustrating this challenge is the detection of biomarkers in blood. One can in principle extract over a liter of blood from a healthy human being, so it is possible to get a very high sample volume. Of course, such a diagnostic test will not always be applicable, but the point is that even if we only extract 10 mL blood, this is most likely sufficient for the assay. One can also get quite large volumes of, for example, saliva or urine without too much problem. In these situations, one typically has a relatively large number of target molecules in total even if they are present at a low concentration. It should be noted that biomarkers are often present in pM concentrations [24]. Even if we flush substantial volumes of, for example, blood over our sensor, it will not increase the number of molecules on the surface once equilibrium has been reached. Using (10.2) to describe this situation, it can be seen that K_D stands in direct relation to the surface coverage for a given concentration. Thus, we need very high affinity probes (see below) to detect biomarkers.

Low Molecular Weight Analytes (Fig. 10.2d)

Another characteristic challenge for the future of nanoplasmonic sensors is the detection of targets that have low molecular weight. In these situations, the problem is again that the final surface coverage Γ in terms of mass per area unit will be low. However, in this case relatively many molecules may be captured, but the eventual surface mass coverage is still challenging to detect. This situation is principally different from all those mentioned above in the sense that sample volume, target concentration, and receptor affinity all can be very high; there is still a major challenge to detect small molecules. As for the previous challenge, miniaturization of the sensor is in this case completely irrelevant. It will most likely make the sensor worse due to higher noise levels. Instead, the challenge again lies in detecting the low surface mass coverage.

The most important type of application which illustrates this point is most likely the studies of interactions between medical drugs and their receptors. Drug molecules are typically low in molecular weight and can be produced in relatively large amounts and even high concentrations. The "sample" is thus ideal except for the fact that the analyte is small.

In a recent work, Kabashin et al. showed that a vertical nanorod metamaterial can be used in total internal reflection mode to reach sensitivities which are actually sufficient for detecting small molecules [25]. In this case, biotin (mass of 244 D) was detected with S/N of ~5 as it bound to avidin on the surface (instead of the other way around). It appears from the data that it was really the high sensitivity to changes in RI of this structure (for bulk changes it was higher than conventional surface plasmon resonance [SPR]) which enabled detection of biotin rather than low noise in the measurement (the fluctuations in λ_{peak} were ~0.5 nm). This noise level can most likely be improved by changing the experimental methodology [10, 26]. Although the actual surface coverage of biotin was not reported and possible

conformational changes [27] were not discussed, the nanorod metamaterial appears very useful for improving detection limits in terms of surface coverage.

Surface Functionalization

An important factor which is not often considered when evaluating sensor performance is the influence from the chemistry used to achieve the desired surface functionalization for specific detection. In practice, improving surface chemistry to avoid non-specific binding is perhaps the most important problem to address in order to improve the practical usefulness of nanoplasmonic biosensors. In practically all surface-based detection schemes, the observed signal only represents molecular binding and does not contain any information about the type of interaction. The sensor is "blind" in this sense and accurate results rely on the assumption that binding is specific.

Probe Affinity

Increasing the affinity of the immobilized probe for the target is generally an applicable strategy to improve sensor performance, even if the ideal case of irreversible binding rarely can be achieved. Instead, the reversibility of biomolecular interactions implies that the number of molecules on the active sensor area at equilibrium depends on the affinity of the interaction between the target and the recognition element (10.2).

For typical antibody–antigen interactions, the dissociation constant K_D is on the order of 1 nM at best, while engineered antibodies can reach dissociation constants slightly lower [22]. This means that at equilibrium, around 50% of the antibodies on the surface have a target captured when it is present at a concentration of 1 nM (10.2). This value holds for bioengineered antibodies especially designed for specific detection. In biology, many interactions are even weaker. An alternative to antibodies is bioengineered oligonucleotides, generally referred to as *aptamers*. Aptamers may be advantageous for certain surface functionalization strategies due to their small size and robustness, but show binding affinities on the same order as for antibodies [28].

Probe Density

Increasing the number of receptors on the active sensing area will increase the signal for reactions that reach equilibrium, since a higher number of molecules will be bound per area unit. For instance, a way to immobilize more active antibodies on a given sensor surface area would be useful when trying to detect an antigen present

in low concentration. However, it should be noted that increasing the number of receptors on the surface can in some situations lead to a decrease in performance if the analyte is electrostatically repelled or if the probes on the surface interfere with each other at too high coverage.

Also, for a system dominated by mass transport limited binding which has not reached equilibrium (10.1), increasing the number of receptors (or their affinity) normally has no effect. This is because the surface is already "capturing molecules as fast as possible," since otherwise the system would not exhibit mass transport limited binding. The only advantage of more surface receptors in such a system would be to increase the number of captured molecules at saturation. If all binding sites become occupied, more binding sites naturally give more bound molecules and a higher signal eventually. However, in such a situation the surface coverage is probably sufficient, at least for qualitatively detecting that binding has occurred, considering the assumptions under which (10.1) holds (i.e., a surface that captures molecules efficiently and irreversibly). The surface mass coverage may still be small if the molecules are small. In this case the system is normally reaction limited instead due to the high D.

A typical example where the number of recognition elements often needs be increased is the case of interactions with membrane proteins, which are difficult to produce in high density on a surface. It is a major challenge alone to immobilize membrane-residing proteins on a surface with retained biological activity. Naturally, the presence of an artificial biological membrane is a prerequisite, which has led to the development of various artificial cell membrane constructs on plasmonic nanostructures (as described in Chap. 4). In addition, many reactions with membrane proteins involve binding of small analytes [29].

Parasitic Signals

There are in principle three different types of parasitic signals. First, there may be other molecules than the target binding directly to the surface. Second, there may be other molecules binding to the recognition element, i.e. the "bait" may not be specific enough. Third, the analyte itself may end up binding to the surface instead. These types of interactions, illustrated in Fig. 10.3, will always occur to some extent when analyzing complex biological mixtures. Thus, even when using nanoplasmonic sensors to *study* a biomolecular interaction rather than *detecting* the presence of a specific target, there may be problems from unspecific binding. Imagine that a solution containing only a particular antigen is added to a surface functionalized with, e.g., an antibody. In this case it is clearly possible that the target may not interact with the probing molecule, but rather bind directly to the underlying surface unless it is properly functionalized. This will lead to inaccurate determinations of, for example, affinity constants. As an example, in several reports utilizing the biotin–avidin interaction, there is often no way to tell whether avidin actually binds to biotin on the surface or if it just interacts with the surface directly.

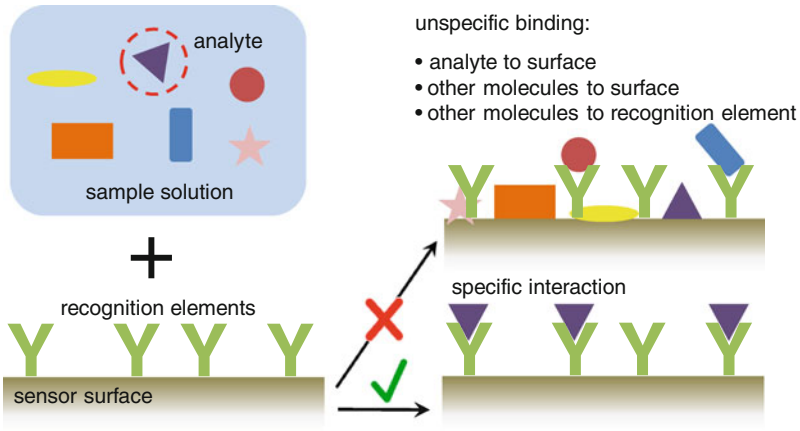

Fig. 10.3 Principle operation of a surface-based sensor. A complex biological sample is added to the surface, but only the specific interaction should occur, since any type of binding results in a signal

A suitable control is to add avidin in the presence of excess free biotin [2], which should result in no binding.

Chemical approaches for creating inert backgrounds that suppress interactions between molecules and the surface support are so far usually based on poly (ethyleneglycol) (PEG), which has proven an effective strategy [30–34]. The basic function of the flexible PEG chains is twofold: First, they form a gel-like layer which presents a steric hindrance, since a molecule entering the film would reduce the conformational entropy of the PEG. Second, any electrostatic interactions between molecules and the surface are screened by the PEG layer [34]. The latter effect requires a reasonably thick layer and not too low salinity (the PEG should, as a rule of thumb, be thicker than the electric double layer). Overall, thicker and denser PEG layers give better resistance to non-specific binding to the surface [32, 33, 35].

When exposing PEG-modified surfaces to, for example, serum, the recorded response can correspond to very low uptakes (<1 ng/cm^2) [33]. Still, the very fact that this amount of unspecific binding can be detected at all shows that further improvements in creating inert surfaces are absolutely necessary in order to improve the performance of nanoplasmonic sensors when detecting analytes in complex biological samples [36, 37]. Indeed, as long as unspecific binding *can* be observed, the physical detection limit of a system in terms of surface coverage *cannot* be realized in a biomedical sensing application. It should also be recalled that not even the best PEG layer in the world can prevent unspecific interactions associated with the recognition element. Furthermore, there is also the challenge of putting the recognition element on top of the PEG layer, which requires some terminal group for further functionalization after PEG layer formation [38]. Finally, the thicker the PEG layer is, the further out from the surface binding will occur. In

the case of nanoplasmonic sensing, this results in a loss of signal due to the rapid decay of the electric field [8].

Gold is generally the most interesting metal for developing surface functionalization strategies since it is, for good reasons (see below), the most commonly used metal in nanoplasmonic biosensors. Thick and dense PEG coatings on Au can be achieved by using surface-initiated polymerization (SIP), in which case the PEG is synthesized directly from initiators on the surface. This generates a high density of PEG chains since the small initiator molecules can be assembled in dense monolayers [32]. In particular, Au can be made highly inert and also long-term stable by assembling a thiol monolayer on the surface, followed by SIP. Another option presented for creating inert Au surfaces is poly(propylenesulphide) with grafted PEG chains [30].

However, other materials than Au are usually present on a nanoplasmonic sensor surface. For instance, Au nanoparticles and thin Au films with nanoholes are typically supported by glass surfaces. Some [37], or even a large part [39, 40], of the response from such a sensor will be associated with binding to the glass and strategies for making silica surfaces inert are thus of utmost importance for nanoplasmonic sensors. For this purpose, the copolymer consisting of PEG grafted to poly(L-lysine) (PLL-g-PEG) has proven suitable [33, 34]. The molecule assembles on oxide surfaces with the lysine units adhering to the surface by electrostatic interactions, making the PEG chains face outwards into the liquid [31]. This occurs for oxide surfaces that are negatively charged at reasonable pH (for instance, pK_a for pure SiO_2 is around 2). A high density of PEG can be achieved since the grafting ratio (lysine backbone monomer per PEG chain) can be tuned during bulk synthesis of the molecule. PLL-g-PEG can also easily be functionalized further by introducing, for example, biotin at the end of a fraction of the PEG chains [38].

In any situation where two or more materials are present, the strategy for making one inert may affect the other surface and functionalization becomes more difficult. As mentioned above, the materials typically encountered in nanoplasmonic biosensors are gold and silica. In this situation, thiolated PEG (or thiolated oligoethyleneglycols) can be used to first specifically modify gold without influencing silica [40]. Alternatively, a small carboxylated thiol can be self-assembled on gold and PLL-PEG introduced to both materials [2, 10, 26]. These strategies also work for Au and silicon nitride [19] or Au and titanium oxide [4].

Sensitivity Maximization

After discussing possible improvements in terms of surface functionalization, we turn to the question of signal enhancement. We recall that sensitivity is defined as the sensor response per unit change of some variable to be analyzed. Here we choose to let this variable be the RI of the liquid environment in order to make performance comparisons simple. Every model that aims to understand the plasmonic properties of a nanostructure will introduce the dielectric function (refractive index) of the

environment surrounding the metal as a variable and this is the parameter which is changing in most sensing experiments. Therefore, defining the sensor variable in terms of RI changes is convenient also when dealing with analytical expressions. Naturally, in a biosensing experiment, the actual RI change is caused by a certain surface coverage of biomolecules and the sensor responds to a *local* RI change. Fortunately, there are ways to translate adsorbed biomolecule mass into an *effective* environmental RI. In this situation, it is critical to take the unhomogenous distribution of the plasmonic field into account [2, 8, 41].

What Kind of Sensitivity?

One might also ponder on what parameter the sensitivity should be expressed in when discussing sensor performance. A common parameter of choice is the plasmon resonance wavelength λ_{peak}. In fact, using the change in λ_{peak} per RI unit appears to be the most common way to express the performance of a given nanostructure for sensing applications. This parameter has some convenience due to the fact that, for nanoparticles, the sensitivity is then independent of the number of particles analyzed as long as there are no coupling effects. Also, shifts in resonance wavelength are typically presented in biosensing experiments. However, this does not mean shifts in λ_{peak} is the best way to define performance.

We note that spectroscopy equipment does not directly measure λ_{peak}, but simply probes intensity changes. Even when a full optical spectrum of a sample is acquired, the data consists merely of independent intensity values for different wavelengths [10, 42]. Whatever method that is used to determine a change in λ_{peak} it will be based on the associated intensity changes at wavelengths close to λ_{peak}. Hence, the sensitivity of a particular structure in terms of shift in λ_{peak} per RI unit is not sufficient to evaluate the sensor performance. Instead, a performance parameter should reflect how large changes in *relative intensity* (e.g., extinction or transmission in percent) can be acquired using a particular nanostructure [26, 43, 44].

One effect besides λ_{peak} which actually is commonly considered when estimating the performance of a nanoplasmonic sensor is the width of the resonance peak. The width is often taken into account using a so-called figure-of-merit (FoM), which is usually defined as ratio between the bulk resonance wavelength sensitivity and the full width at half maximum [45]. This is an improvement compared to looking only at changes in λ_{peak}, but it should be noted that the reason why peak width is important for performance is simply that sharper peaks tend to give higher intensity changes as they shift. (This can be realized simply by drawing a sharp mountain peak next to a flattened hill and imagine moving them both laterally.) Also, the full picture is not provided unless peak *magnitude* is also taken into account [43, 46]. In the same manner, a high magnitude is preferable simply because it causes higher changes in extinction when the peak shifts. The importance of peak magnitude is conceptually illustrated in Fig. 10.4, showing that a FoM that only introduces peak width does not necessarily provide the full picture.

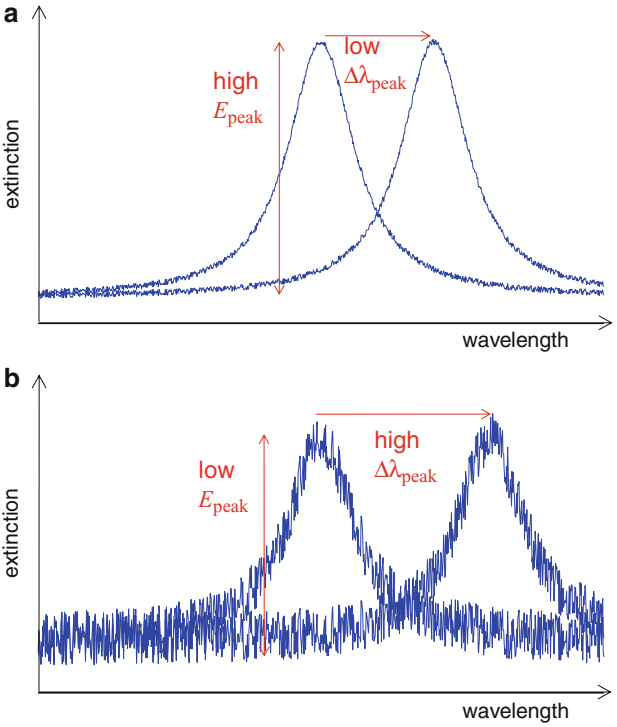

Fig. 10.4 Simulated spectral peak shifts. The peak in (**a**) shifts less than the one in (**b**), but has a magnitude which is one order of magnitude higher. The simulated noise is the same for both peaks

The peak in Fig. 10.4b shifts more than that shown in Fig. 10.4a, but the peak magnitude is ten times lower in Fig. 10.4b compared to Fig. 10.4a. In both plots, the same noise level was introduced. It is evident that the upper peak will be more suitable for sensing, because it results in much higher extinction changes, even if the sensitivity in terms of peak shift is lower. The peak width parameter was set to the same value in both simulated peaks, so the FoM is lower for the peak in Fig. 10.4b according to the most common definition. However, it should be noted that a FoM that also takes peak magnitude into account has been discussed by Masson and colleagues [46].

When it comes to the importance of peak magnitude, quantitative information is rarely reported in the literature. This, in turn, actually complicates the search for nanostructures that are good for sensing. In fact, extinction is often displayed as "arbitrary unit" in graphs, and sometimes information on changes in extinction is lost due to normalization of spectra. This way of treating data makes sense in order to characterize the physical properties of nanoplasmonic structures, but although extinction values have no *physical* unit (length, time, . . .), it is a misconception that it is not of utmost importance with respect to sensor performance (compare with, for example, refractive index that also has no physical unit). Indeed, a surface containing a defined

nanostructure will have an absolute extinction value for each wavelength of incident light. The measured changes in this extinction spectrum during a sensing experiment do *not*, in principle, depend on the instrumentation used and provide, as detailed further below, critical information for evaluating sensor performance.

Considering the reasoning above, we suggest it is simpler and more relevant to define the sensing performance of a nanostructure in terms of relative intensity (e.g., extinction) changes per RI unit, rather than a sensitivity in λ_{peak} per RI unit or a FoM based on arithmetic combinations of various resonance peak parameters. It means, in turn, that the performance parameter will depend on wavelength. Preferably, the full spectral changes should be visualized and the wavelength where the change induced by an altered environmental RI is maximized specified [26], as was recently discussed also by Sönnichsen [43].

General Guidelines

Overall, there is no obvious method to choose a nanostructure for maximized signal, in particular when striving towards high relative intensity changes as explained above. Still, there are a few general guidelines which can be useful. Admittedly, a large sensitivity in terms of $\Delta\lambda_{peak}$ per RI unit is often, though not necessarily, correlated with higher sensitivity in terms of relative intensity changes (see Fig. 10.4). A higher sensitivity to RI in terms of λ_{peak} can thus serve as an *indication* of a suitable nanostructure for sensing. Also, λ_{peak} is a convenient parameter to monitor in experiments (see below).

The Lazarides group presented a convenient rule of thumb for estimating the resonance wavelength sensitivity to RI [47]. For ellipsoidal nanoparticles in the electrostatic dipole limit, the sensitivity of a nanoparticle plasmon resonance wavelength to the RI (n) of the environment can be written as:

$$\frac{\delta\lambda_{peak}}{\delta n} = \frac{2}{n}\left[\lambda_{peak} - \frac{a}{b}\right] \tag{10.3}$$

Here a and b are constants used to describe the real part of the dielectric function of gold in the wavelength region from 500 to 800 nm as $a - b\lambda$ with $a = 34$ and $b = 0.072$ [47, 48]. The relation thus works best for Au nanoparticles in the VIS-NIR region. It should also be noted that the validity of the electrostatic approximation is poor for any particle larger than some tens of nm. Furthermore, for shapes that deviate strongly from ellipsoids, there might not be only dipole modes involved. Still, the formula is useful as a rule of thumb since it states that the sensitivity is simply proportional to λ_{peak}. The parameter n cannot really be changed since all biosensing experiments will take place in a water environment with n close to 1.333 (water at room temperature).

In summary, we can expect that nanoparticles with higher resonance wavelengths have a better sensitivity. For Au in particular, it is also worth noting that the

imaginary part of the dielectric function is minimal in the interval from 700 mm to 900 nm [48]. A low imaginary part of the dielectric function generally results in sharper resonance peaks and higher intensity changes. Indeed, this spectral window has been identified as the optimal sensing region due to the highest FoM [49] (when defined as peak shift sensitivity divided by peak width). Interestingly, this conclusion holds also for surface plasmons in thin films as it is only derived from the material properties of Au. Furthermore, this wavelength region is known as the "biological window" where human tissue is most transparent [50]. For instance, the absorption of hemoglobin in blood occurs at shorter wavelengths and water absorption occurs at longer wavelengths. This helps providing high light throughput, which is desirable (see below), in applications where transmission occurs through tissue or bodily fluids.

Most of the discussion has so far been focused on Au nanoparticles, although in principle any metal, or even any material with free electrons, can exhibit plasmon resonances. Most other metals are unsuitable for plasmonic sensing due to their dielectric functions, which makes their resonances weak (low magnitude, high broadness) or at wavelengths that are not easily accessible. However, some metals may still be interesting for nonbiological sensing. This has been showed by the Kasemo group who has investigated resonances in palladium [51], platinum [51], aluminum [52], and tin [53] nano disks and processes associated with these material (Chap. 9).

There are at least two metals, namely silver and copper, which are competitive for biosensing in comparison to Au from a sensitivity perspective due to their dielectric functions [48]. However, these metals are usually not a better choice in practice due to their susceptibility to oxidation. Still, the van Duyne group has investigated the resonances in Cu nanoparticles [54] and successfully use Ag nanoparticles regularly for sensing [36, 55]. On the nanoscale, Cu particles are practically completely oxidized and special conditions are needed to measure the proper spectrum [54]. It has also been shown that for Ag, the situation is in fact not that bad and freshly fabricated samples are useable, at least as "single use sensor chips." However, it should be noted that Ag does not provide a higher sensitivity than Au in terms of λ_{peak} for all nanostructure geometries [56]. Still, in order to have surfaces that are stable and can be cleaned and regenerated, Au appears to be the best choice. By proper adhesion to the underlying substrate, Au nanoparticles or holes in thin Au films can be cleaned with efficient methods such as hydrogen peroxide under basic conditions [10, 35], which is an efficient wet etch cleaning method to remove organic material.

The Spatial Sensitivity Distribution

A final critical aspect that must be considered in discussions about sensitivity is the spatial distribution of the plasmonic field around the nanostructure. A molecule binding to a plasmonic nanostructure will induce a different response depending on

where it is located. In particular, due to the rapid decay of the nanoplasmonic field (tens of nm) [2, 8, 37, 41], the distance to the metal surface is important and the maximum signal is generally achieved when molecules attach directly to the metal. This is often not possible in a real surface-based biosensor as there is generally a recognition layer present. Thus, optimizing the recognition layer so that it maintains specificity without being too thick is a very important challenge for optimal performance in nanoplasmonic sensors. For practically all sensing applications, a monolayer of bound analytes, plus the underlying functionalization layer, must be smaller than the extension of the sensitivity to RI into the liquid environment. The sensitivity extension into the liquid environment depends on nanoparticle geometry and exhibits quite large variation, but seems to always be somewhere between 10 and 100 nm [2, 8, 37, 41].

When comparing conventional SPR [57] and typical nanoplasmonic (LSPR) sensors under practically identical conditions, the magnitude of the spectral changes induced by a biomolecular monolayer is quite similar for the two systems [45]. This is because although SPR has a bulk sensitivity to RI which is >10 times higher, the surface sensitivity is much lower, i.e., SPR can sense RI changes even if they occur a micrometer away from the metal surface [3]. This is conceptually illustrated in Fig. 10.5a. However, there are methods available to utilize the full probing volume in SPR by introducing a 3D gel matrix [58] (Fig. 10.5c). This usually results in a higher signal since more receptors can be immobilized on the surface. It can also be argued that the gel provides an environment which better mimics the native environment of biomolecules since it is "more 3D like" compared to molecular monolayers on surfaces. However, many receptors will also be located in less sensitive regions, so it is not always obvious that the gel matrix provides the highest signal (compare Fig. 10.5a, b). If equilibrium is not reached, the bound molecules might induce lower response if they end up in less sensitive regions [4].

We argue that it is suitable to maintain a definition of performance as relative intensity changes per RI change of the whole liquid bulk environment, simply because in many cases there are methods available to utilize the full probing volume. This is not always the case though and it is important to be aware that the structure with highest spectral changes due to bulk RI changes will not be the best choice for all applications because the end result will always depend on the exact type of surface functionalization used. The degree of surface localization of the sensitivity must be kept in mind and will normally play an important role as many surface functionalization techniques create layers that are thinner than the sensitivity extension. When detecting low molecular weight targets or low analyte concentrations (see above), it is of interest to utilize the full probing volume. On the contrary, for detecting few molecules or for achieving single molecule resolution, it is important that molecules are directed to the most sensitive regions of the nanostructure and knowledge of the sensitivity distribution becomes critical.

One can from this reasoning conclude that it is generally important to match the characteristic sensitivity extension into the liquid to the eventual molecular

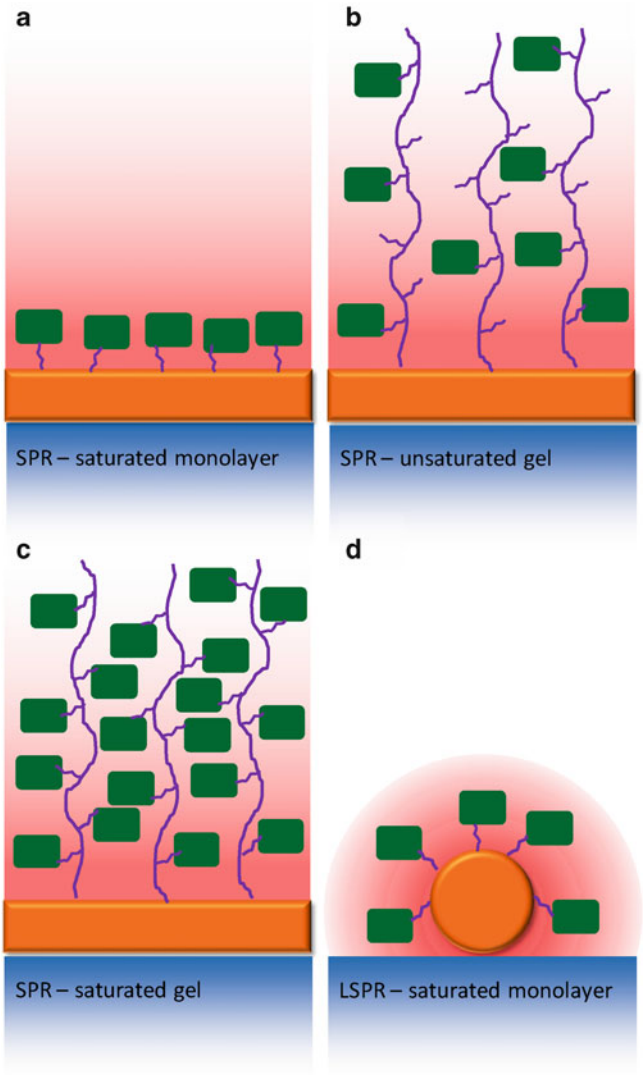

Fig. 10.5 Illustration of how the sensitive volume is utilized in different plasmonic sensors. (**a**) and (**d**) result in similar signals. The configuration in (**b**) might provide higher signal than (**a**) if the receptor density is higher, but the sensitivity decrease with distance from the surface needs to be taken into account. The highest signal is normally achieved in (**c**)

construct on the surface in the real sensing application. In some situations, creative solutions have been found, such as lipid vesicle multilayers for cell-membrane-related sensing applications [59]. For some types of surface modifications, a 3D structure will clearly be difficult to realize. For instance, self-assembled thiol-based monolayers on gold are a convenient basis for further surface functionalization

[8, 11, 12, 15, 37, 40], but will normally result in layers that are thinner than the characteristic extension of the sensitivity. However, after immobilizing, e.g., an antibody and detecting an antigen, the eventual thickness of the biomolecular layer on the surface might well match the sensitivity extension [2, 8].

Noise Minimization

We now assume that we have our functionalized nanostructure and thus the spectral changes of the system are defined, with a sensing performance preferably expressed in terms of relative intensity changes per RI unit. A completely separate challenge is to design an experimental setup that can probe these changes with as low noise as possible. The S/N performance will then be determined by the spectroscopy setup (noise), together with the optical properties of the functionalized nanostructure (signal). The discussion below is mainly focused on minimizing noise and not to improve stability. This is mainly because it is difficult to provide simple answers to why a spectroscopy system exhibits bad stability. It can be related to just about any slow change in the environment, such as the temperature in the lab. Finally, we assume that the sample is reasonably transparent so that it allows transmission of light.

Accuracy and Precision

In surface-based sensing techniques, a physical parameter is monitored and the *change* in this parameter corresponds to the signal. This means that the *accuracy* when measuring the physical parameter is less of interest, while the *precision* becomes more important. Accuracy is defined as the difference between the measured and the true value, while precision is defined as the reproducibility in repeated estimates of the true value. Precision is thus what defines the noise in the system. Also, since it is the change in the monitored parameter that matters, a constant offset between the measured value and the true value will not influence the signal. Figure 10.6 conceptually illustrates accuracy and precision.

Optical Configuration for Spectroscopy

All optical spectroscopy configurations contain a light source emitting all wavelengths of interest, typically tungsten or halogen for VIS-NIR and deuterium, mercury or xenon when UV illumination is necessary. Also, some form of dispersion element is needed to sort out wavelengths, as well as one or several photodetectors to measure intensity of light. Alternatively, a laser [60], VCSEL [61],

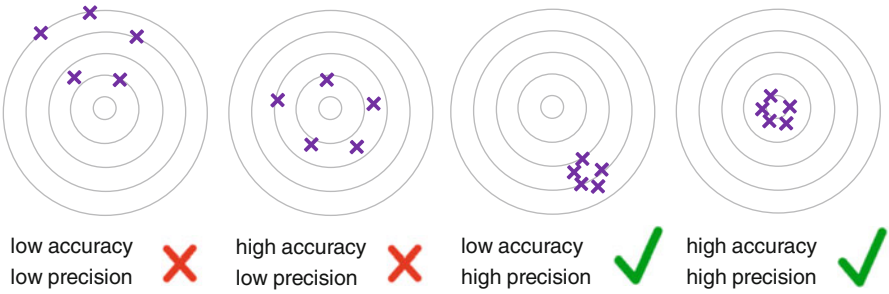

Fig. 10.6 Illustration of the different concepts of accuracy and precision. For surface-based sensors, precision is typically much more important than accuracy in the measurement

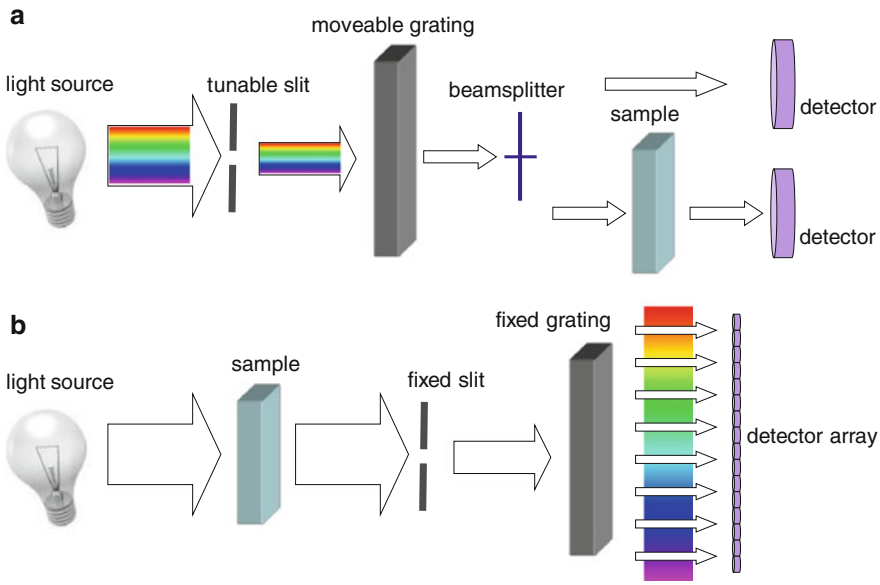

Fig. 10.7 The two most common arrangements for optical spectroscopy. In (**a**) is shown a double beam setup with a moveable grating and tunable slit. In (**b**) is shown a setup with fixed grating and slit together with an array of pixels

or LED [62] source can be used for single wavelength measurements when the full spectrum is not of interest.

Figure 10.7 shows the two most common experimental setups for acquiring the extinction spectrum using spectroscopy in transmission mode. The configuration shown in Fig. 10.7a is typically found in conventional spectrophotometers (which are usually quite large). Here a narrow wavelength interval (a few nm) of light is selected from the light source by a slit and a grating. A beamsplitter sends a fraction (normally 50%) of this essentially monochromatic light through the sample, while

the rest goes to a detector that measures the reference intensity I_0. The full spectrum is generated by moving the grating, thereby scanning the available wavelengths. By comparing I_0 with the intensity I measured by the sample detector, the extinction (E) of the sample is calculated, typically in absorbance units, according to:

$$E(\lambda) = \log_{10}\left(\frac{I_0(\lambda)}{I(\lambda)}\right) \tag{10.4}$$

Figure 10.7b shows an alternative configuration. Here dispersion of light occurs after the sample and an array of photodetectors is used to measure the intensity at multiple wavelengths simultaneously. The reference intensity is not continuously measured, but instead acquired before the sample is mounted and then stored in memory. The advantage of this setup is that the full spectrum is generated much faster (a few ms) compared to the setup in Fig. 10.7a where the grating must be moved to scan all wavelengths (which typically takes a few minutes). Acquiring the full spectrum simultaneously naturally improves the temporal resolution for sensing applications where the full spectrum is of interest. The configuration in Fig. 10.7b also has the advantage that spectral data analysis can be applied for each acquisition and more information is acquired faster.

In principle, a beam splitter could be introduced and the reference spectrum $I_0(\lambda)$ continuously measured also in the setup in Fig. 10.7b. In the same manner, it is not necessary, only very common, to have a double beam configuration in the moveable grating setup (Fig. 10.7a). The advantage of double beam configurations for continuous acquisition of the reference intensity is that light source fluctuations are compensated for. However, for reasonably stable light sources, the major source of noise often originates from the detector [10, 26, 42, 60]. Double beam configurations may also reduce accuracy in data since it is difficult to construct perfectly identical beams, beam paths, and detectors.

One advantage with the moveable grating setup is that it is more flexible and provides better *spectral* resolution since the choice of wavelength is continuous and high precision can be achieved in the wavelength steps. The slit width can also usually be tuned to further increase the precision of the *wavelength* at the expense of lower intensity. In the fixed grating setup, each pixel is always associated with a certain wavelength. Still, narrow spectral features can be resolved if a narrow slit and a high number of detector pixels are used together with a suitable grating. In any case, the broad (typically $>$100 nm) resonance peaks associated with plasmon excitation usually make fine spectral resolution in terms of wavelength irrelevant.

A convenient way to perform spectroscopy on smaller samples, or smaller regions on a sample, is to connect a spectrometer to a conventional optical microscope. Spectrometers that have fixed slit, grating, and pixel arrays (Fig. 10.7b) are commercially available as "black boxes," simply designed to measure spectra by connecting an optical fiber. If such a spectrometer is placed with the entrance slit in the image plane from the objective of a microscope (no fiber is necessary), a microspectroscopy setup is created. When the sample surface is in focus, the

effective area from which the spectrum is acquired is roughly equal to the physical size of the entrance slit divided by the magnification of the objective [10]. However, this is under the assumption that the full *height* of the spectrometer slit is utilized, i.e., that all light going through the slit eventually reaches the detector. This usually requires a 2D pixel array. A minor complication with microscope setups is that there are often components designed to only handle visible light, while plasmon resonances often lie in the NIR. For instance, heat filters may need to be removed.

Detector Noise

Assume that a stable light source is illuminating a sample mounted in a mechanically stable setup, so that there is a certain intensity $I(\lambda)$ reaching the photodetector pixels and generating photoelectrons. The pixel array is exposed for a certain time and the number of electrons generated is counted. This number (can be on the order of 10^7) is digitalized with various degrees of resolution, usually 16 bit (a number from one to $2^{16} = 65{,}536$). The most common pixel array detector types are charge coupled device (CCD) or photodiode array (PDA), which are both silicon-based and sensitive to UV–VIS-NIR light (200–1,100 nm). Most plasmon resonance peaks are found in this region, but for, e.g., nanoring resonances at longer wavelengths [63], PDA detectors based on other semiconductor materials (such as InGaAs) must be used.

There are four types of noise present in the value measured by a detector pixel. First, there are thermal electrons generated in the detector even without illumination, which is referred to as *dark noise*. Dark noise can be greatly reduced by cooling the detector. Second, there is always an error introduced by additional electrons in the actual measuring process for a pixel, which creates *readout noise*. This type of noise can be practically eliminated by introducing amplification (gain) in the photoelectron sensitivity. Third, there are photons not originating from the sample that generate electrons in the detector, i.e., *background noise*. (The solution is to turn off the light in the lab.) Finally, there is always noise in intensity because of the simple fact that light consists of photons, which are discrete energy quanta. A certain intensity value represents an *average* photon flux and the number of photons passing a cross-section area during a certain time is thus a random variable. This phenomenon, known as *shot noise*, has an analogy in current measurements (electron flux) and is well described by Poisson statistics. For high numbers, the Poisson distribution of estimates of I approaches a normal distribution with standard deviation equal to $I^{1/2}$.

It is important to note that the challenge in plasmon spectroscopy for sensing applications is not about detecting low intensities or "capturing every single photon." This is the case in many imaging techniques based on, e.g., fluorescence. For plasmonic sensing, we focus instead on detecting small *changes* in the *optical properties* of a surface. By choosing a probing intensity that is as high as possible,

the optical signal in terms of absolute intensity is maximized. Dark noise, readout noise, and background noise do not increase when measuring at higher intensities, so their relative contributions become smaller. In addition, they can be reduced in simple ways as discussed above. In contrast, shot noise is always present and increases with $I^{1/2}$. However, the signal in terms of photon flux is *proportional* to I and the S/N is thus increased for higher I with a square root dependence. In other words, shot noise increases, but the signal in absolute intensity change increases more. Two conclusions follow from this: First, measuring at high intensity is preferable. Second, the dominating form of noise (related to the detector) will then most likely be shot noise.

Choosing Optical Components

Now that we are illuminated by the discussion above, picking a suitable type of light source and spectrometer becomes relatively straightforward. It is a matter of maximizing the number of photoelectrons generated in the detector per time unit. The light source should be able to provide as high intensity as possible while still being stable (and not causing too much heating to the particles). All optical components in the setup should be chosen so that as much light as possible is guided through the sample and to the detector. One important component is the slit width of the spectrometer. A wider slit obviously gives more light, but also reduces the spectral resolution. However, the widest possible slit is normally preferable since the resolution in terms of wavelength always will be adequate for looking at plasmon resonance peaks (due to their high broadness). The grating of the spectrometer should simply be chosen so that the resulting wavelength interval illuminating the detector pixels includes all spectral regions of interest.

The important characteristics of the pixel array detector are the minimum exposure time, the well depth (number of electrons generated before saturation), and the probability to generate a photoelectron from incident light (the photon sensitivity). The minimum exposure time should be as short as possible to be compatible with high temporal resolution and enable more averaging operations to be performed. The detector should have a high well depth so that many electrons can be generated before saturation occurs. High photon sensitivity is preferable, but only relevant in the case when the light source does not provide enough light to saturate the detector at the shortest possible exposure time. CCD detectors are more sensitive than PDA detectors, but the latter have a much higher (at least 100 times) well depth. In practice, this means that a PDA detector is preferable unless measurements are done on very small areas (spot size of a few μm), from which low absolute intensities are collected even under very strong illumination [10]. The physical pixel size and the number of pixels in the detector are usually not relevant since these factors can be compensated for by each pixel having a higher well depth.

Data Analysis

When the optical extinction spectrum has been measured, the next task is to analyze the data and provide at least one parameter representing the sensor result. This parameter should be calculated with high precision when analyzing several spectra. We recall that each extinction spectrum consists of a set of uncorrelated relative intensity measurements at different wavelengths, i.e., each pixel value fluctuates within a normal (high number Poisson) distribution and does not care about the values of the other pixels [10, 42].

Following the discussion above, the peak position is not the best parameter to use when defining performance, but may be a useful parameter in other ways. For instance, it is not influenced much by fluctuations in light source intensity during a measurement (see below). λ_{peak} may also be important in terms of physics since it defines the resonance energy. In summary, it is suitable to *present* sensing data using λ_{peak}. The question is then how to best calculate it (simply zooming in on the peak will not help much). Data analysis algorithms that define λ_{peak} mathematically from the discrete spectral data points are needed.

Much work has been done on data analysis in SPR systems since the technique is commercialized and in use. These algorithms can be applied also to spectroscopy of plasmonic nanostructures [10, 26] (or just about any analysis of "peak features"). In general, algorithms that calculate the *centroid*, i.e., the geometrical center of mass of a resonance peak, greatly reduce noise because more data values are taken into account compared to only considering the values close to the peak position [60]. In a continuous extinction spectrum $E(\lambda)$, the centroid wavelength (C) is defined as:

$$C_{\text{continuous}} = \frac{\int_{\lambda_1}^{\lambda_2} (\lambda[(E(\lambda) - E_{\text{base}})])\, \mathrm{d}\lambda}{\int_{\lambda_1}^{\lambda_2} (E(\lambda) - E_{\text{base}})\, \mathrm{d}\lambda} \tag{10.5}$$

In reality, the data set will be discontinuous, in which case the centroid can be defined as:

$$C_{\text{discrete}} = \frac{\sum_{i=1}^{m} (\lambda_i[E(\lambda_i) - E_{\text{base}}])}{\sum_{i=1}^{m} (E(\lambda_i) - E_{\text{base}})} \tag{10.6}$$

In the centroid equations, E_{base} is a constant baseline extinction value, while λ_1 and λ_2 define the interval used to calculate the centroid. E_{base} is usually chosen so that $E(\lambda_1) = E(\lambda_2) = E_{\text{base}}$. For discontinuous data, the integral is replaced with a sum. Note that unless the peak is symmetric, there is typically a small offset between the peak position and the centroid. However, this offset is usually constant, i.e., the centroid can be related to the peak position as $C = p + q\lambda_{\text{peak}}$ where $p \ll \lambda_{\text{peak}}$ and $q \approx 1$ and thus $\Delta C \approx \Delta\lambda_{\text{peak}}$ [26]. The exact method used to calculate C varies, depending on how the interval (λ_1 and λ_2) and E_{base} are defined.

As shown by the integrals in (10.5), C is essentially a sum of extinction changes. Also for other algorithms that calculate peak position or peak broadness, the noise and the signal will in some way be caused by extinction changes, because this is the only information present in a series of spectra. Indeed, when the system exhibits low noise in extinction, the noise in C will be reduced while ΔC still remains roughly equal to the change in λ_{peak} [26]. The peak shape also greatly affects the noise level in C and narrow peaks with high magnitude are generally preferable [10, 26]. Thus, in some sense, the centroid approach takes all important peak factors (shift, magnitude, and broadness) into account which makes it a useful parameter.

The primary challenge in applying centroid algorithms on spectral data is that there is no continuous function $E(\lambda)$ to perform the calculation on, only discrete data points. Although centroids can be defined also for discontinuous functions as in (10.6), problems arise when the peak shifts, since the values close to the beginning or end of the interval cause discontinuities depending on whether a pixel is included or not. This can be overcome by special treatment of those values [42, 60] or by simply fitting a continuous function to the data [10, 26]. Such a function may also act as an additional reduction in noise if extinction values at particular wavelengths are measured. It should be noted that the function does not have to "make sense" physically since it is only used for mathematical purposes.

Scattering Spectroscopy

While the discussion above is somewhat focused on extinction measurements, an alternative spectroscopy mode is the collection of light which is scattered by radiative plasmons in holes [64] or particles [9, 11–15]. This mode of spectroscopy requires *dark-field* illumination, i.e., light that is freely transmitted should not end up at the detector and objects are detected on a dark background. Scattering spectroscopy has proven useful in single nanoparticle measurements and is often performed in optical microscopes since an effective collection lens (an objective) is needed to collect as much scattered light as possible. In contrast, the lens collecting transmitted light in extinction measurements should be placed far from the sample for high accuracy, thereby *preventing* collection of scattered light [10].

A sample for which the extinction originates only from elastic scattering of light $(\sigma_{\text{sca}} \gg \sigma_{\text{abs}})$ has a scattering spectrum that looks identical to the extinction spectrum. However, it should be noted that scattering spectra are not quantitative in the same way as extinction spectra. For an extinction spectrum, given that the number of, for example, nanoparticles per area unit on the sample surface is known, it is possible to determine $\sigma_{\text{ext}}(\lambda)$ from the ratio of $I_0(\lambda)$ and $I(\lambda)$. For scattering mode, on the other hand, there is little quantitative information in the measured intensity. For one thing, normalizing to the reference intensity is usually difficult since it cannot be easily measured. This is because under dark-field illumination, no transmitted light is collected per definition. In addition, it is difficult to estimate what fraction of the scattered light is collected (the parameter β discussed below).

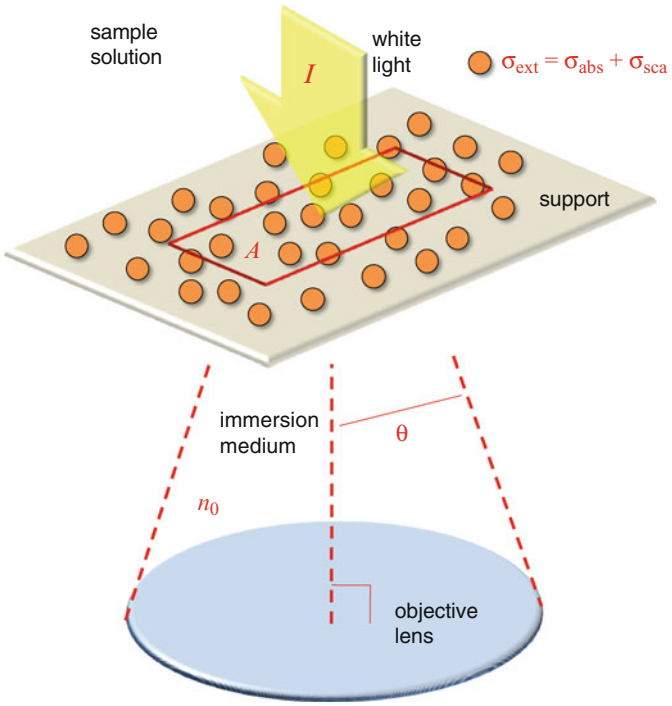

Fig. 10.8 Schematic of a model for estimating the intensity of collected light when performing microspectroscopy. Figure reproduced from ref. [10] with permission, © American Chemical Society

Still, the centroid can obviously be determined also from a scattering spectrum. For particles, the resonance peak position in the scattering spectrum is almost equal to that in the extinction spectrum, while for nanoholes the metal film influence on transmission mode can make the resonance peaks appear at slightly different wavelengths [39].

When optimizing S/N, it is interesting to compare spectroscopy in transmission and scattering mode [10]. Figure 10.8 shows a principle schematic of plasmonic nanoparticles on a surface in a microspectroscopy setup. White light illuminates the sample with a plane wave intensity I_0 (photons per area and time unit) and the light from an area A is analyzed. Extinction of light is caused by nanoparticles (or holes) that have a surface coverage of m/A entities per area unit. If the fraction of the scattered intensity which is collected by the lens is denoted β, we can write the number of photons collected per time unit (N) in transmission mode (index T) as:

$$N_{\mathrm{T}}(\lambda) = I_0(\lambda)[A - m\sigma_{\mathrm{ext}}(\lambda) + m\beta\sigma_{\mathrm{sca}}(\lambda)] \tag{10.7}$$

For comparison, in scattering mode (index S) under dark-field illumination, the number of collected photons is:

$$N_s(\lambda) = I_0(\lambda) m \beta \sigma_{sca}(\lambda) \tag{10.8}$$

Following the previous discussion, it is important to maximize N to reduce noise. Therefore, a problem with scattering spectroscopy is that it is normally difficult to achieve high illumination intensity I_0 combined with efficient collection of light (β) in dark-field [10]. If we assume that the scattering is isotropic, β can be approximated by geometry as $[1 - \cos^2(\theta)]/2$, where θ is the collection angle of the objective (Fig. 10.8). (This follows from the formula for the area of a sphere segment.) Next, θ can be determined from the numerical aperture $n_0 \sin(\theta)$ of the objective. Looking at commercially available microscope objectives, the highest value of β that can be achieved is then around 35%. However, this will require complex illumination configurations, such as evanescent excitation in TIR [65], to avoid collecting transmitted light.

In reality, the exact collected fraction of the scattering intensity is much harder to determine. First, the scattering is far from isotropic, which can be realized by considering the emission pattern from an infinitely small dipole. The emitted field is then proportional to $\sin(\theta)$ and inversely proportional to the distance from the dipole. With this model, the maximum possible value of β is around 46% (derivation not shown). Especially in microscopy, it is difficult to avoid collecting scattered light entirely, but by using long working distance objectives β can be reduced down to a few percent. Finally, it should be noted that β will be affected by refraction of light before the collecting lens, which normally occurs at the backside of the solid support of the plasmonic nanostructure (typically glass to air). The simplified model in Fig. 10.8 only holds when using an oil immersion and matching the RI of the solid support (normally glass) of the nanoparticles.

Note that in scattering mode, the area A is not directly relevant for the measured intensity, although implicitly it may affect the number of particles analyzed (m). In this sense, scattering spectroscopy is "background free" under the assumption of perfect dark-field illumination. This might appear as a desirable property for spectroscopy, but it must be recalled that in plasmonic sensing the challenge is not to image nanoparticles on a surface, but to investigate the properties of their nanoplasmons. Reducing background light is only of interest for detecting the particles or holes themselves, which may be relevant in, for example, bioimaging applications with Au nanoparticles [66], but irrelevant for the biosensing applications discussed here. Another important property to consider for spectroscopy is the relative scattering contribution to the extinction ($\sigma_{sca}/\sigma_{ext}$), since signals associated with changes in σ_{abs} are not detected when using scattering mode. It is possible, however, to illuminate and collect light from the same side of the sample surface when using scattering spectroscopy [67], which can have great value in many applications.

Using the model illustrated in Fig. 10.8 and assuming a shot noise limited system, signals and noise levels can be expressed and compared for scattering and transmission mode (see Dahlin et al. for details [10]). The results show that only the extinction of the sample is needed for a relative comparison of performance between scattering and transmission mode, as illustrated in Fig. 10.9. When

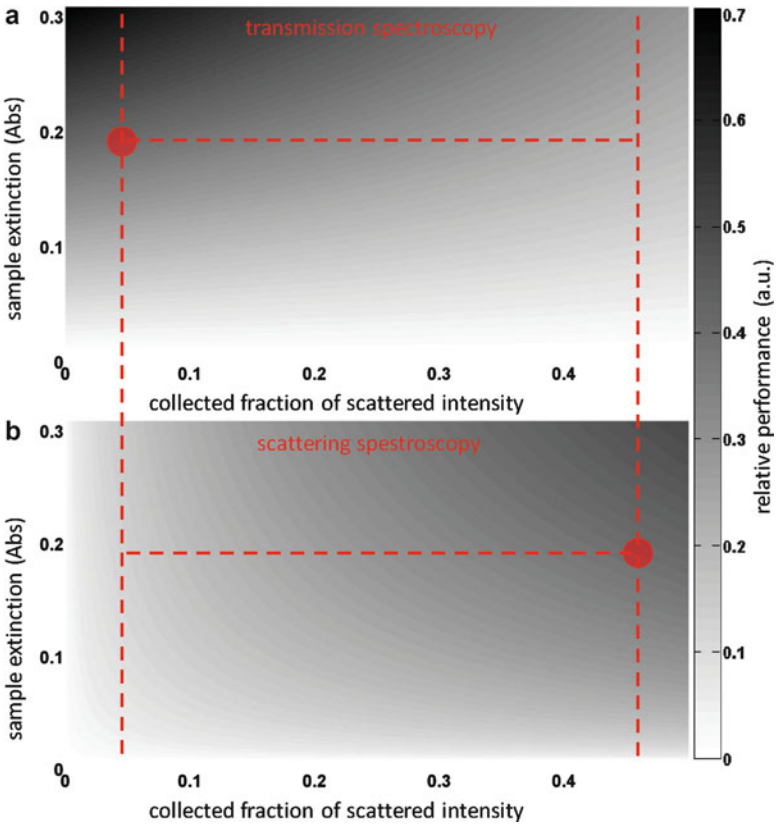

Fig. 10.9 Performance comparison of transmission mode and scattering mode under the assumption of a shot noise limited system. The *vertical lines* show the interval of realizable values for the collected fraction of the scattered light. Above a critical sample extinction value (slightly below 0.2 Abs, *vertical line*) the highest performance is always achieved in transmission mode. Reproduced in part from ref. [10] with permission, © American Chemical Society

β is increased, the performance increases for scattering mode and decreases for transmission mode due to the nature of the spectroscopy methods. The maximum and minimum values of β that can be achieved in practice (here illustrated by dashed lines) are thus of interest in principle, although they actually have little effect on the outcome of the analysis.

The results in Fig. 10.9 show that as long as the sample has an extinction of more than a critical value, transmission mode will give better performance. This value is below 0.2 Abs, which is lower than the extinction values for most nanoplasmonic structures when λ is close to λ_{peak} (see discussion by Dahlin et al. [10] and references therein). The comparison is done under the assumptions that the illumination intensity is equal for transmission and scattering mode and that the nanoparticles on the surface only scatter light without absorbing $(\sigma_{\text{ext}} = \sigma_{\text{sca}})$. This situation cannot be realized which thus makes scattering mode *even less*

preferable. The interval of possible values for β does not significantly influence the critical extinction value resulting from the analysis. In summary, scattering spectroscopy in dark-field is, in most situations, not a very bright idea.

Imaging

Since light is dispersed in one dimension in grating-based spectrometers, one spatial dimension remains available and it is possible to perform one-dimensional spectral imaging on the sample by using a 2D pixel array detector [44]. An alternative to spectroscopy and peak position determinations altogether is to simply look at the extinction value at a single wavelength, preferably chosen to be on the longer wavelength side of the resonance peak for maximum signal as the peak shifts [26, 39]. A (possibly monochromatic) light source can then be used together with a camera to measure intensity variations in 2D on the surface, thereby enabling array-based parallel plasmonic sensing in a simple manner [68]. It is also possible to use two wavelengths as was shown for nanoparticle dimer imaging [69]. However, we emphasize again that it is important to distinguish imaging *mode* for sensing (as an alternative to spectroscopy) from applications where the images themselves represent the data of interest, because different principles apply.

The imaging approach can provide high S/N by reducing shot noise since all probing light can be of the wavelength at which extinction changes are maximal and lasers can be used as light sources. For the case of SPR, imaging mode can be performed in TIR configuration [70], enabling simultaneous readout of multiple sensing spots, which can be down to around 100 μm in size [57]. The detector in the camera should be chosen according to the same principles as for the detector in a spectrometer (see above). The primary disadvantage of imaging is arguably that the full spectrum is lost and important parameters, such as the resonance peak position, cannot be measured. Still, when optimal S/N is all that matters, imaging at a single wavelength may be preferable over spectroscopy even if there is no need for simultaneous readout of multiple spots in an array.

This overview of spectroscopy techniques concludes the chapter and we wish to end with a few very brief remarks. There is certainly potential for nanoplasmonic sensors to be competitive in comparison to conventional SPR, although it appears unlikely that they will ever become better than SPR or imaging SPR, at least not in terms of *surface coverage* detection limits. For a few of the future challenges where the sensitivity *per molecule* is important, nanoplasmonic sensors may contribute. Nanoplasmonic sensors can, however, have the advantage that they are cheaper and easier to work with. Also, for the case of nanohole structures, the actual structure itself may be utilized for flow-through configuration [18–20] and size exclusion [35].

References

1. Healy DA, et al. Biosensor developments: application to prostate-specific antigen detection. Trends Biotechnol. 2007;25(3):125–31.
2. Dahlin AB, et al. Synchronized quartz crystal microbalance and nanoplasmonic sensing of biomolecular recognition reactions. ACS Nano. 2008;2(10):2174–82.
3. Jung LS, et al. Quantitative interpretation of the response of surface plasmon resonance sensors to adsorbed films. Langmuir. 1998;14(19):5636–48.
4. Feuz L, et al. Improving the limit of detection of nanoscale sensors by directed binding to high-sensitivity areas. ACS Nano. 2010;4(4):2167–77.
5. Hibbert DB, Gooding JJ, Erokhin P. Kinetics of irreversible adsorption with diffusion: application to biomolecule immobilization. Langmuir. 2002;18(5):1770–6.
6. Sheehan PE, Whitman LJ. Detection limits for nanoscale biosensors. Nano Lett. 2005;5 (4):803–7.
7. Squires TM, Messinger RJ, Manalis SR. Making it stick: convection, reaction and diffusion in surface-based biosensors. Nat Biotechnol. 2008;26(4):417–26.
8. Bendikov TA, et al. Biological sensing and interface design in gold island film based localized plasmon transducers. Anal Chem. 2008;80(19):7487–98.
9. Curry A, et al. Analysis of total uncertainty in spectral peak measurements for plasmonic nanoparticle-based biosensors. Appl Opt. 2007;46(10):1931–9.
10. Dahlin AB, et al. High-resolution microspectroscopy of plasmonic nanostructures for miniaturized biosensing. Anal Chem. 2009;81(16):6572–80.
11. Nusz GJ, et al. Label-free plasmonic detection of biomolecular binding by a single gold nanorod. Anal Chem. 2008;80(4):984–9.
12. Baciu CL, et al. Protein-membrane interaction probed by single plasmonic nanoparticles. Nano Lett. 2008;8(6):1724–8.
13. McFarland AD, Van Duyne RP. Single silver nanoparticles as real-time optical sensors with zeptomole sensitivity. Nano Lett. 2003;3(8):1057–62.
14. Raschke G, et al. Biomolecular recognition based on single gold nanoparticle light scattering. Nano Lett. 2003;3(7):935–8.
15. Sannomiya T, Hafner C, Voros J. In situ sensing of single binding events by localized surface plasmon resonance. Nano Lett. 2008;8(10):3450–5.
16. Nair PR, Alam MA. Performance limits of nanobiosensors. Appl Phys Lett. 2006;88 (23):233120.
17. Andersson H, van den Berg A. Microtechnologies and nanotechnologies for single-cell analysis. Curr Opin Biotechnol. 2004;15(1):44–9.
18. Eftekhari F, et al. Nanoholes as nanochannels: flow-through plasmonic sensing. Anal Chem. 2009;81(11):4308–11.
19. Jonsson MP, et al. Locally functionalized short-range ordered nanoplasmonic pores for bioanalytical sensing. Anal Chem. 2010;82(5):2087–94.
20. Yanik AA, et al. Integrated nanoplasmonic-nanofluidic biosensors with targeted delivery of analytes. Appl Phys Lett. 2010;96(2):021101.
21. Green NM. Avidin. 1. The use of [14c] biotin for kinetic studies and for assay. Biochem J. 1963;89(3):585–91.
22. Hock B, Seifert M, Kramer K. Engineering receptors and antibodies for biosensors. Biosens Bioelectron. 2002;17(3):239–49.
23. Gresham D, Dunham MJ, Botstein D. Comparing whole genomes using DNA microarrays. Nat Rev Genet. 2008;9(4):291–302.
24. Service RF. Proteomics ponders prime time. Science. 2008;321(5897):1758–61.
25. Kabashin AV, et al. Plasmonic nanorod metamaterials for biosensing. Nat Mater. 2009;8 (11):867–71.
26. Dahlin AB, Tegenfeldt JO, Hook F. Improving the instrumental resolution of sensors based on localized surface plasmon resonance. Anal Chem. 2006;78(13):4416–23.

27. Swann MJ, et al. Dual-polarization interferometry: an analytical technique to measure changes in protein structure in real time, to determine the stoichiometry of binding events, and to differentiate between specific and nonspecific interactions. Anal Biochem. 2004;329 (2):190–8.
28. Song SP, et al. Aptamer-based biosensors. Trac Trends Anal Chem. 2008;27(2):108–17.
29. Cooper MA. Advances in membrane receptor screening and analysis. J Mol Recognit. 2004;17 (4):286–315.
30. Bearinger JP, et al. Chemisorbed poly(propylene sulphide)-based copolymers resist biomolecular interactions. Nat Mater. 2003;2(4):259–64.
31. Kenausis GL, et al. Poly(L-lysine)-g-poly(ethylene glycol) layers on metal oxide surfaces: attachment mechanism and effects of polymer architecture on resistance to protein adsorption. J Phys Chem B. 2000;104(14):3298–309.
32. Ma HW, et al. "Non-fouling" oligo(ethylene glycol)-functionalized polymer brushes synthesized by surface-initiated atom transfer radical polymerization. Adv Mater. 2004;16 (4):338–41.
33. Pasche S, et al. Poly(L-lysine)-graft-poly(ethylene glycol) assembled monolayers on niobium oxide surfaces: a quantitative study of the influence of polymer interfacial architecture on resistance to protein adsorption by ToF-SIMS and in situ OWLS. Langmuir. 2003;19 (22):9216–25.
34. Pasche S, et al. Relationship between interfacial forces measured by colloid-probe atomic force microscopy and protein resistance of poly(ethylene glycol)-grafted poly(L-lysine) adlayers on niobia surfaces. Langmuir. 2005;21(14):6508–20.
35. Dahlin AB, Jonsson MP, Hook F. Specific self-assembly of single lipid vesicles in nanoplasmonic apertures in gold. Adv Mater. 2008;20(8):1436–42.
36. Haes AJ, et al. Detection of a biomarker for Alzheimer's disease from synthetic and clinical samples using a nanoscale optical biosensor. J Am Chem Soc. 2005;127(7):2264–71.
37. Marinakos SM, Chen SH, Chilkoti A. Plasmonic detection of a model analyte in serum by a gold nanorod sensor. Anal Chem. 2007;79(14):5278–83.
38. Huang NP, et al. Biotin-derivatized poly(L-lysine)-g-poly(ethylene glycol): a novel polymeric interface for bioaffinity sensing. Langmuir. 2002;18(1):220–30.
39. Dahlin A, et al. Localized surface plasmon resonance sensing of lipid-membrane-mediated biorecognition events. J Am Chem Soc. 2005;127(14):5043–8.
40. Marie R, et al. Generic surface modification strategy for sensing applications based on Au/ SiO2 nanostructures. Biointerphases. 2007;2(1):49–55.
41. Whitney AV, et al. Localized surface plasmon resonance nanosensor: a high-resolution distance-dependence study using atomic layer deposition. J Phys Chem B. 2005;109 (43):20522–8.
42. Nenninger GG, Piliarik M, Homola J. Data analysis for optical sensors based on spectroscopy of surface plasmons. Meas Sci Technol. 2002;13(12):2038–46.
43. Becker J, et al. The optimal aspect ratio of gold nanorods for plasmonic bio-sensing. Plasmonics. 2010;5(2):161–7.
44. Stewart ME, et al. Quantitative multispectral biosensing and 1D imaging using quasi-3D plasmonic crystals. Proc Natl Acad Sci U S A. 2006;103(46):17143–8.
45. Svedendahl M, et al. Refractometric sensing using propagating versus localized surface plasmons: a direct comparison. Nano Lett. 2009;9(12):4428–33.
46. Murray-Methot MP, Ratel M, Masson JF. Optical properties of Au, Ag, and bimetallic Au on Ag nanohole arrays. J Phys Chem C. 2010;114(18):8268–75.
47. Miller MM, Lazarides AA. Sensitivity of metal nanoparticle surface plasmon resonance to the dielectric environment. J Phys Chem B. 2005;109(46):21556–65.
48. Johnson PB, Christy RW. Optical-constants of noble-metals. Phys Rev B. 1972;6(12):4370–9.
49. Otte MA, et al. Identification of the optimal spectral region for plasmonic and nanoplasmonic sensing. ACS Nano. 2010;4(1):349–57.
50. Weissleder R. A clearer vision for in vivo imaging. Nat Biotechnol. 2001;19(4):316–7.

51. Langhammer C, et al. Plasmonic properties of supported Pt and Pd nanostructures. Nano Lett. 2006;6(4):833–8.
52. Langhammer C, et al. Localized surface plasmon resonances in aluminum nanodisks. Nano Lett. 2008;8(5):1461–71.
53. Schwind M, et al. LSPR study of the kinetics of the liquid-solid phase transition in Sn nanoparticles. Nano Lett. 2010;10(3):931–6.
54. Chan GH, et al. Plasmonic properties of copper nanoparticles fabricated by nanosphere lithography. Nano Lett. 2007;7(7):1947–52.
55. Anker JN, et al. Biosensing with plasmonic nanosensors. Nat Mater. 2008;7(6):442–53.
56. Jonsson MP, et al. Supported lipid bilayer formation and lipid-membrane-mediated biorecognition reactions studied with a new nanoplasmonic sensor template. Nano Lett. 2007;7(11):3462–8.
57. Homola J. Surface plasmon resonance sensors for detection of chemical and biological species. Chem Rev. 2008;108(2):462–93.
58. Johnsson B, Lofas S, Lindquist G. Immobilization of proteins to a carboxymethyl dextran-modified gold surface for biospecific interaction analysis in surface-plasmon resonance sensors. Anal Biochem. 1991;198(2):268–77.
59. Graneli A, Edvardsson M, Hook F. DNA-based formation of a supported, three-dimensional lipid vesicle matrix probed by QCM-D and SPR. Chemphyschem. 2004;5(5):729–33.
60. Johansen K, et al. Surface plasmon resonance: instrumental resolution using photo diode arrays. Meas Sci Technol. 2000;11(11):1630–8.
61. Hedsten K, et al. Optical label-free nanoplasmonic biosensing using a vertical-cavity surface-emitting laser and charge-coupled device. Anal Chem. 2010;82(4):1535–9.
62. Mazzotta F, Wang G, Hägglund C, Höök F, Jonsson MP. Biosensors and Bioelectronics. 2010;(26): 1131–1136. doi:10.1016/j.bios.2010.07.008.
63. Larsson EM, et al. Sensing characteristics of NIR localized surface plasmon resonances in gold nanorings for application as ultrasensitive biosensors. Nano Lett. 2007;7(5):1256–63.
64. Rindzevicius T, et al. Plasmonic sensing characteristics of single nanometric holes. Nano Lett. 2005;5(11):2335–9.
65. Sonnichsen C, et al. Drastic reduction of plasmon damping in gold nanorods. Phys Rev Lett. 2002;88(7):077402.
66. Jain PK, et al. Review of some interesting surface plasmon resonance-enhanced properties of noble metal nanoparticles and their applications to biosystems. Plasmonics. 2007;2(3):107–18.
67. Braslavsky I, et al. Objective-type dark-field illumination for scattering from microbeads. Appl Opt. 2001;40(31):5650–7.
68. Endo T, et al. Multiple label-free detection of antigen-antibody reaction using localized surface plasmon resonance-based core-shell structured nanoparticle layer nanochip. Anal Chem. 2006;78(18):6465–75.
69. Rong GX, et al. Resolving sub-diffraction limit encounters in nanoparticle tracking using live cell plasmon coupling microscopy. Nano Lett. 2008;8(10):3386–93.
70. Scarano S, et al. Surface plasmon resonance imaging for affinity-based biosensors. Biosens Bioelectron. 2010;25(5):957–66.

Chapter 11
Engineering Through Mode Shaping and Lithographical Nanofabrication of Ultrasensitive Nano-plasmonic Sensors for Molecular Detection

Srdjan S. Aćimović, Mark P. Kreuzer, and Romain Quidant

Abstract The resonance change of plasmonic nanostructures to a small variation of the shallow refractive index as induced by the binding of molecules to the metal surface determines the sensitivity of plasmonic sensors. The magnitude of this change is strongly determined by a number of factors including dielectric constant of the metal at the working wavelength, refractive indices of analyte, and surroundings [J Phys Chem B 109:21556–21565, 2005], but also the spatial overlap between the region of local refractive index change and the plasmon mode. In this chapter we discuss how the plasmon modes of lithographically prepared plasmonic nanostructures can be accurately engineered to design bio-chemical sensors with improved sensitivities.

We first describe how metal nanostructures can be designed to control the confinement of light modes down to the nanometer scale. Using 3D calculations based on the finite element method, we then discuss the influence on the sensitivity of the nanostructure geometry and location of the sensed molecule. Finally, we present experimental results that demonstrate this enhanced sensitivity to the detection of small molecules in arrays of gold dimers.

S.S. Aćimović • M.P. Kreuzer
ICFO-Institut de Ciencies Fotoniques, Mediterranean Technology Park, 08860 Castelldefels, Barcelona, Spain

R. Quidant (✉)
ICFO-Institut de Ciencies Fotoniques, Mediterranean Technology Park, 08860 Castelldefels, Barcelona, Spain

ICREA-Institució Catalana de Recerca I Estudis Avançats, 08010 Barcelona, Spain
e-mail: romain.quidant@icfo.es

A. Dmitriev (ed.), *Nanoplasmonic Sensors*, Integrated Analytical Systems,
DOI 10.1007/978-1-4614-3933-2_11,

Mode Engineering and Nanoscale Light Confinement in Lithographically Fabricated Plasmonic Structures

Motivations for Using Lithographically Prepared Structures

One of the main advantages of resonant metallic nanoparticles (MNP) over metal films relies on the possibility for an accurate engineering of their optical properties by controlling their size, shape, composition, and environment [1–3]. The sensitivity of localized surface plasmon (LSP) sensors is determined by both the magnitude of the frequency shift and the minimum resonance shift that can be detected [4, 5]. In this first section, we discuss how top-down lithography approaches can be used to accurately engineer plasmon modes, both spatially and spectrally, in order to enhance the sensitivity of LSP sensors.

Optimizing Biosensing with LSPR Sensors

The maximum resonance shift of a plasmonic sensor upon binding of molecules is determined by various parameters related to the sensor itself, its surrounding medium, and the target molecule. It has been established that such dependence can be formalized into the following equation, adopted from exact theory for planar surface plasmon resonance sensing, and accepted to some extent as a valid approximation for LSPR.

$$\Delta\lambda \approx m(n_{\text{analyte}} - n_{\text{medium}})(1 - e^{(-2d/L_{\text{d}})}) \tag{11.1}$$

where m is the bulk sensitivity in RIU change per nanometer, n_{analyte} and n_{medium} are the refractive indexes of the adsorbing molecule and medium surrounding the system, respectively, d is the thickness of the adsorbed layer, and L_{d} is the EM field decay length. Equation (11.1) suggests that there are quite a number of parameters that influence the change in the resonance. In the case in which the system is adopted for a particular analyte (n_{analyte} and d are fixed), to increase resonance shift one can tune m, n_{medium}, and L_{d}. The only tunable parameter independent of the plasmonic sensor is n_{medium}, and its decrease benefit to the sensitivity. However, the refractive index of the medium surrounding nanoparticle is a very rigid parameter, and as a rule, mostly governed by the analyte's nature. For instance, when employing free colloidal nanoparticles in solutions as sensors, n_{medium} usually falls in the small range around 1.33 (refractive index of water), and it follows requirements of the analyte's solubility, pH, etc. In case of nanoparticles fixed on a substrate, the medium in principle can be varied depending on sensing protocols. In limiting case, the medium refractive index can be decreased to 1 as in the case of measurements in air, but it is not favorable to molecular binding tracking or kinetic

studies, thus imposing restrictions to only applications for molecular concentration detection in equilibrium [6, 7] or for detection of gases [8]. Natural environment of biomolecules (proteins, antibodies) are aqueous media (blood and other body liquids). Drying or removing this media after binding increases the shift induced by molecular binding [6], but for accurate concentration determination it complicates detection procedures and protocols. Frequent drying also brings issues of molecules stability when exposed to air, poor reproducibility of measurements due to instability of nanoparticles when exposed to different media (section "Solvent Annealing"), and uncertainty on whether the solvent is completely removed [9].

The remaining two parameters, the bulk refractive index sensitivity, m, and the EM field decay, L_d, are strongly correlated, accounting for the near-field enhancement and modal distribution, respectively. In an SPR configuration using a flat metal film, m is related to the maximum field value on the dielectric-metal interface, while L_d depends on the normal component of the incident wave vector.

While simple and intuitive, the 2D model of (11.1) fails in accounting for the inhomogeneous spatial 3D distribution of the near field in LSPR sensing as well as the nonuniform assembly of molecules due to steric hindrance. It supposes indeed a uniform molecular coverage (thin layers) [10–12], and consequently does not apply to single or few molecule-binding events [13].

One of the more rigorous approaches, based on perturbation theory, attempting to address the important differences between LSP and SPP, yields complicated expressions. Derived initially from dielectric nonlossy resonators, (11.2) gives more insight into the contributions of spatial near-field distribution around 3D particles and the location and size of the perturbation. C stands for the mode-analyte overlap. More details about the derivation, approximations, and viability of this equation can be found in Unger et al. [4].

$$\Delta\lambda \approx \lambda \frac{(n_{\text{analyte}} - n_{\text{medium}}) \int_{V_{\text{analyte}}} \varepsilon_{\text{medium}} |\vec{E}^2| \mathrm{d}V}{n_{\text{medium}} \int_{V_{\text{nearfield}}} \varepsilon_{\text{metal}} |\vec{E}^2| \mathrm{d}V} = \lambda \frac{\Delta n}{n_{\text{medium}}} C \tag{11.2}$$

Although emphasizing the role of spatial mode-analye overlap, (11.2) still remains inappropriate to some LSPR sensing configurations. For instance, it gives that if one matches the resonance of a single metallic nanocylinder with the resonance of nanocylinder dimer formed by slightly smaller disks, both systems feature the same bulk refractive sensitivity. This is not correct and it is the consequence of the initial approximation that the perturbation is very small. Indeed, Unger et al. show that this expression is more valid for small perturbation (smaller molecules with refractive index close to the medium), while it fails for infinite perturbation case (bulk refractive index sensing). Thus, by convenience, most of the LSPR modeling utilizes (11.1), although the parameter L_d can be misleading for nonuniform modal distribution, as we will see later.

Spatial Plasmon Mode Engineering

Over the last decade, the intensive research in plasmon optics has shown the huge potential of metallic nanostructures to concentrate light into nanoscale volumes in which the field amplitude can be enhanced by several orders of magnitude over the incident field. From the early stage of research in surface-enhanced Raman scattering (SERS), the so-called *hot spots* were found partially responsible for the enhancement of the Raman cross-section [14, 15]. *Hot spots* generally arise from a surface charge accumulation that preferentially occurs at sharp metallic tips [16, 17] and across dielectric gaps between adjacent metallic structures [18, 19]. The resulting strong charge gradients oscillating with the driving electromagnetic field lead to a large field magnitude within highly localized regions.

While intense *hot spots* appear in random ensembles of metallic nanoclusters, either prepared by annealing of thin metallic films or agglomeration of colloidal metal particles, their location and density can rarely be controlled. In that sense, a very attractive aspect of lithographically prepared plasmonic nanostructures is in the possibility of accurately controlling the location and density of *hot spots* within a well-defined region of the surface. Moreover, top-down approaches also enable to control the shape of each individual particle that directly affects the plasmonic mode distribution [20]. All these advantages need to be balanced though by the limitations of state-of-the-art lithography techniques in the definition of sharp edges or dielectric gaps between adjacent particles that limit the magnitude and volume of *hot spots*.

Spectral Plasmon Mode Engineering

While the mode confinement has a direct influence on the magnitude of the resonance shift, the accuracy in resolving a tiny frequency shift of the LSP resonance is influenced by the signal strength and full width at half-maximum (FWHM) of the resonant peak. Although the absorption of metals in the optical range is responsible for rather broad resonances, great emphasis has recently been placed on identifying systems that can give a tunable plasmonic peak with a narrow linewidth. For the majority of colloids, linewidth has been a problem due to polydispersity of the synthetic approach rendering a wide distribution of sizes and thus a broadening of the plasmonic peak. It is worth commenting, however, that as more effort is being invested in fully understanding the chemical pathways in making said colloidal nanoparticles, improvements are already seen towards monodispersed systems [21] as well as in controlled arranged positioning of colloidal nanoparticles [22]. Coupled with the current optical capability of performing single-particle spectroscopy [23], it is now possible to perform binding study experiments on a dispersion of colloids and selecting the particle with the optimum spectral peak width [24, 25]. In fact these single experiments can now be multiplexed in what is known as HT-LSPR (High Throughput) and

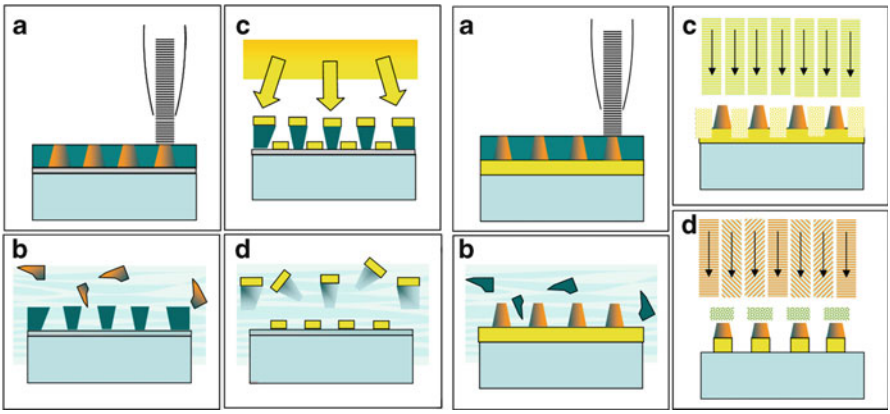

Fig. 11.1 (*Left*) Fabrication steps using positive resist approach. (**a**) Exposure of spin-coated resist on ITO covered glass substrate by e-beam. (**b**) Developing process. (**c**) Metal evaporation. (**d**) Lift-off process. (*Right*) Fabrication steps using negative resist approach and RIE. (**a**) Resist exposure on previously evaporated metallic film. (**b**) Developing process. (**c**) Selective gold etching by Ar plasma. (**d**) Selective mask stripping by O_2 plasma

more quantitative information can be harnessed which otherwise was very time-consuming [26, 27].

Nevertheless, the nanoparticle toolbox for colloidal chemists, though vast, is somewhat more difficult to exploit as each synthesis relies on some fine-tuning and experience to prepare mono-dispersions of one size, material, or shape. As an alternative, lithographic methods offer here a great potential to accurately control the shape and size parameters with nanometric precision and manage areas of thousands of identical particles. Nevertheless, this gain in the control on the resonance linewidth has to be balanced by the intrinsically larger absorption losses associated to the amorphous metal, usually used in lithography that leads to broader plasmon resonances as compared to colloidal particles. On the other hand, several works have lately pointed out configurations of electromagnetically coupled metal nanoparticles that enable the achievement of sharp spectral features [28–30].

Fabrication of LSPR Sensors by Top-Down Approaches

Fabrication of plasmonic nanostructures with nanometric control over size, shape, and spatial arrangement can be performed by what is considered as the most flexible technique at the research laboratory level, electron beam lithography (EBL). EBL is based on precise scanning and exposure of electro-sensitive polymer resist by a focused electron beam. In order to achieve the final nanostructures, different procedures of pattern transfer need to be followed depending on type of resist employed (Fig. 11.1a). Within the framework of plasmon optics, most EBL

applications employ procedures based on positive resists (typically PMMA). Thus, the designed pattern, once the exposed resist is developed (Fig. 11.1 left a, b), is transferred to the substrate by material evaporation into the developed polymer template (Fig. 11.1 left c) and followed by a lift-off step (removal of remaining polymer and excess of metal material; Fig. 11.1 left d). In the standard procedure, a transparent conductive layer indium tin oxide (ITO) is deposited on top of a glass substrate prior to polymer resist spin coating. This layer allows for charge evacuation and minimizes back-scattered electrons in order to attain maximum resolution. Additionally, thin conductive layers (1 nm) of titanium (Ti) or chromium (Cr) are deposited below the metal of interest to assure good particle adhesion to glass. However, these layers (Cr or Ti, as well as ITO) represent additional pathways of plasmon decay, thus dampen and broaden resonance, with consequent red shift due to increased refractive index in comparison to glass substrate. An alternative to the ITO layer is deposition of thin metal film (10 nm) on top of the resist for charge evacuation during exposure and subsequent selective removal [31]. This approach gives good results if a high voltage system is utilized (100 kV). Additional improvements can be introduced by two layer resist combination [32]. The most commonly available EBL systems (30 kV) by default use the ITO method. While small features can be achieved with positive resist at the single structure level, the somewhat uncontrolled nature of the lift-off process restricts the level of reproducibility, particularly when attempting patterns where gaps between adjacent structures are smaller than 15 nm. In order to circumvent these problems, we have developed an alternative approach based on high-resolution negative resist and reactive ion etching (RIE) using a standard 30 kV EBL system. In this process, negative resist is spin-coated onto a continuous metallic film, which serves as a building block for the nanostructures as well as charge evacuation layer during exposure.

After the resist exposure and development (Fig. 11.1 right a, b), the pattern is transferred by selective argon (Ar) plasma etching of metal (Fig. 11.1 right c), followed by mild O_2 plasma mask stripping that removes only the remaining resist (Fig. 11.1 right d). In the absence of any conductive layers beneath, plasmonic structures exhibit resonances that are more intense, narrower, and blue shifted. Closer inspection by SEM also reveals smaller level of defects and higher reproducibility in the minimum attainable gap size in large nanoparticle dimer arrays (see Fig. 11.2) as compared to standard lift-off procedure-fabricated dimer arrays done with the same EBL system.

It is also worth noting that other methods like focused ion beam (FIB) milling [33] and electron beam-induced deposition (EBID) [34] are attractive when dealing with nonflat substrates, for instance for fabrication of plasmonic nanostructures at the extremity of a scanning near-field optical probe [35]. However, they usually suffer from heavy ion contamination or low metal purity that tends to affect the quality factor of the plasmon resonance. While scanning beam methods are well suited for patterning with their optimum resolution small surface areas, typically of $100 \times 100\ \mu m^2$, they become inappropriate when much larger areas need to be patterned and/or when high sample fabrication throughput are needed. Alternatively, there are various other top-down approaches, like colloidal sphere nanolithography techniques [36] which offer fast, simple, and good quality

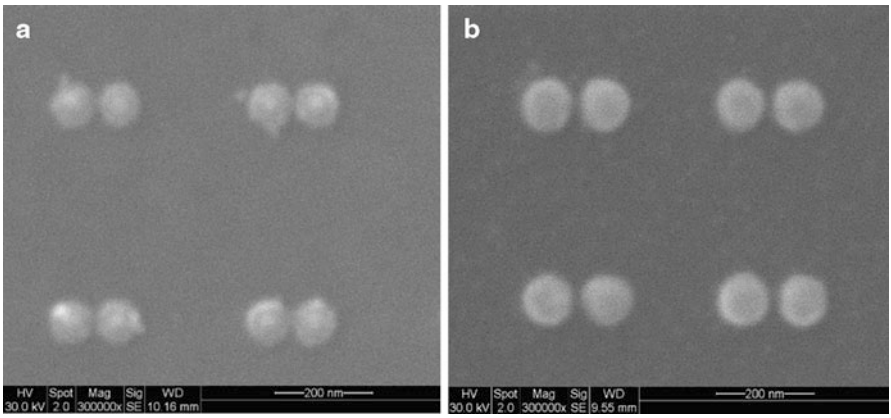

Fig. 11.2 SEM images comparing dimer structures obtained by (**a**) positive resist (PMMA) and lift-off (**b**) negative resist and RIE fabrication procedures

patterning of large areas, but rather limited particle geometry and arrangements, and thus are not suitable for strongly coupled nanoparticle configuration. In that sense, nano-imprint lithography, that uses EBL-fabricated molds, provides a faster and relatively cheaper alternative that offers a comparable spatial resolution [37, 38].

Mode Engineering in Plasmonic Dimers

An attractive elementary geometry that concentrates light into nanoscale volumes at a predefined location of the surface of a substrate is the so-called "plasmonic dimers" geometry, also known as "optical gap antenna" in which two identical metal particles are brought very close from each other to form a nanometric dielectric gap (Fig. 11.3a). Driving the dimers with an incident field linearly polarized along the particles alignment leads to an intense and strongly localized optical field within the gap region as illustrated in Fig. 11.3b. Since the magnitude of the charge gradient across the gap is directly associated to the dimension of the latter, one can accurately control the *hot spot* volume by adjusting the relative position between both particles. The amplitude of the local field within the gap, like the resonance wavelength, increases exponentially with the inverse of the interparticle distance leading to an enhancement of the incident field that can theoretically reach several orders of magnitude for nanometer-sized gaps [39].

Independently of the gap size, the geometry of the particles forming the antenna has substantial influence on the optical properties of the antenna, both on its spectroscopy and the distribution of the local field. As an illustration, using triangular particles or rods instead of cylinders tends to broaden the resonance bandwidth and increase the ratio between the field within the gap and at the outer edges [40].

Subsequent to the fabrication process, the optimization of plasmonic dimers also requires their optical characterization. While the spectroscopic features of the

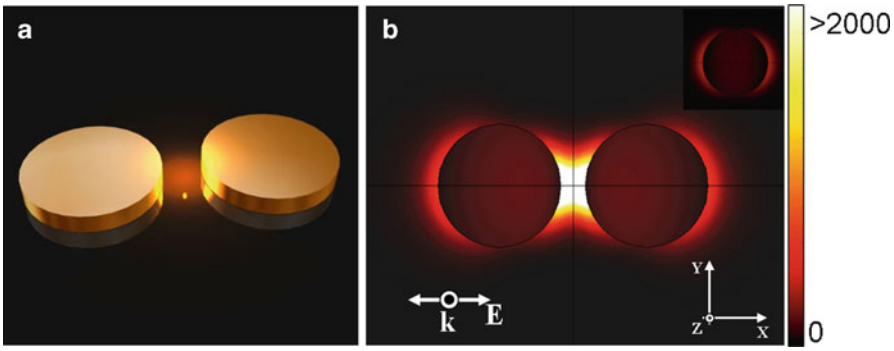

Fig. 11.3 (**a**) Dimer (or gap optical antenna) geometry formed by two gold cylinder (50 nm diameter and 20 nm height) (**b**) FEM calculations of the normalized electric field intensity distribution at resonance (659 nm). (*Inset*) single gold disk at resonance

fabricated structures can be measured by standard extinction or scattering spectroscopy, local field mapping requires specific optical methods able to probe the evanescent plasmonic fields bound to the metal. Although scanning near-field optical microscopy (SNOM) is usually well suited to detect evanescent fields, the actual influence of the optical probe along with its polarization sensitivity raise some issues in the specific case of gap antenna [41, 42]. Consequently, one is rather interested in tip-less techniques despite their limited resolution. Among the possible approaches, two-photon-induced luminescence (TPL) in gold provides direct insight in the optical near-field bound to a gold nanostructure [43]. In particular, we recently showed that mapping the TPL emission over gold antennas provides direct insights on their actual mode distribution [44]. Figure 11.4 displays the TPL distribution of a gap antenna formed by two adjacent 500 nm gold bars separated by a 40 nm gap along with the associated distribution of the fourth power of the electric field. Beyond capturing a snap shot of the antenna mode for a fixed incident wavelength, TPL microscopy can be extended to spectroscopic mode mapping, by monitoring the evolution of the TPL maps as a function of the wavelength of the incident pulsed laser. Such data provides an efficient way to perform near-field spectroscopy of the local field at specific regions of the antenna [45, 46]. Since plasmonic sensing, like SERS, involves the interaction of molecules with the local fields, such information is particularly valuable especially when considering structures large enough to experience some retardation effect for which far-field and near-field spectra can significantly differ.

How to Design a Good Nanosensor?

In this section, we derive the general rules to design an efficient LSP sensor for the detection of small molecules. To this end, firstly it is important to remind ourselves what dictates the sensitivity of an optical sensor. The change in the optical response

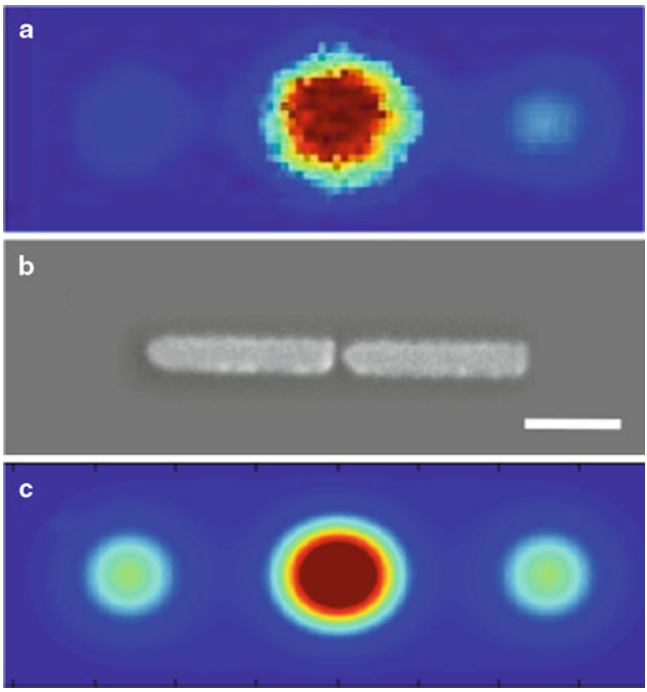

Fig. 11.4 Experimental TPL map (**a**) recorded over a gold gap antenna formed by two gold bars (**b**) (scale bar = 250 nm). (**c**) Comparison with the corresponding calculated distribution of the $|E|^4$ convoluted with a 200 nm Gaussian profile

of the sensor is in part determined by the magnitude of the perturbation to the optical mode induced by the binding of the target molecules. In the particular case of a sensor based on plasmon nanoparticles, one aims at maximizing the induced shift in the LSP resonance central wavelength. Here, we illustrate with finite elements method (FEM) numerical simulations how this can be achieved by properly engineering the plasmon mode of the sensor and adapt it to detect a given target molecule.

Influence of the Sensor Geometry

We illustrate a configuration in which a single molecule, such as a protein, binds to the sensor. Such protein can be reasonably mimicked in our model by an 8 nm dielectric sphere of refraction index 1.5. Let us first consider an isolated cylindrical gold nanoparticle lying upon a glass substrate. Figure 11.5b shows the unperturbed electric near-field distribution in the half-height plane of the particle in resonance

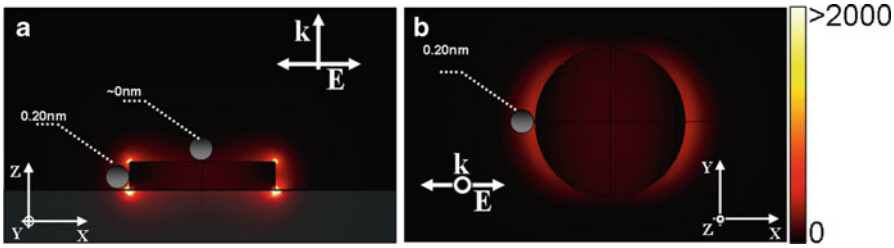

Fig. 11.5 Near-field intensity distribution computed for an isolated cylindrical gold particle (50 nm diameters and 20 nm height) illuminated by a linearly polarized plane wave at 626 nm and resonance shift induced by the presence of a single 8 nm dielectric sphere ($n = 1.5$). (**a**) Side cross-section view, (**b**) top cross-section through the middle of nanoparticle

for an incident plane wave polarized along the *X*-axis. Upon this illumination condition, the plasmon mode features two lobes located at opposite edges of the particle and aligned along the incident electric field direction. For a single molecule binding to the metal, there is a strong mismatch between the volume of the target molecule and the plasmon mode volume leading to a very small resonance shift (Fig. 11.5). Note that this shift would be even smaller if the molecule would be bound in the "dark regions" located along the *Y*-axis or *Z*-axis (Fig. 11.5a).

In order to increase the perturbation, one needs to squeeze the mode volume to dimensions that are commensurable with the size of the target molecule, as can be done using plasmonic dimers. Locating the target molecule in the gap of a gold dimer formed by two identical gold cylinders leads to a resonances shift about ten times larger than that with a single particle (Fig. 11.6).

Influence of the Target Position

In a configuration involving a large number of molecules binding all over the dimer, the different molecules do not all have the same contribution to the resonance shift depending on where they are located. Figure 11.6 illustrates the influence of the location of a single molecule on the magnitude of the shift. It is shown that a molecule sitting in the gap leads to a shift at least one order of magnitude larger than for any other location of the structure. Such ratio becomes even larger for gap antennas formed by two adjacent elongated gold rods instead of cylinders. This underlines the importance of specifically binding the target molecules within the gap regions where the antenna effect could be fully exploited, especially when the analyte molecules are not abundant enough to cover the whole structure.

Recently, it has been shown that for sensors based on nanoholes in metallic films, a faster kinetics and therefore shorter read-out time is achieved when the analyte selectively binds on the hole walls where the plasmonic mode is

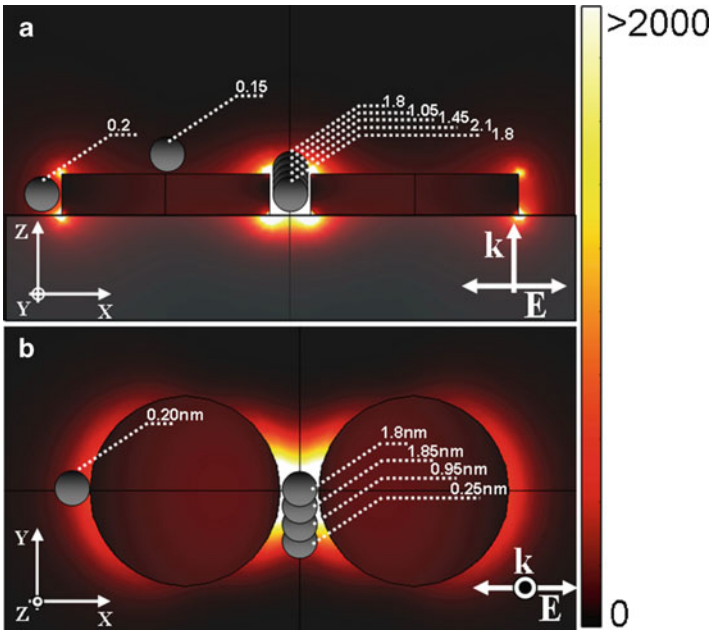

Fig. 11.6 Near-field intensity distribution computed for a gold dimer illuminated by a linearly polarized plane wave at 659 nm and resonance shift induced by the presence of a single 8 nm dielectric sphere ($n = 1.5$). (**a**) Side cross-section view, (**b**) top cross-section through the middle of nanoparticle

mostly confined. This was managed by coating the bottom of holes and the top surface of the gold film by a thin layer of TiO_2, enabling selective functionalization of the gold wall of the hole [47]. The improvement lays in the decrease of averaged depletion zone near the sensor interface, since molecules cannot be consumed by nonactive regions of metallic film. Besides, the detected signal originates from the smaller number of analytes. In the case of dimer structures, a similar approach where the top surface is covered can be considered. In practice though, analyte delivery of a few molecules represents a major challenge, since molecule transport is then governed by diffusion. This makes the detection time of a few molecules, diffusing into the sensing volume, excessive. Possible improvements can be foreseen by further miniaturization from microfluidics to nanofluidics or using the very promising flow-through sensing configuration [48–50].

A substantial enhanced resonance shift of dimers over isolated particle is still expected when considering a large ensemble of molecules binding uniformly all over the nanoparticles. In that case the bound molecules can be modeled by a thin dielectric layer covering the substrate. Simulations based on the Fourier Modal Method showed an enhancement in the resonance shift of about five as compared to isolated particles [52].

Experimental Implementation of Enhanced Small Molecule Detection in Plasmonic Antennae (and Other Recent Works on Litho Structures)

When Enoch et al. proposed in 2004 to use plasmonic dimers for enhanced sensitivity sensing [51], EBL structures of dimer dots [52] and bowties [53] were prepared and started to be intensively characterized optically. At this time, however, the fabrication capability was somewhat limited and with the exception of the work of Atay, gap sizes shorter than 20 nm were difficult to prepare with high reproducibility. In the interim years, based on the initial plasmonic ruler work of Sönnichsen et al. [54], this concept was fully developed both theoretically and experimentally by Jain & El Sayed, which eventually derived the universal scaling behavior or the plasmon ruler equation principle [31, 55]. The group of El Sayed was able to prepare highly ordered, reproducible small gap dimers by EBL, but without studying their enhanced sensing capability. One work of note, however, for bulk refractive index measurements used particle pairs and reported an enhanced sensitivity value of ca. 300 nm/RIU [9] when compared to other single structured LSP sensors with sensitivities of between 150 and 200 nm/RIU [6, 7, 56].

We have recently made some advances toward engineering nano-plasmonic structures for enhanced sensitivity sensing, where we have used a standard EBL setup of 30 kV in conjunction with negative e-beam resist and RIE to produce well-defined and highly reproducible structures [13]. For sensing purposes, we utilize arrays of particle pairs with varying gaps in order to investigate the influence of the analyte/mode overlap. For conducting such experiments, it is important to precisely determine the actual gap size within each array. A standard way of accomplishing this is to apply statistical analysis to a collection of high-resolution SEM images of dimer pairs in each particular array. However, this is time-consuming and cost-ineffective, and therefore, we use a versatile and faster calibration alternative that relies on far-field spectra measurements.

Interparticle Distance Calibration

In order to fully characterize our nano-plasmonic sensors, we focus on the evolution of their spectral response as a function of the gap size. In recent times, the response of particles in near-touching and touching regimes has been investigated both theoretically and experimentally, with focus on small gaps and towards the single point touching limit [19, 52]. In support of these works, our FEM simulations in Fig. 11.7 show that the scattering spectrum of dimers is dominated by different modes depending on whether the particles are fused or separated.

Figure 11.7a gives an illustrative overview of the evolution of the plasmon peak position in the Vis-NIR spectrum. The arrow height and thickness relates to the relative intensity and broadness of the peaks, respectively. For fused particles

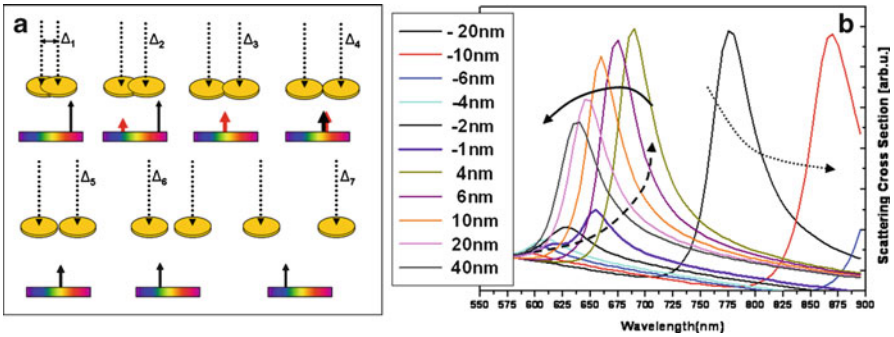

Fig. 11.7 Theoretical evolution with the gap size of the scattering spectrum of a gold dimer formed by gold cylinders (50 × 10 nm). (**a**) Schematic illustration: *black arrows* represent dipolar modes while *red arrows* represent multipolar modes. (**b**) FEM computed scattering spectra evolution from fused to separated particles

(negative gap values), the dimer behaves like a nanorod whose dipolar resonance continuously red shifts toward the near-IR as overlap decreases, and therefore, the size of this equivalent nanorod increases (Fig. 11.7b, dotted arrow). At some point, the dipolar peak shifts to the IR region, out of the range of our spectrometer. Further separation between the nanoparticle pairs provides even longer nanorod-shaped structures and leads to the appearance of a multipolar peak around 600 nm (Fig. 11.7b, dashed arrow), which also continually red shifts with the overlap decrease. Once the conductive bridge between the two particles breaks, the multipolar peak evolves into the coupled dipolar mode. Thereafter, the resonance exponentially blue shifts as the gap increases (Fig. 11.7b, solid arrow) and finally stabilizes around 630 nm, when the particles become nearly uncoupled [62].

Monitoring the transition between the multipolar peak of the fused particles and the dipolar of the separated dimers provides thus an efficient way to accurately identify the touching condition (gap = 0 nm).

In practice, we fabricated a complete series of dimer matrices ranging from well-separated to fused particles with increments of 2–4 nm and measured their extinction spectrum. The experimental data (Fig. 11.8) are found to be in good qualitative agreement with the simulations of the Fig. 11.7. From them, we identify the matrix associated to touching dimers. At this stage, one can retrieve the actual particles diameter from the EBL pattern design, (Δ_4 in Fig. 11.7a) as well as the gap/overlap of each exposed arrays. Matrices from touching dimers to dimers with gaps shorter than 30 nm form the basis of our enhanced sensitivity nano-plasmonic sensors.

Enhanced Biosensing in Arrays of Gold Dimers

Once determined the optical properties of the fabricated arrays, molecular binding experiments were conducted to test and prove the enhanced sensitivity of small molecule detection with gold dimers.

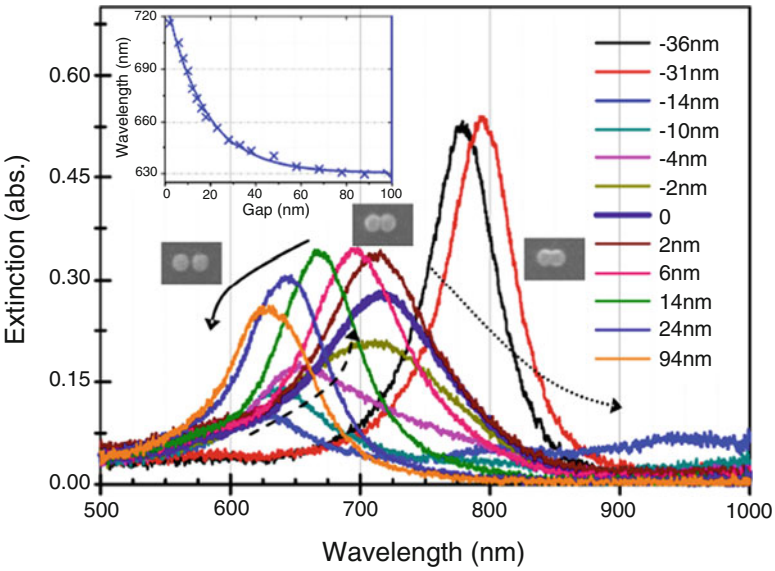

Fig. 11.8 Experimental evolution with the gap size of the extinction spectrum of arrays of gold dimers (100 × 40 nm). *Inset*: resonance peak position as function of gap (overlapping particle arrays are disregarded)

Solvent Annealing

Recently, it has been reported that metallic particles produced by nanospheres lithography (NSL) are prone to structural changes induced by surface tension alterations after changing the liquid environment surrounding the nanoparticle [6]. Although rarely reported, these transformations might play an important role in the operation of LSP sensing platforms. Changes of surface tension when transferring NSL structures from air or nitrogen to solvents provoke a substantial resonance shift that can reach up to 100 nm as a consequence of nanoparticle edge smoothing, in-plane size shrinkage, and out-of-plane height increase. Even though total solvent annealing decreases with time, particles have to be stabilized prior to any molecular binding in order to correctly ascertain the true plasmon shift associated with such binding events. Interplay of surface tension on glass/metal and metal/environment particle interfaces determine the extent of shape modification. Since these modifications to dimer configuration are difficult to observe by AFM or SEM, we monitor the annealing by resonance shift measurements to evaluate the approximate particle shape changes.

For EBL-fabricated dimers, after immersion of the particle arrays into an ethanolic solution, the resonances subsequently shift to the blue (lower wavelengths) by an amount nearly exponentially dependent on the initial gap size. Blue shift of gold, single (uncoupled) particle arrays can reach typically up to 10 nm. This implies that particle diameter is on average shrinking with larger

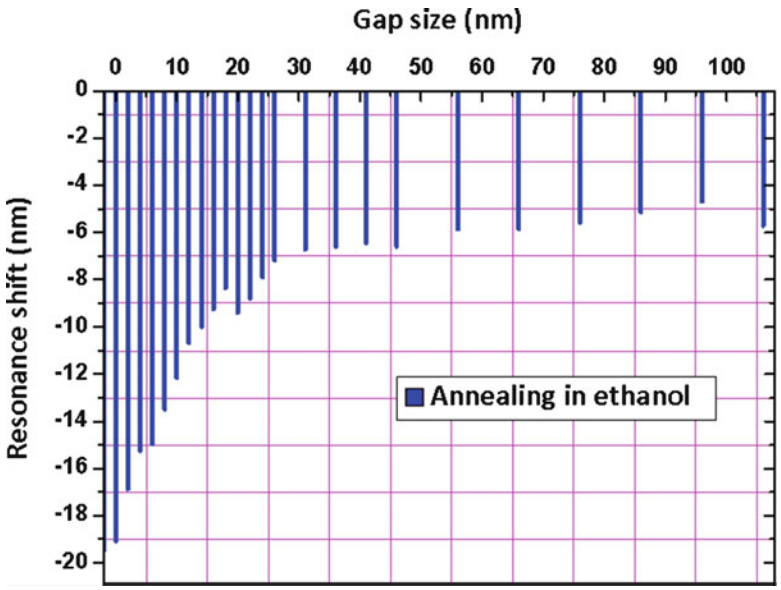

Fig. 11.9 Solvent annealing curve for fully annealed sample in ethanol for 7 days

change noted farther from the glass interface, while out-of-plane height is slightly increasing. Yet another indication of diameter shrinkage is the gap dependence where a blue shift for closest dimers can reach down to 30 nm. Figure 11.9 shows the result of solvent annealing after a 7 day time. When compared to organic solvents, water annealing is significantly less pronounced. Thus in order to preserve gaps, it is in practice more suitable to work with water-based solvents.

Monolayer (MUA) and Protein (BSA) Detection

Gold nanoparticle functionalization is performed by self-assembly of mercapto undecanoic acid (MUA) molecules. Despite the small size of MUA (<1.5 nm), the monolayer formation is easily monitored by resonance shifts [7]. Typical response of our system after binding of MUA is shown in Fig. 11.10. One can clearly observe that squeezing the mode volume increases the induced resonant shifts exponentially.

Subsequent to the formation of the MUA layer and its activation, the dimer sensors are exposed to a buffered solution of BSA molecules. After drying the sample, the resonance shift resulting from the binding of BSA to MUA-coated arrays is shown in Fig. 11.11. Contrary to the curve in Fig. 11.10, BSA binding curves are far richer in features. Pertaining to previous observations, starting from isolated MNs, the red shift magnitude follows an exponential rise with decreasing separation. The maximum resonance shift is obtained when the gap reaches the size

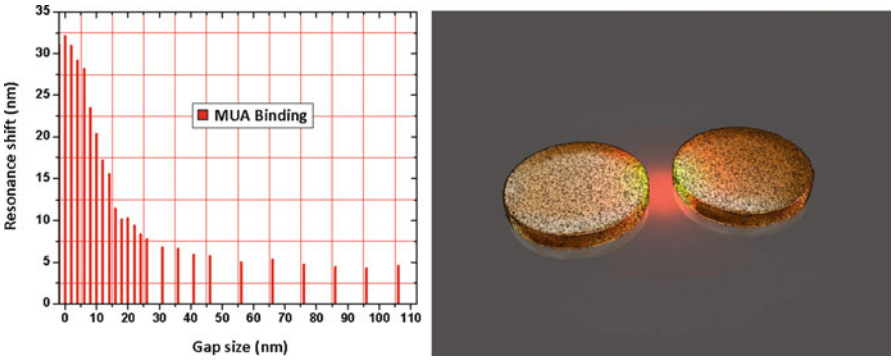

Fig. 11.10 (*Left*) Equilibrium resonance shift induced by MUA for dimers as a function of gap size, and (*Right*) depiction of self-assembling monolayer formation

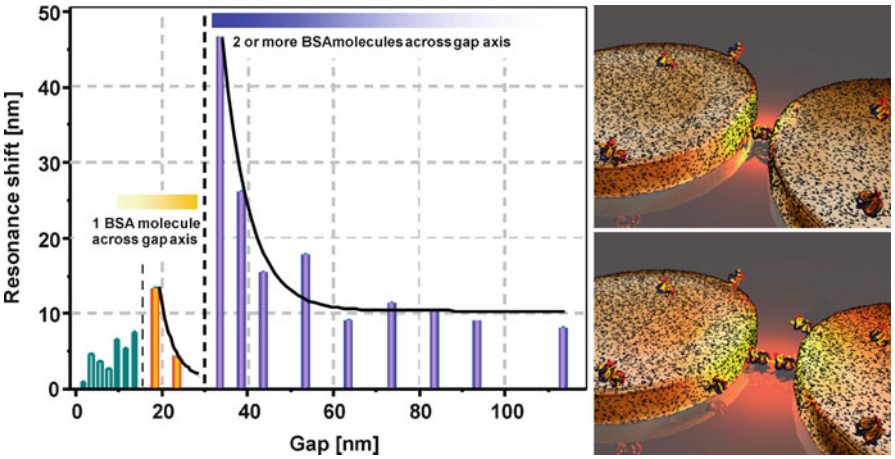

Fig. 11.11 (*Left*) Equilibrium resonance shift induced by BSA and (*Right*) depiction representing both binding regimes

of ca. 30 nm. Thereafter, as the gap further decreases, a sudden drop is observed, followed by an additional increasing trend. Again, when the gap size reaches ca. 15 nm, another discrete drop occurs. We attribute these discrete drops to the relation between the geometry of the dimer gap and the protein size. The shape of a BSA molecule is rod-like ($4 \times 4 \times 14$ nm^3) [57]. When the gap is big enough ($\geq$30 nm), two such molecules can fit across the shortest distance between the dimer structure. By reaching this limiting gap size of 30 nm, large resonance shifts are expected due to the optimum overlap of mode volume and BSA molecules. When the gap decreases further below the first critical value, only one molecule can now fit along the dimer axis, bound either to one or the other particle forming the dimer. As the gap further diminishes, overlap of hot spot and molecule increases again, up to a point when the molecule can no longer fit inside (gap of ca. 15 nm).

This interpretation may look simplified considering BSA is not a spherical molecule and that binding orientation inside the gap could vary. However, it is known that binding of BSA to glass substrates at the protein's isoelectric point favors a long axis linking and therefore suggests that BSA will protrude perpendicularly out from the surface [58, 59]. Although this system is not glass, the protein could behave in an analogous fashion under similar binding conditions and thus on average extend from the surface. Additionally, this effect is reproducible, and strikingly, it has been found repeatedly within 4 nm around this critical 30 nm gap distance. The second drop, although less pronounced, occurs at 15 $\pm$ 2 nm, corroborating the hypothesis of specific BSA binding orientation. After the second drop, we observed smaller BSA-induced shifts than for the isolated MN case (Fig. 11.11), as a consequence of reduced mode extension away from the gap and the inability of the BSA molecules to now penetrate into this area due to size exclusion.

Concluding Remarks and Outlook

As a way to summarize the main results of this study, we show in Fig. 11.12 the comparative normalized resonance shift with gap decrease (normalized to resonance shift of quasi-isolated particles) for a number of sensing conditions.

The bulk refractive index sensitivity m (see (11.1)) is mostly related to both the mode distribution and the electromagnetic field enhancement. Near-field coupling in dimers induces a mode redistribution that leads to a hot spot in the gap whose

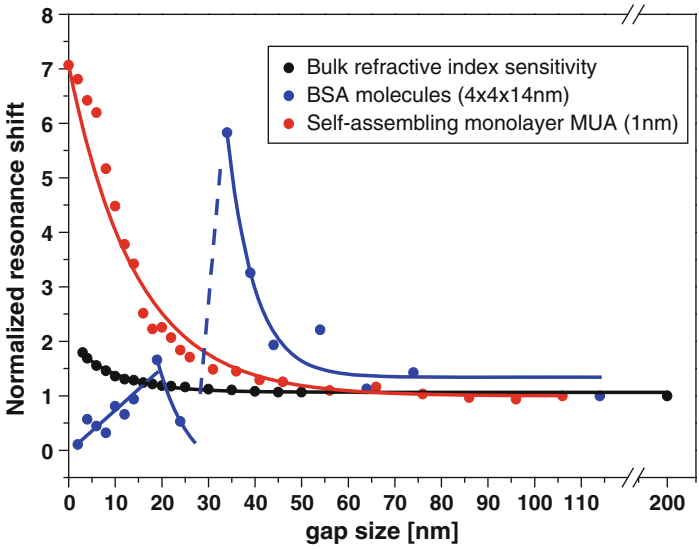

Fig. 11.12 Normalized resonance shift as a function of gap size in the case of bulk refractive sensitivity (*black*), self-assembling monolayer of 1 nm thickness (*red*), and BSA protein molecules ($4 \times 4 \times 14$ nm)

confinement and field enhancement increase with dimer gap shrinkage. This enhancement provides higher m, as illustrated by the black curve in Fig. 11.12, typically twice as large as compared to isolated particles [63].

Contrary to bulk refractive index sensing where the mode-perturbation overlap is always maximized to 1, when dealing with very small molecules, the mode redistribution due to different coupling strengths, i.e., different gaps, affects the mode-analyte overlap. Figure 11.12 (red data points) shows the evolution of the normalized resonance shift with the gap size upon formation of a self-assembling monolayer of approximately 1 nm thickness. A maximum increase of 7 is achieved for smallest gaps of few nm.

However, a majority of significant biomolecules (proteins, antibodies, DNAs) are considerably bigger, typically 5–15 nm. These sizes of dimer gaps are readily achievable with state-of-the-art lithography processes, and the binding of such molecules cannot be described with (11.1). In particular, as shown in Fig. 11.11, steric hindrance and molecular binding orientation influence the magnitude of resonance shift. For sensing protocols in which the total molecular layer thickness (SAM + recognition molecule + target molecule) is smaller than one half of the smallest considered gap, the resonance shift curve exhibits continuous exponential growth with decreasing gaps (red data). On the other hand, for molecules like BSA, the maximum shift occurs when the overlap is maximized, i.e., when the molecular layer thickness (MUA + BSA molecule) is equal to half of the gap. For smaller gaps, the overlap abruptly falls, and then reaches local maximum for gap equal to one molecular layer thickness. Further decrease of the gap size increases the mismatch between the hot spot and the protein, inducing very small shifts.

Figure 11.12 points out parameters that are not crucial for the majority of LSPR schemes based on "quasi-isolated" particles [6–8], but become crucial in the optimization of more sensitive close coupling base LSPR platforms. For every detection protocol involving a particular molecule of interest, it is thus necessary to optimize the distance between particle pairs to obtain the highest sensitivity. It is shown in Fig. 11.12 (blue data set) that the shift enhancement can reach 5 for optimized gap. We though foresee that other sensor geometry may enable higher enhancements.

Assessing the absolute sensitivity of our dimer sensor requires implementing few additional technical steps. One of them being its integration into a microfluidic platform [60]. The controlled delivery of different samples to the sensing area along with a high-speed and high-resolution read-out should provide more competitive LSP sensing platforms, and most likely turn LSPR sensors into an important player on the chemical and biomedical sensor market [61].

References

1. Miller MM, Lazarides AA. Sensitivity of metal nanoparticle surface plasmon resonance to the dielectric environment. J Phys Chem B. 2005;109:21556–65.
2. Willets KA, Van Duyne RP. Localized surface plasmon resonance spectroscopy and sensing. Annu Rev Phys Chem. 2007;58:267–97.

3. Liz-Marzán LM. Tailoring surface plasmons through the morphology and assembly of metal nanoparticles. Langmuir. 2006;22:32–41.
4. Unger A, Kreiter M. Analyzing the performance of plasmonic resonators for dielectric sensing. J Phys Chem C. 2009;113:12243–51.
5. Andreas B. Dahlin and Magnus P. Jonsson, Performance of Nanoplasmonic Biosensors in A. Dmitriev (ed.), Nanoplasmonic Sensors, Integrated Analytical Systems. 2012
6. Malinsky MD, Kelly KL, Schatz GC, Van Duyne RP. Chain length dependence and sensing capabilities of the localized surface plasmon resonance of silver nanoparticles chemically modified with alkanethiol self-assembled monolayers. J Am Chem Soc. 2001;123:1471–82.
7. Barbillon G, Bijeon JL, Plain J, Lamy de la Chapelle M, Adam PM, Royer P. Electron beam lithography designed chemical nanosensors based on localized surface plasmon resonance. Surf Sci. 2007;601:5057–61.
8. Kreno LE, Hupp JT, Van Duyne RP. Metal−organic framework thin film for enhanced localized surface plasmon resonance gas sensing. Anal Chem. 2010;82(19):8042–6.
9. Grigorenko AN, Gleeson HF, Zhang Y, Roberts NW, Sidorov AR, Panteleev AA. Antisymmetric plasmon resonance in coupled gold nanoparticles as a sensitive tool for detection of local index of refraction. Appl Phys Lett. 2006;88:124103.
10. Haes AJ, Van Duyne RP. A nanoscale optical biosensor: sensitivity and selectivity of an approach based on the localized surface plasmon resonance spectroscopy of triangular silver nanoparticles. J Am Chem Soc. 2002;124(35):10596–604.
11. Chen S, Svedendahl M, Kall M, Gunnarsson L, Dimtriev A. Ultrahigh sensitivity made simple: nanoplasmonic label-free biosensing with an extremely low limit-of-detection for bacterial and cancer diagnostics. Nanotechnology. 2009;20:434015.
12. Barbillon G, Bijeon J-L, Lérondel G, Plain J, Royer P. Detection of chemical molecules with integrated plasmonics glass nanotips. Surf Sci. 2008;602:119–22.
13. Aćimović SS, Kreuzer MP, González MU, Quidant R. Plasmon near-field coupling in metal dimers as a step toward single-molecule sensing. ACS Nano. 2009;3:1231–7.
14. Xu H, Aizpurua J, Käll M, Apell P. Electromagnetic contributions to single-molecule sensitivity in surface-enhanced Raman scattering. Phys Rev E. 2000;62:4318–24.
15. Ringler M, Klar TA, Schwemer A, Susha AS, Stehr J, Rasche G, Funk S, Borowski M, Nichtl A, Kurzinger K, Phillips RT, Feldman J. Moving nanoparticles with Raman scattering. Nanoletters. 2007;7(9):2753–7.
16. Stockman MI. Nanofocusing of optical energy in tapered plasmonic waveguides. Phys Rev Lett. 2004;93:137404.
17. De Angelis F, Patrini M, Das G, Maksymov I, Galli M, Businaro L, Andreani LC, Di Fabrizio E. A hybrid plasmonic-photonic nanodevice for label-free detection of a few molecules. Nano Lett. 2008;8:2321–7.
18. Li K, Stockman MI, Bergman DJ. Self-similar chain of metal nanospheres as an efficient nanolens. Phys Rev Lett. 2003;91:227402.
19. Romero I, Aizpurua J, Bryant GW, GarcíaDeAbajo FJ. Plasmons in nearly touching metallic nanoparticles: singular response in the limit of touching dimers. Opt Express. 2006;14:9988–99.
20. Kottmann J, Martin O. Retardation-induced plasmon resonances in coupled nanoparticles. Opt Lett. 2001;26:1096–8.
21. Pérez-Juste J, Pastoriza-Santos I, Liz-Marzán LM, Mulvaney P. Gold nanorods: synthesis, characterization and applications. Coord Chem Rev. 2005;249(17–18):1870–901.
22. Malaquin L, Kraus T, Schmid H, Delamarche E, Wolf H. Controlled particle placement through convective and capillary assembly. Langmuir. 2007;23:11513–21.
23. Biswas A, Wang T, Biris AS. single metal nanoparticle spectroscopy: optical characterization of individual nanosystems for biomedical applications. Nanoscale. 2010;2:1560–72.
24. Nehl CL, Liao H, Hafner JH. Optical properties of star-shaped gold nanoparticles. Nano Lett. 2006;6(4):683–8.

25. Sannomiya T, Hafner C, Voros J. In situ sensing of single binding events by localized surface plasmon resonance. Nano Lett. 2008;8:3450–5.
26. Becker J, Schubert O, Sönnichsen C. Gold nanoparticle growth monitored in situ using a novel fast optical single-particle spectroscopy method. Nano Lett. 2007;7(6):1664–9.
27. Bingham JM, Willets KA, Shah NC, Andrews DQ, Van Duyne RP. Localized surface plasmon resonance imaging: simultaneous single nanoparticle spectroscopy and diffusional dynamics. J Phys Chem C. 2009;113(39):16839–42.
28. Hicks EM, Zou S, Schatz GC, Spears KG, Van Duyne RP, Gunnarsson L, Rindzevicius T, Kasemo B, Käll M. Controlling plasmon line shapes through diffractive coupling in linear arrays of cylindrical nanoparticles fabricated by electron beam lithography. Nano Lett. 2005;5:1065–70.
29. Kravets VG, Schedin F, Grigorenko AN. Extremely narrow plasmon resonances based on diffraction coupling of localized plasmons in arrays of metallic nanoparticles. Phys Rev Lett. 2008;101:087403.
30. Auguie B, Barnes WL. Collective resonances in gold nanoparticle arrays. Phys Rev Lett. 2008;101:143902.
31. Jain PK, Huang W, El-Sayed MA. On the universal scaling behavior of the distance decay of plasmon coupling in metal nanoparticle pairs: a plasmon ruler equation. Nano Lett. 2007;7:2080–8.
32. Zhang WH, Fischer H, Schmid T, Zenobi R, Martin OJF. Mode-selective surface-enhanced Raman spectroscopy using nanofabricated plasmonic dipole antennas. J Phys Chem C. 2009;113:14672–5.
33. Smythe EJ, Cubukcu E, Capasso F. Optical properties of surface plasmon resonances of coupled metallic nanorods. Opt Express. 2007;15(12):7439–47.
34. Graells S, Alcubilla R, Badenes G, Quidant R. Growth of plasmonic gold nanostructures by electron beam induced deposition. Appl Phys Lett. 2007;91:121112.
35. Farahani JN, Pohl DW, Eisler HJ, Hecht B. Single quantum dot coupled to a scanning optical antenna: a tunable superemitter. Phys Rev Lett. 2005;95:017402.
36. chapters 2–4
37. Chou SY, Krauss PR, Zhang W, Guo LJ, Zhuang L. Sub-10nm imprint lithography and applications. J Vac Sci Technol B. 1997;15:2897–904.
38. Guo LJ. Nanoimprint lithography: methods and material requirements. Adv Mater. 2007;19:495–513.
39. Zhdanov A, Kreuzer MP, Rao S, Fedyanin A, Ghenuche P, Quidant R, Petrov D. Detection of plasmon-enhanced luminescence fields from an optically manipulated pair of partially metal covered dielectric spheres. Opt Lett. 2008;33(23):2749–51.
40. Fischer H, Martin OJF. Engineering the optical response of plasmonic nanoantennas. Opt Express. 2008;16:9144–54.
41. Lereu AL, Sánchez-Mosteiro G, Ghenuche P, Quidant R, van Hulst NF. Individual gold dimers investigated by far- and near-field imaging. J Microsc. 2008;229:254–8.
42. Schnell M, García-Etxarri A, Huber AJ, Crozier K, Aizpurua J, Hillenbrand R. Controlling the near-field oscillations of loaded plasmonic nanoantennas. Nat Photon. 2009;3:287–91.
43. Bouhelier A, Bachelot R, Lerondel G, Kostcheev S, Royer P, Wiederrecht GP. Surface plasmon characteristics of tunable photoluminescence in single gold nanorods. Phys Rev Lett. 2005;95:267405.
44. Ghenuche P, Cherukulappurath S, Taminiau TH, van Hulst NF, Quidant R. Spectroscopic mode mapping of resonant plasmon nanoantennas. Phys Rev Lett. 2008;101:116805.
45. Wissert MD, Ilin KS, Siegel M, Lemmer U, Eisler HJ. Coupled nanoantenna plasmon resonance spectra from two-photon laser excitation. Nano Lett. 2010;10(10):4161–5.
46. Messinger BJ, von Raben KU, Chang RK, Barber PW. Local fields at the surface of noble-metal microspheres. Phys Rev B. 1981;24:649.
47. Sheehan PE, Whitman LJ. Detection limits for nanoscale biosensors. Nano Lett. 2005;5 (4):803–7.

48. Ferreira J, Santos MJL, Rahman MM, Brolo AG, Gordon R, Sinton D, Girotto EM. Attomolar protein detection using in-hole surface plasmon resonance. J Am Chem Soc. 2009;131 (2):436–7.
49. Eftekhari F, Escobedo C, Ferreira J, Duan X, Girotto EM, Brolo AG, Gordon R, Sinton D. Nanoholes as nanochannels: flow-through plasmonic sensing. Anal Chem. 2009;81:4308–11.
50. Jonsson MP, Dahlin AB, Feuz L, Petronis A, Hook F. Locally functionalized short-range ordered nanoplasmonic pores for bioanalytical sensing. Anal Chem. 2010;82(5):2087–94.
51. Enoch S, Quidant R, Badenes G. Optical sensing based on plasmon coupling in nanoparticle arrays. Opt Express. 2004;12:3422–7.
52. Atay T, Song JH, Nurmikko AV. Strongly interacting plasmon nanoparticle pairs: from dipole-dipole interaction to conductively coupled regime. Nano Lett. 2004;4:1627–31.
53. Fromm DP, Sundaramurthy A, Schuck PJ, Kino G, Moerner WE. Gap-dependent optical coupling of single bowtie nanoantenas resonant in the visible. Nano Lett. 2004;4:957–61.
54. Sönnichsen C, Reinhard BM, Liphardt J, Alivisatos AP. A molecular ruler based on plasmon coupling of single gold and silver nanoparticles. Nat Biotechnol. 2005;23:741–5.
55. Huang W, Qian W, Jain PK, El-Sayed MA. The effect of plasmon field on the coherent lattice phonon oscillation in electron-beam fabricated gold nanoparticle pairs. Nano Lett. 2007;7 (10):3227–34.
56. Félidj N, Grand J, Laurent G, Aubard J, Lévi G, Hohenau A, Galler N, Aussenegg FR, Krenn JR. Multipolar surface plasmon peaks on gold nanotriangles. J Chem Phys. 2008;128:094702.
57. Malmsten M. Ellipsometry studies of the effects of surface hydrophobicity on protein adsorption. Colloids Surf B. 1995;3:297–308.
58. Fukuzaki S, Urano H, Nagata K. Adsorption of bovine serum albumin onto metal oxide surfaces. J Ferment Bioeng. 1996;81(2):163–7.
59. Brewer SH, Glomm WR, Johnson MC, Knag MK, Franzen S. Probing BSA binding to citrate-coated gold nanoparticles and surfaces. Langmuir. 2005;21:9303–7.
60. Thorsen T, Maerkl SJ, Quake SR. Microfluidic large-scale integration. Science. 2002;298 (5593):580–4.
61. Gerion D, Day G. Label-free and labeled technology for protein characterization and quantitation. Biopharm Int. 2010;23(9):38–45.
62. Rechberger W, Hohenau A, Leitner A, Krenn JR, Lamprecht B, Aussenegg FR. Optical properties of two interacting gold nanoparticles. Opt Commun. 2003;220:137–41.
63. Jain PK, El-Sayed MA. Plasmonic coupling in noble metal nanostructures. Chem Phys Lett. 2010;487:153–64.

Chapter 12
Nanoplasmonic Structures in Optical Fibers

Gustavo F.S. Andrade and Alexandre G. Brolo

Abstract The intense research efforts on the development, fabrication, characterization, and application of metallic nanostructures and films that support surface plasmon resonance (SPR) constitute a field called nanoplasmonics. Although SPR biosensing is well established, the development of new nanoplasmonic approaches for biosensing is still a very active research area, as it can be attested by the range of topics covered in this book. The SPR approach is widely used in biochemistry and biomedical research, because it offers a "label-free" alternative for the detection and quantification of biomolecular interactions. The objective of this chapter is to focus on the approaches for the integration of the nanoplasmonic sensing elements to the optical fiber technology. Initially, selected examples of applications of optical fiber in analytical sciences are presented. Next, techniques used to fabricate optical fiber-based devices developed for SPR and SERS sensing are discussed. Examples of applications of optical fiber based plasmonic devices are provided. The field of optical fiber applications in nano- plasmonics has been in effervescence in the recent years, and the wide-coverage review of the field in this chapter is intended to give a more comprehensive understanding of the current state-of-the-art to the interested reader.

Introduction and Scope

The intense research efforts on the development, fabrication, characterization, and application of metallic nanostructures and films that support surface plasmon resonance (SPR) constitute a field called nanoplasmonics. This book focuses on

G.F.S. Andrade
Departamento de Quimica, Universidade Federal de Juiz de Fora, Juiz de Fora, Brazil

A.G. Brolo (✉)
Department of Chemistry, University of Victoria, 3055, Victoria, BC, Canada V8W 3V6,
e-mail: agbrolo@uvic.ca

A. Dmitriev (ed.), *Nanoplasmonic Sensors*, Integrated Analytical Systems,
DOI 10.1007/978-1-4614-3933-2_12,

the application of nanoplasmonic platforms as sensors. In fact, SPR has been already proved to be an extremely powerful bioanalytical technique [1]. Although SPR biosensing is well established, the development of new nanoplasmonic approaches for biosensing is still a very active research area [2, 3], as it can be attested by the range of topics covered in this book. In the last decades, the use of SPR spread over a large range of applications in bioanalysis, culminating on commercial SPR systems based on the so-called Kretschmann configuration [4], which explore the properties of extended-surface plasmon modes generated on thin (about 50 nm) gold films. The surface plasmons excited in this way are characterized by their propagation distance along the metallic surface (about 10 mm SP waves excited on a silver thin film using visible, ~500 nm, radiation) and their penetration depth into the analyte layer (about half of the excitation wavelength) and into the metal (about a tenth of the penetration depth into the analyte). The SPR approach is widely used in biochemistry and biomedical research, because it offers a "label-free" alternative for the detection and quantification of biomolecular interactions. The method is also useful for the determination of kinetic parameters and binding constants [5]. The advent of imaging SPR [6] allows the detection of multiple binding events simultaneously, making this methodology very attractive for disease diagnostic, drug development, and screening.

The conditions for SPR can also be satisfied for light interacting with metallic nanoparticles with diameters smaller than the exciting wavelength [7]. For SPR in the visible-NIR region of the spectra, the required dimension for these nanoplasmonic materials are in the range of tens of nanometers [3]. The resulting excitation is usually called "localized surface-plasmons" (LSPs) and the surface-plasmon properties of the nanostructures are strongly dependent on the nanoparticle size and shape [8]. A very important consequence of localized surface plasmon resonance (LSPR) excitation is field localization. The focusing of light in sub-wavelength regions due to LSPR is widely accepted as the main contribution to surface-enhanced spectroscopic methods, such as surface-enhanced Raman scattering (SERS). SERS is particularly powerful for sensing applications, since it provides vibrational information unique to the adsorbed species.

Principles and application of nanoplasmonic sensor elements based on LSPs have been covered in previous chapters. The objective of this chapter is to focus on the approaches for the integration of the nanoplasmonic sensing elements to the optical fiber technology. Initially, selected examples of applications of optical fiber in analytical sciences will be presented, and the actual delimitations of the present text around this broad issue will be discussed. Next, techniques used to fabricate optical fiber-based devices developed for SPR and SERS sensing will be presented. The fabrication techniques were arbitrarily divided into "lithographic" and "non-lithographic methods." Examples of applications of optical fiber based plasmonic devices will also be provided. The field of optical fiber applications in nanoplasmonics has been in effervescence in the recent years, and the wide-coverage review of the field in this chapter is intended to give a more comprehensive understanding of the current state-of-the-art for the interested reader. It is not our objective to provide an in-depth description of every nanoplasmonic integrated

optical fiber approach, and the reader is encouraged to follow the references to find more details regarding a specific system.

Optical Fibers in Analytical Chemistry

The importance of optical fibers in a variety of transducers used in analytical chemistry is outstanding, because it allows the detection of analytes in environments that are prohibitive for traditional spectroscopic probes [9]. This versatility stimulates a very significant amount of work on the application of optical fibers in sensing, as it has been well presented in the series of reviews by Wolfbeis [10–13]. In addition, there are several review papers devoted to specific aspects of optical fiber sensing, such as in vivo detection [14], fluorescence probes [15], laser induced breakdown spectroscopy (LIBS) [16], and near-infrared spectroscopy [17], just to name a few.

The actual role of the optical fiber on the measurement may vary widely from technique to technique. One of the possibilities is the use of the optical fiber as the optical delivery (or collection) system, without any other involvement in the actual measurement. This is obviously the most fundamental usage for optical fibers, but the discussion of such a broad subject is outside the objectives of the present text. In this chapter, the focus is on nanoplasmonic elements integrated inside or on the tips of optical fibers. The application of optical fiber in this manner may range from the use of single modified fibers as optrodes for the delivering and collection of the excitation, to more complexes systems of multiple fibers, each modified with different nanoplasmonic structures.

Approaches for the Use of Optical Fibers for Remote SPR and SERS Measurements

The integration of SPR sensing in optical fibers can be achieved mainly in two ways: (1) the modification of the exposed core by cladding etching; (2) the modification of one of the fiber ends with the plasmonic probe.

The first approach consists of an initial cladding etching step to expose the fiber core at an intermediate point between the excitation and collection ends of the fiber. The initial report on this kind of procedure dates back to 1988 [18, 19]. The cladding is usually etched to a small thickness, so that the exposed region is only a few micrometers away from the core. A thin Au layer, usually around 50 nm, is then deposited on the exposed surface [20], as depicted in Fig. 12.1.

The SPR sensing is obtained by the coupling of light to one end of the fiber and detection from the other end; the SPR excitation occurs due to the evanescent field from the core coupled to the surface-plasmon of the thin Au film exposed to the sample. The modified portion of the fiber is immersed in the probe solution and changes in the position of the transmission minimum are monitored during the sensing event.

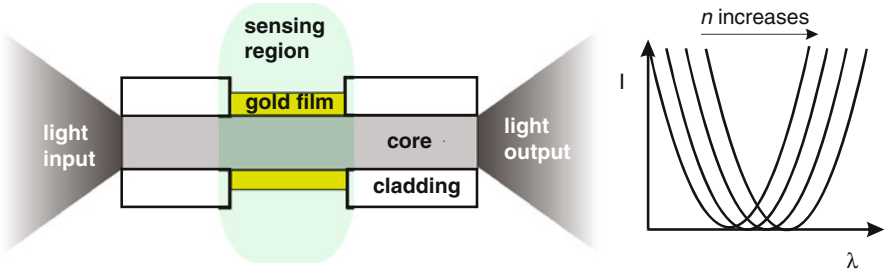

Fig. 12.1 Scheme for the etched cladding procedure for SPR device in optical fiber (the sensing region is not drawn to scale—the gold film is only about 50 nm). Surface plasmons are excited in the gold film surface by the evanescent field of the light guided through the core. The valley in the output light spectrum is due to the light absorption that excites the SPR. The position of the minimum of the curve is expected to redshift as the refractive index (n) in the sensing region increases

In this sort of procedure, the necessity of polishing or dissolution of the fiber cladding decreases the fiber mechanical resilience. Even with this drawback, this design has been extensively applied throughout the last 20 years for the construction of surface-plasmon sensors integrated with optical fibers [21–24]. The details of this device will not be discussed in any more extension in this chapter, because there are already several very interesting recent reviews on this class of SPR devices [2, 20].

The second approach for the modification of optical fiber for nanoplasmonic sensing also relies on the evanescent field of the exciting radiation for the detection, but it used the surface modification of one fiber tip by a metallic layer. The modification may be carried out on only one fiber end, and the back-reflected light is detected. This class of devices is called optrodes. The resulting modified fiber may be used as both SPR and SERS nanosensors. In addition to single, individual, "optrodes," bunches of modified optical fibers has also been realized [25]. The use of microstructured optical fiber (MOF) as carriers for SPR and SERS devices has been recently proposed theoretically [26–28], and some of them have been recently demonstrated experimentally [29–32]. Most of the remaining of this chapter will be focused on the construction strategies of LSP-based devices that use subwavelength metallic nanostructures on optical fiber surface for sensing by SPR and SERS. The optrode approach for the building of nanoplasmonic sensor also lead to the design of SPR and SERS imaging systems with remote capabilities [33], as will be discussed later in the text. Other approaches, such as the use of Bragg structures to excite SPR through cladding modes will also be presented.

Nanoplasmonic Optical Fibers Fabrication Techniques

An overview of the main fabrication methodologies that are covered in this review is presented in Fig. 12.2. Nanoplasmonic optrodes for SPR and SERS are obtained by the modification of the optical fiber tip with a metallic layer. This modification

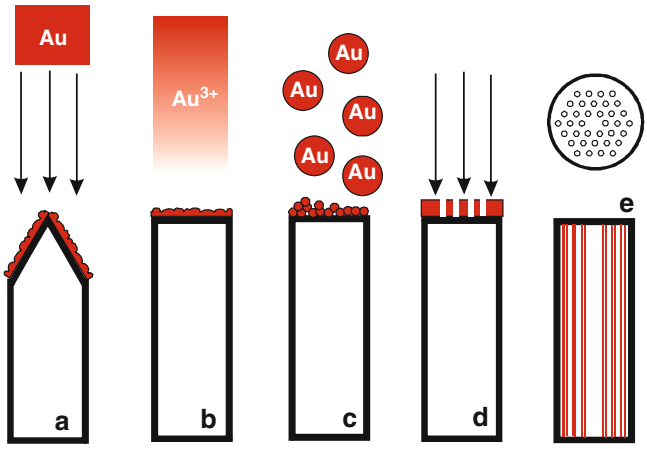

Fig. 12.2 Schematic representation of the fabrication methodologies and types of fibers and optrodes that are covered in this review. (**a**) Vacuum deposition of metals (gold in this case) directly in metallic tip. A shaped (*conical*) optical fiber tip is represented; (**b**) metal deposition by the reduction of metal ions from a solution; (**c**) deposition of pre-formed metal colloids from a suspension; (**d**) tip modification by nanolithographic methods; (**e**) MOF (*top view* and *side view*) with internal channels modified by a metal film

may be done by thin film nanoisland deposition (Fig. 12.2a, b), by immobilization of pre-formed nanoparticles (Fig. 12.2c) and by nanofabrication techniques, such as nanolithography and nanoimprinting that can result in metallic nanostructures on the fiber (Fig. 12.2d). MOFs, also known as photonic crystal fibers, have been developed lately in great scale [34, 35], and they offer a very interesting platform for the integration of a sensing system (Fig. 12.2e). The nanoplasmonic integration in this case might be accomplished by depositing a metal film directly on the walls inside the microstructures of the fiber. In the last few years, there have been growing efforts towards the integration of MOF and SPR or SERS. The efforts in this direction will be discussed in the last part of this section.

The description of the fabrication techniques methods is divided rather arbitrarily in four parts: (1) non-lithographic procedures that include the vacuum and Ar^+ sputtering deposition of metals in different fibers (Fig. 12.2a, b); (2) metallic nanoparticles deposition on optical fibers, which includes the immobilization of pre-formed nanoparticles on optical fiber tips by several methods (Fig. 12.2c); (3) lithographic methods and nanopatterning that include, among others, the focused ion-bean and electron-beam milling of metallic nanostructures on optical fiber tips (Fig. 12.2d); (4) sensors based on MOF (Fig. 12.2d), which is discussed in a separate section due to the unique characteristics of this sort of optical fibers. The separation is intended to allow the readers to select the procedures that best suits their own experimental setup availability and techniques of choice for the device fabrication.

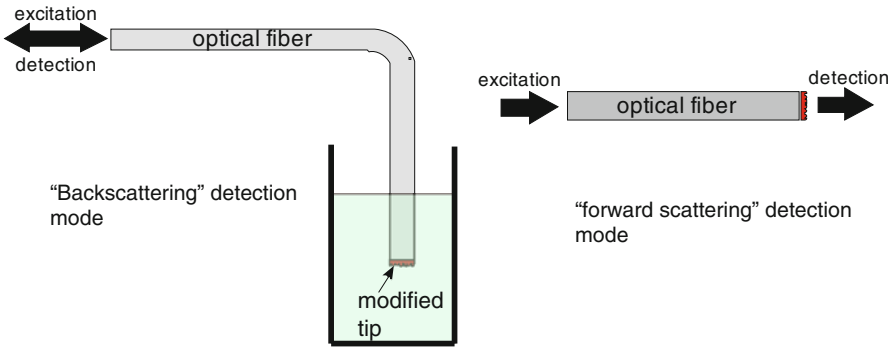

Fig. 12.3 Schematic representation of the most common detection modes for nanoplasmonics optical fibers

Nanoplasmonic Optical Fibers Fabricated Using Non-lithographic Techniques

Optical-fiber SERS substrates were developed earlier than SPR substrates. To the best of our knowledge, the first report on optical fibers used as the complete optrode, which means that the optical fiber was used as the waveguide for the exciting and scattered light for SERS detection (provided by the modification of the tip with a metallic layer), was done by Mullen and Carron [36]. A mechanically roughened 600-μm core optical fiber tip was treated with ammonium hydroxide and Ag nanoislands were deposited on the fiber tip by thermal evaporation (AgNI-OF). The SERS measurements were in a "forward scattering" configuration, as indicated in Fig. 12.3: the laser light was coupled to the distal end of the fiber, and the Raman intensity was measured from the light transmitted through the modified AgNI-OF tip. The detection of adsorbed cobalt phthalocyanine (CoPc) was demonstrated both for an analyte solution dried off on the fiber tip and for the tip immersed in an aqueous solution of CoPc. A maximum SERS intensity for a 20 nm-thick Ag film was reported. The SERS enhancement factor calculated for this substrate was 1.2×10^5. It was later shown that the AgNI-OF substrate presents a larger tolerance to laser power, without damaging the structures; [37, 38] the higher stability in performance relative to planar SERS substrates was attributed to the more evenly distributed laser power over a larger area than for macroscopic SERS substrates. Subsequently, Meriaudeau et al. [39] verified that an AgNI-OF have a sensitivity of ca. 110 nm RIU^{-1} when employed as LSPR sensor.

Modifications to the fabrication of the AgNI-OF substrates were later proposed by Viets and Hill [40]. The authors compared the usage of alumina nanoparticles and sandblasted template to create the required roughness in the optical fiber tip, followed by the thermal deposition on the metal. The SERS signal was detected in a "backscattering" mode, illustrated in Fig. 12.3, which is more suitable for remote sensing: the modified tip of the AgNI-OF was immersed in the interrogated solution, and the laser was coupled to the unmodified fiber tip end using an optical

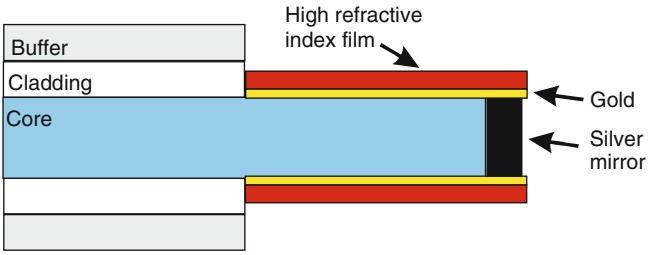

Fig. 12.4 Optical fiber tip with the cladding closed to the tip etched off, followed by deposition of a Au thin film, followed by the deposition of an Ag mirror on the fiber tip. The high-refractive index film was zirconium oxide (18 nm). Adapted from Jorgenson and Yee [44]

microscope; the Raman signal was generated in the modified end and back-scattered collected from the unmodified tip. The authors verified that the SERS enhancement factor for both procedures is equivalent; suggesting that the suitability of the different procedure should be left to the specific chemical needs. Stokes and Vo-Dinh [41] showed that the AgNI-OF built with a Ag thin-film over alumina microparticles can be used for in situ detection using SERS in backscattering configuration. They showed that the AgNI-OF obtained with this procedure can be used for SERS detection of the cresyl fast violet (CFV) dye down to a limit-of-detection (LOD) of 50 ppb.

De Maria et al. [42] polished a single-mode optical fiber at a defined angle relative to the fiber long axis and after covering one of the tips with a 480 Å of Ag thin film a total-internal reflection-based optical fiber (TF-TIR-OF) SPR sensor was obtained. Fontana et al. [43] used an Au film 50 nm thick in a 45° angled-tip to obtain a TF-TIR-OF sensor, coupled to an external detection of the light diffracted out of the fiber by the Au film.

A modification to this methodology was proposed by Jorgenson and Yee: [44] ca. 1 cm of the cladding of an optical fiber was etched off at the tip region; the etching was followed by Au thin film (ca. 55 nm) deposition on the side of the etched-tip region by electron-beam evaporation. This deposition was followed by 300 nm-thick Ag mirror deposition on the fiber tip. Figure 12.4 illustrates the resulting device. As the metals were deposited on the optical fiber tip, the remote sensing was straightforward, and it was demonstrated by the authors. The dynamic detection range of this sort of sensor was increased by the deposition of a high-refractive index material over the Au layer, namely zirconium oxide, reaching a dynamic range in the 1.000–1.375 refractive index range. The use of higher refractive index optical fiber materials can increase the high-end refractive index limit of detection. When a sapphire rod connected to the optical fiber system was used, the high-end limit refractive index was shown to go up to 1.7. Suzuki et al. [45] studied the dependence of the performance of this device on the Au-layer thickness. The results showed the maximum sensitivity of 1,557 nm RIU^{-1} reached for a 65 nm thick Au layer on a 400 μm core optical fiber.

Obando and Booksh [46] reported a merging method between the propositions of Fontana, Jorgenson, and Lee. The exposed part of the core was tapered in several forms, spanning from trapezoid to pyramidal shapes, before the deposition of the SPR active layer. The SPR was detected in a backscattering mode. This procedure allowed achieving a better control over the SPR wavelength, maintaining the usefulness of the devices in the visible range for a larger range of adsorbates. Later optimization of this sort of sensor led to improvements in the reproducibility and temporal stability of the devices [47]. The better performance were obtained by greater control over the polishing procedures and the use of Ar^+ sputtering to improve the orientation of the optical fiber during the deposition of the LSPR Au-active layer.

Several developments followed these initial works on tapered fiber tip modified for SPR sensing. Chang et al. [48] verified that a conically tapered optical fiber with a 100 nm tip may be used as a SPR sensor with low background light and small sample volume. The sensitivity of 4,000% RIU^{-1} was measured using a fixed excitation laser (650 nm), within the SP resonance, and recording relative changes in the reflected intensity. Masson et al. [49] designed an NIR excited SPR sensor based on this technology, and reported an optimization for the relative angles of tapering of the fiber tip. The best-performance devices presented a sensitivity of 2.4×10^4 nm RIU^{-1}, a ca. 10 times improvement relative to the 1.9×10^3 nm RIU^{-1} for the 90° relative angle. Kim et al. [50] proposed that the use of sapphire waveguides improve the resistance of the device to high pressure and temperatures, which could have considerable advantages in harsh environments. Scaffidi et al. [51] used a commercial pipette puller to produce a tapered optical fiber with a tip of ca. 100 nm diameter. The tapered fiber tip had a 5 nm Ag thin-layer vacuum-deposited and was used in remote sensing as a SERS-based pH-sensor. This device was proved to be able to determine the pH of cells in vivo.

Chaigneau et al. [52] deposited AgNI on tapered optical fibers and measured the transmitted light in forward scattering mode. Using this procedure the authors were able to detect both SPR and SERS from microdroplets of samples, emphasizing the small sample volume necessary for the measurement. The SPR sensitivity reported was 6.2×10^3 nm RIU^{-1}, and the SERS of tetrahydronaphtalene was obtained with high signal-to-noise ratio. This sort of tapered OF-based device has not been used in more complex LSPR sensing schemes, but their good sensitivity indicate that they should be an interesting alternative for practical remote sensing applications.

Kurihara et al. [53] used a selective chemical etching (SCE) method to produce a cone-shaped single-mode optical fiber tip. Their solution for SCE was a mixture of NH_4F (40wt.%), HF (50wt.%) and pure water in the 5:1:1 volumetric relation. The etched fiber tip was sputter-covered with 10 nm thick gold film. The resulting device was tested in a microfluidic chip as SPR sensor in a forward scattering detection scheme, and presented sensitivity to changes of 8×10^{-3} RIU after a suitable modification to avoid non-specific binding to the surface. Very strong and localized field localization on tapered optical fiber covered with Au/Ag thin-films have been suggested by Janunts et al. [54] and Ding et al. [55]. The field localization can allow for the used as both SPR and SERS device of high performance after the experimental conditions are optimized.

White and Stoddart [56] used an etching procedure on imaging optical fibers, consisting of 10,000 "single fiber" imaging elements hexagonally arranged, to obtain microwells. An example of one of these imaging fiber bundles is shown in Fig. 12.5. The etching was followed by the vacuum-deposition of 100-nm thick Ag layer. The SERS spectra of thiophenol on the resulting surface were obtained with reasonable signal-to-noise ratio. White et al. [57] further investigated the etching time dependence on the SERS enhancement factor and verified that there is actually a variation in the overall shape of the nanostructures produced by different etching times. The process was optimized to allow predictable structures, such as microrods, microtriangles, and microwells. The SERS intensity resulting from Ag thin-film deposition on those surfaces was measured. A higher SERS efficiency was observed for the microrods and microtriangles with smaller interspacing when compared to the microwells. The order of magnitude of the measured enhancement factors were in the 10^6. Guieu et al. [58] obtained SERS spatial mappings of these devices, shown in Fig. 12.5, and the mappings showed appreciable SERS intensity coming only from the sharp tips produced by the etching process. This was later confirmed by confocal Raman and scanning near-field optical microscopy (SNOM) [25].

Schevchenko and Albert [59] drew a Bragg-diffraction grating (BDG) in the fiber core of a single-mode optical fiber and covered the nearby cladding with a 20 nm Au thin film. When light is coupled through this device, part of the light is reflected back by the BDG and an interference pattern is observed in the transmitted spectra. The scheme of the device is presented in Fig. 12.6a together with the measured transmission spectra for the device immersed in a sucrose solution in Fig. 12.6b. The surface plasmon peak position may be obtained from the fitting of the intensity maxima by a suitable curve. The measured sensitivity was 454 nm RIU^{-1}, in agreement with theoretical predictions. Spackova et al. [60] varied systematically both grating lines spacing and gold layer thickness and optimized the BDG on OF device using a figure of merit that took into account the SPR line width, absorption depth and the sensitivity. The optimized values were a grating length of 2 mm and gold film 50 nm-thick.

Kitahama et al. [61] constructed a surface-enhanced resonance Raman scattering (SERRS) substrate by photo-reducing Ag nanoparticles on a sharp tip optical fiber used for SNOM. The fiber was initially modified in a 0.1 wt.% poly-L-lysine solution, followed by immersion in a 1 mM $AgNO_3$ and 1 mM sodium citrate aqueous solution; the reduction was carried out by excitation with evanescent field in the SNOM fiber tip when excited with a 532 nm laser for 1 min. The resulting AgNPs on the SNOM-fiber tip was used to detect 100 nM Rhodamine-6G in the presence of KSCN, an efficient chelating agent for the residual Ag^+ ions on the surface of the AgNPs. KSCN slowly dissolves the AgNPs; this process caused increase in the SERS spectra for the initial 20 min of immersion, followed by a fast intensity decreasing. The authors suggest that this was due to the increase in the amount of efficient SERS hot-spots by the creation of nanogaps between the AgNPs; as the dissolution of the Ag kept going, the nanogaps become too large to allow efficient coupling of the dipoles between the AgNPs, decreasing the SERRS enhancement factor.

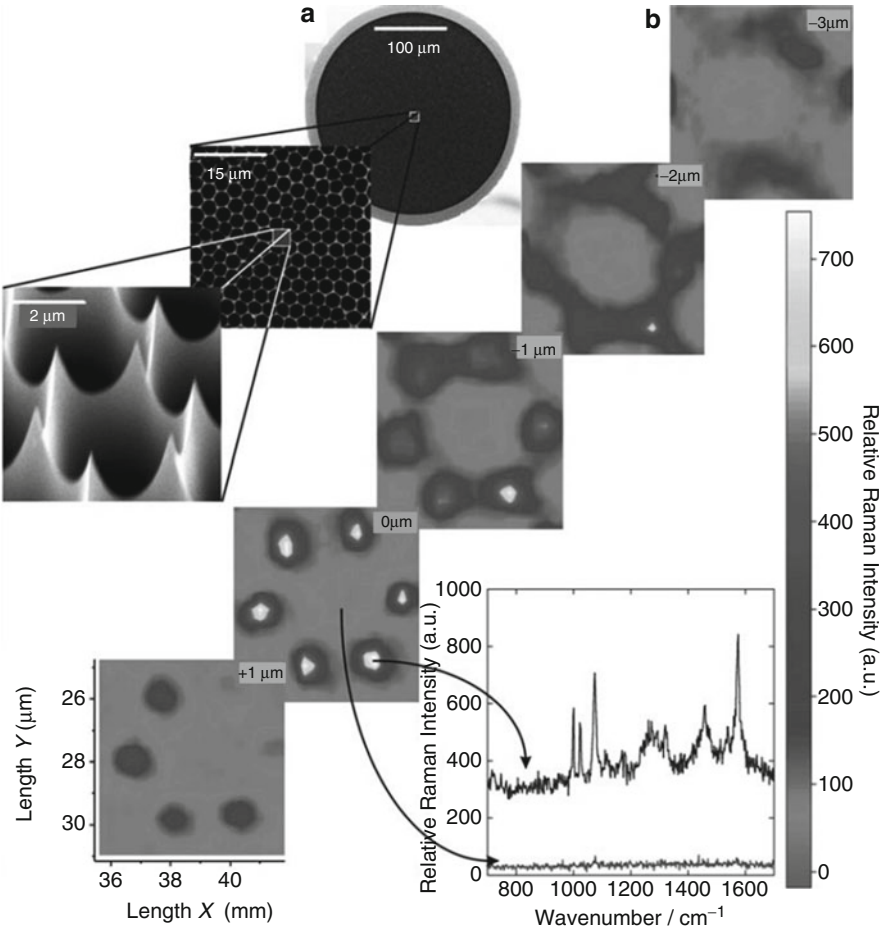

Fig. 12.5 (**a**) SEM images of an imaging fiber bundle coated with a 40-nm-thick gold film; (**b**) confocal Raman images from a fiber modified with benzenethiol. Adapted from Guieu et al. [58] © 2008 Wiley

Zheng et al. [62] photochemically modified the tip of a 6-cm long OF by producing Ag from an Ag^+-citrate solution. The silver clusters were formed by reducing the ions using the excitation of a 4.2 mW laser at 514.5 nm wavelength. The laser was coupled through the fiber core and Ag^+ ions were reduced preferably on the OF tip, resulting in highly-aggregated 35 nm Ag-NPs clusters. SERS measurements were then realized in the absence of Ag^+ ions. The authors verified that the laser tip fabricated by 4.5 min laser illumination gave the best performance for SERS. The resulting modified optical fiber tip was used to detect decreasing concentrations of R6G; the LOD for this dye was 1 nM for a 514.5 nm laser excitation. This LOD was comparable to other reports on the literature [63].

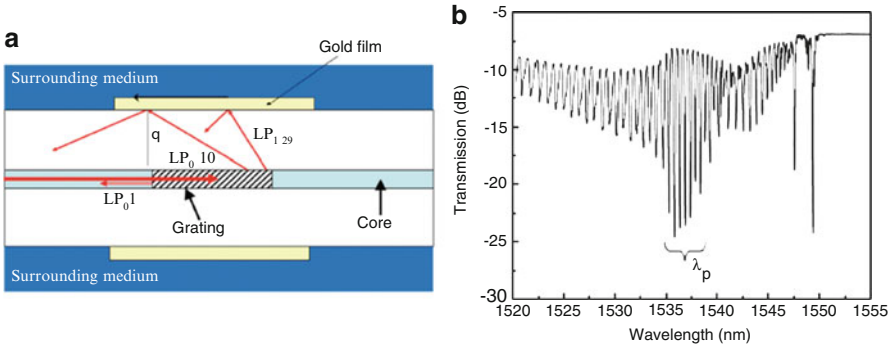

Fig. 12.6 (**a**) Scheme of the BDG-based SPR sensor. (**b**) Transmission spectra for the device immersed in a sucrose solution with $n_D = 1.4378$. The *bracket* indicates the position of the surface-plasmon excitation. Adapted from Shevchenko and Albert [59] © 2007 Optical Society of America

Table 12.1 Comparison of the optimized SPR sensitivity for the devices discussed in section "Nanoplasmonic Optical Fibers Fabricated Using Non-lithographic Techniques"

Procedure	Metal	Sensitivity (nm RIU^{-1})	References
Ag-NI-OF	Ag	110	[39]
TF-TIR-OF	Au	1,557	[45]
NIR-TF-TIR-OF	Au	2.4×10^4	[49]
OFtapered-AgNI	Ag	6.2×10^3	[52]
BDG-OF	Au	454	[59]

Lan et al. [64] laser-ablated a freshly cleaved OF tip with a femtosecond laser, resulting in a rough tip surface. The roughened tip was immersed in a $[Ag(NH_3)_4]^+$ solution and α-lactose was added as a reducing agent. AgNPs deposited on the roughened tip, with diameters ranging from 20 to 60 nm. The resulting AgNPs on laser-ablated OF (AgNP-LAOF) was used as a remote SERS sensor, with an all-through fiber excitation and detection of the Raman spectra. The SERS detection of R6G was demonstrated for concentrations as low as 10 nM in the backscattering detection scheme. The authors also verified a small influence of the OF length in the SERS performance of the AgNP-LAOF fiber, with an increase in SERS intensity of about 16% with the decrease in the fiber length from 100 to 50 cm. This small dependence was mostly attributed to the imperfect coupling of light due to mismatch between the numerical aperture of the focusing objective and the optical fiber.

In this section we provided seven different methodologies for the fabrication of SPR and SERS surfaces based on the evaporation of metal (Au or Ag) thin-films on optical fiber tips. In some of the works the authors verified the device's SPR sensors sensitivity, which allows the quantification of the sensing properties of the devices. The available data for the optimized devices are presented in Table 12.1.

The evaluation of the relative efficiency of each device as a chemical or biosensors goes necessarily through the figure-of-merit of each device, and this

should be taken as an essential data in the divulgation of any new nanoplasmonic sensing scheme. Unfortunately, the evaluation of figures-of-merit is not always observed throughout the literature. Figure of merits values are very important for researchers interested in finding applications for the OF-based nanoplasmonic devices, since it allow them to estimate which platform will suit their needs.

Metallic Nanoparticles Deposition on Optical Fibers

Polwart et al. [65] reported on the immobilization of pre-formed metallic nanoparticles on optical fibers as optrode for SERS remote sensing. The Ag-NPs were obtained by the Lee and Meisel method [66] and the authors silanized a clean distal tip of a 100 mm OF with (3-aminopropyl)trimethoxysilane and, after curing of the silane layer formation at 110°C, the tip was immersed during 16–24 h in the Ag-NPs suspension. The SERS performance of the NPs-modified OF was checked by the immersion of the distal tip in solution of two dyes: 1×10^{-7} M solution of the azo dye 4-(5′-azobenzotriazol)-3,5-dimethoxyphenylamine (ABT-DMOPA), and 1×10^{-6} M solution of crystal violet (CV). The ABT-DMOPA dye has an absorption band at 450 nm and, because the SERS was excited with the 514.5 nm line of an Ar^+ laser, the measurements were actually the coupling of SERS with the resonance Raman effect, usually referred to as SERRS. CV presents an absorption maximum at 590 nm, and the SERS is also pre-resonant with an internal electronic absorption of the dye at 514.5 nm. The resulting SERRS spectra presented Raman characteristics bands from the OF silica body, in addition to strong SERRS bands of the dyes with a reported sample-to-sample intensity reproducibility of 10%. Lucotti and Zerbi [63] used a similar modification with Ag-NPs on a hydrofluoric acid tapered OF tip that presented a final conical shape. The tapered OF tip was modified in two ways: one was very similar to Polwart et al. [65]; the second was the casting of the fiber by silver-decanoate in xylene solution, followed by annealing at 300°C, forming a film of Ag-NPs on the fiber tip. The SERRS performance of the devices ($\lambda_0 = 514.5$ nm) was tested with CV, and a LOD of 1 nM of CV was reported.

Recently, Andrade et al. [67] prepared multiplayer Ag-NPs on OF tip as an optrode for SERS. The scheme for the substrate fabrication is illustrated in Fig. 12.7a. The initial Ag-NPs layer was deposited by a procedure similar to that of Polwart et al. [65]. The subsequent Ag-NPs layers were deposited by additional dipping of the tip in the APTMS solution followed by immersion in the Ag-NPs suspension [68]. The deposition procedure results in a higher Ag-NPs coverage of the fiber tip than previously reported in the literature; the procedure was optimized, and the number of Ag NPs deposition steps that led to the highest SERS intensity was five. Typical SERS spectra from rhodamine 6G (R6G) solutions of different concentrations obtained in backscattering mode is shown in Fig. 12.7b. With the optimized substrate, it was shown that the AgNP-OFT substrate presented a 3 nM LOD for R6G for $\lambda_0 = 632.8$ nm; it has also been shown that this substrate

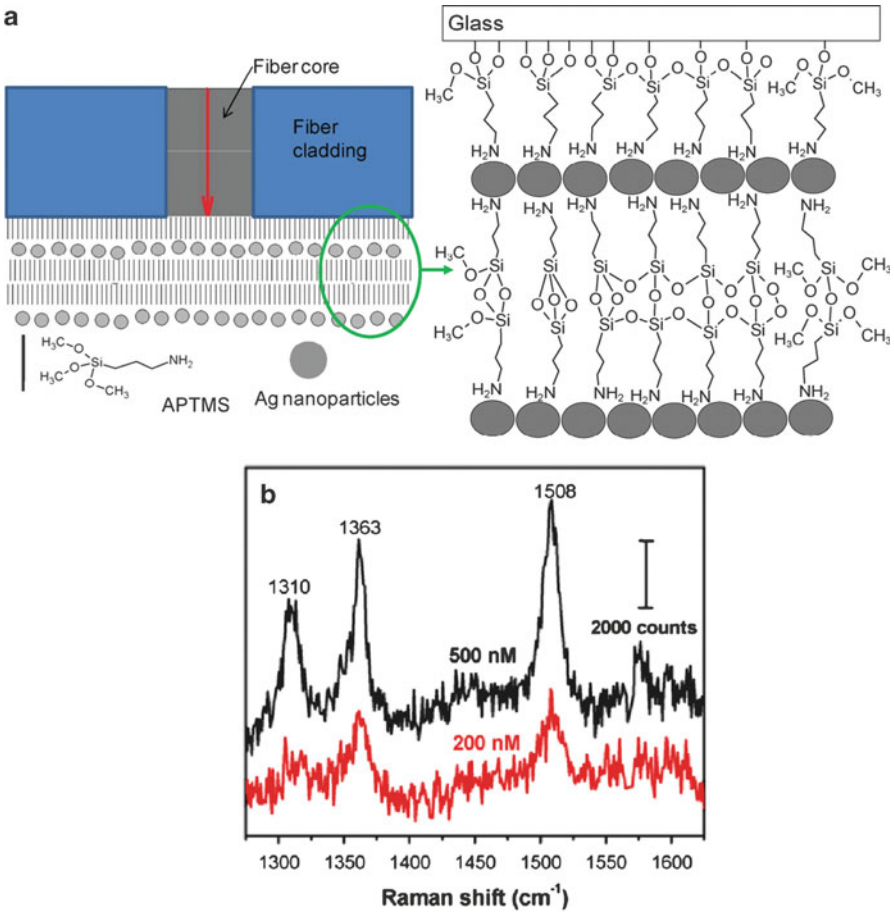

Fig. 12.7 (**a**) Schematic structure for the multilayer Ag-NP deposited on an OF-tip. *The right hand side* is a detailed structure of the bonding of the Ag-NP to the fiber glass; (**b**) representative spectra from R6G solution obtained with an optimized fiber tip. Reproduced from Andrade et al. [67] © 2010 Elsevier B.V. All rights reserved

can be used for the detection of dyes with different charges, such as Nile blue (a cation), Congo red (an anion), and the neutral 4-dicyanomethylene-2-methyl-6-(*p*(dimethylamino)styryl)-4H-pyran (DCM), all in remote sensing (backscattering) configuration.

A different approach based on silanization for the immobilization of Au-NPs on OF tips (AuNP-OFT) for nanoplasmonic-based LSPR remote sensing was reported by Mitsui et al. [69]. The authors silanized the distal tip of an OF with *N*-2-(aminoethyl)-3-aminopropyltrimethoxysilane, and immobilized chemically synthesized Au-NPs on the silanized tip. This procedure resulted in a 20% coverage of AuNPs on the fiber tip. The unmodified tip end was mounted in a multimode fiber coupler, and two detection schemes were used: (1) halogen lamp excitation to obtain the whole SPR spectrum; and

(2) red LED excitation for single-wavelength measurements. The SPR spectra were acquired from the back-coupled light ("backscattering mode" in Fig. 12.3). The reported resolution of the AuNP-OFT device was 2×10^{-5} RIU.

Volkan et al. [70] reported the modification of a tapered OF tip modified with Ag-NPs embedded in a poly(vinyl alcohol) (PVA) thin film. The tip of a 200 mm OF was tapered by a 10 W CO_2 laser-based rod extraction system. The tapered tip was immersed in a PVA-$AgNO_3$ solution for 3 s and then kept in a vacuum oven for 6 h at 60°C. The modified tip was immersed in an aqueous 4% in weight $FeSO_4 \cdot 7H_2O$ solution to reduce the Ag^+ ions in the film to obtain embedded Ag-NPs in the PVA film. Finally, the fiber was dried at 100°C for 15 min. The device was used for the detection of 1×10^{-3} M solutions of dopamine. In addition, the reproducibility of the device was tested using the probes CFV, brilliant cresyl blue, and aminopyrene, leading to a relative standard deviation of 10–17%. The PVA-AgNP devices can be stored in the unreduced form. The initial step involves the immersion for 3 s in the PVA-$AgNO_3$ bath, followed by vacuum oven drying, and a great number of sensors may be done in one single step. The two last characteristics of the PVA-AgNP device turn its production into a relatively low-cost process, which could make single-measurements affordable, avoiding cleaning procedures to reuse the device.

The modification of the unclad last 2 cm of an plastic cladding optical fiber with Au-NPs and the tip with an Ag-mirror was proposed by Lin and Lou [71] for SPR sensing in high-pressure environments. The Au-NPs were immobilized by interaction with a thiol layer resulting from the silanization of the glass surface with (3-mercaptopropyl)trimethoxysilane (MPTMS). The resulting device was used as an optrode with the excitation light reflected back to the detector by the Ag-mirror. The refractive index resolution of the probe at ambient pressure was 1.2×10^{-3} RIU, which decreased for increasing in the applied pressure, although the sensor kept a linear response to refractive index changes.

Xie et al. [72] used tip-tapered polymeric-OF (POF). The tapering was realized by partially etching off the fiber close to the OF tip by immersion in cyclohexanone. The nanoplasmonic function was obtained by the casting of Au nanorods (Au-NRs) on the polymeric surface of the OF. The Au-NRs were synthesized by a surfactant-mediated Au-NPs seed growth [73]. The Au-NRs casted on the POF tip surface were held in place by the polymer. A limitation of the Au-NR-POF is the intrinsic Raman signal from the polymeric material of the POF. SERS from a 1×10^{-9} M R6G solution could not be detected in the optrode, remote sensing configuration, in spite the fact that this level of R6G was detected with external excitation of the fiber tip, indicating successful modification of the fiber tip with the Au-NRs.

The chemical etching procedure was used in OF-bundles (OFB) and the resulting microwells were filled up with Au-NP [74]. The selective etching was done by a NH_4F/HF/HCl aqueous solution, and allowed for a fine tuning of the wells depth. The resulting microwells were sputtered with an Au thin-film, followed by the deposition of polystyrene microbeads as template for the deposition of microporous Au. The polymer microbeads were added to the OFB microwells by controlled solvent evaporation. Au were deposited on this template by electroless

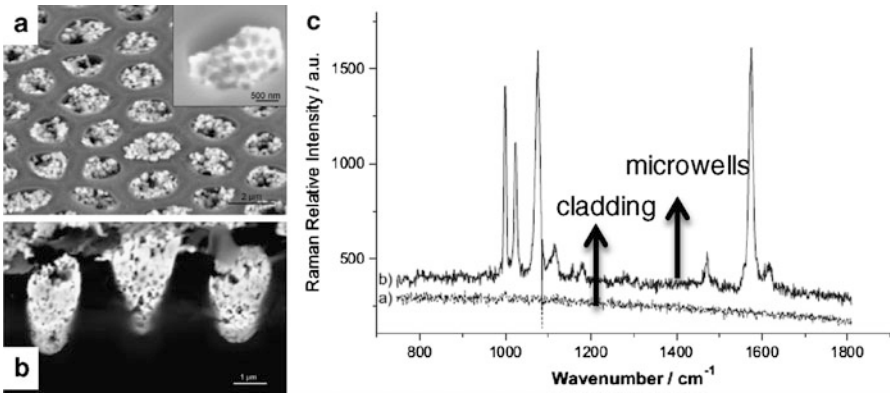

Fig. 12.8 (**a**) SEM image of the Au layer deposited on the OFB microwells after PS-microbead dissolution; the *inset* presents a high-magnification image of one microwell in the structure. (**b**) Cross-section of the OFB, showing the depth of the deposited Au-microstrucutres; (**c**) SERS spectra of benzethiol on the substrates on the cladding and on one of the microwells. Adapted from Zamuner et al. [74] © 2009 WILEY-VCH Verlag GmbH & Co. KGaA, Weinheim

deposition from a $Na_3Au(SO_3)_2$/formaldehyde solution. The SEM image of the resulting macroporous Au-layer on the OFB is presented in Fig. 12.8a, b.

The authors reported the SERS spectra from benzenethiol (Fig. 12.8c) directly on the microwells-containing tip, with a SERS enhancement factor of 4×10^4. There is no mention of the use of this device in a remote sensing (backscattering) configuration to obtain the spectra. If realizable, the remote sensing configuration could allow the use of the Au-microporous-OFB substrate as an imaging device for SERS studies. This is a very promising direction to be followed for this sort of substrate, as soon as the issues related to the adhesion of the Au-nanostructures to the OFB are worked out.

It is interesting to notice that the fabrication methods reviewed in this section are mostly directed to the use of the modified fibers as SERS substrate, due to intrinsic nanostructure-dependence of the enhanced-Raman effect [7]. The LSPR that these structures support would also be of great interest as biosensors, because they present several unique characteristics that make their application in sensing very interesting, such as narrow plasmon-resonance absorption bands, easy coupling to microfluidics devices, among others [3]. It is expected that some of these fabricated structures will be tested for LSPR in a near future.

Nanoplasmonic Optical Fibers Fabricated Using Nanolithographic Techniques

The use of lithographic techniques is a latest development of OF-based nanoplasmonic. This is due in great part to the widespread availability of advanced

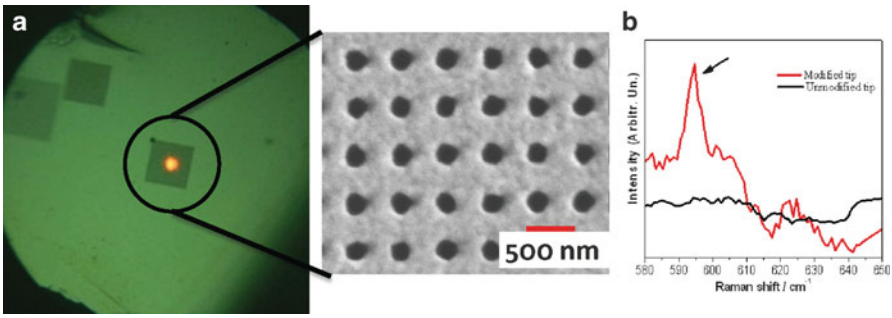

Fig. 12.9 (**a**) optical micrograph of an optical fiber tip coated with 100 nm layer of a Au film and patterned with an array of nanoholes. The *bright dot* is the laser excitation, introduced from the opposite end of the fiber, exiting the core. A SEM of the nanoholes is also shown; (**b**) NERS spectrum from a dye (oxazine 720) adsorbed on the array-modified tip obtained using the backscattering configuration. A spectrum from a blank fiber is also shown for comparison

lithography in a number of research centers in recent years. Initially, Chen et al. [75] proposed a chessboard-like Au structure with nanogaps in the 6–15 nm range, lithographically drawn on distal OF tips as a high-performance substrate for the excitation of LSPR. Based on finite-difference time-domain (FDTD) calculations, the authors predicted a maximum SERS-EF on the order of 1×10^{10} for an optimized structure with a 2 nm gap between the micro-squares. The field localization of the structure is predicted to be strongly dependent on the nanometric gap between the micro-squares, and also on the polarization of the incident light.

Dhawan et al. [76–79] showed in a series of articles the fabrication of Au nanoholes (NH)arrays on an optical fiber tip by focused ion-beam (FIB) milling of a previously deposited 100–250 nm-thick gold layer. The dielectric constant sensing was based on the extraordinary optical-transmission from the Au nanoholes arrays that has been used in the last few years as high-performance biosensing platforms [80]. In this series of papers, it was demonstrated a sensitivity of 533 nm RIU^{-1} to bulk dielectric constants change, in a transmission mode of operation.

Andrade et al. [81] verified that a NH array on OF-tip can be used as nanoholes-enhanced Raman scattering (NERS) [82] substrate, as illustrated in Fig. 12.9. The NH array was fabricated by FIB on a 200-nm thick Au layer deposited on the OF-tip. The periodicity of the array and NH diameter used were those previously optimized in planar NERS substrates for the excitation with the 632.8 nm laser line [82]. Enhanced signal from oxazine 720 dye adsorbed on the arrays were obtained in both forward and back scattering configurations. It was also verified that this sort of substrate may be used as a plasmonic biosensor for the detection of the protein streptavidin, in a well-established proof-of-concept experiment [83], in which the 4-step modification was successfully monitored by the forward transmitted white light through the array of nanoholes as depicted in Fig. 12.9a.

Smythe et al. [84] used a decal-transfer technique to build an array of 100-nm Au-nanostructures obtained with electron-beam lithography on an OF-tip. The Au-

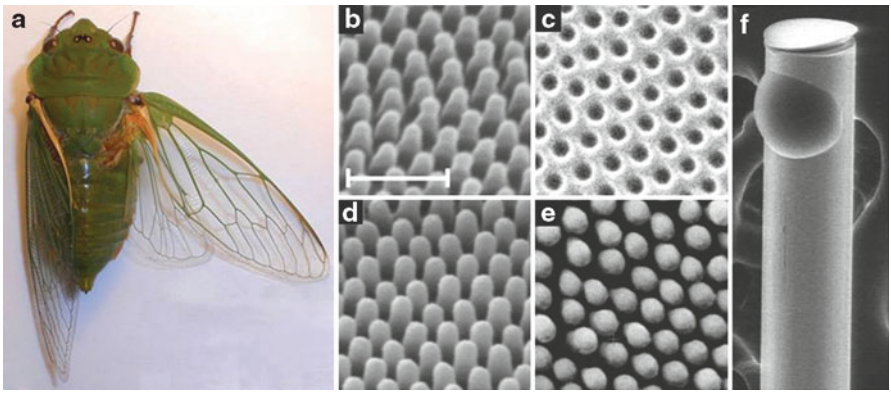

Fig. 12.10 (**a**) A photograph of the *Cyclochila australasiae* and SEM images of (**b**) the wing nanotemplate (**c**) the inverse h-PDMS mold (**d**) the polymer replica on an optical fiber end face (**e**) the silver coated replica and (**f**) a macroscopic view of the imprinted optical fiber. Scale bar is 500 nm. Reproduced from Kostovski et al. [85]

NS were transferred from a Si support to a poly(thiol-ene) film with a mechanical support of poly(dimethylsiloxane) (PDMS), which was then pressed against the OFT, transferring the pattern to the tip. The resulting device was employed as a SERS optrode, and it was shown to be able to detect deposited layers of benzenethiol and 4-[(E)-2-pyridin-4-ylethenyl]pyridine after the subtraction of the OF-silica background. The authors report a SERS enhancement-factor of five orders of magnitude in the optrode configuration.

Kostovski et al. [85] used a nanoimprint lithography technique in the development of SERS-active substrates on OF-tips. The dense 2D array of natural nanorods from the "*Cyclochila australasiae*" wings (Fig. 12.10a) was used as a nanotemplate for the Ag-nanopillars deposition on an OF-tip, resulting in nanostructures shown in Fig. 12.10e.

The resulting Ag-nanopillar on OFT was used as a SERS optrode, with a deposition-and-dry of thiophenol as the molecular probe, showing a high-performance enhancement. In addition, a 100 μM R6G solution was measured, resulting in a SERS spectrum with high signal-to-noise ratio, but with a very strong interference from the normal Raman of the silica background. For future applications, the silica background could be subtracted with relative ease, in a procedure similar to that proposed by Viets and Hill [40].

Nanoplasmonic Structures in Microstructured Optical Fibers

The creation of MOFs is one of the greatest developments in the photonics research field. MOF are optical fibers that present a set of holes running throughout the fiber.

As a consequence, the light-guiding mechanism for these fibers is different than the conventional ones. The photonic band gap created by the regular arrangement of the holes needs to be taken into account, in addition to the modified total-internal reflection, when considering the guiding [35]. The possibility of utilizing the interior of the air-holes that run along the fiber holes for chemical sensing open up very interesting opportunities. Among the advantages of this platform are the ultralow sample volume required, and the possibility of integrated optofluidic microflow-system. The integration of nanoplasmonic materials inside the holes of MOFs is a very recent field, and, as we hope to demonstrate in this section, there are still a lot of open opportunities and challenges for its full realization.

To the best of our knowledge, the first report of nanoplasmonic devices in solid-core MOF was the one by Amezcua-Correa et al. [86]. The authors used the precursor Ag(hfac)(1,5-COD) (hfac = 1,1,1,5,5,5-hexafluoroacetylacetonato, COD = cyclo-octadiene) as the Ag^+ source, and pumped the precursor through a MOF using a HPLC pump operating at 17 MPa. The precursor was then heat-decomposed on the internal walls of the MOF. The result was Ag-NPs deposited on the MOF internal walls, with the nanoparticle filling of the holes dependent on the reaction time. A monolayer of benzenthiol was the SERS probe for this Ag-NP-MOF device. The SERS spectra were obtained by focusing the laser on the silica-core of the MOF, and collecting in back-scattering. SERS intensity was obtained both from the cladding and from the core of the MOF, and the SERS enhancement factor for benzethiol was estimated to be 10^4. The initial work was followed by a comparative study of different core-size MOFs [30], in which the authors shows that the choice of small-core MOF improve the SERS intensity by one order of magnitude when the Ag-NPs have a average diameter of 40-nm.

Yan et al. [31] modified the inner-part of 4-holes MOF with pre-formed Au-NP by dipping-and-drying a suspension of nanoparticles inside the fiber. The Au-NPs entered the first 2 cm of the fiber immersed in the suspension by capillarity, leaving a partially filled MOF after the drying step, as the scheme in Fig. 12.11b shows. A solution of RhB was inserted by capillarity into the MOF holes, and the solution was dried naturally off the holes. SERS spectra were obtained in the optrode configuration (Fig. 12.11a); after the background from the MOF silica core was subtracted, the SERS spectrum indicated a similar profile to the spectrum from a silicon wafer drop-coated with the Au-NP covered with the probing dye (Fig. 12.11c).

Oo et al. [87] reported a forward scattering scheme for an Ag-NP filled solid-core MOF as SERS substrates. Negatively charged Ag-NPs were immobilized inside the holes through a polycation layer electrostatically bound to the fiber internal walls. The authors report that the transmitted light loss increased by ca. 6 times with the immobilization of the Ag-NP; most of the loss has been attributed to the strong scattering of the evanescent field by the nanoparticles. The transmitted intensity decay increased from 3 dB/30 cm to 20 dB/30 cm. In spite of this loss, the metallic modification still allowed for an appreciable transmitted intensity. After Ag-NP immobilization, a 30 cm modified MOF was filled with an aqueous 1 μM R6G solution and the SERS spectrum presented the characteristic bands of the dye, with

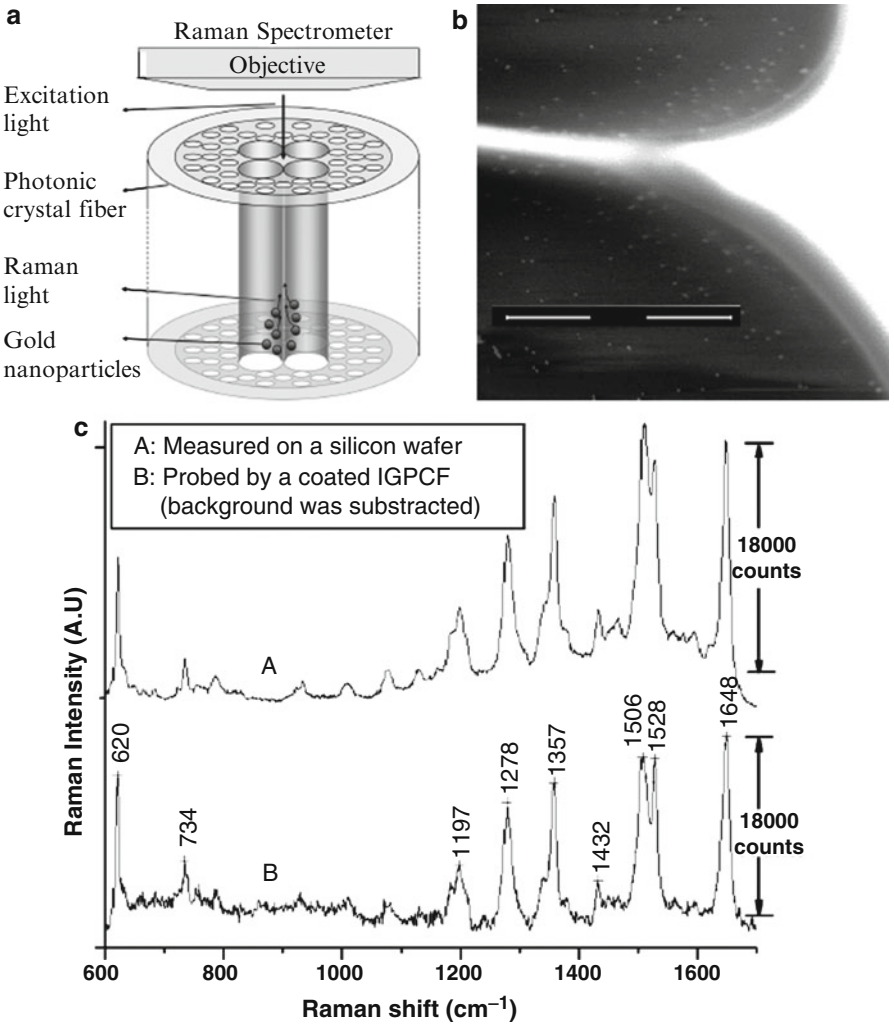

Fig. 12.11 (**a**) Scheme of the excitation and collection for the SERS on the partially Au-NP filled MOF; (**b**) SEM image of the cross-section of the Au-NP modified fiber; (**c**) A—SERS of RhB on Au-NP modified sicion wafer and B—background-subtracted SERS of RhB in the optrode configuration shown in (**a**). Adapted from Yan et al. [31] © 2008 OSA

considerably high signal-to-noise ratio [88], although the authors didn't report any attempt to estimate the SERS-enhancement factor. Similarly, de Matos et al. [89] immobilized pre-formed gold and silver nanoparticles inside a hollow core MOF. A NaOH solution was inserted into the fiber by applying a moderated pressure, ~0.4 MPa, with a syringe, to deprotonate the glass walls. Then an aqueous 10^{-5} wt.% poly-(L)-lysine (PL) solution was injected. The PL polycation interacts with the negatively charged glass surface forming a strongly bounded overlayer. The excess

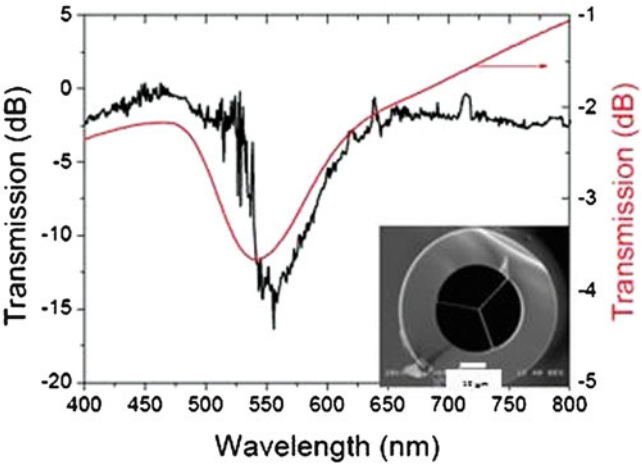

Fig. 12.12 Transmission spectra of an Au nanoparticle suspension (*red*) and for Au nanoparticles immobilized in the internal walls of the MOF (*black*). A SEM picture of the MOF is shown in the *inset*

PL was washed out by water injection cycles and then the nanoparticle suspension was inserted into the fiber. The nanoparticles are negatively charged and readily attach to the PL layer. Figure 12.12 shows an example of a successful functionalized fiber. The SPR peak shown in Fig. 12.12 shifted when solutions of different refractive indexes were inserted into the fiber, although no surface binding results were reported. Preliminary SERS measurements were also realized in backscattering configuration. A 1 μM R6G solution was inserted into the fiber, and the fiber was subsequently washed with water; the SERS spectrum in backscattering configuration showed high S/N ratio, and the amount of dye that actually acted as SERS scatterers has yet to be determined.

Most of the initial reports on the nanoplasmonic properties of metallic nanoparticles immobilized on MOF were on the SERS properties of the devices. Results from modeling of metallic-NP filled microholes of MOF indicated the possibility of creating devices for SPR sensing as well [27, 28, 90, 91]. The main identified challenges that need to be overcome by the experimentalists were the necessity of phase matching and flow-optimizations, but the feasibility of the devices were reinforced by several numerical calculations [92, 93]. Yu et al. [94] also suggested that the selective modification of some of the microholes in a hollow core MOF with nanoplasmonic structures can result in a better phase matching between the guided and the plasmonic modes.

The implementation of a reliable SPR sensor, capable of detection surface binding event, such as antibody–antigen interactions, based on metallic nanoparticles immobilization on MOF looks like the next challenge to this very exciting field. The development of this sort of device will necessarily take advantage of the great deal of knowledge on the controlled synthesis and modification of

metallic nanoparticles developed in the last years. The development of such devices may lead the detection schemes SPR to new levels of miniaturization and applicability in trace detection, because the MOF may be as long as necessary to the detection, which makes the availability of path length very flexible.

Applications in Remote Sensing

These first decade of the effervescent efforts in the direction of SPR and SERS sensing by the modification of OF-tips have been mostly focused on different strategies for the development of the devices. This is different from the unclad OF, which had a great deal of application-directed development in the last years, as have been pointed out in recent reviews [2, 95]. But one can notice an increase in the chemical application directed also in the metallic-modified OF-tip devices.

Attempts of application of OF-based SERS sensors beyond the device development were made by Crane et al. [96]. In that paper, the authors deposited a 40 nm-thick Ag film on a roughened optical fiber tip, and modified it with 4-(2-pyridylazo) resorcinol disulfide. The SERRS spectra with $\lambda_0 = 514.5$ nm of the modifier was used for the detection of Pb^{2+}, Cu^{2+} and Cd^{2+}, when the intensity-ratio of two SERS bands at 1,005 and 1,023 cm^{-1} was plotted against the concentration of the cations. The device was tested for the detection of mM concentrations Pb^{2+} in a flow system and the possibility of quantitative detection of the cation was claimed by the authors.

Many OF-tip modified SERS sensors have been used for the detection of low-concentration of dyes. These include the detection of CFV down to 560 ppb by Stokes and Vo-Dinh [41], the detection of R6G with a LOD in the 10–100 nM range [61, 64], and 1,4-bis[2-(4-pyridyl)-ethenyl]-benzene with a LOD of 1 nM with photochemically deposited Ag-NP on the OF-tip by Zheng et al. [62]. Andrade et al. [67] reported the possibility of detection of dyes with different charges such as the cation R6G, the anion CV, and the neutral dye DCM.

Stokes et al. [97] reported the possibility of using Ag-islands modified tip-tapered OF to detect CFV in an essay in which the SERS signal was detected only when the fiber touched the sample. This detection scheme evolved to the work of Scaffidi et al. [51], which reported the monitoring of intracellular pH using a SERS probe immobilized on the tip-tapered OF device in HMEC-15/hTERT immortalized human mammary epithelial cells and PC-3 human prostate cancer cell lines. This preliminary result indicates an interesting future for OF-based SERS sensors for the probing of the internal cellular environment. It seems that efforts in the direction of improving specificity and analyte-range of the nanoplasmonic—optical fiber devices can be a very productive line of investigation for future works.

The application of LSPR sensing nanoplasmonic devices to chemical or biosensing is just starting to acquire momentum in the literature. Kim et al. [98] have shown that the use of a selectively tapered OF tip, with one sensing layer of Au, and a mirror can be used for the direct remote detection of organic vapors. The detection scheme was all-through-fiber excitation and detection, without the

necessity of surface modifications of the nanoplasmonic surface to match the refractive index of the silica core. The authors also demonstrate the possibility of quantitative detection of ammonia vapor in concentrations in the range 0.08–2.00% in mass.

Mitsui et al. [69] reported the use of an Au-NP modified optical fiber in the biotin-avidin affinity essay, and demonstrated that real-time measurements are feasible. Kunz et al. [99] deposited a 50 nm-thick layer of Ag on the side of an OF close to the tip, followed by a Cr-mirror deposition on the tip, to improve reflection, in a procedure similar to that of Jorgensen and Yee [44]. The Ag surface was protected against oxidation by the modifications with dithio-bis-succinimidyl-propionate, which also modifies the surface for the binding of proteins. The protected Ag surface was exposed to the human heart-type fatty acid binding protein (H-FABP), an early heart infarction marker. The signaling was made by an anti-H-FABP antibody, in a competitive assay in flow-system. A SPR-based calibration curve was constructed and the detection limit for H-FABP in competitive essays was 200 ng mg^{-1}, which is enough to detect the marker in an acute infarction.

Lin and Lou [71] demonstrated the LSPR-sensing capabilities of a device with an Ag-mirror OF-tip with the side close to the tip modified with Ag-NP as a function of applied pressures. The authors show that the device is still functional for the detection of Ni^{2+}, the biotin-avidin affinity essay and the immobilization of IgG in pressure as high as 20 MPa. The RIU resolution decreases for increasing pressures, but it is still linear with the refractive index changes.

Final Remarks

As it can be noticed in the preceding pages, there have been impressive scientific efforts in the development on the integration of nanoplasmonic devices with OF. The efforts resulted in high-performance SERS devices that can be used as dyes sensors for concentrations down to the nM range, and LSPR sensor with competitive performance in the field to the available commercial planar platforms. In addition, there has been effort from several groups in the modification of MOFs with nanoplasmonic structures, which can transform the optical fiber devices in both the sensing layer and a flow system for these plasmonic-based sensing schemes. These efforts show that the field is moving strongly and fast, and new discoveries are found in the literature in a rate that increased in the last years.

Examples of their applicability in real chemical and biochemical problems are still limited, in spite of the great efforts in the device development. We hope to have shown in the few examples presented in this chapter that several of these devices already have the necessary requirements in terms of robustness and generality for applications in complex sensing schemes. There is no doubt that the OF-based devices still need to be improved, this is clearer for the MOF-based nanoplasmonic approach. It is then essential that the groups dedicated to the development of these

integrated systems have feedback from examples of applications, so improvements in fabrication and analytical figure of merits can be better guided by the requirements of potential end users.

Acknowledgment This work was supported by operating grants from NSERC and by the NSERC Strategic Network for Bioplasmonic Systems (BiopSys), Canada. G.F.S.A. thanks Canadian Bureau for International Education—Department of Foreign Affairs and International Trade (CBIE-DFAIT) of Canada for a post-doctoral fellowship.

References

1. Homola J, Yee SS, Gauglitz G. Surface plasmon resonance sensors: review. Sens Actuators B Chem. 1999;54(1–2):3–15.
2. Homola J. Surface plasmon resonance sensors for detection of chemical and biological species. Chem Rev. 2008;108(2):462–93.
3. Stewart ME, Anderton CR, Thompson LB, Maria J, Gray SK, Rogers JA, Nuzzo RG. Nanostructured plasmonic sensors. Chem Rev. 2008;108(2):494–521.
4. Kretschmann E, Raether H. Radiative decay of non radiative surface plasmon excited by light. Z. NATURFORSCH. PT. A. 1968;A23(12):2135.
5. Jung LS, Nelson KE, Stayton PS, Campbell CT. Binding and dissociation kinetics of wild-type and mutant streptavidins on mixed biotin-containing alkylthiolate monolayers. Langmuir. 2000;16(24):9421–32.
6. Campbell CT, Kim G. SPR microscopy and its applications to high-throughput analyses of biomolecular binding events and their kinetics. Biomaterials. 2007;28(15):2380–92.
7. Moskovits M. Surface-enhanced Raman spectroscopy: a brief retrospective. J Raman Spectrosc. 2005;36(6–7):485–96.
8. Kelly K, Coronado E, Zhao L, Schatz G. The optical properties of metal nanoparticles: the influence of size, shape, and dielectric environment. J Phys Chem B. 2003;107(3):668–77.
9. Lee B. Review of the present status of optical fiber sensors. Opt Fiber Technol. 2003;9 (2):57–79.
10. Wolfbeis OS. Fiber optic chemical sensors and biosensors. Anal Chem. 2000;72(12):81r–9.
11. Wolfbeis OS. Fiber-optic chemical sensors and biosensors. Anal Chem. 2002;74(12):2663–77.
12. Wolfbeis OS. Fiber-optic chemical sensors and biosensors. Anal Chem. 2004;76(12):3269–83.
13. Wolfbeis OS. Fiber-optic chemical sensors and biosensors. Anal Chem. 2006;78(12):3859–73.
14. Vo-Dinh T. Nanosensing at the single cell level. Spectrochim Acta B At Spectrosc. 2008;63 (2):95–103.
15. Wolfbeis OS. Materials for fluorescence-based optical chemical sensors. J Mater Chem. 2005;15(27–28):2657–69.
16. Lee WB, Wu JY, Lee YI, Sneddon J. Recent applications of laser-induced breakdown spectrometry: a review of material approaches. Appl Spectrosc Rev. 2004;39(1):27–97.
17. Benito MTJ, Ojeda CB, Rojas FS. Process analytical chemistry: applications of near infrared spectrometry in environmental and food analysis: an overview. Appl Spectrosc Rev. 2008;43 (5):452–84.
18. Markatos S, Zervas MN, Giles IP. Optical fiber surface-plasmon wave devices. Electron Lett. 1988;24(5):287–8.
19. Johnstone W, Stewart G, Hart T, Culshaw B. Surface-plasmon polaritons in thin metal-films and their role in fiber optic polarizing devices. J Lightwave Technol. 1990;8(4):538–44.
20. Sharma AK, Jha R, Gupta BD. Fiber-optic sensors based on surface plasmon resonance: a comprehensive review. IEEE Sens J. 2007;7(7–8):1118–29.

21. Jorgenson RC, Yee SS. A fiberoptic chemical sensor-based on surface-plasmon resonance. Sens Actuators B Chem. 1993;12(3):213–20.
22. Homola J, Slavik R, Ctyroky J. Interaction between fiber modes and surface plasmon waves: spectral properties. Opt Lett. 1997;22(18):1403–5.
23. Ko WS, Oh SB, Kim SH. Development of fiber type surface plasmon resonance sensor for protein detection. In Culshaw B, Marcus MA, Dakin JP, Crossley SD, Knee HE, editors. Industrial and highway sensors technology, Proceedings of SPIE, USA. Vol. 5272; 2003. pp. 100–9.
24. Themistos C, Rahman BMA, Rajarajan M, Kalli K, Grattan KTV. Characterization of surface-plasmon modes in metal-clad optical waveguides. Appl Opt. 2006;45(33):8523–30.
25. Guieu V, Talaga D, Servant L, Sojic N, Lagugne-Labarthet F. Multitip-localized enhanced Raman scattering from a nanostructured optical fiber array. J Phys Chem C. 2009;113 (3):874–81.
26. Hassani A, Skorobogatiy M. Design of the microstructured optical fiber-based surface plasmon resonance sensors with enhanced microfluidics. Opt Express. 2006;14(24):11616–21.
27. Hassani A, Gauvreau B, Fehri MF, Kabashin A, Skorobogatiy M. Photonic crystal fiber and waveguide-based surface plasmon resonance sensors for application in the visible and near-IR. Electromagnetics. 2008;28(3):16.
28. Hassani A, Skorobogatiy M. Design criteria for microstructured-optical-fiber-based surface-plasmon-resonance sensors. J Opt Soc Am B Opt Phys. 2007;24(6):1423–9.
29. Cox FM, Argyros A, Large MCJ, Kalluri S. Surface enhanced Raman scattering in a hollow core microstructured optical fiber. Opt Express. 2007;15(21):13675–81.
30. Peacock AC, Amezcua-Correa A, Yang JX, Sazio PJA, Howdle SM. Highly efficient surface enhanced Raman scattering using microstructured optical fibers with enhanced plasmonic interactions. Appl Phys Lett. 2008;92(14):141113.
31. Yan H, Liu J, Yang CX, Jin GF, Gu C, Hou L. Novel index-guided photonic crystal fiber surface-enhanced Raman scattering probe. Opt Express. 2008;16(11):8300–5.
32. Wang A, Docherty A, Kuhlmey BT, Cox FM, Large MCJ. Side-hole fiber sensor based on surface plasmon resonance. Opt Lett. 2009;34(24):3890–2.
33. Lv Q, Huang DX, Yuan XH, Hou R. Fiber optic surface plasmon resonance sensors for imaging systems. Opt Eng. 2007;46(5):054403.
34. Knight JC. Photonic crystal fibres. Nature. 2003;424(6950):847–51.
35. Zolla F, Renversez G, Nicolet A, Kuhlmey B, Guenneau S, Felbacq D. Foundations of photonic crystal fibres. London: Imperial College Press; 2005. p. 326.
36. Mullen KI, Carron KT. Surface-enhanced Raman-spectroscopy with abrasively modified fiber optic probes. Anal Chem. 1991;63(19):2196–9.
37. Viets C, Hill W. Laser power effects in SERS spectroscopy at thin metal films. J Phys Chem B. 2001;105(27):6330–6.
38. Viets C, Hill W. Fibre-optic SERS sensors with conically etched tips. J Mol Struct. 2001;563:163–6.
39. Meriaudeau F, Wig A, Passian A, Downey T, Buncick M, Ferrell TL. Gold island fiber optic sensor for refractive index sensing. Sens Actuators B Chem. 2000;69(1–2):51–7.
40. Viets C, Hill W. Comparison of fibre-optic SERS sensors with differently prepared tips. Sens Actuators B Chem. 1998;51:92–9.
41. Stokes DL, Vo-Dinh T. Development of an integrated single-fiber SERS sensor. Sens Actuators B Chem. 2000;69(1–2):28–36.
42. Demaria L, Martinelli M, Vegetti G. Fiberoptic sensor-based on surface-plasmon interrogation. Sens Actuators B Chem. 1993;12(3):221–3.
43. Fontana E, Dulman HD, Doggett DE, Pantell RH. Surface plasmon resonance on a single mode optical fiber. IEEE Trans Instrum Meas. 1998;47(1):168–73.
44. Jorgenson RC, Yee SS. Control of the dynamic-range and sensitivity of a surface-plasmon resonance based fiber optic sensor. Sens Actuators A Phys. 1994;43(1–3):44–8.

45. Suzuki H, Sugimoto M, Matsui Y, Kondoh J. Effects of gold film thickness on spectrum profile and sensitivity of a multimode-optical-fiber SPR sensor. Sens Actuators B Chem. 2008;132 (1):26–33.
46. Obando LL, Booksh KS. Tuning dynamic range and sensitivity of white-light, multimode, fiber-optic surface plasmon resonance sensors. Anal Chem. 1999;71(22):5116–22.
47. Obando LA, Gentleman DJ, Holloway JR, Booksh KS. Manufacture of robust surface plasmon resonance fiber optic based dip-probes. Sens Actuators B Chem. 2004;100(3):439–49.
48. Chang YJ, Chen YC, Kuo HL, Wei PK. Nanofiber optic sensor based on the excitation of surface plasmon wave near fiber tip. J Biomed Opt. 2006;11(1):014032.
49. Masson JF, Kim YC, Obando LA, Peng W, Booksh KS. Fiber-optic surface plasmon resonance sensors in the near-infrared spectral region. Appl Spectrosc. 2006;60(11):1241–6.
50. Kim YC, Masson JF, Booksh KS. Single-crystal sapphire-fiber optic sensors based on surface plasmon resonance spectroscopy for in situ monitoring. Talanta. 2005;67(5):908–17.
51. Scaffidi JP, Gregas MK, Seewaldt V, Vo-Dinh T. SERS-based plasmonic nanobiosensing in single living cells. Anal Bioanal Chem. 2009;393(4):1135–41.
52. Chaigneau M, Balaa K, Minea T, Louarn G. Plasmon resonance microsensor for droplet analysis. Opt Lett. 2007;32(16):2435–7.
53. Kurihara K, Ohkawa H, Iwasaki Y, Niwa O, Tobita T, Suzuki K. Fiber-optic conical microsensors for surface plasmon resonance using chemically etched single-mode fiber. Anal Chim Acta. 2004;523(2):165–70.
54. Janunts NA, Baghdasaryan KS, Nerkararyan KV, Hecht B. Excitation and superfocusing of surface plasmon polaritons on a silver-coated optical fiber tip. Opt Commun. 2005;253 (1–3):118–24.
55. Ding W, Andrews SR, Maier SA. Internal excitation and superfocusing of surface plasmon polaritons on a silver-coated optical fiber tip. Phys Rev A. 2007;75(6):063822.
56. White DJ, Stoddart PR. Nanostructured optical fiber with surface-enhanced Raman scattering functionality. Opt Lett. 2005;30(6):598–600.
57. White DJ, Mazzolini AP, Stoddart PR. Fabrication of a range of SERS substrates on nanostructured multicore optical fibres. J Raman Spectrosc. 2007;38(4):377–82.
58. Guieu V, Lagugne-Labarthet F, Servant L, Talaga D, Sojic N. Ultrasharp optical-fiber nanoprobe array for Raman local-enhancement imaging. Small. 2008;4(1):96–9.
59. Shevchenko YY, Albert J. Plasmon resonances in gold-coated tilted fiber Bragg gratings. Opt Lett. 2007;32(3):211–3.
60. Spackova B, Piliarik M, Kvasnicka P, Themistos C, Rajarajan M, Homola J. Novel concept of multi-channel fiber optic surface plasmon resonance sensor. Sens Actuators B Chem. 2009;139:199–203.
61. Kitahama Y, Itoh T, Aoyama J, Nishikata K, Ozaki Y. SERRS fiber probe: fabrication of silver nanoparticles at the aperture of an optical fiber used for SNOM. Chem Commun. 2009;43:6563–5.
62. Zheng XL, Guo DW, Shao YL, Jia SJ, Xu SP, Zhao B, Xu WQ, Corredor C, Lombardi JR. Photochemical modification of an optical fiber tip with a silver nanoparticle film: a SERS chemical sensor. Langmuir. 2008;24(8):4394–8.
63. Lucotti A, Zerbi G. Fiber-optic SERS sensor with optimized geometry. Sens Actuators B Chem. 2007;121(2):356–64.
64. Lan XW, Han YK, Wei T, Zhang YN, Jiang L, Tsai HL, Xiao H. Surface-enhanced Raman-scattering fiber probe fabricated by femtosecond laser. Opt Lett. 2009;34(15):2285–7.
65. Polwart E, Keir RL, Davidson CM, Smith WE, Sadler DA. Novel SERS-active optical fibers prepared by the immobilization of silver colloidal particles. Appl Spectrosc. 2000;54 (4):522–7.
66. Lee PC, Meisel D. Adsorption and surface-enhanced Raman of dyes on silver and gold sols. J Phys Chem. 1982;86(17):3391–5.
67. Andrade GFS, Fan M, Brolo AG. Multilayer silver nanoparticles-modified optical fiber tip for high performance SERS remote sensing. Biosens Bioelectron. 2010;25:2270–5.

68. Fan M, Brolo AG. Silver nanoparticles self assembly as SERS substrates with near single molecule detection limit. Phys Chem Chem Phys. 2009;11:7381–9.
69. Mitsui K, Handa Y, Kajikawa K. Optical fiber affinity biosensor based on localized surface plasmon resonance. Appl Phys Lett. 2004;85(18):4231–3.
70. Volkan M, Stokes DL, Tuan VD. Surface-enhanced Raman of dopamine and neurotransmitters using sol–gel substrates and polymer-coated fiber-optic probes. Appl Spectrosc. 2000;54 (12):1842–8.
71. Lin TJ, Lou CT. Reflection-based localized surface plasmon resonance fiber-optic probe for chemical and biochemical sensing at high-pressure conditions. J Supercrit Fluids. 2007;41 (2):317–25.
72. Xie ZG, Tao J, Lu YH, Lin KQ, Yan J, Wang P, Ming H. Polymer optical fiber SERS sensor with gold nanorods. Opt Commun. 2009;282(3):439–42.
73. Nikoobakht B, El-Sayed MA. Preparation and growth mechanism of gold nanorods (NRs) using seed-mediated growth method. Chem Mater. 2003;15(10):1957–62.
74. Zamuner M, Talaga D, Deiss F, Guieu V, Kuhn A, Ugo P, Sojic N. Fabrication of a macroporous microwell array for surface-enhanced Raman scattering. Adv Funct Mater. 2009;19(19):3129–35.
75. Chen SQ, Han L, Schulzgen A, Li HB, Li L, Moloney JV, Peyghambarian N. Local electric field enhancement and polarization effects in a surface-enhanced Raman scattering fiber sensor with chessboard nanostructure. Opt Express. 2008;16(17):13016–23.
76. Dhawan A, Gerhold MD, Muth JF. Plasmonic structures based on subwavelength apertures for chemical and biological sensing applications. IEEE Sens J. 2008;8(5–6):942–50.
77. Dhawan A, Muth JF. Engineering surface plasmon based fiber-optic sensors. Mater Sci Eng B. 2008;149(3):237–41.
78. Dhawan A, Muth JF, Leonard DN, Gerhold MD, Gleeson J, Vo-Dinh T, Russell PE. Focused in beam fabrication of metallic nanostructures on end faces of optical fibers for chemical sensing applications. J Vac Sci Technol B. 2008;26:2168–73.
79. Dhawan A, Gerhold M, Madison A, Fowlkes J, Russell PE, Vo-Dinh T, Leonard DN. Fabrication of nanodot plasmonic waveguide structures using FIB milling and electron beam-induced deposition. Scanning. 2009;31(4):139–46.
80. Gordon R, Sinton D, Kavanagh KL, Brolo AG. A new generation of sensors based on extraordinary optical transmission. Acc Chem Res. 2008;41(8):1049–57.
81. Andrade GFS, Hayashi JG, Rahman MM, Cordeiro CMB, Brolo AG. Au nanohole arrays on optical fiber tips as SPR and SERS chemical and bio-sensors; 2012. Submitted for publication.
82. Brolo AG, Arctander E, Gordon R, Leathem B, Kavanagh KL. Nanohole-enhanced Raman scattering. Nano Lett. 2004;4(10):2015–8.
83. Grabarek Z, Gergely J. Zero-length crosslinking procedure with the use of active esters. Anal Biochem. 1990;185(1):131–5.
84. Smythe EJ, Dickey MD, Bao JM, Whitesides GM, Capasso F. Optical antenna arrays on a fiber facet for in situ surface-enhanced Raman scattering detection. Nano Lett. 2009;9(3):1132–8.
85. Kostovski G, White DJ, Mitchell A, Austin MW, Stoddart PR. Nanoimprinted optical fibres: biotemplated nanostructures for SERS sensing. Biosens Bioelectron. 2009;24:1531–5.
86. Amezcua-Correa A, Yang J, Finlayson CE, Peacock AC, Hayes JR, Sazio PJA, Baumberg JJ, Howdle SM. Surface-enhanced Raman scattering using microstructured optical fiber substrates. Adv Funct Mater. 2007;17(13):2024–30.
87. Oo MKK, Han Y, Martini R, Sukhishvili S, Du H. Forward-propagating surface-enhanced Raman scattering and intensity distribution in photonic crystal fiber with immobilized Ag nanoparticles. Opt Lett. 2009;34(7):968–70.
88. Oo MKK, Han Y, Kanka J, Sukhishvili S, Du H. Structure fits the purpose: photonic crystal fibers for evanescent-field surface-enhanced Raman spectroscopy. Opt Lett. 2010;35 (4):466–8.
89. de Matos CJ, Cordeiro CMB, Andrade GFS, Brolo AG, Brito-Silva AM, Temperini MLA, Galembeck A, de Araújo CB. Creating and fixing a metal nanoparticle layer on the holes of

microstructured fibers for plasmonic applications. In CLEO/QLES conference on photonic applications of systems technologies, San Jose, CA, USA; 2008.
90. Florous NJ, Saitoh K, Koshiba M. Numerical modeling of cryogenic temperature sensors based on plasmonic oscillations in metallic nanoparticles embedded into photonic crystal fibers. IEEE Photonics Technol Lett. 2007;19(5–8):324–6.
91. Hautakorpi M, Mattinen M, Ludvigsen H. Surface-plasmon-resonance sensor based on three-hole microstructured optical fiber. Opt Express. 2008;16(12):8427–32.
92. Hassani A, Skorobogatiy M. Photonic crystal fiber-based plasmonic sensors for the detection of biolayer thickness. J Opt Soc Am B Opt Phys. 2009;26(8):1550–7.
93. Kejalakshmy N, Rahman BMA, Agrawal A, Tanvir HM, Grattan KTV. Metal-coated defect-core photonic crystal fiber for THz propagation. J Lightwave Technol. 2009;27(11):1631–7.
94. Yu X, Zhang Y, Pan SS, Shum P, Yan M, Leviatan Y, Li CM. A selectively coated photonic crystal fiber based surface plasmon resonance sensor. J Opt A Pure Appl Opt. 2010;12 (1):015005.
95. Orellana G, Haigh D. New trends in fiber-optic chemical and biological sensors. Curr Anal Chem. 2008;4(4):273–95.
96. Crane LG, Wang DX, Sears LM, Heyns B, Carron K. SERS surfaces modified with a 4-(2-pyridylazo)resorcinol disulfide derivative—detection of copper, lead, and cadmium. Anal Chem. 1995;67(2):360–4.
97. Stokes DL, Chi ZH, Vo-Dinh T. Surface-enhanced-Raman-scattering-inducing nanoprobe for spectrochemical analysis. Appl Spectrosc. 2004;58(3):292–8.
98. Kim YC, Banerji S, Masson JF, Peng W, Booksh KS. Fiber-optic surface plasmon resonance for vapor phase analyses. Analyst. 2005;130(6):838–43.
99. Kunz U, Katerkamp A, Reinhard R, Spener F, Cammann K. Sensing fatty acid binding protein with planar and fiber-optical surface plasmon resonance spectroscopy devices. Sens Actuators B Chem. 1996;32(2):149–55.

Chapter 13
Figures of Merit for Refractometric LSPR Biosensing

Marinus A. Otte and Borja Sepulveda

Abstract The aim of this chapter is to describe routes to improve the features of plasmonic nanoparticles as refractometric based biosensors. Taking advantage of the tunability of their localized surface plasmon resonance (LSPR), we explore the sensing performance as a function of the LSPR spectral position. Firstly, we show the ambiguities that can arise from the description of the sensitivity in the wavelength and energy scales. However, we will see how such ambiguities can be circumvented with the introduction of the figure of merit (FOM), defined as the quotient between sensitivity and width of the resonance peaks, since this parameter is equivalent in both energy and wavelength scales. The spectral analysis reveals that the sensitivity to local changes of refractive index close to the metal surface can be comparable or even larger than that of conventional SPR sensors when the resonance position of the nanoparticles is properly selected. Indeed, for a fixed nanoparticle volume, we show that the surface sensitivity only depends on the spectral position of the resonance, whereas the shape of the particle only plays a secondary role. In addition, the FOM displays an optimized spectral region, located between 700 and 900 nm in the case of gold, which coincides with the region where the quotient between real and imaginary parts of the dielectric constant of the metal is maximized.

Finally, we study the influence of the supporting substrate and adhesion layers, required to improve the mechanical stability of the nanoparticles, on their

M.A. Otte
NanoBiosensors and Bioanalytical Applications Group, Research Center on Nanoscience and Nanotechnology (CIN2: CSIC-ICN), ETSE. Campus UAB -Edificio Q 3rd floor, 08193 Bellaterra, Barcelona, Spain

B. Sepulveda (✉)
NanoBiosensors and Bioanalytical Applications Group, Research Center on Nanoscience and Nanotechnology (CIN2: CSIC-ICN), ETSE. Campus UAB -Edificio Q 3rd floor, 08193 Bellaterra, Barcelona, Spain

CSIC-ICN, ETSE. Campus UAB -Edificio Q 3rd floor, 08193 Bellaterra, Barcelona, Spain
e-mail: borja.sepulveda@cin2.es

A. Dmitriev (ed.), *Nanoplasmonic Sensors*, Integrated Analytical Systems,
DOI 10.1007/978-1-4614-3933-2_13,

refractometric FOMs. Just the presence of the substrate can induce a sensitivity reduction larger than 40%, especially in substrates with high refractive index. On the other hand, the adhesion layer can drastically downgrade the sensing performance of plasmonic nanoparticles due to the large decrease of their scattering or extinction cross-sections and the substantial broadening of their LSPR peaks. In the particular case of Cr adhesion layers, the FOM can show a fourfold decrease, while the scattering cross-section can be reduced close to one order of magnitude, adding drastic constraints to the limit of detection and performance of nanoplasmonic sensors. Therefore, minimization of the substrate refractive index and the thickness of the adhesion layers are prerequisites to ensure excellent limits of detection in refractometric nanoplasmonic sensors.

Introduction

Nanoplasmonic biosensors [1–3] can be classified according to the optical phenomena employed for the detection of the bioanalytical interactions in elastic or inelastic plasmonic sensors. Inelastic sensors include fluorescence or Raman detection schemes, making use of interesting phenomena such as fluorescence quenching, surface enhanced fluorescence, or SERS. However, these sensors typically require tagging the bioreceptors or target analytes with Raman or fluorescence labels. In contrast, sensors based on elastic optical processes can allow the label-free detection of the analytes, being typically based on two different sensing principles [2]: near-field interaction sensing or refractometric sensing. The first group employs the well-known drastic color change of colloidal metal nanoparticles upon aggregation. Generally, in the simplest case of two metal nanoparticles, the resonance peak redshifts as the particles get closer when the polarization is parallel to the dimer axis. This color change is induced by the near field coupling between particles. Thus, if two sets of metal nanoparticles are functionalized with complementary biomolecules, the biochemical interaction between them will trigger the aggregation of the nanoparticles, which can be easily detected through the color change of the aggregate. However, biofunctionalization of colloidal particles is a complex process due to the delicate balance between attractive Van der Waals forces and repulsive electrostatic forces in the nanoparticles. Changes in the ionic strength, pH or temperature of the buffer can lead to precipitation of the colloids. In addition, the biofunctionalization process can screen or modify the charge distribution at the nanoparticles surface, breaking the colloidal equilibrium. To avoid these difficulties biosensing with attached or fabricated nanostructures at solid surfaces can be an alternative. These assays are usually based on the dependence of the localized surface plasmon resonance (LSPR) on the refractive index of the surrounding medium. Although generally less sensitive than the aggregation assays, refractometric sensing offers several advantages, as the possibility of miniaturization and multiplexing, reaching the single nanostructure limit, or the compatibility with microfluidics and in-flow assays. The range of functionalization chemistries available is broader and can

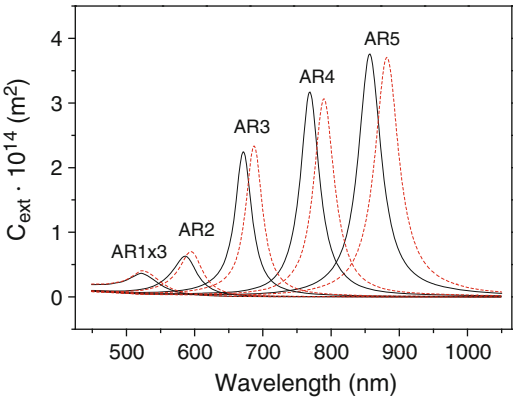

Fig. 13.1 Illustration of the spectral changes when the aspect ratio (AR) of prolate ellipsoidal nanoparticles is varied and the refractive index of the external medium is increased (*red-dashed lines*). The volume of the nanoparticles is kept constant at 1.6×10^4 nm^3

take advantage from the knowledge acquired in conventional surface plasmon resonance (SPR) sensors based on thin metal films.

Likewise conventional SPR sensors, the LSPR of metal nanoparticles is very sensitive to small changes of the refractive index close to the metal surface. Such dependence can be easily recognized by considering the metal nanoparticle as a resonant induced dipole. For simplicity, we assume an ellipsoidal nanoparticle, whose components of the polarizability tensor in the quasi-static regime can be analytically described by [4]:

$$\alpha_i = 4\pi abc \frac{\varepsilon_m - \varepsilon_d}{3L_i(\varepsilon_m - \varepsilon_d) + 3\varepsilon_d} \tag{13.1}$$

where a, b and c are the semi-axis of the ellipsoids, ε_m and ε_d are the dielectric constants of the metal and the external dielectric medium, respectively, and L_i is the shape depolarization factor, which is given by:

$$L_i = \frac{abc}{2} \int_0^\infty \frac{dq}{(s_i^2 + q)\sqrt{(q + a^2) + (q + b^2) + (q + c^2)}} \tag{13.2}$$

The LSPR of the nanoparticle is excited when the following condition is satisfied:

$$\mathrm{Re}[\varepsilon_m] = -\frac{1 - L_i}{L_i}\varepsilon_d \tag{13.3}$$

At first glance (13.3) shows that the resonance position is controlled by the shape of the nanoparticle and the external dielectric constant. For a fixed volume, elongation of the particle in one dimension causes a redshift of the resonance in that direction (see Fig. 13.1) and a blueshift in the perpendicular one, which confers metal nanoparticles an extremely high spectral tunability. In addition, the spectral position of the resonance is highly dependent on the external dielectric constant, which constitutes the basis of refractometric plasmonic sensing. Therefore,

refractometric sensors rely on the redshift (blueshift) of the resonance peak when the refractive index around the nanoparticle increases (decreases), as Fig. 13.1 displays. Thus, local changes of refractive index induced by interacting biomolecules at the surface of the nanostructures can be monitored via the spectral shifts in the scattering or extinction cross-sections of the nanoparticles.

In order to extract the most favorable and sensitive configuration for the refractometric detection of the biosensing interactions, we analyze the sensing performance of nanoparticles with different shapes, i.e., different LSPR spectral positions. In addition, we will study the effect of the surface and the commonly used adhesion layers, required to enhance the mechanical stability of the nanostructures, particularly important for in-flow assays in microfluidic channels, thus improving the robustness of the sensing platforms.

Sensitivity and Figures of Merit, Wavelength vs. Energy Scales

To quantify and compare the performance of LSPR based sensors, the most commonly employed parameter has been the sensitivity to changes of bulk refractive index, or bulk sensitivity, defined as the variation of the resonance position (P_{LSPR}) as the refractive index of the dielectric (n_{d}) changes:

$$\eta_{\mathrm{bulk}} = \frac{\delta P_{\mathrm{LSPR}}}{\delta n_{\mathrm{d}}} \tag{13.4}$$

So far, the majority of the sensitivity analyses have employed the wavelength scale, monitoring the wavelength shifts of the LSPR, i.e., $P_{\mathrm{LSPR}} = \lambda_{\mathrm{LSPR}}$. Such studies have debated and experimentally shown that the sensitivity of plasmonic nanostructures to bulk changes of refractive index increases as the resonance position is tuned to longer wavelengths. Interestingly, reference [5] has analytically demonstrated that the sensitivity η_{bulk} is proportional to the real part of the dielectric constant of the metal and, consequently, η_{bulk} is approximately proportional to the LSPR wavelength position [5]. These evidences have encouraged the development of metal nanostructures with long resonance wavelengths such us nanorods [6], bipyramids [7], nanorings [8], or core-shell [9] nanoparticles. Indeed, this behavior can be readily visualized in the case of prolate ellipsoidal Au nanoparticles presented in Fig. 13.1, where the peak redshift is evidently larger in nanoparticles with high aspect ratios and therefore longer LSPR wavelengths.

However, the sensitivity increase is accompanied with a substantial broadening of the resonance peaks when the resonance wavelength increases, thus reducing the resolution and ability to discriminate small wavelength shifts. Such behavior can be observed in Fig. 13.2a, where we compare the sensitivity and full-width-half-maximum (FWHM) of ellipsoidal prolate nanoparticles of different aspect ratio, but keeping a constant volume of 1.6×10^4 nm^3. On the other hand, if we compare the sensitivity and peak widths in wavelength ($P_{\mathrm{LSPR}} = \lambda_{\mathrm{LSPR}}$) and energy scales

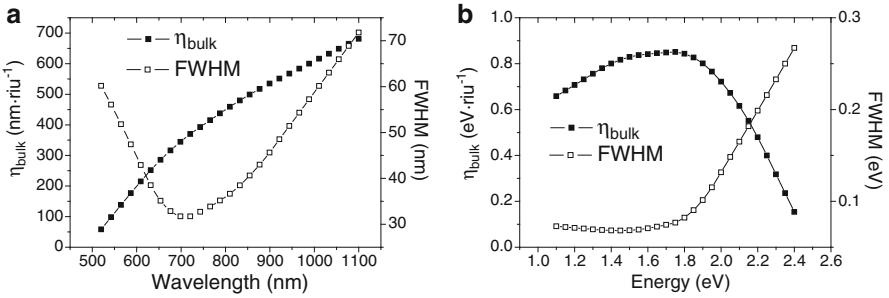

Fig. 13.2 Comparison of the bulk sensitivity and FWHM in the quasi-static (QS) regime in (**a**) wavelength and (**b**) energy scales

($P_{LSPR} = E_{LSPR}$), controversy may arise (see Fig. 13.2b). For example, in the wavelength domain, the LSPR bulk sensitivity monotonically increases as λ_{SPR} augments, whereas in the energy representation a switch of the overall trend is found at $E_{LSPR} \approx 1.75$ eV. When considering the peak widths, computed as the FWHM of the resonance peaks, the observed tendencies are even more controversial. In this case, Au nanoellipsoids show an abrupt FWHM increase of the resonance peaks in the energy domain at a threshold value of $E_{LSPR} \approx 1.8$ eV, whereas for smaller energies the peak width is more or less constant; this shows very little resemblance when compared to the FWHM tendency in wavelength scale, clearly displaying a minimum in the peak widths at $\lambda_{SPR} = 700$ nm.

Such controversies, together with the necessity of correlating sensitivity and resolution, motivate the introduction of the figure of merit (FOM), which is defined as the sensitivity (bulk or surface) divided by the FWHM:

$$\mathrm{FOM} = \frac{\eta}{\mathrm{FWHM}} \tag{13.5}$$

As we will demonstrate, the FOM is equivalent in energy and wavelength scales. If we consider a typical resonance peak with Lorentzian shape, as the one schematized in Fig. 13.3, the following relation between the FOM in energy and wavelength domains can be established:

$$\begin{aligned}\mathrm{FOM}(\lambda) &= \frac{\partial \lambda_R/\partial n}{\Delta\lambda} = -\frac{(1/E_R^2)(\partial E_R/\partial n)}{(1/E_2)-(1/E_1)} = \frac{E_2E_1}{E_R^2}\frac{\partial E_R/\partial n}{E_2-E_1} \\ &= \frac{E_2E_1}{E_R^2}\mathrm{FOM}(E)\end{aligned} \tag{13.6}$$

According to Fig. 13.3, the factor accompanying the FOM(E) in (13.6) can be rewritten as:

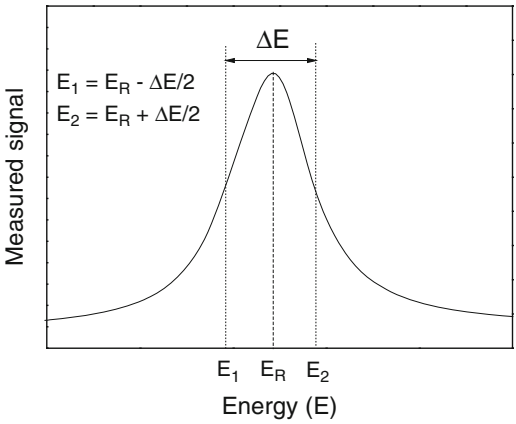

Fig. 13.3 Schematic resonant peak to show the equivalence of the FOM in energy and wavelength scales

$$\frac{E_2 E_1}{E_R^2} = \frac{(E_R + \Delta E/2)(E_R - \Delta E/2)}{E_R^2} = 1 - \left(\frac{\Delta E}{2E_R}\right)^2 \tag{13.7}$$

As a consequence, the FOM in wavelength and energy domains are equivalent if the following condition is satisfied:

$$\mathrm{FOM}(\lambda) = \mathrm{FOM}(E) \Leftrightarrow \Delta E \ll 2E_R \tag{13.8}$$

As can be observed in Fig. 13.2, E_{LSPR} is at least one order of magnitude larger than the corresponding FWHM, therefore ensuring the validity of (13.8) in the whole spectral range, even close to Au interband transitions, where the absorption substantially increases.

Figure 13.4 numerically demonstrates the equivalence of the FOM in energy and wavelength scales. It is worth noticing that the ratio between sensitivity and resolution ability displays a maximum in the spectral region comprised between 700 and 900 nm (i.e., 1.37–1.77 eV), which indicates that tuning the LSPR indefinitely towards the infrared does not give additional improvements in the refractometric sensing performance, as it has been experimentally observed [10, 11]. Besides, more accurate calculation methods, such as the modified long wavelength approximation (MLWA) or the finite different time domain (FDTD), that account for the finite size effects of the nanoparticles, give rise to very similar tendency in the FOM at this volume range of nanoparticles (see Fig. 13.4b). For larger particle volume, the difference between MLWA or FDTD and the dipolar approximation becomes more evident. The divergence is due to the dipolar underestimation of the peak widths caused by dephasing effects related to the finite size of the particles. Such increase of the peak widths is logically accompanied with a decrease in the refractometric FOM, although similar spectral trends can be observed, with an

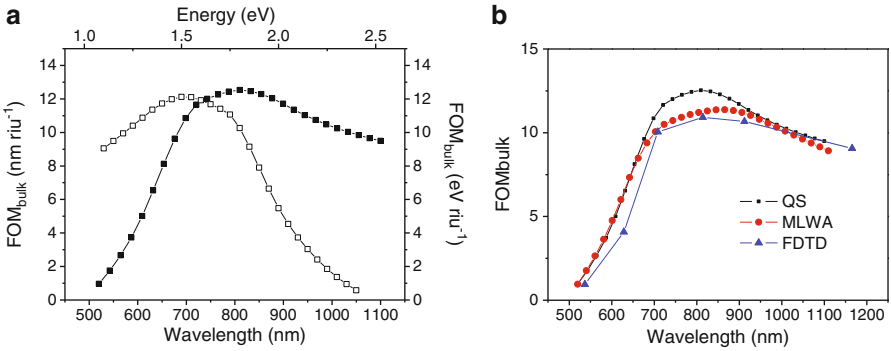

Fig. 13.4 (**a**) Comparison of the bulk FOM and FWHM in energy and wavelength scales. (**b**) Comparison of the bulk FOM for the quasi-static (QS), MLWA, and FDTD calculation methods assuming a constant volume of the nanoparticles of 1.6×10^4 nm^3

optimal sensing region between 700 and 900 nm. In the next section we will discuss the origin of such optimal sensing region.

Surface Sensitivity and Figure of Merit

When comparing the bulk sensitivity of conventional SPR sensors based on thin metal films and that of plasmonic nanostructures, a remarkable observation can be extracted. While nanoplasmonic sensors can hardly exhibit bulk sensitivities exceeding 800 nm RIU^{-1}, thin metal films can easily achieve sensitivities over 10,000 nm RIU^{-1} [10, 12, 13]. One could then obviously consider plasmonic nanostructures as very poor refractometric sensors and have doubts about their interest for biosensing applications. However, it is exactly this application what conferees relevance to plasmonic nanostructures. Typical biosensing applications rely on the highly specific biochemical recognition of a target analyte by a previously immobilized receptor at the transducer surface. The size of the most commonly used receptors and analytes, such as those related to genomic or proteomic applications (DNA or proteins), is in the range of a few nanometers. Therefore, the complete biodetection process takes place at distances of a few nanometers from the metal surface. This feature together with the very different electromagnetic field distribution associated to the SPR in thin films and nanostructures constitutes the key of the importance of plasmonic nanostructures for biosensing applications.

A simple way to probe the electromagnetic field distribution close to the metal surface in plasmonic structures consists of computing the wavelength shifts of the SPR as a function of the thickness of a surrounding dielectric coating. Since the sensitivity to the changes of refractive index is highly dependent on the spectral

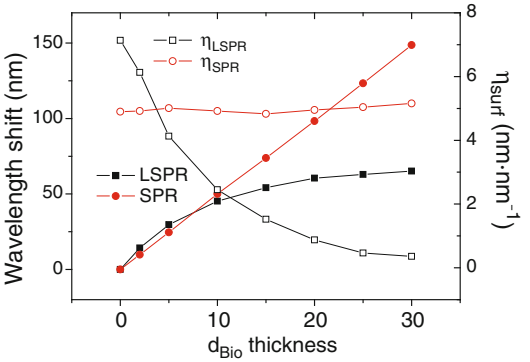

Fig. 13.5 (*Left axis*) Wavelength shifts due to the adsorption of a dielectric layer d_{Bio} as a function of the layer thickness, for a gold prolate ellipsoid ($a = 40$ nm, $b = c = 10$ nm) and a gold film 50 nm thick. (*Right axis*) Corresponding surface sensitivities in both plasmonic systems

position of the resonance (Fig. 13.2), we compare the wavelength shifts for a prolate ellipsoid and a gold film whose resonance wavelengths coincide when the external dielectric medium is water ($n = 1.33$), and we assume that the refractive index of the coating is 1.5, close to that of biomolecules. In the case of metal films, the resonance is tuned by varying the light incidence angle, and the wavelength shifts due to the uniform dielectric coating are computed via transfer matrix method formalism for planar multilayers [14]. On the other hand, in the case of ellipsoidal nanoparticles it is possible to obtain a very useful analytical formula to describe the polarizability and retrieve the spectral shifts of the LSPR induced by a uniform dielectric shell surrounding the particle, which is expressed by [4]:

$$\alpha_i \cong v \frac{(\varepsilon_{\text{Bio}} - \varepsilon_{\text{e}})(\varepsilon_{\text{Bio}} + (\varepsilon_{\text{M}} - \varepsilon_{\text{Bio}})(L_{1i} - fL_{2i})) + f\varepsilon_{\text{Bio}}(\varepsilon_{\text{M}} - \varepsilon_{\text{Bio}})}{(\varepsilon_{\text{Bio}} + (\varepsilon_{\text{M}} - \varepsilon_{\text{Bio}})(L_{1i} - fL_{2i}))(\varepsilon_{\text{e}} + (\varepsilon_{\text{Bio}} - \varepsilon_{\text{e}})L_{2i}) + fL_{2i}\varepsilon_{\text{Bio}}(\varepsilon_{\text{M}} - \varepsilon_{\text{Bio}})} \tag{13.9}$$

where

$$v = \frac{a_2 b_2 c_2}{3} \tag{13.10}$$

and

$$f = \frac{a_1 b_1 c_1}{a_2 b_2 c_2} \tag{13.11}$$

being a_2, b_2, c_2 and a_1, b_1, c_1 the semi-axes of the ellipsoids with and without the dielectric shell, respectively; L_{2i} and L_{1i} the depolarization factors in the i direction with and without the dielectric coating, and ε_{Bio} the dielectric constant of the coating. It is straightforward to demonstrate that (13.9) tends to (13.1) when $\varepsilon_{\text{bio}} = \varepsilon_{\text{e}}$.

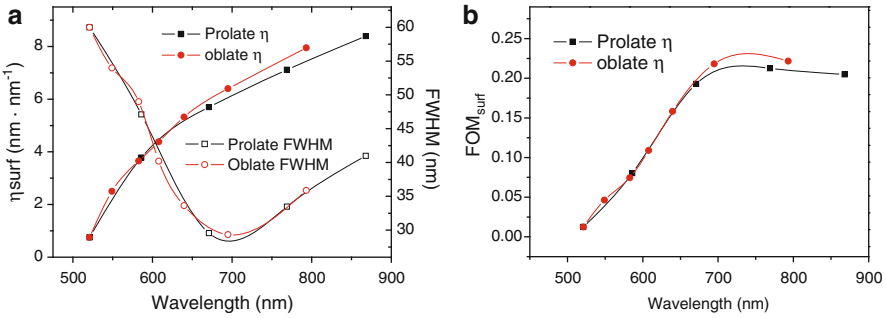

Fig. 13.6 (**a**) Surface sensitivity and FWHM of oblate and prolate ellipsoids with identical volume, but different aspect ratios. (**b**) Corresponding surface FOMs

As can be seen in Fig. 13.5, the wavelength shift of the nanoparticle resonance is larger than that of the film close to the metal surface. In contrast, the resonance shift of the nanoparticle rapidly decreases when the thickness of the dielectric coating d_{Bio} is larger than 20 nm, whereas the shift of the metal film shows a roughly linear dependence on d_{Bio}. Such behavior clearly evidences the strong confinement of the electromagnetic field in metal nanostructures. In contrast, the electromagnetic field decay of the surface plasmon in metal films can be in the order of hundreds of nanometers. The different field distribution explains both the much larger bulk sensitivity obtained in metal films and the similar or even larger sensitivity to local changes of refractive index close to the metal surface found in metal nanoparticles [10, 13]. As a result, in order to compare the biosensing performance of any refractometric sensor, it is then more interesting to define the surface sensitivity parameter as:

$$\eta_{\text{S}} = \frac{\delta P_{\text{LSPR}}}{\delta d_{\text{Bio}}} \tag{13.12}$$

thus quantifying the shift of the measured spectra as the thickness of dielectric coating varies. The surface sensitivities of the metal film and the nanoparticle are compared in Fig. 13.5, showing how the sensitivity close to the metal surface can be up to a 50% larger for the nanostructures. The enhanced surface sensitivity in conjunction with the narrower resonance peaks add even more interest to the biosensing applications of plasmonic nanostructures. It is worth noticing that the surface and bulk sensitivities exhibit similar spectral dependences when the volume of the nanoparticle is kept constant (see Fig. 13.6a). Therefore, the surface FOM also displays an optimal sensing region between 700 and 900 nm (Fig. 13.6b). Within this region a threefold improvement in the surface FOM compared to that of thin films can be achieved [10].

Another interesting and rather surprising feature of the surface sensitivity of metal nanoparticles can be extracted from (13.9). If we assume that the dielectric shell uniformly covers the nanoparticle and the coating thickness is much thinner than the length of the ellipsoid axes, then the main effect of the shell in the polarizability is

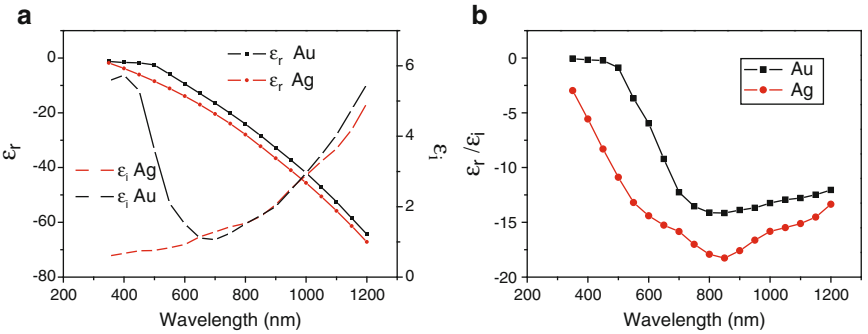

Fig. 13.7 (**a**) Real and imaginary parts of the dielectric constant of silver and gold. (**b**) Quotient between real and imaginary parts of the dielectric constant

generated by the factor *f*, which simply represents the ratio of the nanoparticle volume with and without shell. As a direct consequence from such dependence, nanoparticles with oblate and prolate shapes can exhibit identical surface sensitivities, if the total volume of the nanoparticle is preserved. A proof of such behavior is represented in Fig. 13.6, where the surface sensitivity, FWHM, and FOM of prolate and oblate ellipsoids with different aspect ratios are depicted. These results are confirmed by FDTD calculations, showing a very similar spectral trend and amplitude in the FOM as those gathered in Fig. 13.6. As a result, the surface sensitivity and FOM of the LSPR sensors is mainly dominated by the spectral position of the LSPR, whereas the shape of the nanoparticle plays a secondary role, i.e., selecting the resonance position.

The results of Fig. 13.6 clearly highlight the interdependence between the FOM of plasmonic sensors and the dielectric constants of the metal. As it was mentioned above, the sensitivity to changes of refractive index is proportional to the real part of the dielectric constant of the metal [5]. In contrast, the resonance peak widths are directly related to the imaginary part of the dielectric constant of the metal. The interdependence becomes more evident when quotient between the real and imaginary parts of the dielectric constant of the plasmonic metal is calculated. Figure 13.7 displays a peak-shaped tendency with a range of maximum values located at the same spectral region as the FOM, between 700 and 900 nm. Therefore, we can conclude that the overall spectral behavior of the FOM can be directly attributed to the intrinsic optical properties of gold.

Even better plasmonic characteristics than gold are found in silver. However its poor chemical stability has so far limited the development of robust LSPR sensors. As Fig. 13.7 displays, the real part of the dielectric constant of silver has a similar spectral dependence although blueshifted with respect to gold. Such difference implies that, for a given particle shape and volume, the LSPR spectral position will be always blueshifted with respect to that of a gold particle. In addition, for a given resonance wavelength, the sensitivity will be slightly better in silver due to the larger real part of the dielectric constant. Another difference between silver and gold comes from the imaginary part of the dielectric constant, which is smaller in silver especially for short wavelengths (below 700 nm), although a great

discrepancy is found for these values in the literature. A weaker absorption is manifested in narrower resonance peaks and larger dipole amplitudes. The former feature leads to improved spectral resolution, whereas the latter can help to enhance the signal-to-noise ratio of the spectral measurements, for an overall contribution that could help to improve the limit of detection of plasmonic sensors (Fig. 13.7b).

So far, we have considered the sensitivity of metal nanoparticles to homogeneous changes of refractive index. However, the necessity to link the nanostructures to a solid support in practical applications can reduce the sensing performance of the nanostructures, making difficult to achieve the results presented above. In fact, the experimental surface FOM of Au nanorods on a glass support has only shown a slight improvement with respect to that of Au films [10]. Besides, the substrate can induce significant spectral changes in the LSPR of the nanostructures [15–17]. Therefore, the aim of the next section is to analyze how the substrate influences the sensitivity and FOM of nanoplasmonic sensors.

Effect of the Substrate and Adhesion Layers in the FOM

The compatibility with microfluidic technology for lab-on-a-chip applications, high throughput assays and surface regeneration require that the metal nanostructures are firmly attached to a solid support. Such attachment can be made either chemically, linking colloidal nanoparticles to the surface by means of covalent bonds, or using lithographic methods to nanopattern the surface. Since the adhesion of silver and gold to common transparent substrates such as silica or organic polymers is generally very poor, chemical surface modification or the use of adhesion layers like Cr and Ti is needed to ensure the stability of the nanostructures. However, Cr and Ti are highly absorptive metals that can induce damping of the LSPR and, therefore, reduce the sensing capabilities of plasmonic nanostructures. In this study we select, as model plasmonic nanostructure, gold nanodisks, commonly employed in biosensing applications due to the simplicity of their fabrication by lithographic methods [18–20].

The first obvious effect related to the attachment of the nanoparticles to the substrate is the reduction of the metal surface available for the biofunctionalization, thus limiting the number of molecules than can be employed in the biodetection processes. On the other hand, the majority of the transparent substrates used for biosensing applications have a refractive index larger than that of water based solutions required in biosensing applications. Such difference breaks the symmetry of the electromagnetic field distribution around the nanoparticle and tends to shift the maximum intensity towards the higher refractive index region, i.e., the substrate (see Fig. 13.8). Therefore, as the refractive index of the substrate n_s increases, the electromagnetic field is more concentrated in the region that is not accessible for biosensing, which results in a substantial reduction of the bulk and surface sensitivities of the nanoparticles, ranging from a 30% decrease when $n_s = 1.5$ (borosilicate glass) up to 43% for $n_s = 2.4$ (TiO_2), as can be extracted from Fig. 13.9a. In addition, the sensitivity decrease is accompanied by a large

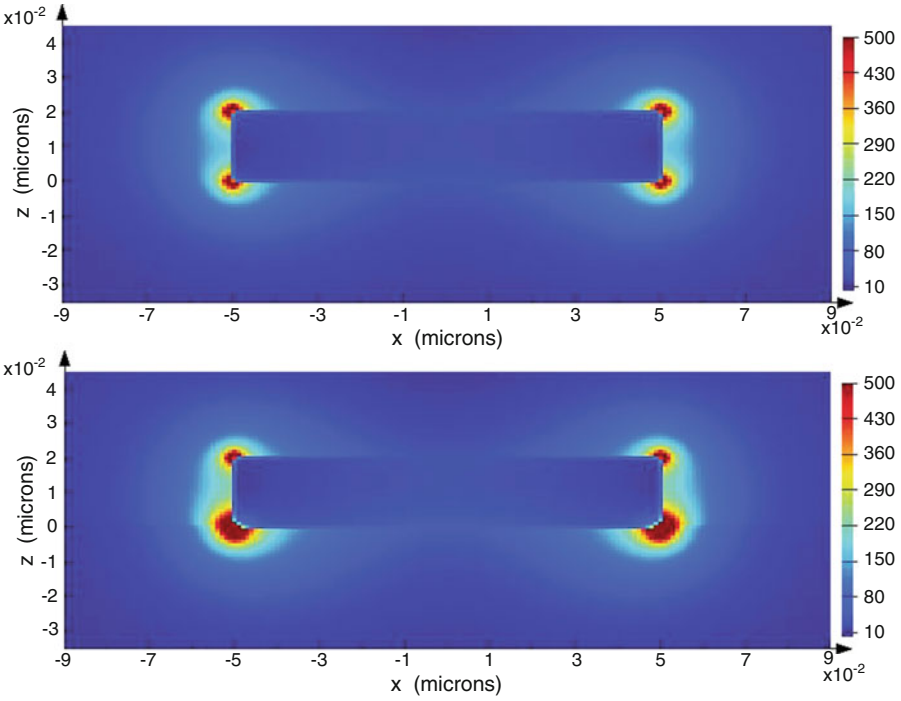

Fig. 13.8 Electromagnetic field distribution at the resonance wavelength for a nanodisk in a homogeneous dielectric medium with refractive index 1.33 (*top*) and when the nanodisk is on a substrate with refractive index $n_s = 2$ (*bottom*)

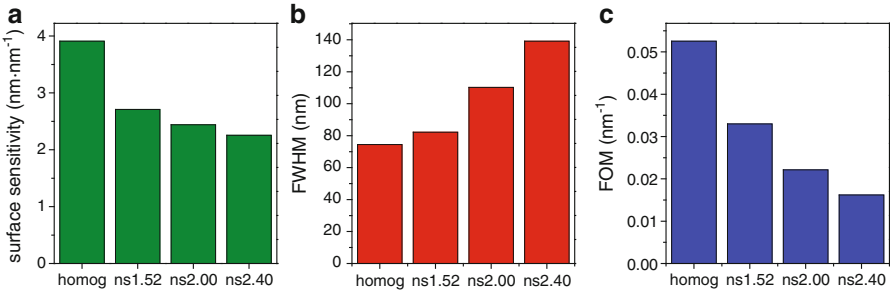

Fig. 13.9 Evolution of the (**a**) surface sensitivity, (**b**) FWHM, and (**c**) FOM of Au nanodisks (diameter $D = 100$ nm, and height $h = 20$ nm) as a function of the refractive index of the substrate

broadening of the resonance peaks (Fig. 13.9b), which can lead to a threefold decay of the FOM (Fig. 13.9c). Consequently, to maximize the biosensing response, it is important the use of substrates with low refractive index [17] or, as an alternative,

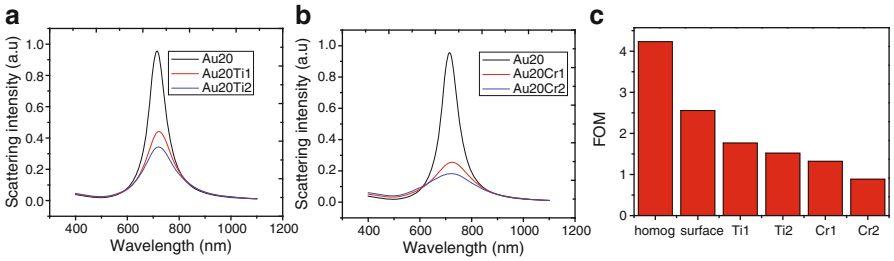

Fig. 13.10 FDTD scattering spectra of Au nanodisks with (**a**) Ti and (**b**) Cr adhesion layers. (**c**) Bulk FOM of Au nanodisks with different adhesion layers compared to that of a nanodisk in a homogeneous medium

nanoparticles on dielectric nanoposts [21], to reduce the effective refractive index around the nanoparticles.

The adverse effect of the substrate on the sensing performance of plasmonic nanostructures is even more pronounced when the typical adhesion layers, such as Ti and Cr, are introduced. Figure 13.10 displays the change of the scattering spectra of Au nanodisks on a glass substrate ($n_s = 1.5$) when an increasingly thick Ti or Cr layer is introduced between Au and the substrate. As can be observed, just 1 nm of Ti induces a 60% reduction of the scattering intensity, while the decrease is even more dramatic for Cr, being close to 80%. Even though the surface sensitivity is not altered by the adhesion layer, the induced LSPR damping is also manifested in a large broadening of the resonance peaks, yielding a fourfold diminution of the FOM when 2 nm of Cr are introduced. The combination of peak broadening and reduction of the scattering cross section will be reflected in a drastic drop of the signal-to-noise ratio of the biosensing measurements and a concomitant limitation of the refractometric sensing capabilities of nanoplasmonic sensors.

Conclusions

In this chapter we have examined several strategies to maximize the performance of metal nanoparticles as refractometric biosensors. Firstly, we have discussed the importance of using the FOM, defined as the ratio between sensitivity and width of the resonance peaks, to describe and quantify the sensing performance, due to the equivalence in wavelength and energy scales, thus eliminating any possible ambiguity. On the other hand, it is crucial to distinguish between surface and bulk sensitivity in order to compare the quality of different refractometric sensors due to their dissimilar electromagnetic field distribution. Taking these factors into account, the strategy to maximize the biosensing performance of refractometric plasmonic sensors is rather general (valid for nanostructured media and planar films) and can be summarized in two steps:

1. Selection of the plasmonic resonance wavelength in the region in which the quotient between the real and imaginary parts of the dielectric constant of the metal is maximized. In the case of gold, the optimal sensing region is comprised between 700 and 900 nm. In order to tune the LSPR within this wavelength range, it is convenient to select nanoparticles with high aspect ratio and low volume to avoid additional peak broadenings associated to dephasing effects. In this sense, nanospheres are the worst candidates for refractometric sensing, whereas disk-like or rod-like nanoparticles can exhibit similar features.
2. Attenuation of the adverse effects related to the attachment of the nanostructures to a solid support, being advantageous to minimize both the refractive index of the substrate and the thickness of the adhesion layers required to promote their mechanical stability.

The combination of both strategies can provide nanoplasmonic biosensors with very competitive features, especially for real-time, label-free, and multiplexed applications.

References

1. Anker JN, Hall WP, Lyandres O, et al. Biosensing with plasmonic nanosensors. Nat Mater. 2008;7(6):442–53.
2. Sepulveda B, Angelome PC, Lechuga LM, et al. LSPR-based nanobiosensors. Nano Today. 2009;4(3):244–51.
3. Lal S, Link S, Halas NJ. Nano-optics from sensing to waveguiding. Nat Photonics. 2007;1:641–8.
4. Bohren CF, Huffman DR. Absorption and scattering by small particles. New York: Wiley-Interscience; 1983.
5. Miller MM, Lazarides AA. Sensitivity of metal nanoparticle surface plasmon resonance to the dielectric environment. J Phys Chem B. 2005;109(46):21556–65.
6. Lee KS, El-Sayed MA. Gold and silver nanoparticles in sensing and imaging: sensitivity of plasmon response to size, shape, and metal composition. J Phys Chem B. 2006;110 (39):19220–5.
7. Chen HJ, Kou XS, Yang Z, et al. Shape- and size-dependent refractive index sensitivity of gold nanoparticles. Langmuir. 2008;24(10):5233–7.
8. Larsson EM, Alegret J, Kall M, et al. Sensing characteristics of NIR localized surface plasmon resonances in gold nanorings for application as ultrasensitive biosensors. Nano Lett. 2007;7 (5):1256–63.
9. Wang H, Brandl DW, Le F, et al. Nanorice: a hybrid plasmonic nanostructure. Nano Lett. 2006;6(4):827–32.
10. Otte MA, Sepulveda B, Ni WH, et al. Identification of the optimal spectral region for plasmonic and nanoplasmonic sensing. ACS Nano. 2010;4(1):349–57.
11. Becker J, Trugler A, Jakab A, et al. The optimal aspect ratio of gold nanorods for plasmonic bio-sensing. Plasmonics. 2010;5(2):161–7.
12. Homola J. Present and future of surface plasmon resonance biosensors. Anal Bioanal Chem. 2003;377(3):528–39.
13. Svedendahl M, Chen S, Dmitriev A, et al. Refractometric sensing using propagating versus localized surface plasmons: a direct comparison. Nano Lett. 2009;9(12):4428–33.

14. Schubert M. Polarization-dependent optical parameters of arbitrarily anisotropic homogeneous layered systems. Phys Rev B. 1996;53(8):4265–74.
15. Knight MW, Wu YP, Lassiter JB, et al. Substrates matter: influence of an adjacent dielectric on an individual plasmonic nanoparticle. Nano Lett. 2009;9(5):2188–92.
16. Vernon KC, Funston AM, Novo C, et al. Influence of particle-substrate interaction on localized plasmon resonances. Nano Lett. 2010;10(6):2080–6.
17. Brian B, Sepulveda B, Alaverdyan Y, et al. Sensitivity enhancement of nanoplasmonic sensors in low refractive index substrates. Opt Express. 2009;17(3):2015–23.
18. Gunnarsson L, Rindzevicius T, Prikulis J, et al. Confined plasmons in nanofabricated single silver particle pairs: experimental observations of strong interparticle interactions. J Phys Chem B. 2005;109(3):1079–87.
19. Acimovic SS, Kreuzer MP, Gonzalez MU, et al. Plasmon near-field coupling in metal dimers as a step toward single-molecule sensing. ACS Nano. 2009;3(5):1231–7.
20. Fredriksson H, Alaverdyan Y, Dmitriev A, et al. Hole-mask colloidal lithography. Adv Mater. 2007;19(23):4297.
21. Dmitriev A, Hagglund C, Chen S, et al. Enhanced nanoplasmonic optical sensors with reduced substrate effect. Nano Lett. 2008;8(11):3893–8.

Chapter 14
Localized Surface Plasmon Resonance (LSPR) Transducers Based on Random Evaporated Gold Island Films: Properties and Sensing Applications

Alexander Vaskevich and Israel Rubinstein

Abstract Methods based on localized surface plasmon resonance (LSPR) spectroscopy have gained popularity in recent years, notably for label-free biosensing. This chapter summarized our progress in the development of LSPR transducers based on random evaporated gold island films. Systematic results on the preparation of Au island films with desired morphology and optical properties, as well as studies of the stability and sensitivity of such LSPR transducers, are presented. Schemes described here allowing tunability of the surface plasmon band wavelength, decay length and refractive index sensitivity of the LSPR transducers enable optimization of the transducer performance. Actual biosensing applications are exemplified using immunosensing (antigen-antibody interactions) and specific protein-carbohydrate interactions. It is concluded that random gold island films prepared by evaporation and annealing present a promising platform for the preparation of sensitive and cost-effective LSPR transducers offering scalability and simplicity.

Introduction

Nano-sized structures of various metals exhibit an extinction band which is not present in the bulk metal spectrum [1]. This band is attributed to localized surface plasmon resonance (LSPR), i.e., excitation of localized surface plasmons (SPs), also known as plasma polaritons. The physics of SPs have been studied extensively for over a century, starting from the pioneering works of Mie [2] and Maxwell-Garnett [3]. A discussion of the physical principles underlying the phenomenon can be found in Chaps. 1 and 2 of this book.

A. Vaskevich (✉) • I. Rubinstein (✉)
Department of Materials and Interfaces, Weizmann Institute of Science, Rehovot 76100, Israel
e-mail: alexander.vaskevich@weizmann.ac.il; israel.rubinstein@weizmann.ac.il

A. Dmitriev (ed.), *Nanoplasmonic Sensors*, Integrated Analytical Systems,
DOI 10.1007/978-1-4614-3933-2_14,

In general, the LSPR spectrum depends on both structural and environmental parameters, and can be measured using different experimental setups including transmission as well as specular and diffuse reflectance. The wavelength, shape, and intensity of the LSPR band are sensitive to changes in the geometric and environmental features. The latter, together with the simplicity of obtaining the experimental data with sufficient accuracy using low-cost equipment, have stimulated rapid development of sensing applications based on LSPR spectroscopy in the past decade.

Initial applications of LSPR spectroscopy to sensing have exploited changes of the spectrum upon analyte-induced aggregation of nanoparticles (NPs) in solution, causing coupling of the SPs of individual NPs. Intense color changes indicating SP coupling, easily observed by the naked eye, were used in immunoassay [4] and later in studies involving DNA hybridization [5]. This type of biosensors, most commonly used in solution, is outside the scope of this chapter. Here we focus on systems where the spatial distribution of the metal nanostructures is assumed to remain unchanged and the LSPR transducer response is attributed to changes in the contacting environment upon analyte binding/release. The wavelength of the SP band of coinage metals is located in, or close to, the visible range; this, combined with the chemical stability of silver and especially of gold, has made them the metals-of-choice in the development and study of LSPR transducers.

The sensitivity of localized SPs to the dielectric properties of the immediate environment has been well understood for many years [2, 3]. Experimental results have been obtained for plasmonic nanostructures on various substrates, including chemically deposited [6, 7] and evaporated [8–10] metal island films, as well as immobilized metal NPs [11]. The results of Underwood and Mulvaney on Au NPs immersed in media of variable refractive index (RI) showed quantitative agreement with the Mie theory [12]. In marked contrast with the relative simplicity of LSPR measurements, exact theoretical calculation of the LSPR spectrum of metal nanostructures immobilized on dielectric substrates is not possible; therefore, substantial effort has been invested in simplified model calculations and numerical modeling (see recent reviews [10, 13–16] for references).

The development of LSPR transducers is closely related to the discovery of surface enhanced Raman scattering (SERS) and the introduction of an electromagnetic enhancement mechanism for SERS [17, 18], promoting numerous studies of metal island films as SERS substrates (see recent reviews [19, 20] for references). An early experimental observation of the shift of the LSPR band in the transmission spectrum of Ag island films after adsorption of 4,4′-bipyridine was published by Schlegel and Cotton [21].

Application of LSPR to sensing of its dielectric environment was suggested by Meriaudeau et al. [22], while Foss and coworkers demonstrated determination of an analyte (phenol) in aqueous solution based on the concentration dependence of the RI of the medium [23]. Both groups used LSPR transducers comprised of Au island films evaporated on glass and annealed. Systematic studies of the refractive index sensitivity (RIS) and sensing applications of ordered metal (Ag, Au) island films prepared by evaporation through a sacrificial mask of closely packed polystyrene NPs were reported by Van Duyne and coworkers [10, 24–26]. LSPR transducers

designed for reflection measurements were prepared by Takei and coworkers by evaporating Au caps on polystyrene NPs assembled on an Au mirror [27, 28].

In general, several platforms have been developed for LSPR sensing. Hence, evaporated island films, either random [22, 23, 29–32] or ordered [10, 24–27]; solution based [33–35] and immobilized [36–38] metal NPs; continuous metal films perforated with nanoholes [39–41]; and sandwich structures combining continuous and nanostructured parts [27, 42, 43], have been used in numerous sensing and biorecognition applications.

In recent years studies of LSPR sensing have been pursued primarily along two directions: achieving record sensitivity of detection down to the single NP/single molecule level, and preparation of LSPR transducers for practical applications. These two directions are distinct in the use of sophisticated vs. simple equipment, respectively. Examples of this difference are dark-field microscopy combined with spectrophotometry [40] on the high end, and transmission/reflection spectrophotometry, available in low-cost configurations of fiber optics-based systems [10] or compact integrated devices [44], on the low end. The two directions are related: The LSPR sensing concept, realized in the late 1990s using ensembles of NPs and nanoislands, was demonstrated in single-particle experiments a few years later, in 2003 [45–47]. Recently monitoring single binding [48] and desorption [49] events was reported, achieving record sensitivity.

An intriguing issue in the quest to achieve high sensitivity of LSPR systems is the shape of individual particles that best suits specific sensing tasks, and the possibility to prepare ensembles of such particles [50]. Numerical modeling showed that variations in the strength of the local electromagnetic field influence the local sensitivity of the individual LSPR nano-objects; therefore, directing the analyte to more sensitive binding locations should improve the transducer performance [25]. Experimental results indicated increase in the transducer sensitivity for analyte bound to the edges of Au nanoplates [51, 52], supporting the model calculations. It is expected that further work on individual LSPR nanostructures will lead to optimization of the shape and spatial positioning of the analyte binding sites.

Thermal evaporation of metals to form nanostructured metal films on inert supports represents one of the earliest techniques for the preparation of localized plasmon systems. Notable advantages of metal evaporation are simplicity and scalability. Post-deposition annealing of the films affords additional tuning of the morphology and optical properties. However, obtaining a narrow distribution of island shape and size usually requires the use of masks, such as e-beam [53, 54] or colloidal [55] lithographies. The latter has been widely used in laboratory studies, but has not reached the level of industrial application. In cases where only shape-control is needed, a variant of colloidal lithography based on immobilization of a random array of template spheres [56] has shown potential of scalability in the preparation of nanoisland [57] and nanohole films [39]. The latter approach also provides the possibility to prepare plasmonic structures with vertically separated layers [58].

In the last decade our group has concentrated on the systematic development of LSPR transducers based on thermally evaporated random island films [29–31, 59]. We have studied the morphological and spectroscopic properties of such films, as

well as their stability and sensitivity when used as optical transducers [32, 60–63]. Sensing applications of LSPR systems based on random Au island films have been demonstrated in the detection of gas-phase [64] and biological [65–67] analytes, the latter including biotin-avidin recognition, immunosensing, and carbohydrate–protein interactions.

This chapter describes our progress to date in the study of LSPR transducers based on random evaporated Au island films.

Preparation of Random Gold Island Films by Metal Evaporation/Annealing

Thermal Evaporation of Discontinuous Au Films on Transparent Substrates

Vacuum evaporation of metal island films on transparent substrates (glass, quartz, mica, polymers) presents a convenient approach to the preparation of LSPR transducers. This method has been used for the preparation of metal island films as well as arrays of nanoholes in continuous metal films. Specific issues related to sensor optimization include control over the size, shape, and surface density of the metal islands or holes, and the adhesion between the metal and the substrate, affecting the stability of the optical signal.

The weak adhesion of evaporated Au and Ag films to oxide substrates such as glass or mica is well known, frequently resulting in uncontrolled detachment and/or aggregation of the metal islands upon exposure to solvents and drying. The common way to improve the adhesion is precoating the substrate with an adhesion layer, either metallic (Cr, Ti, Ni) or organic (polymers, functionalized silanes, dendrimers). It should be noted that preparation of noble metal island films commonly includes post-deposition annealing (see sections "Low-Temperature Annealing" and "High-Temperature Annealing and Stabilization") to achieve desired island morphologies by coalescence, but the heating may be incompatible with organic adhesion promoters. We have shown that Au island films prepared by evaporation on amino- or mercapto-silane functionalized oxide surfaces (glass, quartz) undergo thermal reshaping while retaining their stability upon low-temperature (200°C) annealing in air for several hours [32, 60].

The morphology of evaporated Au island films was characterized by atomic force microscopy (AFM), high-resolution scanning electron microscopy (HRSEM), and cross-sectional transmission electron microscopy (TEM). The latter two techniques provide complementary quantitative information on the 3D topography and projection of the metal islands. Representative images of as-prepared and annealed Au island films of various nominal thicknesses, thermally evaporated on silanized glass, are shown in Fig. 14.1. (The film nominal thickness, or mass thickness, corresponds to homogeneous distribution of the material on the entire surface.) In the usual resistive evaporation using deposition rates of 0.005–0.01 nm s^{-1} [31, 32, 60], the

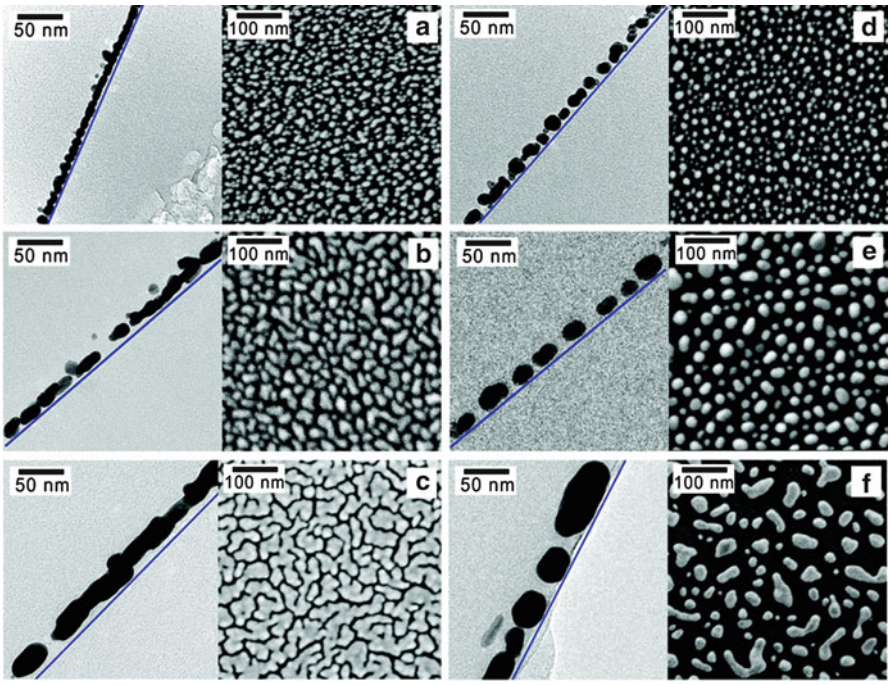

Fig. 14.1 Cross-sectional transmission electron microscopy (TEM) (*left*) and high-resolution scanning electron microscopy (HRSEM) (*right*) images of gold films evaporated on silanized glass. Nominal thickness: 2.5 nm (**a**, **d**), 5.0 nm (**b**, **e**), and 7.5 nm (**c**, **f**). Samples before (**a**, **b**, **c**) and after (**d**, **e**, **f**) annealing 20 h at 200°C are shown. The *solid lines* in the cross-sectional TEM images serve as a guide to the eye, representing the glass substrate removed before sectioning. Note the different *scale bar* in (**f**) (adapted with permission from Karakouz et al. [60])

substrate temperature increases by 10–20°C above room temperature during the evaporation. Under these conditions the mobility of Au adatoms and clusters is high enough to promote formation of small islands and larger aggregates during evaporation [21, 30–32], as seen in the unannealed films (Fig. 14.1a–c). The islands' coalescence process is not complete, as seen in the HRSEM image of the 5.0 nm Au film (Fig. 14.1b), presenting a large fraction of elongated structures. Further increase in the nominal thickness of the Au film induces formation of wormlike, near-percolated structures (Fig. 14.1c) [30, 32, 60]. The average island size remains relatively small, such that TEM images of cross-sectional slices (30–50 nm thick) of the unannealed samples show more than one row of islands (Fig. 14.1a–c).

Low-Temperature Annealing

Evaporated films annealed 20 h at 200°C present larger Au islands spaced farther apart compared to the unannealed ones, as a result of thermally induced coalescence

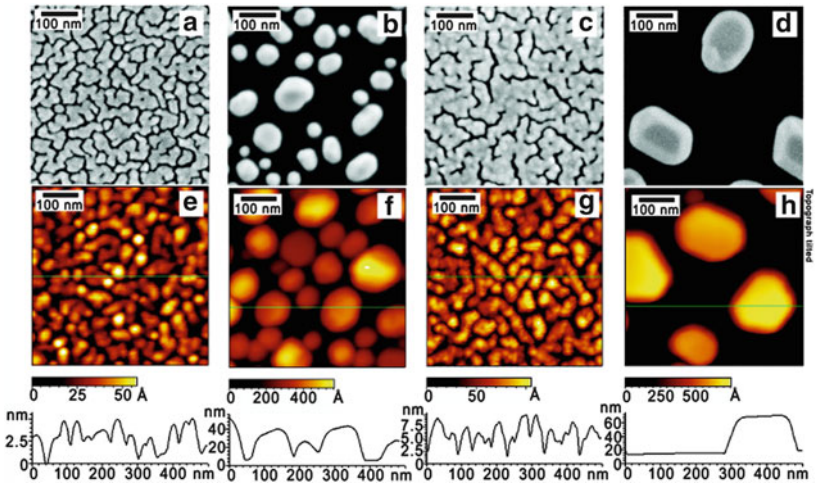

Fig. 14.2 HRSEM (**a**–**d**) and AFM (**e**–**h**) images (500 × 500 nm^2) of gold films evaporated on bare glass. Nominal thickness: 7.5 nm (**a**, **b**, **e**, **f**) and 10 nm (**c**, **d**, **g**, **h**). Samples before (**a**, **c**, **e**, **g**) and after (**b**, **d**, **f**, **h**) annealing 10 h at 550°C are shown. A typical cross-section is shown below each atomic force microscopy (AFM) image; note the different *z*-scales in the cross-sections (adapted with permission from Karakouz et al. [60])

(Fig. 14.1d–f). After annealing the 2D projection of the islands becomes more regular (Fig. 14.1d, e) with increased interisland spacing compared to the unannealed films. The respective cross-sectional TEM images show individual islands with substantially increased island height (Fig. 14.1d, e). Thermal transformation of the near-percolated film into islands (Fig. 14.1c, f) proceeds through dewetting, rather than coalescence. Due to the low rate of surface diffusion of Au adatoms and recrystallization at 200°C, part of the islands remains odd-shaped with a characteristic size of hundreds of nanometer (Fig. 14.1f).

High-Temperature Annealing and Stabilization

Elevating the annealing temperature allows dewetting of thick, near-percolated or percolated films, to form well-defined islands [23]. Transformation of the morphology from percolated films to separated islands was followed by AFM and HRSEM imaging for Au evaporated on bare glass (Fig. 14.2). The unannealed 7.5 and 10 nm films display a largely percolated structure with a network of voids, the latter becoming shorter as the nominal thickness increases (Fig. 14.2a, c, e.g.). High-temperature annealing in air of the near-percolated (7.5 nm) and just-percolated (10 nm) films leads to formation of large, well-separated islands (Fig. 14.2b, d, f, h). Selected-area electron diffraction shows that the individual islands are single

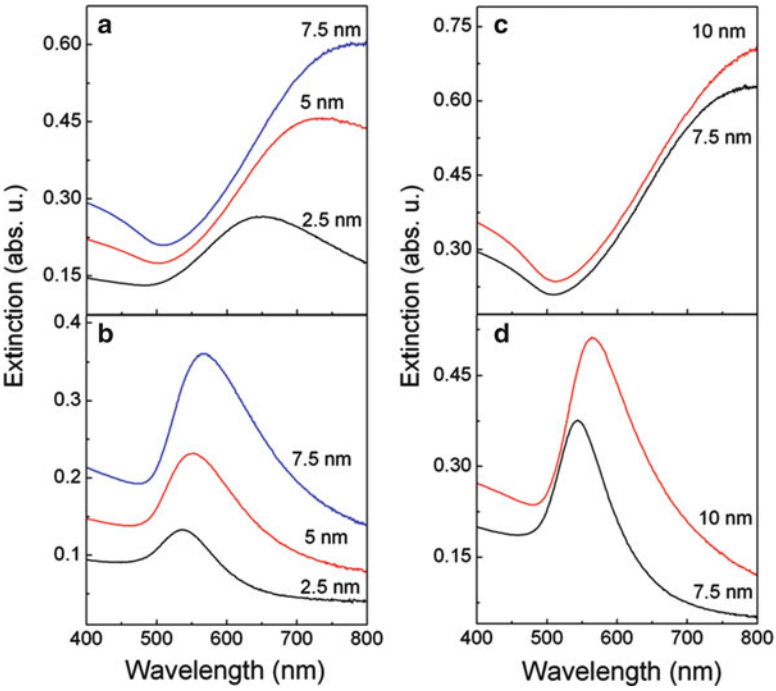

Fig. 14.3 Transmission UV–vis spectra of Au films evaporated on silanized glass (**a**, **b**) and on bare glass (**c**, **d**). (**a**, **c**) As evaporated; (**b**) after annealing 20 h at 200°C; (**d**) after annealing 10 h at 550°C. Nominal thicknesses are indicated (adapted with permission from Karakouz et al. [60])

crystalline [68]. The top surface of larger faceted islands formed after annealing of 10 nm films is more developed, as seen in the HRSEM and AFM images (Fig. 14.2d, h). The AFM measured roughness of the top surface of the annealed films is ca. 0.1 over 100 nm scan, indicating largely atomically flat surfaces. XRD analysis of high-temperature annealed 10 nm Au films shows a strong {111} texture [68], confirming that the top surface of individual Au islands (Fig. 14.2d, h) presents (111) faces.

Typical transmission UV–vis spectra of Au films before and after annealing are shown in Fig. 14.3. Unannealed films presenting an island structure (small nominal thicknesses, 2.5 and 5.0 nm) show an SP band in the visible spectral range. The SP band is barely distinguishable in the spectra of the nonconductive 7.5 nm unannealed films (Fig. 14.3a, c), approaching the spectrum of a continuous Au film, in agreement with the HRSEM imaging results (Figs. 14.1c and 14.2a). The unannealed, just-percolated 10 nm film is highly electronically conductive and exhibits a transmission UV–vis spectrum (Fig. 14.3c) characteristic of a continuous Au film, showing an extinction minimum at ca. 520 nm and the absence of an SP band [69]. High-temperature annealing in air transforms the 7.5 and 10 nm Au films to isolated islands, resulting in the appearance of a well-defined SP band (Fig. 14.3b, d).

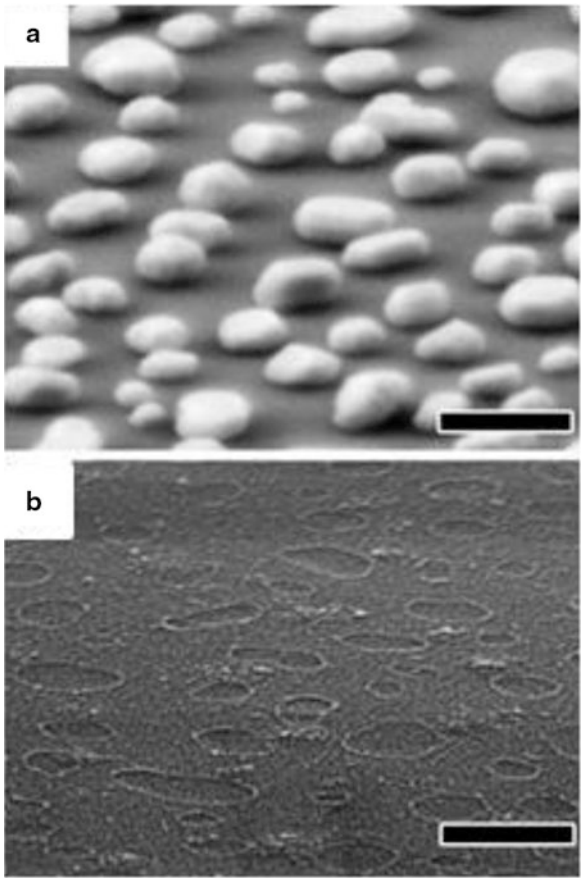

Fig. 14.4 HRSEM isometric view images (projection view, 20°) of a 10 nm Au film after annealing 10 h at 550°C (**a**) followed by dissolution of the islands in cyanide (**b**) [68]. *Scale bars*: 200 nm

When the annealing temperature approaches the glass transition temperature T_g of the glass substrate, the stability of the formed island film is greatly improved [60, 61]. Kinetic studies showed that the film morphology is transformed within less than an hour and remains essentially unchanged during long annealing. However, the morphology of the glass substrate undergoes a slow modification. HRSEM 3D images of island film and the glass substrate after long high-temperature annealing and dissolution of the gold (Fig. 14.4) revealed island footprints in the glass.

Development of the footprints was correlated with softening of the glass substrate at temperatures in the vicinity of T_g and gradual embedding of the islands in the glass over many hours. For films evaporated on glass cover slips ($T_g = 557$°C), indication of glass transformation was observed after long annealing at 500°C (Fig. 14.5b); however, stabilization of the island morphology and optical response was reached only after long annealing at higher temperatures, at which island (partial) embedding in the glass was attained (Fig. 14.5d, f). Elevating the annealing

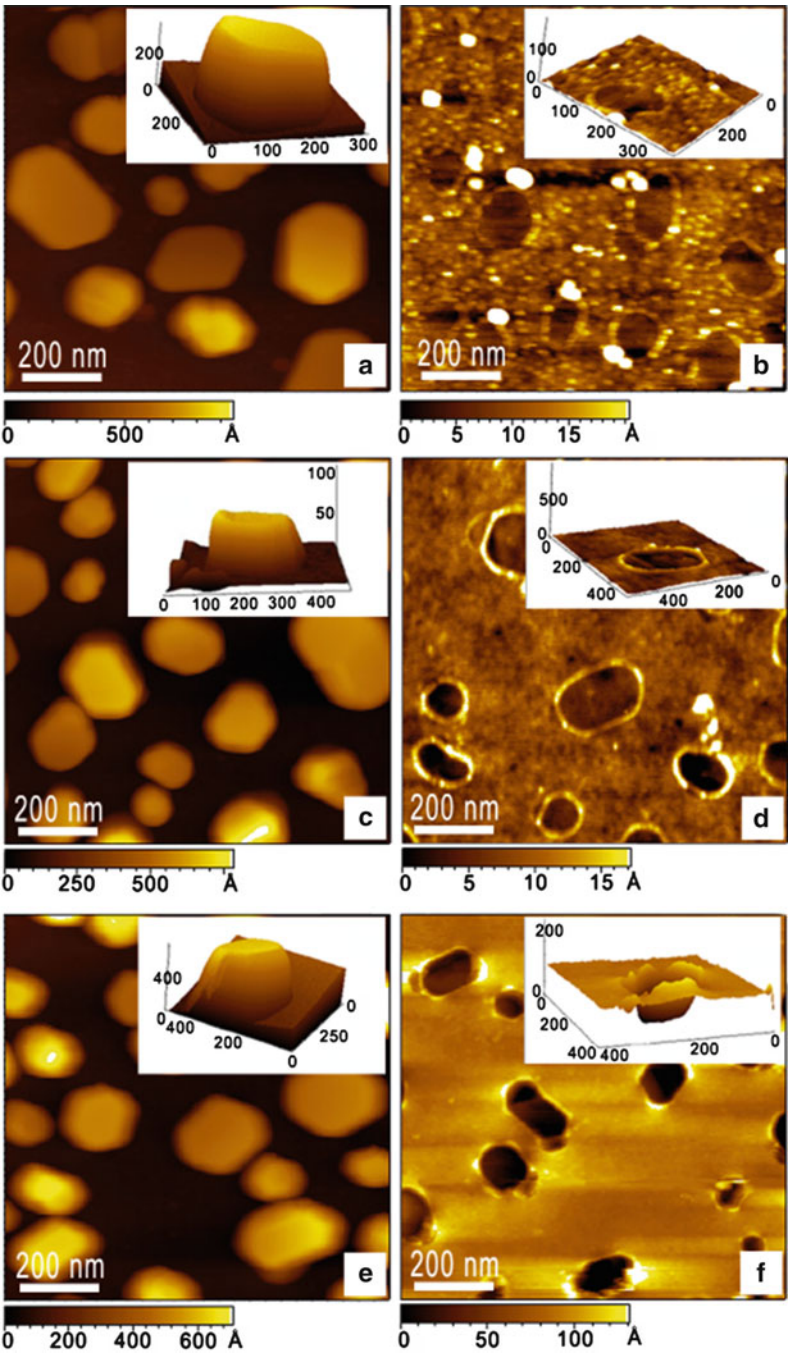

Fig. 14.5 AFM images (1 × 1 μm [2] scan) of 10 nm Au island films on cover-glass (T_g = 557 °C), annealed 10 h at: 500°C (**a**, **b**), 550°C (**c**, **d**), 600°C (**e**, **f**). Samples before (**a**, **c**, **e**) and after (**b**, **d**, **f**) Au dissolution in aqua regia are presented. *Insets* show 3D images of single features. Note the different *z*-scales in different images (adapted with permission from Karakouz et al. [61])

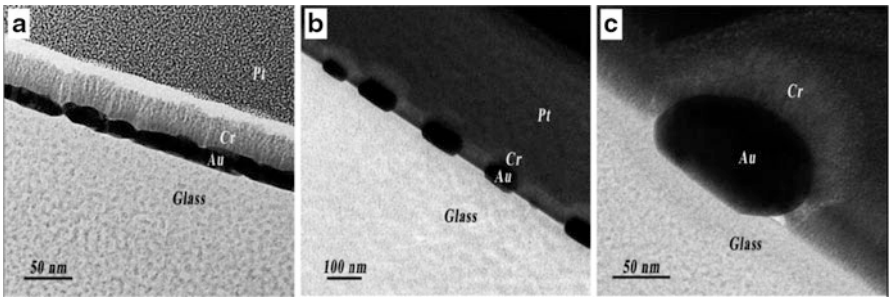

Fig. 14.6 Cross-sectional TEM images of 10 nm gold films evaporated on bare glass. Samples before (**a**) and after (**b**, **c**) 10 h annealing at 600°C are shown. Samples for imaging were prepared by focused ion beam slicing (adapted with permission from Karakouz et al. [60])

temperature enhanced the kinetics of embedding and increased the embedding depth (Fig. 14.5) [60, 61]. The latter, however, decreases the sensitivity of the LSPR transducer due to reduction of the island area available for analyte binding [70]. Higher annealing temperatures lead to deformation of the glass substrate and sticking to the underlying support, preventing use of the LSPR transducer.

The detailed morphology of the embedded islands was studied by cross-sectional TEM (Fig. 14.6). As seen in Fig. 14.6c, the softened glass wets the partially embedded Au island. The same general behavior of gradual embedding was observed with Au NPs immobilized on glass and annealed at similar temperatures [71, 72]. Note that our claim that oxygen is essential for the embedding [61] proved to be wrong (it originated from unsatisfactory temperature control under gas flow). Improving the experimental system showed that annealing in vacuum and under inert atmosphere (N_2) also results in island embedding, with the atmosphere influencing the kinetics of embedding [72].

The driving force for NP embedding in the softened glass appears to be capillary forces at the glass-NP-air three-phase contact; however, a detailed study of the chemical composition of the interface is needed to elucidate the mechanism of island embedding. Recently wetting of Au islands on sapphire by an intermediate anorthite layer was shown [73], where a nanometer-thick amorphous layer of anorthite separated the Au islands and the sapphire surface, forming an intergranular film at the interface. The kinetics of Au island embedding in the glass (Fig. 14.7) show decrease of the mean height of the non-embedded part of the island above the glass, and concurrent increase of the mean embedding depth. The sum of the two (ca. 50 nm) remains constant throughout the process, indicating that the average island overall height remains essentially constant, while the islands gradually sink into the glass as the annealing proceeds.

The ability to systematically change the optical properties of LSPR systems is essential for transducer optimization, as discussed in section "Sensitivity of LSPR Transducers." Preparation of random Au island transducers by evaporation

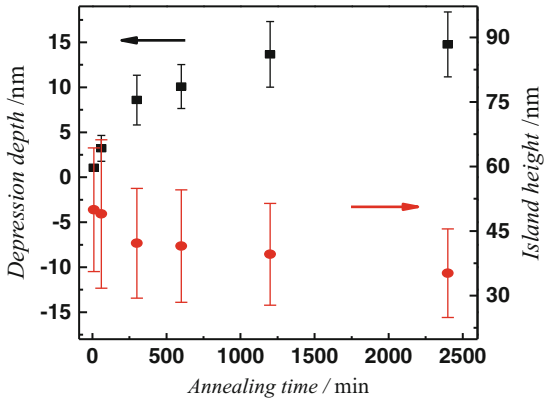

Fig. 14.7 Kinetics of island embedding during annealing at 600°C of a 10 nm Au island film on cover-glass, measured by AFM. *Circles*—island height above the glass, *squares*—depression depth after Au dissolution in aqua regia. Mean values and standard deviations (the latter shown as *error bars*) were calculated from measurements of 50 islands and depressions for each point (adapted with permission from Karakouz et al. [61])

followed by high-temperature annealing presents an effective means of achieving stable and tunable LSPR transducers. Transmission spectra of a series of Au island films with a nominal thickness from 3.0 to 10 nm, annealed at a high temperature, show a regular increase in the extinction and a SP band shift (Fig. 14.8a). The latter can be correlated with the known dependence of the SP band position on the island aspect ratio (Fig. 14.8b). In numerical modeling using the discrete dipole approximation (DDA) taking into account the experimentally determined size distribution of the islands, splitting of the SP band to transverse and longitudinal components was not observed as a result of averaging over the ensemble [68].

The reproducibility of the transducer preparation procedure presents a critical parameter in the development of practical LSPR sensors. In the present system the standard deviation of the nominal thickness of slides evaporated resistively using a rotating sample holder (a batch of ca. 20 slides) is $\leq$4%, attesting to the homogeneity of the evaporated samples [74]. Statistical analysis of extinction spectra was carried out using 6 batches of 18–24 slides each, nominal thicknesses of 2.5–10 nm, and different annealing procedures. The standard deviation of the SP band wavelength for a given batch varied between 1 and 4 nm, with an average of 2.3 nm, while the relative standard deviation of the SP maximum extinction was $\leq$2% [60, 67]. These statistical results indicate that resistive evaporation of thin Au films followed by thermal annealing in air presents a viable route to large-scale preparation of LSPR transducers. It should be noted, however, that the standard deviation of the SP band increases with increase of the nominal thickness, and additional work is necessary to achieve a satisfactory reproducibility for transducers prepared by annealing of near-percolated and just-percolated Au films.

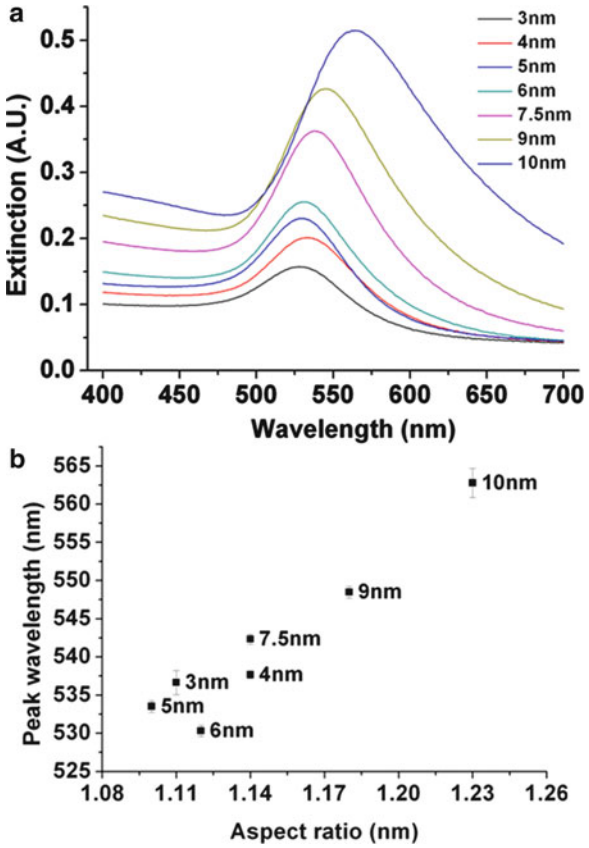

Fig. 14.8 (**a**) Representative extinction spectra of gold island films of various nominal thicknesses (indicated), evaporated on bare glass and annealed 10 h at 580°C. (**b**) The Au SP peak wavelength as a function of the mean island aspect ratio; nominal thicknesses are indicated (adapted with permission from Kedem et al. [76])

Sensitivity of LSPR Transducers

General Properties and Sensitivity of LSPR Transducers Based on Random Evaporated Au Island Films

Development of LSPR-based optical transducers involves general issues, such as sensitivity to analyte binding and choice of the measured parameters. The wavelength, intensity, and shape of the LSPR band are sensitive to changes in the dielectric properties of the surrounding medium, including changes induced by binding of analyte species to the metal structures. In LSPR sensing, analyte accumulates on the transducer surface (either directly or via a recognition layer),

displacing air or solvent and thereby changing the dielectric properties (i.e., the effective RI) of the surrounding medium. As a result the conditions for excitation of SPs change (the simplest case is given by the Mie relationship), expressed as modification of the LSPR spectrum.

Quantitative calculation of the wavelength-dependent intensity of the SP evanescent field for random metal island systems, taking into account the island size and shape, size distribution, influence of the solid support, and electromagnetic coupling between islands, is practically impossible. However, the general optical behavior of the system can be described by a simple phenomenological model, developed to describe the behavior of propagating surface plasmon resonance (SPR) sensors [75] and later applied successfully to LSPR transducers. The model assumes that the response R to change of the RI η of the adjacent bulk medium depends only on the difference in RI (14.1). Over a narrow range of RI change, the LSPR response R can be approximated as a linear function of the change in the bulk RI, $\Delta\eta = \eta_{\text{final}} - \eta_{\text{initial}}$:

$$R = f(\eta_{\text{final}} - \eta_{\text{initial}}) \approx m(\Delta\eta) \tag{14.1}$$

The empirical coefficient m in (14.1) is denoted the bulk RIS. It represents averaging of geometrical factors and sensitivity of individual islands in the ensemble. The response R can be measured as change in one or more of several parameters, such as the SP wavelength, maximum extinction, extinction at a constant wavelength, etc., and corresponding m values can be calculated experimentally for each parameter. As an example, Fig. 14.9 presents experimental data for an Au island transducer immersed sequentially in a series of solvents with different RI values. While the optical parameters change nearly linearly in the narrow RI range covered by the different solvents, in agreement with the approximate (14.1), the experimental points in air ($\eta = 1.00$) exhibit a nonlinearity, which should be taken into account if calculations are performed in a wide RI range. The RIS values extracted from the linear part of Fig. 14.9b, c are 72 nm/RIU (RIU = RI unit) for SP wavelength shift, and 0.32 a.u./RIU for change in maximum extinction.

The RIS m represents an upper limit of the sensitivity of LSPR nanostructures to local RI change, as it involves change of the contacting medium up to infinite distance from the transducer surface. In case of an adsorbed layer of a finite thickness d, which is the common situation in analyte binding, the sensor response depends, in addition, on a characteristic length l associated with the exponential decay of the SP evanescent field. This dependence is presented in (14.2), where d is the dielectric (adsorbate) layer thickness and l is the SP effective decay length [24, 75]:

$$R = m(\Delta\eta)[1 - \exp(-d/l)] \tag{14.2}$$

Note that (14.2) is commonly written with a factor of 2 in the exponent numerator [75]; we chose to eliminate this factor as the relationship expressed in (14.2) is largely empirical. We therefore refer to l as the effective decay length.

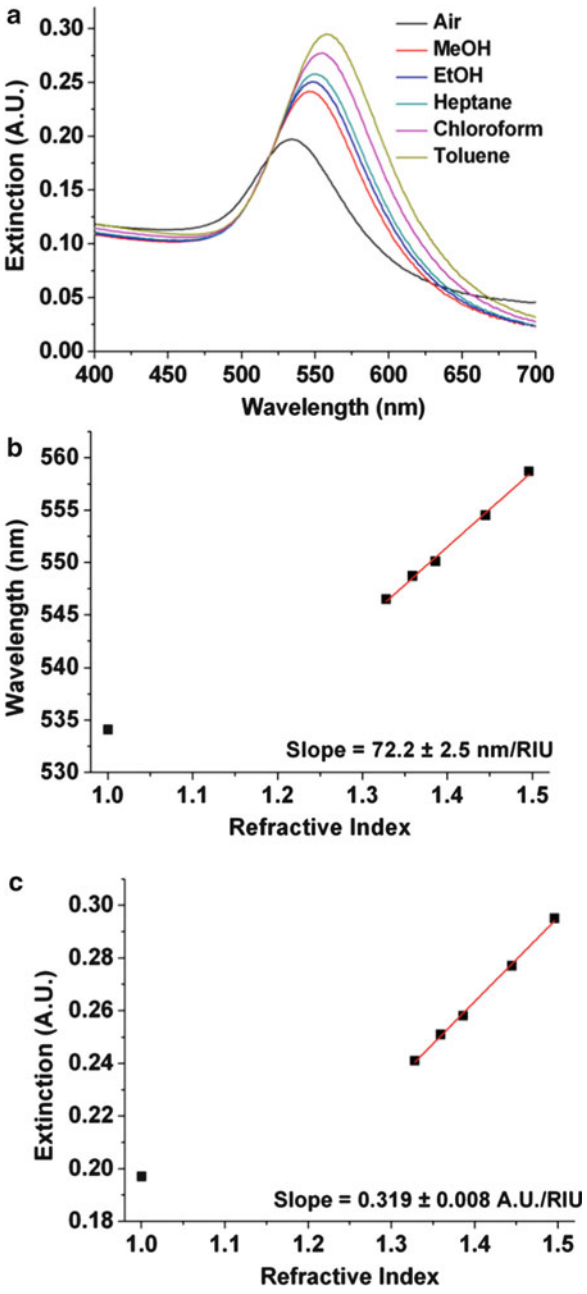

Fig. 14.9 Representative results for a 4 nm Au island film, annealed 10 h at 580°C. (**a**) Transmission spectra in air and in various solvents. (**b**) SP peak wavelength vs. RI of the medium. (**c**) Maximum extinction vs. RI of the medium. The *lines* in (**b**) and (**c**) are linear regression of the results. *Error bars* in (**b**) and (**c**) are too small to be seen (adapted with permission from Kedem et al. [76])

The physical model presented by (14.2) relates to the measurement of extinction and does not distinguish between absorbance and scattering; however, it can serve as a good approximation in sensing applications.

Distance Dependence of the LSPR Transducer Response

The sensitivity of LSPR transducers to the dielectric properties of the local environment can be exploited for sensing purposes. Typically, a recognition layer is first immobilized on the metal nanostructures (e.g., an antibody) and a UV/vis/NIR spectrum (depending on the specific transducer) is recorded, showing the LSPR band. The transducer is then exposed to the tested medium; if the latter contains a specific analyte (e.g., an antigen specific to the immobilized antibody), it will bind to the recognition layer, and a change in the spectrum will be detected. In such a scenario, both the RIS and the decay length of the evanescent field determine the transducer sensitivity toward the given analyte.

While the quest for maximal RIS is straightforward, the issue of the decay length is more complex. Binding of the analyte takes place at a certain distance from the metal surface, determined by the dimensions of the recognition layer and the analyte. If the decay length is small with respect to the dielectric layer thickness, the rapid exponential decay will lead to a weak response to the binding event. If, on the other hand, the decay length is large compared to the dielectric layer thickness, the analyte will occupy a small fraction of the sensing volume, leading, again, to a weak response. Thus, for optimal response a transducer has to be chosen such that the combined RIS and decay length maximize the response to the specific analyte–receptor system [37, 76, 77]. The decay length of the response of a given LSPR transducer can be determined experimentally using overlayers with a variable thickness, controlled on the nanometer scale. Recently we have obtained systematic distance sensitivity data for a series of island films, using electrostatic layer-by layer (LbL) assembly of polyelectrolyte multilayers [78]. This widely used approach is noted for its simplicity and repeatability [79]. To determine the effective decay length and RIS of Au island films of different thicknesses, polyelectrolyte multilayers were deposited on the island films using the standard LbL self-assembly procedure (Fig. 14.10a) [76, 78]. The LbL process was carried out until the characteristic parameters (plasmon peak wavelength and intensity) showed a tendency to stabilize.

Figure 14.10b, c presents, respectively, HRSEM plan-view images of gold island samples before and after coating with a polyelectrolyte multilayer, displaying a rather uniform polymer layer around the islands following LbL assembly. Figure 14.10d, e shows 3D isometric views of the same sample using different detectors, presenting the surface and internal composition. The thickness of the 40-layer film, determined from the images, is 40 ± 4 nm, in agreement with spectroscopic ellipsometry data for a similar multilayer prepared on a continuous Au substrate [76].

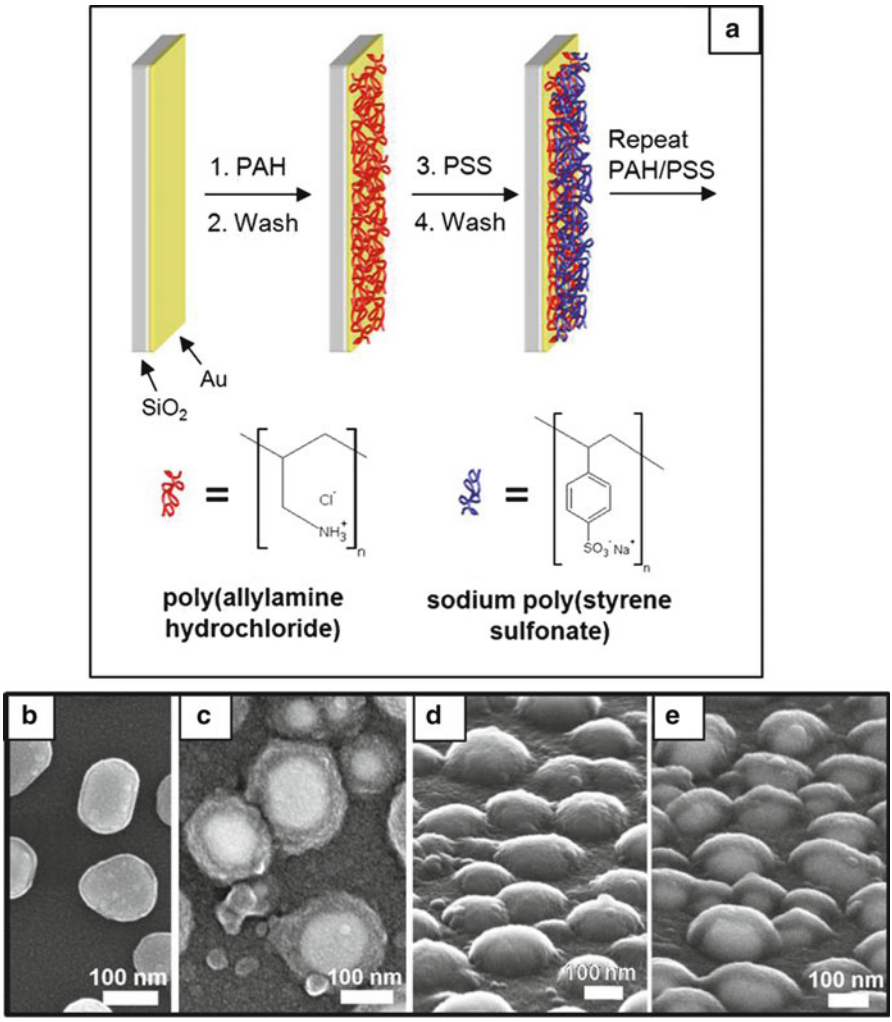

Fig. 14.10 Schematic representation of the polyelectrolyte layer-by layer (LbL) assembly procedure (**a**) and HRSEM images of 10 nm Au island films, annealed 10 h at 580°C, without (**b**) and with (**c**, **d**, **e**) a 40-layer polyelectrolyte overlayer. Plan view (**b**, **c**) and isometric projection (tilted 60° from normal) (**d**, **e**) are presented, the latter showing the surface (**d**) and internal composition (**e**). Samples were coated with 3 nm Cr prior to imaging (adapted with permission from Kedem et al. [76])

Representative spectra and SP peak wavelength and intensity for polyelectrolyte LbL assembly on 3 and 10 nm Au island films are shown in Fig. 14.11, exhibiting the increase in the decay length with nominal thickness. Figure 14.12 shows the SP wavelength shift and extinction intensity change for a 3 nm Au island film coated with polyelectrolyte multilayers of increasing thickness, as well as exponential fits to (14.2). Given the experimentally measured R (the response, as wavelength shift,

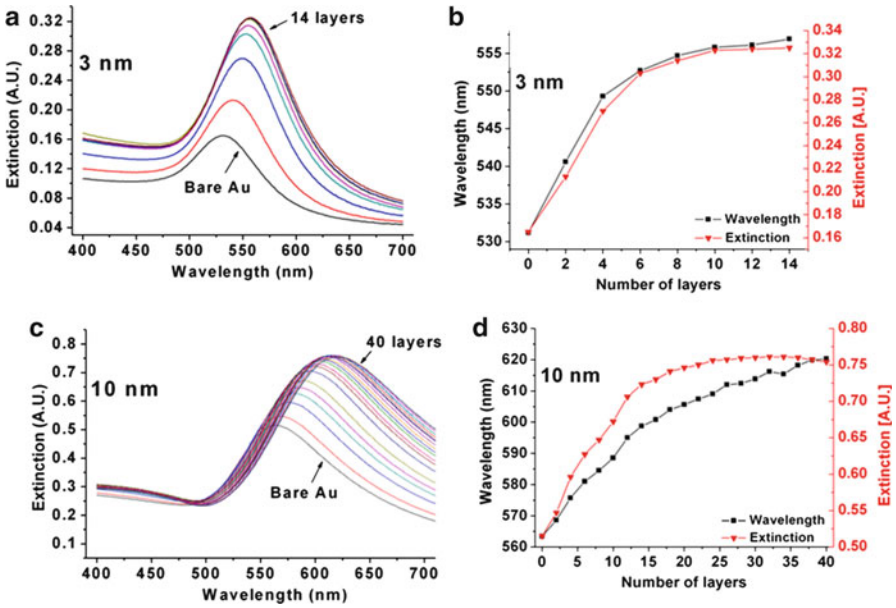

Fig. 14.11 Representative spectra (**a**, **c**) and SP peak wavelength and extinction (**b**, **d**); experimental points are connected for viewing convenience and for increasing number of polyelectrolyte layers assembled on Au island films of indicated nominal thicknesses, annealed 10 h at 580°C. Spectra recorded after assembly of each polyelectrolyte bilayer (adapted with permission from Kedem et al. [76])

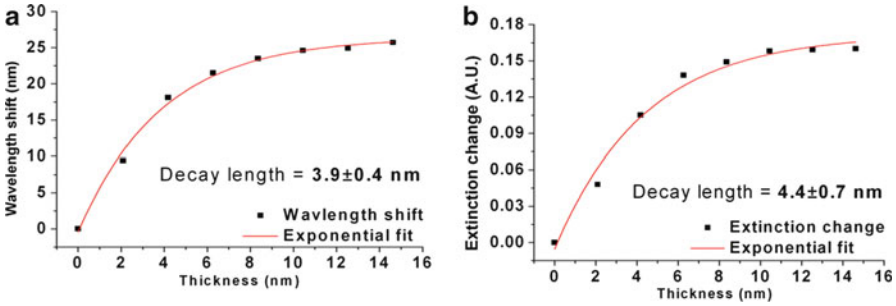

Fig. 14.12 Exponential fit of the SP wavelength shift (**a**) and extinction change (**b**) as a function of polyelectrolyte multilayer thickness; data extracted from Fig. 14.11b (adapted with permission from Kedem et al. [76])

R_λ or extinction change, R_{ext}) and d (polyelectrolyte multilayer thickness), the exponential regression provides the effective decay length l for wavelength (l_λ) or intensity (l_{ext}) change. Also extracted from the same exponential regression is the product $m\Delta\eta$ of the RIS, m (as m_λ or m_{ext}) and the difference in RI between the medium (in the present case, air) and the dielectric layer, $\Delta\eta$.

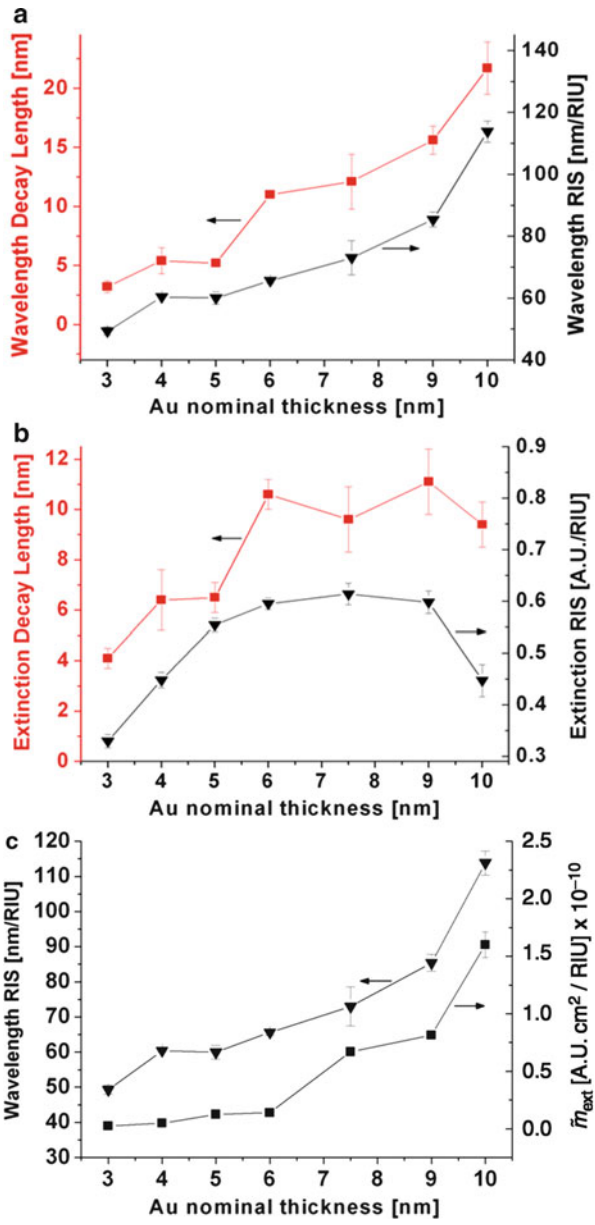

Fig. 14.13 Wavelength (**a**) and extinction (**b**) decay length and refractive index sensitivity (RIS) from exponential regression, and wavelength RIS and refractive index sensitivity normalized to the surface density of particles (**c**), vs. gold nominal thickness. *Error bars* represent standard deviation or average standard error (larger of the two) of four samples per Au thickness (adapted with permission from Kedem et al. [76])

Average decay length and RIS values, determined from the exponential fit, are summarized in Fig. 14.13. The wavelength decay length and RIS values exhibit a regular increase with increasing nominal thickness, i.e., average island size (Fig. 14.13a). The extinction decay length values increase with a tendency to

saturate, while the values of the extinction RIS show an initial increase and a decrease for larger islands (Fig. 14.13b). The difference in the general behavior and in the values of the wavelength and extinction decay length for larger islands may be related to the antireflective effect of the multilayer; a discussion of the latter is beyond the scope of this chapter [76].

The values of the wavelength RIS m_λ increase with Au layer thickness (Fig. 14.13a), while the corresponding extinction RIS m_{ext} reaches a maximum for 7.5 nm films, above which a decrease in the values is observed (Fig. 14.13b). To understand this apparent discrepancy it is useful to consider the physical basis of these variables. The two experimental parameters, m_λ and m_{ext}, are commonly treated in the same manner, as both are similarly used for sensing purposes. However, for a physical discussion the fundamental difference between the two becomes relevant. While the peak wavelength is a basic property of the islands and is independent of the quantity of particles in the optical path (other than coupling effects), the extinction is an additive variable which depends directly on the amount of particles sampled. In the present case, a higher surface density of islands will not affect m_λ (neglecting plasmon coupling effects, which are minor here), but will lead to a higher extinction, and correspondingly, to a higher RIS, m_{ext}. Therefore, while for sensing purposes the values of m_λ and m_{ext} are the relevant parameters, for a discussion of physical aspects of the system, including a comparison of different island films, the value of m_{ext} should be normalized to the surface density of particles. The normalized parameter $\tilde{m}_{ext} = m_{ext}/c$, where c is the number of islands per unit surface area, is thus a quantity-independent variable, analogous to m_λ as an intrinsic physical property of the island ensemble.

Values of $\tilde{m}_{ext}$ are plotted in Fig. 14.13c vs. film nominal thickness. The normalized values display a generally monotonous increase with Au film thickness, similar to the behavior of m_λ. Hence, while the larger islands exhibit larger values of $\tilde{m}_{ext}$, their low surface density results in lower values of m_{ext}.

As shown in Fig. 14.13a, films with larger islands feature both higher RIS and decay length values. Hence, the two parameters are strongly linked; the experimental relationship is presented in Fig. 14.14. The correlation between decay length and RIS in LSPR systems has been recognized previously [37, 77, 80], but not studied systematically before. The implications of this correlation are far-reaching in terms of sensing. Common analytes and recognition interfaces (notably, biological molecules) are smaller than the decay length of most LSPR systems, hence the larger the decay length, the weaker the transducer response. To maximize the response it is therefore imperative to find the optimal combination of RIS and decay length, which has to be tuned to the specific analyte and recognition layer dimensions.

Spatial Distribution of the Sensitivity of LSPR Transducers

In homogeneity of the LSPR transducer surface on the nanometer scale and the existence of regions with different local RIS present the possibility of spatial

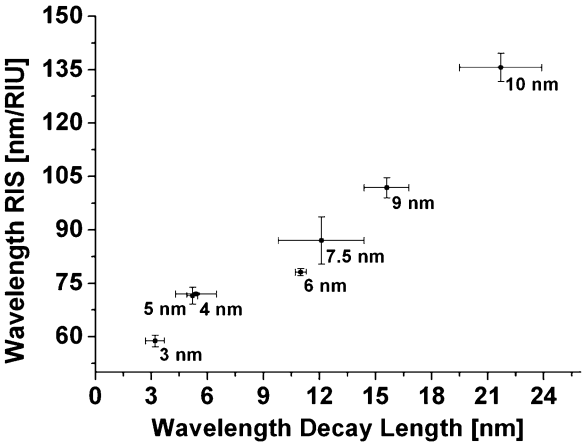

Fig. 14.14 RIS for wavelength shift as a function of wavelength decay length (both from exponential regression of LbL results), for the various Au nominal thicknesses studied (indicated) (adapted with permission from Kedem et al. [76])

distribution of different analyte binding sites [25]. Variation of the optical sensitivity for binding to the metal nanostructures and to the exposed hole bottom was demonstrated for nanohole arrays [39, 40, 81]. Hence, in the application of (14.1) and (14.2) to the analysis of the response of heterogeneous LSPR substrates, the bulk RIS m may represent a local value or a weighted average, depending on the particular spatial distribution of the bound analyte.

A basic issue in LSPR spectroscopy concerns the quantitative relationship between surface coverage by the analyte (in the sub-monolayer regime) and the LSPR response. We have addressed this point by studying the sensitivity of the SP band to change in the fractional coverage of a chromophoric self-assembled monolayer (SAM) on an Au island film, up to a full monolayer coverage [29, 30]. Au island films similar to the one presented in Fig. 14.1a were used as LSPR transducers, and the disulfide chromophoric molecule **1** (Fig. 14.15a) [29] or Co tetraphenylporphyrin (Co-TPP) [30] (not shown) served as a target analyte. The spectral separation between the molecular absorption band and the Au SP band allowed independent determination of the fractional surface coverage and the SP change at different stages of SAM formation. The results for a SAM of **1**, presented in Fig. 14.15, show a direct relationship between the two absorption bands. Hence, the wavelength and intensity of the SP band are linearly correlated with the chromophore absorption (Fig. 14.15b), the latter directly proportional to the fractional surface coverage by the SAM.

A linear correlation similar to the one shown in Fig. 14.15 was also observed for binding of Co-TPP to an imidazole receptor SAM on an Au island transducer, up to a monolayer coverage [30]. The latter established a linear response of the LSPR transducer to change of the analyte surface coverage in the case of analyte binding at a certain distance via a specific receptor layer.

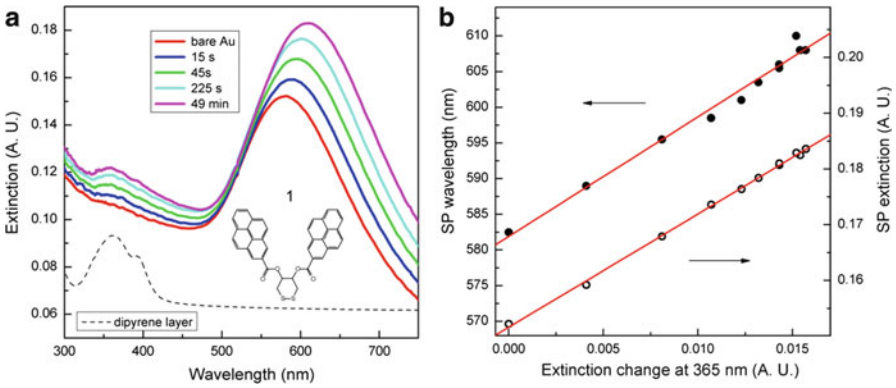

Fig. 14.15 Transmission UV–vis spectroscopy for the formation of a monolayer of **1** (*inset* in (**a**)) on a 2.5 nm (nominal thickness) Au island substrate prepared by evaporation on a quartz slide (see [29] for details). (**a**) Absolute spectra; the lower *black line* is a spectrum of a thick layer of **1**, obtained by evaporation of a drop on quartz (original spectrum divided by 3). (**b**) Correlation between the wavelength and extinction of the SP band and the maximum absorbance of **1** at 365 nm (both from (**a**)). UV–vis spectra were taken ex situ, after rinsing the sample with chloroform and ethanol and drying under a nitrogen stream (adapted with permission from Kalyuzhny et al. [29])

The examples described above provide a solid experimental basis for application of LSPR spectroscopy to quantitative analysis of analyte binding. The linear dependence of the SP optical signal on the analyte surface coverage allows quantification of kinetic data and determination of binding constants, either to the metal or to a receptor layer, using experimental and calculation schemes similar to those applied in the well-established propagating SPR technique.

LSPR Biosensing: Case Studies

General Considerations

Biosensing applications of LSPR transducers require preparation of a biorecognition interface exposing specific receptors to target analytes. In general, immobilization of the receptors follows established schemes developed for the preparation of biorecognition layers [82]. Introduction of a recognition interface of a given thickness between the Au islands and the analyte should be taken into account in the calculation of the response of the LSPR transducer. Assuming an exponential dependence of the kind presented in (14.2), the response of an LSPR transducer coated with a recognition interface of a thickness d_i to binding of a specific analyte of an effective dimension d_a is given by (14.3):

$$R = m(\Delta\eta)\exp(-d_i/l)[1 - \exp(-d_a/l)] \tag{14.3}$$

Equation (14.3) indicates that changes in the thickness of the biological interface d_i are expected to affect the sensitivity of the LSPR systems. Therefore, maximizing the LSPR transducer response to a given analyte requires optimization, taking into account the bulk RIS (m), the decay length (l), and the thicknesses of the recognition interface (d_i) and analyte (d_a) [37, 76, 77].The influence of these parameters on the LSPR response in model biosensing systems is demonstrated below.

Note that in the present chapter we only discuss LSPR spectroscopy carried out in the transmission mode. However, the sensitivity can be enhanced by the choice of measurement configuration, i.e., scattering, transmission, or reflection; additional work in this direction is needed [83, 84].

LSPR Immunosensing

Immunoglobulin (IgG) antibody–antigen recognition plays a major role in the immune system. To demonstrate LSPR sensing of protein–protein recognition, the specific interactions of rabbit and mouse IgG antigens with anti-rabbit and anti-mouse IgG antibodies were studied by LSPR spectroscopy [67].

The LSPR transducers comprised 5 nm (nominal thickness) Au island films prepared by evaporation on silanized glass followed by annealing 20 h at 200°C (Fig. 14.1e), subsequently derivatized with a biological interface (IgG antigens) for IgG antibody recognition/binding. A schematic representation of the stepwise procedure for functionalization of the Au island films is shown in Fig. 14.16. To show the effect of the recognition interface structure and dimensions, three types of interfaces were studied, presented as routes **1**, **2**, and **3** in Fig. 14.16. In route **1** the specific receptor (antigen) was immobilized directly on the bare Au island surface [85]; in route **2** the Au islands were coated with a monolayer of 3-mercaptopropyl trimethoxysilane (MPTS) [62]; while in route **3** the MPTS was further modified with a ca. 2 nm sol–gel derived silica layer [62]. In routes **2** and **3** the silane or silica surface, respectively, was chemically modified in a stepwise manner to expose carboxylate functionalities, capable of covalently linking to amino groups of the antigen by forming an amide bond.

An issue of major importance is the known instability of Au island films toward immersion in various solvents and drying. We have previously shown that Au island films can be stabilized by coating the islands with a thin (ca. 2 nm) sol–gel derived silica layer (as in route **3**, Fig. 14.16) [62]. In the present case we found that all three routes led to stable transducers with biologically active protein (antigen) layers, showing effective antibody recognition [67].

Spectroscopic and imaging results of four cross-experiments, two specific and two nonspecific, are shown in Fig. 14.17. In the two cases of specific binding (rabbit–anti-rabbit and mouse–anti-mouse, Fig. 14.17a, c) the difference spectra show substantial increase of ca. 0.04 a.u. in plasmon peak intensity, while in the two nonspecific cases (rabbit–anti-mouse and mouse–anti-rabbit, Fig. 14.17b, d) the spectra before and after antibody binding are nearly indistinguishable and the

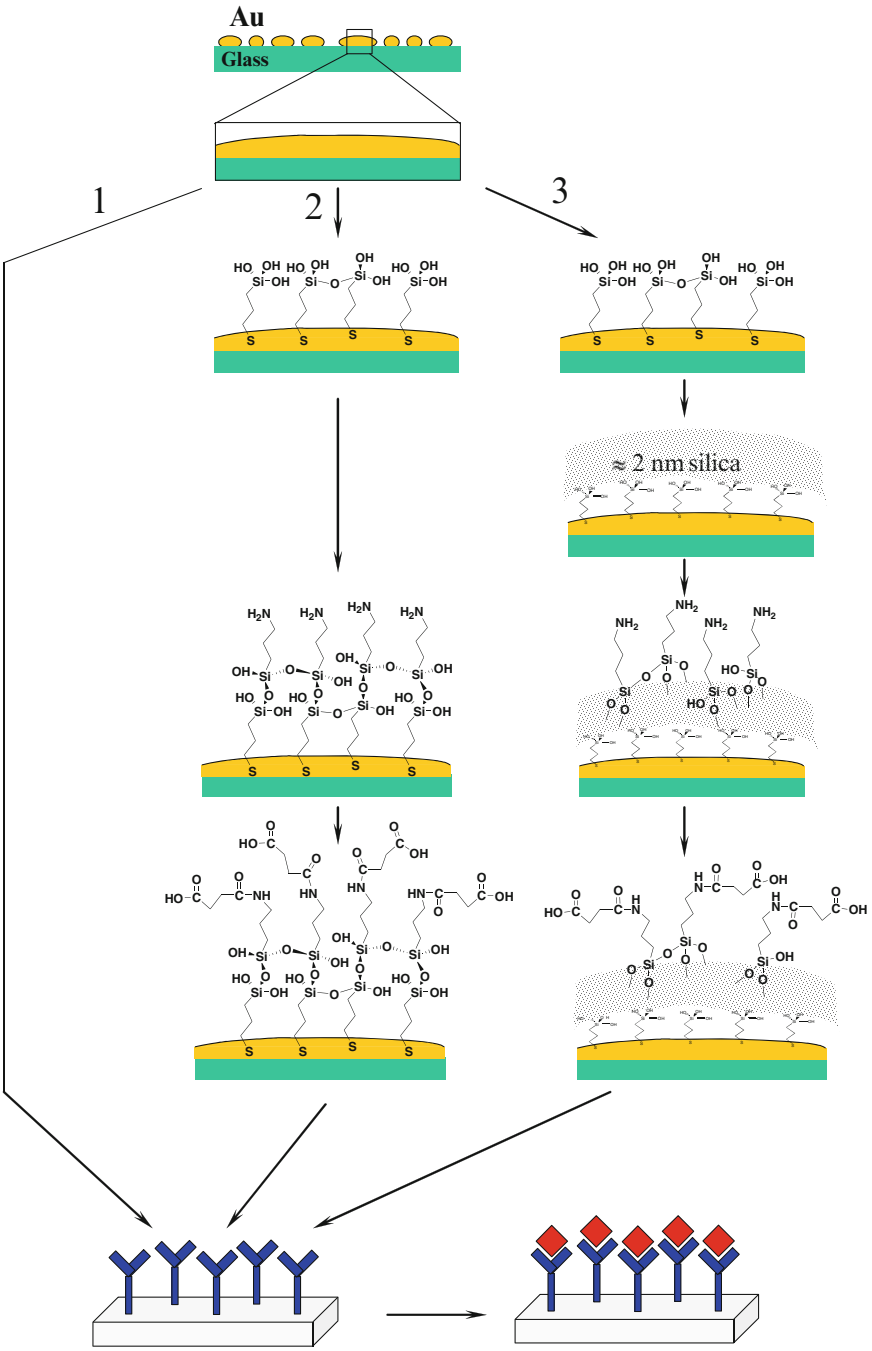

Fig. 14.16 Schematic presentation of the stepwise procedures for the derivatization of Au island films with a layer of antigens, followed by antibody binding. The three routes leading to the different recognition interfaces are *numbered* (adapted with permission from Bendikov et al. [67])

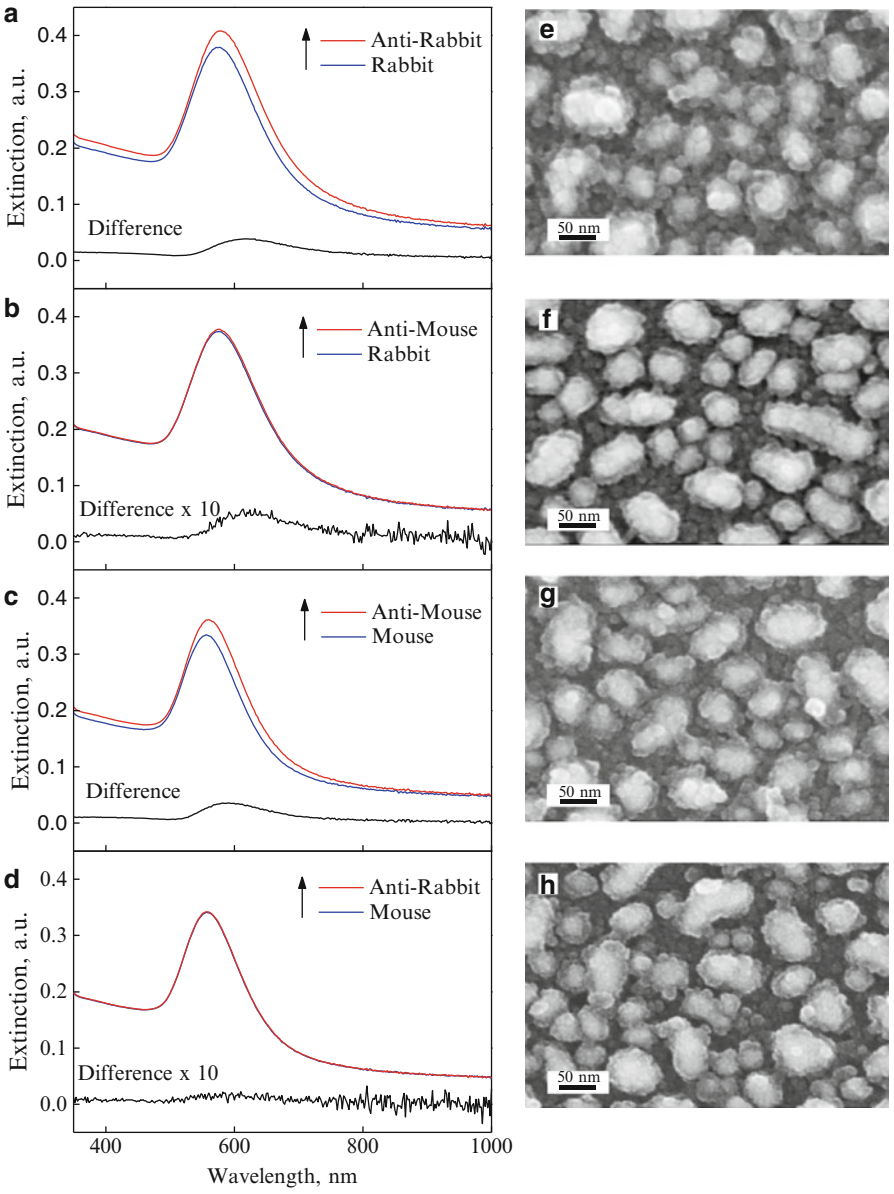

Fig. 14.17 Specific recognition of IgG antibodies; experiments carried out according to route **3** (Fig. 14.16) using 5 nm Au island films, annealed 20 h at 200°C. (**a**–**d**) Absolute and difference spectra for two specific and two nonspecific antibody–antigen interactions (indicated), showing the last step consisting of antibody binding to antigen-derivatized surfaces (see Fig. 14.16). (**e**–**h**) HRSEM images corresponding to the spectra in (**a**–**d**), showing the final state after specific/nonspecific antibody binding (adapted with permission from Bendikov et al. [67])

difference spectra (expanded $\times 10$) show insignificant change in SP peak intensity, i.e., minimal nonspecific binding.

The respective HRSEM images (Fig. 14.17e–h) support the spectroscopic data. Specific antibody binding (Fig. 14.17e, g) is seen as Au islands heavily covered with protein molecules, while the images corresponding to the nonspecific cases (Fig. 14.17f, h) show a thinner protein coating, consistent with no antibody binding to the antigen layer.

The results presented in Fig. 14.17 demonstrate the applicability of Au island based LSPR transducers to monitoring protein–protein interactions. The effect of the recognition interface thickness on the optical response was evaluated by comparing the immunosensing results obtained with interfaces prepared according to routes **1**–**3** (Fig. 14.16), using rabbit IgG protein as the antigen. The maximum SP intensity difference for the antibody binding step was 0.067, 0.055, and 0.039 a.u. for routes **1**–**3**, respectively, in qualitative agreement with the increasing thickness of the recognition interface (d_i in (14.3)).

Carbohydrate–Protein Interactions: LSPR Sensing and System Optimization

Carbohydrate–protein interactions are a major factor in fundamental biological processes, such as cell-to-cell adhesion and communication [86, 87], and host–pathogen recognition [88].

Study of such interactions is therefore crucial for the understanding of basic biological processes, as well as for the development of biosensors, primarily for diagnostics and drug development. For a demonstration of LSPR sensing of such interactions, the specific recognition between the lectin Concavalin A (Con A) from *Canavalia ensiformis* and the sugar mannose [89] was selected [66]. Binding of Con A to mannose-functionalized linkers in LSPR experiments was reported previously [90, 91], making it a good model system.

Figure 14.18 shows schematically the set of experiments carried out in order to demonstrate specific recognition between Con A and mannose immobilized on Au island transducers. The islands were derivatized with synthetically modified carbohydrates, to obtain LSPR transducers for monitoring, quantifying, and imaging of mannose–Con A interactions. These include specific interaction of Con A with mannose-linker **2** (Fig. 14.18a), as well as three controls, i.e., no SAM (Fig. 14.18b), a SAM of linker **1** (Fig. 14.18c), and a SAM of the nonspecific galactose-linker **3** (Fig. 14.18d). Transmission spectra for the series of experiments described in Fig. 14.18 are shown in Fig. 14.19 (transducers: 5.0 nm Au films, annealed 10 h at 570°C) using, for convenience, the same A–D notation as in Fig. 14.18. The increase in intensity and red shift of the SP band observed after incubation of the transducers with molecules **1**–**3** (Fig. 14.19a, c, d) indicate the formation of the respective SAMs on the Au island films.

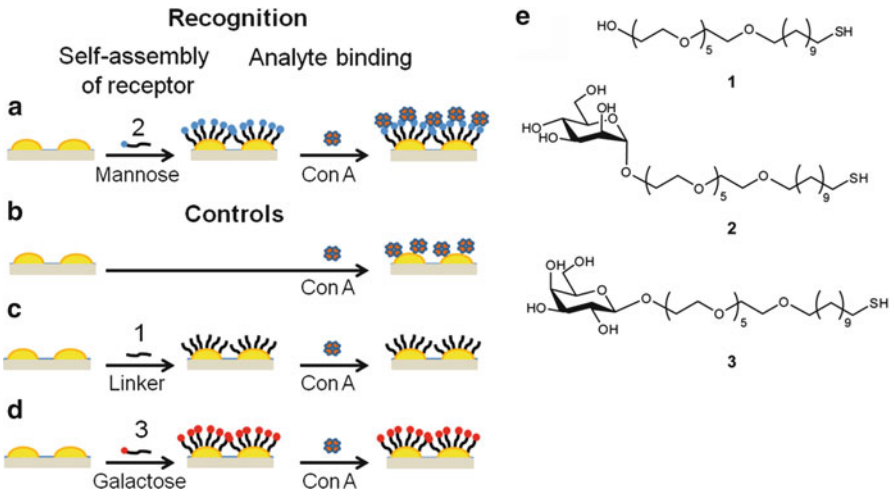

Fig. 14.18 (**a**–**d**) Schematic presentation of carbohydrate–protein recognition and control experiments using Au island transducers. (**a**) Specific binding of Concavalin A (Con A) to a self-assembled monolayer (SAM) of **2** (mannose-linker); (**b**) nonspecific adsorption of Con A on bare Au; (**c**, **d**) nonspecific interaction of Con A with SAMs of **1** (linker) and **3** (galactose-linker), respectively. (**e**) Chemical structure of molecules **1**–**3** (adapted from Bellapadrona et al. [66])

Specific recognition of Con A was assayed using the scheme in Fig. 14.18 by incubation of the different transducers with 1 μM solution of Con A. Figure 14.19a shows a marked response to specific binding of Con A to the mannose SAM, evident as a distinct increase in the maximum intensity and a red shift of the SP band position. A control experiment with no SAM showed the expected binding of Con A directly to the bare Au (Fig. 14.19b). On the other hand, when the Au island transducers were coated with a linker SAM or the nonspecific galactose SAM, no response was observed to Con A (Fig. 14.19c, d).

Visual evidence for specific mannose–Con A binding is obtained using HRSEM imaging of samples which underwent fixation, staining, and coating with 3 nm sputtered Cr [67]. The images are presented in Fig. 14.20; note that the grainy texture results from the Cr layer. Binding of Con A to the mannose SAM is clearly seen in Fig. 14.20b as an added layer on the Au islands with a distinctly different morphology, reminiscent of the imaged protein layers in Fig. 14.17 [67], whereas the images corresponding to the linker and galactose SAMs (Fig. 14.20d, f) appear identical to the bare Au islands.

As discussed in section "Sensitivity of LSPR Transducers," optimization of LSPR sensors for an analyte and recognition interface of given dimensions requires a choice of transducer for which the combined RIS and decay length produce a maximal signal. To perform optimization of LSPR transducers for Con A recognition, Au island films of 1.5, 2.5, 5.0, and 10 nm, annealed 10 h at 570°C, were treated with PEG-silane, derivatized with a SAM of mannose-linker and incubated in Con A, as depicted in Fig. 14.18a. The optical response to the sequence of treatments was measured and changes in the spectral parameters accompanying Con A binding (i.e., the last step in Fig. 14.18a) were compared for the different transducers.

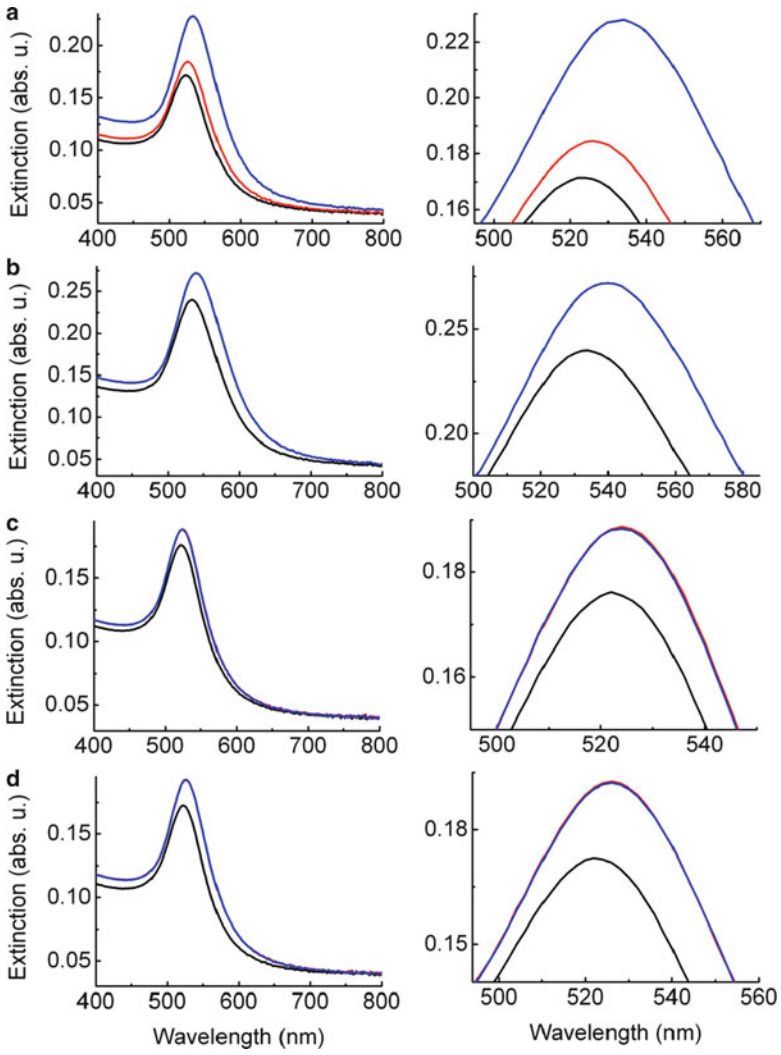

Fig. 14.19 Localized surface plasmon resonance (LSPR) spectra of 5.0 nm (nominal thickness) Au island films, annealed 10 h at 570°C. (**a**–**d**) correspond to the experiments depicted in Fig. 14.18. The different spectra were recorded after modification with PEG-silane to prevent protein binding to the glass substrate between islands (*black lines*); formation of a carbohydrate or linker SAM (*red lines*); and incubation in Con A (*blue lines*). Note that in (**c**) and (**d**) the *red* and *blue lines* coincide (adapted from Bellapadrona et al. [66])

Figure 14.21 summarizes the results of this series of experiments, showing the SP extinction change at a constant wavelength (chosen for each transducer) as well as the plasmon peak shift. The results in Fig. 14.21 indicate a general trend, i.e., the response, in terms of both extinction intensity and wavelength shift, shows a maximum for Au island films of intermediate thickness (2.5–5.0 nm). These Au

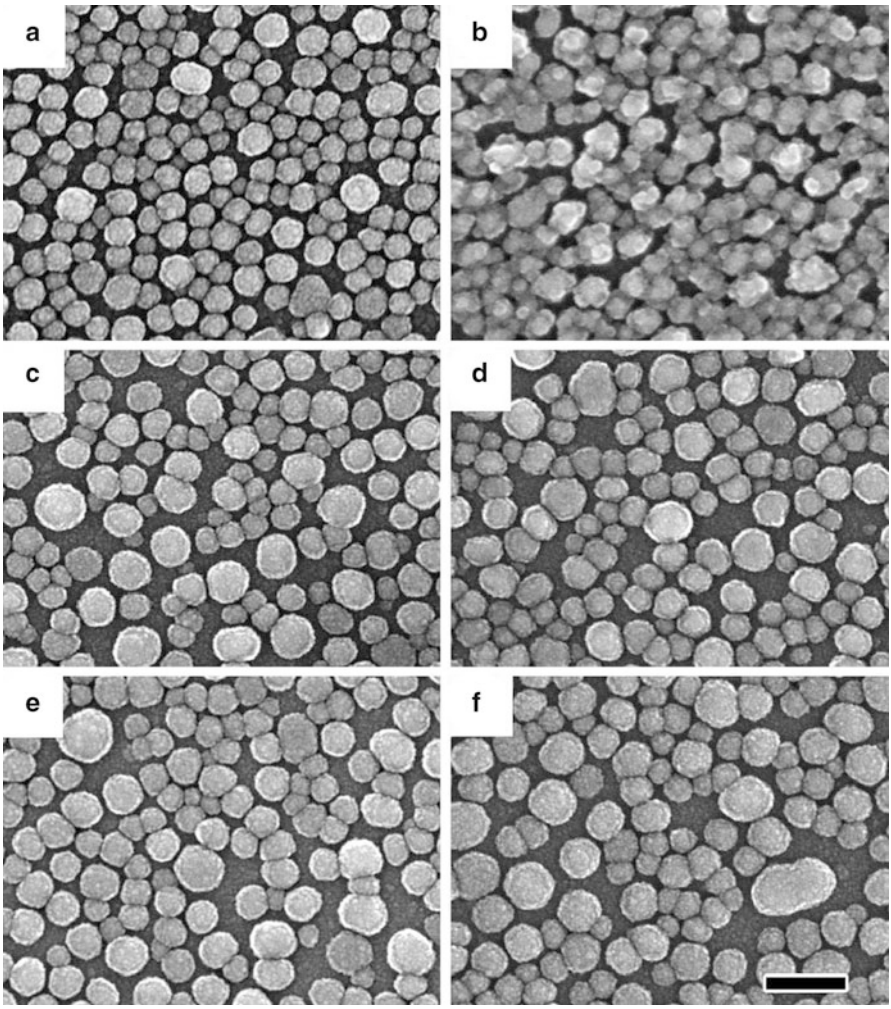

Fig. 14.20 HRSEM images of Au island films (as in Fig. 14.19) after formation of SAMs of (**a**) **2** (mannose); (**c**) **1** (linker); (**e**) **3** (galactose). (**b**), (**d**), and (**f**) are respective images after incubation in Con A. All samples were fixated, stained, and coated with 3 nm sputtered Cr. *Scale bar*: 100 nm (adapted from Bellapadrona et al. [66])

transducers therefore represent an optimal combination of RIS and decay length that best fits the analyte and recognition layer thickness [76].

LSPR Kinetic Measurements

In biorecognition systems, kinetic measurements using a flow-cell configuration present a standard scheme for lowering the detection limit as well as for determination of affinity constants of biomolecules. The latter is achieved using

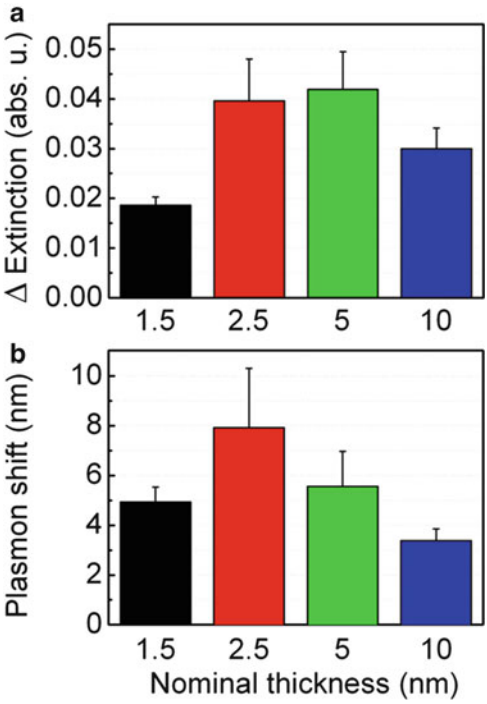

Fig. 14.21 Optimization of the LSPR transducer response using Au island films of different nominal thicknesses (1.5, 2.5, 5.0, and 10 nm, annealed 10 h at 570°C). Changes in extinction at a constant wavelength (**a**) and in plasmon wavelength (**b**) are shown for binding of Con A to mannose-modified transducers. The constant wavelengths in (**a**), chosen near the maximum differential extinction, were 545, 554, 545, and 609 nm for Au transducers of 1.5, 2.5, 5.0, and 10 nm, respectively (adapted from Bellapadrona et al. [66])

measurements with variable concentration of the analyte. Application to our LSPR systems was exemplified using the binding of Con A to a mannose-linker SAM, as described in section "Carbohydrate–Protein Interactions: LSPR Sensing and System Optimization." The kinetic measurements were carried out using a flow system comprising a controlled syringe-based pumping unit, manual selection valves, and a micro flow cell (Fig. 14.22) [66]. The kinetics of Con A binding to a mannose SAM were monitored using 5.0 nm Au island films, annealed 10 h at 570°C, chosen to provide a high sensitivity (Fig. 14.21).

The results in Fig. 14.22 confirm the specificity of the LSPR transducer response under flow conditions. Specific binding of Con A to the mannose SAM is evident as a sizeable extinction increase, followed by a slow release upon change to buffer solution. On the other hand, essentially no response was detected with the linker-coated transducer, and only a weak response with the nonspecific galactose-functionalized transducer.

The kinetics of Con A binding to the mannose-coated transducer were measured as a function of protein concentration (1.0, 0.5, 0.25, 0.1 μM, 50, 25, 5.0 nM) in order to determine the kinetic parameters of the interaction between Con A and mannose (Fig. 14.23a, b). In kinetic terms, the formation of a [Con A–mannose] complex can be described by (14.4):

$$[\text{Con A}]_{(\text{solution})} + [\text{mannose}]_{(\text{surface})} \underset{k_{\text{off}}}{\overset{k_{\text{on}}}{\rightleftharpoons}} [\text{Con A} - \text{mannose}]_{(\text{surface})} \tag{14.4}$$

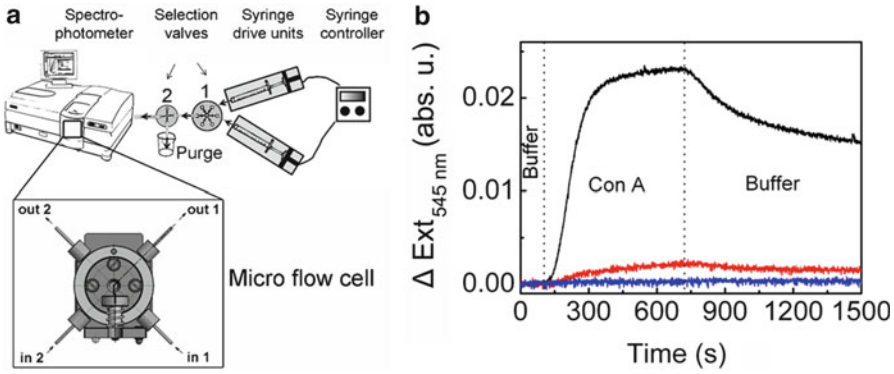

Fig. 14.22 (**a**) Schematic presentation of the home-made flow system and the micro flow cell (60 μL internal volume) used for the kinetic experiments. (**b**) Con A association and dissociation kinetics, recorded as change in the extinction at a constant wavelength of 545 nm in the micro flow cell. The flow sequence included buffer solution, 0.5 μM Con A in buffer, and buffer solution again. Transducers: 5 nm Au island films, annealed 10 h at 570°C, modified with SAMs of **2** (mannose) (*black line*), **1** (linker) (*blue line*), and **3** (galactose) (*red line*) (adapted from Bellapadrona et al. [66])

in which the association (k_{on}) and dissociation (k_{off}) rate constants determine the surface concentration of [Con A–mannose] complex at each time, given by [92]:

$$[\text{Con A}-\text{mannose}]_{(t)} = [\text{Con A}-\text{mannose}]_{(\infty)}[1 - \exp(-t/\tau)] \tag{14.5}$$

The response of the LSPR transducers is directly proportional to the surface concentration of the complex (section "Spatial Distribution of the Sensitivity of LSPR Transducers"), hence for extinction change:

$$\Delta_{\text{ext(t)}} = \Delta_{\text{ext}(\infty)}[1 - \exp(-t/\tau)] \tag{14.6}$$

and

$$1/\tau = k_{on}[\text{Con A}] + k_{off} \tag{14.7}$$

Figure 14.23c shows data analysis according to (14.7). The slope and intercept were obtained by linear fitting of the $(1/\tau)$ vs. [Con A] data, giving the values $k_{on} = 2.0 \times 10^4\ \text{M}^{-1}\ \text{s}^{-1}$ and $k_{off} = 2.6 \times 10^{-3}\ \text{s}^{-1}$ for the association and dissociation rate constants, respectively. The apparent association equilibrium constant is $K_a = k_{on}/k_{off} = 7.7\ \mu\text{M}$.

Table 14.1 presents a comparison of our measured kinetic values with literature data on the interaction between Con A and mannose derivatives, obtained using a variety of techniques. The wide variability of the literature values ($10^3 < k_{on} < 10^5\ \text{M}^{-1}\ \text{s}^{-1}$; $10^{-2} < k_{off} < 10^{-4}\ \text{s}^{-1}$) suggests a marked dependence on the experimental conditions and the technique used. Our LSPR-derived k_{on} and k_{off} values fit well within the range of published values.

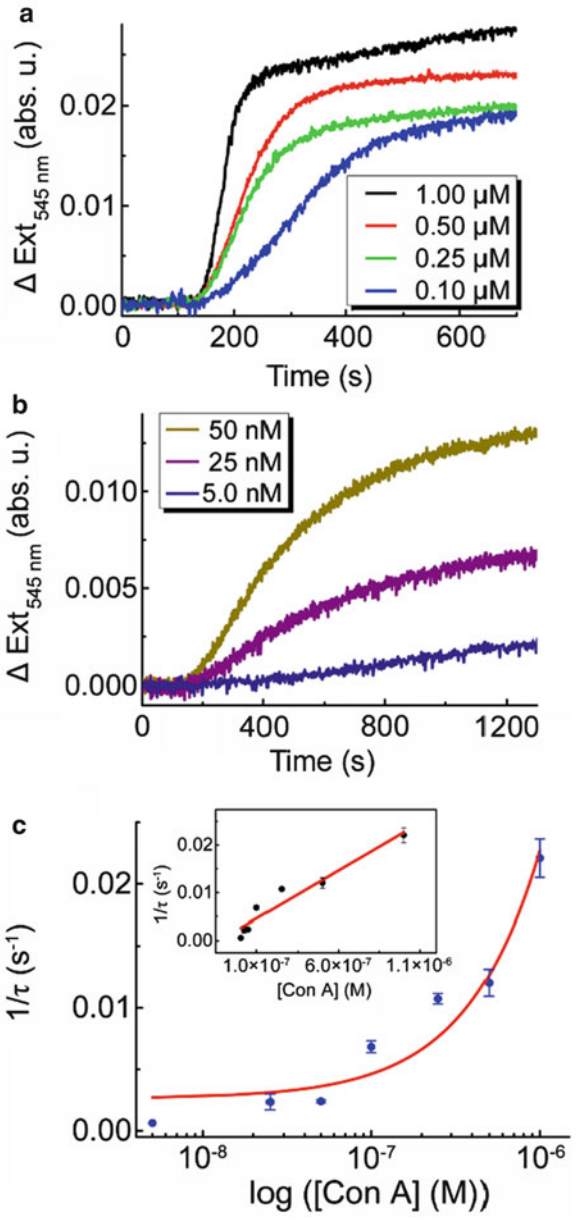

Fig. 14.23 Determination of the binding affinity of Con A to a mannose SAM. The kinetic curves in (**a**) and (**b**) were obtained as in Fig. 14.22, using mannose-functionalized transducers and different Con A concentrations. (**c**) Treatment of the results according to (14.7), showing logarithmic and linear scales (adapted from Bellapadrona et al. [66])

The results indicate that application of optimized Au island based LSPR transducers in a flow mode enables lowering of the detection limit to the nM range, as well as determination of the association (k_{on}) and dissociation (k_{off}) rate constants for the interaction between proteins and immobilized carbohydrates.

Table 14.1 Kinetic parameters for the interaction between Con A and mannose derivatives, obtained using a variety of techniques

Method	k_{on} (M^{-1} s^{-1})	k_{off} (s^{-1})	References
SPR	5.72×10^4	2.48×10^{-4}	[94]
SPR	1.07×10^5	4.47×10^{-3}	[95]
QCM	$(4 \pm 1) \times 10^4$	$(1.2 \pm 0.2) \times 10^{-2}$	[96]
QCM	$(1.4 \pm 0.2) \times 10^5$	$(7 \pm 2) \times 10^{-3}$	[96]
LSPR	5.2×10^3	2.2×10^{-3}	[91]
LSPR	7.4×10^3	1.0×10^{-3}	[91]
LSPR	2.0×10^4	2.6×10^{-3}	[66]

Conclusions

Despite substantial progress in understanding the condition needed for obtaining high sensitivity of LSPR transducers, a gap still exists between the advanced methods of preparation of individual nanostructures and the possibility of technological scale-up for mass-production necessary for actual sensing applications. It has been commonly argued that "uniformity in nanoparticle size, shape, and composition improve sensitivity and reliability" of LSPR transducers [93], implying that a major effort in the preparation of practical LSPR systems should be directed to achieving well-defined shape and spatial positioning of the plasmonic nanostructures. The present results show that LSPR transducers comprised of random evaporated Au films present a viable alternative to those based on ordered arrays. In fact, the LSPR sensitivity achieved with random nanoisland ensembles is quite similar to that demonstrated with uniformly shaped arrays. Moreover, optimization of the average island shape, as well as inducing spatially selective analyte binding (see section "Introduction"), can be attained, to some extent, in the random systems as well. Therefore, low-cost LSPR transducers based on evaporated random island ensembles are promising candidates for actual sensing applications.

References

1. Kreibig U, Vollmer M. Optical properties of metal clusters. Berlin: Springer; 1995.
2. Mie G. Beiträge zur Optik trüber Medien, speziell kolloidalen Metallösungen. Ann Phys. 1908;25:377–445.
3. Maxwell-Garnett JC. Colours in metal glasses and in metallic films. Philos Trans R Soc Lond A. 1904;203:385–420.
4. Leuvering JHW, Thal P, Waart MVD, Schuurs A. Sol particle agglutination immunoassay for human chorionic-gonadotropin. Fresenius Z Anal Chem. 1980;301:132.
5. Mirkin CA, Letsinger RL, Mucic RC, Storhoff JJ. A DNA-based method for rationally assembling nanoparticles into macroscopic materials. Nature. 1996;382:607–9.
6. Papavassiliou GC. Optical absorption spectra of silver, gold, and copper thin films chemically deposited on quartz plates. Z Phys Chem (Leipzig). 1976;257:241–8.
7. Papavassiliou GC. Optical properties of small inorganic and organic metal particles. Prog Solid State Chem. 1979;12:185–271.

8. Doremus RH. Optical properties of thin metallic films in island form. J Appl Phys. 1966;37:2775–81.
9. Royer P, Goudonnet JP, Warmack RJ, Ferrell TL. Substrate effects on surface-plasmon spectra in metal-island films. Phys Rev B. 1987;35:3753–9.
10. Jensen TR, Duval ML, Kelly KL, Lazarides AA, Schatz GC, Van Duyne RP. Nanosphere lithography: effect of the external dielectric medium on the surface plasmon resonance spectrum of a periodic array of sliver nanoparticles. J Phys Chem B. 1999;103:9846–53.
11. Chumanov G, Sokolov K, Gregory BW, Cotton TM. Colloidal metal-films as a substrate for surface-enhanced spectroscopy. J Phys Chem. 1995;99:9466–71.
12. Underwood S, Mulvaney P. Effect of the solution refractive-index on the color of gold colloids. Langmuir. 1994;10:3427–30.
13. Noguez C. Surface plasmons on metal nanoparticles: the influence of shape and physical environment. J Phys Chem C. 2007;111:3806–19.
14. Myroshnychenko V, Rodriguez-Fernandez J, Pastoriza-Santos I, Funston AM, Novo C, Mulvaney P, Liz-Marzan LM, de Abajo FJG. Modelling the optical response of gold nanoparticles. Chem Soc Rev. 2008;37:1792–805.
15. Zhao J, Pinchuk AO, McMahon JM, Li SZ, Ausman LK, Atkinson AL, Schatz GC. Methods for describing the electromagnetic properties of silver and gold nanoparticles. Acc Chem Res. 2008;41:1710–20.
16. Smajic J, Hafner C, Raguin L, Tavzarashvili K, Mishrikey M. Comparison of numerical methods for the analysis of plasmonic structures. J Comput Theor Nanosci. 2009;6:763–74.
17. Jeanmaire DL, Vanduyne RP. Surface Raman spectroelectrochemistry: 1. Heterocyclic, aromatic, and aliphatic-amines adsorbed on anodized silver electrode. J Electroanal Chem. 1977;84:1–20.
18. Moskovits M. Surface-roughness and enhanced intensity of Raman-scattering by molecules adsorbed on metals. J Chem Phys. 1978;69:4159–61.
19. Lin XM, Cui Y, Xu YH, Ren B, Tian ZQ. Surface-enhanced Raman spectroscopy: substrate-related issues. Anal Bioanal Chem. 2009;394:1729–45.
20. Camden JP, Dieringer JA, Zhao J, Van Duyne RP. Controlled plasmonic nanostructures for surface-enhanced spectroscopy and sensing. Acc Chem Res. 2008;41:1653–61.
21. Schlegel VL, Cotton TM. Silver-island films as substrates for enhanced Raman-scattering—effect of deposition rate on intensity. Anal Chem. 1991;63:241–7.
22. Meriaudeau F, Downey TR, Passian A, Wig A, Ferrell TL. Environment effects on surface-plasmon spectra in gold-island films potential for sensing applications. Appl Opt. 1998;37:8030–7.
23. Gluodenis M, Manley C, Foss CA. In situ monitoring of the change in extinction of stabilized nanoscopic cold particles in contact with aqueous phenol solutions. Anal Chem. 1999;71:4554–8.
24. Haes AJ, Van Duyne RP. A nanoscale optical biosensor: sensitivity and selectivity of an approach based on the localized surface plasmon resonance spectroscopy of triangular silver nanoparticles. J Am Chem Soc. 2002;124:10596–604.
25. Haes AJ, Zou SL, Schatz GC, Van Duyne RP. Nanoscale optical biosensor: short range distance dependence of the localized surface plasmon resonance of noble metal nanoparticles. J Phys Chem B. 2004;108:6961–8.
26. Malinsky MD, Kelly KL, Schatz GC, Van Duyne RP. Chain length dependence and sensing capabilities of the localized surface plasmon resonance of silver nanoparticles chemically modified with alkanethiol self-assembled monolayers. J Am Chem Soc. 2001;123:1471–82.
27. Takei H. Biological sensor based on localized surface plasmon associated with surface-bound Au/polystyrene composite microparticles. Proc SPIE. 1998;3515:278–83.
28. Himmelhaus M, Takei H. Cap-shaped gold nanoparticles for an optical biosensor. Sens Actuators B. 2000;63:24–30.
29. Kalyuzhny G, Schneeweiss MA, Shanzer A, Vaskevich A, Rubinstein I. Differential plasmon spectroscopy as a tool for monitoring molecular binding to ultrathin gold films. J Am Chem Soc. 2001;123:3177–8.

30. Kalyuzhny G, Vaskevich A, Ashkenasy G, Shanzer A, Rubinstein I. UV/vis spectroscopy of metalloporphyrin and metallophthalocyanine monolayers self-assembled on ultrathin gold films. J Phys Chem B. 2000;104:8238–44.
31. Kalyuzhny G, Vaskevich A, Schneeweiss MA, Rubinstein I. Transmission surface-plasmon resonance (T-SPR) measurements for monitoring adsorption on ultrathin gold island films. Chem Eur J. 2002;8:3850–7.
32. Doron-Mor I, Barkay Z, Filip-Granit N, Vaskevich A, Rubinstein I. Ultrathin gold island films on silanized glass. Morphology and optical properties. Chem Mater. 2004;16:3476–83.
33. Englebienne P. Use of colloidal gold surface plasmon resonance peak shift to infer affinity constants from the interactions between protein antigens and antibodies specific for single or multiple epitopes. Analyst. 1998;123:1599–603.
34. Khlebtsov NG, Melnikov AG, Dykman LA, Bogatyrev VA. Optical properties and biomedical applications of nanostructures based on gold and silver bioconjugates. In: Videen G, editor. Photopolarimetry in remote sensing. Dordrecht: Kluwer Academic; 2004. p. 265–308.
35. Englebienne P, Van Hoonacker A, Verhas M. Surface plasmon resonance: principles, methods and applications in biomedical sciences. Spectrosc Int J. 2003;17:255–73.
36. Nath N, Chilkoti A. A colorimetric gold nanoparticle sensor to interrogate biomolecular interactions in real time on a surface. Anal Chem. 2002;74:504–9.
37. Nath N, Chilkoti A. Label-free biosensing by surface plasmon resonance of nanoparticles on glass: optimization of nanoparticle size. Anal Chem. 2004;76:5370–8.
38. Okamoto T, Yamaguchi I, Kobayashi T. Local plasmon sensor with gold colloid monolayers deposited upon glass substrates. Opt Lett. 2000;25:372–4.
39. Dahlin A, Zach M, Rindzevicius T, Kall M, Sutherland DS, Hook F. Localized surface plasmon resonance sensing of lipid-membrane-mediated biorecognition events. J Am Chem Soc. 2005;127:5043–8.
40. Rindzevicius T, Alaverdyan Y, Dahlin A, Hook F, Sutherland DS, Kall M. Plasmonic sensing characteristics of single nanometric holes. Nano Lett. 2005;5:2335–9.
41. Brolo AG, Gordon R, Leathem B, Kavanagh KL. Surface plasmon sensor based on the enhanced light transmission through arrays of nanoholes in gold films. Langmuir. 2004;20:4813–5.
42. Aussenegg FR, Brunner H, Leitner A, Lobmaier C, Schalkhammer T, Pittner F. The metal island coated swelling polymer over mirror system (micspoms)—a new principle for measuring ionic-strength. Sens Actuators B. 1995;29:204–9.
43. Hutter E, Pileni MP. Detection of DNA hybridization by gold nanoparticle enhanced transmission surface plasmon resonance spectroscopy. J Phys Chem B. 2003;107:6497–9.
44. Hedsten K, Fonollosa J, Enoksson P, Modh P, Bengtsson J, Sutherland DS, Dmitriev A. Optical label-free nanoplasmonic biosensing using a vertical-cavity surface-emitting laser and charge-coupled device. Anal Chem. 2010;82:1535–9.
45. McFarland AD, Van Duyne RP. Single silver nanoparticles as real-time optical sensors with zeptomole sensitivity. Nano Lett. 2003;3:1057–62.
46. Mock JJ, Smith DR, Schultz S. Local refractive index dependence of plasmon resonance spectra from individual nanoparticles. Nano Lett. 2003;3:485–91.
47. Raschke G, Kowarik S, Franzl T, Sonnichsen C, Klar TA, Feldmann J, Nichtl A, Kurzinger K. Biomolecular recognition based on single gold nanoparticle light scattering. Nano Lett. 2003;3:935–8.
48. Sannomiya T, Hafner C, Voros J. In situ sensing of single binding events by localized surface plasmon resonance. Nano Lett. 2008;8:3450–5.
49. Mayer KM, Hao F, Lee S, Nordlander P, Hafner JH. A single molecule immunoassay by localized surface plasmon resonance. Nanotechnology. 2010;21:255503.
50. Sepulveda B, Angelome PC, Lechuga LM, Liz-Marzan LM. LSPR-based nanobiosensors. Nano Today. 2009;4:244–51.
51. Beeram SR, Zamborini FP. Selective attachment of antibodies to the edges of gold nanostructures for enhanced localized surface plasmon resonance biosensing. J Am Chem Soc. 2009;131:11689–90.

52. Beeram SR, Zamborini FP. Purification of gold nanoplates grown directly on surfaces for enhanced localized surface plasmon resonance biosensing. ACS Nano. 2010;4:3633–46.
53. Krenn JR, Weeber JC, Dereux A, Bourillot E, Goudonnet JP, Schider B, Leitner A, Aussenegg FR, Girard C. Direct observation of localized surface plasmon coupling. Phys Rev B. 1999;60:5029–33.
54. Krenn JR, Wolf R, Leitner A, Aussenegg FR. Near-field optical imaging the surface plasmon fields of lithographically designed nanostructures. Opt Commun. 1997;137:46–50.
55. Zhang XY, Whitney AV, Zhao J, Hicks EM, Van Duyne RP. Advances in contemporary nanosphere lithographic techniques. J Nanosci Nanotechnol. 2006;6:1920–34.
56. Hanarp P, Sutherland DS, Gold J, Kasemo B. Control of nanoparticle film structure for colloidal lithography. Colloid Surf A. 2003;214:23–36.
57. Hanarp P, Kall M, Sutherland DS. Optical properties of short range ordered arrays of nanometer gold disks prepared by colloidal lithography. J Phys Chem B. 2003;107:5768–72.
58. Dmitriev A, Pakizeh T, Kall M, Sutherland DS. Gold-silica-gold nanosandwiches: tunable bimodal plasmonic resonators. Small. 2007;3:294–9.
59. Vaskevich A, Rubinstein I. Localized surface plasmon resonance (LSPR) spectroscopy in biosensing. In: Marks R, Cullen D, Lowe C, Weetall HH, Karube I, editors. Handbook of biosensors and biochips, vol. 1. Chichester: Wiley; 2007.
60. Karakouz T, Holder D, Goomanovsky M, Vaskevich A, Rubinstein I. Morphology and refractive index sensitivity of gold island films. Chem Mater. 2009;21:5875–85.
61. Karakouz T, Tesler AB, Bendikov TA, Vaskevich A, Rubinstein I. Highly-stable localized plasmon transducers obtained by thermal embedding of gold island films on glass. Adv Mater. 2008;20:3893–9.
62. Ruach-Nir I, Bendikov TA, Doron-Mor I, Barkay Z, Vaskevich A, Rubinstein I. Silica-stabilized gold island films for transmission localized surface plasmon sensing. J Am Chem Soc. 2007;129:84–92.
63. Doron-Mor I, Cohen H, Barkay Z, Shanzer A, Vaskevich A, Rubinstein I. Sensitivity of transmission surface plasmon resonance (T-SPR) spectroscopy: self-assembled multilayers on evaporated gold island films. Chem Eur J. 2005;11:5555–62.
64. Karakouz T, Vaskevich A, Rubinstein I. Polymer-coated gold island films as localized plasmon transducers for gas sensing. J Phys Chem B. 2008;112:14530–8.
65. Lahav M, Vaskevich A, Rubinstein I. Biological sensing using transmission surface plasmon resonance spectroscopy. Langmuir. 2004;20:7365–7.
66. Bellapadrona G, Tesler AB, Grünstein D, Hossain L, Kikkeri R, Seeberger PH, Vaskevich A, Rubinstein I. Optimization of localized surface plasmon resonance (LSPR) transducers for sensing carbohydrate-protein interactions. Anal Chem. 2012;84:232–40.
67. Bendikov TA, Rabinkov A, Karakouz T, Vaskevich A, Rubinstein I. Gold island film transducers for immunoglobulin proteins sensing. Anal Chem. 2008;80:7487–98.
68. Tesler AB, Chuntonov L, Karakouz T, Bendikov T, Haran G, Vaskevich A, Rubinstein I. Tunable localized plasmon transducers prepared by thermal dewetting of percolated evaporated gold films. J Phys Chem C. 2011;115:24642–52.
69. Norrman S, Andersson T, Granqvist CG, Hunderi O. Optical properties of discontinuous gold films. Phys Rev B. 1978;18:674–95.
70. Meli MV, Lennox RB. Surface plasmon resonance of gold nanoparticle arrays partially embedded in quartz substrates. J Phys Chem C. 2007;111:3658–64.
71. Natan MJ, Reiss BD, Keefe MH. Thermal immobilization of colloidal metal nanoparticles in a glass matrix. 2000-US32854 2001040132, 4 Dec 2000; 2001.
72. Karakouz T, Vaskevich A, Rubinstein I. Stabilization of gold nanoparticle films on glass by thermal embedding. ACS Appl Mater Interfaces. 2011;3:978–87.
73. Baram M, Kaplan WD. Intergranular films at Au-sapphire interfaces. J Mater Sci. 2006;41:7775–84.
74. Vaskevich A, Sehayek T, Rubinstein I. Mass thickness analysis of gold thin films using room temperature gas-phase chlorination. Anal Chem. 2009;81:2877–83.

75. Jung LS, Campbell CT, Chinowsky TM, Mar MN, Yee SS. Quantitative interpretation of the response of surface plasmon resonance sensors to adsorbed films. Langmuir. 1998;14:5636–48.
76. Kedem O, Tesler AB, Vaskevich A, Rubinstein I. Sensitivity and optimization of localized surface plasmon resonance (LSPR) transducers. ACS Nano. 2011;5:748–60.
77. Nusz GJ, Curry AC, Marinakos SM, Wax A, Chilkoti A. Rational selection of gold nanorod geometry for label-free plasmonic biosensors. ACS Nano. 2009;3:795–806.
78. Decher G, Hong J, Schmitt J. Buildup of ultrathin multilayer films by a self-assembly process: III. Consecutively alternating adsorption of anionic and cationic polyelectrolytes on charged surfaces. Thin Solid Films. 1992;210–211:831–5.
79. Decher G. Fuzzy nanoassemblies: toward layered polymeric multicomposites. Science. 2009;277:1232–7.
80. Svedendahl M, Chen S, Dmitriev A, Käll M. Refractometric sensing using propagating versus localized surface plasmons: a direct comparison. Nano Lett. 2009;9:4428–33.
81. Marie R, Dahlin AB, Tegenfeldt JO, Höök F. Generic surface modification strategy for sensing applications based on Au/SiO_2 nanostructures. Biointerphases. 2007;2:49–55.
82. Chen D, Wang G, Li J. Interfacial bioelectrochemistry: fabrication, properties and applications of functional nanostructured biointerfaces. J Phys Chem C. 2007;111:2351–67.
83. Khlebtsov NG. Optical models for conjugates of gold and silver nanoparticles with biomacromolecules. J Quant Spectrosc Radiat Transf. 2004;89:143–53.
84. Kedem O, Vaskevich A, Rubinstein I. Improved sensitivity of localized surface plasmon resonance transducers using reflection measurements. J Phys Chem Lett. 2011;2:1223–26.
85. Casero E, Vazquez L, Martin-Benito J, Morcillo MA, Lorenzo E, Pariente F. Immobilization of metallothionein on gold/mica surfaces: relationship between surface morphology and protein-substrate interaction. Langmuir. 2002;18:5909–20.
86. Rhodes JM, Campbell BJ, Yu LG. Lectin-epithelial interactions in the human colon. Biochem Soc Trans. 2008;36:1482–6.
87. Sarter K, Mierke C, Beer A, Frey B, Fuhrnrohr BG, Schulze C, Franz S. Sweet clearance: involvement of cell surface glycans in the recognition of apoptotic cells. Autoimmunity. 2007;40:345–8.
88. Lloyd DH, Viac J, Werling D, Reme CA, Gatto H. Role of sugars in surface microbe-host interactions and immune reaction modulation. Vet Dermatol. 2007;18:197–204.
89. Lis H, Sharon N. Biochemistry of plant lectins (phytohemagglutinins). Annu Rev Biochem. 1973;42:541–74.
90. Yonzon CR, Jeoungf E, Zou SL, Schatz GC, Mrksich M, Van Duyne RP. A comparative analysis of localized and propagating surface plasmon resonance sensors: the binding of concanavalin a to a monosaccharide functionalized self-assembled monolayer. J Am Chem Soc. 2004;126:12669–76.
91. Kitano H, Takahashi Y, Mizukami K, Matsuura K. Kinetic study on the binding of lectin to mannose residues in a polymer brush. Colloid Surf B. 2009;70:91–7.
92. Homola J. Present and future of surface plasmon resonance biosensors. Anal Bioanal Chem. 2003;377:528–39.
93. Anker JN, Hall WP, Lyandres O, Shah NC, Zhao J, Van Duyne RP. Biosensing with plasmonic nanosensors. Nat Mater. 2008;7:442–53.
94. Nahálková J, Svitel J, Gemeiner P, Danielsson B, Pribulová B, Petrus L. Affinity analysis of lectin interaction with immobilized C- and O-gylcosides studied by surface plasmon resonance assay. J Biochem Biophys Methods. 2002;52:11–8.
95. Vornholt W, Hartmann M, Keusgen M. SPR studies of carbohydrate-lectin interactions as useful tool for screening on lectin sources. Biosens Bioelectron. 2007;22:2983–8.
96. Mori T, Toyoda M, Ohtsuka T, Okahata Y. Kinetic analyses for bindings of concanavalin A to dispersed and condensed mannose surfaces on a quartz crystal microbalance. Anal Biochem. 2009;395:211–6.

Chapter 15
Nano-Scale Electrical Transducers of Surface Plasmons for Integrated Biosensing

Pieter Neutens, Iwijn De Vlaminck, Sergii Lozenko, Liesbet Lagae, and Pol Van Dorpe

Abstract Recent developments in fabrication, characterization, and understanding of local surface plasmon resonances and surface plasmon waveguides have fuelled the development of a new generation of surface plasmon based biosensors, mainly based on local refractive index sensing and surface enhanced Raman scattering [1, 2]. Although the actual sensor has scaled to the nanoscale, the system still requires bulky optical components, such as light sources, lenses, objectives, and detectors. Integrating sources and/or detectors with the plasmonic sensor can pave the way to small-footprint photodetectors. In this chapter, we demonstrate direct electrical detection of surface plasmon resonators and integrated detection and generation of deep-subwavelength guided plasmons in metal-insulator-metal (MIM) waveguides. We will discuss these different devices, including optical/electrical characterization, the comparison with simulations, and their relevance for integrated biosensors.

Electrical Detection of Surface Plasmon Resonance in a Single Plasmonic Resonator

In the context of biosensing applications, direct electrical transduction of LSPR of a single metal nanostructure using a photodetector in its near field holds great promise. First experimental results for integrated electrical detection of surface plasmons on a relatively large area of randomly distributed nanodisks have been reported [3]. Nevertheless, being able to measure each plasmonic resonator separately has several advantages. First, such a device benefits from a rapid signal reading by an integrated

P. Neutens • I. De Vlaminck • S. Lozenko • L. Lagae • P. Van Dorpe (✉)
IMEC, Kapeldreef 75, Leuven 3001, Belgium
e-mail: pvandorp@imec.be

A. Dmitriev (ed.), *Nanoplasmonic Sensors*, Integrated Analytical Systems,
DOI 10.1007/978-1-4614-3933-2_15,

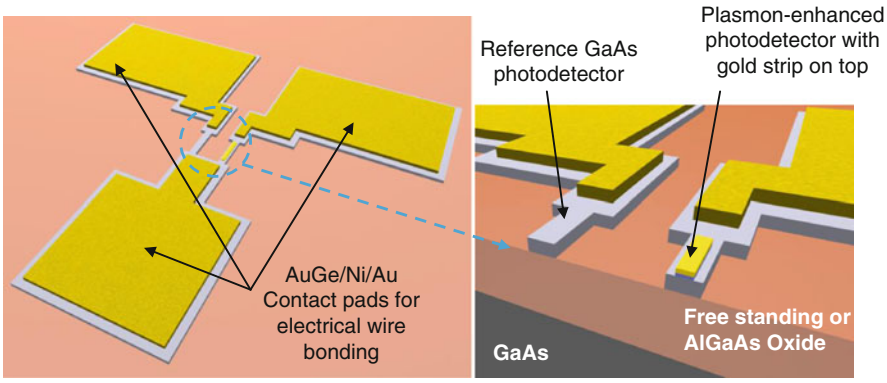

Fig. 15.1 Schematic view of and cross-section of the device comprising reference photodetector and plasmon-enhanced photodetector with a gold strip on top

photodetector. Second, it is compatible with manufacturing technologies used in integrated circuit design. Advancements in nanotechnologies may allow building a large parallel, closely packed array of individual sensing elements on surface plasmon enhanced photodiodes. Thus, the "pixel" size of a sensor is decreased to the size of a single metal nanostructure. Monitoring the signal of single nanostructures also excludes inhomogeneous broadening, which usually occurs when measuring an ensemble of nanoparticles. Such a sensor would allow measurements of the distribution of analyte concentration over the sensor surface as well as perform averaging statistics over large areas. Integration of the sensor arrays together with supporting electronics may lead to development of lab-on-a-chip systems, uniting all steps of the analytical process in a single device.

It is obvious now, that efficient, small, and fast transducing schemes that can directly convert plasmonic signals into electrical signals are needed for LSPR sensors to fully reveal their potential.

A scheme of local electrical transduction of a plasmon resonance of a single metal nanostructure using a photodetector described here is shown in Fig. 15.1. It is based on a surface plasmon polariton (SPP) resonator coupled to a thin GaAs photoresistor [4]. To take advantage of the confinement of the excited surface plasmons and to avoid electrical shorts, the GaAs photoresistors are fabricated either freestanding, or on top of an electrically and optically insulating oxidized AlGaAs layer.

The optical detector used is a GaAs photoresistor with a thin gold strip fabricated directly on top of it, but separated from the GaAs by a thin SiO_2 layer. A photoresistor detector is chosen mainly because of the ease of fabrication and response interpretation. Close to this detector, a reference detector without the metal structure is constructed. By measuring the device and a reference detector simultaneously, irregularities in the source spectrum and wavelength-dependent absorption characteristics of the GaAs detector can be subtracted from the device response.

The strip supports surface plasmon modes on top of the strip (at the Au/air interface) and at the bottom of the strip (at the Au/SiO_2/GaAs interface). The finite width of the strip results in discrete Fabry–Perot resonances at specific resonance wavelengths. Especially the resonances related to the Au/GaAs interface couple strongly to the photodetector and are expected to show up in the spectral photoresponse measurements. Indeed, a comparison of the response of a plasmon-enhanced detector with a gold strip, and a reference detector without the strip reveals a resonance peak in the absorption spectrum at the wavelength corresponding to the excitation of standing wave mode of a SPP at the interface between a gold strip and a semiconducting detector.

Both finite difference time domain (Lumerical FDTD) and finite element (Comsol Multiphysics, RF module) simulations were used to study the response of the surface-plasmon enhanced detector. In Lumerical FDTD, the dielectric properties of the materials were described modeled using a combination of Drude and Lorentz models, which were obtained by curve-fitting experimental data found in literature (GaAs and Au permittivity data taken from Palik and Johnson&Christy). This works very well except for energies below the GaAs bandgap, as the fitted imaginary part of the permittivity does not turn exactly zero and some "parasitic" absorption remains. A calculation grid size of 2 nm × 2 nm was chosen for simulations after a convergence analysis.

COMSOL multiphysics [5] implements finite element frequency domain algorithm (FE/FD). Material properties can be described by specifying experimental values of their dielectric constants for each wavelength, which allows a more precise description of GaAs near the bandgap.

Modeling Results

The purpose of the computational study is to predict the optimal design of the strip-line plasmonic detector, to tailor maximum possible absorption enhancement with the resonance energy lying above to the GaAs band gap.

The geometry of the strip-line plasmonic photodetector (in cross-section) used in the simulations is depicted in Fig. 15.2a. The gold strip on top of the detector is designed as a fragment of a SPP waveguide with sidewalls acting as reflectors, resulting in a Fabry–Perot cavity. The resonant properties of this cavity depend greatly on the dielectric environment and the geometry of the resonator. We assumed that the GaAs photodetector is freestanding.

The relative absorption spectrum of the detector is obtained by monitoring the power flow in and out of the GaAs semiconductor volume and comparing it to the reference detector without the gold strip. In Fig. 15.2b the calculated relative absorption spectrum is presented for different widths of the Au strip. Clearly, strong resonance peaks are observed at λ between 700 and 1,000 nm, corresponding to the excitation of a SPP cavity mode. SPPs, excited with TM-polarized light at the edges of the gold strip and propagating on the Au-SiO_2-GaAs interface interfere and

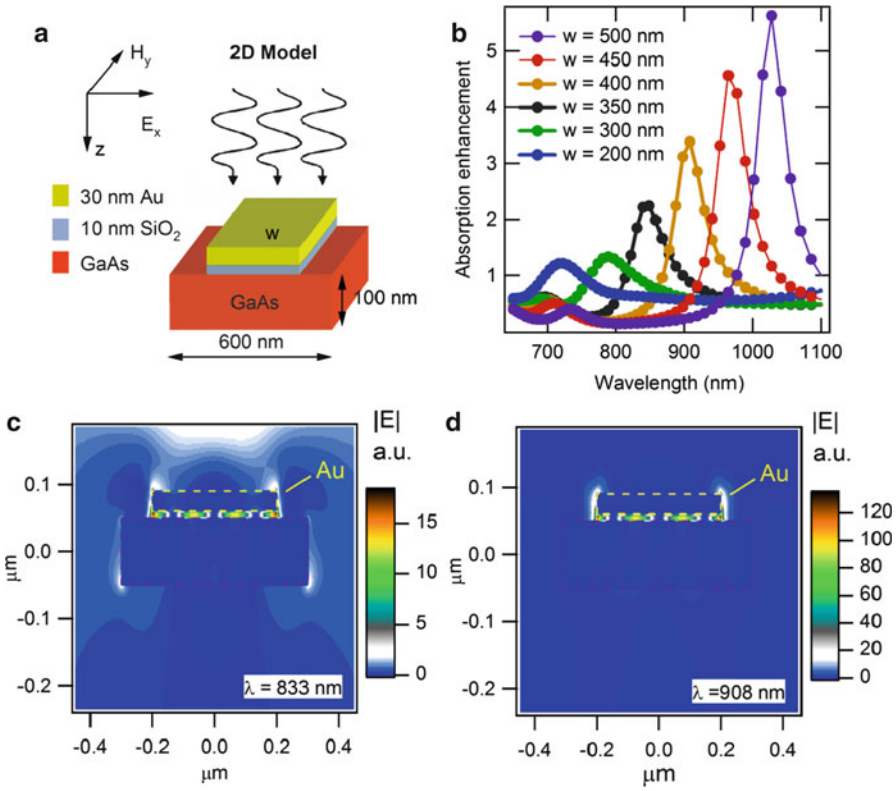

Fig. 15.2 (**a**) Geometry of the plasmonic detector, used in the simulation. (**b**) Relative absorption spectrum of the surface plasmon enhanced detector for different widths of the Au strip. (**c**, **d**) Electrical field intensity distribution of the surface plasmon polariton (SPP) cavity mode for the off-resonant and resonant excitation wavelengths correspondingly. Note the large difference in electric field enhancement (adapted from [4])

create a standing wave pattern. The electrical field intensity distribution of the SPP mode is visualized for an Au width of 400 nm in Fig. 15.2 for off-resonant ($\lambda = 833$ nm) (Fig. 15.2c) and resonant ($\lambda = 908$ nm) (Fig. 15.2d) excitation wavelengths. The modal profile exhibits four spots of high electric field intensity which corresponds to the establishment of a standing wave pattern with an order number $j = 3$. Lower- and higher-order modes can also exist in the same cavity. At the resonant excitation wavelength electric fields of the cavity mode are greatly amplified which leads to enhanced light absorption through transfer of the SPP cavity mode energy to the photodetector. It is evident from the picture that most of the mode energy is confined within the SiO_2 spacer layer.

As is clear from Fig. 15.2b, the strength of the resonance and its wavelength depend on the geometry of the cavity: width and thickness of the gold strip, on the efficiency of excitation of the SPP and on the strength of the coupling between the

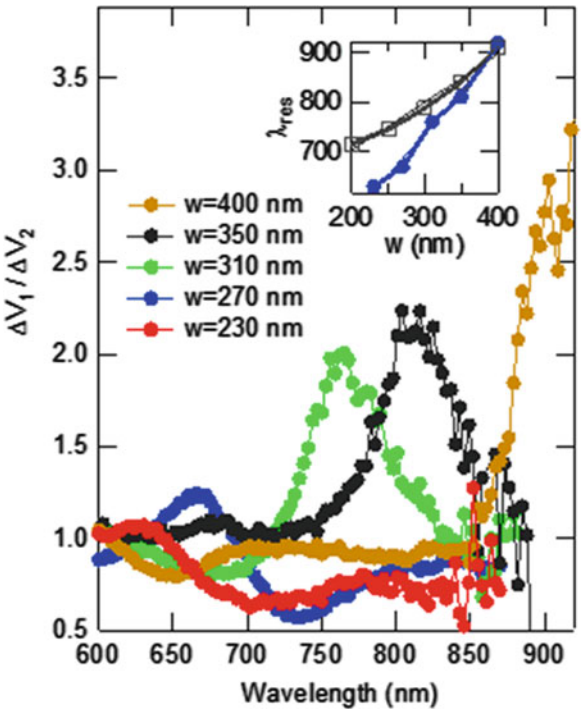

Fig. 15.3 Experimental photodetector enhancement for different widths of the Au strip (*inset*: comparison of the experimental (*blue*) and simulated (*black*) resonance wavelength) (adapted from [4])

cavity mode and the semiconductor. A wide-range tunability of the resonance can be attained by changing the cavity geometry.

This has been confirmed experimentally [4], as shown in Fig. 15.3, which shows the experimentally obtained photosignal enhancement for different Au strip widths. In the experiment, light from a 300 W Xe lamp is passed through a monochromator, and is subsequently linearly polarized, modulated with an optical chopper, and focused on the sample with a lens. A device covered with and without the Au nanostrip is measured simultaneously and their signals are divided to obtain the absorption enhancement. Photosignal enhancements of up to a factor of 3 have been obtained for resonance wavelengths near the GaAs bandgap. For shorter wavelengths, the resonance is strongly damped, as the GaAs absorption strongly increases above the GaAs bandgap.

As for eventual applications, freestanding GaAs wires might not be so appropriate; we also fabricated these GaAs/Au plasmonic detectors on top of an insulating substrate. This has been achieved by oxidizing an underlying $(Al_{0.88},Ga_{0.12})$ As layer with a high Al content, resulting in a transparent AlGaAs oxide, with a refractive index of about 1.65. This is shown in Fig. 15.4a, b, showing the plasmonic and the reference detector.

For this device, clear photosignal resonance signals have been obtained below the GaAs bandgap energy, as illustrated in Fig. 15.4c.

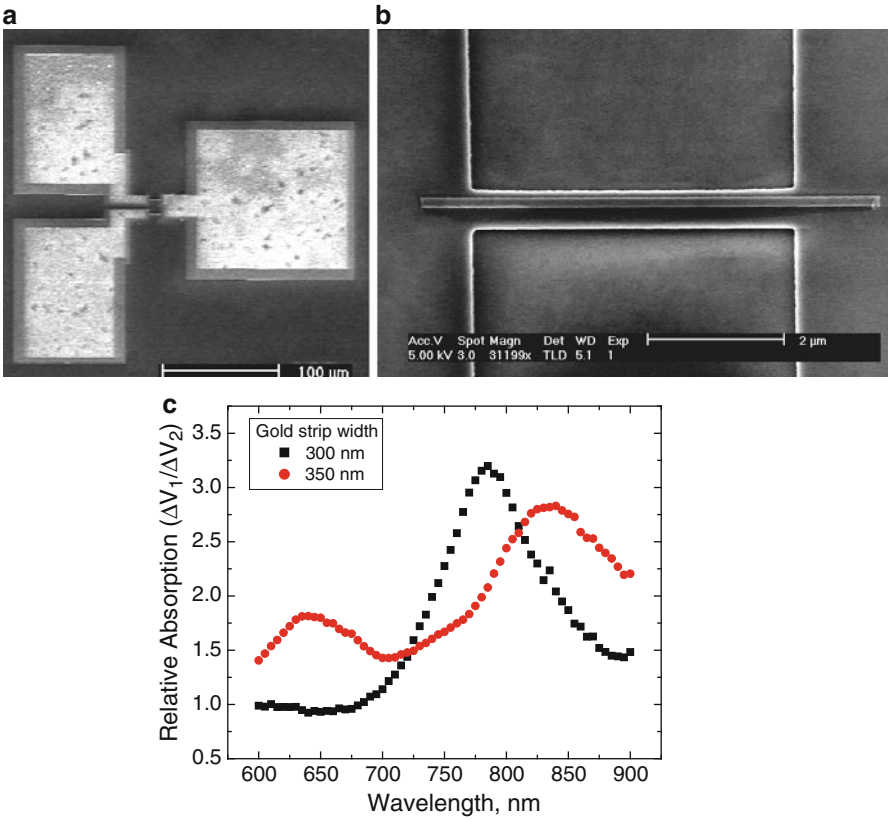

Fig. 15.4 (**a**) SEM picture of the plasmonic and reference detector fabricated on an insulating substrate. (**b**) Zoom of the combined Au strip and GaAs photodetector. (**c**) Optical enhancement spectrum of the plasmonic device for two different widths of the gold strip

Biocompatibility

To turn the plasmon-enhanced photodetector, described here into a device that can be operated as a biosensor, some design considerations have to be taken into account. One of the main requirements for the biosensors is biocompatibility, which means an ability to work under physiological conditions. The design described above has several disadvantages if to be used for biological sensing: first, exposure of the GaAs semiconducting layer to liquids may lead to the problem of chemical instability; second, charges in the liquid can influence the conductivity of the semiconductor detector. The reference detector should be passivated with a material, transparent in the wavelength range of interest, and the region where liquid and detector interact can be limited by definition of a microfluidic channel.

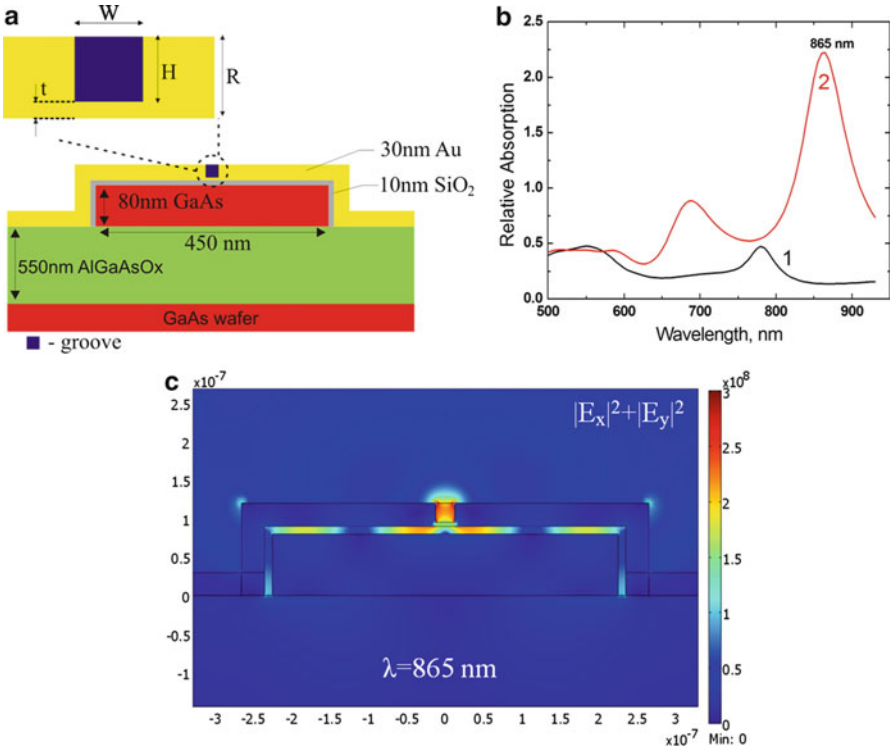

Fig. 15.5 (**a**) Cross-section view of a nano-groove plasmonic detector. (**b**) Simulated relative absorption spectra of the detector in the case of full-metal coverage (*curve 1*), and when a nano-groove is incorporated on the surface (*curve 2*). (**c**) Electrical field intensity distribution of the SPP cavity mode at the resonant excitation wavelength

For biological sensing applications it would be desirable to have all the surface of the detector covered with metal, which will on the one hand, protect it from the influence of the environment, solve the electrical instability problem by screening the charges in the liquid and on the other hand, facilitate biofunctionalization. Extending the gold layer all over the detector area seems to be a promising approach, as gold can be easily functionalized. However SPPs are excited mainly on the edges of the gold strip, so the full metal coverage of the detector will dramatically reduce the efficiency of surface plasmon excitation by screening the electromagnetic fields.

A way to achieve a SPP excitation in case when the detector is fully covered with gold is the incorporation of a single corrugation in the form of a nanosized groove on the top of the smooth gold coverage of the detector.

A schematic view of the device concept, used in simulations is presented in Fig.15.5. In Fig. 15.5a, a cross-section of the fully gold-covered plasmonic detector with a nano-groove incorporated on top is shown.

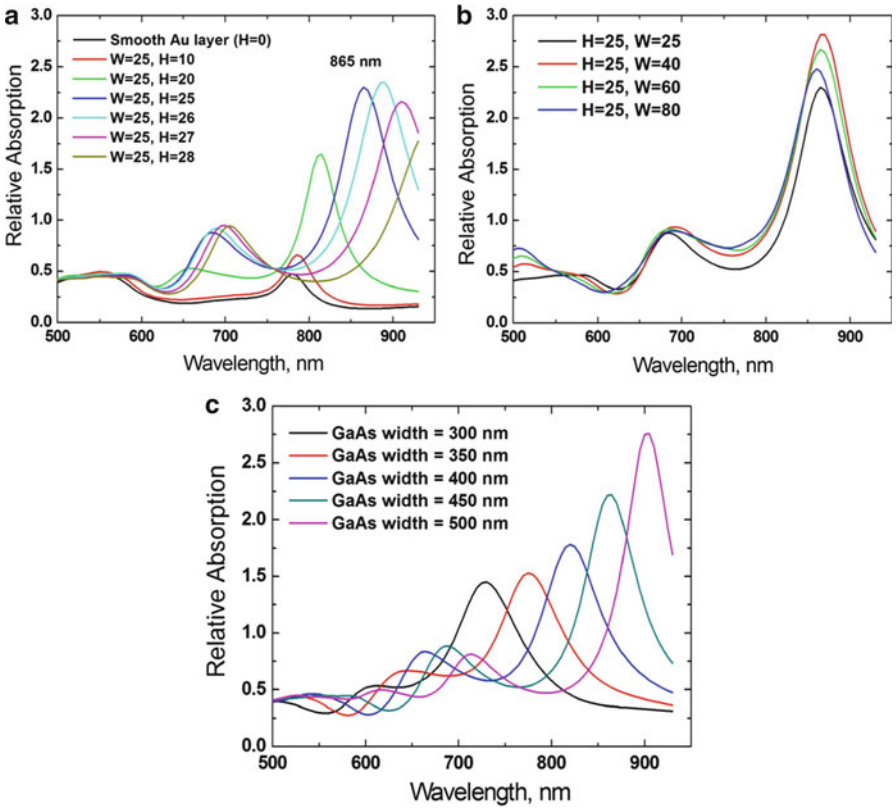

Fig. 15.6 Calculated relative absorption spectra of the nano-groove surface plasmon enhanced detector for a different groove widths and depths. (**a**) Groove depth is varied in the range 10–28 nm at a constant width of $W = 25$ nm. (**b**) Groove width is varied from 25 to 80 nm; depth is $H = 25$ nm. (**c**) Photodetector width is varied in the range 300–500 nm

Simulated relative absorption spectra, shown on Fig. 15.5b, confirm that in case when GaAs detector is fully covered with gold layer, efficiency of SPP cavity mode excitation, seen as a small bump on the spectrum (curve 1) is reduced to a great extent. However, if a nanosized groove is incorporated on the otherwise smooth gold surface, efficient surface plasmon excitation and absorption enhancement may be achieved (curve 2).

An excitation through the nano-groove can provide efficient coupling to a SiO_2–gold interface SPP mode if the groove profile and gold film thickness are suitably related. In Fig. 15.6 dependence of the relative absorption enhancement on the groove parameters—width (W) and depth (H)—is investigated. A GaAs photodetector without the gold layer is taken as a reference in the following calculations.

The simulation results show, that a variation of the groove depth (H) affects the SPP excitation efficiency to a great extent. At a small depth ($H = 10$ nm), excitation efficiency is very low, resembling the case when no groove is present at the

surface. As the depth increases, the plasmon excitation efficiency grows up to a certain depth value and resonant peak shifts to the infrared region. The groove depth of $H = 25$ nm was found to provide the most efficient coupling of incident radiation to a SPP mode of the order $j = 4$ with a corresponding resonant peak at 865 nm (Fig. 15.6a). The second peak, observed at a lower wavelength is related to the excitation of a higher-order cavity mode ($j = 5$). Groove width variation influences the relative absorption spectra to a less extent, causing the change in relative absorption maximum value and slightly shifting the resonance wavelength. The relative absorption magnitude rises as the groove width increases up to an approximately 40 nm, and drops down again if the groove becomes wider (Fig. 15.6b). Low sensitivity of the surface plasmon excitation efficiency to the groove width gives practical advantages, as very narrow grooves are more difficult to manufacture and small variations in groove width will affect the final device performance to a much less extent.

The resonance peak wavelength position can be tuned, as for an Au-strip plasmonic photodetector, by varying the size of the plasmon cavity. In Fig. 15.5c the relative absorption spectra are presented as the width of the GaAs photodetector was varied from 300 to 500 nm. As a result of the plasmon cavity length change, a blue-shift of the resonant wavelength is observed together with the decrease of the peak magnitude due to stronger material damping.

Sensitivity

To evaluate the biosensing capabilities of the described device, the dependence of the response to a change of environmental refractive index above the detector was studied numerically. The nano-groove width was chosen to be $W = 50$ nm, depth $H = 25$ nm, and refractive index above the detector was varied in the range from $n = 1$ to $n = 1.4$ to see the general trends of the device response. Variations of the refractive index due to antibody–antigen interactions in an aqueous environment on the functionalized sensor surface usually lie in the range from 1.3 to 1.4 refractive index units. The corresponding relative absorption spectra are presented in Fig. 15.7a. The resonance peaks corresponding to the quadrupolar ($j = 4$, $\lambda = 870$ nm) and higher-order ($j = 5$, $\lambda = 680$ nm) mode excitation are red-shifted as refractive index of the medium above the detector changes from 1 to 1.4. The relative absorption magnitude varies insignificantly for the quadrupolar resonance peak, however a two times stronger absorption enhancement is achieved for the higher-order mode. The sensitivity of the detector to the refractive index change was estimated to be around ~100 nm/RIU.

The same calculation was repeated with a totally gold-covered photodetector taken as a reference (Fig. 15.7b). Such an approach highlights the role of the nano-groove in the SPP cavity mode excitation. A drop in the magnitude of relative absorption as refractive index increases may be explained, first by the increase in the absorption efficiency of the reference detector due to the lower index contrast and, most importantly by a reduction of the efficiency of coupling between the surface plasmon mode and the active semiconductor volume.

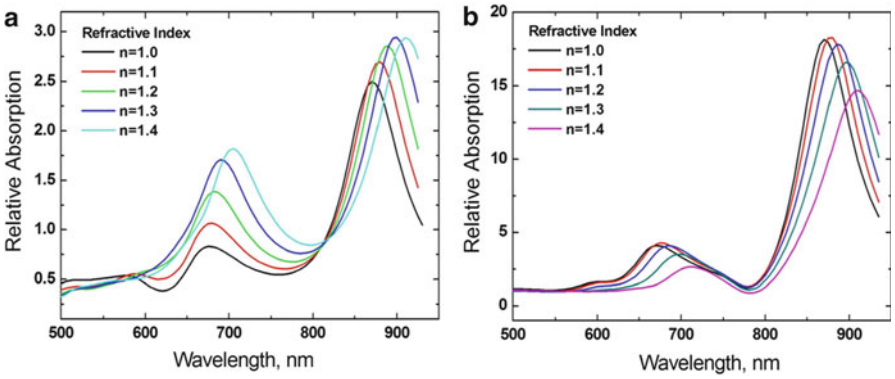

Fig. 15.7 Calculated relative absorption spectra illustrating sensitivity of the nano-groove surface plasmon enhanced detector ($W = 50$ nm, $H = 25$ nm) to refractive index change. (**a**) GaAs photodetector without metal coverage is used as a reference. (**b**) Gold-covered photodetector taken as reference

The previously defined "figure of merit" (FOM) will be used to characterize the sensitivity of the proposed sensors. The estimated sensitivity values are summarized in the table below. The obtained sensitivity values are 2–4 times lower than those, found in literature for nanoparticle LSPR sensors [6, 7]. Ways to increase the refractive index sensitivity need to be found for a device to have biosensing capabilities.

λ_{peak}, $n = 1.0$ (nm)	Sensitivity (nm/RIU)	FWHM (nm/meV)	FOM
870	~100	~80/130	1.2

Advanced Device Design: Nano-Slit Plasmonic Detector

Since in 1998 Ebbesen has reported on an enhanced light transmission through a thin metal film with subwavelength holes [8], a lot of research has been conducted on the optical properties of nano-structured metallic thin films. It has been shown in Lindberg et al. [9] that the enhanced transmission through a subwavelength slit in a metal film can be understood in terms of interfering waveguide modes that propagate in the slit. The position of the transmission resonance depends strongly on the refractive index of the material in the slit that makes sensing applications possible.

An attempt to excite the SPP cavity resonance of the above described device with the help of the enhanced transmission through the slit in the gold layer was made. The high sensitivity of the enhanced transmission to the refractive index change in the slit, reported in Lindberg et al. [9], may increase the sensing potential of the device. The slit in this case can be treated as a MIM waveguide supporting a propagating TM mode. The lowest order TM mode in the planar metallic waveguide, unlike the TE mode, has no cutoff frequency and exhibits a

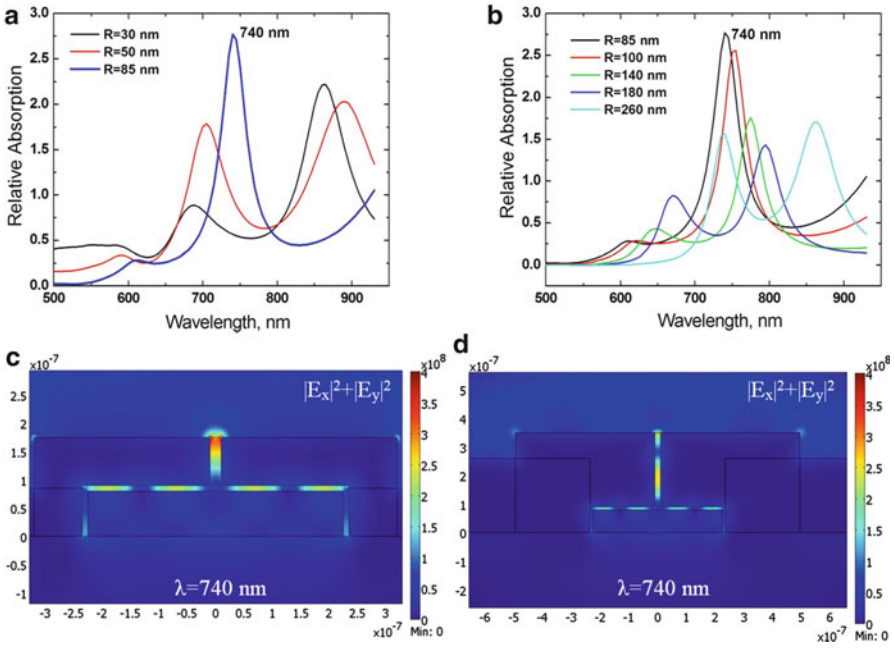

Fig. 15.8 Calculated relative absorption spectra of nano-slit photodetector with $W = 20$ nm, $t = 5$ nm. (**a**) Thickness of the gold layer R is varied from 30 to 85 nm. (**b**) R is varied from 85 to 180 nm. (**c**, **d**) Electrical field intensity distribution of the SPP cavity mode at the resonant excitation wavelength $\lambda = 740$ nm for $R = 85$ nm and $R = 260$ nm

surface-wave-like behavior. The aim of the following set of calculations, presented on Fig. 15.8 is to investigate the dependence of SPP cavity resonance of the plasmon enhanced photodetector device on the thickness of the gold layer (R), while keeping groove parameters W and t constant—t is the thickness of the remaining gold layer in the groove, see Fig. 15.5a.

A variation of the gold layer thickness R significantly influences the spectra. As R increases to 85 nm, a maximum in relative absorption is observed at $\lambda = 740$ nm that corresponds to the excitation of quadrupolar SPP cavity mode through coupling with the guided mode of MIM slit waveguide. The intensity distribution of the electrical field in the slit shows that strong resonances occur at a certain thickness R when an odd number of the quarters of wavelengths of the TM slit waveguide mode fits into the slit. The wavelength of the slit guided mode is estimated from the intensity distributions to be $\lambda \approx 340$ nm. If R is increased to 260 nm, so that three quarters of the wavelength fit into the slit (Fig. 15.8d), the resonance peak is observed at the same wavelength of $\lambda = 740$ nm but is almost two times weaker. This can be explained by the strong attenuation of the propagating mode in the slit waveguide in the visible spectral region.

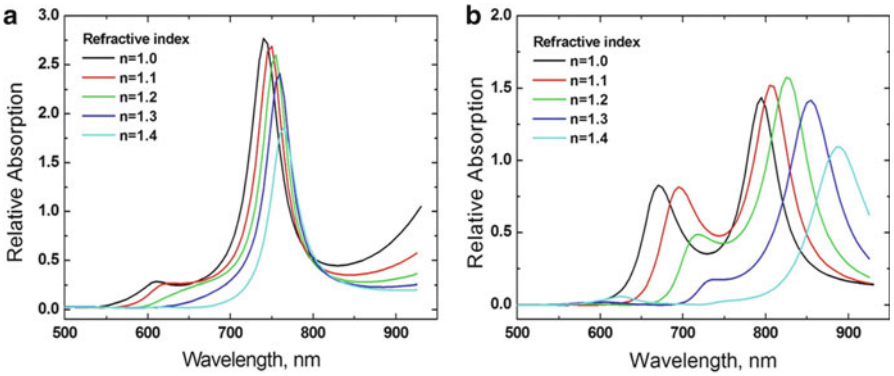

Fig. 15.9 Calculated relative absorption spectra illustrating sensitivity of the nano-slit surface plasmon enhanced detector ($W = 20$ nm, $t = 5$ nm) to the refractive index change. (**a**) Thickness of the gold layer $R = 85$ nm. (**b**) Thickness of the gold layer $R = 180$ nm

The refractive index sensitivity of this device is studied in Fig. 15.9. Calculations have been performed for two values of the gold layer thickness, $R = 85$ nm (Fig. 15.8a) and $R = 180$ nm (Fig. 15.8b). The slit parameters were chosen to be $W = 20$ nm, $t = 5$ nm. The estimated sensitivity values for the main quadrupolar resonance peak are summarized in the table below.

Gold layer thickness (nm)	λ_{peak}, $n = 1.0$ (nm)	Sensitivity (nm/RIU)	FWHM (nm/meV)	FOM
$R = 85$	740	~62	~50/111	1.18
$R = 180$	795	~235	~55/110	3.85

Besides the quadrupolar resonance at $\lambda = 740$ nm, a strong resonance peak corresponding to the excitation of the higher mode of the order $j = 5$ is observed in the spectrum ($\lambda = 670$ nm) when $R = 180$ nm. The higher-order mode resonance peak is significantly influenced by the change of refractive index in the slit: as index value rises to 1.4 peak completely vanishes. By comparing the signals from the reference and plasmon-enhanced detectors, conclusion can be made that the drop of the peak intensity is due to the change of the refractive index in the slit and therefore, change of the guided mode propagation conditions, as the signal of the reference detector, not covered with gold, stays nearly the same for this wavelengths range.

The obtained FOM values from the nano-slit sensor with $R = 180$ nm are comparable with those found in literature for LSPR nanoparticle sensors, making such a device concept a promising candidate for further research. However more deep investigation of the nature of the observed effects and their dependency on geometrical parameters of the nano-slit and the photodetector are needed before proceeding to the practical implementation of the device.

Electrical Generation and Detection of Surface Plasmon Polaritons in Deep-Subwavelength Surface Plasmon Waveguides

SPPs, charge density oscillations at metal-dielectric interfaces, have proven to provide excellent means to probe biochemical events due to their strong local field enhancement near metal surfaces or nanostructures. Multiple detection schemes based on surface plasmon resonance (SPR) have already been developed and commercialized [10] to experimentally characterize molecular binding events. It has also been shown that circuits consisting of plasmon waveguides can provide a deep-subwavelength sensing platform. Nevertheless, all these applications however make use of large external light sources and detectors. By combining SPP waveguides and waveguide circuits with integrated electrical SPP sources and detectors, we can integrate plasmonics with today's electronic devices. Doing so, we pave the way for numerous applications, going from integrated plasmonic circuits to arrays of small-scale, fully-integrated plasmonic biosensors.

In this section we focus on demonstrating efficient electrical transduction between plasmonic and electrical signals, by integrating light-emitting-diodes (LED) and metal-semiconductor-metal (MSM) photodetectors directly in deep-subwavelength MIM plasmon waveguides [11, 12], resulting in a scheme which is scalable down to the nanoscale, allowing a fully operational plasmonic circuit on a very small footprint. Plasmonic MIM waveguides offer the prospect of combining a high spatial field confinement together with micrometer range propagation lengths [13, 14]. Metal-based waveguides provide the unique opportunity to send electrical and optical signals through the same guides. Here we exploit this feature by employing the metal slabs for direct electrical contacting of a semiconductor LED and an MSM photodetector structure. We have fabricated such integrated structures on top of GaAs substrates, containing either a p-i-n-diode with three quantum wells (LED) or an undoped GaAs layer (for the MSM detector). The waveguides were fabricated using standard deposition techniques, electron beam lithography, and Xe ion milling. More details regarding the fabrication procedures can be found in Neutens et al. [11, 12].

Figure 15.9 shows both the integration of a detector and a LED in two different devices. Figure 15.9a shows the schematic operation of an integrated detector: Light is focused on a subwavelength slit of the top metal layer of the MIM waveguide. Through the excitation of a local mode in the slit, the waveguide modes of the MIM waveguide can be efficiently excited. Subsequently the propagating MIM mode is captured in a subwavelength slit in the bottom metal layer of the MIM waveguide, where the light is absorbed in the GaAs through the excitation of electron–hole pairs. These carriers are collected by the electrodes, which are formed by etching a slit in the bottom metal layer. Figure 15.9b shows an SEM picture of the processed device, with the excitation slit on the left and the detection slit on the right side indicated by the triangles. Figure 15.9c shows the schematic operation of an integrated LED: by contacting the semiconductor locally below a subwavelength slit in the bottom metal layer and electrically driving the p-i-n diode, excitons are formed in the three

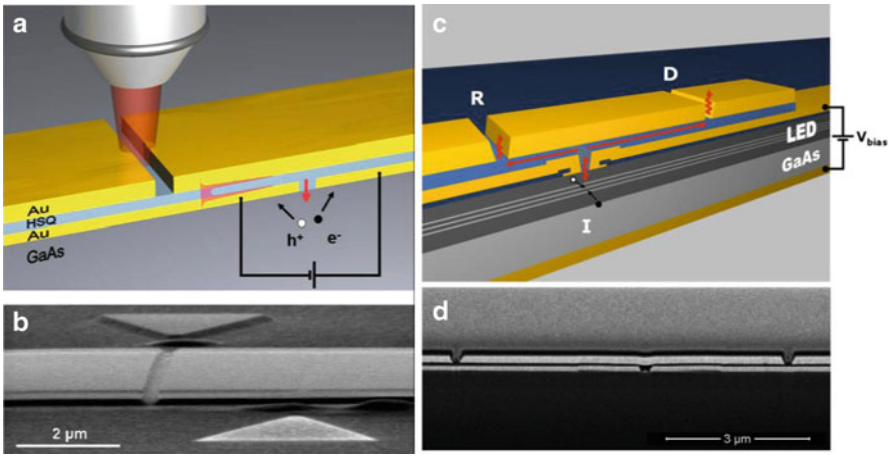

Fig. 15.10 (**a**) Schematic representation of the MSM detector integrated in a MIM plasmonic waveguide. (**b**) SEM picture of the final device. (**c**) Schematic representation of the LED integrated in a MIM plasmonic waveguide. (**d**) SEM picture of the final device (adapted from [11, 12])

quantum wells, giving rise to relatively broad-band light emission. The emitted light can directly couple with the subwavelength slit and couple to propagating modes in the MIM waveguide. In order to detect this, a second slit has been etched in the top metal film, which allows coupling of the plasmons to the far-field, where they can be spectrally analyzed and imaged by a CCD camera. Figure 15.9d shows an SEM picture of a processed device.

The operation principle has been modeled using numerical simulations using the RF module of Comsol Multiphysics. For the detector, a plane wave is incident on the slit in the top metal layer of the MIM waveguide. Figure 15.10a shows that for the light polarization oriented perpendicular to the slit (x-direction), efficient coupling between the incident light and MIM waveguide modes is achieved. The observed standing waves in the MIM waveguide originate from reflections at the injection and detection slits. Similarly, we modeled the LED by a point dipole at the position of the quantum wells in the GaAs substrate. Figure 15.10b shows the electric field profile when we put a point dipole with its polarization perpendicular to the slit axis. Also here, an efficient coupling between the dipole and the MIM waveguide modes is observed.

A first indication of surface plasmon propagation in plasmon waveguides is given by the polarization dependence of the measured signals. For the coupled MIM waveguide/detector device, we have mapped the photocurrent of the device as function of the position of the laser spot for two different polarizations (see Fig. 15.11a). It is clear that efficient coupling has only been achieved for the polarization perpendicular to the slit (TM), as expected for plasmonic waveguides. Similarly, we have analyzed the light coupled to the far-field in the LED/waveguide devices. From Fig. 15.11b it is obvious that the light polarization lies perpendicular to the slit axis.

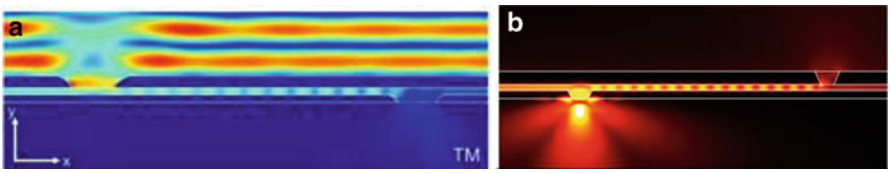

Fig. 15.11 (**a**) Simulated electric field profile of a plasmonic waveguide coupled to MSM detector. (**b**) Simulated electric field profile of a LED coupled to a MIM waveguide

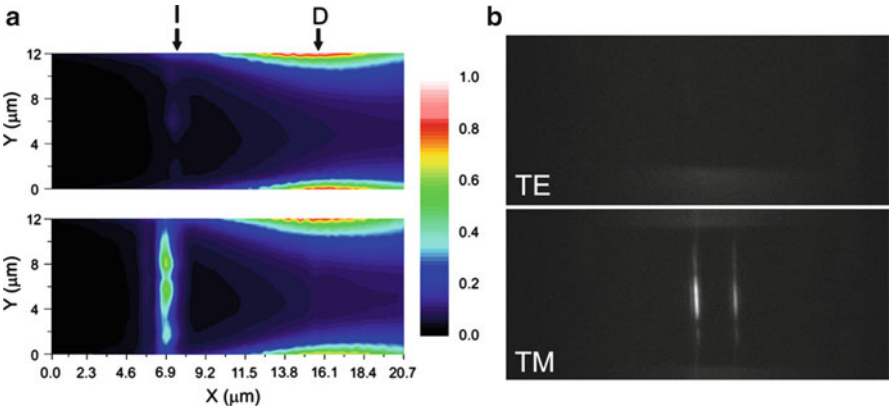

Fig. 15.12 (**a**) Spatial map of the photocurrent as function of the laser spot position for a polarization parallel (*top*) and perpendicular to the slit (*bottom*). The positions of the injection and detection slit are indicated. (**b**) CCD image of the light emitted through two slits in the top metal layer of the MIM waveguide that is integrated on top of an LED. The polarization of the analyzer was set either parallel to the slit (*top*) and perpendicular to the slit (*bottom*)

As surface plasmons decay exponentially along the length of the waveguide due to ohmic losses, this should be manifested in the different devices. Therefore we varied the distance between the injection and detection slits, for both the detector and LED based devices. Figure 15.12a, b indeed shows that the obtained results are consistent with this picture. The obtained plasmon propagation lengths correspond to the simulated results.

This illustrates that we have clearly demonstrated local electrical generation and detection of guided SPPs. The use of such components can be exploited to construct nanoscale SPR-based resonance devices, which can be produced in large arrays, for highly parallelized sensing schemes without the need for external optical components.

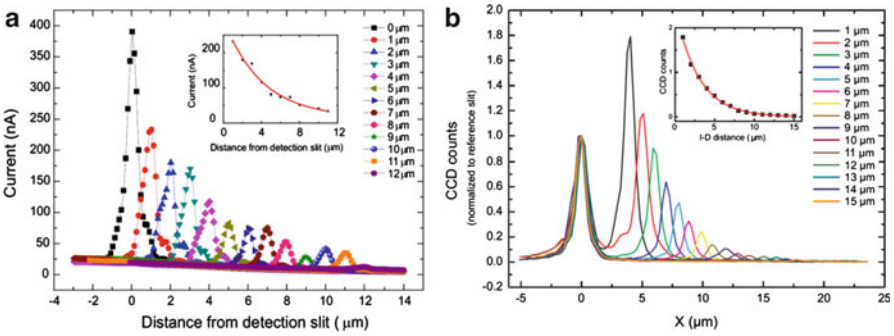

Fig. 15.13 (**a**) Photocurrent of the MSM photodetectors for different distances between the injection and detection slits. (**b**) Measured light emission from the slits in the top metal layer for different distances between the injection slit and the out-coupling slit

References

1. Kneipp K, Wang Y, Kneipp H, Perelman LT, Itzkan I, Dasari RR, Feld MS. Single molecule detection using surface-enhanced Raman scattering (SERS). Phys Rev Lett. 1997;78:1667–70.
2. Haes AJ, Hall WP, Chang L, Klein WL, Van Duyne RP. A localized surface plasmon resonance biosensor: first steps toward an assay for Alzheimer's disease. Nano Lett. 2004;4 (6):1029–34.
3. Mazzotta F, Wang G, Hägglund C, Höök F, Jonsson MP. Nanoplasmonic biosensing with on-chip electrical detection. Biosens Bioelectron. 2010;26(4):1131–6.
4. De Vlaminck I, Van Dorpe P, Lagae L, Borghs G. Local electrical detection of single nanoparticle plasmon resonance. Nano Lett. 2007;7:703–6.
5. www.comsol.com.
6. Sherry LJ, Chang S-H, Wiley BJ, Xia Y, Schatz GC, Van Duyne RP. Localized surface plasmon resonance spectroscopy of single silver nanocubes. Nano Lett. 2005;5(10):2034–8.
7. Sherry LJ, Jin R, Mirkin CA, Schatz GC, Van Duyne RP. Localized surface plasmon resonance spectroscopy of single silver triangular nanoprisms. Nano Lett. 2006;6(9):2060–5.
8. Ebbesen TW, Lezec HJ, Ghaemi HF, Thio T, Wolff PA. Extraordinary optical transmission through sub-wavelength hole arrays. Nature. 1998;391:667–9.
9. Lindberg J, Lindfors K, Setälä T, Kaivola M, Friberg AT. Spectral analysis of resonant transmission of light through a single sub-wavelength slit. Opt Express. 2004;12(4):623–32.
10. www.biacore.com.
11. Neutens P, Van Dorpe P, De Vlaminck I, Lagae L, Borghs G. Electrical detection of confined gap plasmons in metal-insulator-metal waveguides. Nat Photonics. 2009;3:283–6.
12. Neutens P, Van Dorpe P, Lagae L, Borghs G. Electrical excitation of confined surface plasmon polaritons in metallic slot waveguides. Nano Lett. 2010;10:1429–32.
13. Dionne JA, Lezec HJ, Atwater HA. Highly confined photon transport in subwavelength metallic slot waveguides. Nano Lett. 2006;6:1928–32.
14. Dionne JA, Sweatlock LA, Atwater HA, Polman A. Plasmon slot waveguides: towards chip-scale propagation with subwavelength-scale localization. Phys Rev B. 2006;73:035407.

Chapter 16
Future Directions: Nanoplasmonic Sensing Tomorrow

Alexandre Dmitriev

Abstract Nanoplasmonic sensors have made an impressive progress from the conceptual idea to the working devices just in about one decade. It is apparent now that the promises of this technology—high sensitivity, compactness, readily available multiplexing capabilities—can be realized and implemented in a large number of areas, both in research settings and in prototype or even consumer devices. The research interest to the field is also strong—just recently a series of articles appeared that overviewed the current development of the research in nanoplasmonic sensors [1–4]. So, where do we go from here?

It is evident that the functional surface chemistry increasingly becomes the central point in the development of nanoplasmonic sensors that aim at point-of-care diagnostics. Overcoming a dominant background of non-specific interactions seems to be of a paramount importance for the field. Equally important is such proper design of the "linking" chemistry when nanoplasmonic sensing is employed as a quantification tool in molecular biology. As such work would be concentrated in the biophysics and biochemistry labs, the design of proper micro- and nanofludics systems for nanoplasmonics sensors will come hand-in-hand to add to the sensitivity, selectivity, and robustness of these sensing platforms. New conceptual designs are emerging to contribute to further simplification of nanoplasmonic sensors—like the recent advances in paper substrates for nanoplasmonic sensing [5] or in colorimetric detection in nanoplasmonic biosensing with the aid of extra sharp plasmon (Fano) resonances engineering [6, 7]. In line with the latter, the next level of sophistication will be reached by the routine combination of the extreme sensitivity with precise spatial localization of the sensing areas in various nanoplasmonic sensing geometries. The examples of the recent advances are the selective

A. Dmitriev (✉)
Department of Applied Physics, Chalmers University of Technology, Göteborg 41296, Sweden
e-mail: alexd@chalmers.se

A. Dmitriev (ed.), *Nanoplasmonic Sensors*, Integrated Analytical Systems,
DOI 10.1007/978-1-4614-3933-2_16,

decoration with analyte-capturing chemistry of nanostars [8, 9], nanocrescents [10], nanotriangles [11], and others. Proper design of plasmonic nanostructures in combination with surface chemistry can also yield substantially increased and "localized" sensitivity [12–15]. The interplay of several nanoplasmonic resonances in one geometry is promised to produce nanoplasmonic sensors with the capability to resolve the three-dimensional analyte structure [16]. It is also very apparent that nanoplasmonic detectors increasingly find applications beyond biological and chemical sensing. Materials science will greatly benefit from broader implementation of various nanoplasmonic sensing schemes.

Interestingly, as the most advanced and commercially successful plasmonic sensing platforms are those utilizing propagating surface plasmon polaritons in thin noble metal films, there is a trend to combine the both [17]. For example, this is realized in plasmonic nanowires. It is certainly beneficial to further extend the probing volume of the sensor, as with surface plasmon resonance (SPR) technology, yet keeping extreme electromagnetic field enhancement that is characteristic for nanoplasmonic sensors.

On the side of fundamental properties of nanoplasmonic sensors, it is important that reliable predictive models emerge that unambiguously link structure with optical and sensing properties of nanoplasmonic sensing platforms. On more practical side, scalable fabrication techniques are expected to further develop that are able to deliver large arrays of nanoplasmonic structures. Simultaneously, industrial-scale nanofabrication that aims at multiplexed array format is required to further reduce the price-per-chip in nanoplasmonics-based sensing.

All in all, in the coming years we will most probably see an incremental development of nanoplasmonic sensors for various purposes and applications. Nonetheless, exciting fundamental research opportunities are still present in the area of sensors design principles and function.

References

1. Lal S, et al. Nano-optics from sensing to waveguiding. Nat Photonics. 2007;1:641.
2. Anker JN, et al. Biosensing with plasmonic nanosensors. Nat Mater. 2008;7:442.
3. Stewart ME, et al. Nanostructured plasmonic sensors. Chem Rev. 2008;108:494.
4. Mayer KM, Hafner JH. Localized surface plasmon resonance sensors. Chem Rev. 2011;111:3828.
5. Tao H, et al. Metamaterials on paper as a sensing platform. Adv Mater. 2011;23:3197.
6. Yanik AA, et al. Seeing protein monolayers with naked eye through plasmonic Fano resonances. Proc Natl Acad Sci U S A. 2011;108:11784.
7. Wu C, et al. Fano-resonant asymmetric metamaterials for ultrasensitive spectroscopy and identification of molecular monolayers. Nat Mater. 2011;11:69.
8. Hrelescu C, et al. Selective excitation of individual plasmonic hotspots at the tips of single gold nanostars. Nano Lett. 2011;11:402.
9. Dondapati SK, et al. Label-free biosensing based on single gold nanostars as plasmonic transducers. ACS Nano. 2010;4:6318.

10. Unger A, et al. Sensitivity of crescent-shaped metal nanoparticles to attachment of dielectric colloids. Nano Lett. 2009;9:2311.
11. Beeram SR, et al. Selective attachment of antibodies to the edges of gold nanostructures for enhanced localized surface plasmon resonance biosensing. J Am Chem Soc. 2009;131:11689.
12. Feuz L, et al. Improving the limit of detection of nanoscale sensors by directed binding to high-sensitivity areas. ACS Nano. 2010;4:2167.
13. Acimovic SS, et al. Plasmon near-field coupling in metal dimers as a step toward single-molecule sensing. ACS Nano. 2009;3:1231.
14. Sannomiya T, et al. In situ sensing of single binding events by localized surface plasmon resonance. Nano Lett. 2008;8:3450.
15. Otte MA, et al. Improved biosensing capability with novel suspended nanodisks. J Phys Chem C. 2011;115:5344.
16. Liu N, et al. Three-dimensional plasmon rulers. Science. 2011;332:1407.
17. Bolduc OR, et al. Advances in surface plasmon resonance sensing with nanoparticles and thin films: nanomaterials, surface chemistry, and hybrid plasmonic techniques. Anal Chem. 2011;83:8057.

Index

A. Dmitriev (ed.), *Nanoplasmonic Sensors*, Integrated Analytical Systems,
DOI 10.1007/978-1-4614-3933-2,